frontiers | Research Topics

Women in nuclear engineering research

Edited by
Anne Campbell, Tonya Vitova, Charlotte Becquart and
Marta Serrano Garcia

Published in
Frontiers in Nuclear Engineering

ISSN 1664-8714
ISBN 978-2-8325-5823-2
DOI 10.3389/978-2-8325-5823-2

About Frontiers

Frontiers is more than just an open access publisher of scholarly articles: it is a pioneering approach to the world of academia, radically improving the way scholarly research is managed. The grand vision of Frontiers is a world where all people have an equal opportunity to seek, share and generate knowledge. Frontiers provides immediate and permanent online open access to all its publications, but this alone is not enough to realize our grand goals.

Frontiers journal series

The Frontiers journal series is a multi-tier and interdisciplinary set of open-access, online journals, promising a paradigm shift from the current review, selection and dissemination processes in academic publishing. All Frontiers journals are driven by researchers for researchers; therefore, they constitute a service to the scholarly community. At the same time, the *Frontiers journal series* operates on a revolutionary invention, the tiered publishing system, initially addressing specific communities of scholars, and gradually climbing up to broader public understanding, thus serving the interests of the lay society, too.

Dedication to quality

Each Frontiers article is a landmark of the highest quality, thanks to genuinely collaborative interactions between authors and review editors, who include some of the world's best academicians. Research must be certified by peers before entering a stream of knowledge that may eventually reach the public - and shape society; therefore, Frontiers only applies the most rigorous and unbiased reviews. Frontiers revolutionizes research publishing by freely delivering the most outstanding research, evaluated with no bias from both the academic and social point of view. By applying the most advanced information technologies, Frontiers is catapulting scholarly publishing into a new generation.

What are Frontiers Research Topics?

Frontiers Research Topics are very popular trademarks of the *Frontiers journals series*: they are collections of at least ten articles, all centered on a particular subject. With their unique mix of varied contributions from Original Research to Review Articles, Frontiers Research Topics unify the most influential researchers, the latest key findings and historical advances in a hot research area.

Find out more on how to host your own Frontiers Research Topic or contribute to one as an author by contacting the Frontiers editorial office: frontiersin.org/about/contact

Women in nuclear engineering research

Topic editors
Anne Campbell — Oak Ridge National Laboratory (DOE), United States
Tonya Vitova — Karlsruhe Institute of Technology (KIT), Germany
Charlotte Becquart — Centrale Lille Institut, ENSCL, Laboratoire UMET, France
Marta Serrano Garcia — Centro de Investigaciones Energéticas, Medioambientales y Tecnológicas, Spain

Citation
Campbell, A., Vitova, T., Becquart, C., Garcia, M. S., eds. (2024). *Women in nuclear engineering research*. Lausanne: Frontiers Media SA.
doi: 10.3389/978-2-8325-5823-2

Table of contents

frontiers | Frontiers in Nuclear Engineering

TYPE Original Research
PUBLISHED 30 October 2023
DOI 10.3389/fnuen.2023.1240995

EDITED BY
Xiao-Ying Yu,
Pacific Northwest National Laboratory (DOE), United States

REVIEWED BY
Benjamin Lamm,
Oak Ridge National Laboratory (DOE), United States
Yuri Osetsky,
Oak Ridge National Laboratory (DOE), United States

*CORRESPONDENCE
Andrée De Backer,
✉ andree.debacker@gmail.com

RECEIVED 15 June 2023
ACCEPTED 02 October 2023
PUBLISHED 30 October 2023

CITATION
De Backer A, Souidi A, Hodille EA, Autissier E, Genevois C, Haddad F, Della Noce A, Domain C, Becquart CS and Barthe M-F (2023), Readdressing nanocavity diffusion in tungsten.
Front. Nucl. Eng. 2:1240995.
doi: 10.3389/fnuen.2023.1240995

Readdressing nanocavity diffusion in tungsten

Andrée De Backer[1,2,3]*, Abdelkader Souidi[4], Etienne A. Hodille[5], Emmanuel Autissier[6], Cécile Genevois[6], Farah Haddad[6], Antonin Della Noce[7], Christophe Domain[2,8], Charlotte S. Becquart[1,2] and Marie-France Barthe[6]

[1]Universite de Lille, CNRS, INRAE, Centrale Lille, UMR 8207—UMET, Lille, France, [2]EM2VM, Joint Laboratory Study and Modelling of the Microstructure for Ageing of Materials, Moret-sur-Loing, France, [3]Aix Marseille University, CNRS, PIIM, Marseille, France, [4]Universite Dr. Tahar Moulay de Saida, Faculte des Sciences, Departement de Physique, Saïda, Algeria, [5]CEA, IRFM, Saint Paul Lez Durance, France, [6]CNRS-CEMHTI, Orleans, France, [7]IGR, Unite INSERM 981, Villejuif, France, [8]EDF-R&D, Departement Materiaux et Mecanique des Composants, Moret-sur-Loing, France

In nuclear fusion (ITER and the future DEMO), those components that face the plasma are exposed to high temperature and irradiation which, in the long term, modifies their thermal and mechanical properties and tritium retention. Tungsten is a candidate material and is the subject of many studies of microstructure evolution under various irradiation and temperature conditions. One milestone is the characterization of its defect properties. We here readdress the diffusion of nanocavities on broad ranges of size and temperature and compare it with dissociation, a competing process during nanocavity growth. First, at the atomic scale, we used molecular dynamics to explore the variety of elementary events involved in the nanocavity diffusion. Second, an experimental study of ion-irradiated samples, annealed at different temperatures up to 1,773 K, revealed the creation and growth of nanocavities on transmission electron microscopy images. Third, we performed multi-objective optimization of the nanocavity diffusion input of our object kinetic Monte Carlo model to reproduce the experimental results. Finally, we applied a sensitivity analysis of the main inputs of our model developed for these particular conditions—the source term which combines two cascade databases and the impurities whose interaction with the defects is characterised with a supplemented database of density functional theory calculations. Three domains of nanocavity size were observed. The first is the small vacancy clusters, for which atomistic calculations are possible and dissociation is negligible. The second is the small nanocavities, for which we provide new diffusion data and where a competition with the dissociation can take place. The third domain is the large nanocavities, for which, in any case, the dissociation prevents their existence above 1,500 K in the absence of a stabilizing interface.

KEYWORDS

nanocavity diffusion, microstructure evolution, irradiation damage, OKMC, tungsten

1 Introduction

Tungsten is a candidate material for plasma-facing components of fusion reactors because of its resistance to high temperature and its low sputtering property. Two concerns about it are the deterioration of its mechanical properties (the ductile-to-brittle transition temperature is reduced because of the irradiation) and tritium retention due to neutron and ion irradiation. The tritium solubility of perfect tungsten is low, but tritium retention is enlarged by tens of orders of magnitude in the presence of defects created by neutron or high energy particle irradiation. One additional issue is that, in a fusion reactor, the temperature and irradiation conditions experienced by the materials vary significantly—particularly plasma surface interactions, which induce large spatial and temporal temperature gradients.

For the design and safety of ITER and future DEMO power plants, it is necessary to develop numerical models of the evolution of the material microstructure under irradiation and large temperature variations. For this purpose, data on the properties of defects are required. The literature reports a very limited amount of data on the diffusion of vacancy defects and, in particular, on the diffusion properties of nanocavities. In the 1960s, the motion and coalescence of pores in metals were intensively studied in order to understand the microstructural damage in irradiated materials with and without the presence of helium (Nichols, 1969; Goodhew et al., 1981; Zell et al., 1994). The proposed diffusion mechanism is the creation and diffusion of defects at the inner surface of the nanocavity. Theoretical expressions were elaborated, but investigations were limited by the size resolution of the experimental techniques and computational capability. In 2017, Castin et al. (2017) characterized the diffusion properties of vacancy clusters using machine learning, with the drawback that the approach relied on the quality of empirical potentials. Mason et al. (2017) used density functional theory (DFT) to calculate the activation energies for the evolution of small vacancy clusters. They found that the tri-vacancy diffuses faster than the mono-vacancy in W and observed the diffusion of clusters up to 15VAC in atomic kinetic Monte Carlo simulations based on a new empirical potential developed for the study of surfaces and vacancy cluster properties. Perez et al. (2017) studied the diffusion of small vacancy-helium clusters with accelerated MD using a supercomputer. Jansson and Malerba (2013) and Pannier (2017) showed that the migration energy of clusters of similar size in iron can significantly differ depending on their symmetry.

This work relies on complementary approaches to observe, understand, and model the formation and growth of nanocavities due to their diffusion and dissociation. In the first section, we briefly revisit the elementary events observed at the atomistic level using molecular dynamics. In the second section, we summarize the experimental results detailed in Autissier et al. (2023) that characterise the growth of nanocavities in irradiated and annealed samples. The third section describes our object kinetic Monte Carlo (OKMC) model and four main inputs that have been improved since our previous paper (Becquart et al., 2010): the source term, the interactions of defects with impurities, and the diffusion and dissociation of the nanocavities. We emphasise the uncertainty estimation, providing upper and lower limits of the parameter sets. The method we used to obtain the diffusion coefficients of the nanocavities with multi-objective optimisation is detailed in De Backer et al. (2022) and De Backer et al. (2023). In the fourth section, we describe a sensitivity analysis based on systematically combining upper and lower parameter sets. We focus on the most sensible conditions: the impact of empirical potentials in the source term, and the competition between diffusion and dissociation of the nanocavities. Finally, we discuss the results and conclude. For the sake of readability, additional information is reported in the Supplementary Material in numerous places.

2 Diffusion of nanocavities at the atomistic level

In Nichols (1969), Goodhew et al. (1981), and Zell et al. (1994), the motion of a void starts with the creation of a pair of defects at the inner surface: an ad-atom and a surface vacancy. A small change of the *centre of mass* of the void is obtained by the net displacement of one atom from the leading surface to the trailing surface and/or one surface vacancy in the opposite sense. Two mechanisms can be considered: diffusion at the surface, or diffusion via the lattice if the defect *dissociates* before recombination. The flight of an ad-atom through the vacuum or vapour (in a bubble) phase is also possible. Theoretical expressions of the resulting nanocavity diffusion coefficient have been derived; these usually depend on assumptions about the shape of the cavity or the driving process. Mason et al. (2017) showed that small vacancy clusters diffuse by taking successively different configurations. The energy barriers associated with each transformation can be accurately calculated and will determine the diffusion coefficient of the whole cluster. However, this approach rapidly becomes impractical with the increasing number of configurations that must be considered for large clusters. In Castin et al. (2017) and Mason et al. (2017), the diffusion of small nanocavities was simulated using atomic kinetic Monte Carlo simulations where the energy barrier energy calculations rely on assumptions and on the quality of the empirical potential. In this work, we perform exploratory molecular dynamics (MD) simulations of the diffusion of nanocavities of various sizes.

2.1 The molecular dynamics setup

The simulations were performed using the code LAMMPS (Plimpton, 1995) in a cubic cell containing 16,000 W atoms of a bcc lattice. Using the empirical potential, *Ms*—specifically designed for vacancy type defects (Mason et al., 2017)—100 ns simulations at 2,000 K have been calculated. Frames have been saved every 10 ps and analysed (more technical aspects are given in Supplementary Section S1 of the Supplementary Material). Cavities with 12 same-size (110) surfaces were built, this orientation being the most stable for bcc W (Vitos et al., 1998; Byggmästar et al., 2019). We chose a rhombic dodecahedron (one solid of Catalan) in which the 12 surfaces have lozenge shapes of the same area (see Figure 1). Highly symmetric cavity clusters of 15VAC, 65VAC, 175VAC, and 369VAC are easily obtained with this method. In this paper, the description will be limited to 65VAC and 175VAC. The distance between the two opposite vertices is 1.2 nm for 65VAC and 1.9 nm for 175VAC. To remove the perfect crystal and visualise the atoms of the so-called *inner* surface, one uses the atom coordination (CN), with a cutoff of 3.9 Å. Figure 1A shows the *inner* surface atoms of 175VAC from the (100), (110), and (111) lines of sight. The coordination is indicated by the colour coding. The perfect surfaces are in blue (CN = 10), the edges are in green (CN = 12), and the vertices are in red (CN = 13). It can be seen that the 175VAC

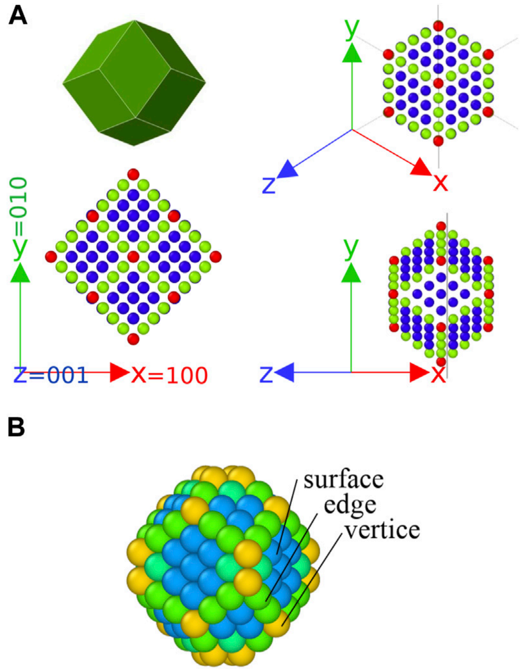

FIGURE 1
(A) Visualisation of the 175VAC nanocavity. Atoms at the inner surface are represented in a different line of sight with their coordination in colour coding. The surface atoms are represented in blue (CN = 10), the edges in green (CN = 12), and the vertices in red (CN = 13). Note a rhombic dodecahedron [14 vertices and 12 lozenge faces in the (110) direction]. **(B)** 3D visualisation of a less symmetrical nanocavity, one 88VAC.

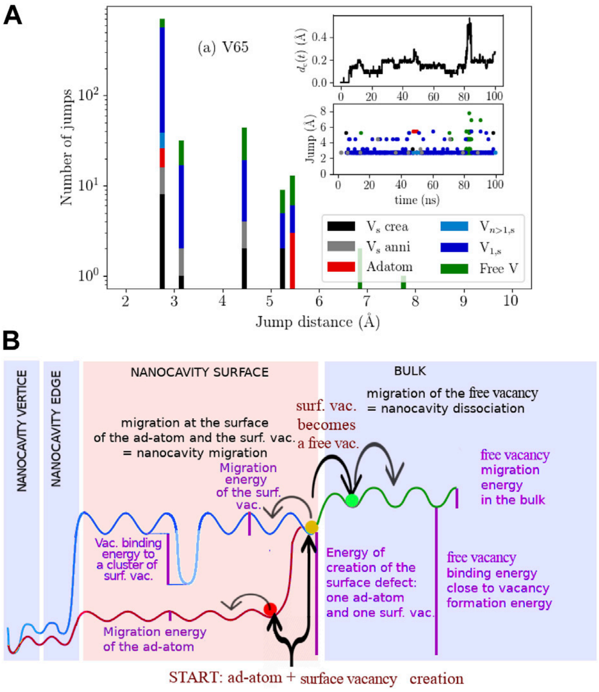

FIGURE 2
(A) Histogram of the number of detected events as a function of the jump distance in the 65VAC simulation; $V_{1,s}$ (blue) is for an isolated *surface* vacancy, and $V_{n>1,s}$ (light blue) is for a jump inside a cluster of *surface* vacancies. The insets show the evolution of the *centre of mass* of the vacancy cluster, $d_c(t)$, and the jump measured for each elementary event as a function of the detection time. **(B)** Energy barriers of the elementary processes, starting in the centre with the creation of a pair of defects: a surface vacancy and an ad-atom. On the left, the ad-atom and the surface vacancy diffuse at the surface until they are trapped at an edge—a vertex or a cluster of surface vacancies. On the right, the surface vacancy penetrates into the bulk, becoming a *free* vacancy. The dissociation, in competition with the diffusion, is when this free vacancy diffuses away.

cluster has nine atoms on the surface, while the 65VAC cluster has only four, which will impact the probability of the elementary events and the variety of the configurations that can be observed in the simulations. The number of possible configurations would be even larger if we had started with less symmetrical clusters. An example of 88VAC is illustrated in Figure 1B, with surfaces of different sizes and vertices involving several atoms.

2.2 Analysis of the simulations

The centre of the mass of the vacancy cluster as a function of time, $d_c(t)$, is plotted in insets in Figure 2A. The effective displacement is very small—0.1–0.4 nm—because of the average number of vacancies in the nanocavity. Its erratic behaviour is strengthened by some elementary processes. For example, for 65VAC at 85 ns, the rapid peak of $d_c(t)$ is due to the emission and recapture of one vacancy—that is, one surface vacancy becomes a free vacancy which rapidly diffuses in the lattice before being recaptured. Here, the periodic boundary conditions of the simulation lead to an artefact: the change of $d_c(t)$ is always temporary, and the free vacancy is always recaptured. Properly calculating the diffusion coefficients requires simulations to be run much longer at different temperatures and with various initial configurations. This is impractical, and we limit our investigations to detecting and counting elementary processes with a few initial configurations.

The method of tracking a defect's creation, motion, and annihilation is based on the detection of a modification between frame (n) and frame (n+1) (see details in Supplementary Section S1 of the Supplementary Material). A frequent sequence of events is observed: i) a pair of defects (an ad-atom and a surface vacancy) are created at the *inner* surface; ii) the ad-atom moves quickly and is trapped first on an edge, and then on a vertex; iii) the surface vacancy migrates until it is also trapped. The six different elementary events by order of increasing frequency are as follows: i) free vacancy jump; ii) single surface vacancy jump; iii) surface vacancy jump in a cluster of surface vacancies; iv) ad-atom jump; v) creation of a surface vacancy and ad-atom pair; vi) annihilation of a surface vacancy (reverse process of v).

One interesting and new process here is the formation of clusters of surface vacancies. The initially perfectly faceted cavity becomes less symmetrical. The creation of several ad-atom and surface vacancy pairs allows the formation of a new ledge which initiates a possible change of surface orientation.

The lengths of each vacancy or ad-atom jump have been measured. The histogram for the 65VAC is plotted and shown in Figure 2. The comparison with 175VAC is possible and shown in

Supplementary Section S1.3 of the Supplementary Material. The main observations follow. First, the large majority of the jumps corresponds to the first nearest neighbours (NN) distance ($\sqrt{3}/2a = 2.74$ Å) and to the displacement of one surface vacancy alone or inside a surface vacancy cluster. Thus, the frequency of frames is good for analysing these vacancy jumps. Second, the free vacancy jumps are not observed with the 175VAC cluster because vacancy emission is rarer than for the 65VAC, in agreement with the increase of the vacancy binding energy with the cluster size. Third, the largest jump distance of an ad-atom or surface vacancy corresponds to the length of an edge. This indicates that the detrapping of the defects from a vertex is possible and is followed by a fast diffusion along an edge. Fourth, the surface defect creation rate is larger for 175VAC than 65VAC because the initial (110) surfaces are larger in 175VAC than in 65VAC. For the same reason, the processes related to the surface vacancy clusters are more frequent for the 175VAC cluster than for the 65VAC cluster. It is possible that the probability of forming these surface vacancy clusters increases with the cavity size. Fifth, the detection of events related to ad-atoms is rare because of the artefact caused by the low frame frequency, and so a flight of one atom inside the vacuum is not observed.

A simple sketch of the energy barriers for the surface defect creation and diffusion leading to the nanocavity diffusion is proposed in Figure 2B. What happens at the inner surface is shown on the left and what happens in the bulk lattice is on the right. The heights of the energy barriers are associated with the frequency of detection in the simulations, taking the bias of the frame frequency into account. It starts with the formation of the pair of defects: one surface vacancy and one ad-atom. The ad-atom and the surface vacancy diffuse independently at the surface until they are trapped or annihilated. The trapping centres are the edges, the vertices, but also clusters of surface vacancies which can appear on large nanocavities. The surface vacancy can also penetrate the bulk of the material, becoming a free vacancy. If it diffuses back to the nanocavity, then it is part of the diffusion process, but if it diffuses far away, then it is part of the nanocavity dissociation process. Thus, the diffusion and dissociation processes share some energy barriers.

3 Experimental observations of the nanocavity growth

Descriptions of the experimental setup, the main experimental results, and the elements of interpretation necessary to this work are explained in the following paragraphs. It is important to remember that irradiation creates interstitial and vacancy defects, which evolve and interact during irradiation and when the material temperature increases.

3.1 Experimental set-up

The experimental scheme is as follows: sample preparation, irradiation, and successive annealing at increasing temperatures. At each stage, the microstructure is characterised using a transmission electron microscope (TEM). Micrographs are recorded and analysed *a posteriori*.

The samples are first polished and annealed at 1,873 K to remove native defects. Zones as thin as 33 nm are obtained with a twin-jet electropolisher. Irradiations of 1.2 MeV W are realised in the JANNuS platform at a fluence of $1.8 \pm 0.2 \times 10^{12}$ cm^{-2} and a temperature of 773 K. The corresponding damage was evaluated with SRIM (Ziegler et al., 2010) in the Quick Kinchin-Pease mode (Stoller et al., 2013) using the displacement energy threshold of 55 eV (Autissier et al., 2023). The average damage dose is about 0.02 dpa. The maximum range of the W ions is located at a depth of 50 nm. This means that a large proportion of the ions passes through the thin parts of the lamella. The same samples are then successively annealed over 1 h at eight fixed temperatures between 873 and 1,773 K.

The TEM is a PHILIPS CM 20 device with a very good resolution of 0.14 nm. The bright field image is recorded in under- and over-focused beam conditions to allow the identification of nanocavities and the measurement of their size (diameter). The analysis of the images combines *manual* and *automatic* inspections that are briefly explained in Supplementary Section S2.2 of the Supplementary Material and detailed in Autissier et al. (2023). The images are also recorded with different operating diffraction vectors to identify dislocation loops.

Note that, in Section 5.2, we also consider one experimental result obtained in the same conditions as just described except for the irradiation temperature, which was 300 K instead of 773 K.

3.2 Experimental results

After irradiation, a large density of 10^{24}-m^{-3} small nanocavities of around 1 nm diameter is apparent. Figure 3 shows bright-field TEM pictures in which nanocavities can be identified by spots whose contrast turns from black in over-focused to white in under-focused conditions. The size histogram is plotted further in the text and compared with the simulations in Figure 10A. The nanocavity sizes range from 0.8 to 2.2 nm—well above the visibility threshold of 0.5 nm. The opposite of the size histogram is obtained in samples irradiated at 300 K plotted in Figure 10B, which start at the visibility limit and decrease exponentially, suggesting that there are also invisible vacancy defects.

During the succession of annealing steps at increasing temperatures, the growth of nanocavities is observed and illustrated by four TEM images taken at 1,173, 1,373, 1,573, and 1,773 K in Figure 3. The size histograms (see Supplementary Figure S12 of the Supplementary Material) exhibit a progressive shift and broadening up to 4 nm.

The nanocavity diffusion cannot be observed *in* situ, and it was not possible to mark the sample surface to localise the nanocavities. Explaining nanocavity growth requires consideration of two possible mechanisms: diffusion and dissociation. Throughout this work, both mechanisms are considered and the modelling results support the final interpretation. Supplementary Figure S2 of the Supplementary Material shows the total density and mean size of the nanocavities as a function of the annealing temperature. The tendency represented by lines adjusted, as described in De Backer et al. (2023), shows that the density decreases and size increases when the temperature increases. The number of experimental data/points is limited, and the saw-tooth variations are mainly

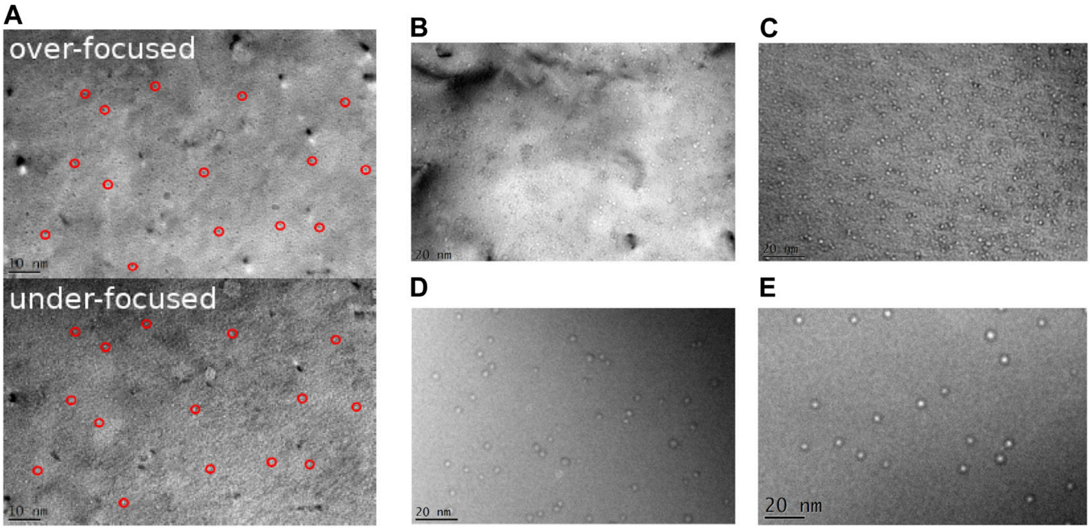

FIGURE 3
(A) Bright-field TEM micrographs in over- and under-focused beam conditions of irradiated samples. A high density of very small nanocavities appear as black (resp. white) spots in over-focused (resp. under-focused) conditions. Some are indicated with red circles. **(B–E)** Bright-field TEM micrographs in under-focused beam conditions of W samples irradiated by 1.2 MeV W ions and annealed up to **(A)** 1,173 K, **(B)** 1,373 K, **(C)** 1,573 K, and **(D)** 1,773 K. Nanocavities appear as white spots. They grow and become less numerous when the temperature increases.

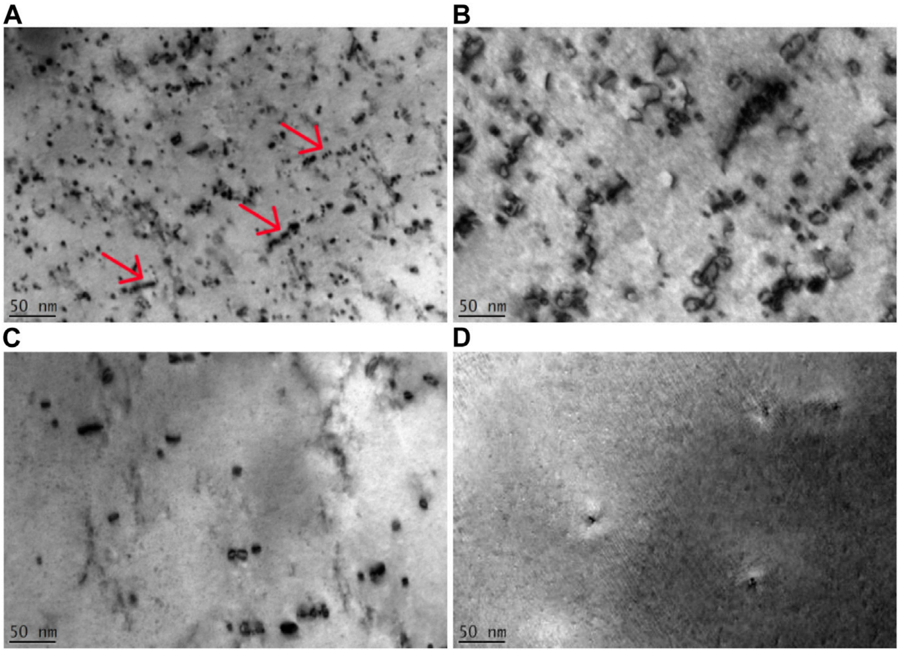

FIGURE 4
Bright-field TEM micrographs acquired with an operating diffraction vector g = ⟨110⟩; **(A)** after irradiation; **(B–D)** after annealing at 973, 1,173, and 1,373 K. After irradiation, isolated dislocation loops and loops gathered in rafts (pointed in red) are apparent. Loops become larger and longer at 993 K, significantly fewer at 1,173 K, and extremely rare at 1,373 K.

due to the counting methods and the variation in the local transparency of the sample.

Figure 4 shows micrographs with interstitial defects—particularly of dislocation loops after irradiation and annealing at 973, 1,173, and 1,373 K. Some dislocation loops gathered in rafts (as in Hasanzadeh et al. (2018)). The total density of isolated dislocation loops is 4.1 ± 0.6 × 10^{23} m^{-3}, and their diameter is about 9 nm. Approximately 60% of loops have a 1/2a ⟨111⟩ Burgers vector, and the others are ⟨100⟩. The total density of the rafts is 0.3 ± 0.6 × 10^{23} m^{-3}, and 90% of loops are 1/2a⟨111⟩.

The isolated dislocation loops and rafts become larger and longer (respectively) at 993 K, significantly fewer at 1,173 K, and extremely rare at 1,373 K.

4 The OKMC model and its main inputs

Our model follows all the experimental steps and simulates the creation, diffusion, dissociation, and interaction of the defects. The core of our model is an object kinetic Monte Carlo (OKMC) simulation implemented in LAKIMOCA (Becquart and Domain, 2009). This approach and its limitations have been explained and reviewed in many papers, as recently in Becquart et al. (2019), Caturla (2019), and Malerba et al. (2021). SIA and vacancy defects of different sizes are objects in a simulation box. They are created by irradiation events described in the following paragraphs. They diffuse and dissociate (emit single defects) according to predefined probabilities which depend on temperature. When the distance between two objects is smaller than a capture distance, they interact—the defects of the complementary type annihilate, and defects of the same type form larger clusters/objects. For this work, the types of defects are limited to ⟨111⟩ SIA dislocation loops, which are very mobile and stable, and spherical vacancy clusters or nanocavities whose properties will be detailed in Section 4.3. To simulate a TEM sample, the simulation box is 33 nm long along the z direction, with absorbing surfaces, and approximately 500 nm long along the x and y directions, with periodic boundary conditions.

In this section, we describe four novelties in the main sub-models or inputs of our model compared to Becquart et al. (2010). Because we will conduct a sensitivity analysis, for each input, we will define two limit parameter sets, labelled *up* and *low*. In some cases, there is also an intermediate parameter set, *ref*. In what follows, the first described input is the source term, which simulates the primary damage created by high-energy ion irradiation. The second input is the interaction model between defects and impurities (necessary to trap SIA loops up to a high temperature as observed in the experiment). We then describe the diffusion of nanocavities, briefly explaining the results of the multi-objective optimisation detailed in De Backer et al. (2023). Finally, we address the nanocavity dissociation.

4.1 The source term or primary damage of high-energy implanted ions

A high-energy ion loses its kinetic energy in the material during nuclear collisions and via energy exchanges with electrons in less than a few picoseconds. The nuclear collision accelerates one atom of the lattice, which triggers cascades/sub-cascades of displacements that create a strongly damaged and heated region. The primary damage is the description of the crystal defects remaining after the cooling down and lattice recovery. As recommended in Nordlund et al. (2018) and Sublet et al. (2019), our approach goes beyond the simple dpa—the number of displacements per atom—and takes into account the formation of clusters of defects and their spatial distribution in the sub-cascades. Our method, illustrated in Figure 5, combines two approaches to simulate the total damage: the binary collision approximation (BCA) and molecular dynamics (MD).

4.1.1 Database of BCA cascades

The BCA is an approximation that permits the modelling, in reasonable CPU time, of the trajectory of one high-energy ion and the kinetic energy transferred to the atoms it encounters. In this approach, only the trajectories of the impinging particle and the collided atoms are simulated. The collective interactions and the crystal recovery are ignored. Each simulation is one random sampling of the possible trajectories, and statistics of several thousands of simulations are simple to acquire. In our approach, the detection of sub-cascades is obtained with the decomposition method described in De Backer et al. (2018). One example of a 1.2-MeV W ion is illustrated in Figure 5. On the left-hand side is the position of the collisions coloured as a function of time. Yellow indicates what happened at the beginning (before 0.05 ps), and purple, what happened at approximately 0.25 ps. This figure illustrates the deployment in space and time of the successive collisions. Next to the BCA trajectories is the decomposition in 10 sub-cascades represented by cubic cells of identical colour.

Statistics on 1.2 MeV ions indicate that they are stopped before 150 nm (indicating an agreement between SDTrimSP and SRIM). In a 33-nm-thick sample are 3.5 sub-cascades of various volumes, per ion. The histogram of sub-cascade volume follows a decreasing power law (De Backer et al., 2016).

A second series of BCA simulations with ions of smaller energies is necessary for establishing the correspondence between the sub-cascade/cascade volume and its energy—that is, the kinetic energy the atom responsible for the displacement cascade/sub-cascade has received (see section below). It is also necessary to estimate the amount of energy transferred to electrons, for which we used Lindhard's formula (Lindhard et al., 1963).

4.1.2 Database of MD cascades

In MD, unlike BCA, all atoms are considered and many body interactions are taken into account through interatomic forces given by empirical potentials that are mostly functions of the interatomic distances. To create the cascade, kinetic energy is given to one atom. As illustrated in Figure 5 (centre), a cascade of collisions is obtained involving atoms of high kinetic energy and exhibiting a tree shape like that observed with the BCA. Linear collision sequences are also seen. At the maximum expansion of the cascade, atoms of low energy are involved in collective interactions. Finally, the defects remaining at the end of the cascade's cooling (after close to a few ps) are visible if all the perfect lattice atoms are removed. They are vacancy defects (usually near the centre of the cascade) and interstitial defects (usually at the surface of the cascade), referred to as "primary damage".

Using the code "DYMOKA" (Becquart et al., 1997), a database[1] of thousands of cascades of energy ranging from 0.25 to 300 keV has been calculated at 100 K using several empirical potentials, as detailed in Supplementary Section S3.2 of the Supplementary Material. It is important to note that, in Becquart et al. (2021)

---

[1] To be available at https://cascadesdb.iaea.org/

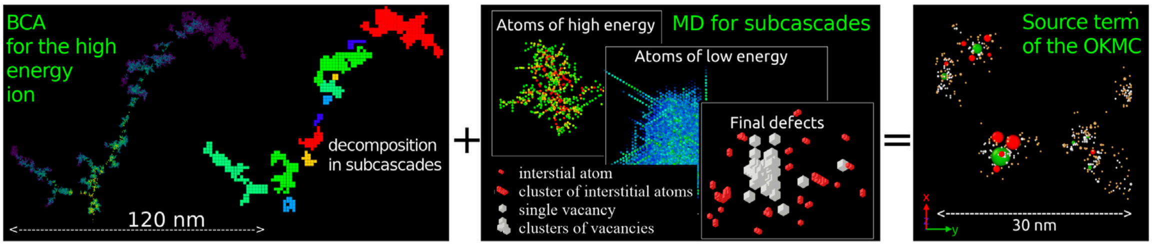

FIGURE 5
Illustration of defect creation modelling by high-energy ions. Left: 1.2-MeV W ion creates cascades/sub-cascades of various volumes simulated with BCA and stored in a first database of thousands of different ion trajectories. Middle: cascades of various energies (0.25–300 keV) are simulated with MD, and the final primary damage is stored in a second database. Right: in the OKMC model, one BCA cascade is picked at random for each irradiation event, and each sub-cascade is replaced by the primary damage of one MD cascade using a correspondence between the sub-cascade volume and the cascade energy. The SIA (resp. VAC) defects in red (resp. green) are larger than 0.5 nm and are considered to be visible by TEM. The smaller and invisible SIA (resp. VAC) defects are in yellow (resp. white).

and De Backer et al. (2021), we studied the effect of the empirical potentials on the primary damage of 50-keV cascades in W and 80-keV cascades in Fe. Based on that study, we selected three potentials for this work. Two came from that developed by Finnis and Sinclair (1984): one version modified by Mason et al. (2017) and labelled *MNs*, and one version modified by Juslin and Wirth (2013) and hardened by Björkas et al. (2009) labelled *JW*. The third potential is Marinica's potential (Marinica et al., 2013), which is the hard version described in Sand et al. (2016) and labelled *MSh*. Quantiles of the vacancy defect in MD cascades performed with *MSh*, *JW*, and *MNs* are calculated to characterise the size distribution. Supplementary Table S1 gives 1% and 0.1%.

Analysis of the primary damage underlines the formation of self-interstitial atoms (SIAs) and vacancies, isolated or agglomerated—forming loops, clusters, or nanocavities.

Many statistical analyses can be performed as a function of the cascade energy. We will focus here on the mean number of defects per cascade and the defect clustering. The latter is illustrated by the mean frequency of defect clusters as a function of the cluster size (SIA and VAC). As expected, the total number of defects increases with the cascade energy. It is larger for *MNs* than for the other potentials. In addition, as expected after Becquart et al. (2019), the cluster frequency generally decreases as a function of the cluster size, following a power law, and dropping to zero at a maximum cluster size (see Supplementary Figure S4 of the Supplementary Material). Overall, the number of clusters increases with the cascade energy. The size of the largest cluster follows the same trends. For all energies, *MNs* creates more defects but smaller clusters than the other two potentials. Potential *JW* creates particularly large clusters, as already observed in the 50-keV cascades analysed in Becquart et al. (2021) and De Backer et al. (2021). To briefly summarize the cascade properties of interest, the *MN* potential creates more defects but less clustering than the *JW* potential. *MSh* causes more intermediate damage. The cascade energy range covers the energy of the sub-cascades created by 1.2-MeV W ions (see the green arrows in Supplementary Figure S3 of the Supplementary Material).

4.1.3 The OKMC source term

The primary damage created by one 1.2-MeV W ion—the source term of our model—is obtained by introducing the primary damage of one MD cascade in each of the BCA sub-cascades, as illustrated in Figure 5. In that figure, a distinction is made between SIA and VAC defects, and between defects that are invisible and visible with TEM (i.e., defects with a diameter smaller or larger than 0.5 nm). In Figure 5, several pockets of defects (sub-cascades) are evident with one visible vacancy cluster (shown in green) surrounded by a few large visible SIA clusters (shown in red) decorated by many defects smaller than the visibility threshold (shown in yellow for SIA and white for VAC).

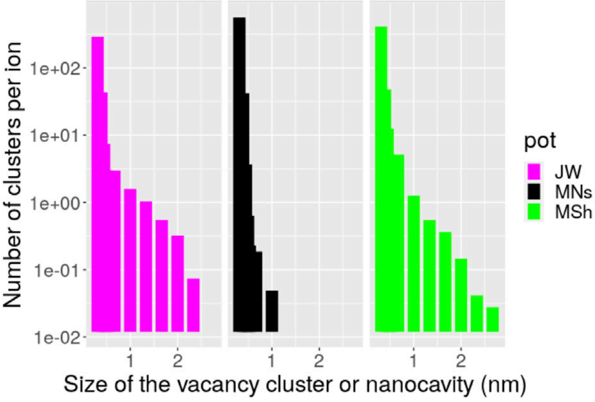

FIGURE 6
Size distributions of the vacancy defects created by 1.2 MeV W ions in a 33-nm-thin sample according to three different interatomic potentials.

On average, in the sample thickness, 700 VAC and 700 SIA defects are created per ion. Defect size distributions follow power laws as a result of the convolution of the defect production per sub-cascade and the histogram of sub-cascades created by the high-energy ion. We calculated defect size histograms for the three empirical potentials (Figure 6) and found that there are more than one nanocavity larger than 1 nm for each ion. These nanocavities are created without vacancies having to diffuse, the time scale of the cascade being too short. Thus, the total number of defects and the width of the distributions depend on the potential. In the following sections, the source term using *JW* will be labelled *up*, *Mhs* will be labelled *ref*, and *MNs* will be labelled *low*. More information can be found in Supplementary Section S3.2 of the Supplementary Material.

4.2 Defect-impurity trapping

The modelling of the microstructure evolution of real material incurs an additional challenge due to the presence of impurities. Even in small quantities, they can impact the microstructure evolution by trapping defects and modifying their properties. Our model takes impurities into account by introducing immobile traps distributed homogeneously in the simulation box. These traps are characterized by their densities and their binding energies with each kind of defect. For this work, we supplement our database in Becquart et al. (2010) of binding energies of mono-vacancies, mono-SIAs, and small SIA loops containing up to 19 SIAs, with up to 30 different elements, which was calculated using density functional theory (DFT). The calculation setup is given in Supplementary Section S4.1 of the Supplementary Material. To facilitate the data analysis, we calculated the *detrapping* temperature $\Theta_{trap}^{i,j}$ at which the detrapping probability of the defect i from the impurity j is 1 per second. The detrapping probability is given by an Arrhenius formula:

$$\Theta_{trap}^{i,j} = \frac{E_b^{i,j} + \min\left(E_M^i, E_M^j\right)}{k_B \log(\Gamma_0)}, \tag{1}$$

where $E_b^{i,j}$ is the binding energy between defect i and impurity j; E_M^i, and E_M^j are the migration energies of the defect and of the impurity; Γ_0 is an attempt frequency (here equal to $6.5 \times 10^{12}\ \mathrm{s}^{-1}$), and k_B is the Boltzmann constant.

The migration energies of SIA clusters are generally much smaller than the mono-vacancy. The migration energies of the impurities have also been calculated (see Supplementary Table S2 of the Supplementary Material) and are generally larger than the migration energy of the mono-SIA and smaller or similar to the migration energy of the mono-vacancy.

As plotted in Supplementary Figure S6 of the Supplementary Material, the binding energies between impurities and a mono-SIA are up to 4.5–5 eV (for P, Ni, and Co), which correspond to de-trapping temperatures as high as 2,000 K. For interstitial solutes such as C, H, N, and O, the binding energy increases with the SIA defect size. On the other hand, substitutional solutes have a large binding energy, which decreases with the SIA defect size. We observed that the binding energy did not evolve much above 19 SIA. Solutes Zr, Hf, Nb, and Ta interact mildly whatever the size of the SIA defect. The binding energies of impurities with the mono-vacancy are generally smaller than those with the mono-SIA. They are up to 2–3 eV (for C, N and O), which corresponds to de-trapping temperatures close to 1,500 K.

According to the material provider, the main impurities of tungsten are H, Mo, C, O, and P, with concentrations ranging from 300 to 900 atomic ppm. Figure 7 illustrates the strength of the trapping of SIA defects and mono-VAC with graphs where the x-axis indicates the impurity concentration. Within this representation, elements situated on the top right are numerous and strong traps, and hence may be the most likely to modify the defects' behaviour and the microstructure evolution. In Figure 7A, red points are used for mono-SIAs and are connected to magenta pentagons which represent SIA loops. The connecting line indicates the de-trapping temperature range for SIA defects. In Figure 7B, the green points are used for the mono-vacancies. De-trapping temperatures below the temperature at which the mono-vacancy starts diffusing possibly reflect the release of the impurity from the vacancy defect. Hence, no trapping of nanocavities is considered because our exploratory simulations (in Section 2) suggest that a single impurity cannot block the elementary events involved in the diffusion of nanocavities. Nevertheless, the question remains for the trapping of small vacancy clusters and in cases of many impurities covering an important proportion of the inner surface of the nanocavity.

The analysis of Figure 7 shows that H probably has little effect on the trapping of either vacancies and SIAs, whereas P, Fe, and Co atoms strongly affect the trapping of SIA defects. For mono-vacancies, C, O, N, and K are the most important impurities. Dotted arrows indicate increased Re concentration under neutron irradiation (by transmutation), according to Gilbert et al. (2017). This element is not a strong trap, but its impact may be non-negligible with time due to the large concentration increase. Re is also an alloying element (Hwang et al., 2018). Interestingly, Re and Os are found to decorate nanocavities in Lloyd et al. (2019).

For the OKMC parameter set related to the trapping, the main unknown is now the densities of the traps. We cannot simply take the material provider concentrations because it is well known that they will be too large as impurities are rarely present as single atoms but in clusters. In our case, the trapping of the SIA defects is the most important as SIA loops are observed in our experiment, indicating that they have been trapped. Indeed, the velocity of loops in pure material is very high. We tried to adjust the trap densities to obtain good agreement with the experimental results. Unfortunately, we were not able to simultaneously obtain good agreement with both the experimental loop sizes and densities. In this work, the amount of information on the loops is very limited, which makes it difficult to further search for a satisfying answer on the trap densities. For the sensitivity analysis, we take as *ref* densities the provider concentration divided by 200. The *up* set then corresponds to four times the *ref* densities and the *low* set to no trap at all.

4.3 The diffusion of the nanocavities

In our OKMC, the diffusion of SIA and VAC defects is simulated by a succession of jumps which mainly differ by their jump probability: SIA defects are highly mobile and diffuse (in 1D), whereas VAC defects diffuse in 3D at high temperature. We focus here on the vacancy jump frequency, knowing that the diffusion coefficient can be obtained by the formula (Kong and Lewis, 2006):

$$D = \frac{\alpha l^2}{2d}\Gamma, \tag{2}$$

where, in the case of bcc crystals, $l = \frac{\sqrt{3}}{2}a$ is the jump length, a the lattice parameter, $d = 3$ the dimension of the diffusion, $\alpha = 8$ the number of possible equivalent jumps on bcc lattice sites, and Γ the jump rate.

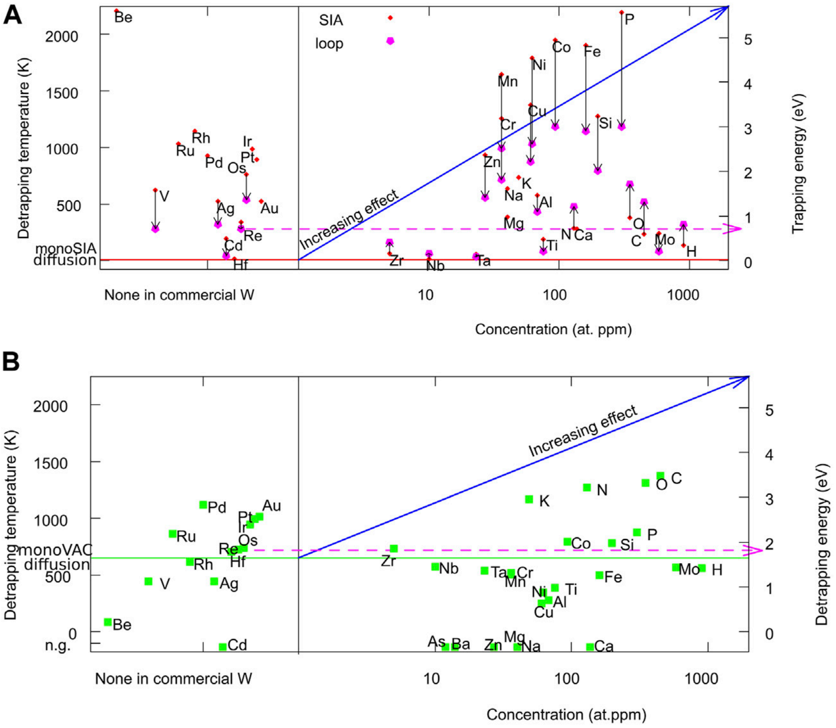

FIGURE 7
(A) Temperature range of the trapping of SIA and a 19-SIA loop by one impurity atom. The *x*-axis represents the impurity concentration in commercially pure W. **(B)** De-trapping temperature of the mono-vacancy defect. Dotted arrows indicate increased Re concentrations (by transmutation) when tungsten is exposed to neutrons during 2 years' operation in the ITER according to Gilbert et al. (2017).

The different simplification stages are as follows. First, the defects jump as a whole onto the first nearest neighbouring sites. Second, the jump length is the same for clusters of all sizes, but the jump probability depends on the defect size and follows an Arrhenius function:

$$\Gamma^m_{nv} = f^m_{nv} \exp\frac{-E^m_{nv}}{k_B T}, \tag{3}$$

where $f^m_{nv}(s)$ is the attempt frequency and E^m_{nv} is the migration energy corresponding to the nVAC defect. k_B is the Boltzmann constant and T is temperature. Third, for the attempt frequencies of the nanocavities, it is possible to use surface diffusion theory; however, information is lacking on the migration energies. Thus, in De Backer et al. (2023), it was decided to fix the attempt frequencies (see Supplementary Section S5 of the Supplementary Material) and adjust the migration energies. Fourth, in De Backer et al. (2023), we adjusted *diffusion* temperatures—the temperature at which the jump frequency is equal to 1 per second. This value depends on both the attempt frequency and the migration energy, which can be obtained using

$$E^m_{nv} = \theta_n k_B \ln\left(f^m_{nv}\right). \tag{4}$$

Finally, n, the number of vacancies in the object, and s, the visible defect size (diameter), are related by the expression $s_n = a\left(\frac{3}{\pi}n\right)^{\frac{1}{3}}$.

The results of the multi-objective optimisation of the diffusion temperatures led to two diffusion parameter sets labelled *up* and *low*, as briefly explained in Supplementary Section S5 of the Supplementary Material and in detail in De Backer et al. (2022) and De Backer et al. (2023). The *up* (resp. *low*) set includes the values which optimised agreement with the observed density (resp. size) of nanocavities as a function of temperature. The fact that these two sets are different indicates the presence of a Pareto front—a domain

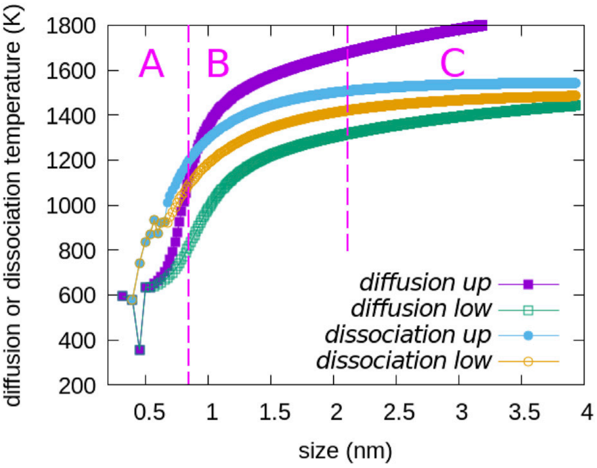

FIGURE 8
Up and *low* values of the diffusion temperatures, results of the multi-objective optimization, and *up* and *low* dissociation temperatures obtained by DFT as a function of the size of the nanocavities. *A*, *B*, and *C* ranges are described in the text.

of solutions where no improvement of any objective can be obtained without losing another objective. We consider that both *up* and *low* limit solutions (plotted in Figure 8) correspond to the uncertainties remaining after the optimisation process.

4.4 Dissociation of nanocavities

The dissociation of the vacancy clusters or nanocavities is simulated by the emission of mono-vacancies from the vacancy defect. In order to determine the uncertainties of the parameters of Becquart et al. (2010), we calculated new formation energies of large size vacancy defects by DFT (see Supplementary Section S6 in the Supplementary Material). Two different capillarity laws representing the upper and lower limit values on the binding energies, labelled as *up* and *low* binding energies, have been adjusted. The dissociation temperature, defined as the temperature at which the emission rate is 1 per second, can then obtained from these binding energies. The results for the *up* and *low* dissociations are shown in Figure 8. The comparison between the *up* and *low* diffusion curves and the *up* and *low* dissociation curves shows three domains. *A*: the diffusion temperature is lower than the dissociation temperature, so diffusion is the dominant process. *B*: the dissociation temperature lies between the *up* and *low* diffusion temperature curves, so diffusion and dissociation are likely to be in competition. Reducing the difference between the *up* and *low* diffusion curves could clarify which process predominates. *C*: the dissociation temperatures become similar to the *low* diffusion temperatures. The dissociation can dominate or be part of the mechanisms of the nanocavity diffusion, as observed in Section 2. Dissociation alone prevents the existence of nanocavities larger than 2 nm at temperatures higher than 1,500 K. However, the presence of nanocavities in the experiment at higher temperature can be explained by the presence of stabilizing interfaces.

5 Sensitivity analysis of the model

The four principal inputs of our model have been described in the previous section: source term, defect trapping, vacancy defect diffusion, and vacancy defect dissociation. The list of parameter sets is recalled in Table 1. The *up* and *low* sets are our upper and lower limit estimates of the parameters. The *ref* sets are the parameters fixed for the multi-objective optimisation which give the *up* and *down* diffusion in De Backer et al. (2022) and De Backer et al. (2023). The possibility "no diffusion," *diff no*, and a source term with only Frenkel pairs, *ST fp*, has been added. The main goal of this sensitivity analysis is to study how strongly the diffusion parameters obtained could be impacted by a change of the other model inputs. We thus perform the sensitivity analysis around both diffusion parameter sets, varying the other parameter sets.

The constraint of the sensitivity analysis is the computing time of one simulation of a few hours. We then tried to limit the number of simulations while sufficiently exploring the high-dimension space of input parameters. To estimate the sensitivity, we were informed by the multi-objective function defined in De Backer et al. (2022) and De Backer et al. (2023). We therefore defined an objective function ranging from 0 to 1. When it is below 0.5, we considered the disagreement with the experimental data to be unacceptable. The sensitivity of our model is indicated by the difference of the objective function calculated in two input configurations: *ref* and *modified*.

The model returns a list of the SIA and VAC defect clusters present in the simulation box at the end of the irradiation and annealing stages. We then focus on the vacancy defects regarding multi-objective optimisation. The outputs will be the total nanocavity densities and mean sizes for each temperature; in this work, these depend on all the input parameters

$$(density\,(T), size\,(T)) \sim OKMC\left(T, \theta^{diff}, \; \left[\theta^{ST}, \theta^{trap}, \theta^{diss}\right]\right), \quad (5)$$

where T is temperature taking one of the M possible values, OKMC is the simulated stochastic process, θ^{diff} is the diffusion parameter set, and $[\theta^{ST}, \theta^{trap}, \theta^{diss}]$ represents the set of the new source term, trapping, and dissociation parameter sets. The sensitivities associated with the $2M$ outputs x which can be a *density* or a *size* can now be expressed by

$$\begin{aligned}\sigma_x^j\left(\theta^{diff}, \left[\theta^{ST}, \theta^{trap}, \theta^{diss}\right]\right) = \mathbb{E}\Big\{\mathcal{F}\left(x_{mod}\left(T_j\right), x_{ref}\left(T_j\right)\right), \\ x_{mod}\left(T_j\right) \sim \mathrm{OKMC}\left(T_j, \theta^{diff}, \left[\theta^{ST}, \theta^{trap}, \theta^{diss}\right]_{mod}\right) \\ x_{ref}\left(T_j\right) \sim \mathrm{OKMC}\left(T_j, \theta^{diff}, \left[\theta^{ST}, \theta^{trap}, \theta^{diss}\right]_{ref}\right)\Big\}\end{aligned} \quad (6)$$

for $j = 1{:}\ M$ where $\mathbb{E}$ represents the mean on OKMC simulations, with either the reference inputs $\theta^{diff}, [\theta^{ST}, \theta^{trap}, \theta^{diss}]_{ref}$ or the modified ones $\theta^{diff}, [\theta^{ST}, \theta^{trap}, \theta^{diss}]_{mod}$. To be similar to the objective function we take

$$\mathcal{F}\left(x_{mod}, x_{ref}\right) = 1 - \exp\left(S\left|\log\left(x_{mod}\right) - \log\left(x_{ref}\right)\right|\right) \quad (7)$$

with $S = 1$ for *density* outputs and $S = 3$ for *size* outputs, indicating that a change in *size* is more meaningful than a change in *density*.

A total of 14 conditions, taking either the *up* or *low* diffusion and changing one of the *ref* parameters by one of its limits, have been simulated and analysed. The cases with significant sensitivity will be studied in the following subsections. The first will concern the dissociation parameters, and the second subsections, the source term. The effect of the trapping is not significant on the nanocavity, but it is necessary for the SIA loops. The results are given in Supplementary Section S7 of the Supplementary Material.

5.1 Sensitivity due to nanocavity dissociation

Figure 9A shows density and size as a function of temperature obtained with the 12 conditions taking either the *up* or the *low* diffusion parameter set and one of the three *ref*, *up*, or *low* dissociation parameter sets. Three cases with the *diff no* parameter set are also shown on these figures. Note that, on these figures, the optimum *density* and *size* are the likelihood curves. One sees that, in absence of diffusion when nanocavities can only dissociate, it is not possible to correctly reproduce the experimental densities and size at the end of the irradiation, while, during the annealing stages, only the size is correct above 1,100 K. This agrees with the domain *B*, where the dissociation starts to compete with the diffusion process. These new simulations confirm that, with the current data, we cannot determine which process dominates in domain *B*. Next, we see that dissociation has no effect with the *low* diffusion model, for which the diffusion coefficients become large at low temperature. On the contrary, there is

TABLE 1 List of parameter sets for sensitivity analysis.

Nanocavity diffusion	*diff up*	Upper solution of the multi-objective optimisation
	diff low	Lower solution of multi-objective optimization
	diff no	No diffusion for vacancy clusters larger than 5VAC
Source term	*ST ref*	With *Msh* potential
	ST up	With *JW* potential
	ST low	With *MN* potential
	ST fp	With Frenkel pair only
Defect trapping	*trap ref*	With 1/200 of provider concentration
	trap up	With 1/50 of provider concentration
	trap low	Without trap
Nanocavity	*diss ref*	No dissociation
Dissociation	*diss up*	Upper capillarity law
	diss low	Lower capillarity law

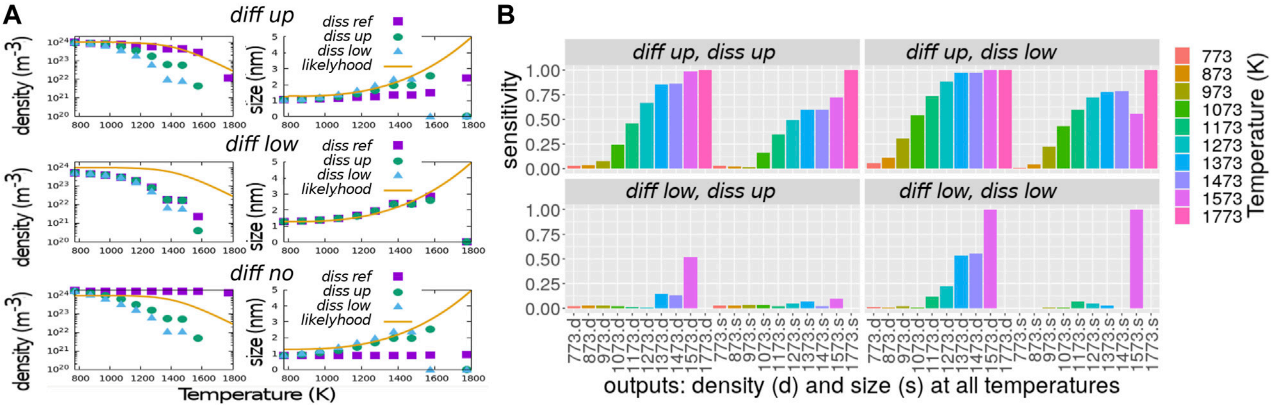

FIGURE 9
Effect of diffusion and dissociation parameter sets. **(A)** *density* and *size* of the nanocavities as a function of temperature for the nine cases obtained combining *no*, *up*, and *low* diffusion parameters and *no*, *up*, and *low* dissociation parameters. **(B)** Sensitivities calculated using Eq. 6 on the outputs of the six cases.

a visible impact of dissociation with the *up* diffusion parameter set to the temperature range of domains *B* and *C*. This is because, in the case of diffusion *low*, the dissociation will never be effective because all nanocavities diffuse, interact, and disappear at lower temperatures than that necessary to observe dissociation. On the contrary, with the *up* diffusion parameter set, the disappearance of nanocavities by dissociation before they are set into motion disagrees with the observed densities.

The sensitivities calculated with Eq. 6 are illustrated by bars on Figure 9B. The sensitivities above 0.5 correspond to the cases described in the previous paragraph. Our equation for the sensitivity is another way of determining the domains *A*, *B*, and *C*. The uncertainty on the dissociation, characterised by the difference between the *up* and *low* dissociation, leads to a shift of around 100 K of the limit between *A* and *B*.

5.2 Sensitivity due to the source term

The sensitivities obtained by varying the source term parameter sets underline a significant effect of *ST low* above 1,300 K with both *up* and *low* diffusion (see Supplementary Figure S11 of the Supplementary Material). This source term is the one obtained using the MD cascades simulated with the *MNs* potential. The reason of this sensibility is due to the fact that 99% of the defect clusters, with the *MNs* potential, are smaller than 4VAC (see 1% quantiles in Supplementary Table S1 of the Supplementary Material) for all energies. These are highly mobile defects. The first consequence is that this increases the amount of recombination with SIA defects during the irradiation, thus reducing the total number of remaining vacancies. The second consequence is that the nanocavities created are less numerous and smaller than the other

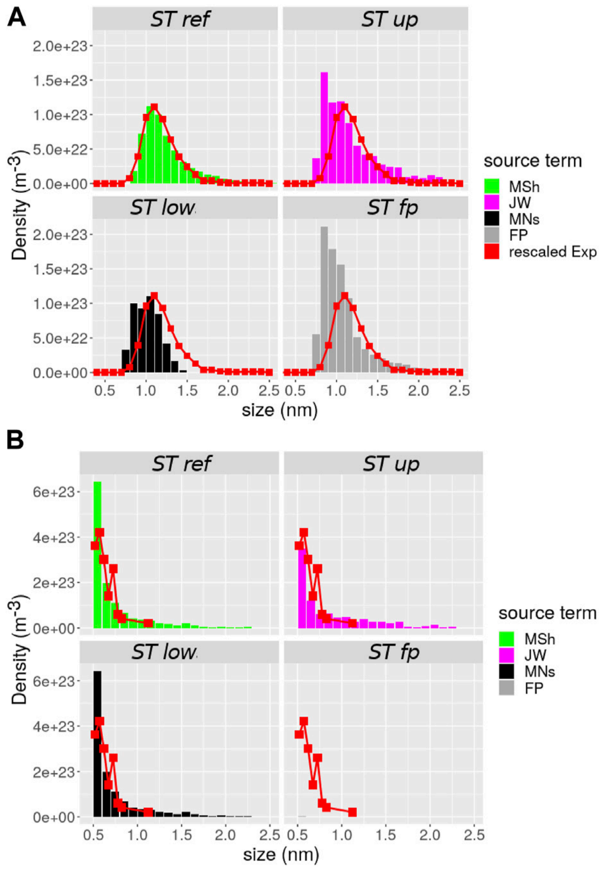

FIGURE 10
Nanocavity size histograms obtained with the different source term parameter sets at 773 K **(A)** and 300 K **(B)**. The corresponding experimental results are in red and had to be rescaled.

source terms, so they cannot grow into large nanocavities during the annealing sequences.

Figure 10A shows the nanocavity size histograms at the end of the irradiation obtained with the different source terms (and the *low* diffusion parameter set). It is evident that *MNs* gives a symmetrical histogram shifted towards smaller nanocavities than the other source terms *ST ref* and *ST up*. The source term made of Frenkel pairs gives the most asymmetrical histogram. On these plots, the red curve represents the experimental results, and there is good agreement with the *ref* source term obtained using the *MSh* potential.

To confirm the sensitivity of our model to the source term, irradiation at a lower temperature of 300 K was simulated and compared to the corresponding experimental results. The size histograms are plotted in Figure 10B. At this temperature, the vacancy defects do not diffuse, and visible nanocavities are created directly within the cascades. Consequently, the size histograms at the end of irradiation are similar to that of the source term (Figure 6). Most vacancy defects are smaller than 0.5 nm and cannot be seen under the microscope. Furthermore, comparing the visible nanocavities obtained with the different empirical potential and in experimental data cannot help demonstrate an effect of the empirical potential unlike that seen with irradiation at 773 K. However, with irradiation at 300 K, one sees that the *fp* source term gives a size histogram which strongly disagrees with the experimental observations as it does not include nanocavities in the source term.

6 Discussion

Exploration by MD of the elementary events involved in the diffusion of nanocavities highlights the role of creating the pair of surface defects, detrapping ad-atom from a nanocavity vertex, and forming a cluster of surface vacancies. The fast surface diffusion of the ad-atom compared to the vacancy agrees with the migration energies calculated by DFT on (110) surface (Hao et al., 2020). It can be explained by the smaller coordination number of the ad-atom compared to the surface vacancy, which has an impact on the strength of the binding of the defect with the surface along its migration path.

The main elements of discussion of the experimental results are in Autissier et al. (2023). We simply issue a reminder here that the saw-tooth variation in the experimental results is attributed to the use of manual and automatic counting, the variation of the sample transparency, and maybe of the sample composition. The characterisation of the dislocation loops requires more work because of the different orientations they can adopt, which requires many images and the absence of automatic counting. This will be achieved and included in the future model development. This should help build evidence of the role of impurities, for which many calculations have been made, because they are necessary to trap loops at high temperature. The current model does not reproduce the density and mean size of loops at the end of irradiation. However, our results agree with the experimental observation that the loops progressively disappear when temperature increases and are not visible above 1,200 K.

Our OKMC model has already shown its ability to reproduce and explain experimental results (De Backer et al., 2012). Its limitations are known and can save computing time. We neglect the long-range elastic interaction between defects (Mason et al., 2018; Mason et al., 2019) which causes the formation of rafts of dislocation loops or the trapping of loops in ultra-pure tungsten. Here, we consider the main source of trapping to be the impurities and we do not try to model the raft formation. Our method of modelling the primary damage created by high energy ions by combining the BCA and the MD databases does not account for the possible interaction between sub-cascades (De Backer et al., 2018). We observed that our model was able to correctly reproduce the experimentally observed size histogram at the end of the irradiation. However, the simulated density was, in that case, twice smaller than that observed. This can be explained by the fact that MD cascades calculated in the perfect bulk (i.e., our database of cascades) produce smaller defects than cascades calculated near the surface, as shown in Si (Tarus et al., 1998) and Fe (Aliaga et al., 2015).

Elements of the discussion of the multi-objective optimisation which leads to the *up* and *low* diffusion parameter sets are in De Backer et al. (2023). It is important to note that we cannot simultaneously reproduce the observed density and size of nanocavities, probably because there is, in the experiment, a source of vacancies not included in the model. We believe that these vacancies are created at the interface between the sample and the native oxide layer when it grows. The sample thickness is small (33 nm). These vacancies could diffuse in the bulk and be a non-negligible quantity as one atomic layer corresponds to 1% of the sample thickness. The growth of the oxide layer is well-known and complex, as explained in research analysing the corrosion mechanisms of zirconium alloys (Lin et al., 2020). Without data in W, this process would introduce many unknown parameters in the optimisation process, and it is thus outside of the scope of this work.

Finally, we consider that the *up* and *low* diffusion parameter sets are the upper and lower limits of the uncertainties on the diffusion results of the current experimental data and the model as it stands. Our results fill the gap between what is known regarding the diffusion of small vacancy clusters, the migration energy of which can be calculated, and the diffusion of large nanocavities for which the classical surface theory is valid. The analysis sensitivity indicates that our results could be different if the source term changes but not with a change of the trapping model. Interestingly, sensitivity associated with the nanocavity dissociation reveals three domains of size and temperature where the competition with diffusion is different. In *A*, the dominating mechanism is the diffusion of the small clusters. In *B*, the unknowns of the diffusion of the nanocavities are too large to give a definitive answer but they are likely in competition. In *C*, dissociation limits the possibility of finding large nanocavities at temperatures larger than 1,200 K without the presence of stabilising interfaces, impurities, or other extended defects.

7 Conclusion

We demonstrated that including the diffusion of nanocavities in our OKMC model is necessary for interpreting the growth of nanocavities observed experimentally in tungsten. A multi-objective optimisation gave the upper and lower limits of the diffusion temperature of nanocavities as a function of their size. This required two novelties: a model of the primary damage of high-energy ions beyond the typical *dpa* and new DFT data on the trapping of point defects by impurities. We have highlighted the variety of elementary events involved in the nanocavity diffusion, and a size threshold of between 1.2 nm (65VAC) and 1.9 nm (175VAC) where the cavity surface is large enough to trap surface vacancies and form a ledge. A sensitivity analysis reveals the importance of the empirical potential chosen to model MD cascades and the source term, and the domains of size (related to temperature) where there is competition with the nanocavity dissociation.

Data availability statement

The original contributions presented in the study are included in the article/Supplementary Material; further inquiries can be directed to the corresponding author.

Author contributions

Category 1, conception and design of the global study: AD, CB, CD, and M-FB; mathematical formulation: AD, ADN, CB, and CD; acquisition of experimental data: EA, CG, FH, and M-FB; acquisition of OKMC data: AD and AS; acquisition of MD data: EH; acquisition of the displacement cascade database and DFT data: CD and CB; analysis and interpretation of experimental data: EA, CG, FH, CD, CB, and M-FB; analysis and interpretation of simulation data: AD, AS, EH, ADN, CD, and CB; Category 2, drafting the manuscript: AD, AS, EH, CD, CB, and M-FB; critical revision of the manuscript for important intellectual content: AD, AS, EH, ADN, CD, CB, and M-FB. Category 3, funding acquisition: CB and M-FB. All authors contributed to the article and approved the submitted version.

Funding

This work was performed within the framework of the EUROfusion Consortium and has received funding from the Euratom research and training program 2014–2018 and 2019–2020 under grant agreement No. 633053. This work was also partly supported by the European project SOTERIA (661913) and contributed to the Joint Program on Nuclear Materials (JPNM) of the European Energy Research Alliance (EERA). The project leading to this publication received funding from the Excellence Initiative of Aix-Marseille University—A*MIDEX, a French Investissements d'Avenir program, as well as from the French National Research Agency (grant no. ANR-18-CE05-0012).

Acknowledgments

Centre de Calcul Intensif d'Aix-Marseille is acknowledged for granting access to its high-performance computing resources. The ICMN laboratory (Orléans, France) is acknowledged for access to the CM20 microscope. The authors thank OVITO developers as images and some analysis were performed with it (Stukowski, 2009).

Conflict of interest

The authors declare that the research was conducted in the absence of any commercial or financial relationships that could be construed as a potential conflict of interest.

Publisher's note

Author disclaimer

The views and opinions expressed herein do not necessarily reflect those of the European Commission.

Supplementary material

The Supplementary Material for this article can be found online at: https://www.frontiersin.org/articles/10.3389/fnuen.2023.1240995/full#supplementary-material

References

Aliaga, M. J., Schäublin, R., Löffler, J. F., and Caturla, M. J. (2015). Surface-induced vacancy loops and damage dispersion in irradiated Fe thin films. *Acta Mater.* 101, 22–30. doi:10.1016/j.actamat.2015.08.063

Autissier, E., Farah, F., Genevois Mazellier, C., Decamps, B., Schaublin, R., and Barthe, M.-F. (2023). *Cavity evolution as a function of temperature in self irradiated tungsten.*

Becquart, C. S., De Backer, A., and Domain, C. (2019). "Atomistic modeling of radiation damage in metallic alloys," in *Handbook of mechanics of materials*. Editors S. Schmauder, C.-S. Chen, K. K. Chawla, N. Chawla, W. Chen, and Y. Kagawa (Singapore: Springer Singapore), 673–701.

Becquart, C. S., De Backer, A., Olsson, P., and Domain, C. (2021). Modelling the primary damage in fe and w: influence of the short range interactions on the cascade properties: part 1 – energy transfer. *J. Nucl. Mater.* 547, 152816. doi:10.1016/j.jnucmat.2021.152816

Becquart, C. S., Decker, K. M., Domain, C., Ruste, J., Souffez, Y., Turbatte, J. C., et al. (1997). Massively parallel molecular dynamics simulations with eam potentials. *Radiat. Eff. Defects Solids* 142, 9–21. doi:10.1080/10420159708211592

Becquart, C. S., and Domain, C. (2009). An object Kinetic Monte Carlo Simulation of the dynamics of helium and point defects in tungsten. *J. Nucl. Mater.* 385, 223–227. doi:10.1016/j.jnucmat.2008.11.027

Becquart, C. S., Domain, C., Sarkar, U., DeBacker, A., and Hou, M. (2010). Microstructural evolution of irradiated tungsten: *ab initio* parameterisation of an OKMC model. *J. Nucl. Mater.* 403, 75–88. doi:10.1016/j.jnucmat.2010.06.003

Björkas, C., Nordlund, K., and Dudarev, S. (2009). Modelling radiation effects using the ab-initio based tungsten and vanadium potentials. *Nucl. Instrum. Methods Phys. Res. Sect. B Beam Interact. Mater. Atoms* 267, 3204–3208. doi:10.1016/j.nimb.2009.06.123

Byggmästar, J., Hamedani, A., Nordlund, K., and Djurabekova, F. (2019). Machine-learning interatomic potential for radiation damage and defects in tungsten. *Phys. Rev. B* 100, 144105. doi:10.1103/physrevb.100.144105

Castin, N., Bakaev, A., Bonny, G., Sand, A. E., Malerba, L., and Terentyev, D. (2017). On the onset of void swelling in pure tungsten under neutron irradiation: an object kinetic Monte Carlo approach. *J. Nucl. Mater.* 493, 280–293. doi:10.1016/j.jnucmat.2017.06.008

Caturla, M. J. (2019). Object kinetic Monte Carlo methods applied to modeling radiation effects in materials. *Comput. Mater. Sci.* 156, 452–459. doi:10.1016/j.commatsci.2018.05.024

De Backer, A., Lhuillier, P. E., Becquart, C. S., and Barthe, M. F. (2012). Modelling of the implantation and the annealing stages of 800keV 3He implanted tungsten: formation of nanovoids in the near surface region. *J. Nucl. Mater.* 429, 78–91. doi:10.1016/j.jnucmat.2012.05.024

De Backer, A., Sand, A. E., Nordlund, K., Luneville, L., Simeone, D., and Dudarev, S. L. (2016). Subcascade formation and defect cluster size scaling in high-energy collision events in metals. *EPL Europhys. Lett.* 115, 26001. doi:10.1209/0295-5075/115/26001

De Backer, A., Domain, C., Becquart, C. S., Luneville, L., Simeone, D., Sand, A. E., et al. (2018). A model of defect cluster creation in fragmented cascades in metals based on morphological analysis. *J. Phys. Condens. Matter* 30, 405701. doi:10.1088/1361-648x/aadb4e

De Backer, A., Becquart, C. S., Olsson, P., and Domain, C. (2021). Modelling the primary damage in fe and w: influence of the short-range interactions on the cascade properties: part 2 – multivariate multiple linear regression analysis of displacement cascades. *J. Nucl. Mater.* 549, 152887. doi:10.1016/j.jnucmat.2021.152887

De Backer, A., Souidi, A., Hodille, E. A., Autissier, E., Genevois, C., Haddad, F., et al. (2022). Multiobjective optimization of the nanocavities diffusion in irradiated metals. *Phys. Sci. Forum* 5, 41. doi:10.3390/psf2022005041

De Backer, A., Souidi, A., Hodille, E. A., Autissier, E., Genevois, C., Haddad, F., et al. (2023). Multi-objective optimization of the nanocavity growth model in irradiated metals. *Submitted.*

Finnis, M. W., and Sinclair, J. E. (1984). A simple empirical n-body potential for transition metals. *Philos. Mag. A* 50, 45–55. doi:10.1080/01418618408244210

Gilbert, M. R., Sublet, J.-C., and Dudarev, S. L. (2017). Spatial heterogeneity of tungsten transmutation in a fusion device. *Nucl. Fusion* 57, 044002. doi:10.1088/1741-4326/aa5e2e

Goodhew, P. J., Tyler, S. K., and Kelly, A. (1981). Helium bubble behaviour in b. c. c. metals below 0.65Tm. *Proc. R. Soc. Lond. A. Math. Phys. Sci.* 377, 151–184. doi:10.1098/rspa.1981.0120

Hao, J., Jin, S., Lu, G.-H., and Xu, H. (2020). Migration energy barriers and diffusion anisotropy of point defects on tungsten surfaces. *Comput. Mater. Sci.* 184, 109893. doi:10.1016/j.commatsci.2020.109893

Hasanzadeh, S., Schäublin, R., Décamps, B., Rousson, V., Autissier, E., Barthe, M. F., et al. (2018). Three-dimensional scanning transmission electron microscopy of dislocation loops in tungsten. *Micron* 113, 24–33. doi:10.1016/j.micron.2018.05.010

Hwang, T., Hasegawa, A., Tomura, K., Ebisawa, N., Toyama, T., Nagai, Y., et al. (2018). Effect of neutron irradiation on rhenium cluster formation in tungsten and tungsten-rhenium alloys. *J. Nucl. Mater.* 507, 78–86. doi:10.1016/j.jnucmat.2018.04.031

Jansson, V., and Malerba, L. (2013). Simulation of the nanostructure evolution under irradiation in Fe–C alloys. *J. Nucl. Mater.* 443, 274–285. doi:10.1016/j.jnucmat.2013.07.046

Juslin, N., and Wirth, B. (2013). Interatomic potentials for simulation of he bubble formation in w. *J. Nucl. Mater.* 432, 61–66. doi:10.1016/j.jnucmat.2012.07.023

Kong, L. T., and Lewis, L. J. (2006). Transition state theory of the preexponential factors for self-diffusion on cu, ag, and ni surfaces. *Phys. Rev. B* 74, 073412. doi:10.1103/physrevb.74.073412

Lin, C., Ruan, H., and Shi, S.-Q. (2020). Mechanical–chemical coupling phase-field modeling for inhomogeneous oxidation of zirconium induced by stress–oxidation interaction. *npj Mater Degrad.* 4, 22. doi:10.1038/s41529-020-00125-6

Lindhard, J., Scharff, M., and Schioett, H. E. (1963). Range concepts and heavy ion ranges (notes on atomic collisions, ii). *Kgl. Dan. Vidensk. Selsk. Mat. Fys. Medd.* 33.

Lloyd, M. J., Abernethy, R. G., Gilbert, M. R., Griffiths, I., Bagot, P. A., Nguyen-Manh, D., et al. (2019). Decoration of voids with rhenium and osmium transmutation products in neutron irradiated single crystal tungsten. *Scr. Mater.* 173, 96–100. doi:10.1016/j.scriptamat.2019.07.036

Malerba, L., Anento, N., Balbuena, J., Becquart, C., Castin, N., Caturla, M., et al. (2021). Physical mechanisms and parameters for models of microstructure evolution under irradiation in fe alloys – part i: pure fe. *Nucl. Mater. Energy* 29, 101069. doi:10.1016/j.nme.2021.101069

Marinica, M.-C., Ventelon, L., Gilbert, M. R., Proville, L., Dudarev, S. L., Marian, J., et al. (2013). Interatomic potentials for modelling radiation defects and dislocations in tungsten. *J. Phys. Condens. Matter* 25, 395502. doi:10.1088/0953-8984/25/39/395502

Mason, D. R., Nguyen-Manh, D., and Becquart, C. S. (2017). An empirical potential for simulating vacancy clusters in tungsten. *J. Phys. Condens. Matter* 29, 505501. doi:10.1088/1361-648x/aa9776

Mason, D. R., Sand, A. E., and Dudarev, S. L. (2019). Atomistic-object kinetic Monte Carlo simulations of irradiation damage in tungsten. *Model. Simul. Mater. Sci. Eng.* 27, 055003. doi:10.1088/1361-651x/ab1a1e

Mason, D. R., Sand, A. E., Yi, X., and Dudarev, S. L. (2018). Direct observation of the spatial distribution of primary cascade damage in tungsten. *Acta Mater.* 144, 905–917. doi:10.1016/j.actamat.2017.10.031

Nichols, F. A. (1969). Kinetics of diffusional motion of pores in solids: a review. *J. Nucl. Mater.* 30, 143–165. doi:10.1016/0022-3115(69)90176-7

Nordlund, K., Zinkle, S. J., Sand, A. E., Granberg, F., Averback, R. S., Stoller, R., et al. (2018). Improving atomic displacement and replacement calculations with physically realistic damage models. *Nat. Commun.* 9, 1084. doi:10.1038/s41467-018-03415-5

Pannier, B. (2017). *Towards the prediction of microstructure evolution under irradiation of model ferritic alloys with an hybrid AKMC-OKMC approach.*

Perez, D., Sandoval, L., Blondel, S., Wirth, B. D., Uberuaga, B. P., and Voter, A. F. (2017). The mobility of small vacancy/helium complexes in tungsten and its impact on retention in fusion-relevant conditions. *Sci. Rep.* 7, 2522. doi:10.1038/s41598-017-02428-2

Plimpton, S. (1995). Fast parallel algorithms for short-range molecular dynamics. *J. Comput. Phys.* 117, 1–19. doi:10.1006/jcph.1995.1039

Sand, A. E., Dequeker, J., Becquart, C. S., Domain, C., and Nordlund, K. (2016). Non-equilibrium properties of interatomic potentials in cascade simulations in tungsten. *J. Nucl. Mater.* 470, 119–127. doi:10.1016/j.jnucmat.2015.12.012

Stoller, R. E., Toloczko, M. B., Was, G. S., Certain, A. G., Dwaraknath, S., and Garner, F. A. (2013). On the use of SRIM for computing radiation damage exposure. *Nucl. Instrum. Methods Phys. Res. Sect. B Beam Interact. Mater. Atoms* 310, 75–80. doi:10.1016/j.nimb.2013.05.008

Stukowski, A. (2009). Visualization and analysis of atomistic simulation data with OVITO–the Open Visualization Tool. *Model. Simul. Mater. Sci. Eng.* 18, 015012. doi:10.1088/0965-0393/18/1/015012

Sublet, J. C., Bondarenko, I. P., Bonny, G., Conlin, J. L., Gilbert, M. R., Greenwood, L. R., et al. (2019). Neutron-induced damage simulations: beyond defect production cross-section, displacement per atom and iron-based metrics. *Eur. Phys. J. Plus* 134, 350. doi:10.1140/epjp/i2019-12758-y

Tarus, J., Nordlund, K., Kuronen, A., and Keinonen, J. (1998). Effect of surface on defect creation by self-ion bombardment of si(001). *Phys. Rev. B* 58, 9907–9915. doi:10.1103/physrevb.58.9907

Vitos, L., Ruban, A. V., Skriver, H. L., and Kollár, J. (1998). The surface energy of metals. *Surf. Sci.* 411, 186–202. doi:10.1016/s0039-6028(98)00363-x

Zell, V., Trinkaus, H., and Schroeder, H. (1994). A simulation study of the migration and coalescence of gas bubbles in metals. *J. Nucl. Mater.* 212-215, 320–324. doi:10.1016/0022-3115(94)90079-5

Ziegler, J. F., Ziegler, M. D., and Biersack, J. P. (2010). SRIM – the stopping and range of ions in matter (2010). *Nucl. Instrum. Methods Phys. Res. Sect. B Beam Interact. Mater. Atoms* 268, 1818–1823. doi:10.1016/j.nimb.2010.02.091

frontiers | Frontiers in Nuclear Engineering

TYPE Original Research
PUBLISHED 23 November 2023
DOI 10.3389/fnuen.2023.1294583

Validation of time-dependent shift using the pulsed sphere benchmarks

Camille J. Palmer[1]*, Jordan Northrop[1], Todd S. Palmer[1] and Aaron J. Reynolds[2]

[1]School of Nuclear Science and Engineering, Oregon State University, Corvallis, OR, United States, [2]TerraPower LLC, Bellevue, WA, United States

OPEN ACCESS

EDITED BY
Charlotte Becquart,
Centrale Lille Institut, ENSCL, Laboratoire UMET, France

REVIEWED BY
Mark David DeHart,
Idaho National Laboratory (DOE), United States
Qingquan Pan,
Shanghai Jiao Tong University, China

*CORRESPONDENCE
Camille J. Palmer,
✉ camille.palmer@oregonstate.edu

RECEIVED 15 September 2023
ACCEPTED 06 November 2023
PUBLISHED 23 November 2023

CITATION
Palmer CJ, Northrop J, Palmer TS and Reynolds AJ (2023), Validation of time-dependent shift using the pulsed sphere benchmarks.
Front. Nucl. Eng. 2:1294583.
doi: 10.3389/fnuen.2023.1294583

The detailed behavior of neutrons in a rapidly changing time-dependent physical system is a challenging computational physics problem, particularly when using Monte Carlo methods on heterogeneous high-performance computing architectures. A small number of algorithms and code implementations have been shown to be performant for time-independent (fixed source and k-eigenvalue) Monte Carlo, and there are existing simulation tools that successfully solve the time-dependent Monte Carlo problem on smaller computing platforms. To bridge this gap, a time-dependent version of ORNL's Shift code has been recently developed. Shift's history-based algorithm on CPUs, and its event-based algorithm on GPUs, have both been observed to scale well to very large numbers of processors, which motivated the extension of this code to solve time-dependent problems. The validation of this new capability requires a comparison with time-dependent neutron experiments. Lawrence Livermore National Laboratory's (LLNL) pulsed sphere benchmark experiments were simulated in Shift to validate both the time-independent as well as new time-dependent features recently incorporated into Shift. A suite of pulsed-sphere models was simulated using Shift and compared to the available experimental data and simulations with MCNP. Overall results indicate that Shift accurately simulates the pulsed sphere benchmarks, and that the new time-dependent modifications of Shift are working as intended. Validated exascale neutron transport codes are essential for a wide variety of future multiphysics applications.

KEYWORDS

Monte Carlo, neutron transport, exascale computing, benchmark evaluation, code validation

1 Introduction

As computing hardware has evolved through the digital age from serial CPU execution to distributed memory, massively parallel, heterogeneous architecture machines, software has often had to be refactored or completely rewritten with different algorithms to ensure that computation efficiency does not suffer. Most recently, the push toward exascale computing Evans et al. (2022) involving machines with millions of cores, mixing CPUs and graphical processing units (GPUs), and a hierarchy of memories with various access speeds, has created significant challenges for simulation across a wide variety of disciplines.

One particularly exacting example is Monte Carlo radiation transport. Simulation tools for the transport of radiation using the Monte Carlo method are ubiquitous in science and engineering fields, including nuclear reactor physics, radiation oncology, high energy density physics, and nuclear criticality safety. These algorithms involve the use of pseudo-random numbers to *sample* from probability distributions that describe the interaction of particles with matter, the *tracking* of these particles throughout the defined heterogeneous spatial domain, and the *tallying* of quantities of interest to the modeler. One attractive feature of Monte Carlo algorithms is that they often can operate without discretizations in the particle phase space—direction, energy, space, and time; this means that convergence of the Monte Carlo solution typically is a function of the number of particle histories (N) used, not any sort of grid imposed on the various independent variables in the simulation. One drawback, however, is that the convergence as a function of particle histories obeys the Central Limit Theorem, which states that mean quantities of interest approach the true mean at a rate that depends on $N^{1/2}$. Often, this means that Monte Carlo methods can be quite computationally expensive.

In the majority of applications, the time scale of the radiation motion is quite small compared to time scale of other processes, and steady-state transport simulations are sufficient. However, there are some specific use cases—ultra fast reactivity excursions in nuclear reactors or high energy density experiments involving nuclear fusion, for example,—where the detailed time dependence of the particle population is needed. Over the years, there have been time-dependent neutron transport codes developed (Buck and Hall, 1999, TART; Cullen, 2000, Mercury; Procassini et al., 2004; MCATK; Shim et al., 2012; Leppänen, 2013; Adams et al., 2015; McCARD), some were optimized for execution on older machines, and others employ approximate treatments of time-dependence to make larger problems solveable in reasonable wall clock times.

Recently, true time-dependence [via census particles and population control Reynolds and Palmer (2022); Reynolds et al. (2022)] has been incorporated in the Shift code originated at Oak Ridge National Laboratory (ORNL). Shift is a general-purpose massively-parallel Monte Carlo radiation transport code with a primary design objective to provide efficient parallel calculations on both CPUs and GPUs on computing scales from laptops to supercomputers. Due to limitations in the CUDA language used to run Shift's code on GPUs, the GPU codebase has been maintained separately from the CPU codebase Hamilton and Evans (2019).

To ensure that Monte Carlo codes are ready for production use, they must undergo both *verification* and *validation*. Verification is the process of determining whether a piece of software is solving a specific set of equations correctly. Typically, verification involves defining a problem with an analytic or manufactured solution and testing the software to make sure it converges to the proper result at the predicted rate. Our verification work has been described in previous publications Reynolds and Palmer (2022); Reynolds et al. (2022). Validation is the process of determining whether a particular simulation tool is solving the correct equations. Comparison with data obtained from experiments is essential for validation. Robust suites of benchmarks exist for nuclear criticality Briggs et al. (2003), and nuclear reactor physics Briggs (2006) problems, but the vast majority of these experiments cannot be used to evaluate the algorithmic features of truly time-dependent Monte Carlo codes.

A number of validation problems have already been simulated with Shift, but none of them were time-dependent problems since Shift did not have time-dependent features Peplow et al. (2019). To validate the new time-dependent features of Shift, we have employed the pulsed sphere benchmarks as they are relatively simple problems that have been used for many validation studies in the past, and incorporate results of a time-dependent nature Miller et al. (2018); Whalen et al. (1992); Procassini and McKinley (2010). The novelty and significance of the work in this paper is two-fold. We present the first validation of the Shift Monte Carlo neutron transport code with the pulsed sphere benchmarks, and we provide comparisons of new, truly time-dependent simulations of the pulsed-sphere benchmarks with time-independent simulations that use a time-of-flight approximation to convert spectral detector responses to time bins. Comparisons of Shift results with those from the widely used MCNP Kulesza et al. (2022) code.

Producing time-dependent results from a time-independent version of Shift requires some approximations, but these results provide a useful baseline for the validation of time-dependent Shift since any discrepancies can be attributed to either existing issues in Shift or the new features.

2 Materials and methods

2.1 Pulsed spheres

The pulsed sphere benchmarks are a series of experiments performed at Lawrence Livermore National Laboratory (LLNL) in the 1960s–1990s. These benchmarks were specifically designed with the goal of validating neutron transport codes and assessing nuclear cross section data Wong et al. (1972). The pulsed-sphere benchmarks are valuable in evaluating time-dependent features and as they measure neutron time of arrival.

The pulsed spheres consist of four main sections: the target assembly, the sphere (of a given material), the experiment pit, and the detector. A simplified version of the setup is shown in Figure 1.

The target assembly is placed into a truncated conical insert in the sphere, and a beam of 400 keV deuterons is directed onto a small tritium-laced titanium target near the center. The result is a $T(d,n)^4He$ reaction that produces ~14.1 MeV neutrons, with a

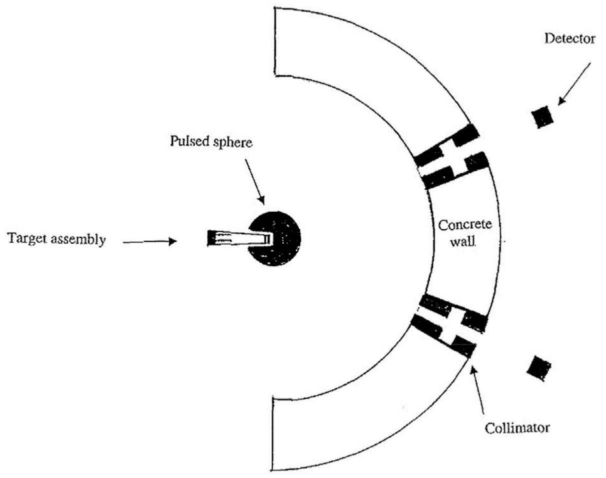

FIGURE 1
Simplified not-to-scale geometry of the setup Marchetti and Hedstrom (1998).

slightly angularly-dependent energy distribution. The experiments measured the time of flight neutron flux at different angles from the incoming deuteron beam. The deuteron beam operated such that a short pulse of neutrons was generated, typically ranging from a full-width half maximum of 2–10 ns depending on the experiment.

Various materials and sphere sizes were measured over the course of the experimental campaigns. Certain fissile and liquid materials were housed in shells of steel or other metals. Other solid materials were assembled as shells with the goal of optimizing material while accommodating different-sized experiments. Scattering, absorption, and sometimes fission reactions in the spheres drive the time-of-flight results measured at the detector. A majority of the spherical setups ranged from 5 to 20 cm, although a couple larger systems were measured as well.

The experiment pit consists of an aluminum floor and concrete walls. The walls are a significant aspect of the simulations as collimators penetrate the walls at specific angles that lead to detectors in separate rooms. This arrangement isolates the detector from neutrons that do not originate directly from the sphere. The flight path from the center of the sphere to the detector ranged from about 750 to 1,000 cm depending on the beamline. The fact that the flight path is significantly larger than the radii of the spheres is important to resolve neutron energy from the time-of-flight measurements. While not explicitly stated if the flight path was measured to the front, middle, or end of the 5 cm detector, previous work indicates that uncertainty is negligible to the results Goricanec et al. (2017). Three different beamlines named 26°, 30°, and 120° were used. The actual angles of interest for the 30° and 120° beamlines were 38.89°, and 116.71° respectively since they were named after the angle with respect to the 26° beamline instead of the axis of symmetry around the incoming deuteron beam.

The detectors used in the experiments were NE213-A or Pilot-B scintillators and measured the neutron flux within each detector in 2 ns time bins. Each detector has its own efficiency curve as a function of the neutron energy, and those response curves can be easily implemented into Monte Carlo codes.

The result of interest is the time at which the neutrons reach the detector. This time-of-flight was experimentally measured in 2 ns time bins. As shown in Figure 2, there is an initial peak of uncollided neutrons that fly straight from the source to the detector, whereas neutrons that collide, slow down, and take longer to reach the detector. The absorption, scattering, and fission cross sections as well as the physical parameters of the sphere determine the behavior of the time-of-flight curve.

2.2 Modeling the pulsed spheres in Shift

An existing set of pulsed sphere models was simulated in the Monte Carlo code MCNP to provide additional comparisons for Shift. Even though MCNP does not have true time dependence, each neutron's time-of-flight can be kept track of by tallying the distance between each collision divided by the speed between those collisions. The MCNP models did not include the entire pit and collimator assemblies. Instead, the beamlines to the detector were modeled as black absorbers with a thin layer of concrete which has been shown to negligibly affect the results Goricanec et al. (2017). This also allowed MCNP to implement a ring detector to take advantage of the symmetry of the problem around the axis of the deuteron beam. A ring detector is a variant of a point detector that can provide accurate results with far fewer histories for problems with axial symmetry.

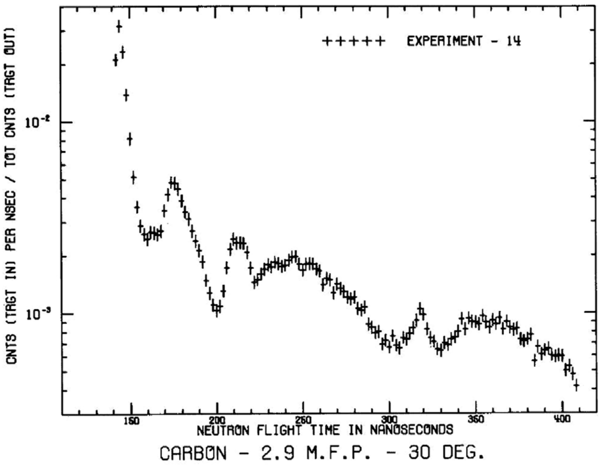

FIGURE 2
Example time-of-flight results for a 2.9 mfp carbon sphere Marchetti and Hedstrom (1998).

To model the pulsed spheres in Shift, ORNL's Lava library was used to translate a portion of the MCNP model into a form readable by the Shift solver. The Lava library ORNL (2022) was included as a package in Shift, and it can replicate the geometry, materials, and neutron source present in an MCNP input.

Tallies had to be manually defined in Shift, which led to several modeling issues that needed to be resolved. Shift does not possess next-event estimator detectors such as the point and ring detectors available in MCNP. A new cell was inserted into the Shift model to represent the detector, and a standard tracklength tally over the cell produced the estimation of the flux. At each collision in the simulation, point and ring detectors tally the probability that the next collision will occur on the point or ring which, in many cases, reduces the variance of the solution. Since Shift used a standard flux tally, it requires significantly more histories to reduce the statistical uncertainty to be on the same order as MCNP.

Neither the time-independent version of Shift nor MCNP possess features such as census particles for true time stepping. MCNP, however, does keep track of a time parameter for each neutron. Time-independent Shift does not have that capability, so the detector cannot collect the results into time bins. For steady-state Shift, the best substitute for time-binned tallies is energy-binned tallies taken at the detector, since the energy of the neutron is directly related to its velocity, and therefore the time the neutron takes to reach the detector. The energy-binned results can be compared directly to MCNP, and although an approximation is required to produced the time-binned spectrum, those results can provide a useful comparison for the time-dependent results. The relativistic

TABLE 1 Description of the spheres simulated in this work.

Material	Radius (cm)	Flight path (cm)	Detector	Pulse width (ns)
Beryllium	12.58	765.2	Pilot-B	4
Carbon	20.96	766.0	NE213-A	4
Iron	4.46	766.0	NE213-A	3
Lead	8.912	766.0	NE213-A	3
Lithium	25.41	765.2	Pilot-B	4
Nitrogen (Liquid)	55.88	765.2	Pilot-B	4
^{235}U	3.145	766.0	NE213-A	3
^{238}U	3.63	765.2	Pilot-B	4

first-flight approximation in can be used to convert the energy of the neutrons into the time-of-flight:

$$E = rme * \left(\left(\frac{1}{\sqrt{\left(1-\left((fp)^2/\left(t^2c^2\right)\right)\right)}}\right)-1\right). \qquad (1)$$

In equation 1, E is the energy of the neutron [MeV], rme is the rest mass energy of the neutron [MeV], fp is the length of the flight path to the detector [cm], t is the time of flight [ns], and c is the speed of light [cm/ns]. This approximation assumes that each neutron travels from the center of the sphere to the detector at its final energy. The assumption that all collisions happen at time 0 at the center of the sphere is only reasonable if the total flight path is significantly longer than the radius of the sphere. For the Monte Carlo codes, energy bin boundaries were defined such that the energy bins would translate to 2 ns wide time bins once

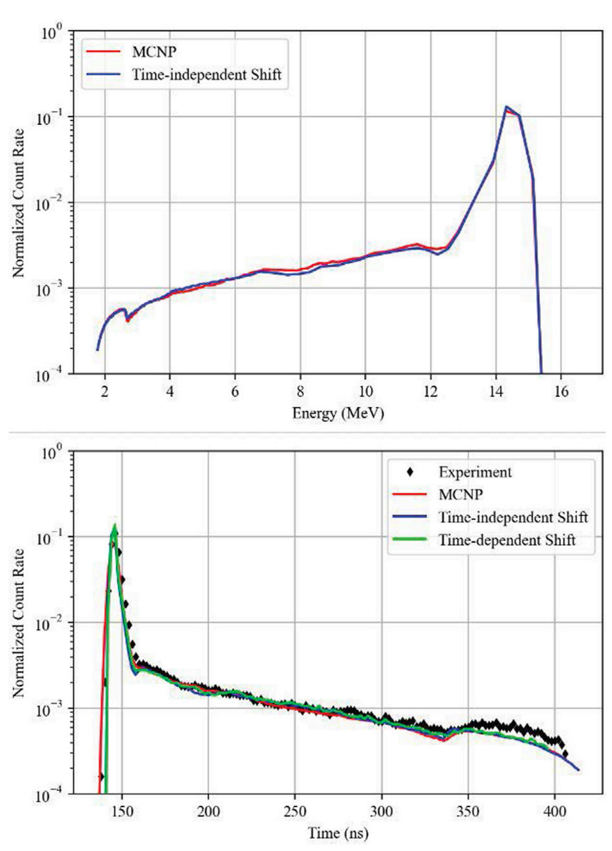

FIGURE 3
Beryllium, top: energy-binned MCNP (10^7 histories) vs. Shift (10^9 histories); bottom: comparison of time-dependent Shift (10^9 histories) with time-independent Shift (10^9 histories) and MCNP (10^7 histories).

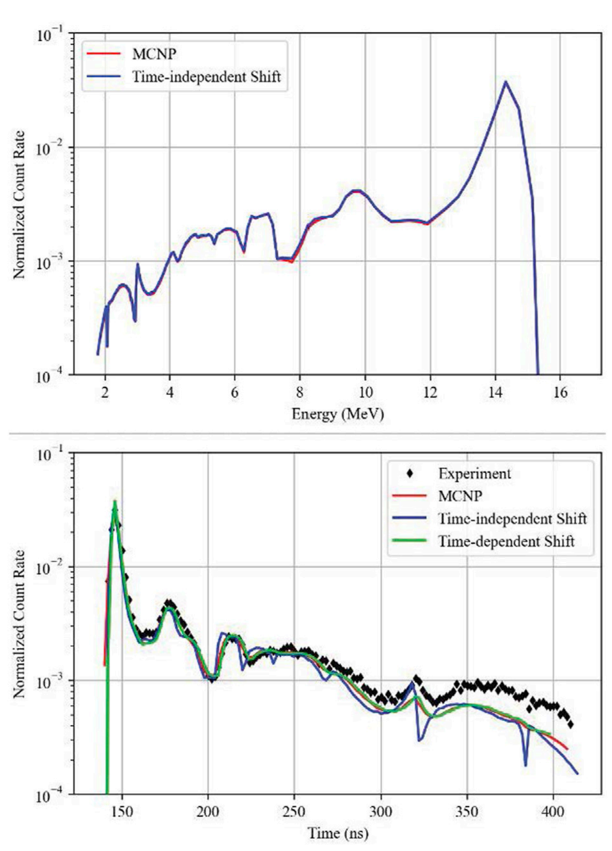

FIGURE 4
Carbon, top: energy-binned MCNP (10^7 histories) vs. Shift (10^9 histories); bottom: comparison of time-dependent Shift (10^9 histories) with time-independent Shift (10^9 histories) and MCNP (10^7 histories).

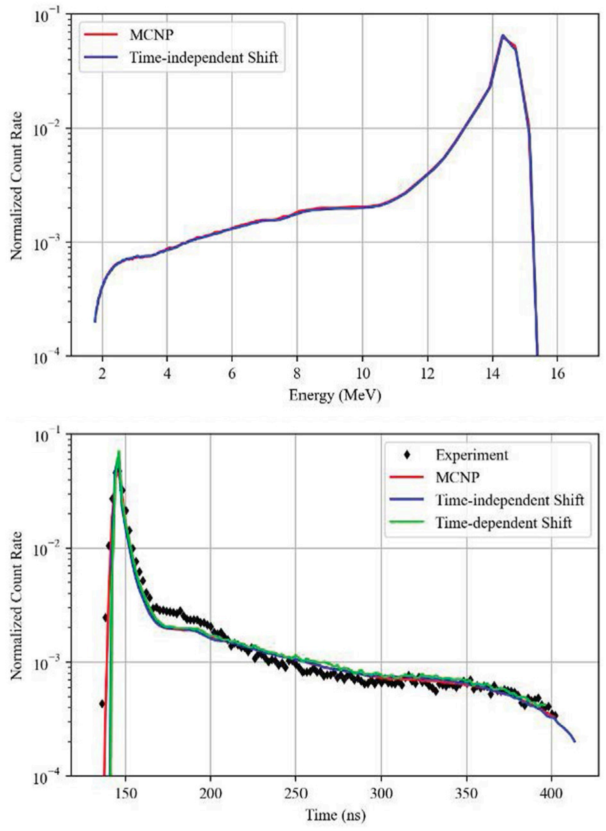

FIGURE 5
Lithium, top: energy-binned MCNP (10^7 histories) vs. Shift (10^9 histories); bottom: comparison of time-dependent Shift (10^9 histories) with time-independent Shift (10^9 histories) and MCNP (10^7 histories).

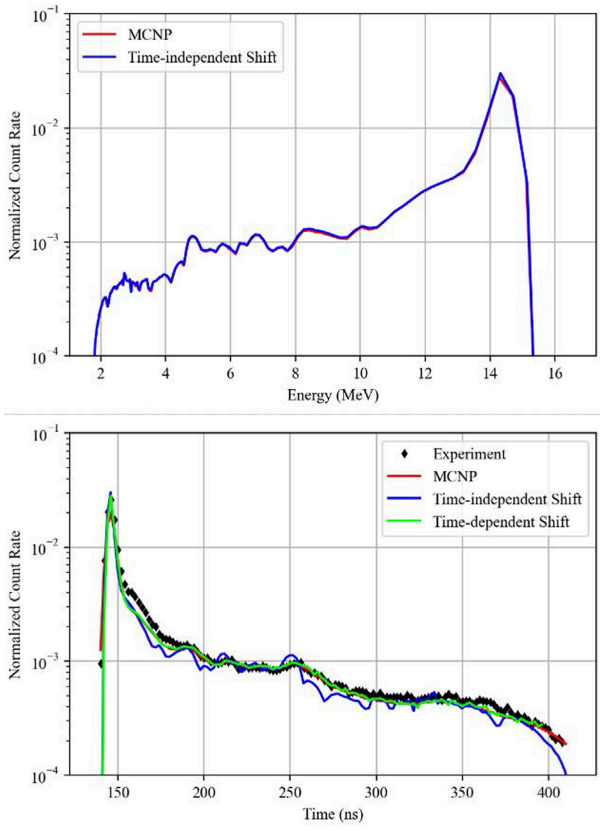

FIGURE 6
Nitrogen, top: energy-binned MCNP (10^7 histories) vs. Shift (10^9 histories); bottom: comparison of time-dependent Shift (10^9 histories) with time-independent Shift (10^9 histories) and MCNP (10^7 histories).

converted to match the experiments and time-binned results. This approximation was used to report energy-binned results for the experiments even though the tallies themselves were only time-binned.

The time-dependent version of Shift does not require such approximation and can be directly compared with MCNP results. There are algorithmic differences in how the two codes treat a time-dependent problem, but as long as the time-of-flight of each neutron is tracked properly, both codes should yield similar results. Both MCNP and time-dependent Shift calculate a time parameter for each neutron, but Shift goes further by adding time steps to the simulation. Instead of transporting neutrons or batches of neutrons to the end of their life and then going back to the beginning and transporting more like MCNP, Shift transports all particles only to the end of the next time step. Shift stores particles and their information in census when they reach the end of the time step until it is ready to begin the next step. Time steps may be of great importance to problems where intermediate solutions are of interest such as transient reactor behavior. The pulsed spheres do not exercise the full extent of transient simulation capabilities that time steps can unlock, but they do test the basic features of the time-dependent build.

All simulations in this work were performed with the ENDF/B-VII.1 nuclear data library for consistency.

Table 1 describes the pulsed sphere models that were simulated in Shift. All these simulations were performed with detectors on the 30° degree beamline. The listed pulse width is the full width half maximum of the source pulse.

3 Results

3.1 Direct comparison to MCNP

The best comparison of time-independent Shift to other codes is the energy-binned detector results, which are shown below in the top half of Figures 3–10. These results are directly comparable since no approximation of the results themselves needs to be made. The energy bin boundaries for both simulations were based on applying the first flight equation to the 2 ns time bins so that the energy-binned tallies could be converted neatly into 2 ns time bins for comparisons. Consequentially, there are limited numbers of wider energy bins at higher energies and denser bins at lower energies. Since Shift is running the exact same problem as MCNP besides the detector setup, the results should match fairly well.

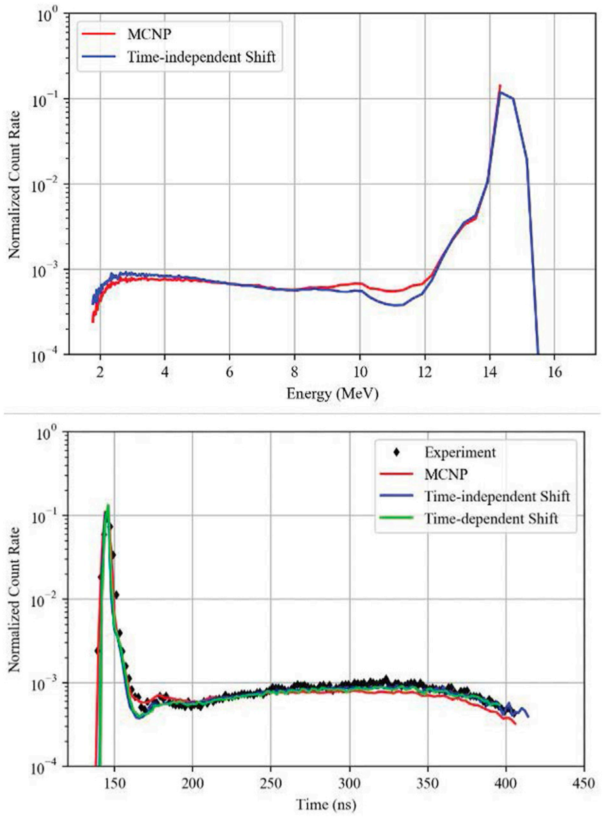

FIGURE 7
Iron, top: nergy-binned MCNP (10^7 histories) vs. Shift (10^9 histories); bottom: comparison of time-dependent Shift (10^9 histories) with time-independent Shift (10^9 histories) and MCNP (10^7 histories).

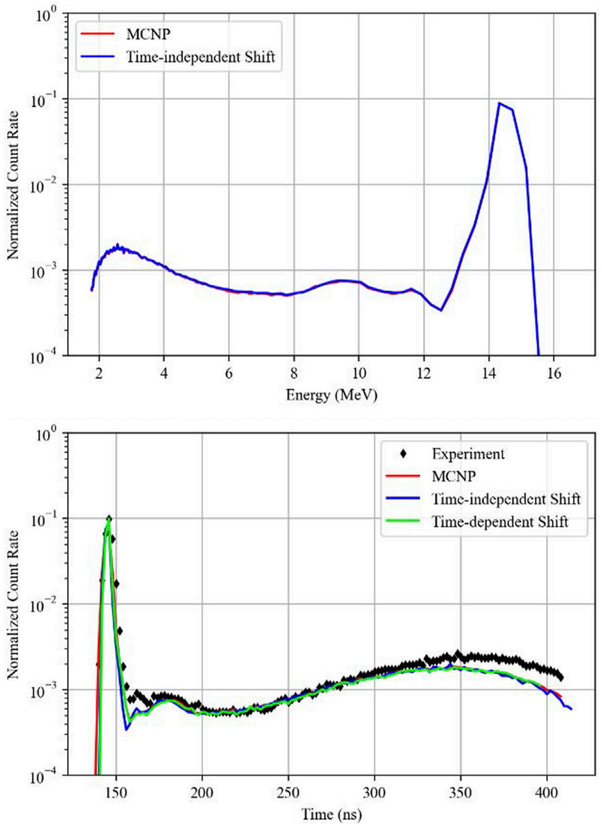

FIGURE 8
Lead, top: energy-binned MCNP (10^7 histories) vs. Shift (10^9 histories); bottom: comparison of time-dependent Shift (10^9 histories) with time-independent Shift (10^9 histories) and MCNP (10^7 histories).

For several spheres including berylium, carbon, lead, lithium, and liquid nitrogen, Shift and MCNP produced nearly identical results.

There are some discrepancies between MCNP and Shift for iron, ^{235}U, and ^{238}U. Shift predicts a dip in the flux around 11 MeV that is not present in MCNP, and Shift predicts a higher flux than MCNP around 13–14 MeV for ^{235}U and ^{238}U. The iron used in the experiments was composed of about 1% ^{55}Mn, and in our modeling we observed that the ENDF/B-VII.1 data libraries had a cross section discrepancy for this isotope which produced errors in Shift. At high energies, the sum of the scattering and absorption cross sections was not equal to the total cross section. The effect was most likely too small to significantly impact the results shown for iron in Figure 7, since the difference between the total cross section and the scattering plus absorption cross sections was typically less than 10%.

3.2 First flight approximation

For the validation of Shift, the results need to be compared with experimental data which can be accomplished by using the relativistic first flight approximation in Eq. 1. This approximation will introduce some error which is dependent on the size and material composition of the sphere. The energy-binned results from Shift in Figures 3–10 were converted and compared with experiment data and MCNP results. The time-of-flight MCNP results were tallied from the same simulations as those energy-binned results using a separate time-binned tally. These converted results, and the comparisons with MCNP, are presented in the bottom graphs of Figures 3–10.

The bottom graphs in Figures 4, 6 show how the first flight approximation can lead to a degradation of results for large spheres with highly scattering media. The carbon and nitrogen spheres in these simulations were about 21 and 56 cm in radius respectively, and there are distinct differences due to scattering behavior over the spectrum. Given that the energy-binned spectrum in Shift was nearly identical to MCNP for both of these spheres, the difference in the time-of-flight results between the codes is most likely entirely due to the errors in the approximation. For the rest of the spheres, where results matched between MCNP and Shift in the energy-binned spectrum, they also matched the time-of-flight results. Small differences at the tail end of the spectrum between the codes and experimental values are expected due to D-D reactions not being modeled in the simulations. These reactions produce an additional 2.5 MeV neutrons Procassini and McKinley (2010); Goricanec et al. (2017). Neither MCNP nor Shift agree with the experimental data for the lithium sphere, with differences approaching 33% in the time period between 170 and 200 ns.

Due to the bins being evenly spaced, some of the more exaggerated differences from the energy-binned uranium results

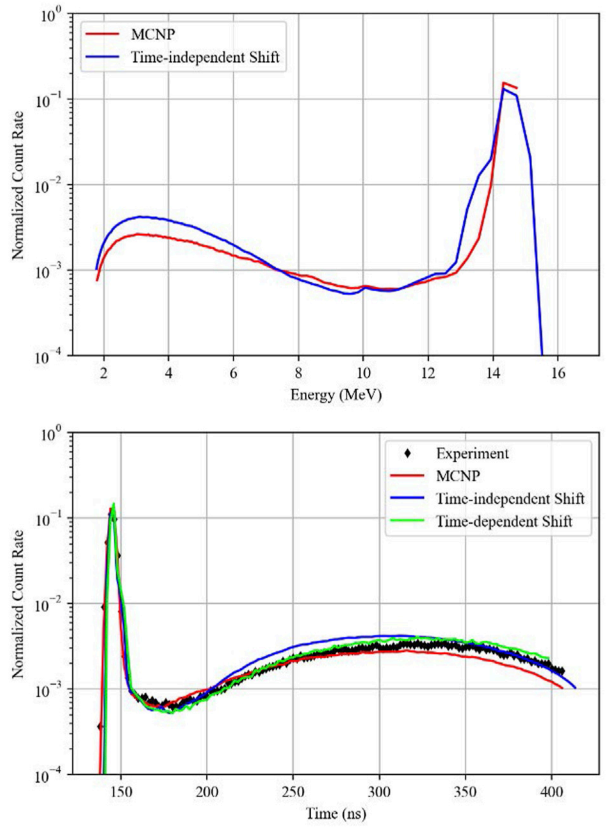

FIGURE 9
^{235}U, top: energy-binned MCNP (10^7 histories) vs. Shift (10^9 histories); bottom: comparison of time-dependent Shift (10^9 histories) with time-independent Shift (10^9 histories) and MCNP (10^7 histories).

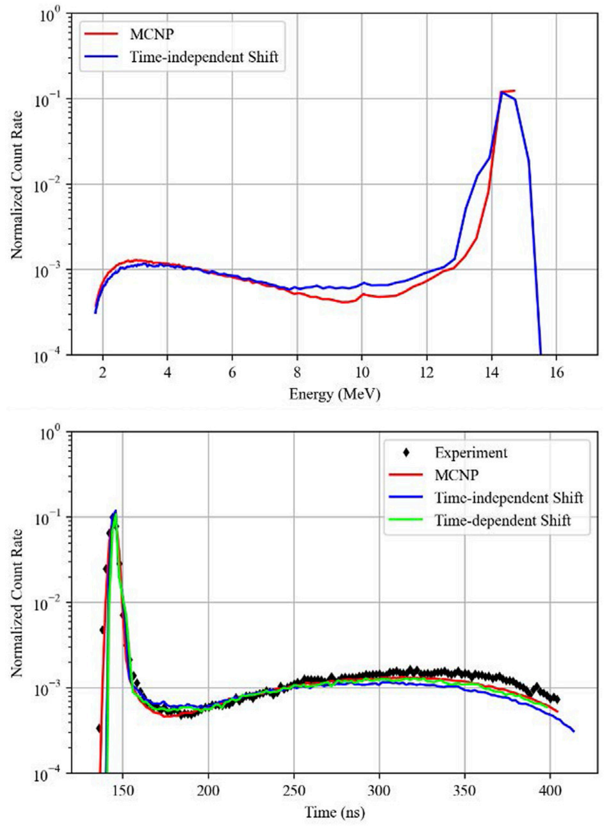

FIGURE 10
^{238}U, top: energy-binned MCNP (10^7 histories) vs. Shift (10^9 histories); bottom: comparison of time-dependent Shift (10^9 histories) with time-independent Shift (10^9 histories) and MCNP (10^7 histories).

are less apparent, but the codes still produce results that are noticeably different for the fissile materials.

3.3 Time-dependent results

The time-dependent CPU code base version of Shift facilitates geometry specifications that correlate directly with MCNP, which means direct comparisons of time-of-flight results can be performed. The current implementation of Shift sets the time-bin boundaries equal to the time step, so the time steps were set to 2 ns to replicate the experimental bins. The bottom graphs in Figures 3–10 contain the results of the time-dependent Shift simulations and comparisons with MCNP.

Small discrepancies between Shift and MCNP still arise in the iron and uranium spheres, but errors are still generally on the same order of magnitude as the differences between the experimental values and the simulation results from either code. Other than the

TABLE 2 Maximum relative difference [%] in the 160–300 ns range.

Material	Shift-TI vs. Exp	Shift-TD vs. Exp	MCNP vs. Exp	Shift-TD vs. MCNP
Be	28.41	14.57	9.21	7.54
C	28.33	19.91	20.13	14.67
Fe	54.89	45.23	20.53	34.25
Pb	56.04	43.19	43.20	11.08
Li	30.84	30.34	32.34	11.87
N	35.34	30.78	31.46	5.66
^{235}U	26.99	24.22	22.04	26.06
^{238}U	30.81	24.82	22.90	23.87

aforementioned carbon and nitrogen spheres, the two uranium spheres showed the greatest differences between time-independent and time-dependent Shift implementations.

Table 2 compares the percent difference of the point of maximum discrepancy for several comparisons. The range was limited to the area of interest between 160 and 300 ns for several reasons. Tally results for the uncollided peak at the start of the time spectrum tend to differ significantly between the codes and experimental data due to the limited number of bins for the rapidly changing behavior. Additionally, the code models do not include the impact of D-D neutrons and tend to drift away from the experimental data near the end of the time spectrum.

To confirm what can be seen graphically, Shift produces results that are very close to MCNP for most spheres. Without the hindrance of the first flight approximation, time-dependent Shift consistently produces more accurate results than time-independent Shift and most of the results compare closely to experiment with both versions of the code. In most cases, where Shift does not align with experimental data, MCNP also experiences some discrepancies. In those cases, the differences most likely originate from the nuclear data.

4 Conclusion

LLNL's pulsed-sphere benchmark experiments were simulated in Shift to validate both the time-independent as well as new time-dependent features. Time-of-flight results for both the time-independent and time-dependent builds of Shift result in errors that are of a similar order of magnitude as MCNP when compared to experimental data. This is the first validation attempt with the Shift code that employed the pulsed sphere benchmarks. Aside from a few minor discrepancies in iron and uranium that could warrant future investigation, Shift aligns with MCNP exceedingly well.

Time-dependent algorithms have been implemented in the GPU version of Shift, but geometry limitations have prevented the easy exploration of problems like the pulsed spheres to date. The pulsed spheres do not exercise the full time-dependent capabilities of Shift. Transient problems that cannot be simulated using time-independent methods such as reactor cores with moving control rods will be the focus of future work.

A study of the computational performance of the time-dependent version of Shift is ongoing, on massively-parallel CPU and GPU architectures, is the subject of a separate article currently in preparation.

Data availability statement

The raw data supporting the conclusion of this article will be made available by the authors, without undue reservation.

Author contributions

CP: Conceptualization, Writing–original draft, Writing–review and editing. JN: Data curation, Formal Analysis, Writing–original draft. TP: Funding acquisition, Writing–review and editing. AR: Methodology, Supervision, Writing–review and editing.

Funding

The author(s) declare financial support was received for the research, authorship, and/or publication of this article. This work was supported by the Center for Exascale Monte-Carlo Neutron Transport (CEMeNT) a PSAAP-III project funded by the Department of Energy, grant number: DE-NA003967.

Conflict of interest

Author AR is employed by TerraPower LLC.

The remaining authors declare that the research was conducted in the absence of any commercial or financial relationships that could be construed as a potential conflict of interest.

Publisher's note

References

Adams, T., Nolen, S., Sweezy, J., Zukaitis, A., Campbell, J., Goorley, T., et al. (2015). Monte Carlo application toolkit (MCATK). *Ann. Nucl. Energy* 82, 41–47. doi:10.1016/j.anucene.2014.08.047

Briggs, J. B. (2006). International handbook of evaluated reactor physics benchmark experiments. *Tech. Rep. NEA/NSC/DOC Paris, Fr.*

Briggs, J. B., Scott, L., and Nouri, A. (2003). The international criticality safety benchmark evaluation project. *Nucl. Sci. Eng.* 145, 1–10. doi:10.13182/NSE03-14

Buck, R. M., and Hall, J. M. (1999). Applications of the COG multiparticle Monte Carlo transport code to simulated imaging of complex objects. *Radiat. Sources Radiat. Interact. (SPIE)* 3771, 127–134. doi:10.1117/12.363699

Cullen, D. E. (2000). *Tart 2000: a coupled neutron-photon, 3-D, combinatorial geometry, time dependent, Monte Carlo transport code*. UCRL-ID-126455-REV-3. Livermore, CA, United States: Lawrence Livermore National Lab.LLNL.

Evans, T. M., Siegel, A., Draeger, E. W., Deslippe, J., Francois, M. M., Germann, T. C., et al. (2022). A survey of software implementations used by application codes in the Exascale Computing Project. *Int. J. High Perform. Comput. Appl.* 36, 5–12. doi:10.1177/10943420211028940

Goricanec, T., Trkov, A., and Noy, R. C. (2017). Analysis of the U-238 Livermore pulsed sphere experiments benchmark evaluations. https://inis.iaea.org/collection/NCLCollectionStore/_Public/49/059/49059862.pdf?r=1.

Hamilton, S. P., and Evans, T. M. (2019). Continuous-energy Monte Carlo neutron transport on GPUs in the Shift code. *Ann. Nucl. Energy* 128. doi:10.1016/j.anucene.2019.01.012

Kulesza, J. A., Adams, T. R., Armstrong, J. C., Bolding, S. R., Brown, F. B., Bull, J. S., et al. (2022). *MCNP® code version 6.3.0 theory & user manual*. Tech. Rep. LA-UR-22-30006. Los Alamos, NM, USA: Los Alamos National Laboratory. doi:10.2172/1889957

Leppänen, J. (2013). Development of a dynamic simulation mode in Serpent 2 Monte Carlo code. *Proc. M&C*, 5–9. https://api.semanticscholar.org/CorpusID:198925618.

Marchetti, A. A., and Hedstrom, G. W. (1998), *New Monte Carlo simulations of the LLNL pulsed-sphere experiments* UCRL-ID-131461. Livermore, CA, United States: Lawrence Livermore National Lab.LLNL.

Miller, T. M., Menedeu, E. L., Mancusi, D., and Zoia, A. (2018). Comparison of mavric/Monaco and tripoli-4® simulations of the llnl pulsed spheres benchmark experiments in 20th Topical Meeting of the Radiation Protection & Shielding Division of ANS, Santa Fe, New Mexico, United States, August 2018.

ORNL (2022). SCALE 6.2 manual. https://scale-manual.ornl.gov/UtilOverview.html.

Peplow, D. E., Banerjee, K., Davidson, G. G., Stewart, I. R., Swinney, M. W., and Wagner, J. N. (2019). Preliminary validation of the Shift Monte Carlo code for fixed-source radiation transport problems. *Nucl. Technol.* 206 (1), 107–125. doi:10.1080/00295450.2019.1625663

Procassini, R., Cullen, D., Greenman, G., and Hagmann, C. (2004). *Verification and validation of Mercury: a modern, Monte Carlo particle transport code*. UCRL-CONF-208667. Livermore, CA, United States: Lawrence Livermore National Lab LLNL.

Procassini, R. J., and McKinley, M. S. (2010).*Modern calculations of pulsed-sphere time-of-flight experiments using the Mercury Monte Carlo transport code* LLNL-PROC-453212. Livermore, CA, United States: Lawrence Livermore National Lab LLNL.

Reynolds, A. J., and Palmer, T. S. (2022). Verification and scaling of time-dependent Shift using the AZURV1 benchmark. *Transactions* 126. doi:10.13182/T126-38060

Reynolds, A. J., Variansyah, I., and Palmer, T. (2022). *Implementation, verification, and scaling of history- and event-based time-dependent Shift*.

Shim, H.-J., Han, B.-S., Jung, J.-S., Park, H.-J., and Kim, C.-H. (2012). McCARD: Monte Carlo code for advanced reactor design and analysis. *Nucl. Eng. Technol.* 44, 161–176. doi:10.5516/NET.01.2012.503

Whalen, D. J., Cardon, D. A., Uhle, J. L., and Hendricks, J. S. (1992). *New Monte Carlo simulations of the LLNL pulsed-sphere experiments*. UCRL-ID-131461. Livermore, CA, United States: Lawrence Livermore National Lab LLNL.

Wong, C., Anderson, J. D., Brown, P., Hansen, L. F., Kammerdiener, J. L., Logan, C., et al. (1972). *Livermore pulsed sphere program: program summary through July 1971*. UCRL-51144. Livermore, CA, United States: Lawrence Livermore National Lab LLNL.

Frontiers in Nuclear Engineering

TYPE Original Research
PUBLISHED 13 December 2023
DOI 10.3389/fnuen.2023.1306529

OPEN ACCESS

EDITED BY
Anne Campbell,
Oak Ridge National Laboratory (DOE),
United States

REVIEWED BY
Shingo Tamaki,
Osaka University, Japan
Karim Ahmed,
Texas A&M University, United States
Elizabeth Sooby,
University of Texas at San Antonio,
United States

*CORRESPONDENCE
Janelle P. Wharry,
✉ jwharry@purdue.edu

RECEIVED 04 October 2023
ACCEPTED 27 November 2023
PUBLISHED 13 December 2023

CITATION
Wharry JP, Guillen DP, Clement CD, Bin Habib S, Jiang W, Zhao Y, Lu Y, Wu Y, Shiau C-H, Frazer D, Heidrich BJ, Knight C and Gandy DW (2023), Materials qualification through the Nuclear Science User Facilities (NSUF): a case study on irradiated PM-HIP structural alloys.
Front. Nucl. Eng. 2:1306529.
doi: 10.3389/fnuen.2023.1306529

Materials qualification through the Nuclear Science User Facilities (NSUF): a case study on irradiated PM-HIP structural alloys

Janelle P. Wharry[1]*, Donna Post Guillen[2], Caleb D. Clement[1,3], Saquib Bin Habib[1], Wen Jiang[1], Yangyang Zhao[1], Yu Lu[4,5], Yaqiao Wu[4,5], Ching-Heng Shiau[4,5], David Frazer[2], Brenden J. Heidrich[2], Collin Knight[2] and David W. Gandy[6]

[1]School of Materials Engineering, Purdue University, West Lafayette, IN, United States, [2]Idaho National Laboratory, Idaho Falls, ID, United States, [3]Westinghouse Electric Company, LLC, Pittsburgh, PA, United States, [4]Micron School of Materials Science and Engineering, Boise State University, Boise, ID, United States, [5]Center for Advanced Energy Studies, Idaho Falls, ID, United States, [6]Electric Power Research Institute, Charlotte, NC, United States

This article presents neutron irradiation and post-irradiation examination (PIE) capabilities available to the nuclear materials research community through the US Department of Energy's Nuclear Science User Facilities (NSUF). The pressing need to deploy advanced nuclear reactors to combat climate change requires qualification of new fuels and materials. Among advanced manufacturing processes, powder metallurgy with hot isostatic pressing (PM-HIP) is nearest to becoming qualified for nuclear applications. This article provides examples from a recent irradiation and PIE program on a series of structural alloys fabricated by PM-HIP to illustrate how NSUF capabilities can be used to generate qualification data. The neutron irradiation experiments are described, and a sampling of results from tensile testing, nanoindentation, transmission electron microscopy, and atom probe tomography are presented, showing the favorable performance of PM-HIP alloys compared to their cast or forged counterparts under irradiation. This article provides a perspective on leveraging NSUF for future nuclear fuels and materials testing and qualification.

KEYWORDS

materials qualification, neutron irradiation, powder metallurgy, mechanical testing, irradiated microstructure, user facility, hot isostatic pressing, structural alloys

1 Introduction

Materials development and qualification for the nuclear power industry have historically been protracted processes by comparison to other industries (Olson and Kuehmann, 2014), in large part due to the need to evaluate the in-reactor performance of materials (Aguiar et al., 2020). Large-scale neutron irradiation and post-irradiation examination (PIE) programs, often termed "campaigns", are the established norms for obtaining irradiation effects and performance data under service-relevant conditions (Crawford et al., 2007; Petti et al., 2010), which can subsequently be used toward materials qualification. Often, sequential campaigns are necessary to take advantage of an iterative materials design cycle. Each campaign can often span a decade and cost multiple millions of US dollars. Consequently, qualification of new materials has long been a bottleneck for the nuclear power industry, and the list of "qualified" materials is mostly limited to those in use since the earliest commercial nuclear power plants in the late 1950s.

Currently qualified nuclear materials will not suffice for advanced reactor designs—the deployment of which is increasingly crucial to combating climate change (Sailor et al., 2000; Chu and Majumdar, 2012; Mathew, 2022). Many of these advanced reactor designs demand materials to operate at higher temperatures, higher irradiation fluences, and in more corrosive environments compared to current light water reactors (LWRs). The recent boon in advanced manufacturing (Kautz et al., 2019; Blevins and Yang, 2020; Morgan et al., 2022) and data-driven, machine learning–based materials design (Stach et al., 2021) has introduced a tremendous breadth of innovative nuclear fuel and material concepts, novel manufacturing methods for established materials, and advanced welding and joining techniques, which show promise for advanced reactors. To bring these materials and methods full circle in an advanced reactor therefore requires a transformation in our capabilities to qualify new nuclear materials.

Wide-ranging efforts to accelerate nuclear fuels and materials qualification are being pursued across the research community (Murty and Charit, 2008; Gong et al., 2016; Aguiar et al., 2020). For example, automation is being used to modularize nuclear manufacturing (Kautz et al., 2019; Blevins and Yang, 2020; Morgan et al., 2022), coupled with *in situ* process monitoring to accelerate and simplify quality assurance of advanced manufactured components (Everton et al., 2016; Sun et al., 2021). High-throughput experiments, separate effects, and small-scale mechanical testing are being developed to improve and accelerate materials screening and downselection before investing in neutron irradiation and PIE campaigns (Terrani et al., 2020; Hensley et al., 2021; Moorehead et al., 2021). Data analytics and machine learning are being leveraged to improve predictive capabilities of modeling tools to maximize the return on investment in irradiation testing (Stach et al., 2021; Morgan et al., 2022).

As irradiation testing remains a cornerstone of nuclear materials qualification, assessing our capacity to conduct these critical experiments will provide the community with a guide for efficient materials qualification campaigns. This article presents irradiation and PIE campaign capabilities within the United States, available through direct and competitive funding from the Department of Energy, Office of Nuclear Energy, Nuclear Science User Facilities (NSUF). An irradiation and PIE campaign on structural alloys fabricated by powder metallurgy with hot isostatic pressing (PM-HIP) is used as an example throughout the article. An overview of results from the campaign are presented to illustrate how NSUF capabilities can be utilized to generate qualification datasets. The article concludes with a perspective on the use of NSUF for future materials testing and qualification efforts.

PM-HIP alloys are the ideal set of materials for this article because among advanced manufacturing technologies, PM-HIP is closest to becoming fully qualified for nuclear applications (Gandy et al., 2019). The nuclear industry is seeking to replace traditional castings or forgings with PM-HIP manufacturing for LWR (Gandy et al., 2012; Gandy et al., 2019) and small modular reactor (SMR) (Gandy et al., 2019) internals, pressure vessels (Morrison et al., 2019), and secondary side components. PM-HIP offers numerous advantages over conventional alloy fabrication, including an equiaxed, fine-grained structure (Clement et al., 2022a; Clement et al., 2022b), chemical homogeneity (Yu et al., 2009; Ahmed et al., 2013; Shulga, 2013; Ahmed et al., 2014; Gandy et al., 2016), exceptional mechanical properties (Metals and and Ceramics Information Center Report No, 1977; Atkinson and Davies, 2000; Rao et al., 2003; Shulga, 2012; Shulga, 2014; Guillen et al., 2018; Morrison et al., 2019; Barros et al., 2022) especially at high temperatures (Bullens et al., 2018; Getto et al., 2019), greater irradiation resistance (van Osch et al., 1996; Lind and Bergenlid, 2000; Rodchenkov et al., 2000; Lind and Bergenlid, 2001; Clement et al., 2022a; Clement et al., 2022b), fewer defects (Gandy et al., 2012; Gandy et al., 2019), and near-net–shaped fabrication which reduces reliance on welding and machining (Mao K. S. et al., 2018; Mao K. et al., 2018; Mao et al., 2021). PM-HIP-manufactured ferritic steels, austenitic steels, and Ni-based alloys are already qualified for non-nuclear applications, alongside castings and forgings, in the ASME Boiler and Pressure Vessel Code (BPVC), Section 2. More recently, the PM-HIP form of austenitic stainless steel 316 L has been qualified for non-irradiation–facing nuclear applications through ASME BPVC, Section 3. The selected results presented herein can expand PM-HIP qualification for irradiation-facing components and for additional alloys.

2 The NSUF program

The NSUF is one of a diverse group of US Department of Energy (DOE) user facilities. It is the DOE Office of Nuclear Energy's (DOE-NE) first and only sponsored user facility and is singularly focused on advancing technologies supporting nuclear energy applications. The NSUF is unique in that it is not formed from a single self-contained facility but is a consortium of facilities distributed across the nation at 21 institutions. The NSUF is centered at and managed from Idaho National Laboratory (INL) where it was originally founded. The partner facilities include twelve universities, seven national laboratories (in addition to INL), and one industry institute as well as the Center for Advanced Energy Studies (CAES) in Idaho Falls, ID. NSUF also has several active international collaborations that leverage capabilities around the world.

The NSUF has one goal: to produce the highest quality research results that will impact and increase the understanding of nuclear energy technologies important to DOE-NE. The NSUF does not have an objective to develop or qualify a particular type of fuel or structural material, but instead, the NSUF performs research projects related to all areas of irradiation effects in nuclear fuels and materials that will increase the knowledge and understanding associated with phenomena or behaviors that will have an impact on advancing nuclear technology. By acting as a user facility and providing the user with no-cost access to its specialized and unique capabilities, the NSUF program fosters the development of novel ideas generated by external contributors from universities, national laboratories, and industry while promoting collaborations between those contributors and the expertise associated with the NSUF partner capabilities. These collaborations define the cutting edge of nuclear technology research in understanding the behavior of materials subjected to radiation environments, contribute to improved performance of current industry and future nuclear reactor systems, and stimulate cooperative research between user groups conducting research in nuclear energy systems.

The NSUF is comprised of many complementary, interrelated components that are fully engaged in building sustainable value over the long term. It delivers high impact results through its outstanding program support staff and partners, its unique facilities, and its unrivaled capabilities. The NSUF seeks to offer the broadest and most advanced technologies to the nuclear research community. The institutions that host the facilities that make up the NSUF offer capabilities that span the entire scope of requirements needed for in-depth nuclear fuels and materials irradiation testing. The capabilities of the NSUF, in conjunction with institutional expertise, can accommodate the simplest to the most complex projects that might require design, fabrication, transportation, irradiation, post-irradiation examination (including advanced materials science characterization), and final disposition. Thus, the NSUF offers nuclear test and research reactor facilities including associated neutronic and thermal hydraulic support calculations, ion irradiation facilities, radiation-qualified fabrication facilities, hot cell capabilities, high-level radiation shielded instrumentation, and low-level radiation instrumentation as well as high performance computing (HPC) and access to neutron, positron, and synchrotron X-ray beam line capabilities.

In addition to physical capabilities and personnel expertise, the NSUF maintains digital resources to support nuclear energy research and researchers. The NSUF developed three databases that can be accessed at the NSUF website: one for nuclear energy associated research and development capabilities known as the Nuclear Energy Infrastructure Database (NEID); one for collaboration, the Nuclear Energy Researcher Database (NERD); and one for nuclear materials available for use by investigators in nuclear energy research projects known as the Nuclear Fuels and Materials Library (NFML). The physical half of the NFML contains specimens of irradiated and unirradiated nuclear fuel and material covering a wide range of material types from past and ongoing irradiation test campaigns, legacy components obtained from decommissioned power reactors, and donations from other laboratories. The NFML is intended to enable time and cost savings by reducing the number of irradiation tests that must be performed to generate material performance data.

Finally, the NSUF, with support from the INL High Performance Computing (HPC) team have developed the Nuclear Research Data System (NRDS). NRDS is intended to store all NSUF project data, available only to the research team during the performance of the awarded work and then open to the public to fuel collaboration and to accelerate the deployment of advanced nuclear energy technologies. NSUF partner facilities and researchers can upload the data and assign one of 20 licenses to guide how it will be used in the future and what attribution is required. NRDS data sets are available from the NSUF and INL HPC websites but will also have individual DOI numbers and will be indexed by major search engines for global accessibility. Since this data is located within the HPC infrastructure at INL, researchers can perform a wide variety of built-in and custom artificial intelligence/machine learning, data processing, and visualization activities without the need to locally download these large data sets.

NSUF was founded in 2007 with one reactor and one hot cell facility. The program continues to grow and adapt to changing national priorities and researcher needs. The program office works with DOE-NE, the US nuclear industry, other user facilities, and its own researchers to inform its operations and growth. While the primary focus of NSUF will always be on nuclear fuels and materials, other areas of endeavor are possible. NSUF works to maintain flexibility and adaptability to the needs of the US nuclear energy community.

3 Methods and materials

3.1 Neutron irradiation

NSUF offers several test reactors for fuels and materials irradiation campaigns, including the Advanced Test Reactor (ATR) at INL, Transient Reactor Test (TREAT) Facility at INL, the High Flux Isotope Reactor (HFIR) at Oak Ridge National Laboratory (ORNL), the Massachusetts Institute of Technology (MIT) Reactor, and the North Carolina State University PULSTAR Reactor. Each of these reactors offers a unique range of fluxes, neutron spectra, and instrumented and controlled testing options, suitable for a wide variety of fuels and materials testing and qualification. For this project, ATR was selected for its relatively high thermal neutron flux (relative to fast flux) and lower temperature capabilities, both of which are more representative of the LWR environments in which the studied alloys are intended to operate. Additionally, ATR offers relatively large test volumes, able to accommodate specimen geometries such as ASTM E8 standardized tensile bars for materials qualification efforts.

For the case study highlighted here, we examined steel and nickel-based alloys intended for nuclear reactor applications. Six structural alloys are included in the irradiation campaign, each fabricated by PM-HIP and by either forging or casting. The alloys were SA508 Grade 3 Class 1 low-alloy RPV steel, Ni-based Alloys 625 and 690, Grade 91 ferritic steel, and austenitic stainless steels 316L and 304 L. The alloys were compliant with ASME BPVC compositional specifications, and were all provided by the Electric Power Research Institute. For all alloys, HIP was conducted at a pressure of 15 ksi for 4 h; HIP temperature was 1149°C for the two Ni-based alloys or 1121°C for all other alloys. The heat treatments for the HIP and cast/forged materials followed standard heat treatment procedures for the specific alloys. The two Ni-based alloys and the two austenitic stainless steels were solution cycled then water quenched; the Grade 91 was normalized and tempered; and the SA508 was solution cycled, quenched, normalized, and tempered. Specimen geometries were ASTM E8 round tensile bars for mechanical property evaluation, transmission electron microscopy (TEM) discs (i.e., coupons) for microstructure characterization and nanoindentation, and pre-cracked miniature compact tension (CT) specimens for fracture toughness testing. More comprehensive description of the alloy compositions, fabrication and heat treatment details, and specimen machining methods are described in ref. (Guillen et al., 2023).

3.2 Mechanical testing

Uniaxial tensile testing of radioactive specimens was conducted using a 13 M Instron load cell in the hot cells at the Hot Fuel Examination Facility (HFEF) at INL. Testing was conducted at ambient temperature in an argon environment following ASTM E8 for threaded grip specimens. The load capacity of the cell was 50 kN, and loading rate range was 0.001 mm/min-500 mm/min. In the present experiments, a strain rate of 8.78×10^{-3} s^{-1} (0.279 mm/min crosshead speed) was used through 10% strain, after which the strain rate increased to 3.15×10^{-2} s^{-1} (1.0 mm/min crosshead speed) until failure. Time, load, and displacement were recorded throughout the test, and have been archived in (Wharry et al., 2023). After tensile testing, fracture surfaces were cut from the broken tensile halves using a diamond wafering blade; this enabled the fracture surfaces to be oriented face-up in a scanning electron microscope (SEM) for fractography. A Lyra3 Tescan SEM at the Electron Microscopy Laboratory (EML) at INL was used for fracture surface characterization. Fractographs are also archived in (Wharry et al., 2023).

Nanoindentation hardness measurement capabilities on the Hysitron TI-950 TriboIndenter are available through NSUF at the Microscopy and Characterization Suite (MaCS), CAES. Nanoindentation is used to rapidly evaluate hardness and elastic modulus, especially in irradiation campaigns that are unable to accommodate ASTM standard-sized tensile bars or for volume-limited specimens (Chen et al., 2020). The TI-950 can be operated with a Berkovich tip in depth-controlled or load-controlled mode, with a maximum load of 2.2 N. In the present work, nanoindentation was conducted in depth-controlled mode to a maximum depth of 3,500 nm at a strain rate of 0.2 s^{-1}. The displacement and load were recorded continuously as a function of time, from which the nanoindentation hardness was calculated using the Oliver-Pharr method (Oliver and Pharr, 2004).

3.3 Microstructure characterization

NSUF has several dedicated radioactive TEM capabilities, including the FEI (now ThermoFisher) Tecnai TF30-FEG STwin TEM at MaCS, CAES, used in this project. The instrument is equipped with energy dispersive x-ray spectroscopy (EDS), electron energy loss spectroscopy (EELS), energy filtered TEM (EFTEM), scanning TEM (STEM), and TopSpin. The instrument has been used across numerous NSUF projects to characterize irradiation-induced defects, including dislocation loops using techniques including two-beam condition (rel-rod) imaging or down-zone STEM (Parish et al., 2015), voids or bubbles using the through-focus technique, phase evolution using diffraction and EDS, and nanoclustering and radiation-induced segregation using EDS line and area mapping. To evaluate the performance of PM-HIP alloys, TEM characterization focused on precipitate and dislocation loop evolution under irradiation. In this work, the TEM was operated in scanning TEM (STEM) mode at 200 kV. STEM high-angle annular dark field (HAADF) imaging was used to observe the precipitate number density and distribution, with high resolution STEM to observe the precipitate structures. Bright-field down-zone STEM imaging was used to observe dislocation loops, following a technique described in (Parish et al., 2015).

Atom probe tomography: NSUF offers capabilities for three-dimensional (3D) atomic-scale chemical characterization using the CAMECA Local Electrode Atom Probe (LEAP) 4000X HR at MaCS, CAES dedicated for radioactive specimens. Atom probe tomography (APT) utilizes the principle of field evaporation on a ~10–100 nm diameter needle specimen; the evaporated species from the needle are collected in a time-of-flight mass spectrometer, enabling atom-by-atom position-sensitive 3D reconstruction of the needles. The LEAP 4000X HR at CAES is capable of laser or voltage pulsing with 250 kHz laser or 200 kHz voltage pulse generator. Metallic specimens can often be analyzed using voltage pulsing for high mass resolution; however, specimens having limited conductivity must be analyzed using laser pulsing, which may limit mass resolution (Sen et al., 2021). In the current work, specimens were tested in laser pulse mode with 60 pJ laser energy, 200 kHz pulse rate, and specimen base temperature ~50 K. APT raw data files were reconstructed using the CAMECA proprietary AP Suite software, with cluster analysis conducted following established procedures (Vaumousse et al., 2003; Hyde et al., 2011; Williams et al., 2013; Swenson and Wharry, 2015; Swenson and Wharry, 2016).

4 Results demonstration

4.1 Neutron irradiation

Irradiation capsules, fixtures, and loading schemes were designed such that each PM-HIP specimen and its cast or forged counterpart would receive consistent fluences and temperatures, enabling a direct comparison of microstructure and mechanical property evolution across fabrication methods. A total of 256 specimens, including 48 round tensile bars, 28 miniature CTs, and 180 TEM discs, were irradiated in a set of seven non-instrumented, drop-in capsules. Melt wires were inserted into the center fixtures of each capsule. Capsules were stacked vertically, with complete loading configurations described in ref. (Guillen et al., 2023). Neutron physics, thermal, and structural analyses were conducted during the design phase to ensure proper fluence and temperature requirements were met for all specimens within this stacked configuration. Details of these calculations are provided in refs. (Brookman, 2018; Hale, 2018). and summarized in ref. (Guillen et al., 2023).

The capsules were inserted for irradiation to the inboard A6, A7, and A8 positions during ATR cycles 164A, 164B, 166 A and 166B, spanning May 2018 through January 2020. Fluxes ranged 8.08–9.61 × 10^{14} neutrons/cm^2·s, with fast (>1 MeV) flux components ranging 1.60–1.96 × 10^{14} neutrons/cm^2·s. As-run fluences (Brookman, 2020) and temperatures (Davis and Hone, 2020; Hale, 2021) are tabulated for each specimen in ref. (Guillen et al., 2023). Actual doses ranged 0.5–1.1 dpa and 2.7–5.4 dpa for the dose targets of 1 and 3 dpa, respectively, corresponding to a dose rate range of 1.0–1.8 10^{-7} dpa/s. Finite element analysis (FEA) based thermal analysis determined actual temperature ranges of 257°C–306°C and 321°C–398°C for the temperature targets of 300°C and 400°C, respectively.

4.2 Uniaxial tensile testing & fractography

As an example, we consider the tensile testing results from neutron irradiated cast and PM-HIP 316 L stainless steel, Figure 1A. The two PM-HIP specimens have irradiation conditions of 3.91 dpa

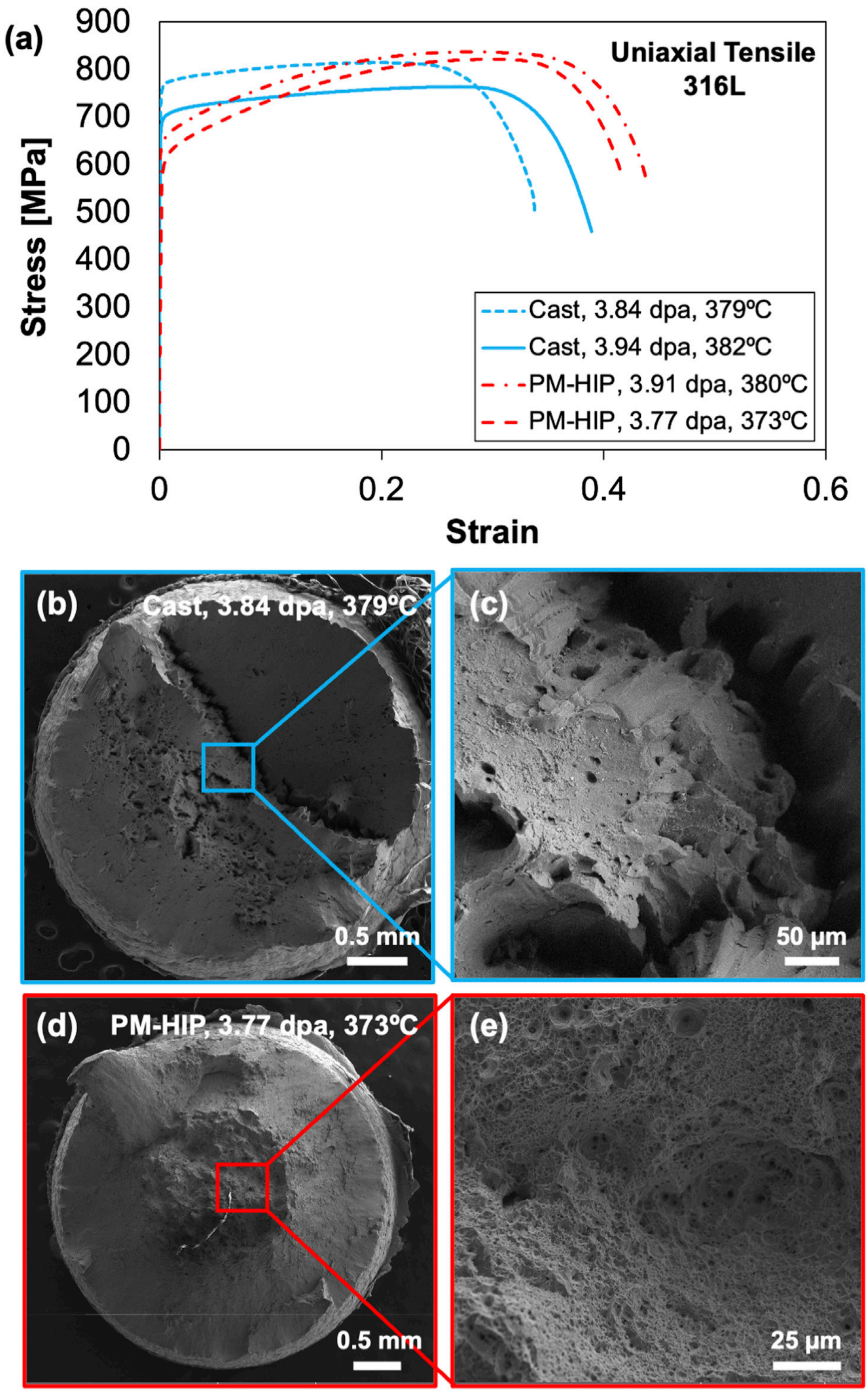

FIGURE 1
Example uniaxial tensile results from cast and PM-HIP 316 L stainless steel, neutron irradiated to nominally 3.8–3.9 dpa at ~370°C–380°C, showing **(A)** stress-strain curves, and SEM fractography of irradiated **(B,C)** cast specimen and **(D,E)** PM-HIP specimen. Micrographs **(B–E)** adapted from (Wharry et al., 2023), licensed under CC BY 4.0.

at an average irradiation temperature of 380°C (specimen 719) and 3.77 dpa at an average irradiation temperature of 373°C (specimen 720). The two cast specimens have irradiation conditions of 3.84 dpa at an average irradiation temperature of 379°C (specimen 704) and 3.94 dpa at an average irradiation temperature of 382°C (specimen 705). The specimen identification numbers correspond to descriptions provided in ref. (Guillen et al., 2023). Results show that after irradiation, PM-HIP specimens exhibit ~10–15% greater

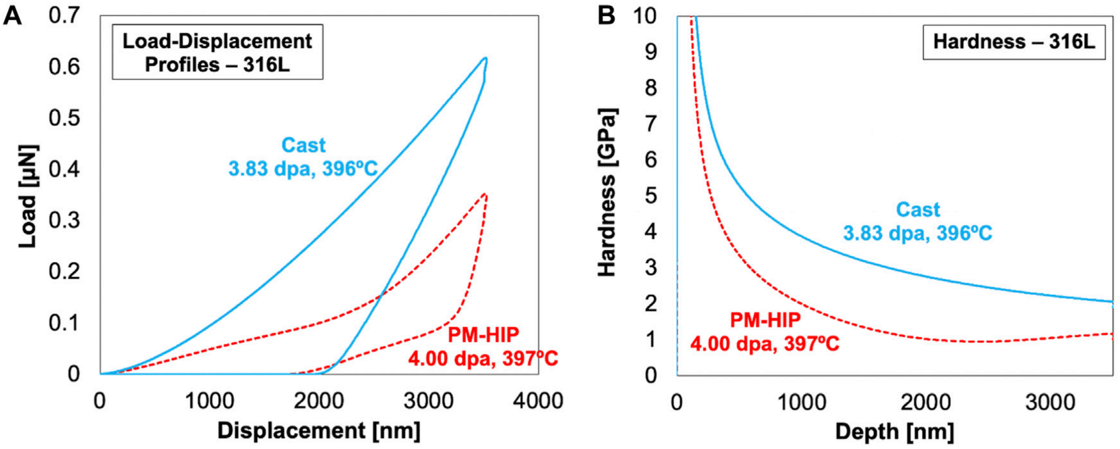

FIGURE 2
Example nanoindentation results from 316 L stainless steel, showing average **(A)** load-displacement curves and **(B)** hardness depth profiles, averaged over 26 indents in cast and PM-HIP specimens irradiated to nominally 3.8–4.0 dpa at ~400°C.

ductility than the cast specimens. Although the irradiated PM-HIP specimens have a lower yield strength than the cast specimens by ~150 MPa, the PM-HIP specimens have greater strain hardening capacity, resulting in a higher ultimate tensile stress (UTS) than the cast specimens. The lower ductility of the cast specimen is evident from fractography, which shows a relative flat fracture surface with possible tearing-type behavior in cast specimen 704 (Figure 1B); by contrast, PM-HIP specimen 720 exhibits a classic ductile cup-cone type fracture surface at low magnifications (Figure 1D). At higher magnification, the PM-HIP fracture surface is heavily dimpled (Figure 1E), providing further contrast to the more brittle, dimple-free cast fracture surface (Figure 1C).

The greater ductility of the PM-HIP specimen may be due to its finer grain structure as compared to the forged specimen. Guillen, et al., (Guillen et al., 2018), used far-field high energy X-ray diffraction (ff-HEDM) *in situ* tensile testing of the unirradiated versions of these exact 316 L PM-HIP and forged materials. They observed the finer PM-HIP grain structure gave rise to a more homogeneous distribution of grain-level stress in the loading direction. This stress homogenization limits the formation of stress concentrations which could lead to more brittle failure. Assuming this stress heterogeneity persists throughout irradiation, the PM-HIP specimen will also be less susceptible to stress concentrations resulting from localized deformation mechanisms that tend to occur in austenitic stainless steels after irradiation (Jiao and Was, 2010; McMurtrey et al., 2011; West et al., 2012; De Bellefon and Van Duysen, 2016; Mao et al., 2020; Wharry and Mao, 2020).

Additionally, in the unirradiated states, the PM-HIP exhibits higher yield strength than the forged specimen (Guillen et al., 2018), explained by the Hall–Petch relationship. However, under irradiation, a finer grain structure provides a high sink density that facilitates recombination of irradiation-induced defects (Odette and Hoelzer, 2010; Yu et al., 2013; Du et al., 2018; Zhang et al., 2018; Patki et al., 2020). Hence, the finer grain structure may make the PM-HIP 316 L more irradiation-tolerant than forged 316L, thus accumulating a lesser extent of irradiation hardening. Future irradiated microstructure examinations will help further rationalize these mechanical behaviors.

4.3 Nanoindentation

Example nanoindentation results are from disc-type specimens of 316 L stainless steel, irradiated to similar conditions as the 316 L tensile bars described in Section 2.2. Specifically, PM-HIP 316 L was irradiated to 4.00 dpa at an average temperature of 397°C (specimen 646), while cast 316 L was irradiated to 3.83 dpa at an average temperature of 396°C (specimen 643). The average nanoindentation load-displacement curves and the corresponding average hardness-depth profiles are shown for both the PM-HIP and cast specimens in Figure 2. Note that the results shown are the average of 26 indents made on each specimen; these load-displacement-time raw datasets are available in (Wharry et al., 2023). The load-displacement curves show that a higher load is required to reach the same indent depth in the cast specimen than in the PM-HIP specimen; correspondingly, the cast material has a higher hardness by ~1.5 GPa. With relatively negligible differences in the actual irradiation dose and temperature between the cast and PM-HIP specimens, the hardness difference is thus likely a true hardness difference that can be ascribed to the material microstructure. This behavior is consistent with the lower yield strength and higher strain hardenability of PM-HIP 316 L observed in uniaxial tension testing (Figure 2B).

4.4 Transmission electron microscopy

Demonstration of TEM work is shown for SA508 Grade 3 Class 1 low-alloy steel in Figure 3. The PM-HIP specimen (431) was irradiated to 0.97 dpa at an average temperature of 388°C, while the forged specimen (437) was irradiated to 0.95 dpa at an average temperature of 384°C. Precipitates in the PM-HIP specimens are spherical and homogeneously dispersed, with average diameter 48 ± 3 nm after irradiation. Meanwhile, precipitates in the forged specimen are needle-like with average length 105 ± 9 nm and appear heterogeneously distributed primarily along grain and subgrain boundaries, with some precipitates located on grain interiors. The PM-HIP precipitates are amorphous, while the

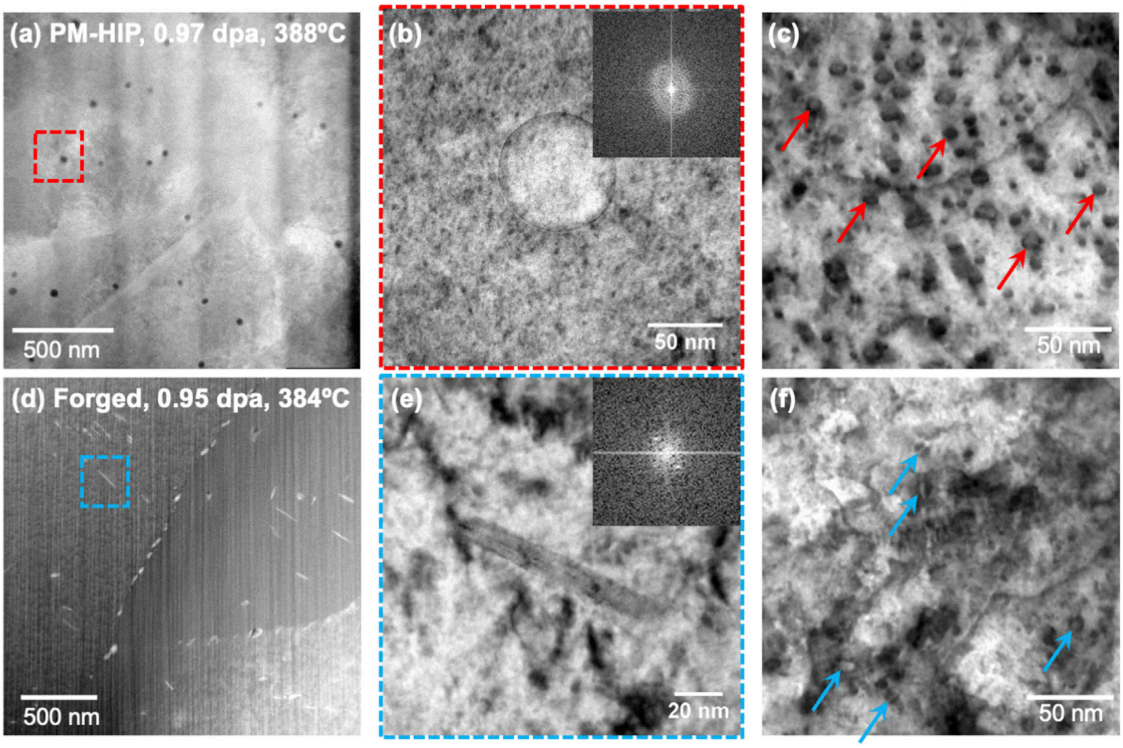

FIGURE 3
TEM micrographs from neutron irradiated SA508 to 0.95–0.98 dpa, 384°C–388°C: **(A–C)** PM-HIP specimen showing **(A)** precipitate distribution, with selected precipitate at higher magnification in **(B)** with inset diffraction pattern suggesting amorphous structure, and **(C)** arrowed dislocation loops; and **(D–F)** Forged specimen showing **(D)** precipitate distribution, with selected precipitate at higher magnification in **(E)** with inset diffraction pattern suggesting semi-crystalline structure, and **(F)** arrowed dislocation loops.

forged precipitates appear at least semi-crystalline given their diffraction spots. Dislocation loops are smaller but more populous in the PM-HIP material than in the forged, suggesting the overall susceptibility to dislocation-type defects may be somewhat comparable between the two fabrication methods.

Differences in the irradiation evolution of the precipitates may be ascribed to their compositions and initial crystal structure. As proposed by Motta (Motta, 1997), irradiation-induced amorphization requires that the change in configurational entropy exceeds the change in enthalpy. This entropy increase can be attained by relaxation of long-range order requirements, consequently leading to an abrupt increase in the available short-range order configurations. Needle-like and preferentially oriented precipitates such as those in the forged material, tend to be incoherent with the matrix, whereas randomly distributed round precipitates such as those in the PM-HIP material, tend to be coherent (Zain-ul-abdein and Nélias, 2016). Since incoherency is associated with higher residual stresses, this may translate to a greater amount of stored mechanical energy in the round PM-HIP precipitates. This greater stored energy contributes to the total entropy required to induce amorphization, effectively making it easier to amorphize the PM-HIP precipitates.

The greater dislocation loop density in the PM-HIP alloy may be due to its chemical composition. In RPV steels at doses above ~0.1 dpa, irradiation drives Mn-Ni-Si (MNS) or Mn-Ni-Si-P (MNSP) nanoclusters to agglomerate on point defect clusters (Meslin et al., 2010; Bonny et al., 2013; Bonny et al., 2014). This muddles the distinction between nanoclusters and defect clusters, the latter of which grow into dislocation loops at higher fluences (Maussner et al., 1999; Kočık et al., 2002; Kuleshova et al., 2002; Gurovich et al., 2009; Meslin et al., 2010). Once these loops become large enough to be resolved in TEM, they are often decorated by Mn and Ni (and Cu, if present in the bulk material) (Fujii et al., 2005; Hamaoka et al., 2010). This underscores the importance of Mn and Ni in stabilizing the loop and nanoprecipitate population. The higher bulk concentration of Mn and Ni in the PM-HIP alloy (1.39 wt% and 0.79 wt%, respectively) than in the forged alloy (0.46 wt% Mn and 0.50 wt% Ni) can explain the higher loop number densities in the PM-HIP alloy. This finding suggests that irradiation susceptibility of RPV steels may be more strongly influenced by bulk alloy chemistry than processing method.

4.5 Atom probe tomography

APT is demonstrated on Grade 91 ferritic steel in Figure 4. Both the PM-HIP and cast specimens were irradiated to 0.99 dpa (specimens 424 and 425) at an average temperature of 389°C. Two

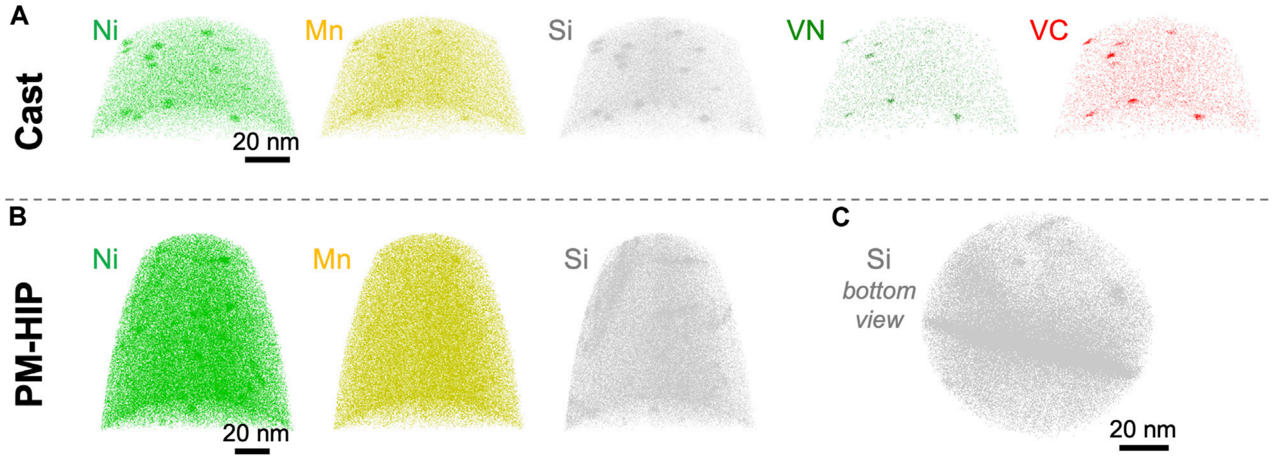

FIGURE 4
APT reconstructions from ~1 dpa, 389°C neutron irradiated Grade 91, showing **(A)** cast specimen with Ni, Mn, Si, VN, and VC nanoclusters, **(B)** PM-HIP specimen with Ni, Mn, and Si nanoclusters with **(C)** Si segregation to dislocation lines.

TABLE 1 Quantitative APT analysis of multiple tips taken from cast and PM-HIP Grade 91 steel, following neutron irradiation to ~1 dpa at 389°C.

Alloy (clustered species)	Tip number	Cluster radius (nm)	Number density (10^{22} m^{-3})	Volume fraction (%)
Cast (Ni, Mn, Si, VN, VC)	1	2.48	5.53	0.41
	2	2.03	4.16	0.16
	Average	2.26 ± 0.32	4.84 ± 0.97	0.28 ± 0.18
PM-HIP (Ni, Mn, Si)	1	1.46	3.06	0.06
	2	1.59	7.58	0.04
	3	1.82	4.66	0.22
	4	1.76	7.17	0.06
	5	2.38	2.00	0.43
	Average	1.80 ± 0.35	4.89 ± 2.46	0.16 ± 0.17

needles were analyzed from the cast specimen, and five from the PM-HIP specimen (Table 1). Qualitatively, representative reconstructions of the analyzed needles show a distribution of fine Ni-Mn-Si nanoclusters in both the cast and PM-HIP specimens (Figures 4A, B). However, nanoclusters in the cast specimen also contain Vanadium Nitride (VN) and Vanadiaum Carbide (VC) molecules, while those in the PM-HIP specimen do not. Additionally, the PM-HIP specimen appears to exhibit Suzuki-like segregation of the clustering species to dislocation features, particularly Si (Figure 4C). Quantitatively, the PM-HIP and cast nanoclusters are statistically identical (Table 1), although the PM-HIP has slightly smaller nanocluster diameters and volume fractions than the cast specimen. The PM-HIP to cast comparison of nanocluster compositions and sizes is somewhat surprising, given that the PM-HIP has a higher bulk Ni, Mn, Si, and V concentration (Wharry et al., 2023). This may suggest that the PM-HIP specimen is inherently resistant to irradiation-induced chemical segregation and redistribution, though the cause has not yet been identified. Alternatively, solute segregation to dislocations in the PM-HIP material may leave few solute atoms available for nucleating nanoclusters. Further microstructure investigation of Grade 91, including at higher irradiation doses, may shed light on the greater resistance of PM-HIP to nanocluster nucleation.

5 Summary and perspective

This work demonstrates the use of a wide range of NSUF capabilities to generate neutron irradiation performance data on nuclear structural materials, through a comprehensive irradiation and post-irradiation examination campaign. The overall irradiation campaign is designed to enable a systematic comparison of mechanical and microstructural evolution between the PM-HIP and cast/forged variants; selected materials and irradiation conditions are shown as four examples herein:

TABLE 2 Summary of irradiation performance of PM-HIP materials compared to their cast or forged counterparts on the basis of mechanical properties and microstructure evolution (favorable = PM-HIP performs better than cast/forged).

Alloy	Mechanical properties	Microstructure evolution	References
Alloy 625	Favorable	Comparable	Clement et al. (2022b)
Alloy 690	Favorable	Comparable	unpublished
Grade 91	Comparable	Comparable	Wharry et al. (2023), this work
SA508	Unfavorable	Unfavorable	Jiang et al. (2023)
316 L	Favorable	TBD	Wharry et al. (2023), this work
304 L	N/A	N/A	N/A

1. Uniaxial tensile testing and fractography reveals that at ~3.8–3.9 dpa at ~370°C–380°C, PM-HIP 316 L stainless steel exhibits lower yield strength, greater ductility, and greater strain hardening capacity than cast 316 L.
2. Nanoindentation shows that after a nominal dose of ~3.8–4.0 dpa at ~400°C, PM-HIP 316 L stainless steel has lower hardness than its cast counterpart, consistent with the aforementioned tensile characteristics.
3. TEM microstructural characterization of SA508 irradiated to ~1 dpa at ~384°C–388°C, reveals that although the PM-HIP material nucleates a higher number density of irradiation-induced dislocation loops, their diameters are smaller than in the forged material.
4. APT characterization presents a finer distribution of Ni-Mn-Si nanoclusters in PM-HIP Grade 91 than in its cast counterpart, following 0.99 dpa, 389°C irradiation, despite the PM-HIP having a higher bulk concentration of the clustering species.

Results generally show favorable irradiation performance of PM-HIP alloys, relative to their cast or forged counterparts, as summarized for all alloys studied within the present irradiation campaign in Table 2. Future code qualification efforts for the respective PM-HIP alloys may leverage these data as evidence of the irradiation resilience of PM-HIP materials relative to the already qualified methods of casting or forging. This NSUF campaign may serve as a model for future irradiation and PIE experiments seeking to generate nuclear code qualification data for new fuels and materials, advanced manufacturing methods, or advanced welding and joining technologies. The breadth of NSUF capabilities leveraged herein can also provide a template for designing future NSUF supported programs to evaluate structure–property relationships in irradiated materials and fuels. Finally, all specimens described in this work are available in the NSUF Nuclear Fuels & Materials Library, through which they are openly and competitively available to the community for follow-on research.

Data availability statement

The datasets presented in this study can be found in online repositories. The names of the repository/repositories and accession number(s) can be found below: https://doi.org/10.1016/j.dib.2023.109092.

Author contributions

JW: Conceptualization, Data curation, Funding acquisition, Methodology, Project administration, Supervision, Writing–original draft. DG: Data curation, Formal Analysis, Funding acquisition, Methodology, Project administration, Writing–original draft, Writing–review and editing. CC: Data curation, Formal Analysis, Investigation, Visualization, Writing–review and editing. SB: Data curation, Formal Analysis, Investigation, Visualization, Writing–review and editing. WJ: Data curation, Formal Analysis, Investigation, Visualization, Writing–review and editing. YL: Data curation, Formal Analysis, Investigation, Writing–review and editing. YW: Data curation, Formal Analysis, Investigation, Writing–review and editing. C-HS: Data curation, Formal Analysis, Investigation, Writing–review and editing. DF: Data curation, Formal Analysis, Investigation, Writing–review and editing. BH: Project administration, Resources, Writing–original draft, Writing–review and editing. CK: Project administration, Resources, Writing–review and editing. DG: Conceptualization, Funding acquisition, Resources, Writing–review and editing.

Funding

The author(s) declare financial support was received for the research, authorship, and/or publication of this article. Work at Purdue is supported by the Electric Power Research Institute Agreement 10015819. Nanoindentation, TEM, and APT experiments are conducted at the Microscopy and Characterization Suite, Center for Advanced Energy Studies through the Nuclear Science User Facilities. Irradiation experiments and post-irradiation examination are supported by the US Department of Energy, Office of Nuclear Energy under DOE Idaho Operations Office Contract DE-AC07-05ID14517 as part of Nuclear Science User Facilities Award #CFA-15-8242.

Acknowledgments

In the spirit of this special issue of Frontiers, thank you to the female trailblazers and Sisters in Nuclear who have inspired my onward pursuit of nuclear energy research. –JW. The authors thankful to the project team at Idaho National Laboratory who managed, designed, analyzed, and assembled this experiment, including Gregory Housley, Cody Hale, Jason Brookman, Katie Anderson, Katelyn Baird, Dave Swank, DC Haggard, and Dave Cottle.

Conflict of interest

Author CC was employed by Westinghouse Electric Company, LLC.

The remaining authors declare that the research was conducted in the absence of any commercial or financial relationships that could be construed as a potential conflict of interest.

Publisher's note

References

Aguiar, J. A., Jokisaari, A. M., Kerr, M., and Allen Roach, R. (2020). Bringing nuclear materials discovery and qualification into the 21st century. *Nat. Commun.* 11, 2556–2612. doi:10.1038/s41467-020-16406-2

Ahmed, R., Ashraf, A., Elameen, M., Faisal, N. H., El-Sherik, A. M., Elakwah, Y. O., et al. (2014). Single asperity nanoscratch behaviour of HIPed and cast Stellite 6 alloys. *Wear* 312, 70–82. doi:10.1016/j.wear.2014.02.006

Ahmed, R., De Villiers Lovelock, H. L., Davies, S., and Faisal, N. H. (2013). Influence of Re-HIPing on the structure-property relationships of cobalt-based alloys. *Tribol. Int.* 57, 8–21. doi:10.1016/j.triboint.2012.06.025

Atkinson, H., and Davies, S. (2000). Fundamental aspects of hot isostatic pressing: an overview. *Metallurgical Mater. Trans. A* 31A, 2981–3000. doi:10.1007/s11661-000-0078-2

Barros, T. S., Pecly, P. H. R., Pardal, J. M., Gonzaga, A. C., and Tavares, S. S. M. (2022). Comparison between hot rolled and powder metallurgy–hot isostatic pressing (PM-HIP) processed duplex stainless steel UNS S32205. *J. Mater Eng. Perform.* 31, 5504–5510. doi:10.1007/s11665-022-06616-8

Blevins, J., and Yang, G. (2020). Machine learning enabled advanced manufacturing in nuclear engineering applications. *Nucl. Eng. Des.* 367, 110817. doi:10.1016/j.nucengdes.2020.110817

Bonny, G., Terentyev, D., Bakaev, A., Zhurkin, E. E., Hou, M., Van Neck, D., et al. (2013). On the thermal stability of late blooming phases in reactor pressure vessel steels: an atomistic study. *J. Nucl. Mater.* 442, 282–291. doi:10.1016/j.jnucmat.2013.08.018

Bonny, G., Terentyev, D., Zhurkin, E. E., and Malerba, L. (2014). Monte Carlo study of decorated dislocation loops in FeNiMnCu model alloys. *J. Nucl. Mater.* 452, 486–492. doi:10.1016/j.jnucmat.2014.05.051

Brookman, J. (2020). *ECAR 4951 BSU-8242 3 DPA as-run physics analysis (INL/EXT-21-64250-Rev000).* Idaho Falls, ID (United States). doi:10.2172/1819757

Brookman, J. V. (2018). *ATR physics evaluation for BSU-8242 in the A-6, A-7, and A-8 ATR irradiation positions (INL/RPT-22-67629).* Idaho: Idaho Falls.

Bullens, A. L., Bautista, E., Jaye, E. H., Vas, N. L., Cain, N. B., Mao, K., et al. (2018). Comparative thermal aging effects on PM-HIP and forged inconel 690. *JOM* 70, 2218–2223. doi:10.1007/s11837-018-2818-z

Chen, T., He, L., Cullison, M. H., Hay, C., Burns, J., Wu, Y., et al. (2020). The correlation between microstructure and nanoindentation property of neutron-irradiated austenitic alloy D9. *Acta Mater* 195, 433–445. doi:10.1016/j.actamat.2020.05.020

Chu, S., and Majumdar, A. (2012). Opportunities and challenges for a sustainable energy future. *Nature* 488, 294–303. doi:10.1038/nature11475

Clement, C., Panuganti, S., Warren, P. H., Zhao, Y., Lu, Y., Wheeler, K., et al. (2022b). Comparing structure-property evolution for PM-HIP and forged alloy 625 irradiated with neutrons to 1 dpa. *Mater. Sci. Eng. A* 857, 144058. doi:10.1016/j.msea.2022.144058

Clement, C., Zhao, Y., Warren, P., Liu, X., Xue, S., Gandy, D. W., et al. (2022a). Comparison of ion irradiation effects in PM-HIP and forged alloy 625. *J. Nucl. Mater.* 558, 153390. doi:10.1016/j.jnucmat.2021.153390

Crawford, D. C., Porter, D. L., Hayes, S. L., Meyer, M. K., Petti, D. A., and Pasamehmetoglu, K. (2007). An approach to fuel development and qualification. *J. Nucl. Mater.* 371, 232–242. doi:10.1016/j.jnucmat.2007.05.029

Davis, K. L., and Hone, L. A. (2020). *NSUF metl wire evaluations for BSU-8242 and GE hitachi-10393 irradiation experiments (INL/EXT-20-58375-Rev0).* Idaho: Idaho Falls.

De Bellefon, G. M., and Van Duysen, J. C. (2016). Tailoring plasticity of austenitic stainless steels for nuclear applications: review of mechanisms controlling plasticity of austenitic steels below 400 °C. *J. Nucl. Mater.* 475, 168–191. doi:10.1016/j.jnucmat.2016.04.015

Du, C., Jin, S., Fang, Y., Li, J., Hu, S., Yang, T., et al. (2018). Ultrastrong nanocrystalline steel with exceptional thermal stability and radiation tolerance. *Nat. Commun.* 9, 5389. doi:10.1038/s41467-018-07712-x

Everton, S. K., Hirsch, M., Stravroulakis, P., Leach, R. K., and Clare, A. T. (2016). Review of *in-situ* process monitoring and *in-situ* metrology for metal additive manufacturing. *Mater Des.* 95, 431–445. doi:10.1016/j.matdes.2016.01.099

Fujii, K., Fukuya, K., Nakata, N., Hono, K., Nagai, Y., and Hasegawa, M. (2005). Hardening and microstructural evolution in A533B steels under high-dose electron irradiation. *J. Nucl. Mater.* 340, 247–258. doi:10.1016/j.jnucmat.2004.12.008

Gandy, D. W., Shingledecker, J., and Siefert, J. (2012). Overcoming Barriers for Using PM/HIP Technology to Manufacture Large Power Generation Components PM/HIP opens up a new method of manufacturing high pressure-retaining components for use in the power-generation industry. *Adv. Mater. Process.* ASM International 170, 1–8.

Gandy, D. W., Siefert, J., Smith, R., Anderson, P., Lherbier, L., Novotnak, D., et al. (2016). Development of a cobalt-free hard-facing alloy — NitroMaxx-PM for nuclear applications, in: World PM2016.

Gandy, D. W., Stover, C., Bridger, K., and Lawler, S., Small modular reactor vessel manufacture/fabrication using PM-HIP and electron beam welding technologies, materials research proceedings (hot isostatic pressing: HIP'17). 10 (2019) 224–234. doi:10.21741/9781644900031-29

Getto, E. M., Tobie, B., Bautista, E., Bullens, A. L., Kroll, Z. T., Pavel, M. J., et al. (2019). Thermal aging and the Hall–petch relationship of PM-HIP and wrought alloy 625. *JOM* 71, 2837–2845. doi:10.1007/s11837-019-03532-6

Gong, X., Li, R., Sun, M., Ren, Q., Liu, T., and Short, M. P. (2016). Opportunities for the LWR ATF materials development program to contribute to the LBE-cooled ADS materials qualification program. *J. Nucl. Mater.* 482, 218–228. doi:10.1016/j.jnucmat.2016.10.012

Guillen, D. P., Pagan, D. C., Getto, E. M., and Wharry, J. P. (2018). *In situ* tensile study of PM-HIP and wrought 316L stainless steel and inconel 625 alloys with high energy diffraction microscopy. *Mater. Sci. Eng. A* 738, 380–388. doi:10.1016/J.MSEA.2018.09.083

Guillen, D. P., Wharry, J. P., Housley, G., Hale, C. D., Brookman, J., and Gandy, D. W. (2023). Experiment design for the neutron irradiation of PM-HIP alloys for nuclear reactors, *Nucl. Eng. Des.* 402, 112114. doi:10.1016/j.nucengdes.2022.112114

Gurovich, B. A., Kuleshova, E. A., Shtrombakh, Ya.I., Erak, D.Yu., Chernobaeva, A. A., and Zabusov, O. O. (2009). Fine structure behaviour of VVER-1000 RPV materials under irradiation. *J. Nucl. Mater.* 389, 490–496. doi:10.1016/j.jnucmat.2009.02.002

Hale, C. (2021). *BSU-8242 as-run thermal analysis (INL/EXT-21-63578-Rev000).* Idaho Falls, ID (United States). doi:10.2172/1813571

Hale, C. D. (2018). *BSU-8242 programmatic and safety compliance structural and thermal analysis (INL/RPT-22-67627).* Idaho: Idaho Falls.

Hamaoka, T., Satoh, Y., and Matsui, H. (2010). One-dimensional motion of self-interstitial atom clusters in A533B steel observed using a high-voltage electron microscope. *J. Nucl. Mater.* 399, 26–31. doi:10.1016/j.jnucmat.2009.12.014

Hensley, C., Sisco, K., Beauchamp, S., Godfrey, A., Rezayat, H., McFalls, T., et al. (2021). Qualification pathways for additively manufactured components for nuclear applications. *J. Nucl. Mater.* 548, 152846. doi:10.1016/j.jnucmat.2021.152846

Hyde, J. M., Marquis, E. A., Wilford, K. B., and Williams, T. J. (2011). A sensitivity analysis of the maximum separation method for the characterisation of solute clusters. *Ultramicroscopy* 111, 440–447. doi:10.1016/j.ultramic.2010.12.015

Jiang, W., Zhao, Y., Lu, Y., Wu, Y., Frazer, D., Guillen, D. P., et al. (2023). Comparison of PM-HIP to forged SA508 pressure vessel steel under high-dose neutron irradiation. Available at: http://arxiv.org/abs/2311.11548.

Jiao, Z., and Was, G. S. (2010). The role of irradiated microstructure in the localized deformation of austenitic stainless steels. *J. Nucl. Mater.* 407, 34–43. doi:10.1016/j.jnucmat.2010.07.006

Kautz, E. J., Hagen, A. R., Johns, J. M., and Burkes, D. E. (2019). A machine learning approach to thermal conductivity modeling: a case study on irradiated uraniummolybdenum nuclear fuels. *Comput. Mater Sci.* 161, 107–118. doi:10.1016/j.commatsci.2019.01.044

Kočık, J., Keilová, E., Čižek, J., and Procházka, I. (2002). TEM and PAS study of neutron irradiated VVER-type RPV steels. *J. Nucl. Mater.* 303, 52–64. doi:10.1016/S0022-3115(02)00800-0

Kuleshova, E. A., Gurovich, B. A., Shtrombakh, Ya.I., Erak, D.Yu., and Lavrenchuk, O. V. (2002). Comparison of microstructural features of radiation embrittlement of VVER-440 and VVER-1000 reactor pressure vessel steels. *J. Nucl. Mater.* 300, 127–140. doi:10.1016/S0022-3115(01)00752-8

Lind, A., and Bergenlid, U. (2000). Mechanical properties of hot isostatic pressed type 316LN steel after irradiation. *J. Nucl. Mater.* 58–59, 451–454. doi:10.1016/s0022-3115(00)00084-2

Lind, A., and Bergenlid, U. (2001). Mechanical properties of hot isostatic pressed type 316LN steel after irradiation to 2.5 dpa. *Fusion Eng. Des.* 58–59, 713–717. doi:10.1016/S0920-3796(01)00541-5

Mao, K., Wang, H., Wu, Y., Tomar, V., and Wharry, J. P. (2018). Microstructure-property relationship for AISI 304/308L stainless steel laser weldment. *Mater. Sci. Eng. A* 721, 234–243. doi:10.1016/j.msea.2018.02.092

Mao, K. S., Wu, Y., Sun, C., Perez, E., and Wharry, J. P. (2018). Laser weld-induced formation of amorphous Mn–Si precipitate in 304 stainless steel. *Mater. (Oxf)* 3, 174–177. doi:10.1016/j.mtla.2018.08.012

Mao, K. S., French, A. J., Liu, X., Wu, Y., Giannuzzi, L. A., Sun, C., et al. (2021). Microstructure and microchemistry of laser welds of irradiated austenitic steels. *Mater Des.* 206, 109764. doi:10.1016/j.matdes.2021.109764

Mao, K. S., Sun, C., Shiau, C.-H., Yano, K. H., Freyer, P. D., El-Azab, A. A., et al. (2020). Role of cavities on deformation-induced martensitic transformation pathways in a laser-welded, neutron irradiated austenitic stainless steel. *Scr Mater* 178, 1–6. doi:10.1016/j.scriptamat.2019.10.037

Mathew, M. D. (2022). Nuclear energy: a pathway towards mitigation of global warming. *Prog. Nucl. Energy* 143, 104080. doi:10.1016/j.pnucene.2021.104080

Maussner, G., Scharf, L., Langer, R., and Gurovich, B. (1999). Microstructure alterations in the base material, heat affected zone and weld metal of a 440-VVER-reactor pressure vessel caused by high fluence irradiation during long term operation; material: 15 Ch2MFA ≈0.15 C–2.5 Cr–0.7 Mo–0.3 V. *Nucl. Eng. Des.* 193, 359–376. doi:10.1016/S0029-5493(99)00192-2

McMurtrey, M. D., Was, G. S., Patrick, L., and Farkas, D. (2011). Relationship between localized strain and irradiation assisted stress corrosion cracking in an austenitic alloy. *Mater. Sci. Eng. A* 528, 3730–3740. doi:10.1016/j.msea.2011.01.073

Meslin, E., Lambrecht, M., Hernández-Mayoral, M., Bergner, F., Malerba, L., Pareige, P., et al. (2010). Characterization of neutron-irradiated ferritic model alloys and a RPV steel from combined APT, SANS, TEM and PAS analyses. *J. Nucl. Mater.* 406, 73–83. doi:10.1016/j.jnucmat.2009.12.021

Metals, and Ceramics Information Center Report No (1977). *MCIC-77-34 (november 1977).* Columbus, Ohio.

Moorehead, M., Nelaturu, P., Elbakhshwan, M., Parkin, C., Zhang, C., Sridharan, K., et al. (2021). High-throughput ion irradiation of additively manufactured compositionally complex alloys. *J. Nucl. Mater.* 547, 152782. doi:10.1016/j.jnucmat.2021.152782

Morgan, D., Pilania, G., Couet, A., Uberuaga, B. P., Sun, C., and Li, J. (2022). Machine learning in nuclear materials research. *Curr. Opin. Solid State Mater Sci.* 26, 100975. doi:10.1016/j.cossms.2021.100975

Morrison, A., Sulley, J., Carpenter, C., Borradaile, B., Jones, G., and Warner, T. (2019). HIPed low alloy steel for nuclear pressure vessel applications – material property and microstructural assessment. *Proc. Int. Conf. Nucl. Eng. (ICONE).* 27, 1021. doi:10.1299/jsmeicone.2019.27.1021

Motta, A. T. (1997). *Amorphization of intermetallic compounds under irradiation-A review.*

Murty, K. L., and Charit, I. (2008). Structural materials for Gen-IV nuclear reactors: challenges and opportunities. *J. Nucl. Mater.* 383, 189–195. doi:10.1016/j.jnucmat.2008.08.044

Odette, G. R., and Hoelzer, D. T. (2010). Irradiation-tolerant nanostructured ferritic alloys: transforming helium from a liability to an asset. *JOM* 62, 84–92. doi:10.1007/s11837-010-0144-1

Oliver, W. C., and Pharr, G. M. (2004). Measurement of hardness and elastic modulus by instrumented indentation: advances in understanding and refinements to methodology. *J. Mater Res.* 19, 3–20. doi:10.1557/jmr.2004.19.1.3

Olson, G. B., and Kuehmann, C. J. (2014). Materials genomics: from CALPHAD to flight. *Scr Mater* 70, 25–30. doi:10.1016/j.scriptamat.2013.08.032

Parish, C. M., Field, K. G., Certain, A. G., and Wharry, J. P. (2015). Application of STEM characterization for investigating radiation effects in BCC Fe-based alloys. *J. Mater Res.* 30, 1275–1289. doi:10.1557/jmr.2015.32

Patki, P. V., Wu, Y. Q., and Wharry, J. P. (2020). Effects of proton irradiation on microstructure and mechanical properties of nanocrystalline Cu–10at%Ta alloy. *Mater. (Oxf).* 9, 100597. doi:10.1016/j.mtla.2020.100597

Petti, D., Maki, J., Hunn, J., Pappano, P., Barnes, C., Saurwein, J., et al. (2010). The DOE advanced gas reactor fuel development and qualification program. *JOM* 62, 62–66. doi:10.1007/s11837-010-0140-5

Rao, G. A., Kumar, M., Srinivas, M., and Sarma, D. S. (2003). Effect of standard heat treatment on the microstructure and mechanical properties of hot isostatically pressed superalloy inconel 718. *Mater. Sci. Eng. A* 355, 114–125. doi:10.1016/S0921-5093(03)00079-0

Rodchenkov, B. S., Prokhorov, V. I., Makarov, O. Y., Shamardin, V. K., Kalinin, G. M., Strebkov, Y. S., et al. (2000). Effect of ITER components manufacturing cycle on the irradiation behaviour of 316L(N)-IG steel. *J. Nucl. Mater.* 283–287, 1166–1170. doi:10.1016/s0022-3115(00)00319-6

Sailor, W. C., Bodansky, D., Braun, C., Fetter, S., and van der Zwaan, B. (2000). A nuclear solution to climate change? *Science* 288, 1177–1178. doi:10.1126/science.288.5469.1177

Sen, A., Bachhav, M., Vurpillot, F., Mann, J. M., Morgan, P. K., Prusnick, T. A., et al. (2021). Influence of field conditions on quantitative analysis of single crystal thorium dioxide by atom probe tomography. *Ultramicroscopy* 220, 113167. doi:10.1016/j.ultramic.2020.113167

Shulga, A. V., Effect of heat treatment on carbon behaviour in the HIPed products of the type EP962P Ni-based superalloys, in: Euro PM 2012 - Hot Isostatic Pressing 3, 2012: pp. 1–6.

Shulga, A. V. (2013). A comparative study of the mechanical properties and the behavior of carbon and boron in stainless steel cladding tubes fabricated by PM HIP and traditional technologies. *J. Nucl. Mater.* 434, 133–140. doi:10.1016/j.jnucmat.2012.11.008

Shulga, A. V. (2014). Effect of thermal aging on the mechanical properties of austenitic and ferritic/martensitic stainless steels manufactured by PM HIP and traditional technologies. 1–6. Euro PM 2014 congress and exhibition. Proceedings, Available at: http://www.scopus.com/inward/record.url?eid=2-s2.0-84959042666&partnerID=tZOtx3y1.

Stach, E., DeCost, B., Kusne, A. G., Hattrick-Simpers, J., Brown, K. A., Reyes, K. G., et al. (2021). Autonomous experimentation systems for materials development: a community perspective. *Matter* 4, 2702–2726. doi:10.1016/j.matt.2021.06.036

Sun, C., Wang, Y., McMurtrey, M. D., Jerred, N. D., Liou, F., and Li, J. (2021). Additive manufacturing for energy: a review. *Appl. Energy* 282, 116041. doi:10.1016/j.apenergy.2020.116041

Swenson, M. J., and Wharry, J. P. (2015). The comparison of microstructure and nanocluster evolution in proton and neutron irradiated Fe–9%Cr ODS steel to 3 dpa at 500 °C. *J. Nucl. Mater.* 467, 97–112. doi:10.1016/j.jnucmat.2015.09.022

Swenson, M. J., and Wharry, J. P. (2016). Collected data set size considerations for atom probe cluster analysis. *Microsc. Microanal.* 22, 690–691. doi:10.1017/S143192761600430X

Terrani, K. A., Capps, N. A., Kerr, M. J., Back, C. A., Nelson, A. T., Wirth, B. D., et al. (2020). Accelerating nuclear fuel development and qualification: modeling and simulation integrated with separate-effects testing. *J. Nucl. Mater.* 539, 152267. doi:10.1016/j.jnucmat.2020.152267

van Osch, E. V., Horsten, M. G., de Vries, M. I., van Witzenburg, W., Conrad, R., Sordon, G., et al. (1996). Low temperature irradiation experiments and material testing in Petten. *J. Nucl. Mater.* 233–237, 1541–1546. doi:10.1016/s0022-3115(96)00134-1

Vaumousse, D., Cerezo, A., and Warren, P. J. (2003). A procedure for quantification of precipitate microstructures from three-dimensional atom probe data. *Ultramicroscopy* 95, 215–221. doi:10.1016/S0304-3991(02)00319-4

West, E. A., McMurtrey, M. D., Jiao, Z., and Was, G. S. (2012). Role of localized deformation in irradiation-assisted stress corrosion cracking initiation. *Metall. Mater Trans. A Phys. Metall. Mater Sci.* 43, 136–146. doi:10.1007/s11661-011-0826-5

Wharry, J. P., Clement, C. D., Zhao, Y., Baird, K., Frazer, D., Burns, J., et al. (2023). Mechanical testing data from neutron irradiations of PM-HIP and conventionally manufactured nuclear structural alloys. *Data Brief.* 48, 109092. doi:10.1016/j.dib.2023.109092

Wharry, J. P., and Mao, K. S. (2020). The role of irradiation on deformation-induced martensitic phase transformations in face-centered cubic alloys. *J. Mater Res.* 35, 1660–1671. doi:10.1557/jmr.2020.80

Williams, C. A., Haley, D., Marquis, E. A., Smith, G. D. W., and Moody, M. P. (2013). Defining clusters in APT reconstructions of ODS steels. *Ultramicroscopy* 132, 271–278. doi:10.1016/j.ultramic.2012.12.011

Yu, H., Ahmed, R., Villiers Lovelock de, H., and Davies, H., Influence of manufacturing process and alloying element content on the tribomechanical properties of cobalt-based alloys, *J. Tribol. Trans. ASME).* 131 (2009) 011601, 1-011601.12. doi:10.1115/1.2991122

Yu, K. Y., Sun, C., Chen, Y., Liu, Y., Wang, H., Kirk, M. A., et al. (2013). Superior tolerance of Ag/Ni multilayers against Kr ion irradiation: an *in situ* study. *Philos. Mag.* 93, 3547–3562. doi:10.1080/14786435.2013.815378

Zain-ul-abdein, M., and Nélias, D. (2016). Effect of coherent and incoherent precipitates upon the stress and strain fields of 6xxx aluminium alloys: a numerical analysis. *Int. J. Mech. Mater. Des.* 12, 255–271. doi:10.1007/s10999-015-9298-x

Zhang, X., Hattar, K., Chen, Y., Shao, L., Li, J., Sun, C., et al. (2018). Radiation damage in nanostructured materials. *Prog. Mater Sci.* 96, 217–321. doi:10.1016/j.pmatsci.2018.03.002

Frontiers in Nuclear Engineering

TYPE Original Research
PUBLISHED 12 January 2024
DOI 10.3389/fnuen.2023.1322209

OPEN ACCESS

EDITED BY
Edgar C. Buck,
Pacific Northwest National Laboratory (DOE), United States

REVIEWED BY
Jacques Lechelle,
Commissariat à l'Energie Atomique et aux Energies Alternatives (CEA), France
Adam Burak,
University of Michigan, United States

*CORRESPONDENCE
Elizabeth Sooby,
✉ Elizabeth.Sooby@utsa.edu

RECEIVED 16 October 2023
ACCEPTED 15 December 2023
PUBLISHED 12 January 2024

CITATION
Stone J, Khair M, Cavazos S and Sooby E (2024), High-temperature thermal imaging to inform the arc-melt synthesis of nuclear materials. *Front. Nucl. Eng.* 2:1322209.
doi: 10.3389/fnuen.2023.1322209

High-temperature thermal imaging to inform the arc-melt synthesis of nuclear materials

Jordan Stone, Mira Khair, Steven Cavazos and Elizabeth Sooby*

Extreme Environment Materials Laboratory, University of Texas at San Antonio, Department of Physics and Astronomy, College of Sciences, San Antonio, TX, United States

The advancement of nuclear energy technology necessitates the development of novel materials and synthesis methods to produce materials which enable new fuel cycles. Alongside the maturation of R&D scale technologies to produce these materials, there is an ongoing effort to develop *in situ* monitoring capabilities to reduce the time to the discovery and development of these fuels. Monitoring data can be leveraged in artificial intelligence platforms to detect phenomena which lead to varied macro- and microstructural features which impact the application and performance of samples synthesized. The present study presents early-stage findings of the implementation of high-temperature, high-frame-rate infrared thermal imaging to monitor the arc-melt synthesis of novel fuels and compounds relevant to advanced nuclear reactors. The study illustrates both the challenges and opportunities of this methodology, highlighting the importance of internal standards while determining emissivity and transmission values as well as visualizing volatilization during melt synthesis.

KEYWORDS

uranium chemistry, melt synthesis, thermal imaging, uranium nitride, palladium silicide

1 Introduction

Researchers across the globe are advancing clean energy solutions (nuclear energy, renewables, and energy storage materials) with the goal of reducing our carbon footprint. The advancement of nuclear energy technologies, such as the introduction of novel fuels and reactor types, and manufacturing capabilities are at the forefront of these efforts. The present investigation provides early-stage findings in a study to assess the feasibility of high-temperature thermal imaging to inform the melt synthesis of compounds and alloys *in situ*. The investigators argue that the development of this novel methodology will enable a capability to shorten the time to material discovery by visualizing the melt and solidification phenomena of high-temperature compounds during synthesis. *In situ* monitoring coupled with computer vision methods (a sub-field of artificial intelligence) will allow researchers to identify melt phenomena and then predict sample homogeneity following fabrication. This effort aims to shortcut the characterization time which traditionally involves labor- and time-intensive sample preparation for diffraction and electron microscopy characterization. Furthermore, the identification of high-temperature phase formation, segregation, solid-state phase transitions, and volatility are critical for thermodynamic modeling of these fuel-cycle material systems, where structure and property data remain scarce. Pairing melting and solidification behavior observations with post-melt characterization will facilitate the discovery of high-temperature crystalline phases not observed in conventional alloy development without extensive post-synthesis microstructural characterization. The methods developed in this study are readily applicable to other melt synthesis methods, including additive manufacturing (AM) techniques used for conventional structural materials.

Research into actinide compound synthesis presents several challenges, including but not limited to safe handling of radiological materials, pyrophoricity, sourcing high-purity precursors, and a general lack of well-defined thermodynamic and thermochemical information. While oxide compounds have seen historic interest due to their application and relevance to civilian nuclear power systems, intermetallic compounds and alloys have been far less investigated. Uranium binary and ternary compounds present a wide range of melt temperatures and thermal properties, and additionally have complex melt and nucleation phenomena, leading to several unexplored material systems for testing the methods developed here (Sooby Wood et al., 2016; Sooby Wood et al., 2017; Lopes et al., 2019; Sooby Wo et al., 2020; Wilson et al., 2020; Gonzales et al., 2021; Watkins et al., 2021; Moczygemba et al., 2022). Furthermore, there are several inconsistencies among experimentally observed phase structures and thermodynamically predicted phase diagrams (Sooby Wood et al., 2017; Moczygemba et al., 2022). These discrepancies provide a material testbed with ample material systems which can meaningfully contribute to the current state of knowledge while concurrently developing a capability applicable to a broader array of material systems.

There does not exist a formal methodology in a research and development (R&D) setting that can collect high-frame-rate thermal images of arc-melt pools during the synthesis of actinide compounds. However, thermal imaging paired with high-speed image capture has been employed to study direct energy deposition (DED) AM melt pool dynamics, as explored in Arrizubieta et al. (2017), Calta et al. (2017), Cheng et al. (2018), Heigel and Lane (2018), Wirth et al. (2018), and Mazzoleni et al. (2019). The challenges of using thermal imaging to resolve microstructural defects originating in melt dynamics include the high-speed dynamics of the melt pool (limitations of the camera frame rate) as well as the spatial resolution required for the imaging technology (Mazzoleni et al., 2019). Cheng et al. (2018) used a near-IR camera to measure melt pool dimensions as a function of build height and found little correlation between the melt pool dimensions (length and width) and the height of the build for nickel-based super alloys. The challenge they encountered was the spatial resolution of the imaging technique, as they were only able to measure the overall dimension of the melt pool rather than the dynamics within the melt pool that would cause microstructural defects. Infrared (IR) camera developers recommend using a 3 × 3 pixel grid to accurately measure the temperature of a spatially resolved feature. While conventionally manufactured materials fabricated through forging, cold-working, and/or sintering produce small crystalline grains (nm to μm sizes), arc-melting is capable of producing materials with tens to hundreds of micrometer size grains. It is argued here that, to resolve microstructural feature formation in the methods presented, each pixel must be in the order of at least 10 μm. Cheng et al. (2018) demonstrated pixel sizes of 47–80 μm, limiting the ability to detect microstructural defect-causing dynamics such as key holing or spatter. A similar pixel size limitation is clear in Wirth et al. (2018), where the melt dynamics, specifically the surface flow field, were studied spatially using a high-speed IR camera.

Mazzoleni et al. (2019) presented the spatial, temporal, and wavelength resolution criteria to observe melt pool dynamics using CMOS imaging techniques. Their analysis settled on a frame acquisition rate of 1,200 frames per second (1.2 kHz), a 4.3 × 4.3 mm field of view, and a 14 μm/pixel spatial resolution. They concluded that the near-IR range was able to provide the most information on melt pool size, and the 1.2 kHz capture frequency proved adequate for resolving the melt pool evolution. However, CMOS detectors cannot be directly calibrated to quantify temperature. At these imaging parameters, microstructural effects were still unobservable using this technology. Instead, a dynamic study of the molten region was presented (Mazzoleni et al., 2019).

These studies investigated bulk (feature size on the order of 100 μm) melt dynamics. To meet the objectives of our broader study, the research team must observe microstructural features during melt and solidification. We recognize a trade-off in the cost of the technology employed to study melt dynamics and the scale of observable phenomena. *In situ* X-ray imaging, employing a synchrotron X-ray source, was utilized to resolve microstructural features, including features such as depressions and pores. (Martin et al., 2019). From a process monitoring perspective, placing AM equipment (or an arc-melt furnace) in a synchrotron facility is impractical for day-to-day process monitoring, although significant information about laser-metal dynamics can be obtained. Therefore, the present study employed an IR camera capable of resolving microstructural features forming in the melt pool of an arc-melt-synthesized sample. The Broadband InSb, 1.5–5.0 μm detector was used to allow for a 1280 × 1024 pixel resolution with a 181 Hz frequency for the full frame that can be windowed to 6 kHz. The extended 1.5–5.0 μm range is necessary to observe dynamics of the melt through the fused quartz observation tube (furnace tube/window). Thermographic calibration filters included with the IR camera facilitate temperature data to be accurately acquired to 3,000°C. However, the study presented here displays the challenges, specifically emissivity and transmission, to accurate calibration, given the physical barriers necessary for the arc-melting process. Emissivity and transmission relate to the ability of the sample to emit infrared radiation. However, as demonstrated in Figure 1, two lenses are placed between the IR camera and the melted sample. A previous study has highlighted the importance of luminance maps for IR observations of arc-melting materials (Hafid El Mir et al., 2010). The protective quartz glass of the arc furnace and the UV shield are in place to prevent intense UV rays emitted from the arc-melting process—an occupational hazard.

Presented here are the findings from three monitored melts, observing the melt behavior of titanium (Ti), palladium silicide (PdSi), and uranium mononitride (UN). These three melts display the challenges as well as the opportunities of this IR observation method. Ti is a pure metal with well-defined and well-behaved melt (minimal to no volatilization). Molten Ti is often used as an internal oxygen “getter” in arc-melt furnaces to scrub ultra-high-purity (UHP) argon (Ar) gas of trace amounts of oxygen (O_2). Palladium silicides are observed in post-irradiation examination (PIE) of particle fuel forms (Tiegs, 1982; Wen et al., 2018; Liu et al., 2023) fabricated by collaborating investigators,

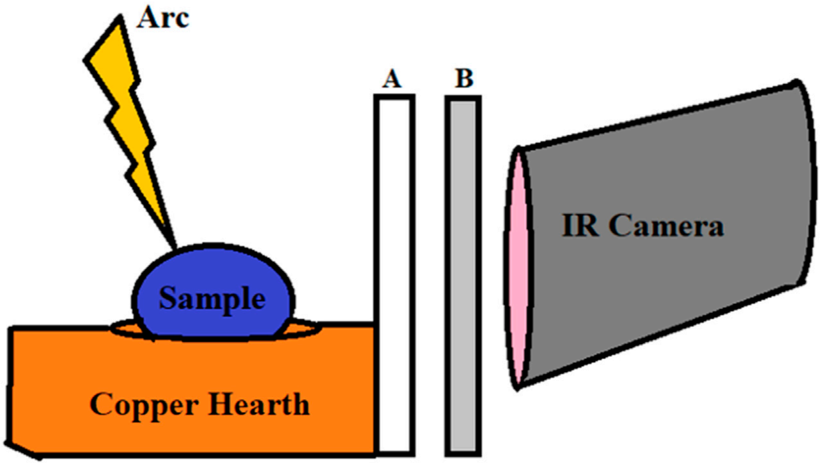

FIGURE 1
Simplified diagram of arc furnace setup with **(A)** the quartz glass of the arc furnace and **(B)** the UV protective film in front of the camera.

FIGURE 2
Downward angled view into the inside of the arc-melter holding chamber: a dimpled copper hearth can be seen below brass fittings which is incased in the fused quartz glass chamber.

FIGURE 3
(A) Arc-melt furnace and IR camera assembly without UV shielding. **($B_{1\text{-}2}$)** Arc-melt furnace and IR camera assembly with UV shielding for researcher safety only; no IR images were taken looking through UV shielding.

with the authoring team observing the melt behavior through the thermal imaging camera. Lastly, uranium mononitride (UN) is an advanced reactor fuel form proposed for reactors which require high temperature stability, high uranium density, and improved thermal transport properties compared to conventional uranium dioxide (Matthews, 1993; Rogozkin et al., 2003; Jaques et al., 2008; Arai, 2012; Brown et al., 2014; Nunez et al., 2014; Jaques et al., 2015; Yang et al., 2015; Johnson et al., 2016; Ortega et al., 2016; Uygur, 2016; Wallenius et al., 2020; Sooby et al., 2021; Watkins et al., 2021). UN, unlike Ti and PdSi, has a high vapor pressure at the melt point, exhibiting volatilization during melt (Nunez et al., 2014).

2 Methods and materials

2.1 Methods

A tri-arc-melting furnace (Centorr Vacuum Industries Model 5 TA) capable of achieving temperatures exceeding 3,000°C was used for the present study. The melting of conductive samples is achieved by resistively heating samples to and often beyond the melt point of the sample. Three independent power supplies provided up to 100 amps (A) of current per electrode to the sample at 8.5–12 volts (V). The current was increased until melting was observed. While samples were in the molten state, they typically exhibited a “pinwheeling” phenomenon observed through the UV

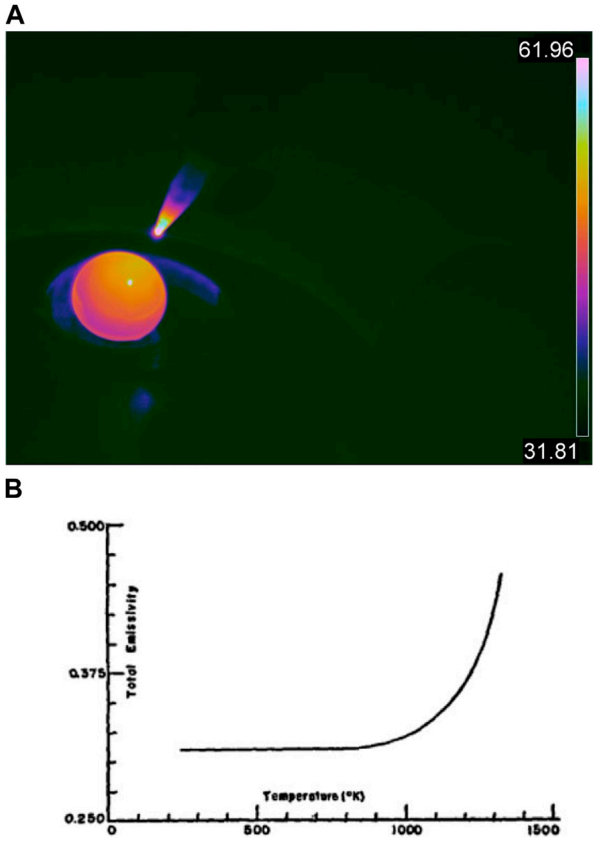

FIGURE 4
(A) Uncalibrated radiometric image of a Ti getter at a liquid state inside an arc furnace, taken with an IR camera, with a temperature range of 31.81°C–61.81°C, showcasing a temperature range that is not reflective of the real temperatures of the surfaces depicted. **(B)** Michels and Wilford's plot of Ti total emissivity vs. temperature (Michels and Wilford, 1949).

shield of the melt furnace. The pinwheeling movement was created by molten material convection within a sample. In the setup described above, each electrode was at an angle to sample on the hearth. As voltage was applied, one side of the sample heated before the other, creating a gradient of heat across the surface of the sample. When liquidation occurred, this temperature gradient caused swirling of the sample, creating the illusion of a completely moving molten ingot that appears like a pin wheel. As displayed in Figure 2, the samples were placed within a cavity of the water-cooled copper hearth. The hearth and Ar atmosphere required to maintain the arc of the electrode were encased in a fused quartz (quartz glass) chamber. While an electric arc resistively heated samples to temperatures in excess of 1,000°C, the copper hearth was actively cooled to prevent fusing of the furnace structural materials. The active cooling quenched the bottom of samples once the arc was removed.

An IR camera (FLIR X8580) was employed to monitor the melt of each sample presented here. Thermal imaging with FLIR X8580 combined a high-definition resolution of 1280 × 1024 pixels with fast frame rates and integration times to allow the recording of fast-moving subjects or, in this case, features such as rapid temperature changes, phase segregation, and cracking. The FLIR X8580 and arc furnace assembly is shown in Figure 3A.

The camera and the data collection were controlled using a desktop PC and commercially available software known as FLIR Research Studio. Multiple parameters were considered when using it: distance from the object of observation (in this case, the wall of the quartz chamber), the atmospheric temperature, emissivity, reflected temperature, and relative humidity. In addition, the setup described above contained a fused quartz chamber acting as an external optical lens (EOL), leading to the inclusion of additional parameters of EOL transmission and EOL temperature. To maintain the consistency of results, each of these parameters was evaluated:

1. Distance from the object of observation. The camera was positioned at a fixed distance of 12 cm (0.12 m) from the wall of the fused quartz chamber to the lens of the camera during Ti and PdSi investigation. Recent techniques were developed to reduce this distance to 7 cm (0.07 m) from the wall of the chamber to the lens, which was employed in dU (depleted uranium) refinement and UN synthesis. This value represented the minimum allowable distance in our IR measurement to minimize potential interference. During refinement and compound synthesis, samples were displaced from their initial position inside the chamber. Future research will include a factor for this change in position during IR data collection. To create a consistent observation methodology, physical lines were placed on the camera tripod to ensure that the setup was assembled so that the camera would be brought to the proper height to ensure a view into the chamber prior to filming. Prior to each filming, the space between the quartz chamber wall and camera was reconfirmed with the values stated above.
2. Atmospheric temperature and relative humidity. The ambient temperature of the system was taken from the room's temperature using a handheld probe (Omega HH802U). The measured temperature was then compared to the ambient temperature of the quartz glass chamber prior melting to establish temperature equilibrium before inducing temperature change via arc heating. Due to the inability to measure humidity in the room of observation, relative humidity measurements were taken from local weather reports and evaluated for accuracy against the relative standard humidity ranges of 30%–50% for ideal indoor humidity from the United States Environmental Protection Agency (US EPA, 2023). High outdoor humidity rates were then correlated to high indoor humidity rates within this range.
3. Emissivity. The emissivity of an object at room temperature ranges from a reflector, emissivity = 0, to a blackbody or absorber, emissivity = 1 (Claudson, 1958; FPI, 2023). At room temperature, approximately 25°C, most objects have a relative emissivity range of 0.9–1. Thus, an emissivity of 0.95 was employed while positioning the camera and for recordings at room temperature. However, emissivity changes inversely as the temperature of a material increases (Baker et al., 1963). Emissivity data are limited for nuclear materials, like UN, due to the recent development of UN for use as a nuclear fuel in experimental reactors. Therefore, inferred ranges of emissivity were taken from the emissive

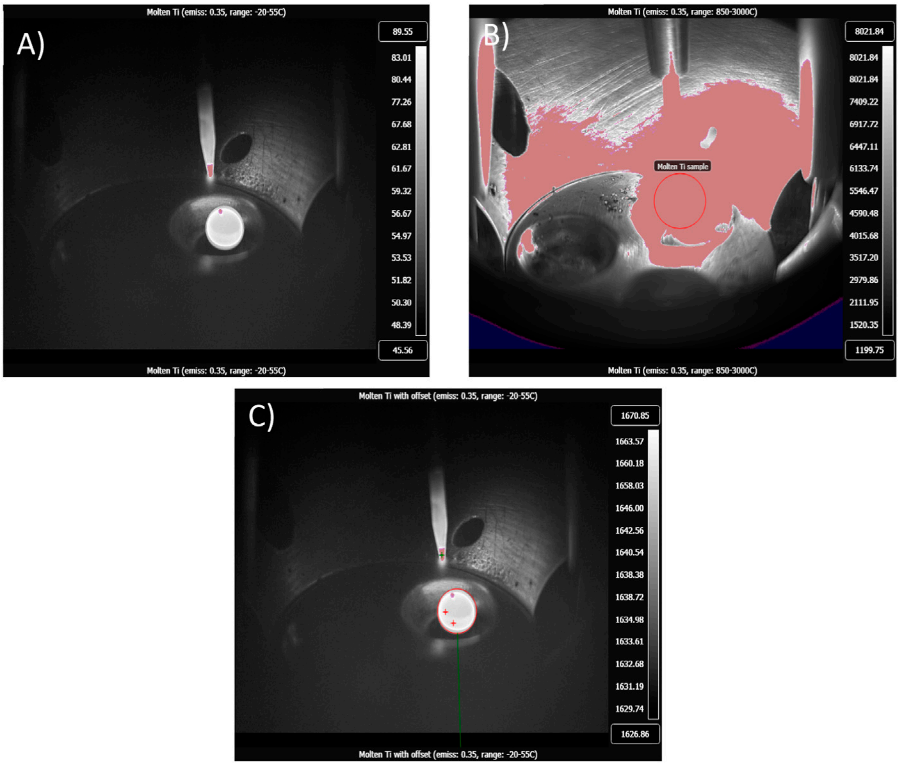

FIGURE 5
(A) Calibrated radiometric image of molten Ti getter with a temperature range of 45.56°C–89.55°C taken in the low-range calibration filter: −20°C to 50°C. **(B)** Calibrated radiometric image of molten Ti with a temperature range of 1,199.75°C–8,021.84°C, taken in the high-range filter: 850°C–3,000°C. A shroud can be seen covering the sample, making it undefinable; therefore, the low range is commonly used to showcase sample position within the chamber during arc-melting. **(C)** Calibrated radiometric image of melted Ti getter with an offset of 1,604°C and a temperature range of 1,626.86°C–1,670.85°C.

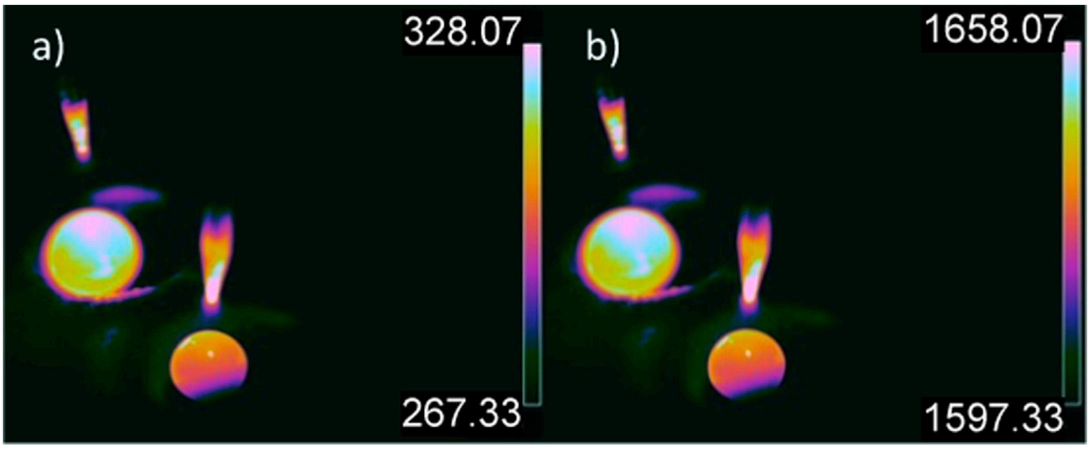

FIGURE 6
(A) Calibrated radiometric image of molten Ti (in the background) and PdSi (in the foreground) ingots inside an arc furnace with a temperature range of 328.07°C–328.07°C, no offset applied. **(B)** Calibrated radiometric image of Ti getter and PdSi ingots with a temperature range of 1,597°C–1,658°C.

properties of pure uranium to compare temperature ranges. In addition, oxidation can tarnish a surface, causing the reflectivity to decrease and, in turn, affecting the emissivity of the surface. To prevent oxidation during the melt process, the crystal chamber of the furnace was flushed with high-purity argon gas until the oxygen content of the chamber reached a magnitude of 10^{-16} ppm. Therefore, during the melt process, all samples were treated as pure/unoxidized. Pure uranium has

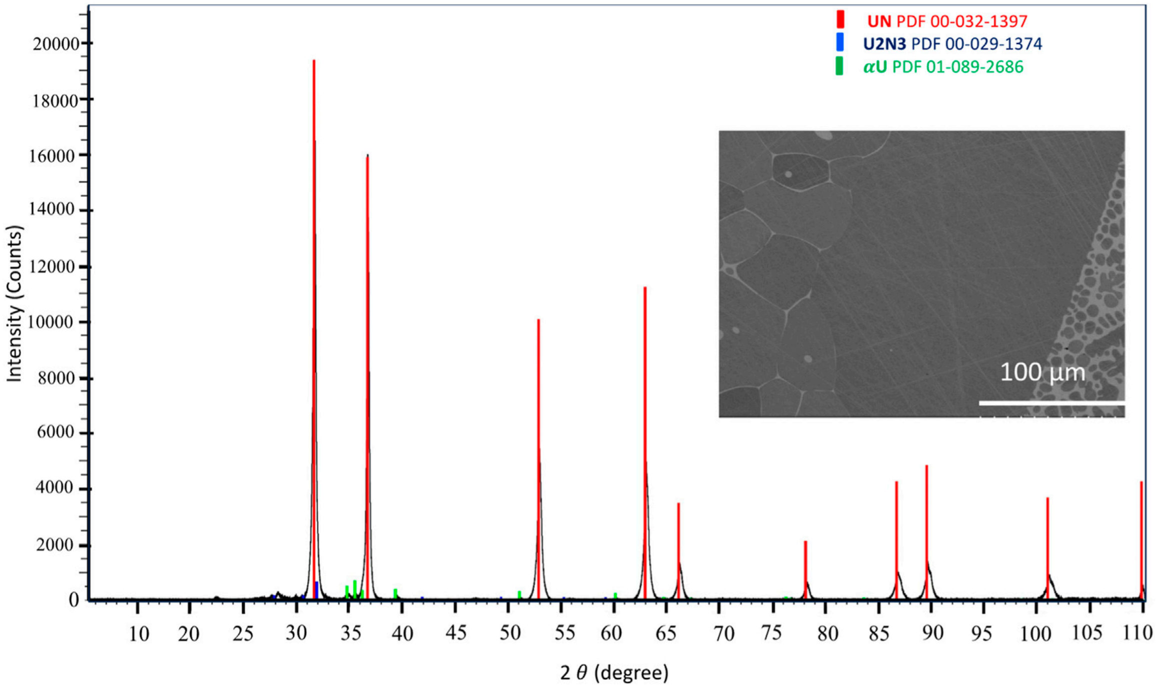

FIGURE 7
X-ray diffraction pattern and SEM micrograph displaying a largely UN sample with some segregated α-U (lighter phase in SEM micrograph) following the melt synthesis.

been found to have an emissivity of approximately 0.3–0.4 at 1,000°C (Baker et al., 1963) and 0.51 below melting temperature (Hole and Wright, 1939). During the refinement process (described in Section 2.2.3), uranium reaches melt temperature multiple times to purify the material. Pure uranium has a melting temperature of 1,132°C (Blumenthal, 1960), while UN has a melting temperature of 2,847°C ± 30°C (Nunez et al., 2014). Therefore, and during the refinement of uranium, the emissivity value was set to 0.3–0.4 for data recording, and during UN synthesis, a range values from 0.2–0.3 was used.

4. Reflected temperature. The metal components which comprise the arc-melting assembly are reflective, polished metals (Figure 2). When ignited with an arc, the IR radiation transmits in an isotropic manner around a sample. These rays reflect off the metallic surface of the chamber, leading to inference by rays encountering the camera lens. This inference can misrepresent the temperature of the sample, leading to a data error. A thermal image of the setup was taken at room temperature using frame image subtraction to prevent reflections caused by lighting and human manipulation of the arc-melting setup. The room temperature reading is discussed further in comparison to molten uranium and UN synthesis in the results. To decrease the number of reflections during refinement, a second thermal image was taken once the sample melted. This subtraction displayed changes to the sample once melt was reached.
5. External optic properties of fused quartz. Research conducted on fused quartz (fused silica and quartz glass) has shown it to have a transmission rate of approximately 0.94 for the IR wavelength range of 700–1,000 nm (Nürnberg et al., 2016). The temperature of the EOL was measured during the refinement of the uranium and UN synthesis process using a handheld thermometer (Omega HH802U) when the sample was observed to have melted and was re-measured for each respective trial.

2.2 Materials

2.2.1 Titanium

Titanium was sourced commercially (Thermo Scientific Chemicals, 99.99% metal basis purity, 12.7 mm rod form), and samples were segmented from this rod stock using electronic discharge machining (EDM). Minimal preparation is required for this type of sample, although EDM residue was removed via grinding with SiC paper and cleaned thoroughly prior to melting using methanol and acetone.

2.2.2 Palladium silicide

Stoichiometric PdSi was of interest due to its stable high-temperature phase between ~820–890°C—a relevant temperature for particle fuels. Palladium foil (sourced from Alfa Aesar, LOT Z20E017, 99.99% purity) of 1.0 mm thickness and granular silicon (virgin poly-fines sourced from Alfa Aesar, LOT M23E014, 99.999% purity) were prepared for arc-melt synthesis. Pd foil was segmented using a CBN metal bonded wafering blade on an Allied TechCut 4 low-speed saw (model 5–5,000). The segmented Pd and Si granules were cleaned using two 10 min successive washes of acetone then methanol in a Crest ultra-sonicator (model 175HTA). Masses of

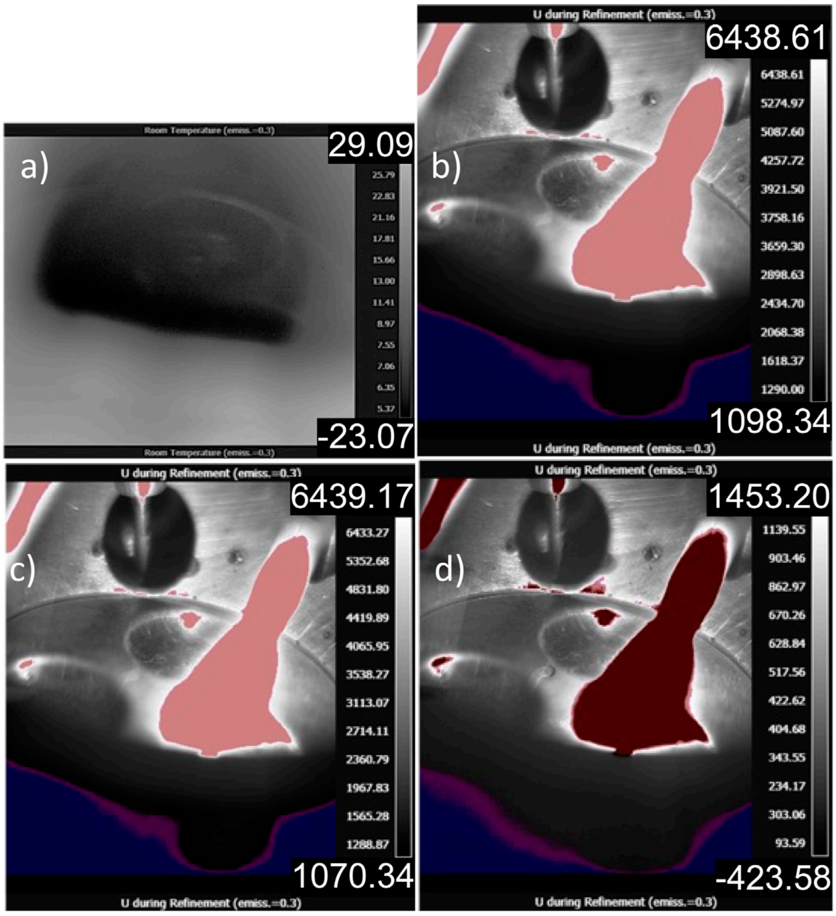

FIGURE 8
(A) Thermal image of a cooling arc-melting chamber post-refinement, allowing a view of the inside of the hearth (emissivity of 0.3 is employed for the clarity of the reader). **(B)** Thermal image of observed molten dU during refinement with a thermal range of 1,098.34°C–6,438.61°C. **(C)** Thermal image of observed molten of dU during refinement with a data subtraction of the room temperature hearth overlaid, thermal range of 1,070.34°C–6,439.17°C displayed. **(D)** Thermal image of observed dU in the molten state with a data subtraction of the molten dU—arc furnace assembly to highlight reflections and operator movement, with a thermal range of −453.58°C to 1,453.20°C.

both materials were measured using an analytical balance (model VWR-210B2). The three-pocketed Cu hearth was assembled with approximately 1.362 g of Pd and 0.3655 g of Si. Both Pd and Si separately occupied two of the three pockets, while Ti, as previously described, occupied the third pocket as a molten internal getter. Both Pd and Si were consolidated into separate ingots, then combined to form the PdSi compound by allowing both ingots to occupy one pocket during melting. The Ti getter remained molten during the consolidation of the PdSi compound and acted as a calibration tool for comparing the IR temperatures of Ti to PdSi.

2.2.3 Uranium mononitride

UN synthesis was used in this study to highlight an opportunity of this method: observing volatilization during melt synthesis. Synthesis of UN in an arc-melt furnace is novel, as are the resulting microstructures, and the detailed experimental procedure as well as resulting microstructural and compositional analysis will be presented in a subsequent publication by the investigative team. The sample observed in the present study was prepared by segmenting ~0.25 g of depleted uranium (dU) from metal feedstock received from Idaho National Laboratory. Since the compounding with nitrogen occurred in a liquid–gas phase interaction, the polished, cleaned uranium metal was the only precursor material placed in the furnace. No internal getter was used in the synthesis of UN due to the nitridization of all available common internal, oxygen-gettering metals. The chamber was subsequently purged using UHP Ar, purified by an external getter assembly comprised of a jeweler's furnace (ProCast, PMC supplies) containing a Zr getter sponge held at 600°C. Once an oxygen level of 10^{-16} ppm was met, the dU ingot was melted using a controlled current of 30 A within an Ar gas environment (with a flow rate of 2 L per minute—LPM). The initial melt of the uranium aimed to refine the uranium metal, removing volatile impurities, before nitrogen (N_2) was introduced to the furnace. The refinement process was repeated four times to ensure the purification of uranium from any impurities.

After precisely 60 s, a calculated introduction of 2 LPM of N_2 gas occurred (purified of trace O_2 using a separate jeweler's furnace, SG-RRL, ToAuto, with an internal Cu getter), coinciding with an increase in current to 89 A. This step led to the formation of a distinct solid phase. Subsequently, the flow of N_2 was terminated, allowing the metal to undergo a pinwheeling motion. N_2 gas was then introduced into the chamber along with argon at a pressure of 2 psi for a duration of 1 min, with an arc of 89 A. Afterward, both the argon and nitrogen were arrested, and the system was allowed to cool to room temperature before removing the sample.

3 Results and discussion

3.1 Titanium

The earliest experimental efforts of this work were conducted on Ti. The experiments were conducted on heritage samples used by the investigators, typically as oxygen scrubbing materials commonly referred to as “getters.” Ti is a common getter employed in the arc-melt synthesis of oxygen-sensitive materials, and thereby is often co-located in the furnace chamber with the actinide or nuclear materials of interest and provides an additional thermal signature during fabrication. A Ti getter was placed in the hearth and brought to melt temperature, reportedly at 1,660°C. Since the getter experienced a phase change (solid to liquid), the temperature of the sample plateaued at 1,660°C, allowing a temperature that could be used to calibrate the IR camera. Figure 4A highlights an uncalibrated measurement of temperatures across the getter with a low temperature range between 31°C and 61°C. Although the calibration is inaccurate, the dramatic change in temperature from the top and bottom of the sample aligns with a reading consistent with a cooled hearth and heated electrode.

Although the emissivity of Ti at 1,660°C has been thoroughly researched, Michels and Wilford (1949) showed that the total emissivity of Ti increases exponentially as heat is applied (Figure 4B). Therefore, it can be implied that the emissivity of Ti at 1,660°C is 0.35. The transmittance rate of quartz glass is 90%, and the transmittance rate of a standard UV shield is 49.1%. This allows for a total transmittance rate of 44.91%. In Figure 5A, the calibrated image of the calibration run shows the temperature range of the sample as 45°C–89°C, with the highest temperature of the getter measured at 78.7°C. This value is then corrected using an offset of 1,581.3°C applied to the image (Figure 5C).

3.2 Palladium silicide

PdSi has a melt temperature of 897°C (Zhenmin Du et al., 2006). When the melt stage of both the Ti getter and PdSi sample was visually checked, the IR camera was set up as in Figure 3B and the UV shield lifted. As shown in Figure 6A, without an offset applied there is an observable difference in temperature between the PdSi sample and the Ti getter. However, the theoretical difference between the two melted materials is greater than the difference between the samples displayed. Therefore, the offset, as shown in Figure 6B, is also inaccurate. Another notable observation for Figure 6A is the increased temperature range of 267°C–328°C. The offset was also recalculated to accommodate the lack of UV shield. With the primary reading of the Ti getter as 300°C, the offset was set to 1,330°C.

3.3 Uranium mononitride

Unlike in the PdSi experiment, an internal getter cannot be used to synthesize UN as Ti, and several other conventional gettering materials like Zr will nitride and react during the synthesis experiment. Therefore, there is no internal IR standard to be used as a correction factor. The pure metallic uranium sample is melted alone in the furnace, and IR data are collected on the sample, furnace, and electrodes. Stills recorded during the melt process using the IR camera are presented in Figure 8. Figure 8A presents the thermal image of a cooling arc-melt chamber post uranium refinement, allowing a view of the inside of the hearth; an emissivity of 0.3 is employed for the clarity of the reader. Figure 8B provides an image of the observed molten dU during refinement with a thermal range of 1,098.34°C–6,438.61°C. Furthermore, Figure 8C provides a thermal image of observed molten dU during refinement with a data subtraction of the room temperature hearth overlaid; a thermal range of 1,070.34°C–6,439.17°C is displayed. While the lower end of the temperature range displayed some decrease, the upper end remained significantly higher than what was experimentally possible. Finally, Figure 8D presents the thermal image of observed dU in the molten state with a data subtraction of the molten dU— furnace setup to highlight reflections and operator movement—a thermal range of −453.58°C to 1,453.20°C. Although this final high temperature range is more representative of the process, the low temperature range is unphysical, and therefore the true temperature range is not captured, as with the PdSi melt. What is not considered in the approximations of the actual melt temperature are the reaction energies during UN formation, which would result in higher temperatures than what is characteristic of molten U and UN. While the temperature calibration failed to capture the true temperature of the melt, what was observed was a continuous, high temperature phenomenon that extended from the sample to the electrode. The authors argue that this is the visualization of volatilization in the chamber. Volatilization is confirmed in the mass measurement following the experiment where the sample lost approximately half of its mass.

It is important to mention that, due to limited visibility within the furnace chamber during the operation of the heating system, one could only observe a small, confined area measuring just a few square centimeters through a small window (Figure 3B). In addition, it must be noted that UN volatilizes at high temperatures. This volatilization surrounds the sample, depositing material on the hearth as well as the electrode due to the decomposition of UN to U and 1/2N_2 (g). In the present study, up to 70% of the original uranium sample was lost in some cases. The decomposition reaction was described in Olson and Mulford (1963). This brilliant light source not only reflects within the metal and gas melt chamber but also off the reflective U/UN sample. As current is increased in the chamber, there is an increase in the intensity of light emitted. Therefore, when melting occurs, reflections form on the hearth’s metallic chamber (Figures 8B–D, highlighted in red). The light and reflections interfere with IR data collection by flooding the chamber with light and a creating false reading on actively cooled surfaces. Future research aims to limit the field of view to decrease emissivity interference caused by the electrode during synthesis and reflections.

X-ray diffraction (XRD) and scanning electron microscopy (SEM) analyses revealed the creation of a UN sample characterized by a dendritic microstructure with islands of α-uranium (Figure 7). The camera successfully captured the entire process of melting uranium and the subsequent diffusion of nitrogen into the sample. The recorded temperature reached approximately 4,000°C, a value significantly distant from the actual melting point of UN. Several factors, including the camera's distance from the sample inside of the furnace, considerations such as the glass's transmission rates, and the emissivity properties of UN, should be addressed to enhance temperature accuracy detection. Importantly, as shown in Figures 5, 8, a shroud can be observed forming over a heated sample. This phenomenon is observed in both volatile, UN, and non-volatile samples, PdSi, and Ti. It must also be noted that the shroud can change in size when the temperature range is changed, as demonstrated in Figures 4A, B. To decrease shroud size, further research on volatizing vs. non-volatizing samples must be done in both the low and high temperature range to fully understand the factors affecting shroud size and shape inside the arc furnace environment.

4 Conclusion

The present study demonstrates the challenges and opportunities to thermal imaging during melt synthesis of novel materials of relevance to advanced nuclear reactor fuels. The melt of pure Ti demonstrates that a linear offset can be applied to correct IR readings to produce near-accurate thermal data for molten samples. While both melts of PdSi and UN produced the targeted compounds with some U segregation for UN alongside some U_2N_3, challenges to determining emissivity and transmission values and the inaccuracy of calibration filters provided by the camera manufacturer produces inaccurate melt readings. Further complications are presented by reflections within the melt furnace. It must be noted that, due to these reflections and continued research into calibration methods, temperature ranges seen in IR images showcase ongoing efforts to increase the accuracy of IR filmography within arc furnace environments in real time. In future research, nonlinear offsets as well as smaller fields of view will be applied to enhance the accuracy and utility of this approach.

Data availability statement

The original contributions presented in the study are included in the article/Supplementary Material; further inquiries can be directed to the corresponding author.

Author contributions

JS: data curation, formal analysis, investigation, methodology, writing–original draft, and writing–review and editing. MK: data curation, formal analysis, investigation, methodology, writing–original draft, and writing–review and editing. SC: investigation and writing–review and editing. ES: conceptualization, funding acquisition, investigation, methodology, project administration, resources, supervision, validation, writing–original draft, and writing–review and editing.

Funding

The author(s) declare that financial support was received for the research, authorship, and/or publication of this article. This material is based upon work supported by the US Department of Energy, Office of Science, Office of Basic Energy Sciences, under the Synthesis and Processing Science Early Career Award "Integration of *in situ* Monitoring and Artificial Intelligence in the Synthesis of Uranium Alloys and Compounds to inform Performance Following Melt Fabrication Processes," Award Number DE-SC0022882. Further support for the fabrication of UN was provided by DOE-Office of Science, Basic Energy Science, Energy Frontiers of Research Center, entitled "Thermal Energy Transport Under Irradiation (TETI)." Lastly, PdSi fabrication was partially funded by a US Department of Energy Integrated Research Project (20-22094) entitled "Multi-physics fuel performance modeling of TRISO-bearing fuel in advanced reactor environments" under Award Number DE-NE0008998.

Conflict of interest

The authors declare that the research was conducted in the absence of any commercial or financial relationships that could be construed as a potential conflict of interest.

Publisher's note

Author disclaimer

This report was prepared as an account of work sponsored by an agency of the United States government. Neither the United States government nor any agency thereof, nor any of their employees, makes any warranty, express or implied, or assumes any legal liability or responsibility for the accuracy, completeness, or usefulness of any information, apparatus, product, or process disclosed, or represents that its use would not infringe privately owned rights. Reference herein to any specific commercial product, process, or service by trade name, trademark, manufacturer, or otherwise does not necessarily constitute or imply its endorsement, recommendation, or favoring by the United States government or any agency thereof. The views and opinions of authors expressed herein do not necessarily state or reflect those of the United States government or any agency thereof.

References

Arai, Y. (2012). *3.02 - nitride fuel A2 - konings, rudy J.M, comprehensive nuclear materials*. Oxford: Elsevier, 41–54.

Arrizubieta, J. I., Lamikiz, A., Klocke, F., Martínez, S., Arntz, K., and Ukar, E. (2017). Evaluation of the relevance of melt pool dynamics in Laser Material Deposition process modeling. *Int. J. Heat Mass Transf.* 115, 80–91. doi:10.1016/j.ijheatmasstransfer.2017.07.011

Baker, L., Jr, Mouradian, E., and Bingle, J. (1963). Determinations of the total emissivity of polished and oxidized uranium surfaces. *Nucl. Sci. Eng.* 15 (2), 218–220. doi:10.13182/nse63-a26423

Blumenthal, B. (1960). The transformation temperatures of high-purity uranium. *J. Nucl. Mater.* 2 (1), 23–30. doi:10.1016/0022-3115(60)90020-9

Brown, N. R., Aronson, A., Todosow, M., Brito, R., and McClellan, K. J. (2014). Neutronic performance of uranium nitride composite fuels in a PWR. *Nucl. Eng. Des.* 275, 393–407. doi:10.1016/j.nucengdes.2014.04.040

Calta, N. P., Guss, G., Wu, S., Ly, S., Deane, D., Crumb, M. F., et al. (2017). "High speed hyperspectral thermal imaging of the melt pool dynamics during metal additive manufacturing," in 2017 Conference on Lasers and Electro-Optics (CLEO), San Jose, CA, USA, 14-19 May 2017 (IEEE), 1–2.

Cheng, B., Lydon, J., Cooper, K., Cole, V., Northrop, P., and Chou, K. (2018). Infrared thermal imaging for melt pool analysis in SLM: a feasibility investigation. *Virtual Phys. Prototyp.* 13 (1), 8–13. doi:10.1080/17452759.2017.1392685

Claudson, T. T. (1958). *Emissivity data for uranium dioxide*. Master of Science (Oregon: Oregon State University).

FPI (2023). *Emissivity - metals, infrared technology: emissivity - metals*. Fluke Process Instruments. Available at: https://www.flukeprocessinstruments.com/en-us/service-and-support/knowledge-center/infrared-technology/emissivity-metals.

Gonzales, A., Watkins, J. K., Wagner, A. R., Jaques, B. J., and Sooby, E. S. (2021). Challenges and opportunities to alloyed and composite fuel architectures to mitigate high uranium density fuel oxidation: uranium silicide. *J. Nucl. Mater.* 533, 153026. doi:10.1016/j.jnucmat.2021.153026

Hafid El Mir, A. J., Bellot, J.-P., Chapelle, P., Lasalmonie, D., Jean, S., and Senevat, J. (2010). Thermal behaviour of the consumable electrode in the vacuum arc remelting process. *J. Mater. Process. Technol.* 210 (3), 564–572. doi:10.1016/j.jmatprotec.2009.11.008

Heigel, J. C., and Lane, B. M. (2018). Measurement of the melt pool length during single scan tracks in a commercial laser powder bed fusion process. *J. Manuf. Sci. Eng.* 140 (5). doi:10.1115/1.4037571

Hole, W., and Wright, R. (1939). Emissive and thermionic characteristics of uranium. *Phys. Rev.* 56 (8), 785–787. doi:10.1103/physrev.56.785

Jaques, B. J., Marx, B. M., Hamdy, A. S., and Butt, D. P. (2008). Synthesis of uranium nitride by a mechanically induced gas-solid reaction. *J. Nucl. Mater.* 381 (3), 309–311. doi:10.1016/j.jnucmat.2008.07.043

Jaques, B. J., Watkins, J., Croteau, J. R., Alanko, G. A., Tyburska-Pueschel, B., Meyer, M., et al. (2015). Synthesis and sintering of UN-UO2 fuel composites. *J. Nucl. Mater.* 466, 745–754. doi:10.1016/j.jnucmat.2015.06.029

Johnson, K. D., Wallenius, J., Jolkkonen, M., and Claisse, A. (2016). Spark plasma sintering and porosity studies of uranium nitride. *J. Nucl. Mater.* 473, 13–17. doi:10.1016/j.jnucmat.2016.01.037

Liu, H., Chen, Y., Gao, Z., Rohbeck, N., and Xiao, P. (2023). A study of reaction between palladium, palladium silver alloy and silicon carbide ceramics at high temperature. *J. Eur. Ceram. Soc.* 43 (8), 3077–3089. doi:10.1016/j.jeurceramsoc.2023.02.032

Lopes, D., Wilson, T., Kocevski, V., Moore, E., Besmann, T., Wood, E. S., et al. (2019). Experimental and computational assessment of USiN ternary phases. *J. Nucl. Mater.* 516, 194–201. doi:10.1016/j.jnucmat.2019.01.008

Martin, A. A., Calta, N. P., Hammons, J. A., Khairallah, S. A., Nielsen, M. H., Shuttlesworth, R. M., et al. (2019). Ultrafast dynamics of laser-metal interactions in additive manufacturing alloys captured by *in situ* X-ray imaging. *Mater. Today Adv.* 1, 100002. doi:10.1016/j.mtadv.2019.01.001

Matthews, R. B. (1993). *Irradiation performance of nitride fuels*. NM (United States): Los Alamos National Lab.

Mazzoleni, L., Demir, A. G., Caprio, L., Pacher, M., and Previtali, B. (2019). Real-time observation of melt pool in selective laser melting: spatial, temporal, and wavelength resolution criteria. *IEEE Trans. Instrum. Meas.* 69 (4), 1179–1190. doi:10.1109/tim.2019.2912236

Michels, W. C., and Wilford, S. (1949). The physical properties of titanium. I. Emissivity and resistivity of the commercial metal. *J. Appl. Phys.* 20 (12), 1223–1226. doi:10.1063/1.1698312

Moczygemba, C., George, J., Montoya, E., Kim, E., Robles, G., and Sooby, E. (2022). Structure characterization and steam oxidation performance of U3Si2 with Zr alloying additions. *J. Nucl. Mater.* 570, 153951. doi:10.1016/j.jnucmat.2022.153951

Nunez, U. C., Prieur, D., Bohler, R., and Manara, D. (2014). Melting point determination of uranium nitride and uranium plutonium nitride: a laser heating study. *J. Nucl. Mater.* 449 (1-3), 1–8. doi:10.1016/j.jnucmat.2014.02.021

Nürnberg, F., Kühn, B., and Rollmann, K. (2016). "Metrology of fused silica, laser-induced damage in optical materials 2016," in Laser-Induced Damage in Optical Materials 2016, Boulder, Colorado, United States, 06 December, 2016 (SPIE), 42–54.

Olson, W., and Mulford, R. (1963). The decomposition pressure and melting point of uranium mononitride1. *J. Phys. Chem.* 67 (4), 952–954. doi:10.1021/j100798a525

Ortega, L. H., Blamer, B. J., Evans, J. A., and McDeavitt, S. M. (2016). Development of an accident-tolerant fuel composite from uranium mononitride (UN) and uranium sesquisilicide (U3Si2) with increased uranium loading. *J. Nucl. Mater.* 471, 116–121. doi:10.1016/j.jnucmat.2016.01.014

Rogozkin, B., Stepennova, N., and Proshkin, A. (2003). Mononitride fuel for fast reactors. *At. Energy* 95 (3), 624–636. doi:10.1023/b:aten.0000007886.86817.32

Sooby, E. S., Brigham, B. A., Robles, G., White, J. T., Paisner, S. W., Kardoulaki, E., et al. (2021). Steam oxidation of uranium mononitride in pure and reducing steam atmospheres to 1200 °C. *J. Nucl. Mater.* 560, 153487. doi:10.1016/j.jnucmat.2021.153487

Sooby Wood, E., Moczygemba, C., Robles, G., Brigham, B., Grote, C. J., Metzger, K., et al. (2020). High temperature steam oxidation dynamics of U3Si2 with alloying additions: Al, Cr, and Y. *J. Nucl. Mater.* 533, 152072. doi:10.1016/j.jnucmat.2020.152072

Sooby Wood, E., White, J. T., and Nelson, A. T. (2016). "The synthesis and air oxidation behavior of U-Si-Al and U-Si-B compositions," in *TopFuel2016* (North Kensington Avenue, La Grange Park, IL: Transactions of the American Nuclear Society).

Sooby Wood, E., White, J. T., and Nelson, A. T. (2017). The effect of aluminum additions on the oxidation resistance of U3Si2. *J. Nucl. Mater.* 489, 84–90. doi:10.1016/j.jnucmat.2017.02.045

Tiegs, T. (1982). Fission product Pd-SiC interaction in irradiated coated-particle fuels. *Nucl. Technol.* 57 (3), 389–398. doi:10.13182/nt82-a26305

US EPA (2023). *Why and where mold grows*. United States: United States Environmental Protection Agency.

Uygur, S. (2016). *Degradation mechanisms of UN and UN–10U_3Si_2 pellets of varying microstructure by comparative steam oxidation experiments*. Stockholm: TRITA-FYS, 48.

Wallenius, J. (2020). "Nitride fuels," in *Comprehensive nuclear materials*. Editors R. J. Konings and R. Stoller (Netherlands: Elsevier).

Watkins, J. K., Gonzales, A., Wagner, A. R., Sooby, E. S., and Jaques, B. J. (2021). Challenges and opportunities to alloyed and composite fuel architectures to mitigate high uranium density fuel oxidation: uranium mononitride. *J. Nucl. Mater.* 553 (153048), 153048. doi:10.1016/j.jnucmat.2021.153048

Wen, H., van Rooyen, I. J., Hunn, J. D., and Gerczak, T. J. (2018). Electron microscopy study of Pd, Ag, and Cs in carbon areas in the locally corroded SiC layer in a neutron-irradiated TRISO fuel particle. *J. Eur. Ceram. Soc.* 38 (12), 4173–4188. doi:10.1016/j.jeurceramsoc.2018.05.003

Wilson, T., Vogel, S., Lopes, D., Kocevski, V., White, J., Wood, E. S., et al. (2020). Phase stability of U5Si4, USi, and U2Si3 in the uranium-silicon system. *J. Nucl. Mater.* 540, 152353. doi:10.1016/j.jnucmat.2020.152353

Wirth, F., Arpagaus, S., and Wegener, K. (2018). Analysis of melt pool dynamics in laser cladding and direct metal deposition by automated high-speed camera image evaluation. *Addit. Manuf.* 21, 369–382. doi:10.1016/j.addma.2018.03.025

Yang, J. H., Kim, D.-J., Kim, K. S., and Koo, Y.-H. (2015). UO2–UN composites with enhanced uranium density and thermal conductivity. *J. Nucl. Mater.* 465, 509–515. doi:10.1016/j.jnucmat.2015.06.039

Zhenmin Du, C. G., Yang, X., Liu, T., and Liu, T. (2006). A thermodynamic description of the Pd–Si–C system. *Intermetallics* 14 (5), 560–569. doi:10.1016/j.intermet.2005.09.008

Frontiers in Nuclear Engineering

TYPE Original Research
PUBLISHED 22 January 2024
DOI 10.3389/fnuen.2023.1340426

OPEN ACCESS

EDITED BY
Tonya Vitova,
Karlsruhe Institute of Technology (KIT),
Germany

REVIEWED BY
Charles M. Folden,
Texas A&M University, United States
Ningappa C.,
Vidya Vikas Institute of Engineering and
Technology, India

*CORRESPONDENCE
Tashiema L. Ulrich,
ulrichtl@ornl.gov

[†]**Present address:**
Tashiema L. Ulrich,
Nuclear Energy and Fuel Cycle Division, Nuclear Fuel Development Section, Nuclear Fuel Performance Group, Oak Ridge National Laboratory, Oak Ridge, TN, United States

RECEIVED 17 November 2023
ACCEPTED 28 December 2023
PUBLISHED 22 January 2024

CITATION
Ulrich TL and Besmann TM (2024), Phase equilibria of advanced technology uranium silicide-based nuclear fuel.
Front. Nucl. Eng. 2:1340426.
doi: 10.3389/fnuen.2023.1340426

Phase equilibria of advanced technology uranium silicide-based nuclear fuel

Tashiema L. Ulrich*[†] and Theodore M. Besmann

Department of Mechanical Engineering, Nuclear Engineering Program, University of South Carolina, Columbia, SC, United States

The phases in uranium-silicide binary system were evaluated in regards to their stabilities, phase boundaries, crystal structures, and phase transitions. The results from this study were used in combination with a well assessed literature to optimize the U-Si phase diagram using the CALPHAD method. A thermodynamic database was developed, which could be used to guide nuclear fuel fabrication, could be incorporated into other nuclear fuel thermodynamic databases, or could be used to generate data required by fuel performance codes to model fuel behavior in normal or off-normal reactor operations. The U_3Si_2 and U_3Si_5 phases were modeled using the Compound Energy Formalism model with 3 sublattices to account for the variation in composition. The crystal structure used for the USi phase was the tetragonal with an *I4/mmm* space. Above 450°C, the U_3Si_5 phase was modeled. The composition of the USi_2 phase was adjusted to $USi_{1.84}$. The calculated invariant reactions and the enthalpy of formation for the stoichiometric phases were in agreement with experimental data.

KEYWORDS

uranium silicides, phase diagram, CALPHAD, nuclear fuel, U3Si2, U3Si5

1 Introduction

The tsunami-initiated nuclear accident that occurred at Fukushima, Japan a decade ago was the impetus behind the world's renewed interest in alternative fuel concepts with enhanced accident tolerance for the current fleet of commercial power reactors (U.S. Nuclear Regulatory Commission, 2011; Kim et al., 2016; Zinkle and Was, 2013; Karoutas et al., 2018; Kurata, 2016). In the United States, the Department of Energy's Office of Nuclear Energy initiated the accident tolerant fuel (ATF) development program, within the Advanced Fuels Campaign (AFC), to identify alternative fuel technologies to further enhance the safety and competitiveness of commercial nuclear power (U.S Department of Energy, 2015; Carmack et al., 2013; Bragg-Sitton et al., 2014; Terrani, 2018).

The U-Si system contains several compounds that are of interest as either a monolithic replacement for the current UO_2 fuel (White et al., 2015; Goddard et al., 2016; World Nuclear News, 2019; Johnson et al., 2020; Westinghouse, 2023), a composite fuel with UN (Johnson et al., 2016; White et al., 2017; Wilson et al., 2018) or metal fuel (Dwight, 1982; Kim and Konings, 2012). The U-Si system has been the subject of various studies detailing thermophysical properties (White et al., 2014; White et al., 2015; White et al., 2015; White et al., 2016). The phase equilibria and thermodynamic properties of the U-Si system has been assessed by Berche et al. (2009) and Wang et al. (2016) however there are concerns regarding the accuracy and completeness of the phase diagram (Remschnig et al., 1992; Berche et al., 2009; White et al., 2015; Middleburgh et al., 2016; Noordhoek et al., 2016; Wang et al., 2016; Lopes et al., 2018; Wilson et al., 2018; Kocevski et al., 2019; Ulrich et al., 2020a; Ulrich et al., 2020b). Companion compositions to U_3Si_2 and U_3Si_5 require further study for a fuller understanding of compositional changes expected to occur in silicide fuel during reactor operation. These include compositions in the range of the USi and $USi_{1.88}$ phases which lie within the 40–66 at% Si region of the phase diagram and can be considered as potential high burn-up phases. Questions remain concerning phase transition, homogeneity range, crystal structure, and potentially new equilibrium phases. As such, further experimental efforts have been suggested (Berche et al., 2009; White et al., 2015; Wilson et al., 2018).

The aim of this project was to develop a self-consistent thermodynamic database for the uranium-silicon system by 1) performing targeted experimental analyses of the potential U_3Si_5 phase transition, homogeneity range for the U_3Si_2, U_3Si_5 and the $USi_{1.88}$ phases, the crystal structure of USi and the stability of the U_5Si_4 and U_2Si_3 phases; 2) using density functional theory (DFT) and molecular dynamics (MD) simulations to predict the energetically and dynamically stable phases in the U-Si system; 3) coupling the computational and experimental results with data from a critically assessed literature to optimize the U-Si system using the CALculation of PHAse Diagram (CALPHAD) method; 4) building and validating a U-Si thermodynamic model. The database generated from this work could be used with other fuel performance codes to predict silicide fuel behavior during normal or off-normal reactor operations, optimize fuel fabrication processes, and support licensing efforts. The focus of this paper is the optimized U-Si phase diagram from the theoretical and experimental data generated from this project as well as literature data.

2 Literature review

2.1 U-Si phase diagram

The first compositional diagram for the uranium-silicon system was based on studies performed by Kaufmann et al., in the 1940s at the Massachusetts Institute of Technology (Cullity, 1945). The original phases reported were $U_{10}Si_3$, U_5Si_3, USi, U_2Si_3, USi_2, and USi_3 (Katz and Rabinowitch, 1951). In 1949, Zachariasen (1949) further refined the original composition diagram by correcting the identification of several compounds; $U_{10}Si_3$ was actually U_3Si, U_5Si_3 was U_3Si_2, and U_2Si_3 (β-USi_2) was an isostructural form of USi_2 (α-USi_2).

Later, in 1957, Kaufmann et al. (1957) published the phase diagram shown in Figure 1A, which contains the compounds U_3Si (ε), U_3Si_2 (δ), USi (ζ), U_2Si_3 (η), USi_2 (θ) and USi_3 (ι). Kaufmann et al. (1957) claimed that the ε phase has a very narrow composition range near 23 at% Si, rather than a stoichiometric ratio of U_3Si and also that the α-USi_2 phase did not transform at high temperature to β-USi_2 and formed the compound U_2Si_3 in its place. U_3Si forms at 1203 K through the peritectic reaction between U_3Si_2 and γ-uranium-silicon solid solution. A eutectic exists between γ-uranium and U_3Si_2 at 9 at% Si and a temperature of 1258 K. The compound U_3Si_2 congruently melts at 1938 K. The USi compound incongruently melts at 1848 K and there is a eutectic between U_3Si_2 and USi at 1843 K. The U_2Si_3 compound incongruently melts at 1883 K and the USi_2 compound is reported to melt congruently at approximately 1973 K. USi_3 is shown to have an incongruent melting point at 1783 K. There is a eutectic at 87 at% Si between USi_3 and silicon at 1588 K. There was appreciable solid solubility of silicon in uranium.

The phase diagram that is currently referenced is shown in Figure 1B and was published in 1990 in ASM international (Massalski, 1990). This phase diagram is characterized by seven intermetallic phases, U_3Si, U_3Si_2, USi, U_3Si_5, $USi_{1.88}$, USi_2, and USi_3. The 0–50 at% Si region remained as previously reported by Kaufmann et al. (1957) except for the temperature where the eutectic reaction occurs between U_3Si_2 and USi. The phase identified as U_2Si_3 by Kaufmann, or β-USi_2 by Zachariasen (1949), is represented as U_3Si_5. In 1959 Brown and Norreys (1959) reported that the U_2Si_3 phase was in fact a modification of the α-USi_2 compound; however, the composition was located between 62–63 at% Si (U_3Si_5). Brown and Norreys (1961) also reported that the phase considered as α-USi_2 is actually $USi_{1.88}$, forming at 65 at% Si and has high melting point. They further claimed that the compound at exact 1:2 stoichiometry does not exist above 723 K.

In an attempt to elucidate the controversy regarding the phases between the 40 to70 at% silicon region of the U-Si system, Vaugoyeau et al. (1972) reexamined the system within this region. The existence of compounds USi, U_3Si_5, U_3Si_2 and $USi_{1.88}$ were confirmed (Vaugoyeau et al., 1972). Vaugoyeau et al. (1972) reported: The USi phase forms at 1853 ± 10 K from a peritectic reaction between liquid and U_3Si_5. The temperature of the eutectic reaction between USi and U_3Si_2 was 1813 ± 10 K, which is approximately 20 K lower than that reported by Kaufmann et al., (Kaufmann et al., 1957). The melting of U_3Si_5 occurred congruently at 2043 ± 10 K instead of incongruently at 1883 K. The $USi_{1.88,}$ reported by Brown and Norreys (1961) forms through a peritectic reaction between liquid and U_3Si_5 at 1983 ± 10 K. The stoichiometric USi_2 compound was not observed by Vaugoyeau et al. (1972).

Additional research since the publication of the phase diagram in Figure 1B shows the need for updates. The U_3Si phase was reported to undergo an allotropic transition at 1043 K (Dwight, 1982). A new phase, U_5Si_4, was reported by Noël et al. (1998) and Berche et al. (2009) claimed that the phase is formed through a peritectic reaction between the liquid phase and U_3Si_2 at 1840 ± 10 K and participates in the eutectic reaction between the liquid phase and the USi phase at 1820 ± 10 K. The stoichiometric USi_2 phase was reported as metastable (Sasa and Uda, 1976; Dwight, 1982; Remschnig et al., 1992; Noordhoek et al., 2016) and the U_3Si_5, U_3Si_2, and $USi_{1.88}$ phases were each reported to have a narrow composition range (Dwight, 1982). A phase transition at 773 K was noted for the U_3Si_5 phase (White et al., 2015).

2.2 Crystallography

The crystal structure properties including the structure types, space groups, prototypes, lattice parameters for the various uranium silicide phases are summarized Table 1. The U_3Si crystal structure reported by Zachariasen (1949) in 1949 was often reproduced (Kaufmann et al., 1957; Dwight, 1982; Remschnig et al., 1992).

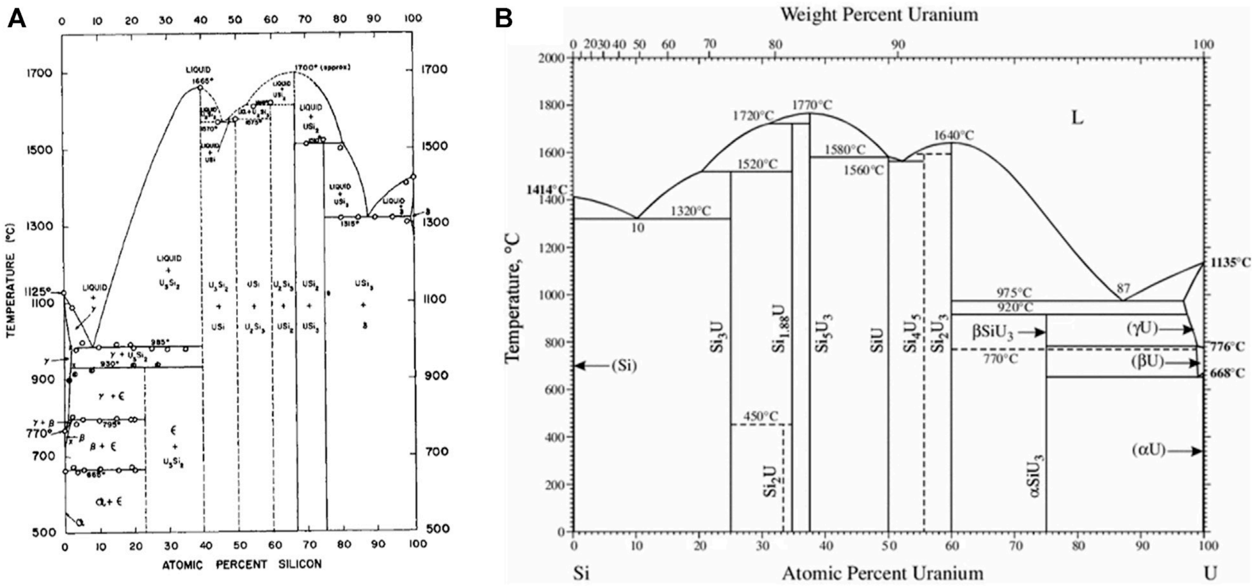

FIGURE 1
Illustration of the 1957 U-Si phase diagram **(A)** compared to the U-Si phase diagram currently referenced **(B)** (Kaufmann et al., 1957; Massalski, 1990).

Kimmel et al. (Kimmel et al., 1980), established that the space group reported earlier (Zachariasen, 1949) was correct; but the assignment of the uranium and silicon lattice sites was incorrect. Noël et al. (2023) also reported that the tetragonal structure undergoes an orthorhombic distortion at 120 K. Dwight, (1982) reported that the tetragonal U_3Si transforms to a cubic Cu_3Au-type structure at 1038 K.

The U_3Si_2 compound has a primitive tetragonal structure belonging to the *P4/mbm* space group and is a prototype for binary ternary rare earth compounds (Pöttgen, 1994; Lukachuk and Pöttgen, 2003). While all published experimental data are in agreement with the early work of Zachariasen (1949), DFT calculations fail to predict the experimental *P4/mbm* as the most stable structure (Noordhoek et al., 2016).

The U_5Si_4 phase reported in 1998 by Noël et al. (1998) has a hexagonal unit cell, *P6/mmm* space group, with lattice parameters a = 10.468 Å and c = 3.912 Å and is isostructural to the $U_{20}Si_{16}C_3$ ternary phase (Lopes et al., 2019; Noël et al., 2023). The crystal structure of the equiatomic compound, USi, is the most controversial of the binary silicides. The compound was reported by Zachariasen (1949) to be orthorhombic of the FeB structure type. His results were based on diffractometer data taken on a powder sample. In later work, Bihan et al. (1996) reported that pure USi has a tetragonal structure with an *I4/mmm* space group as determined from a Weissenberg pattern on a small single crystal. Bihan et al. (1996) further state that the orthorhombic structure by found by Zachariasen (1949) is stabilized by 0.5–1.0 wt% oxygen. Remschnig et al. (1992) and Noordhoek et al. (2016) also reported an orthorhombic structure; however, both differ from the work of Zachariasen, (1949) and each other as the structure by Remschnig et al. (1992) belongs to the *Pnma* space group while the one by Noordhoek et al. (2016) belongs to the *Imma* Space group.

The compound USi_2 with exact 1:2 stoichiometry has all silicon sites occupied and exists in one of two structure types, either AlB_2 or $ThSi_2$, belonging to the *P6/mmm* or the *I4₁/amd* space group. The compound U_3Si_5 is hexagonal, hP3, $A1B_2$-type structure which was reported to undergo an orthorhombic distortion when slightly rich in silicon (63 at% Si) to form the structure belonging to the *Pmmm* space group (Remschnig et al., 1992). The $USi_{1.88}$ phase is tetragonal of the $ThSi_2$-type and experiences an orthorhombic distortion when slightly silicon poor (64 at% Si) (Remschnig et al., 1992).

The silicon-rich compound USi_3 has the cubic Cu_3Au-type structure.

2.3 Thermodynamic values

The tabulated enthalpies of formation for the different U-Si phases are summarized in Table 2. The enthalpies of formation of USi_3, USi_2, USi and U_3Si_2 were measured as −33.05 kJ mol^{-1}, -43.51 kJ mol^{-1}, -40.17 kJ mol^{-1} and -33.89 kJ mol^{-1} by Gross et al. (1962) by measuring the heats evolved in the direct combination of the elements. The enthalpies of formation for USi_3, USi_2, and USi were verified by measuring the heats of reaction of tellurium with the preformed compounds and comparing them with those obtained from reacting equivalent quantities of the uncombined elements with tellurium. The enthalpy of formation for USi_3, USi_2, and USi were measured as −32.22, −42.69, and −43.52 kJ mol $^{-1}$, respectively (Gross et al., 1962). Alcock and Grieveson (1961) measured silicon vapor pressure above the mixtures USi-U_3Si_5, U_3Si_5–USi_2, USi_2–USi_3 and USi_3–Si from the weight loss of a Knudsen cell. From these measurements, the Gibbs energy of U_3Si_5, USi_2 and USi_3 were directly derived. Activities of uranium and silicon for the U–U_3Si_2 mixture were determined from the chemical analysis of the condensate formed from the vapor effusing from the cell.

TABLE 1 Summary of crystallographic properties for the U-Si phases including structure type, space group, prototype, and lattice parameters found in the literature.

Phase	Structure type	Space group	Prototype	Lattice parameters (Å)			Ref.
				a	b	c	
U_3Si (γ)	Cubic	*Pm-3m*	Cu_3Au	4.346	-	-	Massalski (1990)
U_3Si (β)	Tetragonal	*I4/mcm*	U_3Si (β)	6.0328	-	8.6907	Massalski (1990)
U_3Si (δ)	Tetragonal	*I4/mcm*	-	6.029 (2)	-	8.697 (3)	Zachariasen (1949)
U_3Si	Tetragonal	*I4/mcm*	U_3Si	6.029 (2)	-	8.696 (3)	Zachariasen (1949)
				6.033 (1)	-	8.688 (1)	Boucher (1971)
				6.0328	-	8.6907	Vooght et al. (1973)
U_3Si	Orthorhombic	*Fmmm*	U_3Si	8.654 (2)	8.523 (2)	8.523 (2)	Kimmel et al. (1980)
U_3Si (α)	Orthorhombic	*Fmmm*	U_3Si (α)	8.654	8.549	8.523	Massalski (1990)
U_3Si_2	Tetragonal	*P4/mbm*	U_3Si_2	7.3298 (4)	-	3.9003 (5)	Massalski (1990)
				7.3364 (5)	-	3.8900 (8)	Remschnig et al. (1992)
				7.3299	-	3.9004	Zachariasen (1949)
				7.3297	-	3.9003	Laugier et al. (1971)
U_5Si_4	Hexagonal	*P6/mmm*	$U_{20}Si_{16}C_3$	10.467	-	7.835	Noël et al. (1998)
USi	Tetragonal	*I4/mmm*	USi	10.58	-	24.310	Remschnig et al. (1992)
USi	Orthorhombic	*Pnma*		7.585	3.903	5.663	Remschnig et al. (1992)
USi	Orthorhombic	*Imma*		7.585	3.903	5.663	Noordhoek et al. (2016)
USi	Orthorhombic	*Pbmn*	FeB	5.66 (1)	7.67 (1)	3.91 (1)	Zachariasen (1949)
USi	Tetragonal	*I4/mmm*	USi	10.61	24.42	27.490	Laugier et al. (1971)
U_3Si_5	Hexagonal	*P6/mmm*	AlB_2	3.843	-	4.069	Massalski (1990)
				3.8475 (7)		4.074 (1)	Remschnig et al. (1992)
				3.843 (1)		4.069 (1)	Brown and Norreys (1959)
				3.890	6.660	4.040	Dwight, 1982a
o1-U_3Si_5 (at 63 at. % Si)	Orthorhombic	*Pmmm*	Dist. AlB_2	3.869		4.073	Remschnig et al. (1992)
o2-U_3Si_5 (at ~63 at% Si)	Orthorhombic	*Pmmm*	Dist. AlB_2	3.893	6.717	4.042	Remschnig et al. (1992)
USi_{2-z} (at 64 at. % Si)	Orthorhombic	*Imma*	Def. $GdSi_2$	3.953	3.929	13.656	Remschnig et al. (1992)
USi_{2-z} (at 65 at. % Si)	Tetragonal	$I4_1/amd$	Def. $ThSi_2$	3.9423	-	13.712	Zachariasen (1949), Remschnig et al. (1992)
$USi_{1.88}$	Tetragonal	$I4_1/amd$	Def. $ThSi_2$	3.9457 (4)	-	13.739 (7)	Remschnig et al. (1992)
				3.9378 (7)	-	13.729 (6)	Remschnig et al. (1992)
				3.948	-	13.67	Wilson et al. (2018)
				3.98 (3)	-	13.74 (8)	Zachariasen (1949)
USi_3	Cubic	*Pm-3m*	Cu_3Au	4.060	-	-	Zachariasen (1949)
USi_3	Cubic	*Pm3m*	L12 Cu_3Au	4.03	-	-	Kaufmann et al. (1957)
USi_3	Cubic	*Pm-3m*	Cu_3Au	4.0348 (8)	-	-	Ott et al. (1985)
USi_2	Tetragonal	$I4_1/amd$	$ThSi_2$	3.922	-	14.154	Zachariasen (1949)
USi_2	Tetragonal	$I4_1/amd$	$ThSi_2$	3.98 (3)	-	13.74 (8)	Zachariasen (1949)
USi_2	Hexagonal	*P6/mmm*	AlB_2	3.86 (1)	-	4.07 (1)	Zachariasen (1949)

(Continued on following page)

TABLE 1 (*Continued*) Summary of crystallographic properties for the U-Si phases including structure type, space group, prototype, and lattice parameters found in the literature.

Phase	Structure type	Space group	Prototype	Lattice parameters (Å)			Ref.
				a	b	c	
USi_2	Tetragonal	$I4_1/amd$	$ThSi_2$	3.97	-	13.71	Kaufmann et al. (1957)
USi_2	Cubic	-	-	4.053	-	-	Brauer and Haag (1949)
USi_2	Tetragonal	$I4_1/amd$	$ThSi_2$	3.9406 (7)	-	13.778 (7)	Remschnig et al. (1992)
USi_2	Tetragonal	$I4_1/amd$	$ThSi_2$	3.922	-	14.154	Sasa and Uda (1976)
				3.930	-	14.06	Brown and Norreys (1959)
					-		
USi_2	Hexagonal	$P6/mmm$	AlB_2	4.028 (1)	-	3.852 (1)	Brown and Norreys (1961)
$U_{22}Si_{78}$	Cubic	$Pm3m$	Cu_3Au	4.0353 (4)	-	-	Remschnig et al. (1992)

Because of small associated values of uranium activity, a solid/liquid equilibration method using liquid gold–uranium alloys were used for the U_3Si_2–USi mixture. The Gibbs energies of formation of the compounds were derived from the silicon and uranium activity measurements. The results reported by Gross et al. (1962) and Alcock and Grieveson (1961) are in good agreement. OHare et al. (1974) reported the enthalpy of formation of U_3Si as −26.05 ± 4.8 kJ mol-atom^{-1} using fluorine bomb calorimetry. The enthalpy of formation for U_3Si_5 and the tetragonal USi were measured as −43.8 ± 9.0 kJ mol $^{-1}$ and −43.2 ± 6.2 kJ mol $^{-1}$ for using oxidative drop calorimetry (Chung et al., 2018). The heat capacity as a function of temperature for U_3Si, U_3Si_2, USi and U_3Si_5 were measured by White et al. (2015); White et al. (2016) using differential scanning calorimetry from room temperature to 1150 K, 1773 K, 1673 K, and 1773 K, respectively. To the authors knowledge, there are no experimental efforts reported for obtaining the thermodynamic properties of the liquid phase.

3 CALPHAD methodology

3.1 General description of CALPHAD method

The CALPHAD method is commonly used for calculating phase diagrams and predicting thermodynamic properties of a given system through critical assessment of available experimental and/or theoretical data. The CALPHAD method uses mathematical models with adjustable parameters to represent Gibbs energy functions of the phases as a function of temperature, pressure, and composition and calculates the thermodynamic equilibrium by minimizing the Gibbs energy of the system (Kaufman and Bernstein, 1970; Lukas et al., 2007). These functions are stored in a database and are used to calculate phase diagrams and thermodynamic properties. These databases are constructed by incorporating phase diagram data, thermochemical data, and physical and crystallographic properties of the phases (Perrut, 2015).

The first step in the CALPHAD method is to perform a thorough literature search and critically evaluate all the available data. The type of data to search for include; i) experimentally measured thermodynamic quantities such as enthalpies and heat capacity data, ii) the phase diagram data such as the liquidus temperatures and the phase transition reactions, iii) crystallographic information of solid phases (Ferro and Cacciamani, 2002), and first-principles calculations of total energies (Liu, 2009). When evaluating the experimental data, critical attention is paid to the experimental technique, experimental conditions, sample purity, quantities measured, phases present within the system, and accuracy of the measurements as there are many types of equipment utilized to collect the same information. First-principles data are normally used when there are no available experimental data. During the literature search, the possibility of finding previous assessments for the system of interest exists. In such cases, careful examination of the Gibbs energy models used for describing the system is necessary as it may be possible to improve the system. The second step is to develop a mathematical model for G (T, P, composition) for each phase (liquid, solid phases, gas . . .) and to optimize model parameters simultaneously using all available thermodynamic and phase equilibrium data obtained from the first step. The third step is to use the models to calculate phase diagrams and other thermodynamic properties by minimization of the Gibbs energy. The fourth and final step is to use the calculated phase equilibria to develop a database.

3.2 Thermodynamic models

The Gibbs energy of a phase can be expressed as follows in Eqs 1, 2:

$$G_m = {}^{ref}G_m + {}^{id}G_m + {}^{E}G_m + {}^{phy}G_m \tag{1}$$

$${}^{id}G_m = -T^{id}S \tag{2}$$

Where ${}^{ref}G_m$ is the "surface of reference", which represents the Gibbs energy of the mechanical mixture of the constituents of the phase. ${}^{id}G_m$ is the contribution of configuration entropy to the Gibbs energy. T is the absolute temperature in Kelvin and ${}^{id}S$ is the configuration entropy, which is determined by the number of

TABLE 2 Summary of the enthalpy of formation for the various U-Si phases from the literature compared to the values calculated in this work.

Phase	ΔH$_f$ (kJ/mol-atom) 298K	Method	References
USi_3	−33.02 ± 0.13	Direct comb. cal	Gross et al. (1962)
	−32.19 ± 0.84	Tellurium cal	Gross et al. (1962)
	−35.53 ± 4.18	Activity meas	Alcock and Grieveson (1961)
	−32.60	Estimation	Birtcher et al. (1989)
	−32.90	Modelling	Berche et al. (2009)
	−32.90	CALPHAD	This work
USi_2	−43.47 ± 0.42	Direct comb. Cal	Gross et al. (1962)
	−42.64 ± 1.25	Tellurium cal	Gross et al. (1962)
	−43.89 ± 4.18	Activity meas	Alcock and Grieveson (1961)
	−43.19	Estimation	Birtcher et al. (1989)
	−43.33	Modelling	Berche et al. (2009)
	−45.12	CALPHAD	This work
U_3Si_5	−44.26	Estimation	Birtcher et al. (1989)
	−42.9	Modelling	Berche et al. (2009)
	−43.8 ± 9.0	Oxidative drop cal	Chung et al. (2018)
USi	−40.13 ± 0.84	Direct comb. cal	Gross et al. (1962)
	−43.47 ± 1.67	Tellurium Cal	Gross et al. (1962)
	−41.8 ± 4.18	Activity meas	Alcock and Grieveson (1961)
	−42.22	Estimation	Birtcher et al. (1989)
	−41.18	Modelling	Berche et al. (2009)
	−43.2 ± 6.2	Oxidative drop cal	Chung et al. (2018)
	−41.78	CALPHAD	This work
U_3Si_2	−33.2 ± 3.1	High Temp Drop cal	Chung et al. (2018)
	−33.86 ± 0.42	Direct comb. cal	Gross et al. (1962)
	−35.95 ± 3.34	Activity meas	Birtcher et al. (1989)
	−34.11	Estimation	Alcock and Grieveson (1961)
	−34.32	Modelling	Berche et al. (2009)
U_3Si	−26.02 ± 4.8	Fluorine bomb cal	OHare et al. (1974)
	−22.99	Estimation	Birtcher et al. (1989)
	−24.93	Modelling	Berche et al. (2009)
	−24.91	CALPHAD	This work

possible arrangements of the constituents in a phase. $^{E}G_m$ is the excess Gibbs energy, the Gibbs energy change from the ideal solution to the real solution. $^{phy}G_m$ represents the Gibbs energy contribution of physical phenomena, such as magnetic transitions.

3.2.1 The gas phases

The gases in the U-Si system are Si_g, U_g, $Si_{(2g)}$ and $Si_{(3g)}$ gases. The Gibbs energy functions for the gases are taken from the Scientific Group Thermodata Europe (SGTE) database complied by Dinsdale for pure elements (Dinsdale, 1991).

3.2.2 Elements

The molar Gibbs energy $^{\circ}G_i$ of a pure element i in a phase at temperature and pressure of 10^5 Pa, relative to the "Standard Element Reference" H_i^{SER}, is described by a power series such as shown in Eq. 3:

$$^{\circ}G_i - H_i^{SER} = a_0 + a_1T + a_2Tln(T) + a_3T^2 + a_4T^3 + a_5T^{-1} + \ldots, T_1 < T < T_2 \tag{3}$$

$a_0, a_1, a_2, a_3, \ldots$ are coefficients, H_i^{SER} is the enthalpy of the pure element i in its reference state. Since the Gibbs energy has no absolute value, it is

TABLE 3 Phases, composition, crystal structure, and thermodynamic model used for the optimization of the U-Si phase diagram.

Phase	At% Si	Pearson symbol	Space group	Struktur-bericht designation	Prototype	^a^Model
Liquid	0 to 100					TSPIL
Bcc (U)	0 to 3	*cI2*	*Im-3m*	*Ab*	α-U	CEF
Tetragonal (U)	0 to 1	*tP30*	$P4_2/mmm$	*A2*	B-U	CEF
Orthorhombic (U)	0	*oC4*	*Cmcm*	*A20*	W	R-K/Muggianu
Diamond (Si)	100	*cF8*	*Fd-3m*	*A4*	C (Diamond)	R-K/Muggianu
U_3Si (High T)	75	*cP4*	*Pm-3m*	$L1_2$	Cu_3Au	ST
U_3Si (Low T)	75	*tI16*	*I4/mcm*	....	....	ST
U_3Si_2	~40 to ~41.5	*tP10*	*P4/mbm*	*D5a*	U_3Si_2	CEF
USi ($U_{68}Si_{67}$)	~50	....	*I4/mmm*	....	USi	ST
U_3Si_5	~61.5–~63	*hP3*	*P6/mmm*	*C32*	AlB_2	CEF
$USi_{1.84}$	64.5	*tI12*	$I4_1/amd$	C_c	$ThSi_2$	ST
USi_3	75	*cP4*	*Pm-3m*	$L1_2$	Cu_3Au	ST

[a] TSPIL, is the two sublattice partially ionic liquid model; ST, is stoichiometric compound and CEF, is the compound energy formalism. R-K/Muggiaun is the one sublattice Redlich-Kister Muggiaun solution model.

necessary to refer the Gibbs energy of all phases to the same reference point for each element. It is common practice to choose the reference state to be the most stable phase at 298.15 K, 10^5 Pa. The temperature of T_1 and T_2 determines the range of the power series. In this work, the molar Gibbs energy of the pure uranium and silicon are the recommended SGTE values compiled by Dinsdale (1991).

3.2.3 Stoichiometric phases

The molar Gibbs energies for stoichiometric phases can be described by using Eq. 4 where the standard Gibbs energy is equal to the standard enthalpy (see Eq. 5) minus the temperature times the standard entropy (see Eq. 6).

$$°G_T = °H_T - T°S_T \tag{4}$$

$$°H_T = \Delta^{298.15K} H_f^{\circ} + \int_{298.15\,K}^{T} C_p dT \tag{5}$$

$$°S_T = \Delta^{298.15K} S_f^{\circ} + \int_{298.15\,K}^{T} \left(C_p/T\right) dT \tag{6}$$

3.2.4 Two sublattice partial ionic liquid (TSPIL) model

The partially ionic two sublattice model (Lukas et al., 2007) is used to model liquid phases as:

$(C_i^{+\nu_i})_P(A_j^{-\nu_j}, VaB_k^0)_Q$ where C, A, VA and B denotes cation, anion, vacancy, and neutrally charged specie, respectively. ν_i and ν_j represents the charge on the cation, C_i, and anion, A_j, species, respectively. Charge neutrality necessitates that Q and P varies according to Eqs 7, 8 respectively:

$$\mathrm{P} = \sum\nolimits_{\mathrm{A}} \upsilon_{\mathrm{A}} \mathrm{y}_{\mathrm{A}} + \mathrm{Q} \mathrm{y}_{\mathrm{VA}} \tag{7}$$

$$\mathrm{Q} = \sum\nolimits_{\mathrm{C}} \mathrm{v}_{\mathrm{C}} \mathrm{y}_{\mathrm{C}} \tag{8}$$

v_{A} and y_{A} are the charge and site fractions of the anion species, A_j, and v_{C} and y_{C} are the charge and site fraction of the cation species, C_i, respectively. In Eq. 9, the Gibbs energy of the ionic liquid is expressed as:

$$\begin{aligned} G_m = & \sum\sum y_{C_i} y_{A_j} A°G_{C_i:A_j} + Q\left(y_{Va} \sum y_{C_i} °G_{C_i} + \sum y_{B_k} °G_{B_k}\right) + \\ & RT\left[P \sum y_{C_i} \ln y_{C_i} + Q\left(\sum y_{A_j} \ln y_{A_j} + y_{Va} \ln y_{Va} + \sum y_{B_k} \ln y_{B_k}\right)\right] \\ & + {}^{E}G_m \end{aligned} \tag{9}$$

Where $°G_{C_i:A_j}$ is the Gibbs energy of formation for $\nu_i + \nu_j$ moles of atoms of the endmembers C_iA_j while $°G_{C_i}$ and $°G_{B_k}$ are the formation values for C_i and B_k.

3.2.5 Solid solutions

The compound energy formalism (CEF) was introduced by Hillert (2001) to describe the Gibbs energy of solid phases with sublattices. These phases have two or more sublattices and at least one of these sublattices has a variable composition. Ideal entropy of mixing is assumed on each sublattice. This model is generally used to model crystalline solids; but it can also be extended to model ionic liquids.

Here, a solution phases with two sublattices, (A,B)a (C,D)b, will be used as an example to illustrate the compound energy formalism. In this model, components A and B can mix randomly on the first sublattice, as do the components C and D on the second sublattice. a and b are the corresponding stoichiometric coefficients. Site fraction y_i^s (see Eq. 10) is introduced to describe the constitution of the phase and is defined as follows:

$$y_i^s = \frac{n_i^s}{N^s} \tag{10}$$

n_i^s is the number of component *i* on sublattice (s) and N^s is the total number of sites on the same sublattice. When vacancies are considered in the model, the site fraction becomes Eq. 11:

$$y_i^s = \frac{n_i^s}{n_{VA}^s + \sum_i n_i^s} \tag{11}$$

TABLE 4 Optimized thermodynamic parameters for the U-Si system.

Phase	Thermodynamic parameter (J/mol)	References
Liquid: (U^{+4}, Si^{+4}) (VA)	$G^{Liq}_{U+4:\ VA} = G^{Liq}_{U} - {}^{\circ}H^{SER}_{U} = G^{Liq}_{U}$	Dinsdale (1991)
	$G^{Liq}_{Si+4:\ VA} = G^{Liq}_{Si} - {}^{\circ}H^{SER}_{Si} = G^{Liq}_{Si}$	Dinsdale (1991)
	${}^{\circ}L_{U+4,Si+4:\ VA} = -185536.75 + 26.417124T$	Berche et al. (2009)
	${}^{1}L_{U+4,Si+4:\ VA} = -98477.584 + 52.787132T$	Berche et al. (2009)
	${}^{2}L_{U+4,Si+4:\ VA} = 47133.465 - 10.794531T$	This work
BCC_A2: (U, Si) (VA)	$G^{BCC_{A2}}_{U:\ VA} = G^{BCC_{A2}}_{U} - {}^{\circ}H^{SER}_{U} = G^{BCC_{A2}}_{U}$	Dinsdale (1991)
	$G^{BCC_{A2}}_{Si:\ VA} = G^{Diamond}_{Si} + 49999 + 22.5T$	This work
	${}^{\circ}L_{U,Si:\ VA} = -96136.807$	Berche et al. (2009)
Tetragonal_U: (U, Si)	$G^{Tetragonal}_{U} = G^{Tetragonal}_{U} - {}^{\circ}H^{SER}_{U} = G^{Tetragonal}_{U}$	Dinsdale (1991)
	$G^{Tetragonal}_{Si} = G^{Tetragonal}_{Si} - {}^{\circ}H^{SER}_{Si} = G^{Diamond}_{Si} + 4000$	Berche et al. (2009)
	${}^{\circ}L_{U,Si:\ VA} = -78915.524$	This work
Orthorhombic_A20: (U, Si)	$G^{Orthorhombic_{A20}}_{U} = {}^{\circ}H^{SER}_{U}$	Dinsdale (1991)
	$G^{Orthorhombic}_{Si} = G^{Orthorhombic}_{Si} - {}^{\circ}H^{SER}_{Si} = G^{Diamond}_{Si} + 4.2$	Wang et al. (2016)
	${}^{\circ}L_{U,Si:\ VA} = -78590 + 13.25T$	This Work
Diamond_A4: (U, Si)	$G^{Diamond_{A4}}_{U} = G^{Orthorhombic_{A20}}_{U} + 31860.9 + 0.2T$	This work
	$G^{Diamond_{A4}}_{Si} = {}^{\circ}H^{SER}_{Si}$	Dinsdale (1991)
	${}^{\circ}L_{U,Si:\ VA} = -100000 - 18{*}T$	This work
D5A_U$_3$Si$_2$: (U)$_3$(Si)$_2$(Si, VA)	$G^{D5A_{U3Si2}}_{U:\ Si:\ VA} = G^{D5A_{U3Si2}}_{U:\ Si:\ VA} - 3{}^{\circ}H^{SER}_{U} - 2{}^{\circ}H^{SER}_{Si} = -189929 - 36T + 3G^{Orthorhombic_{A20}}_{U} + 2G^{Diamond_{A4}}_{Si}$	This work
	$G^{D5A_{U3Si2}}_{U:\ Si:\ Si} = G^{D5A_{U3Si2}}_{U:\ Si:\ Si} - 3{}^{\circ}H^{SER}_{U} - 3{}^{\circ}H^{SER}_{Si} = -202967 + 7T + 3G^{Orthorhombic_{A20}}_{U} + 3G^{Diamond_{A4}}_{Si}$	
	${}^{\circ}L_{U+4,Si+4:\ VA} = 1000 - 10.245T$	
	${}^{1}L_{U+4,Si+4:\ VA} = 32023 + 58.3232T$	
C32_U$_3$Si$_5$: (U)$_3$(Si)$_5$(Si, VA)	$G^{D5A_{U3Si5}}_{U:\ Si:\ VA} = G^{D5A_{U3Si5}}_{U:\ Si:\ VA} - 3{}^{\circ}H^{SER}_{U} - 5{}^{\circ}H^{SER}_{Si} = -354955.897 - 30T + 3G^{Orthorhombic_{A20}}_{U} + 5G^{Diamond_{A4}}_{Si}$	This work
	$G^{D5A_{U3Si5}}_{U:\ Si:\ Si} = G^{D5A_{U3Si5}}_{U:\ Si:\ Si} - 3{}^{\circ}H^{SER}_{U} - 3{}^{\circ}H^{SER}_{Si} = -222204.02 + 116.89T + 3G^{Orthorhombic_{A20}}_{U} + 3G^{Diamond_{A4}}_{Si}$	
	${}^{\circ}L_{U+4,Si+4:\ VA} = 5000 - 205.297T$	
	${}^{1}L_{U+4,Si+4:\ VA} = 90000 + 78.3232T$	
	${}^{1}L_{U+4,Si+4:\ VA} = 9800 + 10.215T$	
U$_{68}$Si$_{67}$	$G_{U68Si67} = G_{U68Si67} - 68{}^{\circ}H^{SER}_{U} - 67{}^{\circ}H^{SER}_{Si} = -56410000.288 - 672.027T + 68G^{Orthorhombic_{A20}}_{U} + 67G^{Diamond_{A4}}_{Si}$	This work
U$_{12}$Si$_{22}$	$G_{U12Si22} = G_{U12Si22} - 12{}^{\circ}H^{SER}_{U} - 22{}^{\circ}H^{SER}_{Si} = -1544000.01007 - 55T + 12G^{Orthorhombic_{A20}}_{U} + 22G^{Diamond_{A4}}_{Si}$	This work
U$_3$Si	$G_{U3Si} = G_{U3Si} - 3{}^{\circ}H^{SER}_{U} - {}^{\circ}H^{SER}_{Si} = -1544000.01007 - 55T + 3G^{Orthorhombic_{A20}}_{U} + G^{Diamond_{A4}}_{Si}$	This work
	$\Delta H^{\alpha\rightarrow\beta} = 12600\ @\ 1043K$	
USi$_3$	$G_{U3Si} = G_{USi3} - 3{}^{\circ}H^{SER}_{U} - {}^{\circ}H^{SER}_{Si} = -99650.289 - 16.79T + G^{Orthorhombic_{A20}}_{U} + 3G^{Diamond_{A4}}_{Si}$	This work

n^s_{VA} is the number of vacancies on sublattice (s). The site fraction can be transferred to mole fraction (x_i) using the Eq. 12 below:

$$x_i = \frac{\sum_s n^s y^s_i}{\sum_i n^s \left(1 - y^s_{VA}\right)} \tag{12}$$

When each sublattice is only occupied by one component, then end-members of the phase are produced. In the present case, four end-members exist. They are AaCb, AaDb, BaCb and BaDb. The surface of reference ${}^{ref}G_m$ is expressed as in Eq. 13:

$${}^{ref}G_m = y^1 y^2 {}^{\circ}G_{A:\,C} + y^1 y^2 {}^{\circ}G_{A:\,D} + y^1 y^2 {}^{\circ}G_{B:\,C} + y^1 y^2 {}^{\circ}G_{B:\,D} \tag{13}$$

The ideal entropy (${}^{id}S_m$) and the excess free energy are expressed as follows in Eqs 14, 15, respectively:

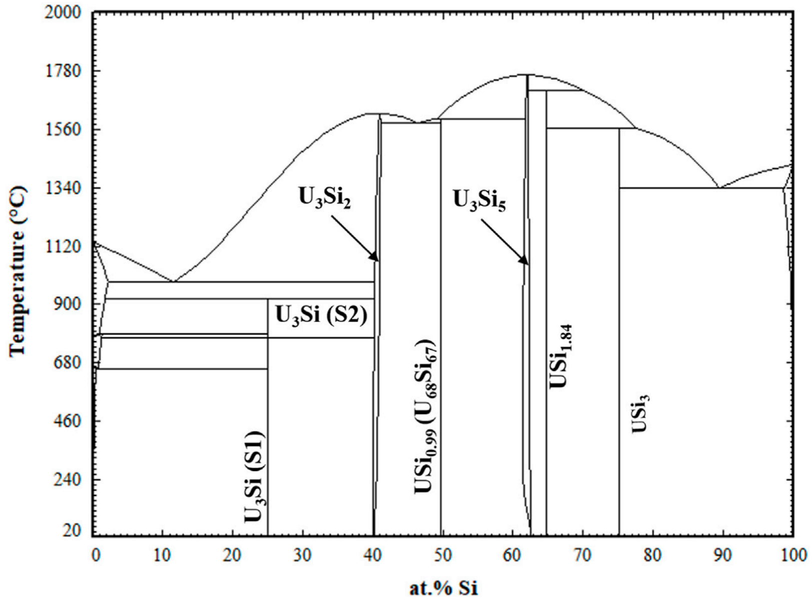

FIGURE 2
Optimized U-Si Phase Diagram. Arrows are pointing to the U_3Si_2 and U_3Si_5 homogeneity range.

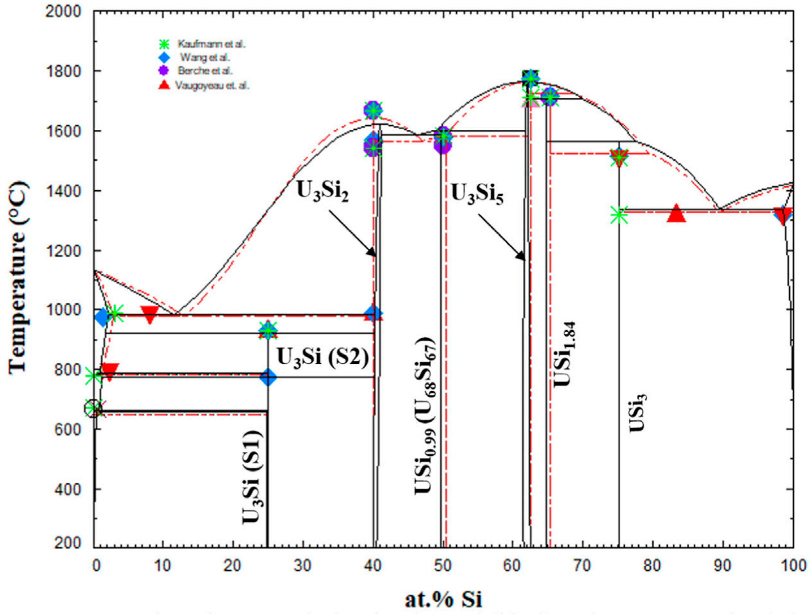

FIGURE 3
U-Si phase diagram calculated in the work (black) and super-imposed with the one from Berche et al., (Berche et al., 2009). The markers are experimental data from (Vaugoyeau et al., 1972; Dwight, 1982; Massalski, 1990; Wang et al., 2016).

$$ {}^{id}S = -R\left[a\left(y_A^1 \ln y_A^1 + y_B^1 \ln y_B^1\right) + b\left(y_C^2 \ln y_C^2 + y_D^2 \ln y_D^2\right)\right] \quad (14) $$

$$ {}^{E}G_m = y_A^1 y_B^1 \left(y_C^2 L_{A,B:\,D} + y_D^2 L_{A,B:\,D}\right) + y_C^2 y_D^2 \left(y_A^1 L_{A:\,C,D} + y_B^1 L_{B:\,C,D}\right) \quad (15) $$

The binary interaction parameters $L_{i,:k}$ represent the interaction between the constituents *i* and *j* in the first sublattice when the second sublattice is only occupied by constituent *k*. These parameters can be further expanded with Redlich-Kister polynomial as follows in Eq. 16:

$$ L_{i,j:\,k} = \sum_{\nu} \left(y_i^1 - y_j^1\right)^{\nu} L_{i,j:k} \quad (16) $$

In the case of a three sublattice model the Gibbs energy is written in Eq. 17 and the excess energy is given in Eq. 18:

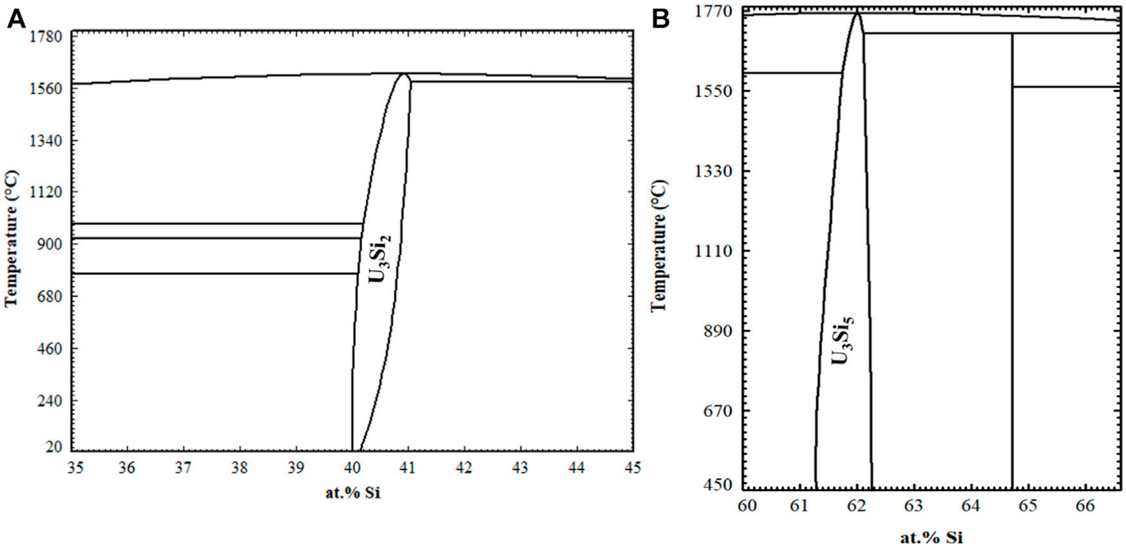

FIGURE 4
Zoomed in region of the U_3Si_2 **(A)** and U_3Si_5 **(B)** phase regions.

$$G_m = \sum_i y_i^I \sum_j y_j^{II} \sum_k y_k^{III} {}^{\circ}G_{i,j,k} + RT \sum_s \sum_i a^s y_i^s \ln y_i^s + {}^E G_m \tag{17}$$

$$\begin{aligned} {}^E G_m = \sum_i y_i^I \sum_j y_j^{II} \sum_k y_k^{III} & \left[\sum_{l>i} y_l^I \sum_\nu {}^\nu L_{i,l:\, j:\, k} \left(y_i^I - y_l^I\right)^\nu \right. \\ & + \left[\sum_{l>j} y_l^{II} \sum_\nu {}^\nu L_{i,j:\, l:\, k} \left(y_j^{II} - y_l^{II}\right)^\nu \right. \\ & + \left[\sum_{l>k} y_l^{III} \sum_\nu {}^\nu L_{i,j:\, k:\, l} \left(y_k^{III} - y_l^{III}\right)^\nu \right. \end{aligned} \tag{18}$$

4 Results

The FactSage thermochemical software (Bale et al., 2016) was used to perform the optimization of the uranium-silicon binary system. Summarized in Table 3 are the phases, with their crystal structure, space groups, prototypes, composition, and the thermodynamic model of the U-Si phases studied in this work. Unlike the previous two models (Berche et al., 2009; Wang et al., 2016), the liquid phase is modeled using the TSPIL model, where the first sublattice contains the U^{+4} and Si^{+4} cations and the second sublattice is occupied by a neutral vacancy as depicted by Eq. 19.

$$\left(U^{+4}, Si^{+4}\right)(VA) \tag{19}$$

This model was chosen because it is the mostly commonly used for modeling liquid phases and will therefore make incorporation of other elements into the U-Si database (e.g., fission product) a straightforward process. The excess energy parameters from Berche et al. (2009) were used for the initial point and adjusted as necessary.

The USi_3, $USi_{1.84}$, $U_{68}Si_{67}$, and U_3Si compositions were modeled as stoichiometric phases. The USi phase was previously assessed with the FeB-type structure; however, neutron diffraction confirmed that the phase has a tetragonal structure with *I4/mmm* space group. Therefore, the phase was modeled based on the recent findings. The recent enthalpy of formation data collected in 2018 (Chung et al., 2018) for the USi phase with tetragonal structure was used in the optimization. The composition of the USi_{2-x} phase was adjusted from $USi_{1.88}$ to $USi_{1.84}$ to reflect the experimental findings (Remschnig et al., 1992).

The U_3Si_5 and U_3Si_2 phases were modeled as a solid solution using the CEF model. The U_3Si_2 phase was modeled with 3 sublattices $(U)_3(Si)_2(Si,VA)$. Originally, a four sublattice model was applied to the system based on Wyckoff positions of the atoms; however, the model was simplified by adding a third sublattice to its stoichiometric representation (i.e., $(U)_3(Si)_2(Si,VA)$). This is justified as the nonstoichiometry in U_3Si_2 is primarily driven by silicon interstitials defects as shown by Ulrich et al. (2020b). Modeling the phase in this manner will facilitate modeling incorporation of light elements that are known to dissolve in the U_3Si_2 lattice such as hydrogen and carbon forms a U_3Si_2X phase (X = H or C). All one would need to do is add these elements to the third sublattice. The model can also be expanded on the first and second sublattices, which will be useful for CALPHAD assessment of fission products with U_3Si_2 fuel.

The U_3Si_5 phase was also modeled using CEF model with 3 sublattices, $(U)_3(Si)_5(Si,VA)$. Although, this phase could have been modeled using 2 sublattices by using the relationship; U_3Si_5 = AlB_2-type USi_{2-x}, modeling with the three sublattice was simpler as there is the $ThSi_2$-type USi_{2-x} structure (i.e., $USi_{1.84}$) close in composition to U_3Si_5, which makes the phase equilibria calculations more difficult.

The optimized parameters for the compounds and solid solutions are provided in Table 4 and the phase diagram is provided in Figure 2.

TABLE 5 Invariant reactions in the U-Si system calculated in the work and compared to literature values.

Reaction	Reaction type	Temperature (°C)	Composition (at. %U)			References
$liquid \leftrightarrow U_3Si_5$	Congruently melting	1770 ± 10			37.5	Kaufmann et al. (1957)
		~1700			37.5	Vaugoyeau et al. (1972)
		1773			37.5	White et al. (2015)
		1762			38	This work
$\alpha U_3Si \leftrightarrow \beta U_3Si$	Allotropic	770			75	Goddard et al. (2016)
		770			75	World Nuclear News (2019)
		769.85			75	This work
$liquid + U_3Si_5 \leftrightarrow USi$	Peritectic	1,580 ± 10		37.5	50	Dwight (1982b)
		1,576	~50	37.5	50	World Nuclear News (2019)
		1,597.4	51	38.3	50.4	This work
$liquid \leftrightarrow U_3Si_2$	Congruently melting	1,540 ± 10			60	Dwight (1982b)
		1,665			60	Dwight (1982b)
		1,664			60	World Nuclear News (2019)
		1,618.9			59.1	This work
$liquid + U_3Si_5 \leftrightarrow USi_{1.88}$	Peritectic	1710 ± 10		37.5	34.7	Dwight (1982b)
		1715	28.5	37.5	34.7	World Nuclear News (2019)
		1706.54	30.2	37.9	35.3	This work
$liquid \leftrightarrow bcc\,U + U_3Si_2$	Eutectic	985	92.1	98.4	60	White et al. (2017)
		985	88.5	98.2	60	World Nuclear News (2019)
		982.5	88.6	97.8	59.8	This work
$\beta U_3Si \leftrightarrow bcc\,U + U_3Si_2$	Eutectoid	930	75	98.2	60	White et al. (2017)
		929	75	98.6	60	World Nuclear News (2019)
$liquid \leftrightarrow dia.\,Si + USi_3$	Eutectic	1,315	10.7	1.4	25	Wang et al. (2016)
		1,317	9.7	1.1	25	World Nuclear News (2019)
		1,335.71	10.6	0.014	25	This work
$tetra\,U + \alpha U_3Si \leftrightarrow ortho\,U$	Eutectoid	665	~100	75	~100	White et al. (2017)
		665	~99.4	75	~99.5	World Nuclear News (2019)
$liquid + USi_{1.88} \leftrightarrow USi_3$	Peritectic	1,510 ± 10	19.1	34.7	25	Dwight, (1982b)
		1,511	17.8	34.7	25	World Nuclear News (2019)
		1,560.43	22.5	35.3	25	This work
$bcc\,U + \alpha U_3Si \leftrightarrow tetra\,U$	Eutectoid	795	98.6	75	97.7	White et al. (2017)
		794	99.4	75	98.7	World Nuclear News (2019)
		784.24	99.2	75	98.8	This work
$liquid \leftrightarrow U_3Si_2 + USi$	Eutectic	1,583.2	53.8	59.0	50.4	This work
$liquid \leftrightarrow dia.Si$	Melting	1,425.26			0	This work
$liquid \leftrightarrow bcc\,U$	Melting	1,134.84			100	This work
$bcc\,U + U_3Si_2 \leftrightarrow U_3Si$	Eutectoid	920.06	98.3	59.8	75	This work
$tetra\,U + U_3Si_2 \leftrightarrow U_3Si$	Eutectoid	769.85	98.8	59.9	75	This work
$tetra\,U \leftrightarrow ortho\,U + U_3Si$	Eutectoid	655.99	99.2	99.7	75	This work

5 Disscussion

The U-Si phase equilibria was modeled using the CALPHAD methodology and for the first time the U_3Si_2 and U_3Si_5 phases were modeled as nonstoichiometric phases using the 3 sublattice CEF model. The optimized diagram is displayed in Figure 3 and is compared to experimental data and calculated diagram by Berche *el. al.* (Berche et al., 2009). The diagram is in good agreement with respect to melting point and the terminal solutions.

Displayed in Figure 4 is a zoomed in region of the U_3Si_2 a) and U_3Si_5 b) phases. The U_3Si_2 phase is modeled with a homogeneity range of $U_3Si_{1.95}$ to $U_3Si_{2.05}$, which is in agreement with the neutron and experimental results from this project (Ulrich et al., 2020b); however, it disagrees with the work of Middleburg et al. (Middleburgh et al., 2016), at low temperatures (i.e., any temperature below 1,000°C). Further experimental work is suggested on samples with a wider homogeneity range to determine the exact width of the solubility range. However, this work shows that modeling the U_3Si_2 phase with the 3 sublattice model is sufficient enough to mimic the experimental composition. Furthermore, it will serve as a starting point for incorporating elements with the affinity for dissolving into U_3Si_2.

Experimentally, it has been shown that the U_3Si_5 phase can exist between the 62.5–63.4 at.% Si phase region; however, since it exists with an unknow, the exact composition of the phase is unknown. Although the phase diagram showed an overall good agreement with experimental data, the model for this phase could use further optimizing as the calculated composition region is narrower than the experimental composition. However, before further optimization of the phase, further experiments and computational analysis would prove useful for understanding the nature of the phase transition associated with the composition. The calculated enthalpy of formation for the stoichiometric compounds and the different invariant reactions are in agreement with literature values, see Table 2 and Table 5, respectively.

6 Conclusion

The aim of this work was to develop a self-consistent thermodynamic database for the uranium-silicon system that can be used to predict silicide fuel behavior during normal or off-normal reactor operations, optimize fuel fabrication processes, and support licensing efforts. To achieve this, the 40–66 at% Si region of the U-Si system had to be investigated for the phases, phase transitions, homogeneity ranges, and crystal structures.

A thermodynamic database for the U-Si phase containing the optimized parameters has been developed and an overall good agreement between the calculated diagram and the experimental phase diagram data was achieved. Representing the U_3Si_2 phase as a 3 sublattice model accurately accounts for Si interstitial defects, which are the primary defects found in this structure. The CALPHAD results for the phase diagram from 40–66 at% Si are summarized below.

- The U_3Si_2 phase exhibits a homogeneity range from room temperature to its melting point.
- U_5Si_4 (*P6/mmm* space group) should not be considered as an equilibrium phase in the U-Si system. The phase could potentially be metastable with negative energy of formation located 2 meV above the U-Si convex hull and has a stable isostructural ternary phase, $U_{20}Si_{16}C_3$ (P6/*mmm*). This suggests that the binary could be stabilized by a third element (Lopes et al., 2018; Kocevski et al., 2019; Ulrich et al., 2020a).
- The crystal structure of the USi phase was confirmed as having a tetragonal supercell with an *I4/mmm* space group and invariant stoichiometry of $USi_{0.99}$ (Ulrich et al., 2020a).
- Above 450°C, the U_3Si_5 phase was found to exhibit a homogeneity range. Below 450°C, U_3Si_5 was found to exist with another unidentified phase. Regarding the equilibrium phase diagram, it is recommended that this phase transition not be included until more knowledge is acquired.
- The composition of the tetragonal α-USi_2 phase was found to be ~$USi_{1.84}$ after annealing for 72 h at 1,200°C.
- The Molar mass of USi and $USi_{1.88}$ were adjusted to represent change in composition, $U_{68}Si_{67}$ and $USi_{1.84}$, respectively.

Data availability statement

The original contributions presented in the study are included in the article/Supplementary material, further inquiries can be directed to the corresponding author.

Author contributions

TU: Conceptualization, Data curation, Formal Analysis, Investigation, Methodology, Visualization, Writing–original draft, Writing–review and editing. TB: Conceptualization, Funding acquisition, Project administration, Resources, Writing–review and editing.

Funding

The author(s) declare financial support was received for the research, authorship, and/or publication of this article. The work done in this paper contributes to the project: Phase Equilibria and Thermochemistry of Advance Fuel: Modelling Burnup Behavior. This work was funded by the Department of Energy Nuclear Energy University Program (NEUP).

Acknowledgments

The authors would also like to acknowledge Sven C. Vogel, Joshua T. White, David A. Andersson, Elizabeth Sooby, Denise A. Lopes, Vancho Kocevski, and Emily Moore for their significant contribution to the project that helped to generate the data needed in order to perform a CALPHAD optimization.

Conflict of interest

The authors declare that the research was conducted in the absence of any commercial or financial relationships that could be construed as a potential conflict of interest.

Publisher's note

References

Alcock, C. B., and Grieveson, P. (1961). A thermodynamic study of the compounds of uranium with silicon, germanium, tin, and lead. *J. Inst. Metals* 90, 304–310.

Bale, C. W., Bélisle, E., Chartrand, P., Decterov, S. A., Eriksson, G., Gheribi, A. E., et al. (2016). FactSage thermochemical software and databases, 2010–2016. *CALPHAD* 54, 35–53. doi:10.1016/j.calphad.2016.05.002

Berche, A., Rado, C., Rapaud, O., Guéneau, C., and Rogez, J. (2009). Thermodynamic study of the U-Si system. *J. Nucl. Mater.* 389, 101–107. doi:10.1016/j.jnucmat.2009.01.014

Bihan, T. L., Noel, H., and Rogl, P. F. (1996). Crystal Structure of the uranium monosilicide (USi). *J. Alloys Compd.* 240, 128–133. doi:10.1016/0925-8388(96)02273-6

Birtcher, R. C., Mueller, M. H., Richardson, J. W., and Faber, J. (1989). Neutron irradiated uranium silicides studied by neutron diffraction and Rietveld analysis. *MRS Online Proc. Libr. Arch.* 166, 437. doi:10.1557/proc-166-437

Boucher, R. R. (1971). X-ray diffraction on U_3Si. *J. Acta Crystallogr.* 4, 326–328. doi:10.1107/S0021889871007088

Bragg-Sitton, S., Merrill, B., Teague, M., Ott, L., Robb, K., Farmer, M., et al. (2014). *Advanced fuels campaign: enhanced LWR accident tolerant fuel performance metrics*. United States: Idaho National Laboratory. Technical Report INL/EXT-13-29957.

Brauer, G., and Haag, H. (1949). Notiz über die Kristallstruktur von Uransilicid. *Z. Fur Anorg. Chem.* 259, 197–200. doi:10.1002/zaac.19492590117

Brown, A., and Norreys, J. (1961). Uranium disilicide. *Nature* 191, 61–62. doi:10.1038/191061a0

Brown, A., and Norreys, J. J. (1959). Beta-polymorphs of uranium and thorium disilicides. *Nature* 183, 673. doi:10.1038/183673a0

Carmack, J., Goldner, F., Bragg-Sitton, S. M., and Snead, L. L. (2013). *Overview of the U.S. DOE accident tolerant fuel development program, TopFuel 2013 Charlotte*. United States: Idaho National Lab. (INL), Idaho Falls.

Chung, C.-K., Guo, X., Wang, G., Wilson, T. L., White, J. T., Nelson, A. T., et al. (2018). Enthalpies of formation and phase stability relations of USi, U_3Si_5 and U_3Si_2. *J. Nucl. Mater.* 523, 101–110. doi:10.1016/j.jnucmat.2019.05.052

Cullity, B. D. (1945). Alloys of uranium and silicon. I. The uranium-silicon phase diagram. U.S.A.E., Report No. CT-3310.

Dinsdale, A. (1991). SGTE data for pure elements. *CALPHAD* 15, 317–425. doi:10.1016/0364-5916(91)90030-N

Dwight, A. (1982a). *Study of the uranium–aluminum–silicon system*. IL, USA: Argonne National Lab. doi:10.2172/6753243

Dwight, A. E. (1982b). *Study of the uranium-aluminum-silicon system*. United States: Argonne National Lab. doi:10.2172/6753243

Ferro, R., and Cacciamani, G. (2002). Remarks on crystallochemical aspects in thermodynamic modeling. *CALPHAD* 26, 439–458. doi:10.1016/S0364-5916(02)00056-1

Goddard, D. T., Mathers, D. P., Eaves, D. G., Xu, P., Lahoda, E. J., and Harp, J. M. (2016). *Manufacturability of U_3Si_2 and its high temperature oxidation behavior*. USA: Boise, Idaho.

Gross, T., Hayman, C., and Clayton, M. H. (1962). Thermodynamic of nuclear materials. *Process Symp.* 1963, 653–665.

Hillert, M. (2001). The compound energy formalism. *J. Alloys Compd.* 320, 161–176. doi:10.1016/S0925-8388(00)01481-X

Johnson, K. D., Raftery, A. M., Lopes, D. A., and Wallenius, J. (2016). Fabrication and microstructural analysis of UN-U_3Si_2 composites for accident tolerant fuel applications. *J. Nucl. Mater.* 477, 18–23. doi:10.1016/j.jnucmat.2016.05.004

Johnson, K. E., Adorno, D. L., Kocevski, V., Ulrich, T. L., White, J. T., Claisse, A., et al. (2020). Impact of fission product inclusion on phase development in U_3Si_2 fuel. *J. Nucl. Material* 537, 152235. doi:10.1016/j.jnucmat.2020.152235

Karoutas, Z., Brown, J., Atwood, A., Hallstadius, L., Lahoda, E., Ray, S., et al. (2018). The maturing of nuclear fuel: past to accident tolerant fuel. *Prog. Nucl. Energy* 102, 68–78. doi:10.1016/j.pnucene.2017.07.016

Katz, J. J., and Rabinowitch, E. (1951). *The chemistry of uranium – Part 1, the element, its binary and related compounds*. New York: McGraw-Hill Book Company, Inc., 226–229.

Kaufman, L., and Bernstein, H. (1970). *Computer calculations of phase diagrams*. New York: Academic Press.

Kaufmann, A. R., Cullity, B. D., and Bitsianes, G. (1957). Uranium silicon alloys. *J. Metals* 9, 23–27. doi:10.1007/BF03398440

Kim, H. G., Yang, J. H., Kim, W. J., and Koo, Y. H. (2016). Development status of accident tolerant fuel for light water reactors in Korea. *Nucl. Eng. Technol.* 48, 1–15. doi:10.1016/j.net.2015.11.011

Kim, Y. S. (2012). "Uranium intermetallic fuels (U-Al, U-Si, U-Mo)," in *Comprehensive nuclear materials*. Editor R. Konings, 3, 391–422.

Kimmel, G., Sharon, B., and Rosen, M. (1980). Structure and phase stability of uranium-silicon U_3Si at low temperatures. *Acta Crystallogr.* B36, 2386–2389. doi:10.1107/S0567740880008783

Kocevski, V., Lopes, D. A., and Besmann, T. M. (2019). Investigation of the on-site Coulomb correction and temperature dependence of the stability of U–Si phases using DFT+U. *J. Nucl. Mater.* 524, 157–163. doi:10.1016/j.jnucmat.2019.07.003

Kurata, M. (2016). Research and development methodology for practical use of accident tolerant fuel in light water reactors. *Nucl. Eng. Technol.* 48, 26–32. doi:10.1016/j.net.2015.12.004

Laugier, J., Blum, P. L., and de Tournemine, R. (1971). Sur la veritable structure du compose USi. *J. Nucl. Mater.* 41, 106–108. doi:10.1016/0022-3115(71)90205-4

Liu, Z. K. (2009). First principles calculations and calphad modeling of thermodynamics. *J. Phase Equilibria* 30, 517–534. doi:10.1007/s11669-009-9570-6

Lopes, D. A., Kocevski, V., Wilson, T. L., and Besmann, T. M. (2018). Stability of U_5Si_4 phase in U-Si system: crystal structure prediction and phonon properties using first-principles calculations. *J. Nucl. Mater.* 510, 331–336. doi:10.1016/j.jnucmat.2018.08.026

Lopes, D. A., Wilson, T. L., Kocevski, V., Moore, E. E., Besmann, T. M., Sooby Wood, E., et al. (2019). Experimental and computational assessment of USiN ternary phases. *J. Nucl. Mater.* 516, 194–201. doi:10.1016/j.jnucmat.2019.01.008

Lukachuk, M., and Pöttgen, R. (2003). Intermetallic compounds with ordered U_3Si_2 and Zr_3Al_2 type structure – crystal chemistry, chemical bonding and physical properties. *Z. für Kristallogr.* 218, 767–787. doi:10.1524/zkri.218.12.767.20545

Lukas, H., Fries, S. G., and Sundman, B. (2007). *Computational thermodynamics: the calphad method*. Cambridge: Cambridge University Press.

Massalski, B. T. (1990). *Binary alloy phase diagrams*. second Ed. (Materials Park, OH: ASM), 3374–3375.

Middleburgh, S. C., Grimes, R. W., Lahoda, E. J., Stanek, C. R., and Andersson, D. A. (2016). Non-stoichiometry in U_3Si_2. *J. Nucl. Mater.* 482, 300–305. doi:10.1016/j.jnucmat.2016.10.016

Noël, H., Chatain, S., Alpettaz, T., Guéneau, C., Duguay, C., and Léchelle, J. (2023). Experimental determination of (U-Si-C) ternary phase diagram at 1000°C and experimental points in the quaternary (U-Pu-Si-C) system. F-BRIDGE, Report No. D-151.

Noordhoek, M. J., Besmann, T. M., Andersson, D., Middleburgh, S. C., and Chernatynskiy, A. (2016). Phase Equilibria in the U-Si system from first-principles calculations. *J. Nucl. Mater.* 479, 216–223. doi:10.1016/j.jnucmat.2016.07.006

Noël, H., Queneau, V., Durand, J. P., and Colomb, P. (1998). *Abstract of a paper at the international conference on strongly correlated electron systems-SCSES98*, 92.

OHare, P. A. G., Hubbard, W. N., Johnson, G. K., and Settle, J. L. (1974). Thermodynamic of nuclear materials. *Process Symp. Vienna* 1975, 452.

Ott, H. R., Hulliger, F., Rudigier, H., and Fisk, Z. (1985). Superconductivity in uranium compounds with Cu_3Au structure. *Phys. Rev. B* 31, 1329–1333. doi:10.1103/physrevb.31.1329

Otto, R., and Kister, A. T. (1948). Algebraic representation of thermodynamic properties and the classification of solutions. *Industrial Eng. Chem.* 40 (2), 345–348. doi:10.1021/ie50458a036

Perrut, M. (2015). Thermodynamic modeling by the calphad method and its applications to innovative materials. *AerospaceLab* 9, 1–11.

Pöttgen, R. (1994). Ternary rare earth metal gold stannides and indides with ordered U3Si2 and Zr3Al2-type structure. *Verl. Z. für Naturforsch.* 49, 1525–1530. doi:10.1515/znb-1994-1112

Remschnig, K., LeBihan, T., Noël, H., and Rogl, P. (1992). Structural chemistry and magnetic behavior of binary uranium silicides. *J. Solid State Chem.* 97, 391–399. doi:10.1016/0022-4596(92)90048-Z

Sasa, Y., and Uda, M. (1976). Structure of stoichiometric USi_2. *J. Solid State Chem.* 18, 63–68. doi:10.1016/0022-4596(76)90079-7

Schindelin, J., Arganda-Carreras, I., Frise, E., Kaynig, V., Longair, M., Pietzsch, T., et al. (2012). Fiji: an open-source platform for biological-image analysis. *Nat. Methods* 9, 676–682. doi:10.1038/nmeth.2019

Terrani, K. (2018). Accident tolerant fuel cladding development: promise, status, and challenges. *J. Nucl. Mater.* 501, 13–30. doi:10.1016/j.jnucmat.2017.12.043

Toby, B. H., and Von Dreele, R. B. (2013). GSAS-II: the genesis of a modern open-source all-purpose crystallography software package. *J. Appl. Crystallogr.* 46, 544–549. doi:10.1107/S0021889813003531

Ulrich, T. L. (2019). "Modeling the uranium-silicon phase equilibria based on computational and experimental analysis," (South Carolina: University of South Carolina). (Doctoral dissertation).

Ulrich, T. L., Vogel, S. C., Lopes, D. A., Kocevski, V., White, J. T., Sooby, E. S., et al. (2020a). Phase stability of U_5Si4, USi, and U_2Si_3 in the uranium–silicon system. *J. Nucl. Mater.* 540, 152353. doi:10.1016/j.jnucmat.2020.152353

Ulrich, T. L., Vogel, S. C., White, J. T., Andersson, D. A., Sooby Wood, E., and Besmann, T. M. (2020b). High temperature neutron diffraction investigation of U_3Si_2. *Materialia* 9, 100580. doi:10.1016/j.mtla.2019.100580

U.S Department of Energy (2015). Development of Light Water Reactor fuels with enhanced accident tolerance. Report to Congress.

US Nuclear Regulatory Commission (2011). Special report on the accident at the Fukushima Diiachi nuclear power station. Report No. INP0 11-005.

Vaugoyeau, H., Lombard, L., and Morlevat, J. (1972). A contribution to the study of the uranium–silicon equilibrium diagram. Report No. AECL-4151.

Vooght, D.De., Verniers, G., and Meester, P.De. (1973). Counter-diffractometer parameter determination of polycrystalline U_3Si. *J. Nucl. Mater.* 46, 303–308. doi:10.1016/0022-3115(73)90045-7

Wang, J., Wang, K., Chunhua, M., and Xie, L. (2016). Critical Evaluation and thermodynamic optimization of the (U+Bi), (U+Si) and (U+Sn) binary systems. *J. Chem. Thermodyn.* 92, 158–167. doi:10.1016/j.jct.2015.08.029

Westinghouse (2023). Westinghouse's Encore fuel inserted in Exelon generation's Byron unit 2. Available at: http://www.westinghousenuclear.com/uknuclear/about/news/view/westinghouse-s-encore-fuel-inserted-in-exelon-generation-s-byron-unit-2.

White, J. T., Nelson, A. T., Byler, D. D., Valdez, J. A., and McClellan, K. J. (2014). Thermophysical properties of U_3Si to 1150 K. *J. Nucl. Mater.* 452, 304–310. doi:10.1016/j.jnucmat.2014.05.037

White, J. T., Nelson, A. T., Dunwoody, J. T., Byler, D. D., and McClellan, K. J. (2016). Thermophysical properties of USi to 1673 K. *J. Nucl. Mater.* 471, 129–135. doi:10.1016/j.jnucmat.2016.01.013

White, J. T., Nelson, A. T., Dunwoody, J. T., Byler, D. D., Safarik, D. J., and McClellan, K. J. (2015). Thermophysical properties of U_3Si_2 to 1773 K. *J. Nucl. Mater.* 464, 275–280. doi:10.1016/j.jnucmat.2015.04.031

White, J. T., Travis, A. W., Dunwoody, J. T., and Nelson, A. T. (2017). Fabrication and thermophysical property characterization of UN/U_3Si_2 composite fuel forms. *J. Nucl. Mater.* 495, 463–474. doi:10.1016/j.jnucmat.2017.08.041

Wilson, T. L., Moore, E. E., Lopes, D. A., KocevskiSooby Wood, V. E., White, J. T., Nelson, A. T., et al. (2018). Uranium nitride-silicide advanced nuclear fuel: higher efficiency and greater safety. *Adv. Appl. Ceram.* 117, S76–S81. doi:10.1080/17436753.2018.1521607

World Nuclear News (2019). US begins first commercial testing of silicide fuel. Available at: http://world-nuclear-news.org/Articles/US-begins-first-commercial-testing-of-silicide-fuel.

Zachariasen, W. H. (1949). Crystal chemical studies of the 5*f*-series of elements. VIII. Crystal structure studies of uranium silicides and of $CeSi_2$, $NpSi_2$, and $PuSi_2$. *Acta Crystallogr.* 2, 94–99. doi:10.1107/s0365110x49000217

Zinkle, S. J., and Was, G. S. (2013). Materials challenges in nuclear energy. *Acta Mater.* 61, 735–758. doi:10.1016/j.actamat.2012.11.004

frontiers | Frontiers in Nuclear Engineering

TYPE Brief Research Report
PUBLISHED 22 January 2024
DOI 10.3389/fnuen.2023.1332377

OPEN ACCESS

EDITED BY
Anne Campbell,
Oak Ridge National Laboratory (DOE),
United States

REVIEWED BY
Jacques Lechelle,
Commissariat à l'Energie Atomique et aux Energies Alternatives (CEA), France
Shingo Tamaki,
Osaka University, Japan

*CORRESPONDENCE
Hazel M. Gardner,
✉ hazel.gardner@ukaea.uk

RECEIVED 02 November 2023
ACCEPTED 18 December 2023
PUBLISHED 22 January 2024

CITATION
Gardner HM, Zilahi G and Wade-Zhu J (2024), Investigating the thermal and irradiation stability of chemical vapor deposited erbium oxide tritium barrier coatings for Li breeder blanket applications.
Front. Nucl. Eng. 2:1332377.
doi: 10.3389/fnuen.2023.1332377

Investigating the thermal and irradiation stability of chemical vapor deposited erbium oxide tritium barrier coatings for Li breeder blanket applications

Hazel M. Gardner*, Gyula Zilahi and James Wade-Zhu

Materials Science and Engineering, UK Atomic Energy Authority, Oxford, United Kingdom

Two-micron thick erbium oxide tritium barrier coatings have been prepared by aerosol injection chemical vapor deposition and subsequently irradiated with 33 MeV Au 6+ ions at fluences up to 2.1 × 10^{16} Au/m^2 at 550°C. Scanning electron microscopy, X-ray diffraction and transmission electron microscopy were used to investigate the coating surface morphologies, phase structures and cross-sectional microstructures as a function of irradiation and thermal treatment. XRD data was also used to extract information about the evolution of lattice strain in the coating. Some of the cubic erbia transformed to the monoclinic phase in the sample that was ion irradiated at temperature, and this was accompanied by a change from columnar to a more equiaxed grain structure. All coatings were found to experience out-of-plane tensile strain, thought to originate from thermal stresses created during coating manufacture. Thermal treatment reduced microstrains present in the as-deposited sample, whilst the cubic-to-monoclinic phase transformation reduced strain in the cubic phase but increased strain in the monoclinic phase.

KEYWORDS

fusion energy, ceramic coatings, erbium oxide, ion beam irradiation, microstructure evolution, chemical vapor deposition, phase transformation

Introduction

Erbium oxide (erbia, Er_2O_3) coatings are being investigated for use in the breeder blanket and tritium extraction system of future fusion power plants owing to their high permeation reduction factor (Nemanič, 2019) and ability to show some degree of resistance to attack by corrosive liquid Li (Pint et al., 2002). However, to perform successfully as a tritium permeation barrier the erbia coating must withstand thermal cycling and remain stable under irradiation during reactor operation.

Erbia has a low temperature cubic (bixbyite) phase with higher temperature monoclinic and hexagonal phases (Zinkevich, 2007; Ushakov et al., 2020), denoted as C, B and H respectively. The phase structure of the erbia affects the properties and performance of the coating. For example, the B phase has higher stability under ion irradiation than the C phase (Tang et al., 2006) but the C phase is harder than the B phase (Li et al., 2012). Studies have shown that coating application method can be tailored to control the phase of as-deposited thin erbia films (Adelhelm et al., 2009; Yan et al., 2019).

Pressure (Guo et al., 2007), temperature (Yan et al., 2019) and ion irradiation (Tang et al., 2006) have all been shown to separately induce cubic-to-monoclinic phase transformations in erbia. This work investigates the combined thermal and ion irradiation response of cubic erbium oxide coatings produced by chemical vapor deposition (CVD), at temperatures and irradiation damage levels that are relevant to breeder blanket operating conditions.

Materials and methods

Grade 91 steel substrate discs were grit blast in preparation for the coating application process. Er_2O_3 coatings were deposited on one side of the substrate using aerosol injection CVD with Er (tmhd)3 precursor and oxygen as a reactive gas. A 2-micron thick erbium oxide coating was deposited at a substrate temperature of 600–700°C, with a total process time of 1–1.5 h. Exact details of precursor partial pressures, deposition temperatures and process times are proprietary to the coating manufacturer (ATL, High Wycombe, United Kingdom).

The coating was ion irradiated at the Dalton Cumbria Facility with 33 MeV Au 6+ ions at fluences up to 2.1×10^{16} Au/m^2 at 550°C, with the incident ions normal to the coated surface. The Monte Carlo program SRIM (Ziegler and Biersack, 1985) was used to estimate the displacement damage distribution under these irradiation conditions. The peak in the displaced atom damage distribution occurs in the steel substrate at a sample depth of 3.5 micron (1.5 microns beyond the coating substrate interface). This corresponds to a peak displacement damage level in the steel of 55 displacements per atom (dpa) at a fluence of 2.1×10^{16} Au/m^2. This is approximately the targeted lifetime dose of the DEMO second generation breeder blanket (Federici et al., 2019). The displacement damage level within the 2 micron coating layer is 20–25 dpa. During the irradiation, a small square of the sample was blanked by a mask such that this region of the sample experienced the same temperature without irradiation. This region of sample is referred to as "irradiated (blanked)." The region of sample that was not blanked by the mask is referred to as "irradiated (exposed)."

The as-deposited, irradiated (blanked) and irradiated (exposed) samples were each analyzed using scanning electron microscopy (SEM), X-ray diffraction (XRD) and transmission electron microscopy (TEM). Secondary electron SEM images were collected from the surface of all three samples using a Tescan Mira3 XMH scanning electron microscope. XRD measurements were made using a Rigaku Smartlab X-ray diffractometer. Cu Kα radiation was used for the as-deposited sample whereas Co Kα radiation was used for the irradiated (blanked) and irradiated (exposed) samples, due to instrument availability. A fixed, 6° angle of incidence was used for the as-deposited sample; a 3° angle of incidence was used for the irradiated (blanked) and irradiated (exposed) samples.

Cross sections were prepared for TEM examination from the as-deposited and both irradiated samples using a focused ion beam. The microstructures were examined using a FEI Tecnai F20 G2 S—Twin FEG-scanning TEM.

Results

Figure 1 shows representative regions of the coated surface of the as-deposited sample and the irradiated (blanked) and irradiated (exposed) samples. The coating morphology was consistent across all three samples, and gaps can be observed in the regions where adjacent coating nodules have nucleated and grown together. XRD spectra collected from the samples are shown in Figure 2, along with simulated spectra that were plotted using data from the Materials Project (Jain et al., 2013). Comparison of the experimental data with the simulated spectra shows that the peaks marked with a circle on Figure 2 in the as-deposited and irradiated (blanked) data match those expected for the cubic erbia phase. In all samples, peaks present at Q = 3.097 1/Å and Q = 4.379 1/Å can be attributed to BCC Fe phase, which originate from the substrate. No other peaks were identified as relating to the substrate or substrate oxides. In the ion irradiated (exposed) sample, additional peaks are present at Q (1/Å) = 2.109, 2.151, 2.274, 3.632, 3.769, and 3.886, which correspond to peaks expected for the monoclinic phase. This suggests that the ion irradiation has induced a phase change.

The ratio of the intensity of the peak at Q = 2.061 1/Å to the peak at Q = 2.383 1/Å changed between the three samples. These peak positions correspond to the (222) and the (400) peaks for the cubic phase, respectively. The (222) peak is the highest intensity peak in the simulated spectrum for the cubic erbia phase, as well as in the as-deposited and ion irradiated (blanked) spectra. For the irradiated (exposed) sample, the (222) peak is less intense than the (400) peak. Multiple mechanisms could be contributing to this change in peak intensity in the irradiated (exposed) sample. For example, it is possible that point defects generated in the irradiated (exposed) sample are favoring diffusion and crystal re-ordering of the Er/O atoms, such that a change in preferred grain orientation from (222) to (400) occurs in the cubic erbia. A similar change in preferred grain orientation from (222) to (400) has been observed in H permeation studies in cubic erbia (Chikada et al., 2011). First principles modelling showed that interactions between the H and O/Er atoms resulted in movement of O/Er atoms, enabling change in grain orientation (Mao et al., 2020). Another mechanism that could be contributing is irradiation-induced grain growth of the (400) oriented grains in the cubic phase, resulting in an increase in intensity of the (400) peak relative to the (222) peak. Further work is needed to fully outline all mechanisms at play, and determine which mechanisms are dominant.

Two different types of lattice strain can be extracted from XRD spectra. The first type manifests as a shift in position of the XRD peaks and occurs when the strain extends over the whole lattice. The second, known as microstrain, results in broadening of the XRD peaks and occurs over only a few lattice spacings (Dolabella et al., 2022). Microstrain is caused by defects such as dislocations and vacancies, which locally distort the lattice (Maniammal et al., 2017).

The major peaks for each of the measured spectra in Figure 2 were all shifted to the left relative to the corresponding peak position in the simulated spectra. Since the spectra are plotted in reciprocal space, this shift indicates that all samples were under a slight tensile strain. Because the XRD measurements have been taken in reflection mode, the peak shift measurements were affected by the out-of-plane strain components. Cubic erbia

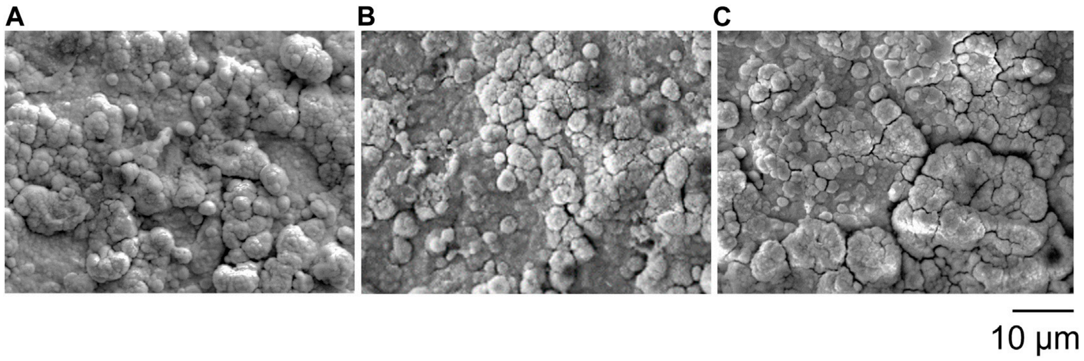

FIGURE 1
SEM images of the surface of the erbia coatings in the **(A)** as-deposited, **(B)** ion irradiated (blanked) and **(C)** ion irradiated (exposed) regions.

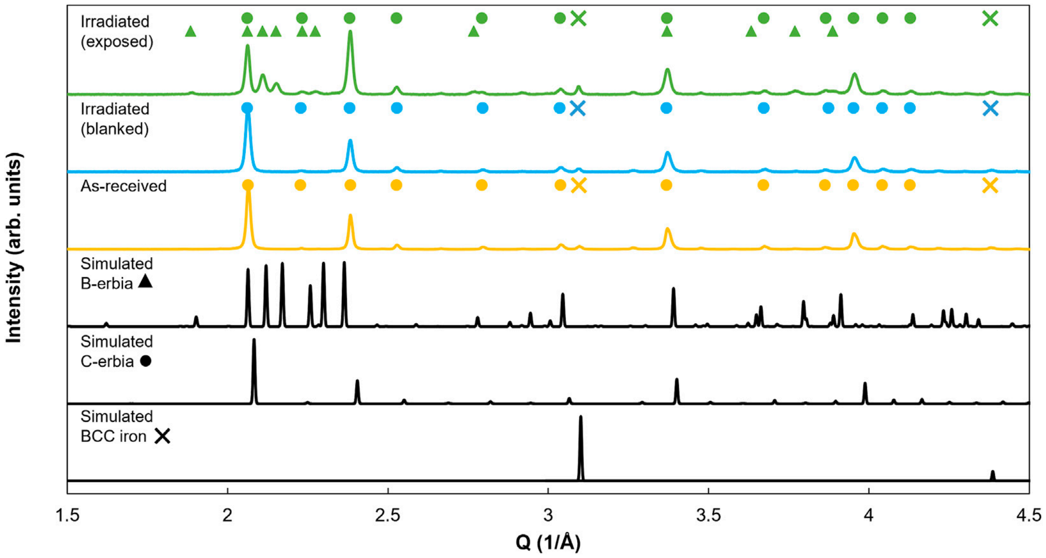

FIGURE 2
XRD patterns of erbium oxide coated Grade 91 steel in the as-deposited, ion irradiated (blanked) and ion irradiated (exposed) state. Simulated patterns for BCC iron, cubic C-erbia and monoclinic B-erbia are included for reference. All patterns have been normalized to the highest peak intensity.

has a coefficient of thermal expansion (CTE) of 6.5 × 10^{-6} K^{-1} (Liu et al., 2010) whereas Grade 91 steel has a CTE of ~13 × 10^{-6} K^{-1} (Norajitra, 2014). This difference in CTE caused the coating to be put under an in-plane compressive stress during cooling from deposition temperature to room temperature. This set up out-of-plane tensile strains, as a result of Poisson's ratio, in the as-deposited coating.

In additional to the thermal strain caused by the difference in CTE between the coating and the steel, microstrains are present within the coating grains. Microstrain within the coatings manifest as the broadening of peaks in the XRD spectrum. However, change in crystallite size can also result in peak broadening. Williamson and Hall (Williamson and Hall, 1953) identified that the microstrain (ε) and crystallite size (L) contributions to peak broadening vary differently as a function of the diffraction half angle, θ, as described by Eq. 1. This enables the microstrain contribution to be extracted.

$$\beta = K_{strain}\varepsilon \tan\theta + \frac{K_{size}\lambda}{L \, Cos\,\theta} \tag{1}$$

where β is the FWHM in radians of the peak at diffraction angle, 2θ, K_{size} is a shape factor set to 0.94 (Pang et al., 2009) and K_{strain} is set to 4 for isotropic growth (Pang et al., 2009).

To obtain β, the XRD spectra were fitted using split pseudo-voigt function with B-spline background fit, using the Rigaku SmartLab Studio II software. For each sample, by plotting βCosθ against 4Sinθ for the peaks of each phase, the microstrain can be extracted from the gradient of the plot, as seen in Figure 3. Peak prominence was used as a metric to determine which peaks should be included in the Williamson-Hall plots; all peaks with a value of prominence greater than 0.035 (for normalized

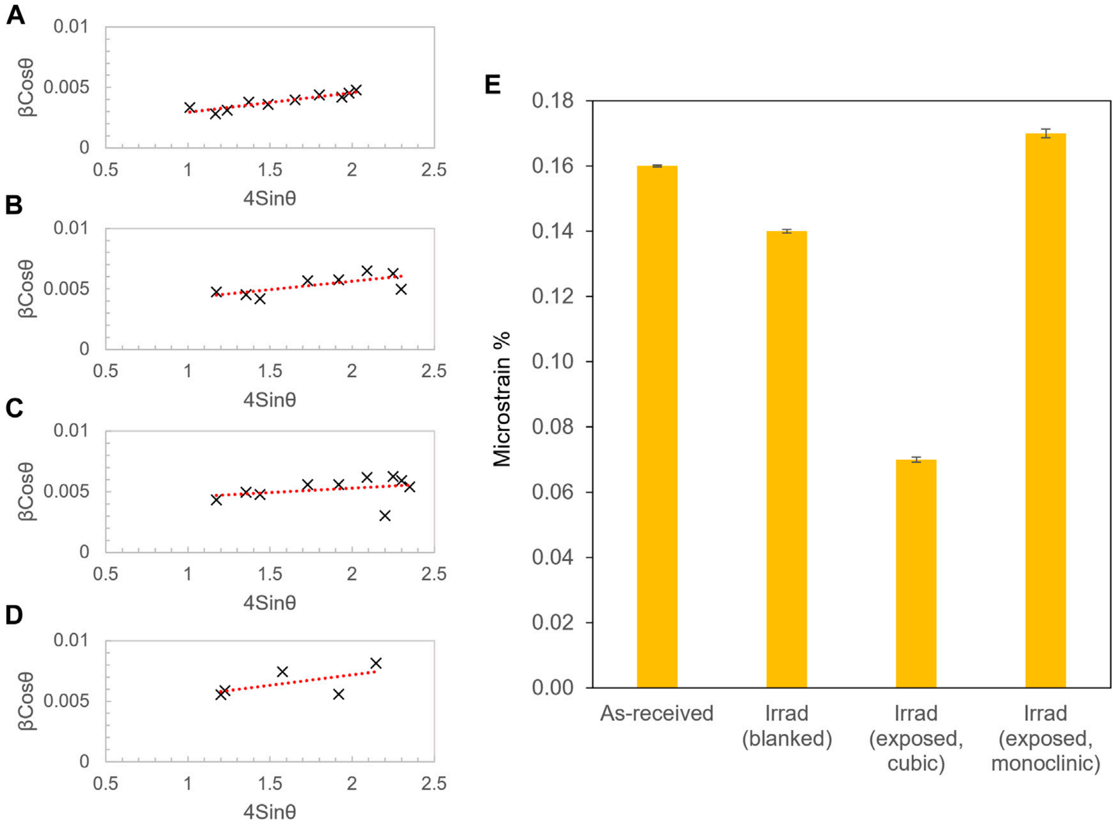

FIGURE 3
Williamson Hall (W-H) plots for **(A)** as-deposited, **(B)** ion irradiated (blanked), **(C)** ion irradiated (exposed, cubic erbia) and **(D)** ion irradiated (exposed, monoclinic erbia) erbia coated samples. **(E)** displays the microstrain extracted from each of the W-H plots.

spectra) were included. A least squares fit was used to determine the gradient, and the error bars plotted on the microstrain values represent the standard deviation associated with the gradient of the fit.

It can be seen from Figure 3E that the microstrain was reduced in the blanked region of the irradiated sample compared to the as-deposited sample. This is likely to be a result of thermal annealing of the residual stresses through reduction of defect density, especially given that the ion irradiations were conducted at temperatures close the deposition temperature of the coatings (T_{irrad} = 550°C vs. T_{cvd} ~650°C) over much longer time periods (53 h vs. ~1–2 h). The microstrain in the cubic phase of the irradiated (exposed) sample was further reduced compared to the blanked sample. By contrast, the microstrain in the monoclinic phase of the irradiated (exposed) sample was much higher. Since microstrain results from the local lattice distortions caused by defects, Figure 3E suggests that the monoclinic phase formed in the irradiated (exposed) sample is highly defective, while the cubic phase that remains has a much lower defect density. The defects present in the monoclinic phase are likely to be a combination of irradiation induced defects and the increase in defect density that results from the ~9% volume contraction associated with the cubic-to-monoclinic transformation.

The microstructural changes that occur in the irradiated (blanked) and irradiated (exposed) coatings can be directly observed in the cross-sectional TEM images in Figure 4. The as-deposited coating seen in Figure 4A, B is crack-free and has a fine columnar microstructure typical of CVD coatings. The surface roughness of the substrate can be seen to affect the coating growth and morphology. For example, the arrows on Figure 4B indicate roughness on the steel substrate that has nucleated regions of coating growth, which have subsequently impinged on each other as they have grown. This often leads to the formation of columnar pores, as demonstrated by the white lines emanating from the substrate surface at consecutive points along the coating. The cross-sectional TEM reveals how the substrate surface roughness gives rise to the nodular coating morphology observed in Figure 1.

The microstructure of the irradiated (blanked) sample in Figure 4C, D was the result of thermal annealing of the as-deposited structure. The grains were still columnar in shape. While it was not possible to quantitatively analyse the grain size in these micrographs, visual inspection shows that the grain size was larger in the irradiated (blanked) sample than the as-deposited sample. This observed grain growth provides confirmation of the occurrence of thermal annealing effects and their contribution to the decrease in microstrain in the irradiated (blanked) sample.

The equiaxed grain structure of the irradiated (exposed) sample in Figures 4E, F was markedly different to the columnar grain structure of the as-deposited and irradiated (blanked) coatings. A combination of the cubic-to-monoclinic phase transformation and annealing/grain growth of the remaining cubic phase has resulted in this microstructure.

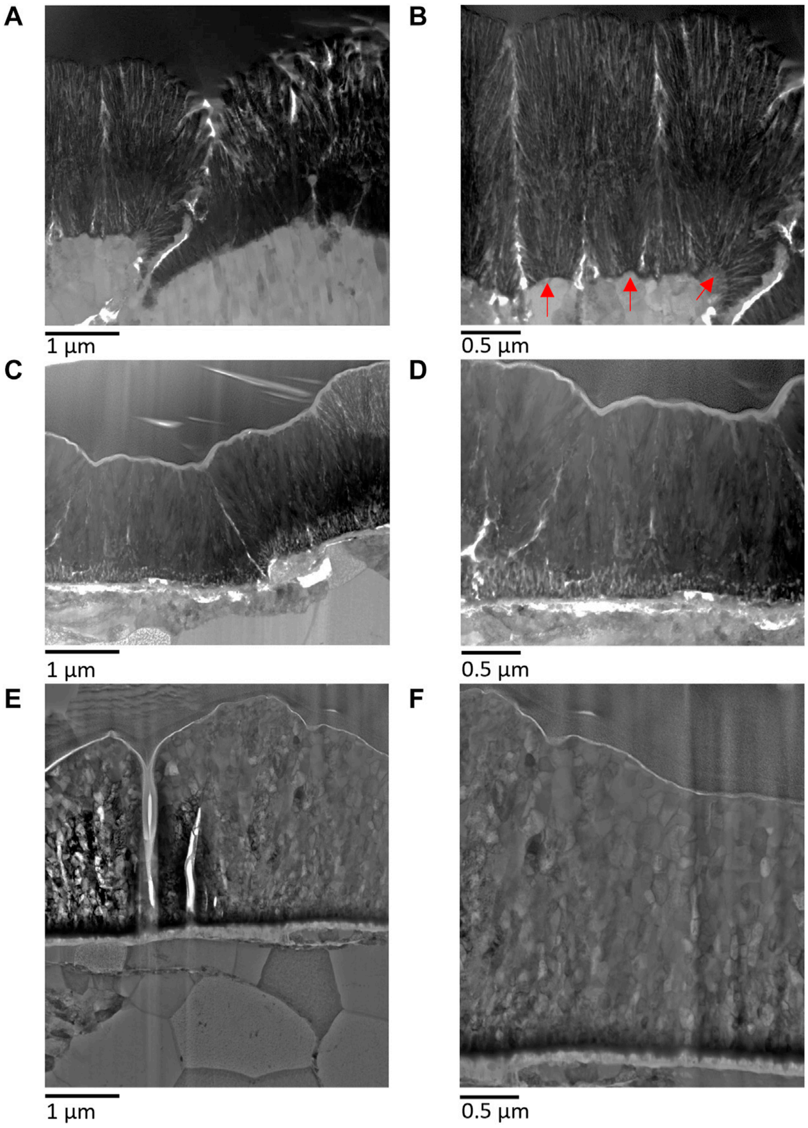

FIGURE 4
Cross sectional TEM images of the erbium oxide coated Grade 91 steel in the **(A, B)** as-deposited, **(C, D)** ion irradiated (blanked) and **(E, F)** ion irradiated (exposed) state.

The microstructures in Figure 4 also reveal changes at the coating-substrate interface, which warrant further investigation. However, this is not the focus of this study and will be reported on in a future publication.

Discussion

The out-of-plane tensile lattice strains measured using XRD have been caused by in-plane thermal stresses created in the coating during manufacture. It is important to control the stress state of the coating since it can dictate the phases formed. For example, presence of a compressive stress during coating growth has been reported to favor monoclinic erbia over cubic erbia (Adelhelm et al., 2009), since the monoclinic phase can be formed at high pressure (Guo et al., 2007). Use of interlayers is currently being explored by the authors to reduce the difference in CTE between the coating and substrate, thus reducing the thermal stress generated in the coating upon cooling from the deposition temperature. Coating application method can also be controlled to tailor the stress state of the coating, thus influencing the coating microstructure and performance (Adelhelm et al., 2009).

The XRD data alone is insufficient to determine that the monoclinic erbia phase is only formed in the irradiated (exposed) sample, due to overlapping cubic and monoclinic erbia peaks and the phase fraction detection limit of the XRD instrument. However, when the XRD data from Figure 2 is taken in combination with the microstructural information from Figure 4, the change from columnar to equiaxed microstructure that occurs only after ion irradiation supports the idea that the phase change is induced by ion irradiation at 550°C, for a damage level of 20–30 dpa. Tang et al. (Tang et al., 2006) observed a cubic-to-monoclinic transformation in erbium oxide under 300 keV Kr++ ion irradiation at cryogenic temperature (−153°C) when the damage exceeded ~15 dpa, and proposed that the phase transformation resulted from a combination of intracascade transformation and damage accumulation. The higher irradiation temperature of 550°C in this study means that the erbia is in the defect cluster swelling regime between Stage I and III recovery, whereas in the study by Tang et al. (Tang et al., 2006) the sample was at cryogenic temperature which is close to the onset of stage I recovery (Zinkle and Snead, 2014). A greater level of defect recovery is occurring at 550°C compared to −153°C, due to a greater number of mobile interstitials. This may reduce the levels of damage accumulation contributing to the phase change in this study compared to the study by Tang et al. (2006).

A previous study (Yan et al., 2019) on the thermally induced cubic-to-monoclinic phase transformation in erbia coatings reports that there is a competition between grain growth and phase transformation. For example, in the case where groups of grains of the cubic phase exist, the energy barrier for phase transformation to the monoclinic phase is higher than the energy barrier for grain growth. In the irradiated (blanked) sample, grain growth occurs in preference to phase transformation whereas in the irradiated (exposed) sample, phase transformation is observed. It is proposed that ion irradiation damage combined with temperature lowers the energy barrier for the cubic-to-monoclinic phase transformation. Further work is needed to understand the role of irradiation temperature in the cubic-to-monoclinic phase transformation of erbium oxide.

This study has shown that some of the cubic erbium oxide phase transforms to the monoclinic phase under ion irradiation at 550°C, for a damage level of 20–30 dpa, meaning that cubic erbium oxide is not stable under these conditions. The monoclinic erbia phase has previously been shown to be more stable under ion irradiation than the cubic phase (Tang et al., 2006). However, the permeation reduction factor of monoclinic erbia is reported to be an order of magnitude lower than that of cubic erbia (Brendel et al., 2011). Furthermore, this study suggests that monoclinic erbia transformed from the cubic phase has a high defect density, which is likely to cause an undesirable increase in tritium retention, with defects potentially acting as trap sites in the coating. The findings of this work may have implications on the use of erbium oxide as a tritium barrier in fusion environments. However, further investigations are needed to understand the permeation performance of as-grown monoclinic erbia compared to cubic to understand whether a compromise can be reached between improved irradiation resistance and acceptable reduction in tritium permeation with minimal tritium trapping.

Data availability statement

The data presented in the study are publicly available. The data can be found here: https://doi.org/10.14468/we5q-sm15.

Author contributions

HG: Writing–original draft, Writing–review and editing. GZ: Writing–review and editing. JW-Z: Writing–review and editing.

Funding

The author(s) declare financial support was received for the research, authorship, and/or publication of this article. HG, GZ and JW-Z acknowledge funding from EPSRC grant EP/W006839/1. The research used UKAEA's Materials Research Facility, which has been funded by and is part of the UK's National Nuclear User Facility and Henry Royce Institute for Advanced Materials.

Acknowledgments

We acknowledge the support of The University of Manchester's Dalton Cumbrian Facility (DCF), a partner in the National Nuclear User Facility, the EPSRC United Kingdom National Ion Beam Centre and the Henry Royce Institute. We recognize Dr. Samir de Moraes Shubeita, Dr. Andy Smith, Dr. Jack Haley, Dr. Max Rigby Bell for their assistance during the ion irradiation experiment. The authors thank Dr. Stuart Robertson for carrying out the TEM sample preparation and imaging at Loughborough Materials Characterisation Centre.

Conflict of interest

The authors declare that the research was conducted in the absence of any commercial or financial relationships that could be construed as a potential conflict of interest.

Publisher's note

References

Adelhelm, C., Pickert, T., Balden, M., Rasinski, M., Plocinski, T., Ziebert, C., et al. (2009). Monoclinic B-phase erbium sesquioxide (Er2O3) thin films by filtered cathodic arc deposition. *Scr. Mater.* 61 (8), 789–792. doi:10.1016/j.scriptamat.2009.06.031

Brendel, A., Adelhelm, C., Werkstetter, M., Pickert, T., Ertl, K., Balden, M., et al. (2011). "Phase formation of Erbia coatings on EUROFER 97, phase stability and deuterium permeability," in Proceedings of the 13th International Workshop on Plasma-Facing Materials and Components for Fusion Applications and 1st International Conference on Fusion Energy Materials Science, Germany, September 2011.

Chikada, T., Suzuki, A., Adelhelm, C., Terai, T., and Muroga, T. (2011). Surface behaviour in deuterium permeation through erbium oxide coatings. *Nucl. Fusion* 51 (6), 063023. doi:10.1088/0029-5515/51/6/063023

Dolabella, S., Borzì, A., Dommann, A., and Neels, A. (2022). Lattice strain and defects analysis in nanostructured semiconductor materials and devices by high-resolution X-ray diffraction: theoretical and practical aspects. *Small Methods* 6 (Issue 2), e2100932. doi:10.1002/smtd.202100932

Federici, G., Boccaccini, L., Cismondi, F., Gasparotto, M., Poitevin, Y., and Ricapito, I. (2019). An overview of the EU breeding blanket design strategy as an integral part of the DEMO design effort. *Fusion Eng. Des.* 141, 30–42. doi:10.1016/J.FUSENGDES.2019.01.141

Guo, Q., Zhao, Y., Jiang, C., Mao, W. L., Wang, Z., Zhang, J., et al. (2007). Pressure-induced cubic to monoclinic phase transformation in erbium sesquioxide Er2O3. *Inorg. Chem.* 46 (15), 6164–6169. doi:10.1021/ic070154g

Jain, A., Ong, S. P., Hautier, G., Chen, W., Richards, W. D., Dacek, S., et al. (2013). Commentary: the materials project: a materials genome approach to accelerating materials innovation. *Am. Inst. Phys. Inc* 1 (Issue 1). doi:10.1063/1.4812323

Li, X., Wu, P., Qiu, H., Chen, S., and Song, B. (2012). Crystallization behavior and mechanical properties of erbium oxide coatings fabricated by pulsed magnetron sputtering. *Thin Solid Films*, 520(6), 2316–2320. doi:10.1016/j.tsf.2011.09.053

Liu, S., Ju, X., Xin, Y., Qiu, J., Li, T., and Cao, J. L. (2010). Investigation of coating CLAM steel substrates with erbium oxide by a magnetron sputtering method. *Fusion Eng. Des.* 85 (7–9), 1401–1405. doi:10.1016/j.fusengdes.2010.03.059

Maniammal, K., Madhu, G., and Biju, V. (2017). X-ray diffraction line profile analysis of nanostructured nickel oxide: shape factor and convolution of crystallite size and microstrain contributions. *Phys. E Low-Dimensional Syst. Nanostructures* 85, 214–222. doi:10.1016/j.physe.2016.08.035

Mao, W., Wilde, M., Chikada, T., Fukutani, K., Matsuzaki, H., and Terai, T. (2020). Hydrogen isotope role in the crystal orientation change of erbium oxide coatings. *J. Nucl. Mater.* 528, 151871. doi:10.1016/j.jnucmat.2019.151871

Nemanič, V. (2019). Hydrogen permeation barriers: basic requirements, materials selection, deposition methods, and quality evaluation. *Nucl. Mater. Energy* 19, 451–457. doi:10.1016/j.nme.2019.04.001

Norajitra, P. (2014). *Development for a future fusion power plant*. Deutschland: KIT Scientific Publishing.

Pang, X., Gao, K., Luo, F., Emirov, Y., Levin, A. A., and Volinsky, A. A. (2009). Investigation of microstructure and mechanical properties of multi-layer Cr/Cr2O3 coatings. *Thin Solid Films* 517 (6), 1922–1927. doi:10.1016/J.TSF.2008.10.026

Pint, B. A., Devan, J. H., and Distefano, J. R. (2002). Temperature limits on the compatibility of insulating ceramics in lithium. *J. Nucl. Mater.*, 307–311. doi:10.1016/S0022-3115(02)01224-2

Tang, M., Lu, P., Valdez, J. A., and Sickafus, K. E. (2006). Ion-irradiation-induced phase transformation in rare earth sesquioxides (Dy 2O 3, Er 2O 3, Lu 2O 3). *J. Appl. Phys.* 99 (6). doi:10.1063/1.2184433

Ushakov, S. V., Hayun, S., Gong, W., and Navrotsky, A. (2020). Thermal analysis of high entropy rare earth oxides. *Materials* 13 (14), 3141. doi:10.3390/ma13143141

Williamson, G. K., and Hall, W. H. (1953). X-ray line broadening from filed aluminium and wolfram. *Acta Metall.* 1 (1), 22–31. doi:10.1016/0001-6160(53)90006-6

Yan, D., Wu, P., Zhang, Y., Zhang, S., Yang, J., Li, Y., et al. (2019). Effect of Er interlayer on microstructure, composition, electrical and mechanical properties of erbium oxide coating on steel. *Appl. Surf. Sci.* 498, 143750. doi:10.1016/j.apsusc.2019.143750

Ziegler, J. F., and Biersack, J. P. (1985). “The stopping and range of ions in matter,” in *Treatise on heavy-ion science* (Berlun, Germany: Springer), 93–129.

Zinkevich, M. (2007). Thermodynamics of rare earth sesquioxides. *Prog. Mater. Sci.* 52 (4), 597–647. doi:10.1016/j.pmatsci.2006.09.002

Zinkle, S. J., and Snead, L. L. (2014). Designing radiation resistance in materials for fusion energy. *Annu. Rev. Mater. Res.* 44, 241–267. doi:10.1146/annurev-matsci-070813-113627

frontiers | Frontiers in Nuclear Engineering

TYPE Review
PUBLISHED 07 February 2024
DOI 10.3389/fnuen.2024.1339222

Check for updates

OPEN ACCESS

EDITED BY
Anne Campbell,
Oak Ridge National Laboratory (DOE),
United States

REVIEWED BY
Jacob G. Fantidis,
International Hellenic University, Greece
Karim Ahmed,
Texas A and M University, United States
Stuart Maloy,
Pacific Northwest National Laboratory (DOE),
United States

*CORRESPONDENCE
Susan Ortner,
✉ susan.r.ortner@uknnl.com

RECEIVED 15 November 2023
ACCEPTED 08 January 2024
PUBLISHED 07 February 2024

CITATION
Ortner S, Styman P and Long E (2024), The effects of flux on the radiation-induced embrittlement of reactor pressure vessel steels: review of current understanding and application to high fluences.
Front. Nucl. Eng. 3:1339222.
doi: 10.3389/fnuen.2024.1339222

The effects of flux on the radiation-induced embrittlement of reactor pressure vessel steels: review of current understanding and application to high fluences

Susan Ortner[1]*, Paul Styman[1] and Elliot Long[2]

[1]National Nuclear Laboratory, D5 Culham Science Centre, Abingdon, United Kingdom, [2]Materials Reliability Program (MRP), Electric Power Research Institute, Palo Alto, CA, United States

It is necessary to quantify the effects of flux on reactor pressure vessel steel embrittlement under neutron irradiation, if surveillance or high-flux test reactor data is used to predict vessel embrittlement occurring at lower fluxes. This is particularly important when considering embrittlement occurring during extended (60–80 years) operation for which there is no direct experience. Dedicated investigations are time-consuming and expensive even when only small flux-fluence ranges are investigated, so collating data from multiple campaigns is necessary to provide sufficient information to cover the wide range of fluxes required for vessel assessment in the long term. This paper collates and reviews such data. The review finds that flux dependences probably differ in sign and strength in different regimes (low flux and fluence, intermediate flux at low and high fluence, high flux at low and high fluence) with the regime limits affected by composition and temperature. The current understanding of diffusion processes and microstructural development are invaluable in interpreting the trends and limits. Many contradictory data sets were found, however, and not all contradictions could be dismissed as resulting from poor quality data. Suggestions are made for investigations to clarify the uncertainties. One wide-ranging model of flux effects, based on an extensive data set, is used to compare high-fluence data from different sources, to assess whether embrittlement rates accelerate after a high, threshold fluence. The model helps to identify experiments which investigated comparable flux-fluence-temperature regimes. The comparable data are split evenly between data sets supporting acceleration after a particular fluence and data sets contradicting it. The model identifies regimes in which further campaigns would clarify the causes of these contrasting observations.

KEYWORDS

flux, embrittlement, reactor pressure vessel, steel, radiation

1 Introduction

Extrapolating from currently-available data to predict reactor pressure vessel (RPV) condition during extended reactor lifetimes is viable only if the correct allowance is made for the dependence of RPV steel embrittlement on neutron flux. The aim of this review is, therefore, to collate and interpret the available data illustrating the effects of flux on steel embrittlement, in support of predicting RPV condition assessment out to 60–80 years of operation. Mention will be made of modelling in support of data interpretation, but the focus of the review is on experimental data.

Although investigations into the effects of flux on embrittlement have been made over many decades, uncertainties remain, and these will be highlighted within the review to show where further work may help to resolve uncertainties and ambiguities. The uncertainties exist because the neutron fluxes relevant to RPV condition assessment cover an extremely wide range and the effect of flux may well vary within this range. For Boiling Water Reactors (BWRs), the neutron flux at the beltline inner wall is of the order 10^8–10^9 n.cm^{-2}s^{-1}[1], while for Pressurized Water Reactors (PWRs) it is around 10^{10}–10^{11} n.cm^{-2}s^{-1}. Through-wall attenuation reduces this by a factor of about 20 for PWRs, less for BWRs with their thinner walls. Information on changes in mechanical properties and microstructure under neutron irradiation comes primarily from surveillance programs and MTR campaigns. Surveillance specimens are generally irradiated at rates up to ×5 faster than the beltline inner wall, while MTR irradiations are, typically, at rates ×10 to $\times 10^4$ more rapid than this. Understanding the relevance of MTR and surveillance data to degradation processes occurring within the RPV wall, thus requires trends in degradation with flux to be identified over many orders of magnitude.

Uncertainties and ambiguities also exist because investigating flux effects presents significant experimental challenges: achieving a meaningful fluence range over even one order of magnitude in flux requires a multiple-year campaign. Most campaigns must examine a small fluence range or compare a trend curve derived at one flux with individual measurements acquired at another, e.g., a trend derived from MTR data is compared with surveillance measurements on a similar material, or MTR measurements are compared with an embrittlement trend curve derived from analysis of a surveillance data base. Some, more extensive campaigns proceed in a stepwise fashion, with data acquired at pairs of low fluxes compared at low fluences and higher flux data compared over increasingly higher fluence ranges. The degree of overlap between steps is balanced between limiting the size of the campaign and limiting the range of fluxes examined. Comparing the results of different campaigns is vital to achieve a broad view and extract trends from scattered data. This paper provides an extensive review, collating data from multiple sources and both large and small campaigns.

The practical constraints on experimental investigations are compounded by the existence of multiple microstructural features capable of contributing to embrittlement and the non-monotonic relation between flux and the rate at which a given feature develops. A mechanistic framework derived from data interpretation and modelling is necessary to define flux/fluence/temperature/composition regimes within which particular processes may dominate and, hence, consistent trends may be observed. This review therefore separates the data based on the different microstructural components leading to embrittlement and the different flux-temperature regimes affecting the mobile point defect concentration or diffusion rate. The combination of the range of data sources and the organisation of the data within the review is intended to provide the clearest possible view of RPV steel behaviour.

1.1 Data organisation within the review

The specific definitions of the components used in this review are:

- Matrix defects or features (MDs or MFs are defined here as individual point defects and clusters of point defects and solute atoms in which the point defect concentration dominates. This includes vacancy or self-interstitial atom clusters, voids and dislocation loops).
- Solute clusters (SCs are clusters of point defects and solute atoms in which the solute content dominates, and which do not correspond to a phase with a lattice structure differing from that of the solid solution).
- Precipitates (These are solute dominated features which are energetically favoured based on the equilibrium or metastable phase diagram for the bulk steel composition or the composition in a local solute-enriched region of the irradiated steel. The equilibrium precipitates significant in MnMoNi RPV steels involve Cu and combinations of Ni, Si and Mn. Depending on the analysis technique used it is not easy to determine whether a solute-rich feature is a SC or a precipitate).
- Grain boundary segregants (Of greatest interest here are the desegregation of C and the segregation of P).

This leads to the division of the data into sub-sets based on steel composition and fluence: bulk Cu levels high enough to induce precipitation (high Cu); local or bulk Ni levels high enough to induce precipitation (high fluence or high Ni); conditions without identifiable precipitates (low Cu, low-moderate Ni and low-moderate fluence).

The different flux-temperature regimes considered here are those proposed originally by Sizmann (1978). The precise locations of the different regimes (in terms of flux, temperature, fluence and composition) are not known, and other regimes have been proposed. Nonetheless, Sizman's description provides a useful starting point, and one aim of the review is to determine whether sufficient data exist to locate the boundaries between the different regimes. Quantitative flux dependences in the different regimes were derived in Sizmann (1978) and are reported below for illustrative purposes, but have not been definitively confirmed.

- The thermal regime (At high temperatures and low fluxes, the radiation-induced defect concentration does not differ markedly from the equilibrium vacancy concentration, so thermal processes dominate. In this *thermal regime*, the diffusion rate is flux-independent, so any diffusion-controlled process is simply time-dependent. Expressing processes in terms of fluence then requires an inverse dependence on flux (damage proportional to $1/\phi$, where ϕ = flux).

---

[1] Note that all fluxes and fluences are given in units of neutrons with energies >1 MeV unless otherwise stated.

- The fixed sink regime (With reducing temperatures and increasing dose rates, the radiation-induced defects begin to dominate. At intermediate temperatures, the point defects remain capable of rapid diffusion so, at low-to-moderate dose rates, they are likely to encounter a microstructural feature such as a dislocation or interface before annihilating with another point defect. In this regime, therefore, defects annihilate primarily at such fixed sinks. Attractions between point defects and the main solutes in RPV steels mean that the flux of defects drags solutes to or away from the sinks. In the *fixed sink regime*, the diffusion coefficient is proportional to ϕ^1, so the mean diffusion distance (a good correlate for the progress of a diffusion-controlled process) is independent of flux).
- The matrix recombination regime (At higher dose rates and lower temperatures still, the diffusion rates decrease, and the point defect concentrations rise until point defects can interact with each other after only short diffusion distances. This is the *recombination-dominated regime* (or *matrix recombination regime*). In this regime, solutes do not move over large distances via point defect interactions. In the matrix recombination regime, the diffusion coefficient is proportional to $\surd\phi$, so the progress of a microstructural change versus fluence is proportional to $1/\surd\phi$, becoming slower, with respect to fluence, at higher fluxes).

Around half the point defects produced initially will cluster within the cascade (i.e., at times < 50 ps) (Stoller, 2020), and cluster numbers increase with increasing dose (Stoller et al., 2003; Soneda, 2007). These clusters become progressively more important as sinks with increasing dose, reducing the rate of increase of mobile point defects with increasing flux and effectively expanding the fixed sink regime as the fluence increases. (Stoller et al., 2003; Odette et al., 2005; Soneda, 2007; Williams et al., 2010; Becquart and Wirth, 2020; Castin et al., 2020; Stoller, 2020).

Based on these descriptions, it is worth further dividing the data into sub-sets based on low, medium and high fluxes. With any choice of specific flux ranges, individual campaigns will often cover more than one range, so overlapping ranges have been chosen: low = surveillance ($<\sim 10^{11}$ n.cm^{-2}s^{-1}), medium = MTR ($\sim 10^{10}$–10^{12} n.cm^{-2}s^{-1}), high = accelerated MTR ($>\sim 5 \times 10^{11}$ n.cm^{-2}s^{-1}).

2 Review of data on flux effects in low-Cu steels

In steels containing low levels of Cu, the hardening and embrittlement caused by irradiation to low-moderate fluences will be dominated by the formation of matrix defects. If point defect clustering is dominated by processes occurring in cascades, then matrix damage is expected to be independent of flux; if, however, longer-range diffusion processes cause significant changes to the post-cascade structures, then flux effects should be observed. Distinguishing between these alternatives is difficult because hardening increments in low-Cu steels tend to be small. Despite this difficulty, the low-Cu steels are considered first as the reduced number of contributors to embrittlement simplify the interpretation of the available data.

2.1 Low fluxes (low-moderate fluences)

Information concerning embrittlement at low fluxes comes from surveillance programs. These are not designed to provide single-variable comparisons, so extracting the flux contribution is hampered by effects of concurrently changing variables: there is a strong correlation between flux and fluence in any surveillance database; when the low-flux data are provided by BWR surveillance schemes and the high flux data by PWR schemes any other differences between BWRs and PWRs (chiefly operating temperature) correlate with flux. Nonetheless, it is worth noting that,

- Of the analyses of the US surveillance database (in which around one sixth of the data come from BWRs), most have not derived a flux-dependence for the matrix damage term but
  - o The 1998 analysis by Eason et al. (1998) contains a flux dependence in the matrix damage (Cu-independent) term,
  - o The 2001 analysis by Server et al. (2001) contains a flux dependence for matrix damage,
  - o The 2007 analysis by Eason et al. contains a flux dependence only below 4.4×10^{10} n.cm^{-2}s^{-1} (Eason et al., 2007), although it is not very strongly supported by the BWR data (EPRI, 2009).
- The French reactor fleet contains only PWRs and the French embrittlement trend curves (FIS and FIM) contain no flux dependence in the matrix damage term.
- The Belgian embrittlement trend curve (RADAMO) contains no flux term (Chaouadi, 2005).
- The embrittlement trend curve (ETC) in the ASTM E900-15 standard (ASTM, 2015) is derived from a database dominated by US data but containing a significant amount of data from other countries. Around one sixth of the data comes from BWRs and the ETC does not contain a flux term in the Cu-independent term.
- The Japanese JEAC4201 ETCs are based on surveillance data derived from a fleet which contains similar numbers of BWRs and PWRs, and the ETCs include a flux term for matrix damage (Tomimatsu et al., 1994; Soneda and Nomoto, 2008; Hashimoto et al., 2021).

On this basis, it is plausible that the thermal regime appears within the range of BWR surveillance data (at fluxes of the order 10^{10} n.cm^{-2}s^{-1}) with the fixed sink regime at higher fluxes, and that this affects matrix damage development.

It should be noted, however, that the temperature dependence in the Japanese ETCs tends to be weaker than in other ETCs, so some conflating of flux and temperature effects may be occurring. A dedicated analysis of international surveillance data with the aim of identifying whether a low-flux regime of flux-dependence is appearing would be useful.

---

2 Reprinted from J. Nuclear Mater., Vol 418, Chaouadi, R.; Gerard, R., Neutron flux and annealing effects on irradiation hardening of RPV materials, Pages 137–142, Copyright (2011), with permission from Elsevier.

2.2 Intermediate fluxes (low-moderate fluences)

Experimental investigations at higher fluxes are dominated by the large campaigns led by the UCSB group of G. R. Odette. Few other programs have been as extensive or as well-controlled, to minimize ambiguity from concurrently changing variables. The results from the UCSB campaigns will, therefore, be presented first, and data from other campaigns (whether conducted earlier or later) will be presented in the context of the UCSB work.

2.2.1 UCSB campaigns

In their IVAR (Irradiation Variables) program, the UCSB group investigated a flux range which overlaps with the range of PWR surveillance fluxes but reaches to higher fluxes (nominally 8×10^{10}, 3×10^{11} and 8×10^{11} n.cm^{-2}s^{-1}). Steels with a wide range of compositions (Cu = 0–0.43, Ni = 0–1.7, Mn = 0–1.7, P = 0.002–0.035 wt%) were irradiated at a range of temperatures (270, 290, and 310°C) to fluences up to 4×10^{18} n.cm^{-2} (low flux) – 3×10^{19} n.cm^{-2} (high flux). Portions of the data are reported and analyzed in multiple publications, but the full set is provided in association with (Eason et al., 2007), where the data trends are discussed in detail.

Of the ten low-Cu (<0.08 wt%), medium-Ni (<1 wt%) and two low-Cu, high-Ni (1.6–1.7 wt%) steels examined in the IVAR campaign, eight showed clear trends with flux in the residuals when the measured hardening was compared with a (flux-independent) trend curve developed for surveillance data by Eason et al. (2007) (four showed negligible trends; none showed a positive trend). This led Odette and co-workers to conclude that there was a small but consistent flux-dependence to stable matrix damage (SMD) in this flux/fluence/temperature range. They incorporated this into a flux-compensated "effective fluence" defined by:

$$Effective\ fluence = \varphi t_e = \varphi t \left(\frac{\varphi_r}{\varphi}\right)^p \tag{1}$$

Equation 1: Odette et al.'s definition of effective fluence
where ϕ_r = reference flux, here 3×10^{11} n.cm^{-2}s^{-1}
p = constant fitted to each composition (=0.42–0.47)

Note that this indicates that increasing the flux delays microstructural development to higher fluences, partly offsetting the advantage of using higher fluxes to identify high-fluence behaviour. An associated rate theory model interpreting this trend was presented in (Odette et al., 2005), but will not be assessed within this review, which is focused on the accumulation of support for particular trends.

2.2.2 Other campaigns

The flux-dependence in the IVAR data was confirmed by other authors and methods (Williams et al., 2010; Mathew et al., 2018). The flux dependence has, however, been difficult to reproduce in other data sets. In the most closely comparable campaign, Dohi et al. (2001) obtained both tensile and Charpy data from two different low-Cu, medium-Ni base metals after irradiation at 3 (tensile) or 4 (Charpy) different fluxes to 10^{18} n.cm^{-2} and after 2 and 3 fluxes at 10^{19} n.cm^{-2}. The fluxes at 10^{18} n.cm^{-2} overlap the IVAR range very closely, but the authors did not find any trend in their data within scatter. Other authors who examined low-Cu material within the IVAR range have fewer materials or measurements (Bourgoin et al., 2001; Wagner et al., 2016), so the absences of flux effects in their individual observations carry less weight. Nonetheless, the accumulation of campaigns in which the IVAR trend was not reproduced is a matter for concern, and confirmation from datasets from other sources would be desirable.

2.2.3 Implications

The immediate importance of the trend in matrix damage seen in the IVAR data was that, if continued to lower fluxes, it would cause higher-flux data to underestimate the hardening rate at lower fluxes. Artificial neural network analysis of IVAR and US LWR surveillance data (a set with very few data below 10^{10} n.cm^{-2}s^{-1}) (Mathew et al., 2018) used a consistent methodology to confirm that the flux dependence was indeed significant within the IVAR data set but not within the (PWR) surveillance set, suggesting that p (Eq. 1) drops to zero below about 10^{11} n.cm^{-2}s^{-1}. Comparing this outcome with the earlier assessment of surveillance data suggests that the fixed sink regime covers the range 10^{10}–10^{11} n.cm^{-2}s^{-1}, with the thermal regime probably intervening at lower fluxes.

Based on the combined observations, the PWR beltline inner wall can be described by surveillance data without a flux correction. Whether through-wall attenuation effects require a flux correction, and whether the state of the BWR beltline inner wall is correctly assessed with a flux-independent trend curve derived from predominantly PWR data, remain unclear from these low-Cu steel data. Given the magnitudes of the effects observed, however, differences between BWR surveillance samples and the BWR inner wall (a ×3 to ×5 change in flux) will be very small, even if one or both lie within the thermal regime.

2.3 High fluxes (low and high fluences)

2.3.1 UCSB and RADAMO campaigns

In the 1990s Odette and co-workers exposed A533B-type steels of multiple compositions at high fluxes 5×10^{11}–6×10^{13} n.cm^{-2}s^{-1}, in the University of Virginia and PLUTO MTRs (the UV-P campaign) (Odette et al., 1993; Mader, 1995). They found that hardening at a given fluence in 0.4 wt% Cu steels decreased with increasing flux while that in 0.11–0.16 wt% Cu steels increased. They interpreted this as indicating that two opposing flux dependences existed, one in MDs and the other in Cu-rich SCs. This MD contribution added increasingly to hardening at fluxes above 4×10^{12} n.cm^{-2}s^{-1}. Data (Mader, 1995) from steels with <~0.01 wt% Cu confirmed that the appropriate trend occurred when only matrix damage was present, as illustrated in Figure 1.

It is important to note that (1) the hardening increments shown are small (15–35 Vickers hardness points) and comparable with measurement uncertainty, even though great care was taken to minimize the uncertainties, and (2) the fluences involved are small.

---

3 Reprinted from Nuclear Engineering and Design., Vol 273, Kryukov, A.; Nanstad, R. K.; Brumovsky, M. Common comparison of the irradiation embrittlement of WWER/PWR reactor pressure vessel steels, Pages 175–180, Copyright (2014), with permission from Elsevier.

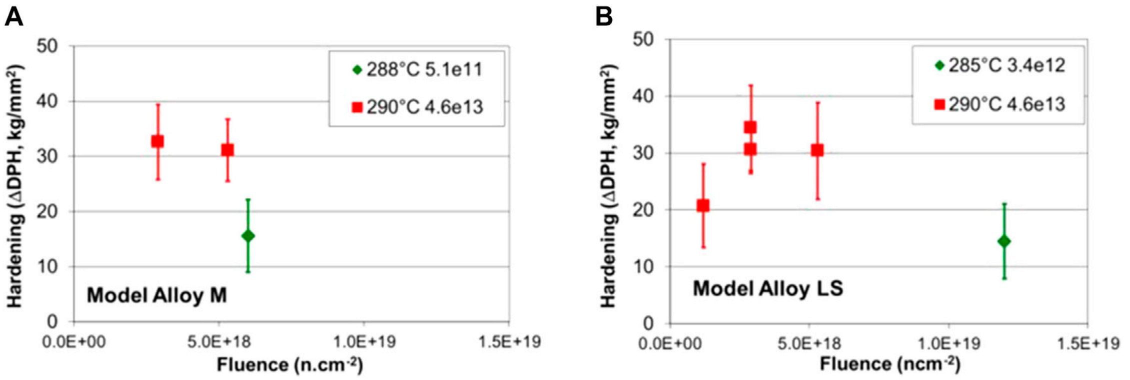

FIGURE 1
Effect of flux on hardening in UV-P campaign **(A)** 0.01Cu 0.6Ni Model Alloy M in temperature range 288°C–290°C **(B)** 0.005Cu 0.74Ni Model Alloy LS in temperature range 285°C–290°C [data from (Mader, 1995)].

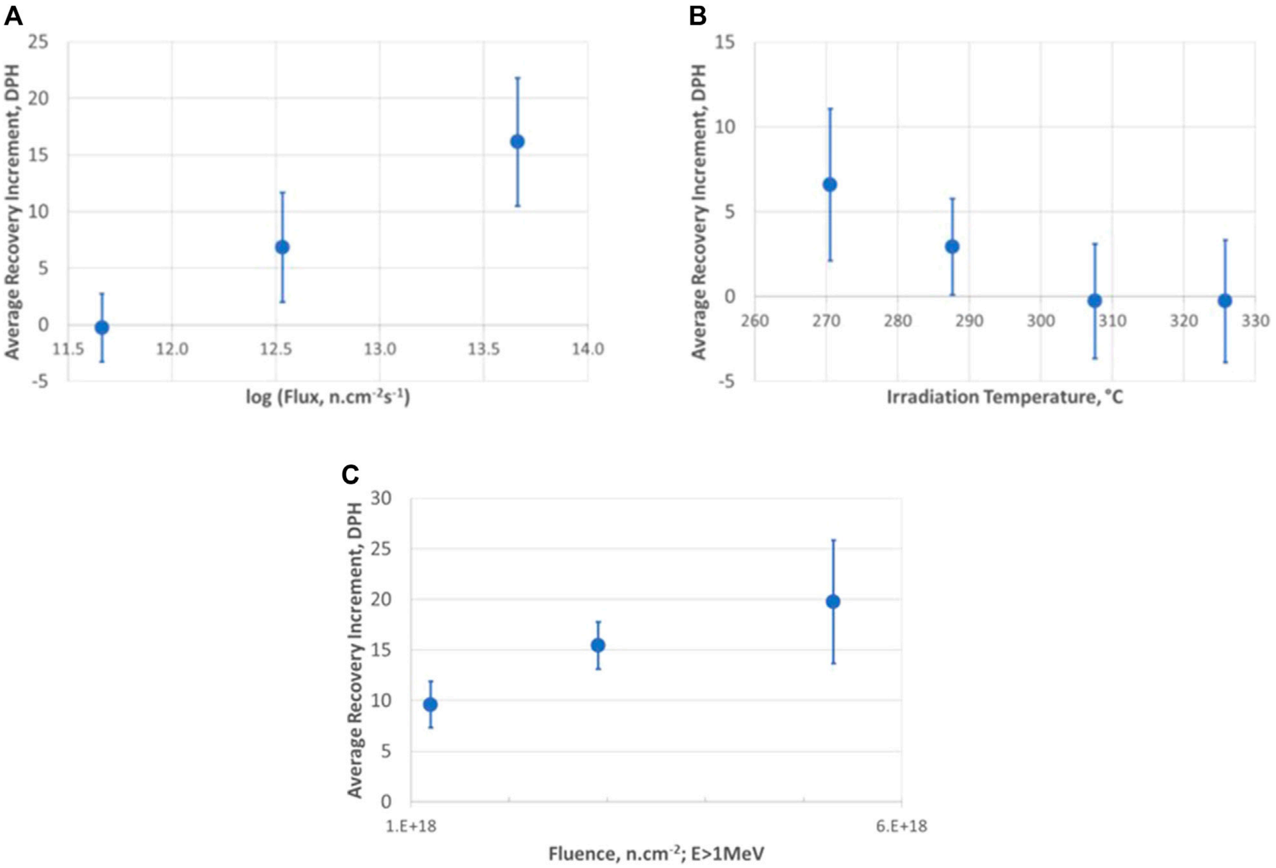

FIGURE 2
Hardness recovered during low temperature (150 h 290°C or 5 h 343°C) annealing of an RPV steel as a function of **(A)** flux (after irradiation to 6 × 10^{19}n.cm^{-2} at 290°C) **(B)** irradiation temperature (after irradiation to 10^{19}n.cm^{-2} at 4.5 × 10^{12}n.cm^{-2}s^{-1} **(C)** fluence (after irradiation at 290°C and 4.6 × 10^{13}n.cm^{-2}s^{-1}) (data from (Castin et al., 2011)).

Associated low-temperature post-irradiation annealing (PIA) indicated that measurable recovery occurred within 5 h 343°C after the higher-flux irradiations, as illustrated in Figure 1. The average recovery increments increase with increasing flux and fluence and decreasing temperature and are similar in magnitude to the additional high-flux hardening illustrated in Figure 1. Odette and co-workers interpreted this as showing that a population of matrix defects, unstable at the irradiation temperature ("Unstable Matrix Defects/Features", UMDs/UMFs) contributed increasingly to hardening at high fluxes. It should, however, be recognized that the PIA behavior could also have indicated an increasing contribution from matrix recombination with increasing flux. (In the fixed sink regime, vacancies and SIAs reach independent equilibria with the fixed sinks, so loss of hardening during PIA would reflect the contribution of only the unstable defects. In the matrix recombination regime, however, loss of unstable vacancy-type defects would involve annihilation with stable SIA defects and *vice versa*, so the loss of hardness during PIA would reflect the loss of both unstable and otherwise stable defects). In addition, the annealing increments displayed in Figure 2 appear to have been averaged over results from steels with Cu levels from 0–0.8 wt%, with the UMD contribution to hardening increasing with increasing Cu (Mader, 1995). This was originally considered to be justified as SANS indicated that the Cu-rich SCs were unaffected by the annealing treatment (Mader, 1995). In later APT analyses of low-temperature annealed steels, however, it appeared that a short annealing treatment does affect the SC population (Soneda, 2010), inducing softening. The average PIA increments in Figure 2 will, thus, be an upper limit to the UMD contribution to annealing, even as the PIA contribution itself is an upper limit to the defects' hardening contribution in low-Cu steels.

Overall, Odette and co-workers observed a consistent trend in the hardening and annealing of several Cu < 0.01 wt% steels in the UV-P campaign. The model they derived included flux dependences for both UMDs and SCs and reconciled the hardening and annealing behavior of multiple steels within this program. Nonetheless, these observations of UMD effects conflicted with the lack of a flux dependence seen in the tensile data in the extensive Belgian RADAMO database (Chaouadi, 2005; Castin et al., 2011; Chaouadi and Gerard, 2011; Chaouadi and Gerard, 2013).

The RADAMO database did not incorporate such a systematic variation in material compositions as the UCSB UV-P campaign but involved multiple steels with a range of compositions within RPV steel specifications. It was built up largely from irradiations in the BR2 MTR at 300°C and covered a similar flux range to the UV-P campaign, although the exposures were generally taken to higher fluences than in the UV-P campaign. The relatively high irradiation temperature would be predicted to reduce the UMD effect (Figure 2C), and there is some tendency for lower-fluence RADAMO data to have been acquired at lower fluxes. Given the small size and upper bound nature of the UMD increments shown in Figures 1, 2, this might be sufficient to account for the flux-independence seen in the RADAMO tensile data.

Another possible contributor to the contrasting observations made within the UCSB and RADAMO campaigns is the fluence range. The UV-P data were mostly acquired at $<10^{19}$ n.cm^{-2}, while the RADAMO data were mostly acquired in the range 0.5–10 × 10^{19} n.cm^{-2}. At the higher fluences, the presence of large numbers of stable matrix features (SMFs) might overwhelm the contribution of the UMDs.

In an effort to clarify the alternative views, Odette et al. irradiated one of the UCSB model steels (LG = 0Cu, 0.8Ni) in the BR2 reactor (Toyama et al., 2020). The hardening at fluences up to 2 × 10^{19} n.cm^{-2} was similar after the high-flux BR2 irradiations (1.4 × 10^{12} n.cm^{-2}s^{-1} or 10^{14} n.cm^{-2}s^{-1}) and IVAR campaigns (0.3 and 0.8 × 10^{12} n.cm^{-2}s^{-1}). The BR2 hardening, however, was almost entirely recovered during low-temperature annealing, while the IVAR samples showed no recovery. After 3.3 × 10^{19} n.cm^{-2}, the BR2 sample showed around 10Hv more hardening than the IVAR sample: the difference was recovered within PIA 5 h 343°C or during isochronal annealing in 20-min, 25°C-increments from 275°C–375°C. The UCSB group concluded that their BR2 campaign confirmed the existence of UMDs and their increasing contribution with increasing flux and fluence. Nonetheless, the difference in the fluence ranges over which UMD hardening increments were seen in the UV-P and IVAR-BR2 campaigns shows again the smallness of the systematic effect with respect to measurement uncertainties. Subsequent PIA of the RADAMO steels by SCK.CEN, found no reductions in hardness after low-temperature PIA of steels which the UCSB group would have predicted to show UMD annealing (Chaouadi and Gerard, 2013).

In their more recent, ATR campaigns (Odette et al., 2016), the UCSB group irradiated very low Cu steels in the range 10^{12}–10^{14} n.cm^{-2}s^{-1} to much higher fluences (from the mid-10^{19} to 10^{21} n.cm^{-2}). Solute clustering dominated by Mn, Ni and Si (possibly precipitation) was observed above 10^{20} n.cm^{-2} in a medium-Ni steel and at lower fluences in a high-Ni (1.6wt%) steel. Unlike in the UV-P and BR2 campaigns, the hardening after irradiation at 10^{14} n.cm^{-2}s^{-1} data in the ATR campaign was not evidently greater than that after 10^{11} and 10^{12} n.cm^{-2}s^{-1}, even at the lowest fluences shown (1-3 × 10^{19} n.cm^{-2}s^{-1} depending on the steel). If this is because the significance of a UMD component diminishes above about 10^{19} n.cm^{-2}, then this would reconcile the ATR and UV-P observations, but it does not clarify the BR2 observations.

At the high fluences above which Mn-Ni-Si clustering was seen, the UCSB group found that the hardening at different fluxes could, again, be made to converge via use of the effective fluence, though now with a smaller value of p (Eq. 1) than at the IVAR fluxes-fluences. The flux-dependence is weaker than in the IVAR data because of the larger number of sinks present at the high fluences of the ATR experiments.

In their most recent analysis of ATR2 data, Odette and co-workers (OWAY) have concluded that there is no net effect of flux in the range 6–14 × 10^{19} n.cm^{-2} and 3.7 × 10^{12}–10^{14} n.cm^{-2} (Nanstad et al., 2022). This is not immediately evident in the plots of (Odette et al., 2016). Possibly (i) the restriction in the flux-fluence range of the OWAY data makes any flux effect more difficult to extract from measurement uncertainty and/or (ii) the aspect of the OWAY analysis which postulates linear hardening versus log fluence in this fluence range affects the apparent contribution of flux.

Summarizing the various UCSB campaigns, the following trends in hardening in low-Cu steels were identified:

- Hardening decreases with increasing flux in the range 0.8–8 × 10^{11} n.cm^{-2}s^{-1} and 0.4–3 × 10^{19} n.cm^{-2} (SMF effect);
- Hardening increases with increasing flux in the range 0.4–46 × 10^{12} n.cm^{-2}s^{-1} and 1–8 × 10^{18} n.cm^{-2} (UMD effect);
- Hardening decreases with increasing flux in the range 10^{12}–10^{14} n.cm^{-2}s^{-1} and 0.5–12 × 10^{20} n.cm^{-2}, but less strongly than at lower fluxes (MNS effect at high fluences).

The UCSB campaigns thus predict that there are transitions in the direction of the flux effect around 10^{12} n.cm^{-2}s^{-1} at low fluences (SMF↔UMD) and around 5 × 10^{19} n.cm^{-2} at high fluxes (UMD↔MNS). In this context, it is possible that some of the RADAMO data may have been acquired over a fluence range between that dominated by UMDs (hardening increases with increasing flux) and that dominated by MNSs (hardening deceases with increasing flux). The contrasting PIA responses in the UCSB and RADAMO steels after BR2 irradiations, however, remain unexplained.

2.3.2 Other campaigns

The different flux dependences found by the UCSB group in each flux-fluence range examined make comparisons between UCSB and other data difficult. Few other campaigns compare hardening in low-Cu steels at different fluxes within only one of the flux-fluence ranges examined by the UCSB group, or to only one side of the transitions. Most studies tend to compare data from within or below the IVAR range with data from within the UV-P range (Petrequin, 1996; Xu et al., 2000; Langer et al., 2001; Yamamoto et al., 2001; Gerard et al., 2006; Hein and May, 2008; Soneda et al., 2008; Soneda et al., 2015; Wagner et al., 2016; Lindgren et al., 2017; Burke et al., 2003; Japan Nuclear Energy Safety Organisation, 2009; Soneda et al., 2009). Under these circumstances, it becomes impossible to distinguish between the presence of a changing flux dependence and the absence of any flux-dependence. In addition, the small sizes of the flux-dependent increments mean that large databases are required to identify the trends. Indeed, most of these groups interpret their data as showing no effect of flux.

A large database was investigated by Kirk and co-workers' analysis of the surveillance and MTR embrittlement data in the PLOTTER database [in (Kirk and Ferreno Blanco, 2022) and Appendix B of (Kirk and Erickson, 2021)]. The surveillance data had been used to derive the E900-15, ETC and were, in consequence, well-described by it without a flux-dependence in the low-Cu term. The MTR low-Cu data, however, showed a bias towards underprediction, interpretable as an increase in hardening with increasing flux. Such a bias would be consistent with the introduction of UMFs, but the fluence ranges involved are higher than that used in the UV-P campaign. In the relevant fluence range (between 10^{19} and 10^{20} n.cm^{-2}) the IVAR and ATR campaigns showed a decrease in hardening with increasing flux and the RADAMO campaign showed no effect of flux. One possible explanation for Kirk and co-workers' contrary observation is that it did not involve a focused, single-variable investigation, but a statistical analysis of data from multiple campaigns in multiple reactors/reactor locations. In some of the MTR irradiations within PLOTTER, the dpa levels associated with a particular fluence (E > 1 MeV) can vary by a factor of 2. The apparent flux effect in PLOTTER may, therefore, reflect the different dpa values in different campaigns. A dedicated analysis program would, however, be required to determine whether this is a significant contributory factor.

Another compilation of data was made by Williams and co-workers at Rolls-Royce (RR) in collaboration with UCSB. In the analysis of their own data on low-Ni and high-Ni submerged-arc welds (SAWs) Williams identified no effects of flux (Williams et al., 2001a; Williams et al., 2001b; Williams and Ellis, 2001). (See Figure 3.) They then added the IVAR data, US and French surveillance data, data from the IAEA Coordinated Research Program IAEA-CRP3, and data from Bettis Laboratory to their compilation, using dpa as the damage correlate to avoid the problem of differing neutron spectra. Considering only low-Cu (<0.075 wt%) materials irradiated at dose rates <=1.5 × 10^{-9} dpa/s (~10^{12} n.cm^{-2}s^{-1}), that is steels damaged by SMFs (Williams et al., 2010), they found hardening to decrease with increasing flux. Essentially, the trend in the IVAR data was supported (or at least not offset by) the additional data. No thermal regime was identified, consistent with previous analyses of the US and French surveillance databases.

Their overall analysis incorporated an effective fluence, $(\varphi t)_{\text{eff}} = Q(\varphi t)$: the flux and temperature dependences of Q are shown in Figure 4, (Williams et al., 2010). This describes a fixed sink (flux-independent) regime below 10^{-10}dpa/s at 320°C, decreasing with decreasing irradiation temperature, and a higher flux trend of decreasing hardening rates with increasing fluxes, intensified if UMDs exist.

Williams and co-workers used a combination of PIA (to isolate any UMD contribution), atom probe tomography (to isolate any Mn-Ni-Si clustering contribution), thermal ageing and modelling to assign increments to the different components and concluded that a UMD effect was introduced above 10^{12} n.cm^{-2}s^{-1} but saturated above 0.1 dpa (about 6 × 10^{19} n.cm^{-2}). A hardening increment due to Mn-Ni-Si-containing SCs (or precipitates) appeared above about 0.07 dpa (5 × 10^{19} n.cm^{-2}) in the high-Ni steels and increased with increasing dose. Since the UMDs could act as sinks for point defects, they were expected to reduce the rate at which SMFs and SCs develop. The presence of UMDs thus does not necessarily result in higher overall hardening at all fluences; under some conditions, it will merely redistribute a similar amount of hardening between different contributors.

The UMD contribution to hardening determined by Williams and co-workers is retained to a higher dose than the 10^{19} n.cm^{-2} limit which would have reconciled the UCSB UV-P and RADAMO data, but the irradiation temperature in the high-dose RR data is lower (255°C) than in the UV-P or RADAMO irradiations, and low temperatures were predicted to enhance the UMD effect (Mader, 1995; Odette and Lucas, 1998), so the difference may not be significant. Retention of a UMD effect up to 10^{20} n.cm^{-2} is, however, difficult to reconcile with the ATR data (Odette et al., 2016) (which show the opposite flux dependence in this fluence range even in the absence of MNS clusters) or the RADAMO data (showing no flux dependence). Saturation of the UMD effect around 6 × 10^{19} n.cm^{-2}, is also not consistent with the original analysis of the UCSB BR2 observations in which low-temperature PIA removed increasing amounts of hardening up to the maximum fluence of 1.2 × 10^{20} n.cm^{-2}.

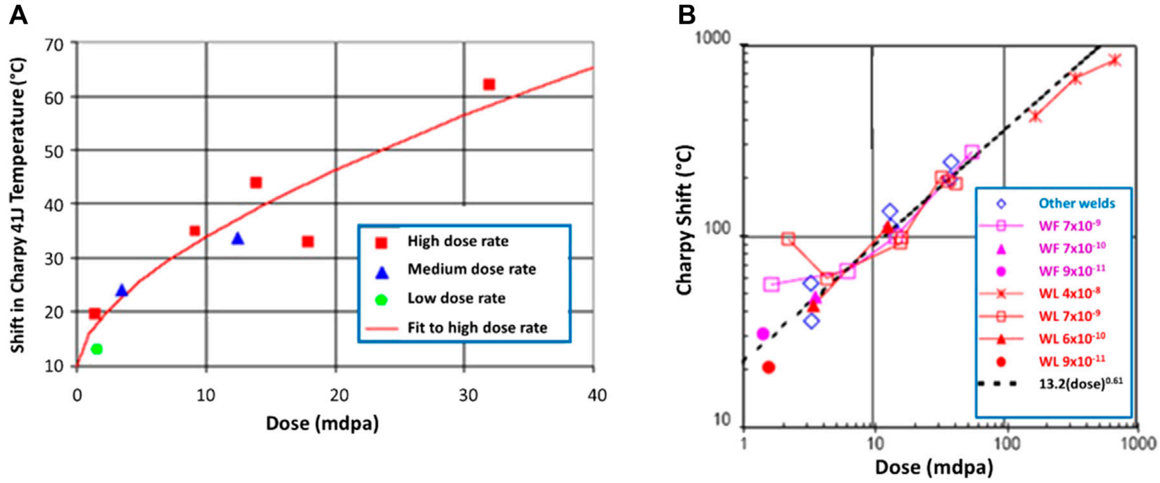

FIGURE 3
Williams and co-workers' hardening data from low-Cu SAWs, compared with trend curves without flux dependences **(A)** low-Ni SAWs, **(B)** high-Ni SAWs (Williams et al., 2001b; Williams and Ellis, 2001).

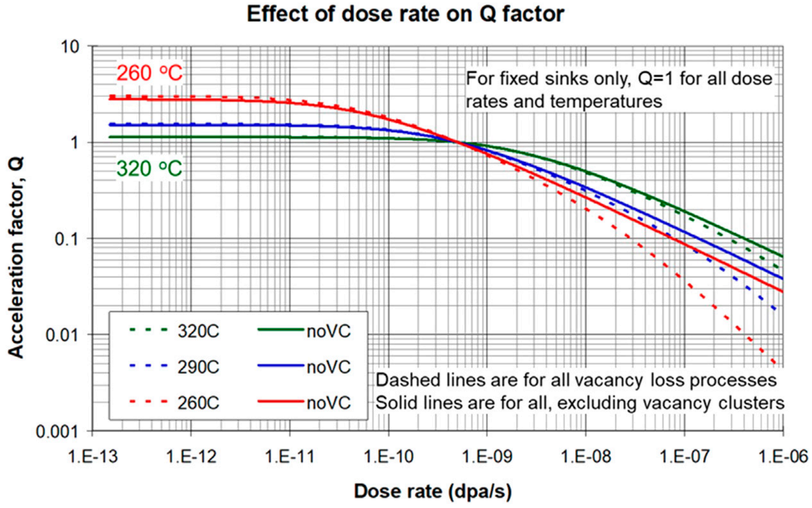

FIGURE 4
Flux-dependence of the fluence acceleration factor at different temperatures with and without a contribution from vacancy clusters (UMDs) from Williams and co-workers' data compilation (Williams et al., 2010).

2.3.3 Summary of flux effects seen in low-Cu steels and implications

A summary of the different studies on low-Cu steels is given in Figure 5. The numbers across the top indicate the log(flux), such that the bars indicate the range of fluxes in each investigation. If the data are found over multiple fluxes within the range, the bar is solid; if the data were acquired at specific, widely separated fluxes within the range, then the fluxes without data are shown hatched. If the authors found an increase in hardening/embrittlement with increasing flux over the flux range, the bar is red; if they found a decrease with increasing flux, the bar is blue; if no trend was observed, the bar is green. The final column shows the number of different materials involved in each campaign. Clearly a trend seen for multiple materials is more significant than when only one material is involved. The overlap in data (i.e., whether low-flux-and-fluence data are compared with extrapolations from trends drawn through high-fluxes-and-fluences or whether similar fluences are reached with different fluxes) is also important, but more difficult to quantify.

The plot makes it clear that the extensive, single-variable experimental campaigns set up by the UCSB group identified small, but consistently measurable effects of flux on hardening in low-Cu steels, with different trends in the flux-fluence range of each campaign. These trends are also seen in Williams et al.'s compilation including UCSB data, but data from other sources often fail to agree with the trends observed in the UCSB campaigns.

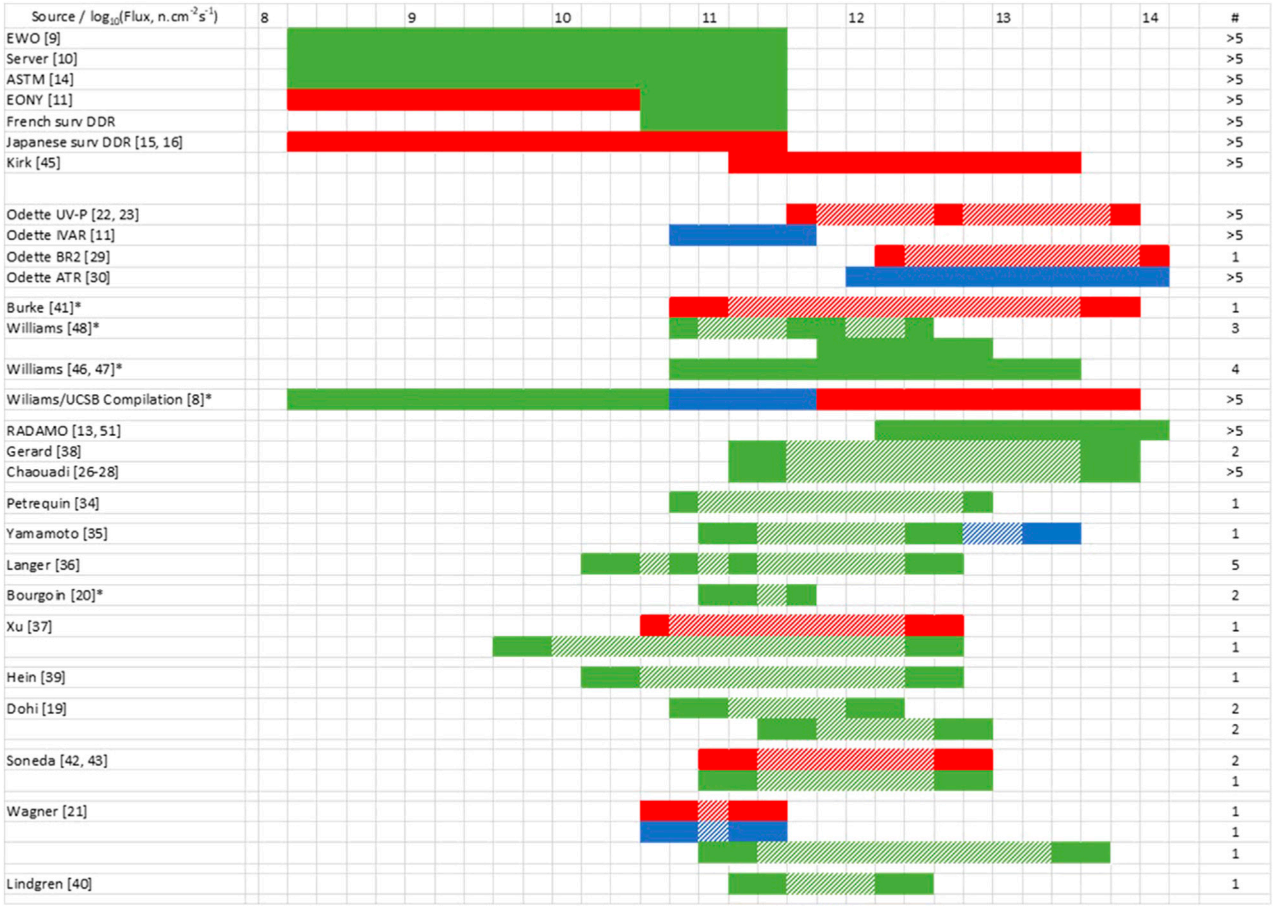

FIGURE 5
Summary of observations on low-Cu steels. Most observations were made at 270°C–310°C. Those marked with an asterisk (*) involved lower irradiation temperatures.

The different trends (or lack of trends) seen in different data sets cannot all be immediately ascribed to measurement uncertainty, even though the absolute values of shifts in low-Cu steels tend to be small. It is feasible that some properties not widely reported (e.g., C or N content, thermomechanical history) affect the transitions between different flux-fluence regimes, such that different materials exposed in a given flux-fluence range can be experiencing different mechanistic regimes. It is also feasible that neutron energy spectra affect comparisons between data acquired in different locations.

The main questions and knowledge gaps concerning low-Cu steels are, thus:

- Does a thermal regime affect hardening in low-Cu steels at BWR surveillance fluxes?
- What causes the contrasting trends observed by different groups in similar MTR flux-fluence ranges?
- Can a program of experiment, analysis/reanalysis, or modelling be defined which would reconcile the currently conflicting trends seen in different data sets (possibly including an updated analysis of dpa/fluence ratios in relevant reactor locations)?
- If UMFs are real, what is the range over which they affect hardening, since reconciliation between UV-P and RADAMO might indicate a limit of around 10^{19} n.cm^{-2}; while the RR/UCSB compilation and analysis of the PLOTTER database would suggest a limit around 10^{20} n.cm^{-2}.
  o Does PIA really characterize a UMF contribution to hardening?

Settling these questions is technologically important because nuclear power plants with low-Cu RPV steels are those for which operators are most likely to apply for license to extend plant lifetimes. If there is no overall effect of flux, then an accelerated irradiation can directly identify the fluence at which a new hardening component appears, allowing operational behaviour to be predicted out to 80 or even 100 years. Allowing for flux dependences of different sign in different flux-fluence-temperature ranges means that no general statement can be made. Based on the various UCSB campaigns and the RR/UCSB compilation analysis, it appears that measurements made on steels irradiated to around 10^{20}n.cm^{-2} or above, after irradiations at 10^{12}–10^{14}n.cm^{-2}s^{-1} will underestimate the embrittlement of low-Cu steels after surveillance or

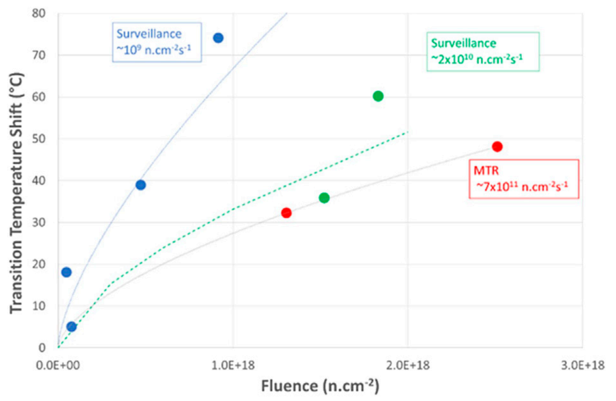

FIGURE 6
Effect of flux on embrittlement of 0.24Cu, 0.6Ni mod A302B base metal SP, irradiated at about 276°C (Data from (Soneda, 2007). Lines indicate best power law fits to data.).

operational exposures to a similar fluence. This is considered further in Section 5.1.

3 Review of data from high-Cu steels at low-moderate fluences

The beltlines of RPVs in modern NPP are not generally manufactured from high-Cu steels (steels with Cu levels >0.08 wt% for the purposes of this review). Nonetheless, information on flux or high-fluence effects in high-Cu steels is relevant to modern plant in that it can aid in the interpretation of otherwise ambiguous data from low-Cu steels. Unlike matrix defects, solute clusters are expected to grow predominantly via diffusion outside cascades. This makes the clustering/precipitation of Cu and other solutes more strongly diffusion dependent than MD formation. At the same time, the overall hardening in the presence of Cu is greater than in low-Cu steels, so trends with material and environmental parameters are easier to distinguish from measurement uncertainty.

More directly, components which were not considered as subject to radiation-induced degradation in current LWRs operating for 40 years may experience sufficient exposure to experience degradation during 60–80 years of operation. The composition control of such components will not have been as tight as that of beltline components, so some will contain high levels of Cu. Any low-flux flux dependences present in the embrittlement of high-Cu steels will affect the prediction of embrittlement in these components.

The behavior of Cu-containing steels is best understood if it is separated into the fluence ranges (1) during which Cu is precipitating and (2) after most of the Cu has precipitated and the Cu contribution to hardening has reached a maximum, or a constant value with further increases in fluence (the "plateau"). Fluences in the range below 10^{19} n.cm^{-2} are generally in the pre-plateau region, with the plateau onset around 1–2 × 10^{19} n.cm^{-2}, depending somewhat on material and irradiation variables.

3.1 Low-intermediate fluxes (<10^{12} n.cm^{-2}) and low fluences (pre-plateau)

As with MD terms, the copper clustering terms in most analyses of PWR-dominated surveillance data are independent of flux, but the Japanese JEAC4201 trend curve (derived from a BWR-dominated fleet) and the part of the EONY analysis of US LWR surveillance data applicable to BWR data both incorporate a flux-dependence for copper clustering (Brillaud and Hedin, 1992; Bourgoin et al., 2001). This supports the possibility that the onset of the thermal regime lies within, rather than below, the flux range of BWR surveillance data.

This interpretation of statistical trends in surveillance data is subject to the caveat that flux is readily conflated with fluence and temperature effects in the statistical analysis of surveillance data. More direct support for the location of the thermal regime is provided by the comparison between BWR surveillance data and higher-flux irradiations illustrated in Figure 6 (Soneda, 2007). The hardening at low fluences (pre-plateau hardening) in the high-Cu steel SP is clearly more rapid at the very low flux ("Surveillance W", ~10^9 n.cm^{-2}s^{-1}) than at the low flux ("Surveillance A″, ~2 × 10^{10} n.cm^{-2}s^{-1}) or intermediate flux ("MTR", 7 × 10^{11} n.cm^{-2}s^{-1}). This is reflected in microstructural analyses which show the Cu coming out of solution more rapidly (with respect to fluence, not time) at the lower flux.

The change in flux between the higher surveillance and MTR exposures is somewhat greater (×35) than that between the two surveillance exposures (×20), but the change in embrittlement is greatest between the two surveillance fluxes in Figure 6. The rate of change of embrittlement with flux is, thus diminishing in this flux range. This would be consistent with a shift from a (more strongly flux-dependent) thermal regime to a (flux-independent) fixed sink regime. More quantitatively, it suggests that (i) the upper limit to the thermal regime is above 10^9 n.cm^{-2}s^{-1}, and below 7 × 10^{11} n.cm^{-2}s^{-1}(ii) the upper limit to the fixed sink regime will be above 7 × 10^{11} n.cm^{-2}s^{-1}. (This places the fixed sink-matrix recombination boundary close to the onset flux for Odette and Mader's UMDs, suggesting that matrix recombination could influence the apparent UMD annealing behaviour.)

In their analysis of SC growth in a number of different steels, Wagner et al. (Wagner et al., 2016) concluded that a fixed sink (flux-independent) regime existed below 1.2 × 10^{12} n.cm^{-2}s^{-1}, with matrix recombination dominant at higher flux. Some authors comparing surveillance and MTR irradiations of Cu-containing steels would agree that there is no effect of flux between 10^{10} and 10^{11} (or even mid-10^{12}) n.cm^{-2} (Hein and May, 2008). Odette and co-workers (Eason et al., 1998), however, identify a finite inverse flux dependence within this range in multiple medium and high-Cu welds and base metals irradiated 0.7–8 × 10^{11} n.cm^{-2}s^{-1} in the IVAR campaign. Some of their data are shown in Figure 7, which illustrates both the consistency of the trend and its magnitude which, once again, is sufficiently small to be indistinguishable from scatter in campaigns with fewer measurements or greater measurement uncertainty.

As with the IVAR low-Cu steels, the hardening of the IVAR high-Cu steels was best described using an effective fluence (p = 0.38 ± 0.12, increasing with increasing Ni and Mn and decreasing

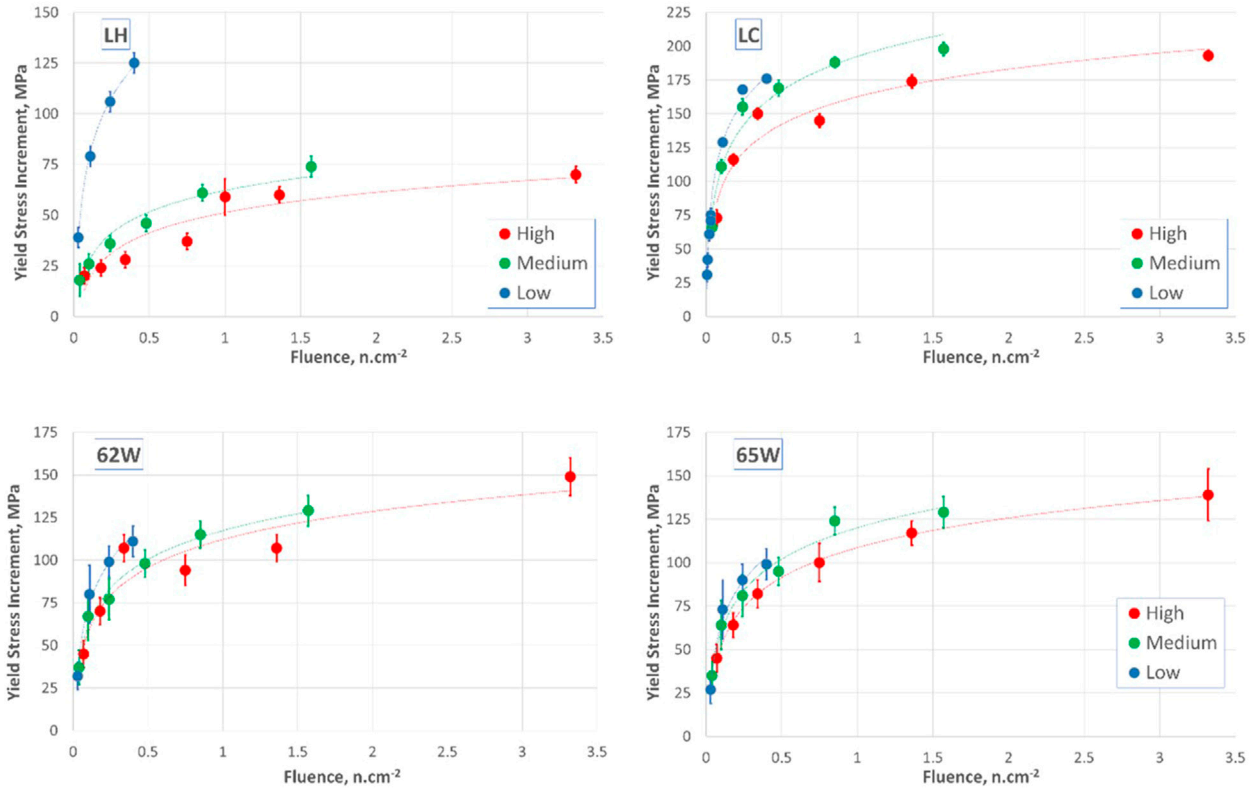

FIGURE 7
Hardening of IVAR high-Cu base metals (LC, LH) and welds (62W, 65 W) at 290°C and high (8–10 × 10^{11} n.cm^{-2}s^{-1}), medium (3 × 10^{11} n.cm^{-2}s^{-1}) and low (8–10 × 10^{10}n.cm^{-2}s^{-1}) fluxes (Data taken from (Eason et al., 2007). LH = 0.11Cu-0.74Ni-1.39Mn-0.005P, LC = 0.41Cu-0.86Ni-1.44Mn-0.005P, 62 W = 0.23Cu-0.60Ni-1.61Mn-0.020P, 64 W = 0.22Cu-0.60Ni-1.45Mn-0.015P. Trend lines are logarithmic best fits to the data.).

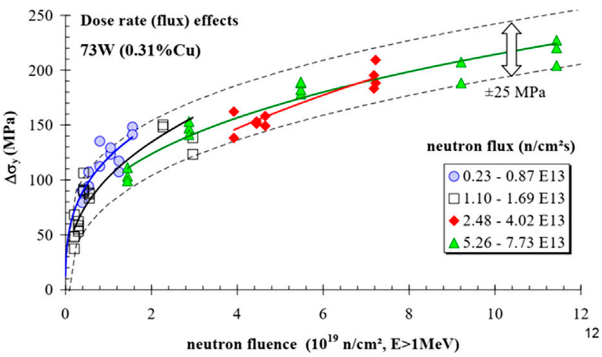

FIGURE 8
Hardening in high-Cu weld at high fluxes (Chaouadi et al., 2008).

Cu) (Eason et al., 1998; Bourgoin et al., 2001; Odette et al., 2001; Odette et al., 2005).

3.2 High fluxes, low fluences (pre-plateau)

Few campaigns obtain much data at fluxes >10^{11} n.cm^{-2} and fluences < 10^{19} n.cm^{-2}.

In their UV-P campaign, Odette, Mader et al. found that increasing the flux from 6 × 10^{11} to 4.6 × 10^{13} n.cm^{-2}s^{-1} decreased the rate of hardening in high-Cu steels. Similarly, Chaouadi et al. observed slight, but consistently decreasing hardening rates with increasing fluxes at low fluences in BR2 irradiations of a 0.31 wt% Cu plate, as illustrated in Figure 8. In consequence of such observations, the RADAMO, ETC contains a flux dependence in the CRP term (although not in the MD term) (Chaouadi et al., 2008). Williams et al. (Williams et al., 1985; Williams et al., 2001b) also saw lower hardening at low-fluences in 0.24–0.56 wt% Cu SAWs irradiated at 2 × 10^{-8} dpa/s versus 6 × 10^{-10} dpa/s(approximately 1.3 × 10^{13} vs. 4 × 10^{11} n.cm^{-2}s^{-1}) with the data converging at higher (plateau) doses. They could not distinguish flux effects in Cu < 0.15 wt % Cu SAWs.

A balance between opposing UMD and CRP responses to increasing flux at fluxes above 10^{12} n.cm^{-2}s^{-1} (plus limited data below 10^{19} n.cm^{-2}) might explain why Hawthorne and Hiser saw higher low-fluence hardening at 6 × 10^{11} n.cm^{-2}s^{-1} than at 9 × 10^{12} n.cm^{-2}s^{-1} in a Linde 80 (0.4 wt% Cu), but not in 0.2 wt% Cu A302B or A533B plates (Hawthorne and Hiser, 1990). The very limited direct support for a UMD effect in studies of low-Cu steels outside UCSB is thus complemented by indirect support from comparative studies of medium-versus high-Cu steels in the UMD range.

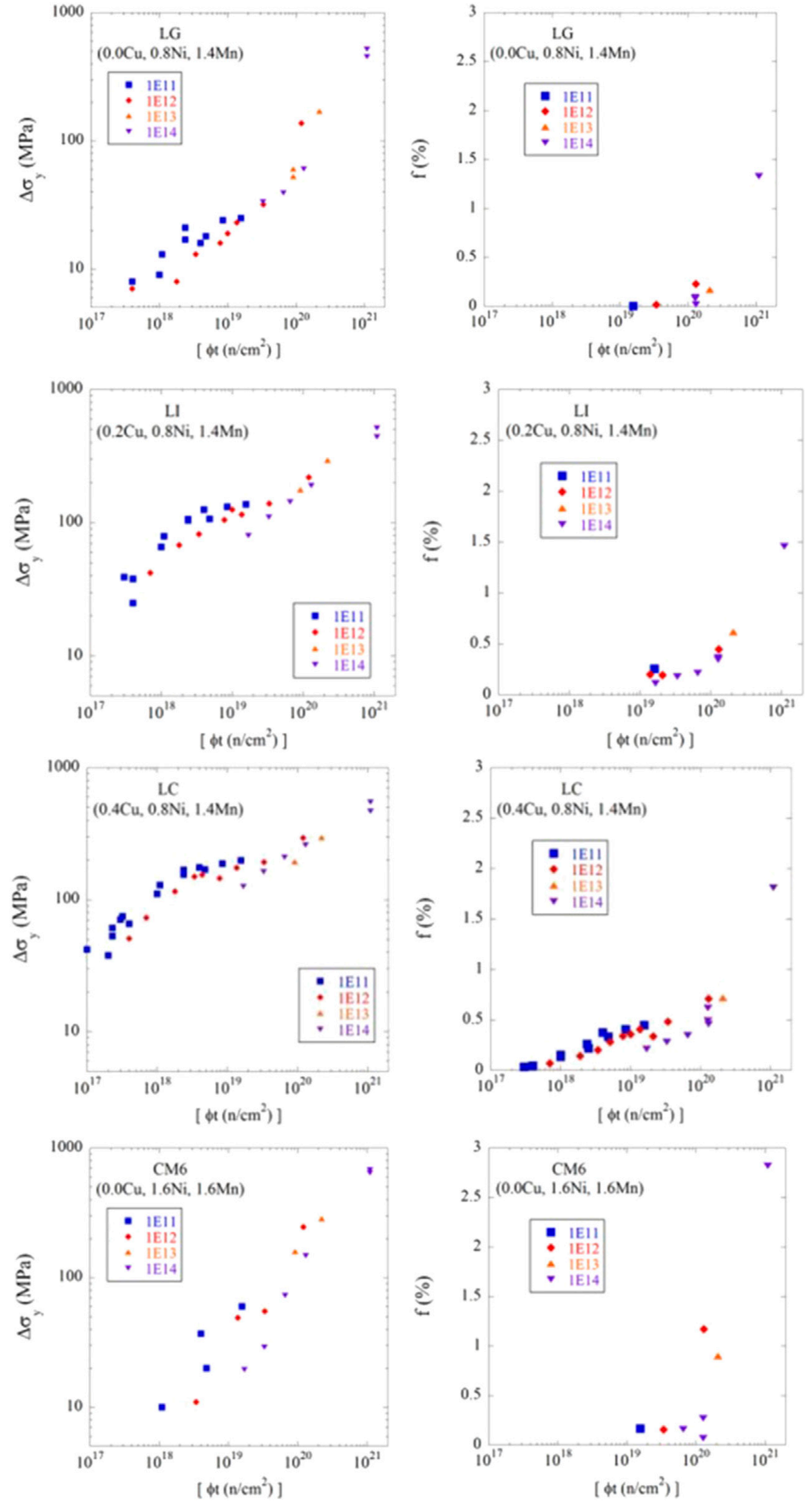

FIGURE 9
Hardening and precipitation in medium -Ni UCSB steels with different Cu and Ni levels (Nanstad et al., 2022).

3.3 Moderate fluences ("on the plateau")

Most authors agree that there is no significant effect of flux on the magnitude of the Cu contribution to hardening or embrittlement once the Cu contribution has reached the plateau. This is found in MTR campaigns at high fluxes (Williams et al., 1985; Langer et al., 2000; Chaouadi et al., 2008) and is also reflected in the forms of the EWO, EONY, ASTM E900-02 and E900-15 embrittlement trend curves derived from US LWR lower-flux surveillance data. Odette et al. (Odette et al., 2005) considered that the plateau level of CRP hardening was generally independent of flux at the low and intermediate dose rates (~8 × 10^{10} n.cm^{-2}s^{-1} and 3 × 10^{11} n.cm^{-2}s^{-1}) but, for some compositions, it was lower at high flux (~8 × 10^{11} n.cm^{-2}s^{-1}).

Microstructurally, increasing the flux tends to produce slightly more, smaller clusters (Williams and Phythian, 1996; Hyde et al., 2001; Dohi et al., 2009; Soneda et al., 2015; Wagner et al., 2016; Hashimoto et al., 2021). Within a classic dispersed barrier model of hardening (DBH), this would be expected to produce a higher plateau in MTR-irradiated materials. In irradiated RPV steels, however, the hardening is more strongly related to $\sqrt{f_v}$ than to $\sqrt{f_v}/r$, (where f_v = volume fraction of SCs and r = SC radius), so the small microstructural change is insufficient to produce a flux-dependence in the plateau which is easily distinguishable from scatter.

3.4 Very high fluences

Even in high-Cu steels, the dissolved Cu is generally reduced to very low levels by 5–10 × 10^{19} n.cm^{-2}. Above this stage, the development of the microstructure is similar in low-and high-Cu steels. In consequence, the flux dependence of hardening and embrittlement follow similar trends.

Once again, much of the systematic data on flux effects comes from UCSB campaigns. Microstructural and hardening data from steels with increasing levels of Cu are shown in Figure 9.

As expected, Figures 9C, E show high initial hardening rate versus fluence (data acquired at 10^{11} and 10^{12} n.cm^{-2}s^{-1}) which diminishes in the range 2–6 × 10^{18} n.cm^{-2} as the Cu precipitation rate diminishes (the onset of the plateau). The data acquired at 10^{12} n.cm^{-2}s^{-1} extend to higher fluences and show an increase in the hardening rate somewhere in the range 6–12 × 10^{19} n.cm^{-2}. The higher rate of hardening is reproduced in the high-fluence data acquired at 10^{13} and 10^{14} n.cm^{-2}s^{-1} although no threshold fluence for a change in hardening rate is evident in these data. In this representation, the 10^{13} and 10^{14} n.cm^{-2}s^{-1} data appear to show a consistent linear hardening rate (on the log-log plot) from low fluences. The hardening and cluster data from 1.6 wt% Ni steels (such as CM6 in Figures 9G, H) also show no change in the rates of increase with fluence but are consistently high.

The UCSB group found that the high-fluence hardening and precipitation data converged when plotted versus the effective fluence with $p = 0.25$, confirming the existence of flux dependence in the regime over which Mn-Ni-Si phases were thought to precipitate. The low derived value of p appears to be due to the density of radiation-induced sinks (solute clusters, dislocation loops, solute-point defect complexes, precipitates) which dominate recombination in contrast to the mutual annihilation of individual point defect anticipated at high flux and low fluences.

In their analysis of the embrittlement data in the PLOTTER database, Kirk and co-workers (Kirk and Erickson, 2021; Kirk and Ferreno Blanco, 2022) were able to reconcile surveillance and MTR data with a trend curve which incorporated a weak negative flux dependence in the term applicable to high-Cu steels, consistent with the UCSB CRP and MNS observations. (The stronger flux effect in high-Cu steels being visible despite the variation in dpa:fluence ratios in the input data.)

3.5 Summary of flux effects in high-Cu steels, knowledge gaps and implication

Hardening and embrittlement in high-Cu steels is greater than in low-Cu steels, making trends easier to observe. In the pre-plateau, low-fluence range:

- The various analyses agree that, in the flux range <~5 × 10^{10} n.cm^{-2}s^{-1}, the embrittlement in Cu-containing steels decreases with increasing flux at a given fluence. The agreement is consistent with understanding that increasing flux will delay the rate at which diffusion-controlled SC growth can occur in the thermal regime, with the thermal regime beginning within the range of fluxes examined in the program. More information is available from high-Cu steels in this flux-fluence regime than was available for the low-Cu steels.
- In the range 5 × 10^{10}–10^{12} n.cm^{-2}s^{-1}, the observations in Cu-containing steels appear split between those who observe no effect of flux within measurement uncertainty and those who observe a decrease in hardening with increasing flux. It is not easy to correlate the alternative observations with fluence range or Cu content. Nonetheless, it is plausible that this is a range of weaker flux-dependence given the data from the low-Cu steels supportive of a fixed sink regime in this flux range.
- At fluxes above 10^{12} n.cm^{-2}s^{-1}, different observations of embrittlement show increases, decreases and no effect with increasing flux. In this flux range, the higher-Cu steels appear more likely to show a decrease and the lower-Cu steels an increase in embrittlement with increasing flux. This is interpretable in terms of a low-fluence UMD effect operating in the opposite sense to a low-fluence, pre-plateau Cu precipitation effect. Alternatively, it could indicate that the effect of flux is monotonic but is more difficult to distinguish from measurement uncertainty at lower fluences and Cu levels.

There is general agreement that hardening in the plateau regime is independent of flux. The importance of diffusion in the development of CRPs allows rate theory models of flux effects on diffusion (e.g. (Williams et al., 2010)) to be applied to mechanical property development in high-Cu as well as low-Cu steels. There are fewer disagreements between campaigns involving higher-Cu steels than were reported for low-Cu steels. This leaves fewer areas of uncertainty. Further investigation in the 5 × 10^{10}–10^{12} n.cm^{-2}s^{-1} range might help clarify when (or whether) hardening is flux dependent in this range.

Studies on low-Cu steels came to conflicting conclusions concerning the presence of the thermal regime in BWR surveillance data. The direct evidence from the behavior of medium-Cu steels in BWR surveillance irradiations supports the existence for a thermal regime which would affect both low- and high-Cu steels. The overall results indicate that flux effects need to be considered when applying trends derived from surveillance data to the BWR beltline and to "expanded beltline" components during plant life extension periods.

Studies on low-Cu steels were also ambiguous concerning the existence of UMDs (Section 2.3) and the flux-fluence range over which they would have an effect on hardening/embrittlement. The indirect evidence from the difference in the pre-plateau behavior of medium-Cu versus high-Cu steels provides support for the existence of UMDs. The flux-fluence range over which they dominate flux effects remains unclear, affecting the extrapolation of information from high-flux MTR irradiations to beltline conditions in the range 10^{19}–10^{20} n.cm^{-2}s^{-1}.

4 Flux effects on grain boundary segregation and non-hardening embrittlement

MnMoNi steels are not generally prone to intergranular failure, so information on flux effects generally comes from CrMoV steels. Kuleshova et al. (2017) used Auger Electron Spectroscopy (AES) to measure grain boundary segregation in a low-Cu (0.03–0.06 wt%) high-Ni (1.61–1.89 wt%) NiCrMo WWER-1000 Sv-10KhGNMAA weld metal after thermal ageing at 300°C or irradiation in a WWER-1000 surveillance scheme, (8–11 × 10^{10} n.cm^{-2}s^{-1}; E > 0.5 MeV at 300°C to 3 × 10^{19} n.cm^{-2}; E > 0.5 MeV). Some of the thermally-aged samples were subsequently irradiated in a research reactor, IR8 (2–18 × 10^{12} n.cm^{-2}s^{-1}; E > 0.5MeV to 5 × 10^{19} n.cm^{-2}; E > 0.5 MeV). The lower-flux irradiation may be in the thermal or fixed sink regime while the higher fluxes are likely to be in the matrix recombination regime.

In both cases the fluences are high enough that the concentration of radiation-induced sinks is significant: TEM found 3–4 × 10^{21} dislocation loops m^{-3}; APT found 6 × 10^{23} solute clusters m^{-3}. The AES showed that the levels of P, Ni and Cr on the grain boundaries all increased with both thermal ageing and irradiation. The higher-flux irradiation was somewhat less effective at attracting P to the grain boundaries, consistent with the shorter diffusion distances over which complexes drag solutes when matrix recombination (and radiation-induced traps) becomes more important.

No intergranular failure (IGF) was observed in the initial material (14% monolayer P), but increasing amounts were observed with increasing thermal ageing or increasing low-flux irradiation, suggesting a threshold for IGF between 15% and 20% monolayer in these steels.

These observations of P segregation in CrMoV steels suggest that the framework described in the Introduction is relevant, and data from high-flux irradiations will underestimate grain boundary segregation at lower fluxes. Insufficient measurements and modelling exist to quantify this overall trend and show how high flux data should be used to predict P accumulation in RPV grain boundaries even in CrMoV steels.

5 Flux effects at high fluences

5.1 Comparison between high fluence data and threshold/flux models

The most important challenge facing LWR operators looking to extend the reactor lifetime is the possibility of accelerated embrittlement at high fluences due to either the onset of intergranular fracture or the conversion of solute clusters into the nuclei of a distinct phase with a higher hardening capacity. As shown in Section 4, there are insufficient data to quantify the effect of flux on the threshold dose for IGF. It is, however, possible to assess whether an acceleration due to Mn-Ni-Si precipitate formation occurs at fluences above a flux-dependent threshold by comparing the available data with predictions of the RR-UCSB model of flux effects.

The data set with the least ambiguous change in the hardening and solute clustering rate at high fluence is that acquired for medium-Ni steels in the UCSB ATR2 campaign at 10^{12} n.cm^{-2}s^{-1} (red points in Figure 9). For these steels, the hardening data suggest an upswing midway between the two highest-fluence datapoints (3–11 × 10^{19} n.cm^{-2}) while the associated f_v data suggest an upswing closer to the last datapoints. This fluence range does not appear affected by the steels' Cu content. For the high-Ni steels in that program (not included in these Figures), there was no clear upswing in the hardening rate, although the rate was generally high, suggesting a much lower threshold, perhaps as low as the lowest-fluence data point for which hardening was measured at 3 × 10^{18} n.cm^{-2}. The cluster volume fraction measurements suggest a higher fluence for the threshold, perhaps around 1 × 10^{19} n.cm^{-2}.

Taking representative threshold fluences of 8 × 10^{19} n.cm^{-2} for medium-Ni steels and 1 × 10^{19} n.cm^{-2} for high-Ni steels at 10^{12} n.cm^{-2}s^{-1} and 290°C, the fluences required for a similar level of diffusion-controlled microstructural development under different fluxes can be derived using the acceleration factor, Q, developed in the RR-UCSB collaboration (Williams et al., 2010) and given in Figure 4. The equivalent values for the medium-Ni steels are:

- 5.5 × 10^{20} n.cm^{-2} at 10^{14} n.cm^{-2}s^{-1} (Q~0.13)
- 1.8 × 10^{20} n.cm^{-2} at 10^{13} n.cm^{-2}s^{-1} (Q~0.4)
- 8.0 × 10^{19} n.cm^{-2} at 10^{12} n.cm^{-2}s^{-1} (Q~0.9)
- 6.0 × 10^{19} n.cm^{-2} at 10^{11} n.cm^{-2}s^{-1} (Q~1.2)
- 5.5 × 10^{19} n.cm^{-2} at 10^{10} n.cm^{-2}s^{-1} (Q~1.3)
- 5.1 × 10^{19} n.cm^{-2} at 10^{9} n.cm^{-2}s^{-1} (Q~1.4)

These fluences can be compared with the hardening seen in other data sets acquired out to high fluences.

- The predicted threshold for the UCSB ATR data (Odette et al., 2016) acquired at 10^{14} n.cm^{-2}s^{-1} in Figure 9 (mauve points)

TABLE 1 Material compositions and irradiation conditions used in the LONGLIFE program (Altstadt et al., 2014; Hein, 2015).

Material	Type	Composition (wt%)			Flux ($n.cm^{-2}s^{-1}$)	Temp. (°C)	Maximum fluence ($n.cm^{-2}$)	Predicted threshold ($n.cm^{-2}$)	Suggested threshold fluence ($n.cm^{-2}$)
		Cu	Ni	Mn					
EDF1	16MND5 bm	0.09	0.65	1.27	0.9–2.5 × 10^{11}	260	1.2 × 10^{20}	7 × 10^{19}	N/S
EDF2	16MND5 bm	0.06	0.69	1.32	2 × 10^{11}	286	7 × 10^{19}	6 × 10^{19}	N/S
EDF3	16MND5 wm	0.03	0.64	1.41	1.5 × 10^{12}	286	5 × 10^{19}	6 × 10^{19}	N/S
RAB1	S3NiMo wm	0.08	1.58	1.46	2 × 10^{11}	283	5.5 × 10^{19}	6 × 10^{19}	N/S
JPB	A533B Cl1 bm	0.01	0.83	1.42	0.3–9.6 × 10^{12}	290	1.6 × 10^{20}	7–28 × 10^{19}	N/S
JPC	A533B Cl1 bm	0.01	0.81	1.45	0.3–9.6 × 10^{12}	290	1.2 × 10^{20}	7–28 × 10^{19}	N/S
JPB	A533B Cl1 bm	0.01	0.83	1.42	0.1–3.5 × 10^{12}	255*	9 × 10^{19}	1.2 × 10^{20}	6–9 × 10^{19}
JPC	A533B Cl1 bm	0.01	0.81	1.45	0.1–3.5 × 10^{12}	255*	9 × 10^{19}	1.2 × 10^{20}	6–9 × 10^{19}

N/S no threshold seen, bm, base metal; wm, weld metal. * Only 3 points shown on plot.

lies between the two highest-fluence data points. The $\Delta\sigma_Y$ and f_v values for steel LG are consistent with the prediction, although the increase in the rate of hardening is not very strong on the log-log scale. The f_v values for the higher-Cu steels LI and LC also support this analysis, although the $\Delta\sigma_Y$ data do not: no increase in hardening rate is evident between the last two data points for these steels. Overall, the data are weakly supportive of the prediction.

- All the UCSB data acquired at 10^{13} $n.cm^{-2}s^{-1}$ in Figure 9 (orange points) lie above the threshold, so no change in hardening or precipitation rate need be evident in the data. In accordance with this, no change in hardening rate is evident in the data for any of the steels, while the f_v levels are similar to those seen in the post-threshold 10^{12} $n.cm^{-2}s^{-1}$ data. Again, the data are weakly supportive.
- The UCSB data acquired at 10^{11} $n.cm^{-2}s^{-1}$ in Figure 9 (blue points) are all below the threshold, so all the hardening should be at the lower rate, and no additional f_v should be evident. This is in accordance with the observed $\Delta\sigma_Y$ and f_v data. Such data cannot really be considered to support or contradict the analysis.
- The Belgian data reaching to the highest fluences in Figure 8 were acquired at 5.2–7.7 × 10^{13} $n.cm^{-2}s^{-1}$ and 300°C (Q~0.15) so the threshold is predicted to be around 4.8 × 10^{20} $n.cm^{-2}$. The data in Figure 8 have been used to suggest that there is no late-onset increase in the rate of embrittlement, but with a maximum fluence around 1.17 × 10^{20} $n.cm^{-2}$, all the data are predicted to lie below the threshold. The monotonic trend curve in the Figure thus neither does supports nor contradicts the analysis.
- The Rolls-Royce low-Ni SAW data in Figure 3 (Williams et al., 2001a; Williams et al., 2001b) showed no high-dose upswing out to 32mdpa (~2.2 × 10^{19} $n.cm^{-2}$) at 255°C and 7 × 10^{-9} dpa/s (about 4.7 × 10^{12} $n.cm^{-2}s^{-1}$). Given the relatively low dose, it is not surprising that the measurements are also all predicted to be below the threshold.

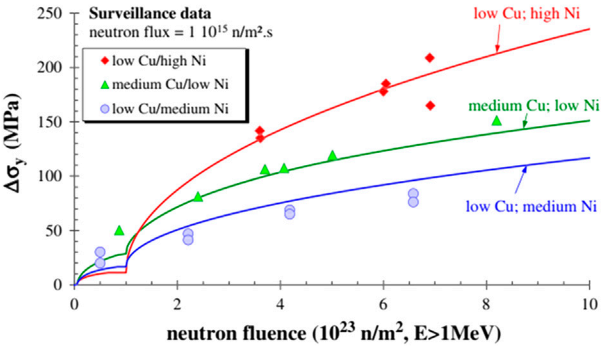

FIGURE 10
Comparison between RADAMO predictions and hardening of a number of steels in the SCK.CEN database (Chaouadi and Gerard, 2013)[2].

- Analysis of the Rolls-Royce high-Ni SAW data is a little more complex, but more consistent with a threshold of 3 × 10^{18} $n.cm^{-2}s^{-1}$ than 1 × 10^{19} $n.cm^{-2}$. With the lower threshold, the RR high-Ni SAW data at 4 × 10^{-8} dpa/s (crosses) are above the threshold and the data at 7 × 10^{-9} dpa/s (open squares) cross the threshold. The location of the lower-dose 7 × 10^{-9} dpa/s data, above the trend line drawn in the Figure, is consistent with a change in hardening rate at the required dose (as well as with measurement uncertainty, as assumed in the plot). The 7 × 10^{-10} dpa/s data (triangles) should also cross the threshold, but the lower-dose data are sufficiently close to the threshold that this might be difficult to observe. Similarly, the 9 × 10^{-11} dpa/s data (circles) should lie below the threshold, but the absolute hardening is so small at the low doses involved that comparison with the higher-dose rate data is difficult. Overall, the RR high-Ni data are consistent with the existence of a threshold in high-Ni steels, if not strongly so. The threshold is sufficiently low

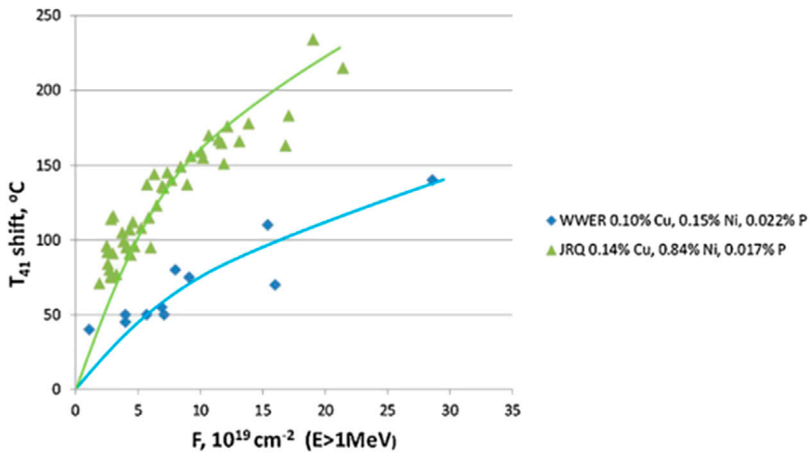

FIGURE 11
High fluence data from 15Kh2MFA CrMoV WWER steel and A533B plate (JRQ) irradiated at 270°C and fluxes between 1011 and 1012 n.cm^{-2}s^{-1} (Castin et al., 2022)[3].

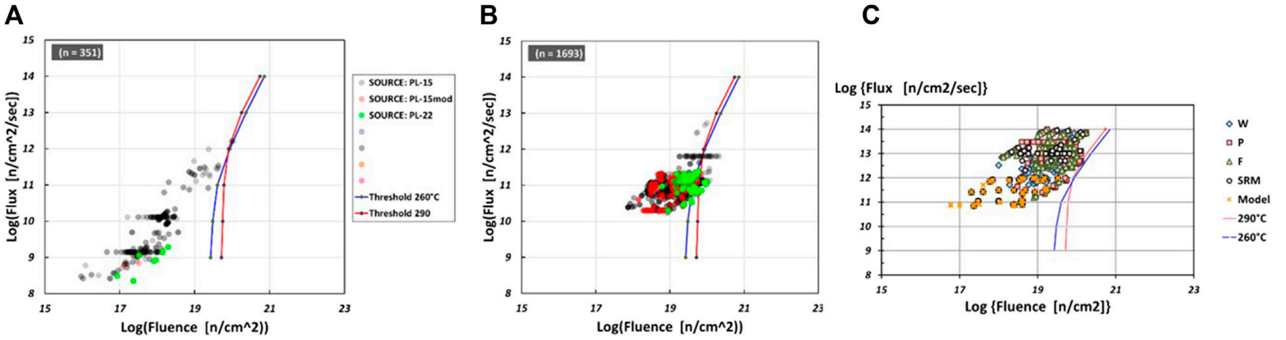

FIGURE 12
Comparison between data in ASTM PLOTTER database and predicted threshold **(A)** BWR surveillance data **(B)** PWR surveillance data **(C)** MTR data. (Blue diamonds = welds, orange squares = plates, green triangles = forgings, open circles = standard reference materials, yellow crosses = model alloys, red line = threshold at 290°C, blue line = threshold at 260°C).

that high embrittlement rates will be expected in high-Ni RPV components from early in life, so no further acceleration is likely to be introduced by long term operation.

- The Euratom-funded LONGLIFE program was set up to collate data from a range of commercial steels irradiated to high fluences (Altstadt et al., 2014; Hein, 2015). The results are summarized in Table 1. In two cases, a high-fluence acceleration in hardening was identified in the data but at a fluence well below prediction. With only three datapoints in each set, however, it was difficult to confirm that a change in hardening rate had, indeed occurred. In five cases, no acceleration was observed and the highest fluence was predicted to be at or below the threshold. These data can neither confirm nor contradict the model. In only one case (EDF-1) were multiple data points acquired both before and significantly beyond the predicted threshold fluence, without an acceleration being identified, contradicting the model.
- Figure 10 shows surveillance data from within the RADAMO database acquired at fluxes around 10^{11} n.cm^{-2}s^{-1} (Chaouadi and Gerard, 2011). The Q-factor analysis suggests that a change in the fluence-dependence of hardening should occur around 6 × 10^{19} n.cm^{-2}s^{-1} for the medium-Ni steel, and at a higher fluence for a low-Ni steel, making all these data pre-threshold. The absence of acceleration in the low- and medium-Ni data sets is consistent with the proposition, but does not confirm it. The predicted threshold for a high-Ni steel would be between 2–8 × 10^{18} n.cm^{-2} (depending on the definition of the CM6 threshold), such that all the high-Ni data would be post-threshold. The higher hardening rate with respect to the lower-Ni steels and the absence of acceleration in the high-Ni data set is also consistent with the proposition.
- Figure 11 shows embrittlement data from the IAEA reference steel JRQ acquired at 270°C and fluxes between 10^{11}–10^{12} n.cm^{-2}s^{-1}. Again, the lower-fluence data were

likely to have been acquired at lower fluxes. With Q values between 0.9 and 1.2, this puts the threshold around 7 × 10^{19} n.cm^{-2}. This is a valuable data set in that it contains a large number of measurements out to high fluences. A monotonic trend line is drawn through the data, although a better fit might be achieved with either (i) a steeper early curve and shallower later curve, or (ii) a more sharply bending curve at lower fluences, plus a threshold to a higher hardening rate above about 1.7 × 10^{20} n.cm^{-2}. If the last two data points in Figure 11 are truly above a threshold, rather than exhibiting scatter, however, this threshold occurs at more than twice the predicted fluence.

Figure 12 compares the predicted threshold fluence values at 260°C and 290°C and different fluxes with the fluxes and fluences of data in the ASTM PLOTTER database. The predicted thresholds are above all the BWR surveillance data (as of 2022), but 5%–10% of the PWR data are above the predicted thresholds at 290°C. The MTR data (as of 2015) are also below the predicted thresholds. Given the uncertainties in the calculations, it is unlikely that any late-onset increase in the embrittlement rate will be evident in the surveillance data. In consequence current embrittlement trend curves will not incorporate any influence from the predicted acceleration. (The absence of a high-fluence increase in the embrittlement rate within the PLOTTER data is also supported by the multiscale modelling shown in (Castin et al., 2022) which successfully predicts the behaviour of the low-Cu steels within PLOTTER via a model which does not allow for precipitation.)

- Nine low- and medium-Ni commercial steels irradiated in surveillance programs (exposures in the range 7 × 10^{18} ~9 × 10^{19} n.cm^{-2} at 0.9–1.6 × 10^{11} n.cm^{-2}s^{-1}) were re-irradiated in an MTR in the UCSB ATR-2 campaign (to ~1.4 × 10^{20} n.cm^{-2} at 3.6 × 10^{12} n.cm^{-2}s^{-1} (Q~0.65) At the surveillance fluxes (Q~1.2), the threshold fluence would convert to around 6 × 10^{19} n.cm^{-2}, so surveillance points would lie below and above the threshold. Around half of the eight steels can be described as showing an acceleration in hardening, generally between the surveillance and MTR points. Given the scatter in the surveillance measurements, the uncertainty in the threshold value and the small number of points likely to be above the threshold, this comparison does provide clear confirmation of the threshold model, but does not contradict it.

In summary, few of the data sets extending to high fluences exhibit a late onset acceleration in hardening/precipitation rates. In the majority of cases, the Q-based analysis suggests that this is because the data all fall above or below a flux-dependent threshold. These campaigns cannot help determine whether or not late-onset acceleration occurs. In only one of the data sets is a threshold predicted to be present (on the basis of the UCSB data acquired at 10^{12} n.cm^{-2}s^{-1} (Odette et al., 2016) and the Q analysis) plausibly observed (irradiations at 10^{14} n.cm^{-2}s^{-1} in (Odette et al., 2016)). In several others, a predicted threshold may or may not be present given the scatter in the data. In two data sets with multiple measurements each side of the predicted threshold, however, no acceleration is seen (EDF-1 (Altstadt et al., 2014; Hein, 2015) and JRQ (Kryukov et al., 2014)). At best, this constitutes only weak support for a late-onset threshold. Nonetheless, because the UCSB data acquired at 10^{12} n.cm^{-2}s^{-1}, plus the RR-UCSB description of flux dependences, lead to a prediction that PWR designs with beltline fluxes around 10^{11} n.cm^{-2}s^{-1} will exceed the threshold in long term operation, it is important to provide clearer confirmation/rejection of the flux-dependent threshold hypothesis. The threshold values listed for different fluxes in this Section provide useful input into the design of appropriate experiments.

6 Summary and conclusion

A framework in which to understand flux effects was suggested in the 1970s. It postulates a thermal region at low fluxes, and intermediate fixed sink regime and a high flux matrix recombination regime. This review has shown that the framework remains useful, identifies ranges for some of the regimes, and recognises that fixed sink regime expands with increasing fluence.

Flux effects in low-Cu steels are more difficult to distinguish from measurement uncertainty, but comparisons between low- and high-Cu steels suggest that flux dependences are present in both composition categories. With different flux-dependences in different regimes, monotonic extrapolation from MTR to surveillance or vessel fluxes is inappropriate in high-Cu steels and would be associated with significant uncertainty in low-Cu steels. The conditions under which unstable matrix defects may be found, and the extent to which they affect hardening, remain unclear. Suggestions have been made for clarifying experiments.

An acceleration in embrittlement at high fluences has been predicted for some years based on the radiation-induced segregation of grain boundary P and consequent introduction of intergranular fracture, but insufficient data exist to identify whether such a threshold occurs under the flux-fluence conditions of long-term operation. This question requires further investigation. A series of campaigns by a well-respected group at UCSB has identified a threshold for accelerated embrittlement at high fluences due to precipitation. An associated model, describing the accelerating effects of flux on precipitation, leads to the conclusion that acceleration will be observed in some PWR RPVs during very long-term operation. The predictions are not, however, well-supported by appropriate data from other sources and, in some cases, are clearly contradicted. Although it can be difficult to obtain funding for "repeat experiments", the technological importance of the issue requires that further observations in flux-fluence ranges encompassing predicted thresholds be performed.

Author contributions

SO: Conceptualization, Writing–original draft. PS: Writing–review and editing. EL: Conceptualization, Project administration, Writing–review and editing.

Funding

The author(s) declare financial support was received for the research, authorship, and/or publication of this article. The authors are grateful to EPRI for the provision of funding to perform this review under Source Agreement MA 10013253 and to NNL for the provision of additional funds for preparation of the paper under Order 30031.221.

Acknowledgments

The authors wish to thank fellow members of EPRI and the UK's Radiation Embrittlement Forum for helpful discussions and insights on the subject of this paper.

Conflict of interest

The authors declare that the research was conducted in the absence of any commercial or financial relationships that could be construed as a potential conflict of interest.

Publisher's note

References

Altstadt, E., Keim, E., Hein, H., Serrano, M., Bergner, F., Viehrig, H.-W., et al. (2014). FP7 Project LONGLIFE: overview of results and implications. *Nucl. Eng. Des.* 278, 753–757. doi:10.1016/j.nucengdes.2014.09.003

ASTM (2015). *ASTM E900-15. Standard guide for predicting radiation-induced transition temperature shifts in reactor vessel materials*. Pennsylvania, United States: ASTM. April.

Becquart, C. S., and Wirth, B. D. (2020). "Kinetic monte CarloSimulations of irradiation effects chapter 1.14," in *Comprehensive nuclear materials*, 393–410.

Bourgoin, J., Rupa, N., Bache, A., Buisine, D., Rouillon, Y., and Bezdekian, G. (2001). "The pressure vessel surveillance program of the French PWRs," in Proc. Workshop on Dose Rate Effects in Reactor Pressure Vesel Materials, Squaw Valley, CA, USA, November 2001.

Brillaud, C., and Hedin, F. (1992). "In-service evaluation of French pressurised water reactor vessel steel," in *Effects of radiation on materials: 15th int. Symp. ASTM STP 1125* (ASTM), 23–49.

Burke, M. G., Stofanak, R. J., Hyde, J. M., English, C. A., and Server, W. L. (2003). "Microstructural aspects of irraiation damage in A508 Gr 4N forging steel: composition and flux effects," in Effects of Radiation on Materials: 21st Int. Symp. ASTM STP 1447, West Conshohocken, PA, USA, January 2003.

Castin, N., Bonny, G., Bakaev, A., Bergner, F., Domain, C., Hyde, J., et al. (2020). The dominant mechanisms for the formation of solute-rich clusters in low-Cu steels under irradiation. *Mater. Today Energy* 17, 100472. doi:10.1016/j.mtener.2020.100472

Castin, N., Bonny, G., Konstantinovic, M. J., Bakaev, A., Bergner, F., Courilleau, C., et al. (2022). Multiscale modelling in nuclear ferritic steels: from nano-sized defects to embrittlement. arXiv preprint, arXiv2204.11441 Available at: https://arxiv.org/abs/2204.11441.

Castin, N., Malerba, L., and Chaouadi, R. (2011). Prediction of radiation induced hardening of reactor pressure vessel steels using artificial neural networks. *J. Nucl. Mater.* 408, 30–39. doi:10.1016/j.jnucmat.2010.10.039

Chaouadi, R., and Gerard, R. (2011). Neutron flux and annealing effects on irradiation hardening of RPV materials. *J. Nucl. Mater.* 418, 137–142. doi:10.1016/j.jnucmat.2011.06.012

Chaouadi, R., and Gerard, R. (2013). Confirmatory investigations on the flux effect and associated unstable matrix damage in RPV materials exposed to high neutron fluence. *J. Nucl. Mater.* 437, 267–274. doi:10.1016/j.jnucmat.2013.02.029

Chaouadi, R. (2005). *An engineering radiation hardening model for RPV materials. SCK.CEN Report R-4235*. Belgium: SCK.CEN, Mol.

Chaouadi, R., van Walle, E., and Gerard, R. (2008). "The RADAMO experimental program in support of the RPV radiation hardening modeling activities at SCK.CEN," in Workshop on Trend Curve Development for Surveillance Data with Insight on Flux Effects at High Fluence: Damage Mechanisms and Modeling, Mol, Belgium, November 2008.

Dohi, K., Nishida, K., Nomoto, A., Soneda, N., Matsuzawa, H., and Tomimatsu, M. (2009). "Effect of additional irradiation at different fluxes on RPV embrittlement PVP2009-77658," in Proc ASME Pressure Vessels And Piping Division Conference, PVP2009, Prague, Czech Republic, July, 2009.

Dohi, K., Soneda, N., Onchi, T., Ishino, S., Odette, G. R., and Lucas, G. E. (2001). "Dose rate effect in low copper steels irradiated in FNR," in Proc. Workshop on Dose Rate Effects in Reactor Pressure Vessel Materials, Squaw Valley, CA, USA, November 2001.

Eason, E. D., Odette, G. R., Nanstad, R. K., and Yamamoto, T. (2007). *A physically based correlation of irradiation-induced transition temperature shifts. ORNL/TM-2006/530*. Oak Ridge, Tennessee: Oak Ridge National Laboratory.

Eason, E. D., Wright, J. E., and Odette, G. R. (1998). *Improved embrittlement correlations for reactor presure vessel steels. NUREG/CR-6551*. Wahsington DC, USA: US Nuclear Regulatory Commission. November.

EPRI (2009). *BWR reactor pressure vessel embrittlement correlation studies. BWRVIP-216NP: BWR Vessels and internals project*. Palo Alto, CA, USA: EPRI.

Gerard, R., Lucon, E., Scibetta, M., Chaouai, R., and Van Walle, E. (2006). "Reactor pressure vessel steels embrittlement at very high neutron doses," in 6th Int. Conf. On Contribution Of Materials Investigtions To Improve The Safety And Performance Of LWRs: Fontevraud VI, Avignon, France, September 2006.

Hashimoto, Y., Nomoto, A., Kirk, M., and Nishida, K. (2021). Development of new embrittlement trend curve based on Japanese surveillance and atom probe tomography data. *J. Nucl. Mater.* 553, 153007. doi:10.1016/j.jnucmat.2021.153007

Hawthorne, J. R., and Hiser, A. L. (1990). *Influence of fluence rate on radiation-induced mechanical property changes in RPV steel NUREG/CR 5493*. Washington, DC, United States: US Nuclear Regulatory Commission.

Hein, H. (2015). "Position paper on RPV radiation embrittlement issues based on the outcome of the Euratom FP7 project LONGLIFE," in *Trans. SMiRT-23* (Manchester, UK).

Hein, H., and May, J. (2008). "Review of irradiation surveillance and test reactor data of RPV steels used in German LWR in relation to the flux effect issue," in Workshop on Trend Curve Development with insight on Flux Effects at High Fluence: Damage Mechanisms and Modeling, Mol, Belgium, November 2008.

Hyde, J. M., Ellis, D. E., English, C. A., and Williams, T. J. (2001). "Microstructural evolution in high-Ni submerged arc welds," in *Effects of radiation on materials: 20th int. Symp. ASTM STP 1405*.

Japan Nuclear Energy Safety Organisation (2009). *Report on radiation embrittlement at high fluences. 08 base metal report-0005*. January.

Kirk, M., and Erickson, M. (2021). *Methods to address the effects of irradiation embrittlement in section XI of the ASME code estimation of an irradiated reference temperature using either traditional Charpy approaches or master curve data. 3002020911*. Palo Alto, CA, USA: EPRI.

Kirk, M., and Ferreno Blanco, D., (2022) "Evaluation of the ASTM E900-15 DT41J prediction equation in light of new data," in ASTM Symposium on Trend Curve Development, Prague, Czech Republic, April 2022.

Kryukov, A., Nanstad, R. K., and Brumovsky, M. (2014). Common comparison of the irradiation embrittlement of WWER/PWR reactor pressure vessel steels. *Nucl. Eng. Des.* 273, 175–180. doi:10.1016/j.nucengdes.2014.03.018

Kuleshova, E. A., Gurovich, B. A., Lavrukhina, Z. V., Maltsev, D. A., Fedotova, S. V., Frolov, A. S., et al. (2017). Study of the flux effect nature for VVER-1000 RPV welds with high nickel content. *J. Nucl. Mater.* 483, 1–12. doi:10.1016/j.jnucmat.2016.10.030

Langer, R., Bartsch, R., and Foehl, J. (2001). "Irradiation results for different reactors," in Proc Workshop on Dose Rate Effects in Reactor Pressure Vessel Materials, Squaw Valley, CA, USA, November 2001.

Langer, R., Bartsch, R., and Nagel, G. (2000). "Irradiation behavior of submerged arc welding materials with different copper contents," in *Effects of radiation on materials: 19th int. Symp. ASTM STP 1366* (West Conshohocken, PA, Unites States: ASTM), 235–244.

Lindgren, K., Boasen, M., Stiller, K., Efsing, P., and Thuvander, M. (2017). Evolution of precipitation in reactor pressure vessel steel welds under neutron irradiation. *J. Nucl. Mater.* 488, 222–230. doi:10.1016/j.jnucmat.2017.03.019

Mader, E. V. (1995). *Kinetics of irradiation embrittlement and the post-irradiation annealing of nuclear reactor pressure vessel steels: D. Phil dissertation. UMI No. 9617674*. Santa Barbara, CA, USA: Deaprtment of Materials Engineering, University of California. August.

Mathew, J., Parfitt, D., Wilford, K., Riddle, N., Alamaniotis, M., Chroneos, A., et al. (2018). Reactor pressure vessel embrittlement: insights from neural network modelling. *J. Nucl. Mater.* 502, 311–322. doi:10.1016/j.jnucmat.2018.02.027

Nanstad, R., Almirall, N., Server, W., Wells, O., Sokolov, M., Long, E., et al. (2022). "On high fluence irradiation hardening of nine RPV surveillance steels in the UCSB ATR-2 experiment: implications to extended life embrittlement predictions," in ASTM Symposium on Trend Curve Development, Prague, Czech Republic, April 2022.

Odette, G. R., and Lucas, G. E. (1998). Recent progress in understanding reactor pressure vessel steel embrittlement. *Radiat. Eff. Defects Solids* 144, 189–231. doi:10.1080/10420159808229676

Odette, G. R., Lucas, G. E., and Klingensmith, D. (2001). "Recent data and analysis on flux effects on RPV embrittlement," in Proc. Workshop on Dose Rate Effects in Reactor Pressure Vessel Materials, Squaw Creek, CA, USA, November 2001.

Odette, G. R., Mader, E. V., Lucas, G. E., Phythian, W. J., and English, C. A. (1993). "The effect of flux on the irradiation hardening of pressure vessel steels," in *Effect of radiation on materials: 16th int. Symp. ASTM STP 1175* (Philadelphia, PA, USA: ASTM), 373–393.

Odette, G. R., Yamamoto, T., and Klingensmith, D. (2005). On the effect of dose rate on irradiation hardening of RPV steels. *Philos. Mag.* 85 (4-7), 779–797. doi:10.1080/14786430412331319910

Odette, G. R., Yamamoto, T., Wells, P. B., and Almirall, N. (2016). *High fluency low flux embrittlement models of LWR reactor pressure vessel embrittlement and a supporting database from the UCSB ATR-2irradiation experiment. Final Report Project No. 11-3176*. Santa Barbara, CA, Unites States: US DOE Nuclear Energy University Program. January.

Petrequin, P. (1996). "IAEA Report IWG-LMNPP-95/5-Vol.1 Proc Specialists meeting on irradiation embrittlement and mitigation," in Proc Specialists meeting on irradiation embrittlement and mitigation, Espoo, Finland, October 23–26, 1995. Vienna, Austria: International Atomic Energy Agency, 95–147.

Server, W., English, C. A., Naiman, D., and Rosinski, S. (2001). *Charpy embrittlement correlations - status of combined mechanistic and statistical bases for US RPV steels: PWR Materials Reliability Program (PWRMRP) EPRI Report 1000705*. Palo Alto, CA, USA: EPRI.

Sizmann, R. (1978). The effect of radiation upon diffusion in metals. *J. Nucl. Mater.* 69-70, 386–412. doi:10.1016/0022-3115(78)90256-8

Soneda, N. (2007). "Multiscale computer simulations and predictive modeling of RPV embrittlement," in *MATGEN-IV, cargese, corsica, France*. September.

Soneda, N. (2010). "Current understanding on the mechanism of neutron irradiation embrittlement," in USNRC Speonsored Workshop on Development of Predictive Models Of Neutron Irradiation Embrittlement In Reactor Pressure Vessel Steels To Support Worldwide Efforts On Nuclear Power Plant Life Extension, Rockville, USA, September 2010.

Soneda, N., Dohi, K., Nishida, K., Nomoto, A., and Matsuzawa, H. (2008). "Effect of fluence and flux on the embrittlement of highly irradiated RPV steels," in Workshop on Trend Curve Development, Mol, Belgium, November 2008.

Soneda, N., Dohi, K., Nishida, K., Nomoto, A., Tomimatsu, M., Matsuzawa, H., et al. (2009). Microstructural characterization of RPV materials irradiated to high fluences at high flux. *J. ASTM Intl* 6 (7), 102128. doi:10.1520/jai102128

Soneda, N., Nishida, K., Nomoto, A., and Dohi, K. (2015). "Flux effect on embrittlement of reactor pressure vessel steels irradiated to high fluences," in Fontevraud 8: International Symposium on Contribution of Materials Investigations and Operating Experience to LWRs' Safety, Performance and Reliability, Avignon, France, April, 2015.

Soneda, N., and Nomoto, A. (2008). "Characteristics of the new embrittlement correlation method for the Japanese reactor pressure vessel steels," in Proceedings of the 17th International Conference on Nuclear Engineering, ICONE17-75320, Brussels, Belgium, May 11-15, 2008.

Stoller, R. E. (2003). "The effect of neutron flux on radiation-induced embrittlement in reactor pressure vessel steels," in *Effects of radiation on materials: 21st int. Symp. ASTM STP 1447*. Editors M. L. Grossbeck, T. R. Allen, R. G. Lott, and A. S. Kumar (West Conshohocken, PA, USA: ASTM), 326–337.

Stoller, R. E. (2020). "Primary radiation damage formation chapter 1.11," in *Comprehensive nuclear materials*, 293–332.

Tomimatsu, M., Urabe, Y., Sanoh, J., Iida, M., Nakamura, T., and Tamura, A. (1994). "Evaluation of RPV steel surveillance programme in Japanese PWR: radiation embrittlement predictions," in Proceedings of the 3rd International Symposium on Contribution of Materials Investigation to the Resolution of Problems Encountered in Pressurized Water Reactors, Fontevraud, France, May 1994.

Toyama, T., Yamamoto, T., Ebisawa, N., Inoue, K., Nagai, Y., and Odette, G. R. (2020). Effects of neutron flux on irradiation-induced hardening and defects in RPV steels studied by positron annihilation spectroscopy. *J. Nucl. Mater.* 532, 152041. doi:10.1016/j.jnucmat.2020.152041

Wagner, A., Bergner, F., Chaouadi, R., Hein, H., Hernandez-Mayoral, M., Serrano, M., et al. (2016). Effect of neutron flux on the characteristics of irradiation-induced nanofeatures and hardening in pressure vessel steels. *Acta mater.* 104, 131–142. doi:10.1016/j.actamat.2015.11.027

Williams, T., Wilford, K., Odette, G. R., and Yamamoto, T. (2010). "A new model of irradiation hardening in low copper RPV steels from stable matrix damage," in Proc IAEA Technical Meeting on Irradiation Embrittlement and Life Management of Reactor Pressure Vessels in Nuclear Power Plant, Znojmo, Czech Republic, October 2010.

Williams, T. J., and Ellis, D. (2001). "A mechanistically-based model of irradiation damage in low alloy steel sumberged arc welds," in *Effects of radiation on materials: 20th int. Symp. ASTM STP 1405* (West Conshohocken, PA, United States: ASTM), 8–27.

Williams, T. J., Ellis, D., English, C. A., and Hyde, J. (2001a). "A model of irradiation damage in high nickel submerged arc welds," in IAEA/LMNPP Specialists Meeting On Irradiation Embrittlement And Mitigation, Gloucester, UK, May 2001.

Williams, T. J., Ellis, D., and O'Connell, W. (2001b). "Dose rate effects in high and low nickel welds," in Proc. Workshop on Dose Rate Effects in Reactor Pressure Vessel Materials, Squaw Valley, CA, USA, November 2001.

Williams, T. J., Ellis, D., Swan, D. I., McGuire, J., Walley, S. P., English, C. A., et al. (1985). "The influence of copper, nickel and irradiation temperature on the irradiation shift of low alloy steels," in Proc. 2nd ANS Int. Symp. Environmental Degradation of Materials in Nuclear Power Systems - Water Reactors, Monterey, California, USA, September 1985.

Williams, T. J., and Phythian, W. J. (1996). "Electron microscopy and small angle neutron scattering study of precipitation in low alloy steel submerged arc welds," in *Effects of radiation on materials: 17th int. Symp. ASTM STP 1270* (Philadelphia, USA).

Xu, Y., Jia, X., Zhang, C., Ning, G., and Yu, Q. (2000). "The effects of flux on radiation embrittlement of low-copper pressure vessel steels," in Effects of Radiation on Materials: 16th Int. Symp. ASTM STP 1366, West Conshohocken, PA, USA, January 2000 (West Conshohocken, PA, United States: ASTM), 118–126.

Yamamoto, T., Matsui, H., Narui, M., and Dohi, K. (2001). "Flux effects on the subsize Charpy impact properties of neutron irradiated A533B steel," in Proc. Workshop on Dose Rate Effects in Reactor Pressure Vessel Materials, Squaw Creek, CA, USA, November 2001.

Nomenclature

ASTM	American Society for Testing and Materials
ATR	Advanced Test Reactor (MTR in US)
BR2	MTR in Belgium
BWR	Boiling water reactor
CRP	Copper-rich SC
Cm	centimetre
dpa	Displacement per atom
ETC	Embrittlement trend curve
FIM, FIS	French median and upper bound embrittlement trend curves
IAEA	International Atomic Energy Agency
IVAR	Irradiation Variables (radiation campaign)
JEAC	Japan Electrical Association Code
LWR	Light water reactor
MD	Matrix defect
MF	Matrix feature
MNS	SC or precipitate containing mainly manganese, nickel and silicon
MTR	Materials test reactor
N	Neutron
PIA	Post-irradiation annealing
ps	Picosecond
PWR	Pressurised water reactor
Q	Hardening acceleration factor
RADAMO	Belgian embrittlement trend curve
RPV	Reactor pressure vessel
RR	Rolls-Royce
S	Second
SAW	Submerged arc weld
SC	Solute cluster
SCK.CEN	Studiecentrum voor de Toepassingen van de Kernenergie. Centre d'Etude de L'Energie Nucleaire (Belgian Nuclear research centre)
SIA	Self-interstitial atom
SMD, SMF	Stable matrix damage/defect, stable matrix feature
T	Time
UCSB	University of California at Santa Barbara
UMD, UMF	Unstable matrix damage/defect, unstable matrix feature
US	United States of America
UV-P	Irradiation campaign carried out in the University of Virginia and Pluto MTRs
$\boldsymbol{\phi}$	Flux
$\boldsymbol{\phi t}$	Fluence
$\boldsymbol{\phi t_e}$	Effective (flux-compensated) fluence

Frontiers in Nuclear Engineering

TYPE Original Research
PUBLISHED 28 February 2024
DOI 10.3389/fnuen.2024.1347322

OPEN ACCESS

EDITED BY
Anne Campbell,
Oak Ridge National Laboratory (DOE),
United States

REVIEWED BY
Charles M. Folden,
Texas A and M University, United States
Tashiema Ulrich,
Oak Ridge National Laboratory (DOE),
United States

*CORRESPONDENCE
Jessica Blenkinsop,
Jessica.blenkinsop@uknnl.com

RECEIVED 30 November 2023
ACCEPTED 16 February 2024
PUBLISHED 28 February 2024

CITATION
Blenkinsop J, Rivonkar A, Robin M, Carey T, Dunnett B, Suzuki-Muresan T, Percin C, Abdelouas A and Street J (2024), Methods for the destruction of oxalic acid decontamination effluents.
Front. Nucl. Eng. 3:1347322.
doi: 10.3389/fnuen.2024.1347322

Methods for the destruction of oxalic acid decontamination effluents

Jessica Blenkinsop[1]*, Aditya Rivonkar[2], Mathurin Robin[2], Thomas Carey[1], Barbara Dunnett[1], Tomo Suzuki-Muresan[2], Cavit Percin[2], Abdesselam Abdelouas[2] and Jonathan Street[3]

[1]National Nuclear Laboratory (NNL), Cumbria, United Kingdom, [2]Subatech Laboratory, IMT Atlantique CNRS/N2P3 Nantes University, Nantes, France, [3]Sellafield Ltd., Cumbria, United Kingdom

Oxalic acid is encountered within industrial processes, spanning from the nuclear sector to various chemical applications. The persistence and potential environmental risks associated with this compound underscore the need for effective management strategies. This article presents an overview of different approaches for the destruction of oxalic acid. The study explores an array of degradation methodologies and delves into the mechanistic insights of these techniques. Significant attention is channeled towards the nuclear industry, wherein oxalic acid arises as a byproduct of decontamination and waste management activities. An integral aspect of decommissioning efforts involves addressing this secondary waste-form of oxalic acid. This becomes imperative due to the potential release of oxalic acid into waste streams, where its accommodation is problematic, and its capacity to solubilize and transport heavy metals like Pu is a concern. To address this, a two-tiered classification is introduced: high concentration and low concentration scenarios. The study investigates various parameters, including the addition of nitric acid or hydrogen peroxide, in the presence of metallic ions, notably Mn^{2+} and Fe^{2+}. These metallic ions are common components of effluents from metallic waste treatment. Additionally, the impact of UV light on degradation is explored. Investigations reveal that at high concentrations and with the influence of hydrogen peroxide, the presence of metallic cations accelerates the rate of destruction, demonstrating a direct correlation. This acceleration is further enhanced by exposure to UV light. At low concentrations, similar effects of metallic cations are observed upon heating the solution to 80°C. The rate of destruction increases proportionally with hydrogen peroxide concentration, with an optimal oxalic acid to hydrogen peroxide ratio of 1:100. Interestingly, a low-power UV light exerted no discernible effects on the destruction rate; heating alone proved sufficient. In essence, regardless of concentration, the degradation of oxalic acid with hydrogen peroxide experiences acceleration in the presence of metallic ions such as Mn^{2+} and Fe^{2+}.

KEYWORDS

oxalic acid, destruction, nitric acid, UV light, hydrogen peroxide, nuclear decommissioning

1 Introduction

Oxalic acid ($C_2H_2O_4$) is a naturally-occurring organic compound found in plants (Mitchell et al., 2019). The use of oxalic acid is observed over a variety of industries and applications. This ranges from the removal of rusts for managing the environmental quality of metals (Wang Q et al., 2023), the conservation of contemporary acrylic paintings (Solbes-García et al., 2017) and the synthesis of graphitic carbon nitrides (Zhang et al., 2022), among many others.

Decontamination is an essential step in the life cycle of nuclear power plants to limit the potential release of radioactive species and reduce the risk to those working on plants. Contamination may be deemed "fixed", where it is firmly adhered to a surface, or "loose", where it may be easily removed from a surface via non-destructive methods; both of these present individual challenges. While washes with water or weakly concentrated nitric acid may be suitable for loose contamination, more invasive techniques may be required for the removal of fixed contamination of metal surfaces. Some decontamination methods explored include, but are not limited to the implementation of laser technology (Wang F et al., 2023), plasma decontamination (Zhong et al., 2021) as well as chemical decontamination encompassing the use of gels and foams (Gossard et al., 2022) and reagents like oxalic acid (Zhong et al., 2021).

Oxalic acid is known to strongly solubilize most iron oxides (Ocken, 1999). It is used as a rust-removal complexing agent that is also good for decontaminating highly damaged corroded surfaces. Oxalic acid dissolves deposited MnO_2. It can also serve as a corrosion inhibitor for carbon steels, limiting over-aggressive digestion during decontamination and so protecting the structural integrity of structures made of such steel. When oxalic acid is used in concentrations of less than 1 wt%, the decontamination process can be slow but has minimal impact on the corrosion of the metal surfaces. Whereas at higher concentrations, typically up to 10 wt%, the decontamination coefficient and treatment time are optimized, but corrosion increases along with chemical secondary waste requiring treatment (Zhong et al., 2021). The treatment of this oxalic acid rich secondary effluents is also an important part of decommissioning activity; this is a necessity due to the potential release of oxalic acid into waste streams where it is unable to be accommodated, or the ability of oxalic acid to solubilize and carry heavy metals such as Pu into waste streams, increasing the criticality risk (Orr et al., 2015).

Oxalic acid can be harmful to both humans and the environment when not properly handled or disposed of. High concentrations of oxalic acid can cause skin and eye irritation, respiratory problems, and even kidney failure (Kliegman and Geme, 2019). Therefore, it is essential to understand the methods for the destruction of oxalic acid to minimize its impact on the environment and human health. Methods for the destruction of oxalic acid to eliminate the risks associated with the secondary waste have been identified in literature. Some techniques, which may be particularly challenging to deploy on licensed nuclear sites and were therefore discarded, include electrolysis (Martinez-Huitle et al., 2004; Shih et al., 2019), ultrasonic degradation (Dükkanci and Gündüz, 2006) and catalytic wet air oxidation (Lee and Kim, 2000; Santos et al., 2021). Other methods from literature which were assessed to be more compatible with nuclear plant operations due to their ease of implementation, potentially using existing plant infrastructure, were identified to be heating with nitric acid (Mason et al., 2008) alongside manganous nitrate ($Mn(NO_3)_2$) (Kubota, 1982; Nash, 2012) and hydrogen peroxide (H_2O_2) (Berry, 1957; Chung et al., 1995; Kim et al., 2000), and well as ultra-violet (UV) light (Beltrán et al., 2002) and ozonation (Ketusky and Subramanian, 2012; Martino et al., 2012). These techniques–thought to be more appropriate for use on nuclear power plants–have been experimented with, as outlined in this paper.

Hydrogen peroxide is used because of the safety of the manipulation and the low cost of the reagents. In the presence of hydrogen peroxide, oxalic acid decomposes to form water and carbon dioxide as shown in Equation 1. UV acts as a catalyst in this reaction and speeds up the process. In parallel, hydrogen peroxide decomposes by a disproportionation reaction to generate water and oxygen, seen in Eq. 2 (Kim et al., 2000).

$$H_2O_2 + H_2C_2O_4 \rightarrow 2CO_2 + 2H_2O \tag{1}$$

$$H_2O_2 \rightarrow H_2O + \frac{1}{2}O_2 \tag{2}$$

In addition to hydrogen peroxide used during the process, it is possible to use manganese as a cation or manganese oxide to increase the reaction kinetics. Indeed, in the presence of nitric acid, manganese is a very powerful catalyst for oxidizing organic compounds such as oxalic acid (Saeed et al., 2013), even in low concentration (few mM). In the case of the Chemical Oxidation Reduction Decontamination (CORD) process, discussed later, various metals are present in solution, including manganese. That is why the catalytic reaction is studied here.

The presence of iron also plays a significant role during this process, acting as the Fenton reagent. Hydrogen peroxide oxidizes iron (II) to iron (III) and produces a hydroxyl radical and a hydroxide ion via the Fenton reaction mechanism shown in Eqs 3–5 (Metelitsa, 1971; Pawar and Gawande, 2015; Haber et al., 1934; Brillas et al., 2009). Iron (III) is then reduced back to iron (II) by another molecule of hydrogen peroxide, producing a hydroperoxyl radical and a proton as seen in Eq. 4. This results in the disproportionation of hydrogen peroxide to create two different oxygen-radical species, with water ($H^+ + OH^-$) as a byproduct.

$$Fe^{2+} + H_2O_2 + H^+ \rightarrow Fe^{3+} + OH^{\cdot} + H_2O \tag{3}$$

$$Fe^{3+} + H_2O_2 \rightarrow Fe^{2+} + HO_2^{\cdot} + H^+ \tag{4}$$

$$RH + OH^{\cdot} \rightarrow R^{\cdot} + H_2O \tag{5}$$

The free radicals generated by this process then engage in secondary reactions. The hydroxyl radical is a powerful, non-selective oxidant. Fenton's reagent is a rapid and exothermic method of oxidizing organic compounds. It results in the oxidation of contaminants to primarily carbon dioxide and water (Kim et al., 2019; Cai et al., 2021). The reactions are accelerated in the presence of UV, therefore known as UV photo-Fenton reaction (Oturan and Aaron, 2014; Kim et al., 2019). The important radical formation steps are seen in Eqs 6, 7 while the radical termination is seen in Eqs 8, 9.

$$H_2O_2 + h\nu \rightarrow 2OH^{\cdot} \tag{6}$$

$$Fe^{3+} + H_2O + h\nu \rightarrow Fe^{2+} + OH^{\cdot} + H^+ \tag{7}$$

$$OH^{\cdot} + OH^{\cdot} \rightarrow H_2O_2 \tag{8}$$

$$Fe^{3+} + OH^{\cdot} + H^+ \rightarrow Fe^{2+} + H_2O \tag{9}$$

As part of the European Union (EU) project 'Pre-disposal management of radioactive waste' (PREDIS), technical work is being carried out internationally across EU-country labs and the United Kingdom. This focuses on innovations in nuclear waste treatments, among which the management of oxalic acid as a secondary waste form is a topic. As previously mentioned, oxalic acid as a decontaminant can be applied at high or low concentrations depending on the desired balance of reaction and corrosion rates (Zhong et al., 2021). This work, carried out at the UK's National Nuclear Laboratory (NNL) and Subatech Laboratory, IMT Atlantique in France has provided an opportunity to test destruction methods using both high and low concentrations of oxalic acid collaboratively. However, the results for the destruction at higher and lower concentrations may not be directly compared due to the differences outlined in the relevant sections. At a higher concentration of oxalic acid (520 mM), destruction using heating with nitric acid with $Mn(NO_3)_2$ and H_2O_2, UV light with H_2O_2 and Fe, and ozonation has been tested by NNL. At a low concentration of oxalic acid (10 mM), the use of H_2O_2 in combination with heating and application of UV light was experimented for oxalic acid destruction at Subatech Laboratory, IMT Atlantique.

2 Materials and methods

2.1 Destruction of oxalic acid at higher concentration

Oxalic acid is being considered for use by Sellafield Ltd. due to its ability to capture and solubilize radionuclides. However, it is considered necessary to establish an effective method for the destruction of oxalic acid as a precaution for its release into waste streams which cannot accommodate it; evaporation methods or *in situ* intervention have both appeared to be attractive destruction methods due to the minimal intervention with existing plant infrastructure which would be required. Hence, for the destruction of oxalic acid at higher concentration starting at 520 mM, methods of heating with nitric acid and use of UV light, Fe (II) and H_2O_2 were experimented. A higher concentration of 520 mM oxalic acid was selected for these experiments, influenced by an existing thermal evaporator at the Sellafield nuclear site where it is thought this destruction process could be carried out, and the solubility limit of oxalic acid in high molarity nitric acid. Experiments were generally run up to a 14-day point, or until analysis indicated that the oxalic acid had been fully destroyed to the limit of detection (3 mM).

Oxalic acid dihydrate ($C_2H_2O_4{\cdot}2H_2O$), standard grade nitric acid (HNO_3, 70% w/w), standard grade sulfuric acid (H_2SO_4, 95%–98% w/w), Mohr salt ($(NH_4)_2Fe(SO_4)_2.(H_2O)_6$), hydrogen peroxide ($H_2O_2$, 30% w/v), chromium nitrate ($Cr(NO_3)_3$), nickel nitrate ($Ni(NO_3)_2$), iron (II) nitrate ($Fe(NO_3)_2$), manganese nitrate ($Mn(NO_3)_2$), potassium permanganate ($KMnO_4$), sodium hyposulfite ($Na_2S_2O_3$), amido sulfuric acid (H_3NSO_3), potassium iodide (KI) and ammonium molybdate ($(NH_4)_6Mo_7O_{24}$) were sourced from Fisher Scientific UK Ltd. to their highest available purity and used. 18 MΩ cm deionized water used was sourced from the laboratory water purifier system.

2.1.1 Heating with nitric acid

For this technique 250 mL of liquor was heated to either 50°C, 75°C or 100°C in a round bottomed flask placed within a thermostatically controlled isomantle accurate to ±3°C. To prevent the evaporation of liquor from each heated round bottomed flask, glass condensers cooled with water at approximately 10°C were employed. Each round bottom flask was equipped with three ports; one of which was used for the condenser, one for the thermostatic temperature probe, and another which was stoppered but used for taking samples of ~2 mL using a Pasteur pipette. Aliquots (1 mL) of this sample were then used for analysis once the solution had cooled to room temperature to ensure accurate volumes were analyzed.

The liquor of all experiments contained 520 mM oxalic acid and 8 M HNO_3. Varying concentrations of $Mn(NO_3)_2$ between 0.025 and 50 mM were also added to the experiments for catalytic purposes. A small number of experiments were also supplemented with minor concentrations of nitrates of Fe, Cr and Ni (100, 25 and 14 ppm, respectively) so as to account for the corrosion products of stainless-steel evaporator systems on the Sellafield site. For solutions also containing H_2O_2, the required amount of 30% w/v H_2O_2 was added. All solutions were made to 250 mL with the addition of 18 MΩ cm deionized water.

2.1.2 Use of UV light, Fe and H_2O_2

For this method, 250 mL solution with a starting concentration of 520 mM oxalic acid was used. Fe (II) in the form of Mohr salt (ammonium iron (II) sulfate) was also added to some experimental solutions, equating to a concentration of 5.2 mM Fe. With the solution in a clear glass Drechsel vessel, UV light at a wavelength of 365 nm was shone towards the solution; the intensity of the UV light was controlled by using either one or two UVP UVGL-58 handheld lamps. In order to initiate a photo-Fenton-like reaction, each experiment was also dosed at regular intervals with 30% w/v H_2O_2 to give an addition of 12 mmoles or 23 mmoles to the solution. Control experiments for this technique were also carried out without exposure of the solution to UV light. For one type of control, the glass Drechsel vessel containing an experimental solution was not exposed to the UV lamp but was left uncovered in the laboratory, therefore being exposed to environmental light. For the other control, the glass Drechsel vessel containing an experimental solution was covered entirely with aluminum foil, thereby preventing the solution from being exposed to any light. In order to direct any gases produced during the destruction process away from the operator, all vessels were fitted with an air condenser (not temperature controlled) in the port of the Drechsel vessel.

For the consistent dosing of the experiments and the regular taking of samples for analysis, the condenser was removed from the Drechsel port. When taking samples, a 1 mL volume was taken from the vessel and used for analysis. The UV lamps, if used, were turned off during dosing or sampling to avoid UV exposure to the operator.

2.1.3 Sampling and analysis

Samples were taken from experiments at regular intervals, each laboratory working day. Oxalic acid concentration was quantified for each sample by two analysis methods: ultraviolet-visible (UV-Vis) spectroscopy and titration with $KMnO_4$. These techniques were selected to allow for simple and quick quantification of oxalic acid while the experiments were ongoing. For both analysis techniques, the 1 mL sample taken from the experiment was first diluted by a dilution factor (DF) of 10.

2.1.3.1 UV-vis analysis

For UV-Vis analysis, 0.25 mL of the DF 10 sample was added to 10 mL of a solution containing 3 M HNO_3 and 0.03 M H_3NSO_3. Then 0.1 mL of 0.1 M $KMnO_4$ was added, and the mixture agitated by swirling the container; this was then left undisturbed for 5 min to allow a pink color to develop. After this point, two Fisherbrand™ disposable semi-micro cell cuvettes were filled with approximately 1.5 mL of the solution. The cuvettes were then each placed in a Thermo Scientific™ GENESYS™ 40 UV-Vis spectrophotometer and the solutions analyzed at 526 nm. The absorbance of the sample at this wavelength was recorded. As analysis at this wavelength produced similar results to analysis with $KMnO_4$ titration, it is not believed that interferences occurred at this wavelength.

A calibration curve using solutions of known concentrations of oxalic acid (0–0.7 M) was plotted to establish the relationship between absorbance and oxalic acid concentration. The straight-line equation from this calibration was used to calculate the concentrations of the samples taken from the experiments.

2.1.3.2 $KMnO_4$ titration for oxalic acid

For the analysis by $KMnO_4$ titration, 7 mL 18 MΩ cm deionized water and 5 mL 1 M H_2SO_4 were added to a conical flask and agitated on a magnetic stirrer heater plate. A 3 mL aliquot of the DF 10 experimental sample was then also added to the flask, and the mixture was heated to 60°C whilst being stirred at 60 rpm. A 0.005 M $KMnO_4$ solution was prepared and added to a burette over the heated solution; this was added to the solution dropwise until a color change from colorless to pale pink. The concentration of oxalic acid in the sample was calculated by using the volume of $KMnO_4$ titrated, taking into account the DF and the molar ratio between the oxalic acid and $KMnO_4$ in the reaction shown by Eq. 10.

$$2KMnO_4 + 3H_2SO_4 + 5(COOH)_2 \rightarrow K_2SO_4 + 2MnSO_4 + 8H_2O + 10CO_2 \tag{10}$$

The limit of detection for this method was established to be 3 mM oxalic acid.

2.1.3.3 Titration with $Na_2S_2O_3$

For experiments where H_2O_2 was added, a further analysis method was also necessary to first quantity the concentration of H_2O_2 in the sample. This was essential as H_2O_2 can react with $KMnO_4$ (Bailey and Taylor, 1937; Li et al., 2011; Sun et al., 2019; Khan, 2021), meaning that its presence interferes with the analysis outlined above and result in an overestimation of the concentration of oxalic acid in a sample.

For this analysis, the DF 10 experimental sample was added to a conical flask along with 50 mL 18 MΩ cm deionized water, 10 mL 1 M H_2SO_4, 12.5 mL 0.09 M KI solution and 2 drops of ammonium molybdate solution. The mixture was stirred at ambient temperature at 60 rpm. $Na_2S_2O_3$ at 0.001 M was then added dropwise from a burette until a subtle color change from colorless to pale yellow was observed. At this point, 2 mL of starch solution was then added to the flask to initiate a color change from pale yellow to black to indicate the presence of iodine. At this point, further additions of $Na_2S_2O_3$ were made from the burette until a color change from black to colorless, indicating the end point of the titration, was observed. The total volume of $Na_2S_2O_3$ titrated was then used to calculate the concentration of H_2O_2 in the sample, taking into account the DF and the molar ratio between the H_2O_2 and $Na_2S_2O_3$ in Equations 11, 12.

$$H_2O_2 + 2KI + H_2SO_4 \rightarrow I_2 + K_2SO_4 + 2H_2O \tag{11}$$

$$I_2 + 2Na_2S_2O_3 \rightarrow Na_2S_4O_6 + 2NaI \tag{12}$$

This analysis technique was used alongside the methods for oxalic acid quantification. Therefore, the calculated concentration of H_2O_2 from this analysis technique was subtracted from the calculated oxalic acid values. This achieved an oxalic acid quantification representative of the sample, as the interference of H_2O_2 with $KMnO_4$ was considered.

2.2 Destruction of oxalic acid at lower concentrations

The lower concentration of oxalic acid comes from the Chemical Oxidation Reduction Decontamination (CORD) process used for decontamination of stainless steels and Ni based alloys. CORD is a decontamination technique used during maintenance and decommissioning of nuclear power plants, mainly for the primary circuit and steam generator circuit (Ocken, 1999). It is a multi-step process where potassium permanganate/permanganic acid is used in the oxidation step as seen in Eq. 13, followed by oxalic acid in the destruction and reduction step, which destroys the MnO_2 formed during the oxidation step, and also dissolves and complexes the iron oxides, as in Eqs 14, 15 respectively (Ocken, 1999; Rivonkar et al., 2022).

$$Cr_2O_3 + 2MnO_4^- + H_2O \rightarrow 2HCrO_4^- + 2MnO_2 \tag{13}$$

$$MnO_2 + H_2C_2O_4 + 2H^+ \rightarrow Mn^{2+} + 2CO_2 + 2H_2O \tag{14}$$

$$Fe_3O_4 + 4H_2C_2O_4 \rightarrow 3FeC_2O_4 + 2H_2O + 2CO_2 \tag{15}$$

The final solution is therefore rich in oxalic acid and its destruction is a precursor to the treatment of CORD effluents, as it is seen to affect the efficiency of precipitation of chrome (Remoundaki et al., 2007; Rivonkar et al., 2022).

2.2.1 Oxidation by H_2O_2 under effects of temperature and UV

The concentration of oxalic acid was determined from the concentrations used during the CORD process (ranging from 5 mM to 18 mM) (Ocken, 1999; Rivonkar et al., 2022). A middle ground concentration of 10 mM oxalic acid (dihydrate, ACS reagent, ≥95.0%, Alfa Aesar) was used and a volume of 100 mL was used. The hydrogen peroxide (30% in water, ThermoFisher) was mixed into the solution once the solution was at the desired temperature, i.e., when the solution reached 80°C, by heating on a heating plate, in the case of high temperature tests. The parameters temperature, concentration of H_2O_2 and UV radiation were evaluated. The concentrations of hydrogen peroxide tested were 100 mM, 500 mM and 1 M. Tests were carried out at 80°C corresponding to the operational temperature of the CORD process. The effects of UV radiation

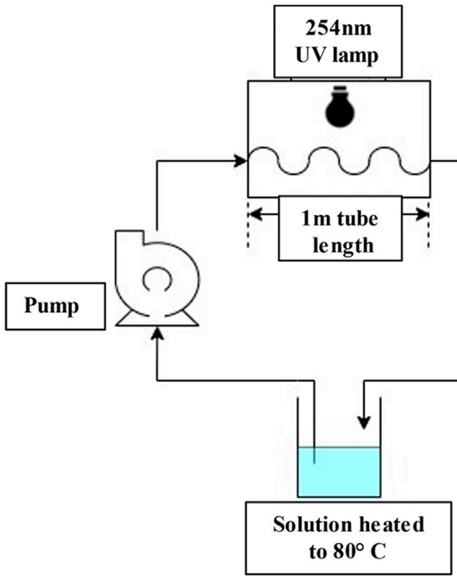

FIGURE 1
Illustration of the dynamic system used with the UV lamp.

were tested at room temperature (22°C) and at 80°C temperature, using an UV lamp (VL-6. C, 254 nm, 6W, Fisher Bioblock Scientific). The summarized methodology of the different conditions is shown in Figure 2. Contact times of 2, 4, 6 and 24 h were applied under all conditions. The measurement of oxalate concentration was carried out by taking 5 mL aliquots at all contact times and done by ion chromatography (881 Compact Pro - Anion, Metrohm) with an anion column (Metrosep A Supp 16–250/2.0, Metrohm), a flow rate of 0.15 mL/min, and a conductivity detector. The eluent used are prepared for 7.5 M Na_2CO_3 (anhydrous, 99.95%, Acros Organics) and 0.5 M NaOH (50%, Merck).

For the high temperature experiments using UV, the sample volume was increased to 300 mL to account for the increased volume of the loop, was placed in a glass bottle and heated on a heating plate up to 80°C and pumped through a UV chamber using a peristaltic pump (Masterflex ISM945D, 4 channels, Ismatec), at a flow rate of 10 mL/min through a Tygon R3607 flexible tube (ID 2.79 mm, Saint-Gobain Tygon LMT-55). A total length of 1 m of tube was exposed to UV which implied a contact time of 38 s. The solution was then mixed into the same bottle on the heating plate. An illustration of this setup can be seen in Figure 1. For room temperature, the solution was placed into 40 mL polypropylene bottles and placed under the UV lamp.

2.2.2 Influence of Mn and Fe ions

To test the influence of manganese and iron cations on the kinetics of oxalic acid destruction, three different solutions were created using salts of manganese (II) chloride (dihydrate, 99%, Merck) and iron (II) chloride (tetrahydrate, 99%, Sigma Aldrich). Concentrations of 0.8, 3 and 7.5 mM Mn^{2+} and 0.14, 0.5 and 1.25 mM Fe^{2+} were used, respectively. A ratio of 6:1 between Mn: Fe was maintained. The reasoning behind these values is explained in Section 3.2.3.

A summary of all the different conditions can be seen in Figure 2.

3 Results

3.1 Destruction of oxalic acid at higher concentration

3.1.1 Heating in nitric acid and Mn

Figure 3 shows the data plotted from the 50°C experiments, with and without the presence of $Mn(NO_3)_2$ as a catalyst. When no manganese was present, very little oxalic acid was destroyed, and after approximately 16 days, the oxalic acid concentration was similar to the starting concentration. As the concentration of manganese increased, so did the rate of oxalic acid destruction. Very little destruction of oxalic acid was also observed at a manganese nitrate concentration of 5 mM, however at 10 mM and above, the rate of destruction increased greatly. At concentrations of 10 and 25 mM of manganese the reaction between the nitric acid and oxalic acid did not start immediately. Complete oxalic acid destruction occurred in approximately 8 days in 50 mM Mn at 50°C.

As illustrated in Figure 4, the time to completely destroy roughly 520 mM of oxalic acid can be further decreased by increasing the temperature from 50°C to 75°C. Different concentrations of manganese were added, from 0.025 to 50 mM to establish at what point the catalytic effect of the Mn at the concentration used would achieve total destruction of the oxalic acid at 75°C. Total destruction could likely be achieved without the presence of Mn, but over a considerably longer timescale than if the catalyst was used. Experiments at the highest Mn concentration (50 M and 25 mM) showed that destruction could be achieved in under 2 days.

Figure 5 shows the rate of oxalic acid destruction when heated with nitric acid at 100°C. Significantly faster oxalic acid destruction was observed with 50 mM Mn, complete destruction occurring in approximately 4 h. This time period was much longer (~30 h) when the Mn catalyst was not present under similar conditions.

Using the experimental data, the half-life (T ½) of oxalic acid under the conditions tested has been calculated, shown in Table 1. In Table 1, the time to destroy 520 mM of oxalic acid to the limit of detection under the conditions is also shown. For experiments using nitric acid only and nitric acid with 50 mM Mn, the activation energy for the destruction reaction has also been calculated. Calculation of activation energy was not possible for other experiments due to these not being carried out at all three temperatures (50°C, 75°C and 100°C). Table 1 corresponds with the trends shown in Figure 3, Figure 4 and Figure 5, with increased temperature and Mn catalyst concentration being associated with quicker oxalic acid destruction.

3.1.2 Treatment via UV light, H_2O_2 and the addition of Fe

Figure 6 shows the results obtained from the tests focused on the destruction of oxalic acid using the photo-Fenton reaction at ambient temperature. Data showed the most effective tested conditions were using UV light, doping with 23 mmoles of H_2O_2

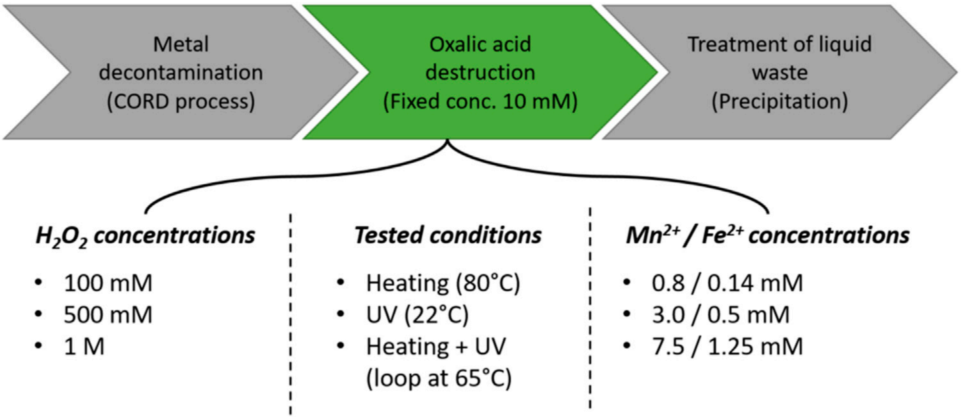

FIGURE 2
Overview of the different parameters tested in order to optimize the low concentration of oxalic acid destruction stage.

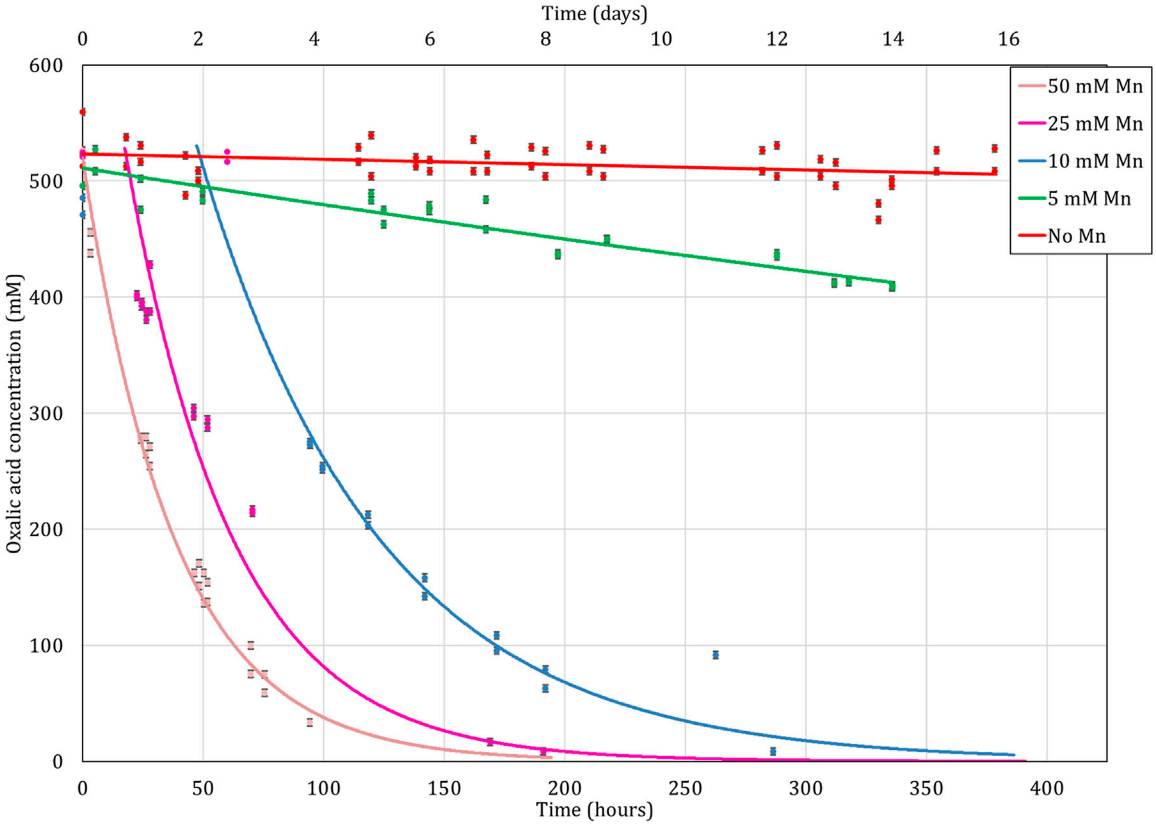

FIGURE 3
Destruction of 520 mM oxalic acid by heating with 8 M nitric acid at 50°C as a function of time. Exponential trendlines fitted.

twice each working day and the solution containing 5.2 mmoles Fe. Complete oxalic acid destruction was achieved within 6 days. When the mmoles of H_2O_2 was approximately halved the destruction time was extended to ~8 days. Note: a plateau in the destruction rate was observed between 2 and 4 days, which coincided with a gap in the H_2O_2 doping over a weekend where addition of the H_2O_2 was not able to be done by an operator. This plateau was not observed when the experiment was doped with 23 mmoles of H_2O_2 as in this case an excess of H_2O_2 was added, meaning there was enough H_2O_2 to sustain the destruction over the weekend. Additional experiments were performed to assess the impact of removing Fe and UV light. Much slower destruction was observed under these conditions, the complete destruction is estimated to be achieved in between 9 and 11 days when the data is linearly extrapolated.

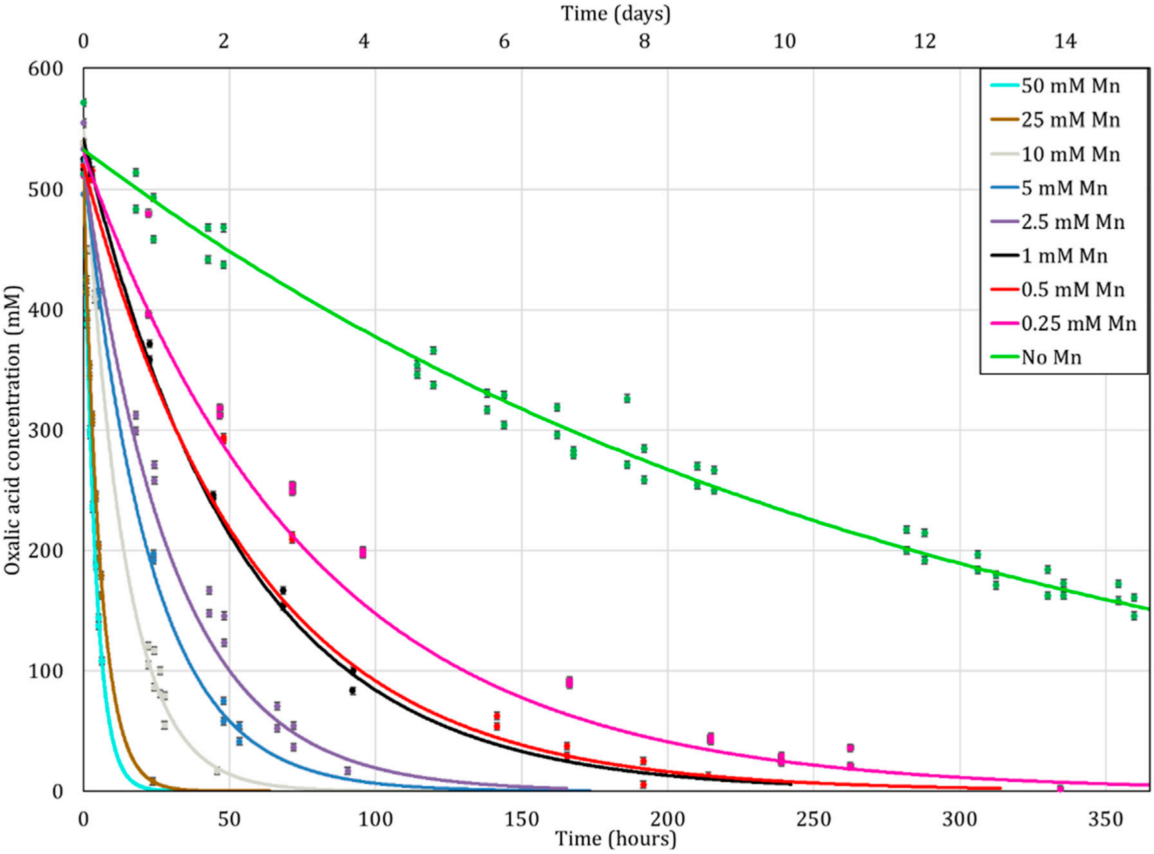

FIGURE 4
Destruction of oxalic acid by heating with 8 M nitric acid at 75°C as a function of time. Exponential trendlines fitted.

3.2 Destruction of oxalic acid at lower concentration

3.2.1 Effects of different concentrations of hydrogen peroxide

Figure 7 shows the effects of different concentrations of hydrogen peroxide observed over 24 h at 80°C, for a fixed concentration of 10 mM oxalic acid. It was observed that the efficiency of oxalic acid destruction increased as the concentration of hydrogen peroxide was increased, with the highest efficiency seen at 1 M H_2O_2, a ratio of 1:100 oxalic acid: hydrogen peroxide (O:H). With this ratio of 1:100, about 94% of the oxalic acid was destroyed in 24 h. It was also observed that the degradation of the oxalic acid is rapid after mixing with hydrogen peroxide and slows down as H_2O_2 starts to be consumed. Due to the excess of hydrogen peroxide, the rate of reaction is initially high but slows down as it is consumed. It could potentially lead to increased gas production or heat generation (exothermic reaction). As there was no sampling carried out between 6 and 24 h, the rate of degradation during this period is not precisely determined. Therefore, it is possible that the degradation stopped before 24 h.

These results were in accordance with the work published by Mailen et al. and Kim et al., who found the oxalic destruction rate increases with increasing concentration of hydrogen peroxide (Mailen et al., 1981; Kim et al., 2019). Kim et al. noticed a significant reduction in oxalic acid concentrations with a ratio of 1:2 in oxalic acid:hydrogen peroxide (O:H), albeit with the use of UV. The minimum ratio in our case was 1:10 (O:H), and the rate of destruction increased at 1:50 and was the highest at 1:100. The best-case ratio of 1:100 (O:H) was therefore selected for further tests going forward.

3.2.2 Effect of different conditions of treatment

Figure 8 shows the influence of UV at room temperature (22°C) and at 80°C using the system in Figure 1, in comparison to only heating at 80°C without UV exposure. At a 1:100 (O:H) ratio, it was observed that heating the solution to 80°C led to the highest degradation of oxalic acid (94% destroyed in 24 h), as in section 3.2.1, whilst exposure to UV at room temperature appeared to be least efficient (29% destroyed in 24 h). This suggests the relative inefficiency of the 6 W, 254 nm UV at the testing conditions. The combination of heating and UV lead to lower destruction efficiency as compared to just heating over 24 h, which was contradictory to section 3.2.1 and not seen in literature either. But after several tests, it was observed that the temperature of the solution at the exit of the UV chamber seen in Figure 1, was roughly 65°C, which was significantly lower than the intended temperature (80°C) used in the heating tests in the absence of UV. The loss of temperature was due to the long length of the loop, and there was no thermal insulation in place. The temperature of the bulk solution was therefore not stable at 80°C and the lower temperature would explain the lower efficiency as it led to a more gradual degradation.

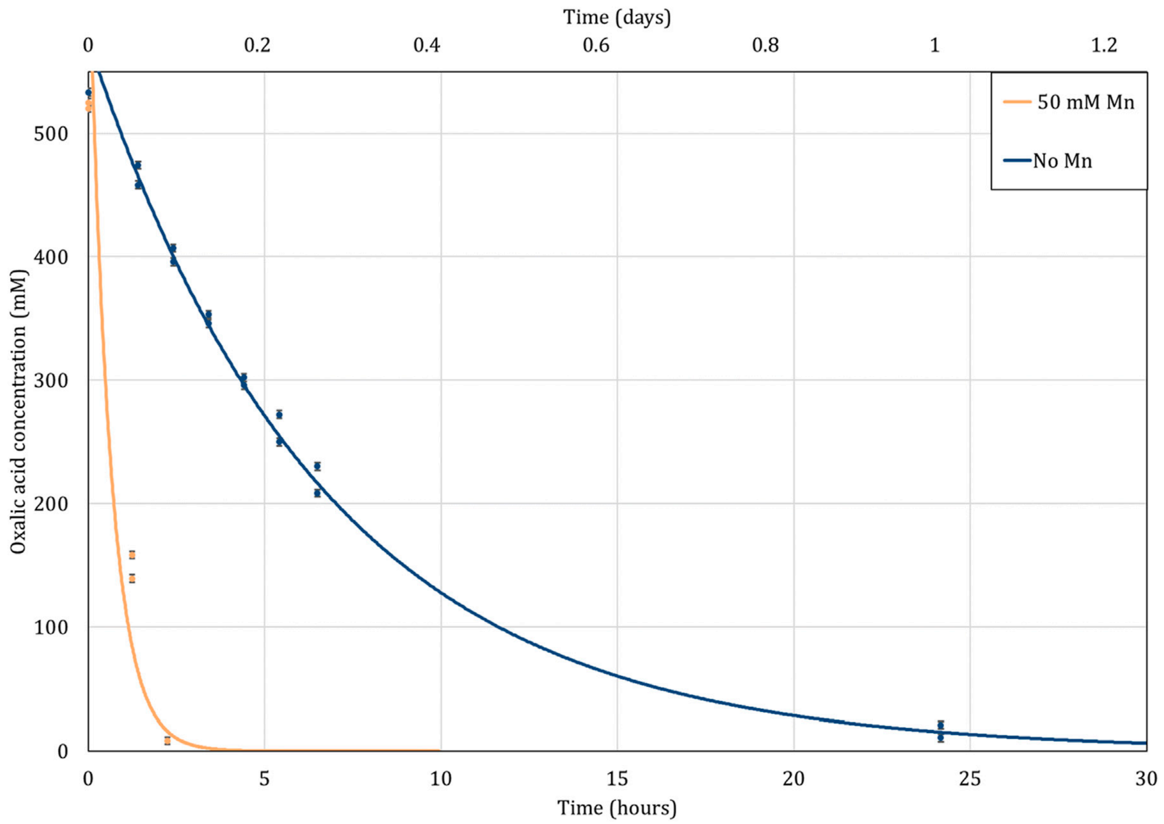

FIGURE 5
Destruction of oxalic acid by heating with 8 M nitric acid at 100°C as a function of time. Exponential trendlines fitted.

TABLE 1 Calculated half-life (hours) and calculated days taken to destroy 520 mM oxalic acid to the limit of detection under experimental conditions tested.

	50°C		75°C		100°C		Activation energy (kJ mol^{-1})
	T ½ (hrs)	*Days to destruction*	*T ½ (hrs)*	*Days to destruction*	*T ½ (hrs)*	*Days to destruction*	
8 M HNO_3	10,599	3,401	205	66	5	2	154
8 M HNO_3 and 0.25 mM $Mn(NO_3)_2$	-	-	55	18	-	-	-
8 M HNO_3 and 0.5 mM $Mn(NO_3)_2$	-	-	40	13	-	-	-
8 M HNO_3 and 1 mM $Mn(NO_3)_2$	-	-	39	12	-	-	-
8 M HNO_3 and 2.5 mM $Mn(NO_3)_2$	-	-	21	7	-	-	-
8 M HNO_3 and 5 mM $Mn(NO_3)_2$	979	314	16	5	-	-	-
8 M HNO_3 and 10 mM $Mn(NO_3)_2$	52	19	10	3	-	-	-
8 M HNO_3 and 25 mM $Mn(NO_3)_2$	31	11	4	1	-	-	-
8 M HNO_3 and 50 mM $Mn(NO_3)_2$	27	9	3	0.9	0.5	0.1	81

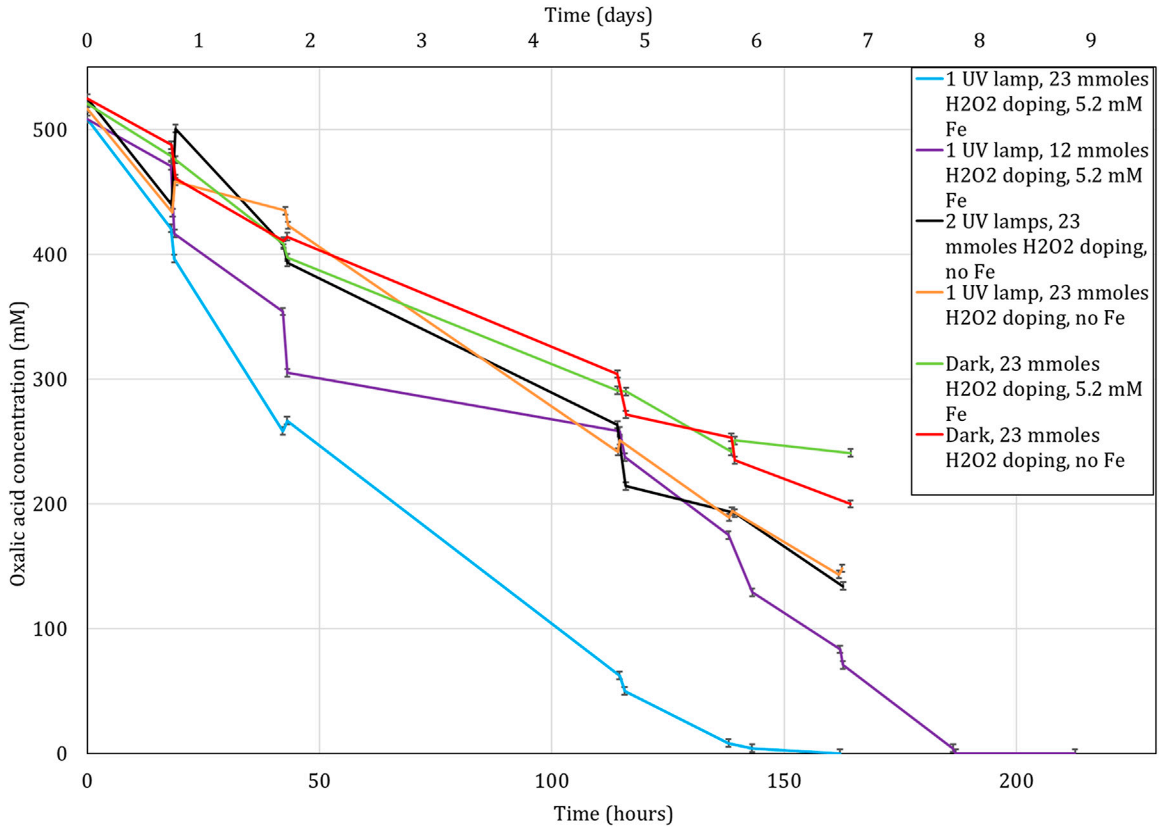

FIGURE 6
Destruction of oxalic acid by UV light, H_2O_2 and Fe as a function of time. H_2O_2 addition is given in mmoles as this is the amount added to the experiment periodically twice each working day. Lines drawn to guide the eye.

These results using the UV source are in contrast to the work done by Kim et al. and Ketusky et al., who found a 254 nm UV source to significantly affect the reaction rate and therefore the oxalic destruction rate even at lower H_2O_2 concentrations. A couple of hypotheses for this could be drawn with the fact that the power of the UV source in our testing was only 6 W as opposed to 120 W used during the testing by Kim et al., and 1500 W used the decomposition loop of Ketusky (2018); Ketusky et al. (2010). Further reducing the efficiency of the 6 W source used, was the fact that our tests utilized comparatively higher concentrations of H_2O_2 beginning from 100 mM up to 1 M, while Kim et al. described a significantly lower UV transmittance (%) even at 50 mM at 120 W (Kim et al., 2019). This would suggest the combination of higher concentration and lower power of the UV, meant an even lower transmittance through the solution.

It appears that in this scenario, the shortcomings of the UV source were overcome with the use of higher concentrations of H_2O_2 alongside mixing at higher temperature, which led to efficient destruction of the oxalic acid over a period of 24 h.

3.2.3 Effects of Mn^{2+} and Fe^{2+} ions on the destruction efficiency

Mn and Fe ions tend to influence the reaction by accelerating the reaction rate in the absence of UV as seen in Eqs 3–5 (Saeed et al., 2013; Kim et al., 2019; Cai et al., 2021). Their influence was studied as they are present in solution after the CORD process (Rivonkar et al., 2022). The selection of 0.8 mM Mn^{2+} and 0.14 mM Fe^{2+} concentrations are based on a previous work (Rivonkar et al., 2022) using the CORD process before effluent treatment. The Mn^{2+} concentration is mainly coming from the $KMnO_4$ used in the CORD process whereas the Fe^{2+} arises from the total dissolved iron after the CORD process. The concentrations of Mn were further increased to 3 mM and 7.5 mM, again arising from the tests done during the optimization of the CORD process published in the same work (Rivonkar et al., 2022). In the initial tests, the Mn^{2+} to Fe^{2+} ratio was set at 6 (with 0.8 mM Mn^{2+} and 0.14 mM Fe^{2+}), the concentrations of Fe^{2+} in the subsequent tests was increased to 0.5 mM (with 3 mM Mn^{2+}) and 1.25 mM (with 7.5 mM Mn^{2+}) in order to preserve the 6:1 ratio. This adjustment was made to simplify the testing process.

The oxalic acid destruction appears to be significantly enhanced with the presence of metallic cations as shown in Figure 9. At 1 M H_2O_2, at 80°C, the oxalic acid is completely decomposed after 6 h of agitation for metal concentrations of 7.5 mM of Fe^{2+} and 1.25 mM of Mn^{2+} whereas for concentrations ten times lower in Fe^{2+} and Mn^{2+} (0.8 and 0.14 mM), 97% of the oxalic acid is destroyed after 24 h of contact time. The impact of the metallic cations is even more apparent at short contact times. For an initial oxalic acid concentration of 10 mM, 6.1 mM is still present in solution for the sample containing the lowest concentrations of iron and manganese, 5.4 mM for the intermediate concentrations (3 mM of Fe^{2+} and 0.5 mM Mn^{2+}) and only 2.8 mM for the highest

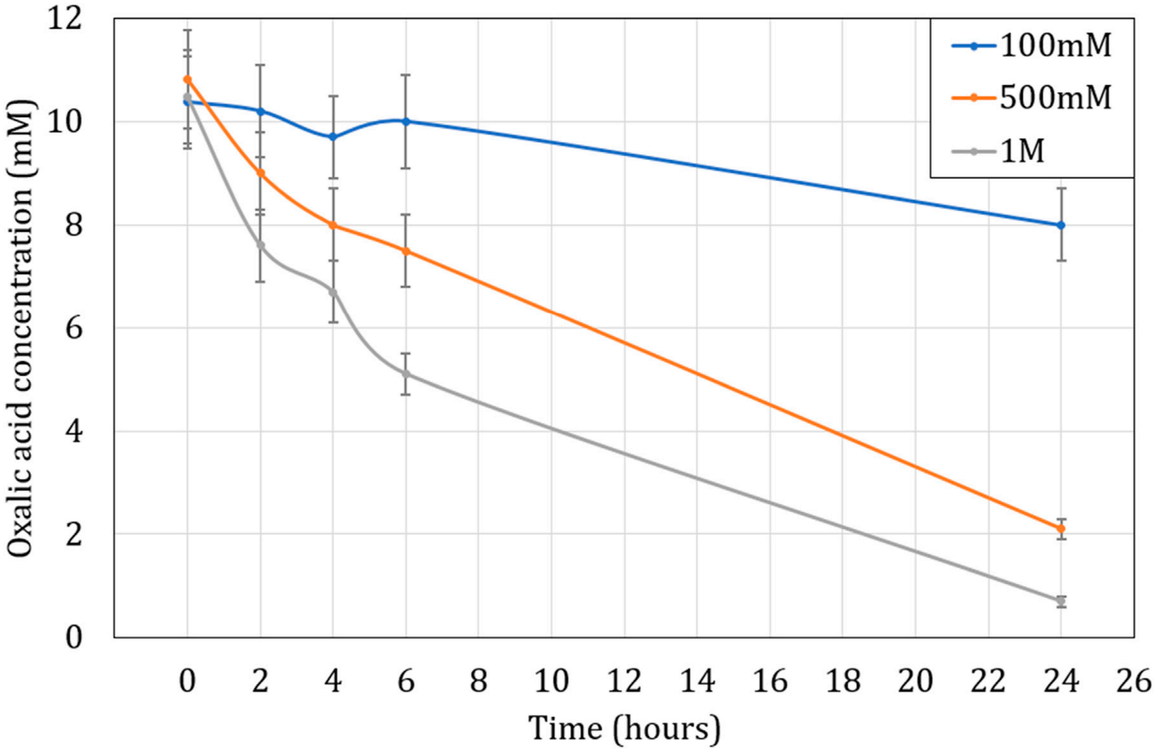

FIGURE 7
Influence of H_2O_2 concentration on oxalic acid concentration over time at 80°C. Initial $H_2C_2O_4$ concentration is 10 mM.

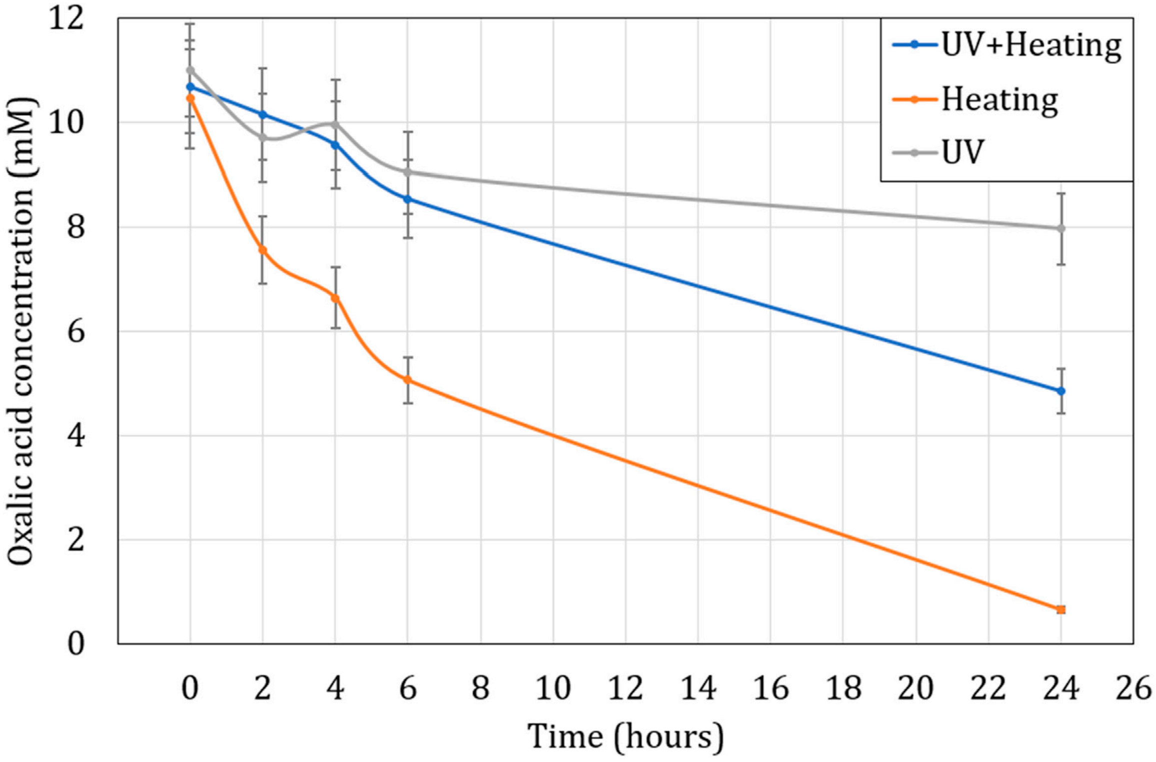

FIGURE 8
Influence of UV radiation and heating on oxalic acid oxidation over time at 80°C. Initial concentration of $H_2C_2O_4$ is 10 mM. Ratio of 1:100 (O:H).

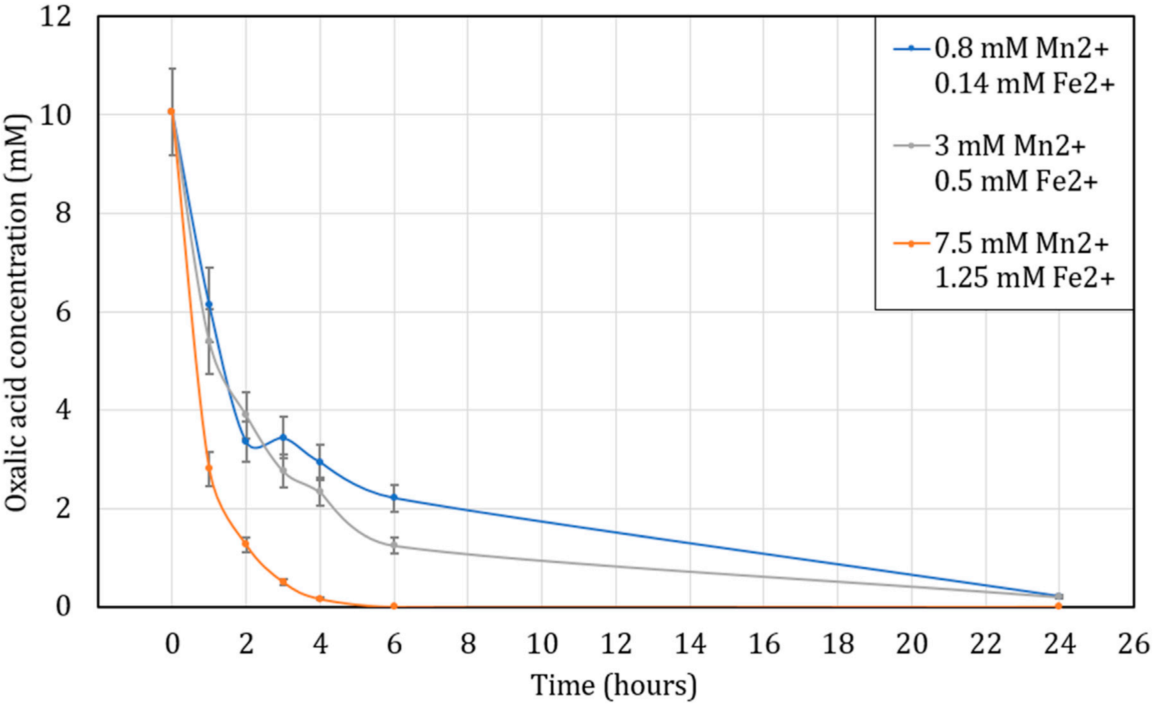

FIGURE 9
Influence of Mn^{2+} and Fe^{2+} concentration on oxalic acid concentration over time while heating the solution to 80°C. Initial concentration of $H_2C_2O_4$ is 10 mM. Ratio of 1:100 (O:H).

concentrations which gives a destruction 39%, 46% and 72% respectively in just 1 h.

These results are in line with the research found in literature (Kubota, 1982; Saeed et al., 2013; Kim et al., 2019; Cai et al., 2021). They found the presence of metal cations and especially Mn^{2+} in solution during the destruction of oxalic acid accelerates the kinetics of this reaction. These results also show the correlation between the metal concentration and the reaction kinetics of oxalic acid destruction. The higher the metal cation concentration, the faster the decomposition of oxalic acid. Due to the presence of both Mn and Fe in CORD solutions, the effects of these ions were not studied individually, and therefore the critical ion amongst Mn and Fe, if any, cannot be identified.

3.2.4 Effects of UV lamp under the influence of Mn^{2+} and Fe^{2+} ions

The influence of metal cations in solution during the destruction of oxalic acid was also tested in a closed loop system in the presence of UV light as in Figure 1. The initial solution was heated to 80°C but the temperature decreased in the loop tube as stated previously, so an average temperature of 65°C is considered during this experiment.

The results are presented in Figure 10 and, as in the previous experiment, the presence of cations accelerates the reaction kinetics of oxalic acid destruction, although slower than in the absence of UV in section 3.2.3, possibly due to lower reaction temperature (65°C). Indeed, in the presence of a high concentration of iron and manganese (7.5 and 1.25 mM) oxalic acid decomposes by more than 70, 86% and 98% after 2, 6 and 24 h of contact respectively. For lower cation concentrations (0.8 mM Mn^{2+} and 0.14 mM Fe^{2+}), the destruction of oxalic acid seems to be slower since its efficiency of destruction is just 32, 50% and 80% for 2, 6 and 24 h of contact time, respectively.

However, the effects of the UV lamp cannot be concretely established as described by Kim et al. (2019); Ketusky (2018); Ketusky et al. (2010). Like in Figure 7, Figure 8 does not show a benefit of using the UV but once again, this is probably due to the reasons mentioned in the previous section 3.2.2, namely, a different power for the UV lamp but also a different solution temperature due to the use of the loop.

4 Discussion and perspectives

This study has provided valuable insights into the crucial factors influencing the destruction of oxalic acid under various conditions and the catalytic effects of Mn coming from $Mn(NO_3)_2$ and metallic cations (Fe and Mn) coming from the decontamination of metallic wastes. The results underscore the significant impact of temperature, catalyst concentration, and UV exposure on the efficiency of oxalic acid degradation.

At higher concentrations of oxalic acid, the presence of Mn as a catalyst demonstrated remarkable potential in accelerating the rate of oxalic acid destruction, showing a positive correlation between catalyst concentration and reaction kinetics. Elevating the reaction temperature to 75°C further expedited the decomposition process, with a minimum concentration of 0.5 mM Mn^{2+} required for complete destruction. Notably, higher concentrations of Mn^{2+}

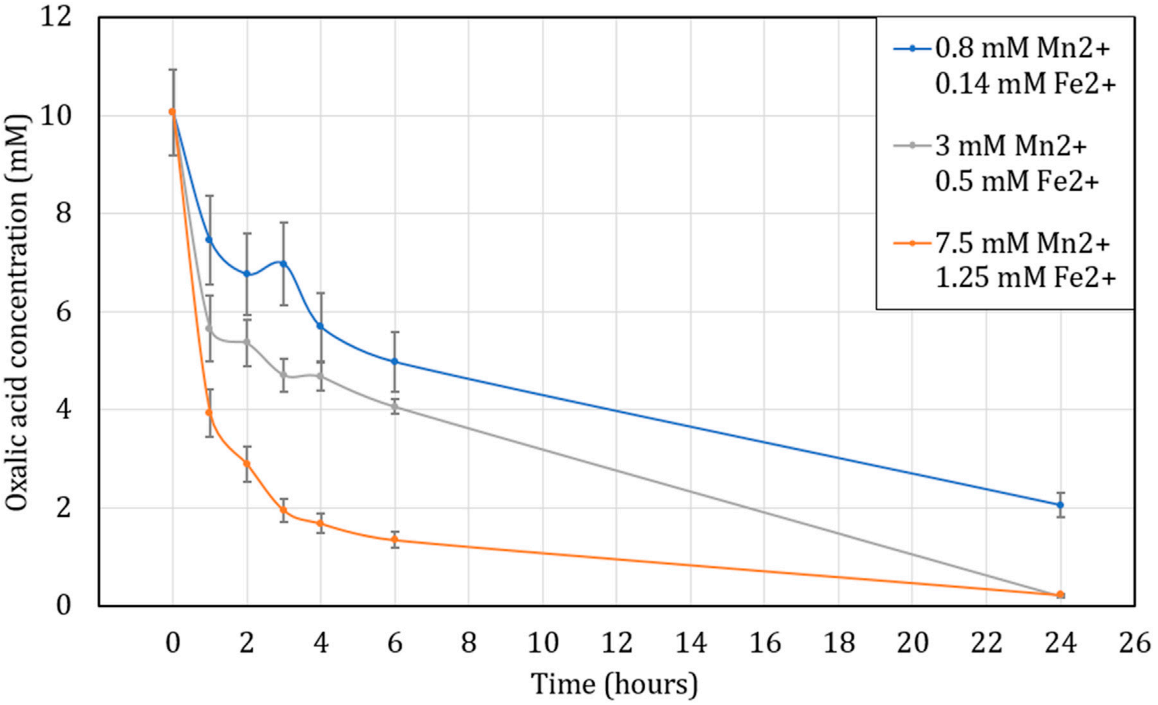

FIGURE 10
Influence of Mn^{2+} and Fe^{2+} concentration on oxalic acid concentration over time while heating the solution to an average of 65°C under UV lamp due to temperature loss through the loop. Initial concentration of $H_2C_2O_4$ is 10 mM. Ratio of 1:100 (O:H).

(25 mM and 50 mM) achieved rapid destruction within just 2 days. Elevating the temperature to 100°C achieved rapid destruction in less than 2 days of the oxalic acid even without presence of the catalyst.

For the photo-Fenton reaction at ambient temperature, the most effective conditions for complete oxalic acid destruction were identified, with an UV lamp, 23 mmoles H_2O_2 doping twice daily, and a solution containing 5.2 mM Fe^{2+} exhibiting optimal results. The absence of Fe^{2+} and UV light resulted in notably slower destruction rates, highlighting their crucial roles as accelerators in the process.

At lower concentrations of oxalic acid, the study investigated the effects of different H_2O_2 concentrations and found a 1:100 ratio of oxalic acid to hydrogen peroxide to be the most optimal for the concentrations tested. Additionally, heating to 80°C displayed high degradation efficiency, while UV exposure at various temperatures showed comparatively lower efficiency, potentially due to limitations in UV transmittance and UV source power in addition to the loss of temperature through the loop.

The presence of metallic cations (Fe^{2+} and Mn^{2+}) significantly enhanced the destruction of oxalic acid, with higher concentrations leading to accelerated degradation rates. The study revealed a notable increase in destruction efficiency as the concentration of Mn^{2+} (and therefore Fe^{2+}) increased, though the individual effects of Mn^{2+} and Fe^{2+} were not studied.

These findings hold significant implications for industrial and environmental applications, particularly in the nuclear industry where oxalic acid plays a critical role in decontamination techniques like the CORD process. Efficient and sustainable methods for destroying oxalic acid wastes are of paramount importance, and the knowledge gained from this study offers a pathway for improved degradation methods.

Future investigations could explore combining the conditions from the lower concentration oxalic acid destruction study, utilizing higher concentrations of H_2O_2 at 80°C in the presence of metallic cations like Mn^{2+} for destruction of higher concentrations of oxalic acid. Additionally, the effects of more powerful UV sources and different wavelengths could be studied under these conditions.

Further research should also include pilot-scale experiments to validate the scalability of these results for practical applications. As the volumes of oxalic acid wastes increase, ensuring scalability is crucial for proper waste management.

Industrial stakeholders seeking effective chemical decontamination options can leverage the information gained from this research to make informed decisions and optimize their waste treatment processes.

5 Conclusion

The key conclusions as a result of the work carried out are.

1. The destruction of oxalic acid at high concentrations can be successfully achieved by heating with nitric acid and a Mn catalyst, and via photo-Fenton reaction.
2. At lower oxalic acid concentrations, oxalic acid destruction was successfully achieved via use of H_2O_2 and heating.
3. The methods tested have identified that metallic cations Fe^{2+} and Mn^{2+} significantly catalyze oxalic acid destruction.

4. While further research could be carried out to combine the learning from oxalic acid destruction at both high and low concentrations, the results presented in this paper indicate that the methods investigated should be considered for the treatment of secondary chemical waste during the decommissioning of nuclear facilities.

Data availability statement

The raw data supporting the conclusion of this article will be made available by the authors, without undue reservation.

Author contributions

JB: Data curation, Formal Analysis, Investigation, Methodology, Validation, Visualization, Writing–original draft, Writing–review and editing. AR: Methodology, Validation, Formal analysis, Investigation, Visualization, Data curation, Supervision, Writing–original draft, Writing–review and editing. MR: Data curation, Formal Analysis, Investigation, Methodology, Validation, Visualization, Writing–original draft, Writing–review and editing. TC: Conceptualization, Funding acquisition, Project administration, Supervision, Writing–review and editing. BD: Conceptualization, Funding acquisition, Project administration, Supervision, Writing–review and editing. TS-M: Methodology, Supervision, Validation, Writing–review and editing. CP: Data curation, Formal Analysis, Investigation, Methodology, Validation, Visualization, Writing–original draft. AA: Conceptualization, Funding acquisition, Project administration, Supervision, Writing–review and editing. JS: Conceptualization, Funding acquisition, Project administration, Supervision, Writing–review and editing.

Funding

The author(s) declare that financial support was received for the research, authorship, and/or publication of this article. This work received funding support from the National Nuclear Laboratory’s Science and Technology programme (Decontamination and Decommissioning Core Science), Sellafield Ltd and the ‘PREDIS’ Euratom research and training programme 2019-2020 under grant agreement No 945098.

Acknowledgments

We would like to thank Nicolas Bessaguet and Valerie Bossé, from Subatech Laboratory, IMT Atlantique, for their support and training during this work.

Conflict of interest

Author JS was employed by Sellafield Ltd.

The remaining authors declare that the research was conducted in the absence of any commercial or financial relationships that could be construed as a potential conflict of interest.

Publisher’s note

References

Bailey, K. C., and Taylor, G. T. (1937). 209. The retardation of chemical reactions. Part VII. The reaction between potassium permanganate and hydrogen peroxide in acid solution. *J. Chem. Soc. (Resumed)* 1937, 994–999. doi:10.1039/JR9370000994

Beltrán, F. J., Rivas, F. J., and Montero-de-Espinosa., R. (2002). Catalytic ozonation of oxalic acid in an aqueous TiO2 slurry reactor. *Appl. Catal. B Environ.* 39 (3), 221–231. doi:10.1016/S0926-3373(02)00102-9

Berry, A. (1957). *Chemical reactions between hydrogen peroxide, nitric acid and oxalic acid.* United Kingdom: United Kingdom Atomic Energy Authority Industrial Group.

Cai, Q. Q., Jothinathan, L., Deng, S. H., Ong, S. L., Ng, H. Y., and Hu, J. Y. (2021). Fenton- and ozone-based AOP processes for industrial effluent treatment. *Adv. Oxid. Process. Effl. Treat. Plants* 2021, 199–254. doi:10.1016/B978-0-12-821011-6.00011-6

Chung, D.-Y., Kim, E.-H., Shin, Y.-J., Yoo, J.-H., Choi, C.-S., and Kim, J.-D. (1995). Decomposition of oxalate by hydrogen peroxide in aqueous solution. *J. Radioanalytical Nucl. Chem. Lett.* 201 (6), 495–507. doi:10.1007/BF02162727

Dükkanci, M., and Gündüz, G. (2006). Ultrasonic degradation of oxalic acid in aqueous solutions. *Ultrason. Sonochemistry* 13 (6), 517–522. doi:10.1016/j.ultsonch.2005.10.005

Gossard, A., Lilin, A., and Faure, S. (2022). Gels, coatings and foams for radioactive surface decontamination: state of the art and challenges for the nuclear industry. *Prog. Nucl. Energy* 149, 104255. doi:10.1016/j.pnucene.2022.104255

Haber, F., Weiss, J., and J Pope, W. (1934). The catalytic decomposition of hydrogen peroxide by iron salts. *Proc. R. Soc. Lond. Ser. A - Math. Phys. Sci.* 147, 332–351. doi:10.1098/rspa.1934.0221

Ketusky, E. (2018). Remediation of spent oxalic acid nuclear decontamination solutions using ozone. *Fac. Sci. Technol.*, 1462344. SRNL-L4500-2018-00011. doi:10.2172/1462344

Ketusky, E., Huff, T., and Sudduth, C. (2010). Enhanced chemical cleaning: effectiveness of the UV lamp to decompose oxalates. Available at: https://www.osti.gov/biblio/971665.

Ketusky, E., and Subramanian, K. (2012). Advanced oxidation: oxalate decomposition testing with ozone. Available at: https://www.osti.gov/biblio/1035776.

Khan, F. (2021). Reaction between hydrogen peroxide and potassium permanganate - is it useful? - bulk peroxide. Available at: https://bulkperoxide.com/reaction-between-hydrogen-peroxide-and-potassium-permanganate-is-it-useful/(Accessed October 24, 2021).

Kim, E. H., Chung, D. Y., Park, J. H., and Yoo, J. H. (2000). Dissolution of oxalate precipitate and destruction of oxalate ion by hydrogen peroxide in nitric acid solution. *J. Nucl. Sci. Technol.* 37 (7), 601–607. doi:10.1080/18811248.2000.9714936

Kim, J. H., Lee, H. K., Park, Y. J., Lee, S. B., Choi, S. J., Oh, W., et al. (2019). Studies on decomposition behavior of oxalic acid waste by UVC photo-fenton advanced oxidation process. *Nucl. Eng. Technol.* 51 (8), 1957–1963. doi:10.1016/j.net.2019.06.011

Kliegman, R., and Geme, J. S. (2019). “Defects in metabolism of amino acids: hyperoxaluria and oxalosis,” in *Nelson textbook of pediatrics* (Elsevier), 695–739.

Kubota, M. (1982). Decomposition of oxalic acid with nitric acid. *J. Radioanalytical Chem.* 75 (1), 39–49. doi:10.1007/BF02519972

Lee, D.-K., and Kim, D.-S. (2000). Catalytic wet air oxidation of carboxylic acids at atmospheric pressure. *Catal. Today* 63 (2), 249–255. doi:10.1016/S0920-5861(00)00466-1

Li, Y., Zhao, Y., and Zhu, Z. (2011). Kinetic investigation of the autocatalytic reaction between potassium permanganate and hydrogen peroxide with soft-modeling methods. *Anal. Sci.* 27 (1), 37–41. doi:10.2116/analsci.27.37

Mailen, J. C., Tallent, O. K., and Arwood, P. C. (1981). *Destruction of oxalate by reaction with hydrogen peroxide*. Oak Ridge, TN (United States): Oak Ridge National Lab. doi:10.2172/6229619

Martinez-Huitle, C. A., Ferro, S., and De Battisti, A. (2004). Electrochemical incineration of oxalic acid: role of electrode material. *Electrochimica Acta* 49 (22), 4027–4034. doi:10.1016/j.electacta.2004.01.083

Martino, C., King, W., and Ketusky, E. (2012). Actual-waste tests of enhanced chemical cleaning for retrieval of SRS HLW sludge tank heels and decomposition of oxalic acid. Available at: https://www.osti.gov/biblio/1033338.

Mason, C., Brown, T. L., Buchanan, D., and Morris, D. (2008). *The destruction of oxalic acid in TPFL evaporators 1 and 2 under normal and potential abnormal conditions*. NNL (08) 9481, 2008.

Metelitsa, D. I. (1971). Mechanisms of the hydroxylation of aromatic compounds. *Russ. Chem. Rev.* 40 (7), 563–580. doi:10.1070/RC1971v040n07ABEH001939

Mitchell, T., Kumar, P., Reddy, T., Wood, K. D., Knight, J., Assimos, D. G., et al. (2019). Dietary oxalate and kidney stone formation. *Am. J. Physiology-Renal Physiology* 316 (3), F409–F413. doi:10.1152/ajprenal.00373.2018

Nash, C. (2012). *Literature review for oxalate oxidation processes and plutonium oxalate solubility*. SRNL-STI-2012-00003. Aiken, SC (United States): Savannah River Site. doi:10.2172/1034748

Ocken, H. (1999). *Decontamination handbook*. TR 112352. Palo Alto, CA: Electric Power Research Institute.

Orr, R. M., Sims, H. E., and Taylor, R. J. (2015). A review of plutonium oxalate decomposition reactions and effects of decomposition temperature on the surface area of the plutonium dioxide product. *J. Nucl. Mater.* 465, 756–773. doi:10.1016/j.jnucmat.2015.06.058

Oturan, M. A., and Aaron, J.-J. (2014). Advanced oxidation processes in water/wastewater treatment: principles and applications. A review. *Crit. Rev. Environ. Sci. Technol.* 44 (23), 2577–2641. doi:10.1080/10643389.2013.829765

Pawar, V., and Gawande, S. (2015). An overview of the Fenton process for industrial wastewater. *IOSR J. Mech. Civ. Eng.* 2015, 127–136.

Remoundaki, E., Hatzikioseyian, A., and Tsezos, M. (2007). A systematic study of chromium solubility in the presence of organic matter: consequences for the treatment of chromium-containing wastewater. *J. Chem. Technol. Biotechnol.* 82 (9), 802–808. doi:10.1002/jctb.1742

Rivonkar, A., Katona, R., Robin, M., Suzuki-Muresan, T., Abdelouas, A., Mokili, M., et al. (2022). Optimisation of the chemical oxidation reduction process (CORD) on surrogate stainless steel in regards to its efficiency and secondary wastes. *Front. Nucl. Eng.* 1. doi:10.3389/fnuen.2022.1080954

Saeed, M., Ilyas, M., Siddique, M., and Ahmad, A. (2013). Oxidative degradation of oxalic acid in aqueous medium using manganese oxide as catalyst at ambient temperature and pressure. *Arabian J. Sci. Eng.* 38 (7), 1739–1748. doi:10.1007/s13369-013-0545-x

Santos, D. F. M., Soares, O. S. G. P., Silva, A. M. T., Figueiredo, J. L., and Pereira, M. F. R. (2021). Degradation and mineralization of oxalic acid using catalytic wet oxidation over carbon coated ceramic monoliths. *J. Environ. Chem. Eng.* 9 (4), 105369. doi:10.1016/j.jece.2021.105369

Shih, Y.-J., Huang, C.-P., Chan, Y.-H., and Huang, Y.-H. (2019). Electrochemical degradation of oxalic acid over highly reactive nano-textured γ- and α-MnO2/carbon electrode fabricated by KMnO4 reduction on loofah sponge-derived active carbon. *J. Hazard. Mater.* 379, 120759. doi:10.1016/j.jhazmat.2019.120759

Solbes-García, Á., Miranda-Vidales, J. M., Nieto-Villena, A., Salvador Hernández, L., and Narváez, L. (2017). Evaluation of the oxalic and tartaric acids as an alternative to citric acid in aqueous cleaning systems for the conservation of contemporary acrylic paintings. *J. Cult. Herit.* 25, 127–134. doi:10.1016/j.culher.2016.11.013

Sun, Y., Liu, H., Tan, X., Zheng, L., Du, Y., Zheng, A., et al. (2019). Highly efficient redox reaction between potassium permanganate and 3,3′,5,5′-tetramethylbenzidine for application in hydrogen peroxide based colorimetric assays. *RSC Adv.* 9 (4), 1889–1894. doi:10.1039/C8RA07758D

Wang, F., Wu, P., Chen, M., Wu, J., Sun, L., Shang, Z., et al. (2023). Green rust sulfate transformation under the impact of Cr(VI) and oxalic acid: mechanism and environmental significance. *Appl. Clay Sci.* 233, 106825. doi:10.1016/j.clay.2023.106825

Wang, Q., Wang, F., Cai, C., Chen, H., Ji, F., Chen, Y., et al. (2023). Laser decontamination for radioactive contaminated metal surface: a review. *Nucl. Eng. Technol.* 55 (1), 12–24. doi:10.1016/j.net.2022.09.020

Zhang, G., Hu, J., and Xu, H. (2022). Oxalic acid induced defect state graphitic carbon nitride with improved photocatalytic performance. *J. Mol. Struct.* 1249, 131611. doi:10.1016/j.molstruc.2021.131611

Zhong, L., Lei, J., Deng, J., Lei, Z., Lei, L., and Xu, X. (2021). Existing and potential decontamination methods for radioactively contaminated metals-A review. *Prog. Nucl. Energy* 139, 103854. doi:10.1016/j.pnucene.2021.103854

frontiers | Frontiers in Nuclear Engineering

TYPE Perspective
PUBLISHED 28 February 2024
DOI 10.3389/fnuen.2024.1335980

OPEN ACCESS

EDITED BY
Tonya Vitova,
Karlsruhe Institute of Technology (KIT),
Germany

REVIEWED BY
Robin Taylor,
National Nuclear Laboratory, United Kingdom

*CORRESPONDENCE
Joanna McFarlane,
✉ mcfarlanej@ornl.gov

RECEIVED 20 November 2023
ACCEPTED 07 February 2024
PUBLISHED 28 February 2024

CITATION
McFarlane J (2024), Cradle to grave: the importance of the fuel cycle to molten salt reactor sustainability.
Front. Nucl. Eng. 3:1335980.
doi: 10.3389/fnuen.2024.1335980

Cradle to grave: the importance of the fuel cycle to molten salt reactor sustainability

Joanna McFarlane*

Oak Ridge National Laboratory, Nuclear Energy and Fuel Cycle Division, Oak Ridge, TN, United States

Advanced reactor technologies are being considered for the next-generation of nuclear power plants. These plants are designed to have a smaller footprint, run more efficiently at higher temperatures, have the flexibility to meet specific power or heating needs, and have lower construction costs. This paper offers a perspective on molten salt reactors, promoted as having a flexible fuel cycle and close-to-ambient pressure operation. A complexity introduced by reducing the reactor footprint is that it may require low-enriched fuel for efficient operation, available from enrichment of the feed salt or by reusing actinides from existing used nuclear fuel (UNF). Recycling UNF has the potential to reduce high-level waste, if done correctly. Release limits from UNF processing are stringent, and processes for waste reduction, fission gas trapping, and stable waste-form generation are not yet ready for commercial deployment. These complex processes are expensive to develop and troubleshoot because the feed is highly radioactive. Thus, fuel production and supply chain development must keep abreast of reactor technology development. Another aspect of reactor sustainability is the non-fuel waste streams that will be generated during operation and decommissioning. Some molten salt reactor designs are projected to have much shorter operational lifetimes than light-water reactors: less than a decade. A goal of the reactor sustainability effort is to divert these materials from a high-level waste repository. However, processing of reactor components should only be undertaken if it reduces waste. Economic and environmental aspects of sustainability are also important, but are not included in this perspective.

KEYWORDS

molten salt reactor fuel cycle, salt fuel preparation, waste generation, fuel salt waste disposition, salt processing

1 Introduction

The challenge to develop a large-scale response to increases in CO_2 emissions and climate change has provided an impetus to develop options for nuclear fission for power generation that address the major issues with the prevalent light-water reactor (LWR) designs. The fleet of LWRs has performed with a strong safety record for several decades, especially when considering dose to the public. Yet, accidents have occurred, highlighting the need to develop designs that have enhanced safety margins, passive safety features, and increased tolerance to fault scenarios (Seghal, 2012). These features have become even more desirable as recent events at the Zaporizhzhia power plant in Ukraine indicate the need to include deliberate sabotage to the list of possible conditions that might impair plant operation (Kurando, 2023). Options for passively safe designs include those with encapsulated tristructural-isotropic (TRISO) fuel (Morris et al., 2004), and low-pressure operation with coolants such as molten metal (King et al., 1991) or molten salt (Holcomb et al., 2021). The latter class of reactors is the subject of this essay. Benefits of molten salt fueled reactors are that they operate slightly above ambient pressure and generally preclude water within containment/confinement, thereby limiting high-energy reactor failure scenarios, airborne transport of radionuclides, and potential dose to the public. Challenges include working with salts that are air sensitive and need to be purified to reduce chemical reactivity (McFarlane et al., 2019).

A decision to adopt a radical change in reactor design must be placed in the context of the production and usage of power. This decision will be made by the electrical utilities and their stakeholders, including customers and government agencies as informed by regulatory review. These decisions also must consider sustainability of the design's supply chain, including the production of nuclear fuel through to the disposition of the waste from the reactor (Krall et al., 2002). Such lifecycle considerations accompany any large-scale adoption of new technologies, one example being the case of electric vehicles and their reliance on new battery technologies (Yang et al., 2022). Molten salt reactors (MSRs) operate at high temperatures with fluoride or chloride salt coolants that can be chemically reactive if not carefully controlled. Development of new materials to contain the salt and research into the chemical stability of these materials in a chloride or fluoride environment are current topics of nuclear research (Raiman and Lee, 2018). The disposition of reactor materials after reactor shutdown and decontamination also must be considered in supply chain feasibility (Riley et al., 2019).

2 Fuel and salt availability

MSRs can burn a variety of actinides, including the standard ^{235}U (Holcomb et al., 2022), higher actinides such as ^{239}Pu and ^{241}Am (Bhomik et al., 2023) recovered from used nuclear fuel (UNF), as well as ^{233}U derived from a thorium fuel cycle (Bogetic et al., 2016). Depending on the design, an MSR may be operated on a single load of fuel, with online processing or addition of fuel, as a breeder, or as a waste or actinide burner. Thus, there have been descriptions of how MSR technology could be coupled with recycling of UNF from other types of nuclear reactors (Moyer et al., 2022). Many reactor designs are being developed in the United States (US) and around the world: some have already taken regulatory steps towards deployment. An example of the latter includes getting permission to construct a prototype, as detailed on the US Nuclear Regulatory Commission Agencywide Documents Access and Management System website (US Nuclear Regulatory Commission, 2023). These demonstration reactors do not rely on currently available commercial fuel suppliers but are collaborating with fuel development programs at the US Department of Energy national laboratories to provide a supply of ^{235}U in the correct form. The choice of fuel and enrichment level will determine the size and configuration of the reactor, preparation of salt for the reactor, safeguards and security requirements, and downstream waste dispositioning. Therefore, design and planning to scale up both the reactor and the fuel cycle must be done in parallel. The advanced reactor development communities in the US and globally have started to address this complex problem by holding workshops that include researchers and other stakeholders, the findings from which will be publicly available (i.e., Rose and Ezell, 2024; Espartero and Grassi, 2024).

The other aspect of salt availability that must be considered is that MSRs depend on having a carrier and/or coolant salt that is transparent to neutron flux. Consequently, fluoride salt reactors that have lithium-based carriers need salt that is enriched in ^{7}Li to reduce the production of ^{3}H through activation (Harrison et al., 2016). Chloride-based carrier salts need enrichment in ^{37}Cl to reduce the production of ^{36}Cl, a long-lived isotope that complicates waste-form disposal, and other activation byproducts such as sulfur (Pigni, 2023). Thermal diffusion has been studied for chlorine isotope separation (Kranz and Watson, 1953), but commercial production is not yet realized. Recovery of ^{6}Li from military applications or fusion could be leveraged to supply ^{7}Li for MSRs, but coupling these different applications may be difficult for both technical and regulatory reasons (US Department of Energy Office of Nuclear Physics, NSAC Isotopes Subcommittee, 2015).

3 Waste generation

One major concern with nuclear power is the accumulation of UNF and difficulties in siting repositories for high-level waste (HLW) (Krall et al., 2002). Although the feasibility of underground disposal of UNF has been thoroughly investigated, public concerns endure regarding the safety and efficacy of permanent disposal at prospective repositories such as Yucca Mountain in the US (Birkholzer et al., 2023). These disparate concerns may arise from the handling of UNF, the safety of transporting UNF canisters long distances to a central location, as well as the indefinite hazard presented by long-lived isotopes sequestered in a dynamic geosphere over many millennia. In the absence of an HLW repository, on-site UNF storage has been the default option (Sindelar, 2022). Although on-site storage is a short-term solution, it has provided the nuclear community time to address the issue of permanent waste disposal.

In the case of MSRs, waste generation will occur at all stages of the lifecycle, as summarized in Table 1. Some of these wastes are analogous to debris from LWR dispositioning, and existing tracking and disposal pathways could be used. Other waste materials are unique to MSRs and will require special consideration (Krall et al., 2002; Riley et al., 2019).

Upstream processing, including salt enrichment, mixing, and transportation to the reactor site, will contaminate vessels and machinery with nuclear materials. Inventories at the production site must be tracked to fulfil material balance accountancy (MBA) requirements, which will be stringent if highly enriched uranium or higher actinides are included in the fuel mixture. Production of ceramic fuel requires similar MBA controls. However, waste from fuel production may meet the low-level waste (LLW) acceptance criteria, unless recycled actinides are part of the fuel mixture. UNF has been considered as a source of material for MSRs because of their flexible fuel cycle. Actinides have been recovered from UNF by pyroprocessing at US Department of Energy installations such as Idaho National Laboratory (Fredrickson and Yoo, 2021).

TABLE 1 Waste generation from molten salt reactors.

Process	Waste form	Disposition
Fuel salt preparation (from unirradiated material)	Contaminated equipment	• Decontaminate and reuse equipment, LLW
Fuel salt preparation (from irradiated material)	Contaminated equipment	• Decontaminate and reuse equipment
	Radiological waste streams (solid debris, liquid, or captured in off-gas)	• Consolidate and stabilize waste streams, LLW, HLW
Reactor operation	Contaminated equipment	• Decontaminate and reuse equipment if possible, LLW, HLW
Fuel handling	Unused fuel salt	• Recover and recycle unused salt, LLW
	Used fuel salt	• Stabilize and contain used fuel salt or separated components, HLW
Reactor operation	Materials replaced during operation	• Out-of-core, minimal contamination, LLW
Maintenance		• In-core, high contamination, Stabilize and contain for storage/disposal
Reactor operation	Volatile radionuclides	• Confine radionuclides until activity is minimal. Capture and stabilize long-lived isotopes. Control decay heat
Off-gas	Spent filters, capture media for off-gas	• Off-gas components and in-core vessels require remote handling as HLW debris. Consolidate and stabilize for storage/disposal
Shutdown & Maintenance	Materials replaced during shutdown (sensors, off-gas filters)	• From out-of-core, minimal contamination, LLW
	Volatile products of radiolysis	• From in-core, high contamination, Stabilize and contain for storage/disposal
		• Minimize conditions contributing to radiolysis
Decommissioning and Decontamination (D&D)	Fuel, carrier, flush salts drained from facility	• Recycle valuable salt components, stabilize used salt against radiolysis, convert to insoluble waste form(s)
	Salt contacted metals and structural materials	• Decontaminate salt wetted materials if feasible. Compact to reduce volume
	Salt contacted carbon wastes	• Off-gas components handled as described for reactor operation
	D&D wastes	• D&D LLW, HLW, depending on contamination
	Off-gas wastes	

Reactor operation will generate wastes from maintenance of the reactor systems such as the off-gas and online processing. The design will dictate the waste generation. For instance, the off-gas system could be enclosed for some reactor designs or have limited throughput (Dunkle et al., 2023), but most will have a flowing cover gas that continuously removes volatile radionuclides similarly to the Molten Salt Reactor Experiment (MSRE) at Oak Ridge National Laboratory (Guymon, 1973). Online processing could include removal of insoluble materials such as graphite particles and noble metals or actinide recovery from the liquid phase. The rationale for online processing has been reviewed in regard to molten salt fuel qualification (Holcomb et al., 2020; 2022). Implementation will depend on a number of factors including relevant regulations and so will be specific to each jurisdiction. Because of salt contamination, wastes from maintenance and operation are likely to be HLW and must be managed accordingly.

Decommissioning, shutdown, and decontamination wastes from MSRs will include materials that are wetted with salt and those that are not. The latter can be handled similarly to LWR reactor materials: volume minimization will be an important consideration (Vestal et al., 2023). The salt-wetted components from MSRs may include the reactor vessel, graphite moderator, filters, and equipment for fuel introduction and sampling. A review of wastes from MSRs delves into each of these categories and suggests ways of managing them for disposal or recycle (Andrews et al., 2021). The feasibility of these options must include safe operation, resistance to diversion, and HLW volume. The salts are water soluble, which may permit decontamination to remove some of the more active fission products (e.g., intermediate half-lived ^{137}Cs and ^{90}Sr) to reduce the decay heat load associated with HLW.

For the fuel salts, indefinite storage is not an option as it is for ceramic fuel. Experience with MSRE has shown that salts drained from the reactor can undergo radiolysis for decades, requiring active monitoring and degassing (National Research Council, 1997). The salts' water-soluble nature complicates waste disposal: they must be processed to an insoluble form. Because some processing is necessary, a once-through fuel cycle is unlikely to be feasible for commercial operation. Reprocessing methods were reviewed by Fredrickson and Yoo, and they highlight the effectiveness of electrorefining for uranium recovery from the converted Experimental Breeder Reactor II (Fredrickson and Yoo, 2021). Capture and reuse of isotopically enriched chlorine and lithium salts may also be desirable. Chemical processing may be avoided by incorporating the UNF salt into an insoluble matrix, such as an intimate mixture of salt and metal, termed a halmet (Del Cul et al., 2018). This approach may be a simpler alternative to chemical or pyrochemical processing. Cermet technology has been developed

TABLE 2 Comparison of MSR and LWR considerations for UNF recycle and waste handling.

	LWR	MSR
Interim storage	On-site dry cask	Drain tank
Incentives for back-end processing	Removal of high-decay heat producing fission products, or long-lived fission products to ameliorate repository requirements Recovery of value-added radionuclides	Recovery of enriched carrier salts, value-added fission products, or high-decay heat producing fission products
UNF Processing	Requires several steps including removal of the matrix surrounding the fuel, cladding and dissolution of the ceramic fuel	Salt can be heated for pyroprocessing or electrorefining
Waste form	Robust clad ceramic fuel matrix can be made more resistant to radionuclide leaching by further encapsulation and geoengineered barriers	Fuel salt is not suitable for permanent disposal without additional processing and stabilization
Volatile and semivolatile fission products (Isotopes of I, Kr, and Xe, Te, Tc, ^{3}H,^{14}C)	Need to be tracked during back-end processing	Largely released and confined in the off-gas system during reactor operation. Disposition of semi-volatile fission products with complex redox chemistry requires further study

over several decades and has been applied to UNF as well as irradiation targets (Kobisk et al., 1981; Robinson et al., 2020). Using halmets to stabilize UNF salt is at an early stage of development. For example, copper, used as the metal phase for a cermet, is typically heated to 1,085°C when forming a mixed phase with UO_2. At this temperature, salt components will volatilize, so a lower temperature process must be considered with a different metal, such as aluminum. Preparation of UNF powder for halmet production will be an engineering challenge because of the requirement for contamination control and MBA considerations. Although halmets have been proposed and patented (Aaron et al., 2012), the durability of these materials has not yet been tested.

4 Conclusion

This paper briefly surveys considerations for the fuel cycle of MSRs from a US perspective. Reactor design and prototype development is more advanced than the supporting fuel preparation and waste management constructs. The choice of fuel to be burned in an MSR will directly affect its design, so these aspects must be considered in tandem. Because irradiated salts used in MSRs undergo radiolysis during storage, the ability to store UNF indefinitely is more complicated for MSRs than for spent LWR fuel, requiring active monitoring and mitigation of acidic gases that may be generated during storage. Because salts are water soluble, they must be processed before disposal, so a once-through fuel cycle is unlikely to be feasible. Stabilizing matrices such as halmets have been proposed to permit direct disposal of salts with minimal processing. Table 2 summarizes the differences in fuel cycle considerations for LWR and MSR designs. In the case of MSRs, the fuel cycle cannot be decoupled from the reactor design and has the potential to be as complex as the reactor itself. Consequently, research and development efforts in all aspects of the MSR fuel cycle—including linkages to the current nuclear materials supply chain, development of fuel processing facilities with or without recycled actinides, and development of insoluble waste forms for permanent disposal—must be considered in tandem. Sharing of information globally is important to addressing complex fuel cycle issues related to MSR technology.

Data availability statement

The original contributions presented in the study are included in the article/Supplementary Material, further inquiries can be directed to the corresponding author.

Author contributions

JM: Conceptualization, Funding acquisition, Writing–original draft, Writing–review and editing.

Funding

The author(s) declare financial support was received for the research, authorship, and/or publication of this article. Funding for this work was provided the US Department of Energy, Office of Nuclear Energy, Advanced Reactor Technology NE-5, Molten Salt Reactor Program. This manuscript has been authored in part by UT-Battelle, LLC, under contract DE-AC05-00OR22725 with the US Department of Energy (DOE). The US government retains and the publisher, by accepting the article for publication, acknowledges that the US government retains a nonexclusive, paid-up, irrevocable, worldwide license to publish or reproduce the published form of this manuscript, or allow others to do so, for US government purposes. DOE will provide public access to these results of federally sponsored research in accordance with the DOE Public Access Plan (http://energy.gov/downloads/doe-public-access-plan).

Acknowledgments

JM would like to acknowledge helpful discussions and insight from Dr. Patricia Paviet (Pacific Northwest National Laboratory and National Technical Director of the US DOE NE-5 Molten Salt Reactor program), as well as colleagues Dr. David Holcomb (Idaho National Laboratory), Dr. Brian Riley (Pacific Northwest National Laboratory), Dr. Melissa Rose (Argonne National

Laboratory) and Dr. Kevin Robb (Oak Ridge National Laboratory).

Conflict of interest

The author declares that the research was conducted in the absence of any commercial or financial relationships that could be construed as a potential conflict of interest.

Publisher's note

References

Aaron, W. S., Collins, E. D., Del Cul, G. D., Jubin, R. T., and Vedder, R. J. (2012). *Cermet high level wasteforms. US Patent No. US2012/02136558 A1*. Washington, DC: US Patent and Trademark Office.

Andrews, H. B., McFarlane, J., Chapel, A. S., Ezell, N. D. B., Holcomb, D. E., De Wet, D., et al. (2021). Review of molten salt reactor off-gas management considerations. *Nucl. Eng. Des.* 385, 111529. doi:10.1016/j.nucengdes.2021.111529

Bhowmik, P. K., Islam, Md. S., and Sabharwall, P. (2023). *Partitioning and transmutation of used nuclear fuel in support of geological waste disposal*. Idaho Falls, Idaho: Idaho National Laboratory. INL/CON-22-70688.

Birkholzer, J. T., Zheng, L., Nair, P., and Gunter, T. (2023). The role of international collaboration in the United States geologic disposal research program. *Saf. Nucl. Waste Dispos.* 2, 29–30. doi:10.5194/sand-2-29-2023

Bogetic, S., Greenop, A., Haneklaus, N., Poresky, C., and Shen, D. (2016). Near-term deployment viability of liquid-fuel molten salt reactors, 2016 ANS winter meeting and nuclear technology expo, November 6–10, 2016. *Trans. Am. Nucl. Soc.* 115.

Del Cul, G. D., Hunt, R. D., and Mattus, C. H. (2018). *Design of the process and equipment that would be required to solidify UNF, NTRD-MRWFD-2018-000144, ORNL/SPR-2018/990*. Oak Ridge, Tennessee: Oak Ridge National Laboratory.

Dunkle, N., Wheeler, A., Richardson, J., Bogetic, S., Chavla, O., and Skutnik, S. E. (2023). Plutonium signatures in molten-salt reactor off-gas tank and safeguards considerations. *J. Nucl. Eng.* 4 (20), 391–411. doi:10.3390/jne4020028

Espartero, A. G., and Grassi, G. (2024). *Joint NEA-IAEA workshop on the chemistry of fuel cycles for molten salt reactor technologies, 2-6 October 2023*. Vienna, Austria. (in preparation) Available at: https://www.oecd-nea.org/jcms/pl_82236/joint-nea-iaea-workshop-on-the-chemistry-of-fuel-cycles-for-molten-salt-reactor-technologies.

Fredrickson, G., and Yoo, T.-S. (2021). *Review – nuclear fuel and reprocessing technologies: a U.S. Perspective, INL-EXT-20-59106*. Idaho Falls, Idaho: Idaho National Laboratory.

Guymon, R. H. (1973). *MSRE systems and components performance, ORNL-TM-3039*. Oak Ridge, Tennessee: Oak Ridge National Laboratory.

Harrison, T. J., Felde, D. K., Logsdon, R. J., McFarlane, J., and Qualls, A. L. (2016). *Preliminary tritium management design activities at ORNL, ORNL/TM-2016/526*. Oak Ridge, Tennessee: Oak Ridge National Laboratory.

Holcomb, D., Poore, W., and Flanagan, G. (2020). *MSR fuel salt qualification methodology*. ORNL/TM-2020/1576. doi:10.2172/1649079

Holcomb, D., Poore, W., and Flanagan, G. (2022). *Fuel qualification for molten salt reactors, NUREG/CR-7299*. Washington, DC: US Nuclear Regulatory Commission, Office of Nuclear Reactor Regulation. ORNL/TM-2022/2754.

Holcomb, D. E., Huning, A. J., Mulheim, M. D., Denning, R. S., and Flanagan, G. F. (2021). *Molten salt reactor fundamental safety function PIRT, ORNL/TM-2021/2176*. Oak Ridge, Tennessee: Oak Ridge National Laboratory.

King, T. L., Landry, R. R., Throm, E. D., and Wilson, J. N. (1991). *Preapplication safety evaluation report for the sodium advanced fast reactor (SAFR) liquid-metal reactor, NUREG-1369*. Washington, DC: US Nuclear Regulatory Commission, Office of Nuclear Regulatory Research.

Kobisk, E. H., Quinby, T. C., and Aaron, W. S. (1981). *Final report on Cermet high-level waste forms, ORNL-5760*. Oak Ridge, Tennessee: Oak Ridge National Laboratory.

Krall, L. M., Macfarlane, A. M., and Ewing, R. (2002). Nuclear waste from small modular reactors. *PNAS* 119 (23), e2111833119. doi:10.1073/pnas.2111833119

Kranz, A. Z., and Watson, W. W. (1953). Chlorine isotope separation by thermal diffusion. *Phys. Rev.* 91 (6), 1469–1472. doi:10.1103/physrev.91.1469

Kurando, M. (2023). Nuclear security in conflict zones: the dangerous case of Zaporizhzhia. *Int. J. Nucl. Secur.* 8 (2), 10. doi:10.7290/ijns372553

McFarlane, J., Taylor, P., Holcomb, D., and Poore, W. P. (2019). *Review of hazards associated with molten salt reactor fuel processing operations*. ORNL/TM-2019/1195.

Morris, R. N., Petti, D. A., Powers, D. A., Boyack, B. E., and Rubin, M. B. (2004). *TRISO-coated particle fuel phenomenon identification and ranking tables (PIRTs) for fission product transport due to manufacturing, operations, and accidents, NUREG/CR-6844*, vol 1. Washington, DC: US Nuclear Regulatory Commission, Office of Nuclear Regulatory Research.

Moyer, B. A., Lumetta, G. J., Bruffey, S. H., Finkeldei, S., Mardsen, K. C., Simpson, M. F., et al. (2022). *Innovative separations research and development needs for advanced fuel cycles, ORNL/SPR-2022/2314*. Oak Ridge, Tennessee: Oak Ridge National Laboratory. doi:10.2172/1844866

National Research Council (1997). *Evaluation of the US Department of Energy's alternatives for the removal and disposition of molten salt reactor experiment fluoride salts*. Washington, DC: National Academies Press.

Pigni, M. T. (2023). Quantification of the ^{35}Cl{n, p} reaction channel. *Prog. Nucl. Energy* 157, 104551. doi:10.1016/j.pnucene.2022.104551

Raiman, S. S., and Lee, S. (2018). Aggregation and data analysis of corrosion studies in molten chloride and fluoride salts. *J. Nucl. Mater.* 511, 523–535. doi:10.1016/j.jnucmat.2018.07.036

Riley, B. J., McFarlane, J., Del Cul, G. D., Vienna, J. D., Contescu, C. I., and Forsberg, C. W. (2019). Molten salt reactor waste and effluent management strategies: a review. *Nucl. Eng. Des.* 345, 94–109. doi:10.1016/j.nucengdes.2019.02.002

Robinson, S. M., Benker, D. E., Collins, E. D., Ezold, J. G., Garrison, J. R., and Hogle, S. L. (2020). Production of Cf-252 and other transplutonium isotopes at Oak Ridge National laboratory. *Radiochim. Acta* 108, 737–746. doi:10.1515/ract-2020-0008

Rose, M. A., and Ezell, D. (2024). *Molten salt reactor fuel cycle chemistry workshop*. Argonne National Laboratory, 2023. ANL/CFCT-23/50 September 19-21. (in preparation).

Sehgal, B. R. (2012). "Light water reactor safety: a historical review," in *Nuclear safety in light water reactors: severe accident phenomenology* (Waltham, Massechusetts: Academic Press), 1–88.

Sindelar, R. L. (2022). The nuclear fuel cycle: safe management of spent nuclear fuel. *J. S. C. Acad. Sci.* 20 (1), 7.

US Department of Energy Office of Nuclear Physics, NSAC Isotopes Subcommittee (2015). *Meeting isotope needs and capturing opportunities for the future: the 2015 long range plan for the DOE-NP isotope program.*

US Nuclear Regulatory Commission. (2023). US NRC ADAMS common web interface. Available at: https://adams.nrc.gov/wba [Updated October 31, 2023, Accessed October 31, 2023].

Vestal, B. K., Travis, J., Albert, A., Bruffey, S., McFarlane, J., Collins, E. D., et al. (2023). A novel protocol to recycle zirconium from zirconium alloy cladding from used nuclear fuel rods. *J. Nucl. Mater.* 578, 154339. doi:10.1016/j.jnucmat.2023.154339

Yang, Z., Huang, H., and Lin, F. (2022). Sustainable electric vehicle batteries for a sustainable world: perspectives on battery cathodes, environment, supply chain, manufacturing, life cycle, and policy. *Adv. Energy Mater.* 12 (26), 2200383. doi:10.1002/aenm.202200383

frontiers | Frontiers in Nuclear Engineering

TYPE Original Research
PUBLISHED 21 March 2024
DOI 10.3389/fnuen.2024.1321627

OPEN ACCESS

EDITED BY
Tonya Vitova,
Karlsruhe Institute of Technology (KIT),
Germany

REVIEWED BY
Sarah C. Finkeldei,
University of California, Irvine, United States
Edgar C. Buck,
Pacific Northwest National Laboratory (DOE),
United States

*CORRESPONDENCE
Rose Montgomery,
✉ montgomeryra@ornl.gov

RECEIVED 14 October 2023
ACCEPTED 19 February 2024
PUBLISHED 21 March 2024

CITATION
Montgomery R, Bevard B, Cantonwine P and Sasikumar Y (2024), Key results from examinations of seven high burnup pressurized water reactor spent nuclear fuel rods.
Front. Nucl. Eng. 3:1321627.
doi: 10.3389/fnuen.2024.1321627

Key results from examinations of seven high burnup pressurized water reactor spent nuclear fuel rods

Rose Montgomery*, Bruce Bevard, Paul Cantonwine and Yadukrishnan Sasikumar

Oak Ridge National Laboratory, Nuclear Energy and Fuel Cycle Division, Oak Ridge, TN, United States

At present, spent nuclear fuel (SNF) assemblies discharged from US commercial power plants are placed into dry storage following a short cooling time (<10 years) in the plant's spent fuel pool. The process of packaging the spent fuel into dry-storage canisters includes a drying step to remove residual water from the canister. During the drying process, the fuel rod cladding may reach temperatures as high as 400°C. Oak Ridge National Laboratory (ORNL) is performing destructive examinations of high burnup (HBU) (>45 GWd/MTU) SNF rods to address knowledge and data gaps related to extended interim storage and eventual transportation for disposal. The rods examined include four different kinds of fuel rod cladding: standard Zircaloy-4 (Zirc-4), low-tin (LT) Zirc-4, ZIRLO, and M5. Three rods were subjected to a thermal transient to assess the effects of decay-heat-driven high temperatures expected during vacuum drying of the fuel as it is prepared for interim dry storage. The examinations focus on the composite fuel rod performance, as compared with the performance of defueled rod cladding, and establish the baseline mechanical properties of a fuel rod before interim dry storage. The key results of these examinations are presented, including the measured mechanical and fatigue properties, observations of cladding hydrogen pickup and hydride reorientation effects on rod performance, effects of the simulated drying temperatures on rod performance, and general conclusions of SNF performance in extended interim dry storage and transport. The rods were found to be strong and durable in the expected loading conditions, even considering the formation of radial hydrides associated with vacuum drying. The combined testing provides a broad body of data supporting extended interim storage and transportation performance of HBU spent fuel.

KEYWORDS

sister rods, sibling pins, spent fuel interim storage, spent fuel transportation, fuel rod mechanical strength, fuel rod fatigue, fuel rod bending test, hydride reorientation

1 Introduction and description of the rods examined

This work presents the key results of destructive mechanical testing of representative high burnup (HBU) fuel rods 1) after reactor discharge and pool storage but before interim dry storage and 2) after a thermal transient simulating the dry storage vacuum drying process, where the fuel rod cladding may reach temperatures as high as 400°C (US Nuclear Regulatory Commission, 2003).

TABLE 1 Summarized nondestructive examination results and measured rod internal pressure, void volume, stack permeability, and fission gas release data (Montgomery et al., 2019a; Montgomery et al., 2019b; Montgomery and Morris, 2019; Montgomery and Bevard, 2023).

Rod →	30AD05	30AE14	3D8E14	3F9N05	3A1F05	F35P17
Cladding alloy	M5	M5	ZIRLO	ZIRLO	LT Zirc-4	Zirc-4
Rod average burnup (GWd/MTU)	54	54	59	54	51	60
Average pellet length (mm)	10.3	10.3	10.1	9.8	9.9	13.6
Estimated number of pellets in the stack	358	357	367	374	371	272
Bottom end plug length (mm)	14	14	19	20	10	11
Top end plug length (mm)	10	9	12	13	10	8
Plenum length (mm)	185	184	175	178	190	172
Fuel stack length (mm)	3,677	3,674	3,687	3,681	3,684	3,699
Overall rod Length (mm)	3,886	3,881	3,894	3,892	3,894	3,890
Maximum nondestructively-measured waterside oxide thickness (μm) and elevation (mm)	20	27	64	65	164	150
	3,245	3,445	3,205	3,075	3,115	3,055
Minimum remaining wall thickness (μm)	0.569	0.569	0.556	0.546	0.462	0.467
Rod outer diameter (mm), maximum, minimum, average	9.50	9.50	9.54	9.52	9.63	9.63
	9.38	9.41	9.43	9.43	9.36	9.44
	9.43	9.45	9.49	9.47	9.49	9.52
Rod growth $\Delta L/L$ (%)	0.32	0.19	0.53	0.48	0.53	0.43
Pellet stack growth $\Delta L/L$ (%)	0.53	0.45	0.80	0.64	0.72	1.13
Maximum change in cladding diameter (%)	0.00	0.00	0.42	0.21	1.37	1.37
Estimated fuel rod free plenum volume (cm^3)	8.2	8.2	7.6	7.8	8.2	7.5
Measured total rod free volume (cm^3)	10.6	11.0	11.7	11.8	12.9	13.3
Rod internal pressure (MPa)	3.46	3.22	4.18	3.98	3.73	4.68
Fission gas release (%)	1.8	1.8	3.6	3.6	3.3	N/A
Measured average stack permeability at 0.1 MPa pressure differential (m^2)	1.15	2.40	4.08	7.30	8.40	9.96

ORNL received 25 HBU spent fuel rods, called *sister rods*, in 2016. After nondestructive examinations were completed on all 25 rods (Scaglione et al., 2016; Montgomery et al., 2019a), destructive examinations were completed on seven of the fuel rods and were focused on four *baseline* rods and three *heat-treated* rods. The baseline rods represent the condition of the HBU rods after reactor operation and storage in a spent fuel pool, and the heat-treated rods provide the condition after a postulated vacuum drying thermal transient during interim storage packaging. The test results of the baseline rods can be compared with the results of the heat-treated rods to determine any effects of the thermal transient.

The fuel rods are 17 × 17 pressurized water reactor (PWR) rods irradiated in the two North Anna Power Station units operated by Dominion Energy in Mineral, Virginia, between 1984 and 2010. The results of the nondestructive tests of the rods, summarized by Montgomery et al. (Montgomery et al., 2019b; Montgomery and Morris, 2019), provide detailed information about the baseline features of the rods. The nondestructive examinations included detailed visual examinations, gamma scans, dimensional measurements, and eddy current liftoff measurements of the combined crud and oxide layer on the rod's waterside surface, and Table 1 summarizes the nondestructively measured dimensions of the sister rods discussed herein. Montgomery (Montgomery et al., 2019b) also provides calculated end-of-life fuel rod and pellet stack growth rates, estimated remaining fuel rod plenum volumes, the percentage change in fuel rod cladding diameter, fission gas release, and gas transmissibility data (Montgomery et al., 2019b; Montgomery and Bevard, 2023). This information is also summarized in Table 1.

The neutron fluence, pellet temperature, and coolant temperature vary axially along the fuel rod during reactor operation. The fuel rod's final condition is path dependent, and rods having the same final burnup may not have been subjected to the same local conditions in the reactor. The local variations of rod condition as a function of rod elevation are evident in the nondestructively acquired gamma count, rod outer diameter, and oxide thickness ("lift off") previously summarized by Montgomery et al. (Montgomery et al., 2019b). The gamma counts are analogous to local fluence/burnup, and the local oxide thickness is directly related to the local cladding and coolant temperatures. The baseline rod outer diameter and oxide thickness are the product of rod

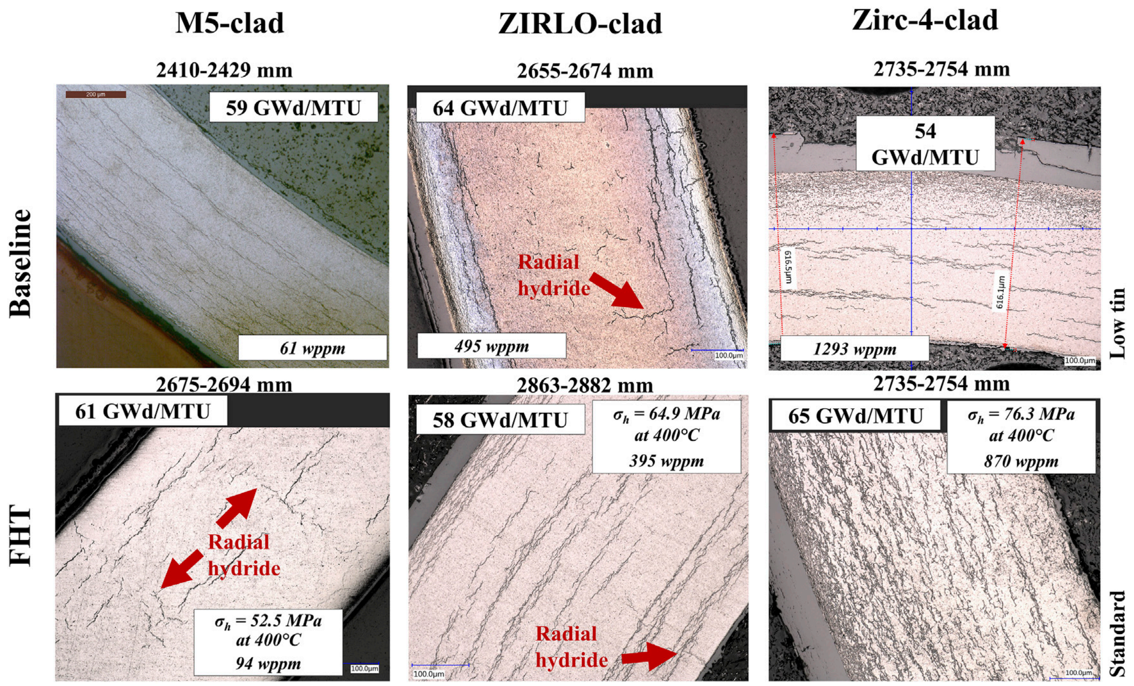

FIGURE 1
A comparison of the cladding hydride precipitates for baseline and FHT examples of the three cladding types.

temperature, fluence, power, and other parameters over operational time; therefore, it is not as directly tied to a single independent parameter.

With the exception of rods from assembly F35, the rods are typical batch fuel. The ZIRLO-clad rods are the Westinghouse North Anna Improved Fuel (NAIF/P + Z) design; the M5-clad rods are Framatome's Advanced Mark-BW design (AMBW); the standard Zircaloy-4 (Zirc-4)-clad rod is the Westinghouse low-parasitic (LOPAR) fuel assembly design; and the low tin (LT) Zirc-4-clad rods are the Westinghouse NAIF fuel assembly design. Thus, four of the examined rods are Westinghouse-designed and manufactured and two are Framatome-designed and manufactured. The rods are thus further grouped by cladding type to look for trends. A more detailed description of the sister rods is provided by Scaglione et al. in the ORNL test plan (Scaglione et al., 2016).

Rod P17 from assembly F35 (F35P17) was a test rod, as documented by Balfour (Balfour et al., 1992). Balfour also describes the cycles of operation: "The North Anna Unit 1 reactor operated with 18-month cycles during Cores 6 and 7 following 12-month cycles for Cores 4 and 5; core design outlet temperatures at hot full power ranged from 618°F (325.6°C) in Core 4°F–624°F (328.9°C) in Core 7. These temperatures were 10°F–27°F (5.6°C–15°C) higher than in previous high-burnup programs at the Farley, Surry, and Zion reactors." Additional detailed data on the operating conditions and the results of the poolside inspections are included by Balfour, and the measurements reported by Balfour compare well with the measurements taken by ORNL during the sister rod program for the two sister rods surveilled in the Electric Power Research Institute program (F35P17 and F35K13). Unfortunately, this level of detail is not publicly available for the other sister rods.

The reactors where the sister rods were irradiated were uprated twice. Some of the sister rod donor assemblies (F35, 30A) were operated during uprate cycles. Assembly F35 was operated early in the life of the reactor and over its lifetime had a lower average linear heat rate during operation than assembly 30A, although it was operated for four cycles. Assembly 30A was operated at the reactor's highest rated power and linear heat rate over three cycles.

Although local segment burnup does not incorporate all parameters that influence the rod's condition, it is publicly available and is used as an independent parameter to examine variations in the destructive examination results. The average coolant temperature—which is assumed to vary linearly from the bottom to the top of the reactor core—at the elevation of the specimen is also used as an independent correlating parameter to examine the results.

2 Heat treatments applied to selected rods

In preparation for dry storage, the volume around the fuel assemblies in the canister cavity is filled with water that must be drained and dried. Typically, the most challenging thermal condition experienced by the fuel during dry storage occurs during the drying sequence or just after drying during canister transfer to the storage pad. To better understand the effects of the drying and transfer sequence, full-length sister rods were subjected to a simulated dry-storage peak cladding temperature before destructive examinations. A comparison of the heat-treated rod data with the baseline rod data can be used to assess differences in

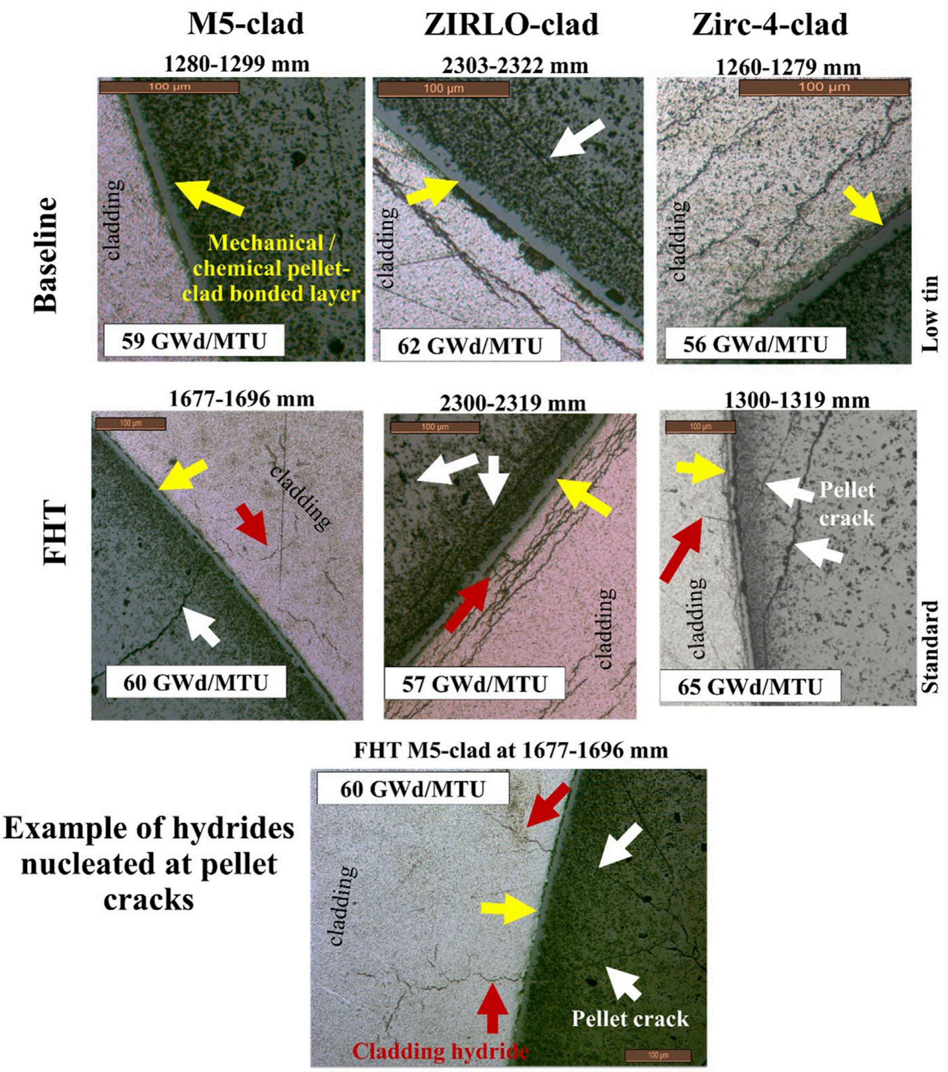

FIGURE 2
Optical micrographs of the pellet intact within the cladding enable the discovery of the pellet's features' effects on the rod performance. For example, pellet cracks (white arrows) were observed as nucleating radial cladding hydrides (red arrows), and this would not have been possible if the pellet were not included within the image. A mechanical/chemical bonded layer (yellow arrow) is developed where the pellet is in contact with the cladding.

rod properties or performance related to increased fuel rod temperature before dry storage.

A heat-treatment oven was designed and fabricated to enable full-length fuel rod heat treatment (FHT). The oven can impose a variety of normal-condition axial temperature profiles and peak cladding temperatures up to 530°C on a full-length fuel rod. In contrast with the heat treatment of rod segments in which the full-length rod is depressurized and segments are cut and repressurized, heat-treating full-length fuel rods before depressurization preserves the as-discharged internal pressure and induces the representative hoop stresses associated with bounding drying temperature conditions.

Three unpunctured fuel rods were heat-treated in the rod oven: one Zirc-4-clad (F35P17), one ZIRLO-clad (3F9N05), and one M5-clad (30AE14). To mimic the desired vacuum drying transient, the rods were heated slowly (10 °C/h), then held at 400°C (all axial elevations) for 8 h, and then slowly cooled (3.7 °C/h) to ambient temperature. A peak temperature of 400°C was selected to be applied to the full-length rods based on regulatory guidance regarding calculated peak fuel cladding temperatures for normal conditions of dry storage and short-term loading operations (US Nuclear Regulatory Commission, 2003).

The main purpose of the FHT was to investigate the effects of a phenomenon known as *cladding hydride reorientation* on the composite rod performance. Past testing at Argonne National Laboratory (Billone, 2019) shows that cladding hydride precipitates can be dissolved into the cladding alloy during the canister drying process, and, when the cladding cools at the slow rate expected during canister operations, the hydrides may reprecipitate in a radial orientation, depending on the cladding hydrogen inventory and the rod internal pressure. However, those tests were completed with empty cladding using aggressive rod internal pressure, whereas the FHT was performed using the whole fuel rod at its as-discharged pressure.

TABLE 2 Destructively-measured average waterside oxide thickness, average cladding hydrogen content, average cladding wall thickness, and transverse load bearing capacity.

Rod ID	Rod elevation, mm	Local burnup, GWd/MTU	Local coolant temp., ˚C	Oxide thickness, μm	Hydrogen content, wppm	Cladding wall thickness, μm	Transverse load capacity, N
30AD05	1,290	59	301	4	34	545	—
	2,333	59	311	9	—	557	17,985
	2,420	59	312	24	61	560	—
	3,163	56	319	17	—	554	17,000
	3,250	55	320	12	142	541	—
30AE14*	1,687	60	305	6	42	564	—
	2,598	60	313	15	—	556	17,632
	2,685	61	314	9	94	560	—
	3,409	50	321	12	152	562	—
	3,431	47	321	27	—	553	19,510
3D8E14	2,335	64	311	18	—	553	15,788
	2,360	64	311	30	—	553	17,752
	2,665	63	314	34	495	549	—
	3,129	60	319	62	—	547	17,210
	3,216	59	319	47/49**	616	545	—
3F9N05*	2,495	59	316	31	—	552	17,444
	1,435	59	305	13	130	559	—
	2,873	58	320	30	395	554	—
	3,341	51	324	39	142	554	—
	3,363	50	325	58	—	545	17,049
	3,388	50	325	55	—	545	18,683
3A1F05	1,270	56	301	15	130	560	—
	1,595	56	304	29	278	550	—
	2016	56	308	64	572	533	—
	2,393	55	312	70	680	530	—
	2,658	55	315	127	—	523	16,232
	2,683	55	315	134	—	523	12,384
	2,745	54	315	90/107**	1,293	546	—
	3,115	53	319	75/88**	667	517	—
	3,137	52	319	145	—	519	12,303
F35P17*	1,310	65	304	47	449	539	—
	2,658	51	318	110	—	523	12,476
	2,683	51	318	101	—	523	15,915
	2,745	66	319	81	870	524	—
	2,973	50	321	124	—	520	12,961
	2,998	50	322	136	—	520	12,500
	3,060	65	322	93/154**	1,440	485	—

*Rod was heat-treated.

**Average/average excluding measurements where spalling occurred.

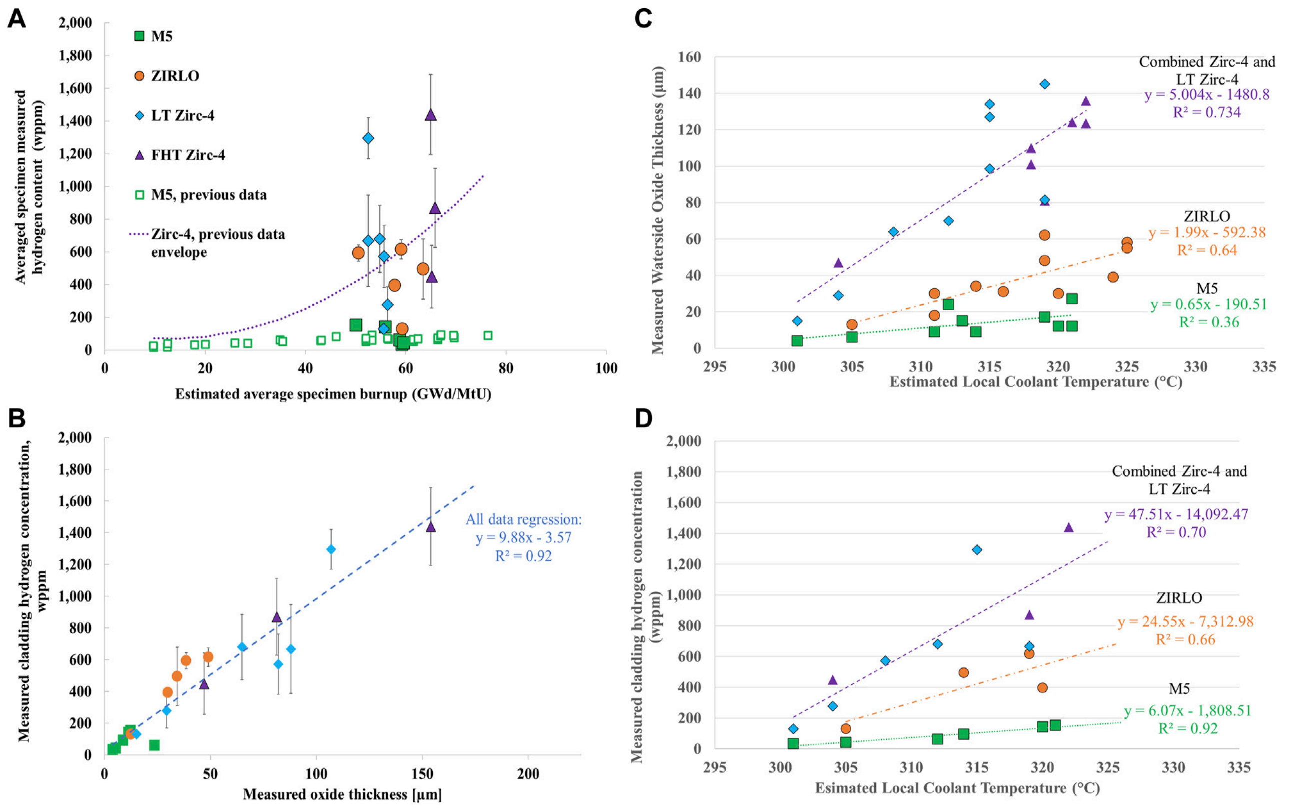

FIGURE 3
The measured cladding hydrogen concentration as a function of **(A)** average specimen local burnup and **(B)** measured local oxide thickness. **(C)** Measured cladding waterside oxide is well-correlated to estimated local coolant temperature, and **(D)** the measured cladding hydrogen concentration related to the waterside oxidation is also well-correlated with estimated local coolant temperature. Two of the graphs shown were originally published in Montgomery and Bevard (2023). The authors have obtained the necessary permissions to use them.

3 Destructive examinations completed, data collected, comparisons and trending

The sister rod examinations were specified to provide general performance characteristics, material property data, and mechanical performance properties on the baseline HBU rods and to discover any changes in performance related to vacuum drying (up to 400°C) during interim storage packaging. The pellets influence rod performance greatly in reactor operation (Cox, 1990), and the same is expected to be true in dry storage and transportation. Towards that end, the following measurements were completed on the baseline and heat-treated rods:

(1) End-of-life rod internal pressure, void volume, fission gas composition and release rate.
(2) Waterside oxide thickness and remaining cladding wall thickness, cladding hydrogen content and hydride precipitate orientation.
(3) Fatigue lifetime.
(4) Flexural modulus, elastic and plastic flexural rigidity, strain at failure in bending.
(5) Bearing capacity in transverse compression, flexural strength, and 0.2% yield strength in bending at room temperature and at 200°C.

A direct comparison of the baseline sister rods with the heat-treated sister rods was performed to identify degradation (or recovery) in mechanical performance of the rods resulting from dry storage. Each of the following subsections summarize the results of the testing completed for the destructive examinations discussed herein.

3.1 Rod internal pressure and void volume measurements

Commercial nuclear fuel rods are pre-pressurized with helium before irradiation. The magnitude of pre-pressurization varies with fuel design; at manufacture, the sister rods were pre-pressurized with helium. During irradiation, the rod internal pressure increases because fission gases (e.g., xenon, krypton) are produced and some portion of the evolved fission gases are released to the rod void volume, which increases the rod internal pressure above the as-manufactured rod pressure. The cladding stress from the rod internal pressure is typically higher in dry storage than during operation because the external pressure in dry storage is low compared to the reactor operating pressure.

The fuel rods are designed with an internal void volume that ensures the rod internal pressure is maintained within its allowable pressure, considering the fission gases that may be released from

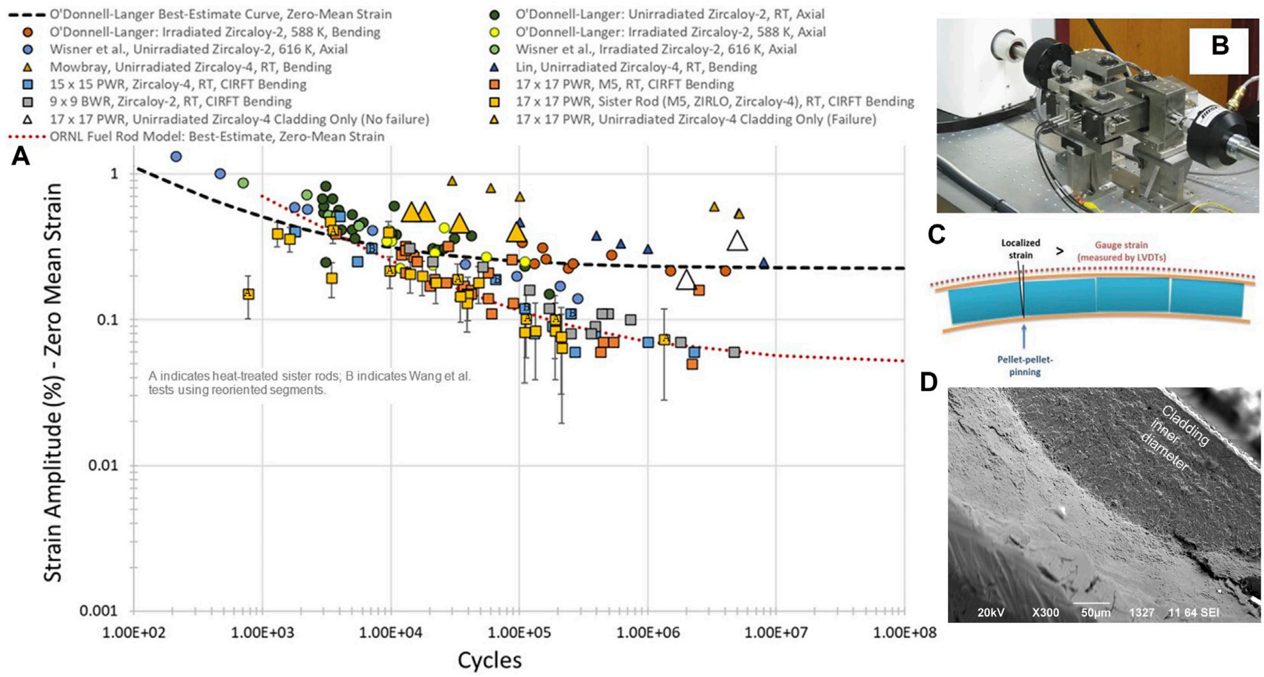

FIGURE 4
(A) The range of fatigue test data evaluated by ORNL for fuel rods using CIRFT (design limit shown in red) and by others for cladding tubing and coupons (design limit shown in black) highlights the differences between cladding-only and fuel rod performance. **(B)** The flexure mechanism used on CIRFT. **(C)** An illustration of the role of the pellets in creating localized strain when the rod is flexed in bending and **(D)** Scanning electron microscopy imaging of a specimen fractured in fatigue testing reveals that the crack nucleated at the cladding inner diameter, rather than as expected at the outer diameter. The likely explanation is that a local strain concentration is applied by pellet fragments during bending. Two of the graphs shown were originally published in Montgomery and Bevard (2023). The authors have obtained the necessary permissions to use them.

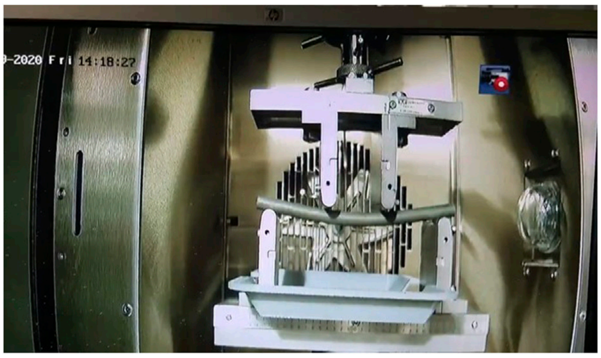

FIGURE 5
Four-point bend setup with a 6 in. fuel rod segment (see Supplementary Video S1).

the pellet stack. The void volume changes during operation as the cladding creeps and grows, and as cracks form within the pellets. For this discussion, the void volume is defined as including the volume in the plenum of the rod that is not occupied by the spring, the gap between the pellet outer diameter and the cladding inner diameter, the volume of any pellet chamfers and dishes, and the volume of pellet cracks or open porosity at the specified temperature. Because rod internal pressure and void volume are important parameters for determining rod performance throughout its lifetime, both were measured for each of the sister rods. These results are listed in Table 1. No difference related to the heat-treatment is visible in the rod internal pressure or void volume measurements. However, Montgomery and Morris also measured the ability of gas to move through the pellet stack (Montgomery and Morris, 2019), and they concluded that the heat-treated rods had better gas transmissibility, which may be related to a permanent increase in the cladding diameter caused by the heat treatment.

3.2 Observations from imaging, dimensional measurements, and cladding hydrogen measurements

Ayanoglu et al., 2024 describes the metallographic and ceramographic imaging, observations, and conclusions reached based on the examinations. This information is important to the discussion herein because the orientation of the cladding hydrides and their influence on the cladding performance has been previously established as directly influencing the mechanical performance (Billone, 2019). Figure 1 provides representative images of the cladding condition, both for baseline and heat-treated fuel rods. The baseline cladding has circumferentially oriented hydrides, and the density and distribution of the hydrides varies depending on whether the cladding is cold-worked stress-relieved (the Zirc-4, low tin Zirc-4, and ZIRLO cladding) or fully recrystallized (the

TABLE 3 Measured and calculated four-point bend data.

	Rod ID	Rod elevation, mm	Local burnup, GWd/MTU	Local coolant temp., °C	Maximum deflection at failure, mm	0.2% yield strength, MPa	Flexural strength, MPa	Failure strain, %	Flexural modulus, GPa	Flexural rigidity, N·m^2
Room temperature tests	30AD05	1,376	60	302	9.57	533	641	2.6	57.88	22.4
	30AE14*	1,055	59	299	13.43	481	609	3.8	57.17	22.5
	3D8E14	1,102	64	299	8.51	617	766	2.3	58.04	23.2
	3F9N05*	2,140	59	312	12.22	526	717	3.3	55.34	21.9
	3A1F05	1,356	57	302	8.59	616	768	2.3	59.25	23.3
	F35P17*	1,396	52	305	6.16	555	640	1.7	54.24	21.7
	F35P17*	1,549	53	307	7.49	565	693	2.2	54.72	22.2
200°C tests	30AD05	927	60	297	6.63	405	461	2.0	51.44	20.0
	30AD05	1877	59	307	6.97	443	502	2.0	53.60	20.7
	30AE14*	902	58	297	13.33	401	503	3.7	55.97	22.0
	30AE14*	2,127	60	309	13.91	385	502	4.6	53.66	21.0
	3D8E14	949	64	298	7.93	518	644	2.2	54.09	21.6
	3D8E14	1984	64	308	8.01	460	583	2.2	50.97	20.3
	3F9N05*	949	59	300	9.07	461	583	2.5	50.60	19.9
	3F9N05*	1987	59	311	10.51	448	588	2.9	50.64	20.0
	3A1F05	1,509	56	303	5.78	519	589	1.6	54.27	21.3
	3A1F05	2,307	54	311	5.64	481	550	1.6	51.25	20.3
	F35P17*	2,306	51	315	8.61	461	588	2.4	48.77	19.6

*Rod was heat-treated.

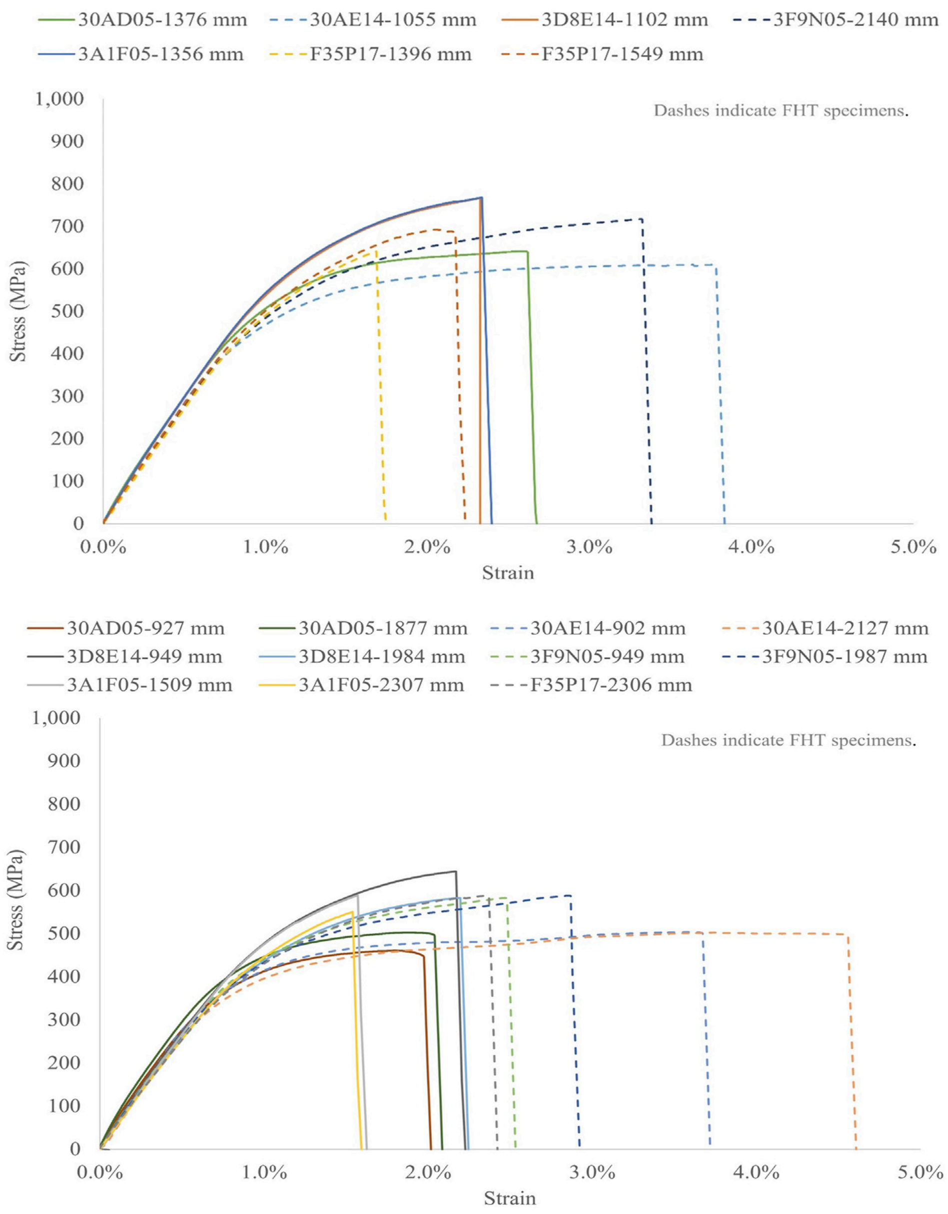

FIGURE 6
Measured stress *versus* strain for 6 in. fuel rods in four-point bending at (top) room temperature and (bottom) 200°C. The data clearly indicate a lower yield and ultimate strength and increased ductility for the FHT rods that is thought to be related to annealing of irradiation defects during the heat treatment. Two of the graphs shown were originally published in Montgomery and Bevard (2023). The authors have obtained the necessary permissions to use them.

M5 cladding). In the heat-treated rods, long radial hydrides were observed in fully recrystallized (RXA) cladding. The cold-worked stress-relieved (CWSR) cladding generally had very short or no radial hydrides. This result is believed to be due to the larger inventory of hydrogen in the CWSR cladding at this burnup. Radial hydrides were located at adjacent pellet cracks. The pellet cracks seem to have influenced the location of hydride precipitates, likely by creating a favorable stress distribution in the adjacent cladding.

Figure 2 shows representative images of the pellet condition for the baseline and heat-treated rods. The pellet crack morphologies were similar in the baseline and heat-treated rods within the burnup range investigated. Consistent with other studies, a mechanical and chemical pellet-clad bonded layer was observed at all investigated rod elevations, except for locations where the pellet does not contact the cladding (e.g., pellet chamfer locations). Past studies have demonstrated that fission products from the pellet are present in the cladding oxide to a depth of ~6 μm and suggest that fission recoil during irradiation is the source of the bonding process (Lach et al., 2019). Just inside the bonded layer, a discontinuous circumferential pellet crack is observed. Both the bonded layer and the circumferential crack are deemed important for consideration in modeling the functionality of how the pellet supports the cladding. No apparent difference is visible between the pellets in the baseline and heat-treated rods.

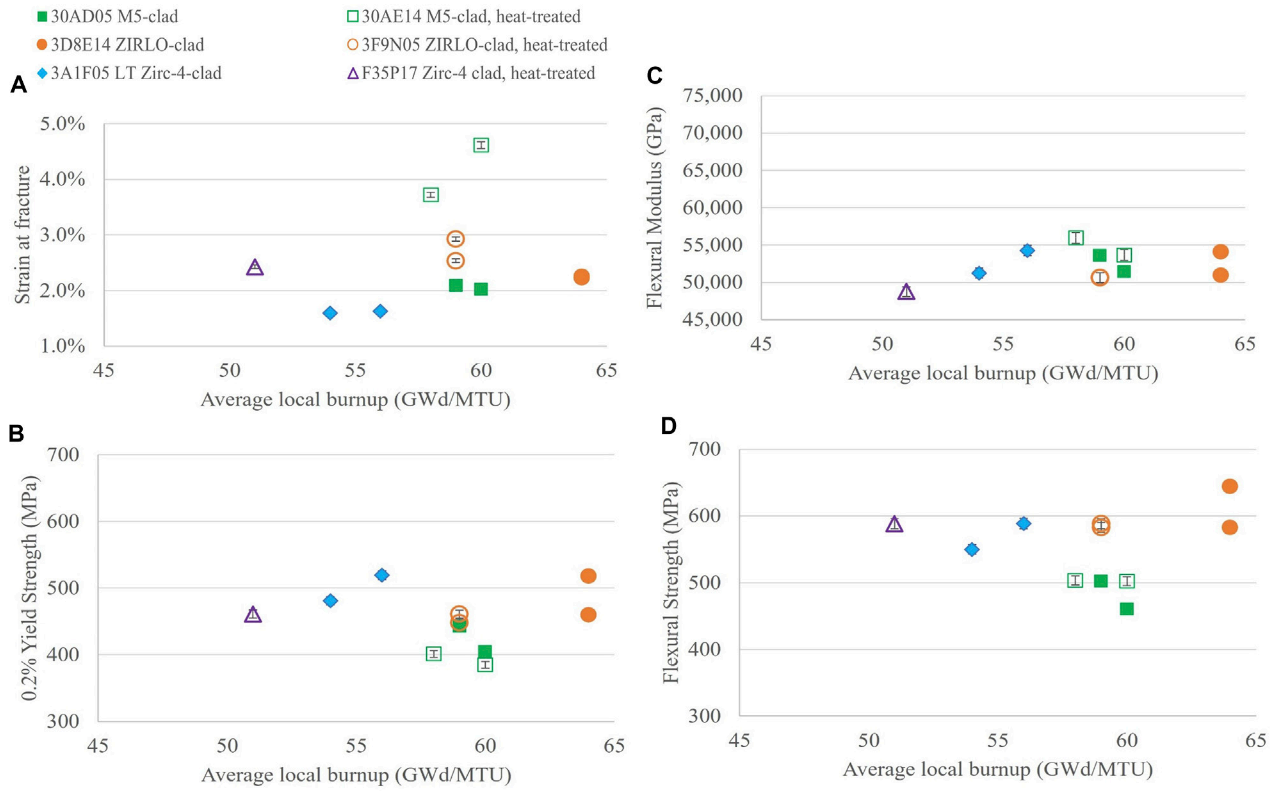

FIGURE 7
Calculated **(A)** strain at fracture, **(B)** 0.2% yield strength, **(C)** flexural modulus, and **(D)** flexural strength derived from the 200°C four-point bend tests plotted as a function of specimen average burnup.

Measurements of the cladding and pellet features derived from the metallographic imaging are summarized in Table 2 with the measured cladding hydrogen concentration for several elevations per rod. The test locations selected are from rod elevations having moderate to thick waterside oxide layers, typically near the 1,500, 2,400, and 3,200 mm rod elevations. For cladding hydrogen concentration measurements, 4 specimens around the circumference of the cladding were analyzed for each elevation and the average is reported in Table 2. The measurement process is discussed in more detail in Montgomery and Bevard, 2023.

Referring to Table 2, the overall results of the examinations indicate that the M5 cladding had the lowest waterside oxide thickness and lowest hydrogen content of the 4 alloys studied, followed by the ZIRLO cladding, the LT Zirc-4, and the Zirc-4 cladding, which had the thickest waterside oxide layer and largest hydrogen inventory. The M5 cladding hydrogen concentration data from the sister rods are very low (<200 wppm) but are slightly higher than previous data (Cole et al., 2012). The Zirc-4 cladding hydrogen concentration data are higher than the previous envelope of data (Cole et al., 2012), but F35P17 was an atypical lead test rod operated over four cycles to HBU. Previous hydrogen concentration data as a function of burnup are not currently available for comparison with the ZIRLO and LT Zirc-4 data. In general, the measured cladding hydrogen concentration for the sister rods is marginally higher than publicly available data (Garde and Slagle, 2009; Cole et al., 2012), and are therefore considered to be conservative examples for demonstration of the effects of hydrogen content on rod performance.

Montgomery and Bevard, 2023 investigated trends for the measured waterside oxide thickness, remaining cladding thickness, cladding hydrogen concentration and hydrogen pickup fractions as a function of local burnup, but they did not correlate well. An example showing cladding hydrogen concentration plotted as a function of local burnup is shown in Figure 3A. However, the cladding hydrogen concentration is very well correlated with the measured oxide thickness (see Figure 3B), which should be expected, as the hydrogen available for cladding pickup is generated through the oxidation process. Further, when plotted with estimated local coolant temperature, a trend of waterside oxide thickness (Figure 3C) and hydrogen concentration (Figure 3D) emerges that is clearly associated with specific alloys. Therefore, while there does not seem to be an alloy-specific hydrogen pickup rate, there is a distinct difference in oxidation rate and related hydrogen concentration for the different alloys.

3.3 Fatigue tests

SNF assemblies must be shipped to other sites for processing and disposal. During shipment, the fuel is typically oriented horizontally,

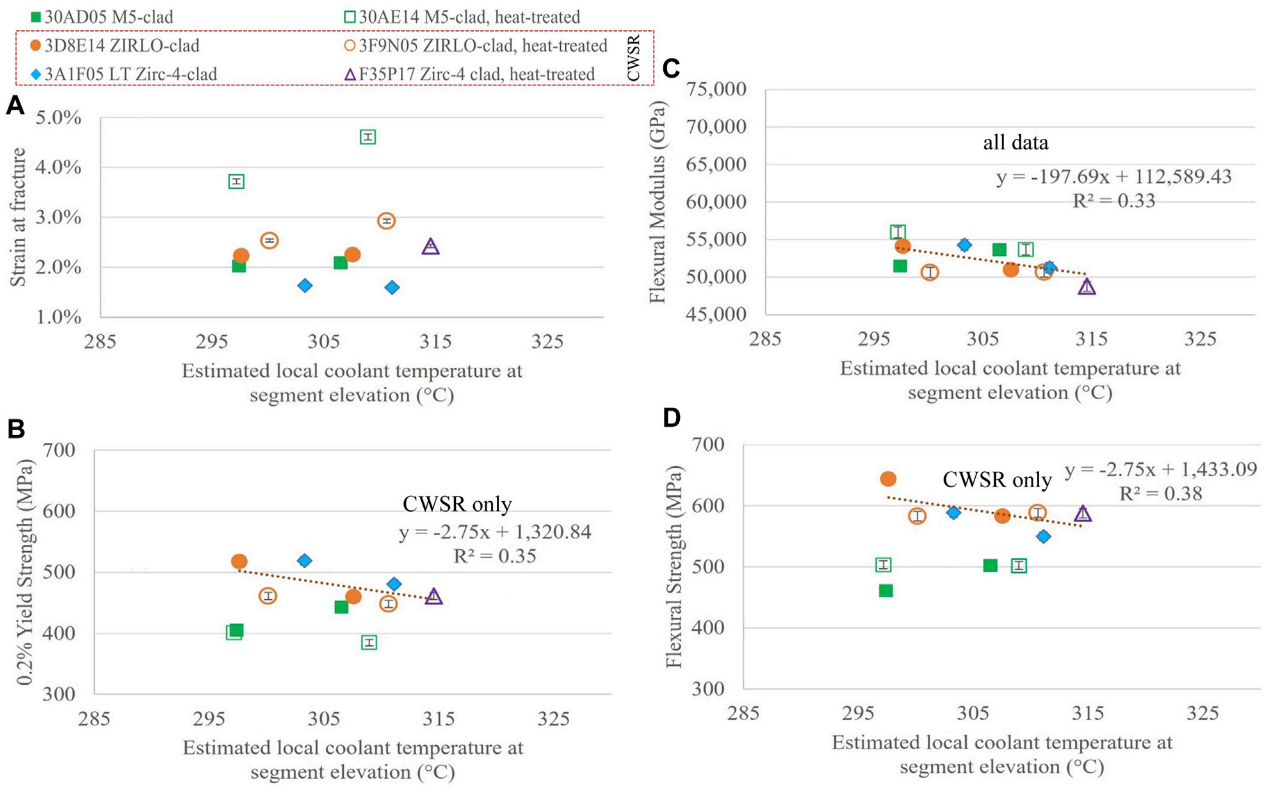

FIGURE 8
Calculated **(A)** strain at fracture, **(B)** 0.2% yield strength, **(C)** flexural modulus, and **(D)** flexural strength derived from the 200°C four-point bend tests plotted as a function of estimated local coolant temperature at the segment elevation.

and the fuel rods are subject to periodic alternating loads related to the movement of the vehicle. These loads result in the alternating bending of the SNF rods. The number of bending cycles is related to the length of the shipping route: longer routes produce more cycles.

Fatigue performance is typically characterized by the number of cycles required to produce failure at a specified strain amplitude. Many tests are completed, and the strain amplitude is varied—even to very high amplitudes not expected during actual service—to characterize fatigue performance over a wide range of fatigue cycles. The strain amplitude data are then plotted against the measured cycles to rod fracture to obtain a characteristic fatigue curve for the tested material. Wang et al. (Wang and Wang, 2017; Wang et al., 2018) developed a method for fatigue testing the SNF segments called the Cyclic Integrated Reversible-Bending Fatigue Tester (CIRFT). A 6 in. long unpressurized fuel rod segment is placed in the CIRFT machine at room temperature and bent in a positive and negative direction (i.e., reversibly) to represent one bending fatigue cycle. The flexure cycle is imposed repeatedly until fracture occurs. The CIRFT machine is run at 5 Hz—five fatigue cycles per second. A strain amplitude is calculated by directly measuring the extent to which the rod segment bends during the test.

The data produced by Wang and Wang (2017), Wang et al. (2018) and supplemented herein through tests of the sister rods, as shown in Figure 4, indicate that the fatigue performance of the SNF segments is relatively insensitive to differences such as cladding alloy type, local oxide thickness, burnup, and reoriented cladding hydrides. The fatigue performance of the baseline fuel rod segments was similar to that of the heat-treated fuel rod segments. No obvious differences were observed between different cladding types or different fuel rod designs (9 × 9 BWR vs. 15 × 15 PWR vs. 17 × 17 PWR). Furthermore, Wang and Wang (2017), Wang et al. (2018) tested several segments that were subjected to high temperature and cladding stress to induce extreme hydride reorientation, and no difference in fatigue performance was observed.

However, the tests from the sister rods indicate that fatigue performance of fuel rods is degraded when compared with tests of cladding alloys. Specifically, the best-estimate fatigue limit of the fuel rod is approximately a factor of five lower than the fatigue limit for cladding alloys (0.25% (O Donnell and Langer, 1964) vs. 0.05%). This difference is attributed to stress risers imposed on the fuel rod cladding by pellet discontinuities such as pellet–pellet gaps and pellet cracks created during reactor operation. Evidence of this phenomenon was observed in examinations of the fatigue fractures, as shown in the scanning electron microscopy image in Figure 4. Traditional solid mechanics evaluations indicate that the peak stresses on the cladding should be at the outer diameter of the cladding, and fracture should nucleate at the outer diameter of the cladding. The fractography revealed crack-like features on the inner diameter of cladding after fatigue failure, and the observed inner diameter crack initiation indicates that fatigue degradation occurs because of local strain concentration at pellet discontinuities such as pellet cracks and pellet–pellet interfaces. Therefore, a primary finding from the fatigue

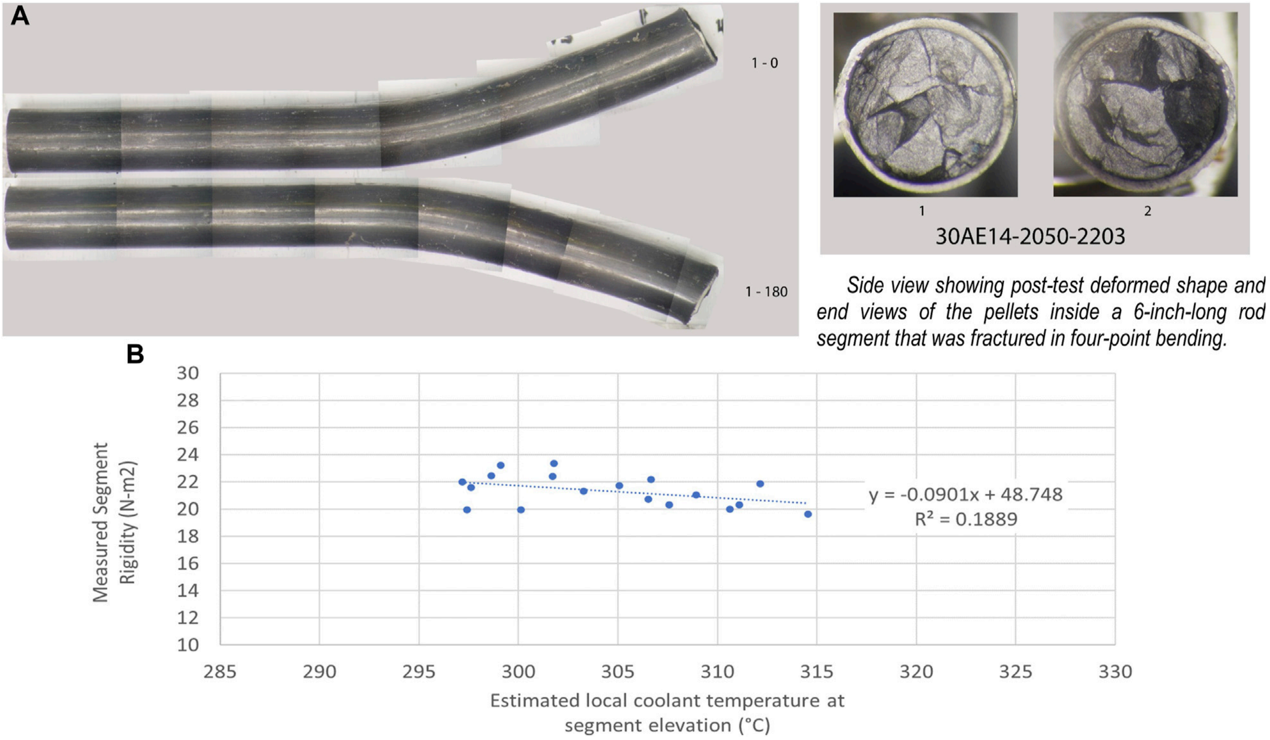

Side view showing post-test deformed shape and end views of the pellets inside a 6-inch-long rod segment that was fractured in four-point bending.

FIGURE 9
(A) The two-halves of a 6 in. M5-clad rod segment fractured in four-point bend clearly indicates a very large amount of deformation sustained up to fracture. This particular rod fractured in the body of a pellet, as opposed to at a pellet–pellet interface location. The vertical lines appearing in the image are an artifact of the imaging process. **(B)** The segment rigidity for all tests vs. the estimated coolant temperature at the segment rod elevation. Two of the graphs shown were originally published in Montgomery and Bevard (2023). The authors have obtained the necessary permissions to use them.

testing is that the pellets must be considered as an integral part of the rod structure in evaluating its performance in bending fatigue. However, as discussed by Montgomery et al. (Montgomery and Bevard, 2023), there is still significant margin to the currently available transportation loads and frequency, suggesting fatigue damage does not accumulate and fatigue failure does not occur as a result of the anticipated transportation conditions.

3.4 Bending tests

Four-point bending was selected to study the strength properties of the fuel rods at room temperature and at 200°C. The test provides values for the elastic modulus in bending and the flexural stress and flexural strain response. It is traditionally used to study brittle materials in which the number and severity of flaws exposed to the maximum stress directly relates to the flexural strength and crack initiation. Bending is the most likely loading scenario for fuel rods. When a rod is loaded in axial compression, it acts as a long, slender column and buckles, creating a bending scenario. When a lateral load is applied, the rod, pinned by the relatively fixed spacer grid supports, is subjected to bending. Therefore, understanding the rod response to bending is extremely important.

The load frame used for the bending tests, with its test fixturing, is shown in Figure 5. The frame applies a constant bending moment over the gauge length of the test specimen. The evaluation method and its uncertainties are discussed in detail by Montgomery et al. (Montgomery and Bevard, 2023); it should be noted herein that elastic beam theory is used as a practical approach to evaluate the mentioned mechanical properties. The resulting evaluated properties should not be considered cladding material properties. The sound of the rod during fracture was recorded, and the consensus is that it resembles the sound of tin cry prior to failure. A link to the video recorded during the test, which includes sound, is provided in Figure 5.

The resulting composite fuel rod mechanical properties are listed in Table 3, and the stress vs. strain data for the room temperature and 200°C tests are plotted in Figure 6. Figure 7 plots the strain at fracture, yield strength, flexural modulus, and flexural strength as a function of the local rod burnup. Figure 8 plots the same information as a function of the average local reactor coolant temperature.

The trends investigated in Figure 7 with specimen average burnup at the specimen rod elevation did not produce a significant correlation, but the dataset is small and limited to high burnup observations. At high burnup, all of the examples have pellet-cladding interaction and pellet-cladding bonding, which could be significantly different from the performance at low burnup. Referring to Figure 7B, the M5-clad rod segments have the lowest yield and flexural strength, even though they have the thinnest waterside oxide layer and thus the most remaining cladding wall thickness. The lower strength of the M5-clad segments is attributed to its RXA microstructure and corresponding inherently ductile characteristic (Motta et al., 2015). When plotted against the estimated local coolant temperature

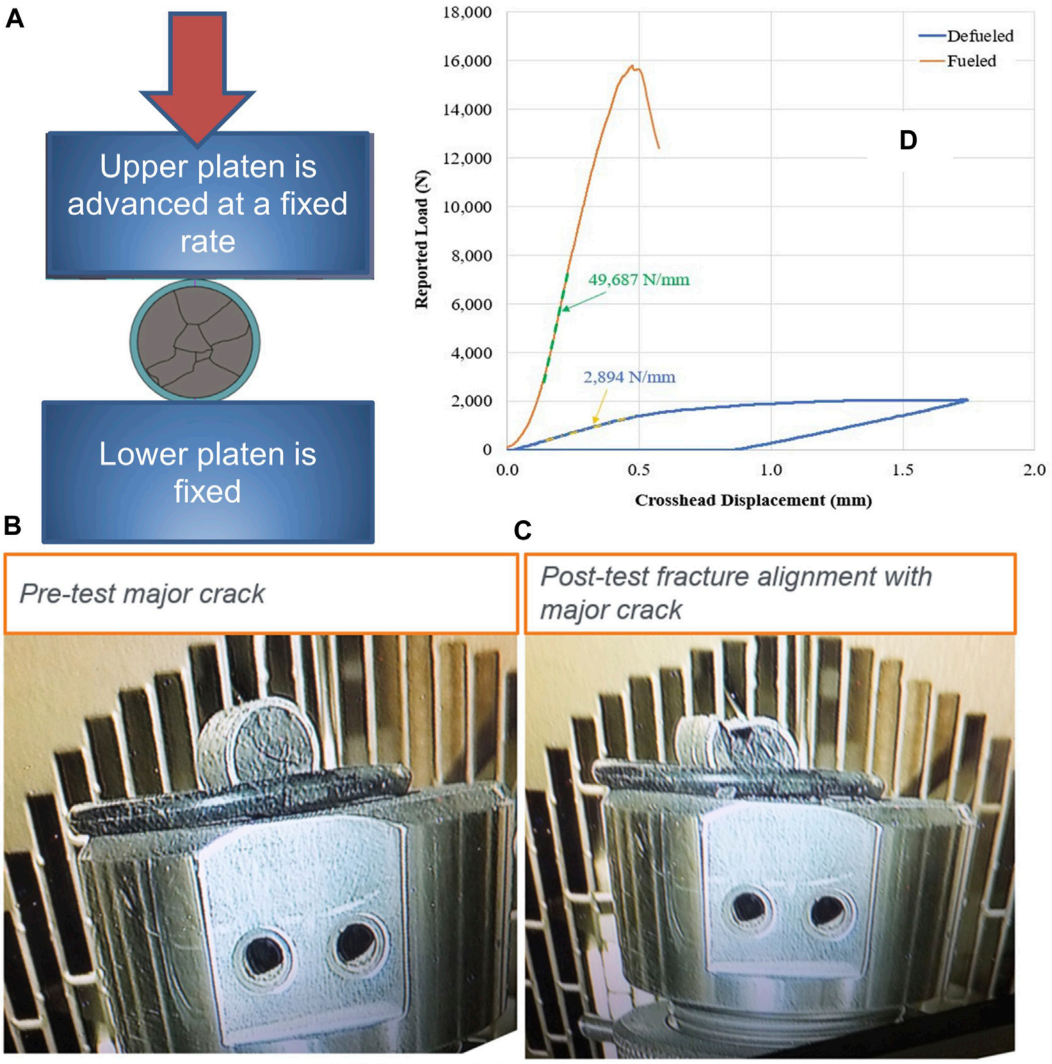

Pre-test major crack

Post-test fracture alignment with major crack

RCT fracture path along major pellet crack.

FIGURE 10
Transverse compression tests, **(A)** test configuration, **(B)** and **(C)** the pretest and posttest alignment of a preexisting pellet crack that influenced the rod segment fracture plane under the tested loading condition, and **(D)** the crosshead displacement vs. reported load compared for a rod segment and cladding-only test illustrates that the rod can carry ~8 × the load in transverse compression. Two of the graphs shown were originally published in Montgomery and Bevard (2023). The authors have obtained the necessary permissions to use them.

(Figure 8), a potential correlation is observed for the CWSR cladding types (LT Zirc-4, ZIRLO, Zirc-4) for yield strength and flexural strength. The flexural modulus of all specimens (CWSR and RXA) also trends reasonably well with local coolant temperature. Montgomery et al. also investigated trends with measured local waterside oxide thickness, hydrogen concentration and reorientation, and remaining cladding thickness with limited success (Montgomery and Bevard, 2023).

Referring to Figure 6, the heat-treated rods had significantly more ductility than the baseline rods (on the order of 2 × for the M5-clad rods), which suggests that annealing of irradiation damage may have occurred during the simulated vacuum drying heat treatment. This is further indicated by the decreased yield strength and increased strain at fracture as compared with the corresponding baseline rods. Significant flexure before fracture was observed for the FHT M5 rod segments, as shown in Figure 9A for one specimen, post-fracture.

The measured elastic flexural modulus was comparable among all rod segments tested and did not change much for the temperatures tested (room temperature and 200°C), as expected. Although the heat treatment did not appear to affect the flexural rigidity of the rod, when all data are pooled, flexural rigidity seems to depend on the local coolant temperature during reactor operation, as shown in Figure 9B. This is likely related to annealing of irradiation defects in the cladding that occurred in reactor, as higher coolant temperature resulted in a more ductile and less rigid rod.

3.5 Ring compression tests

During the last decade, Argonne National Laboratory has developed a significant body of data on cladding hydride reorientation and the associated effects on cladding ductility

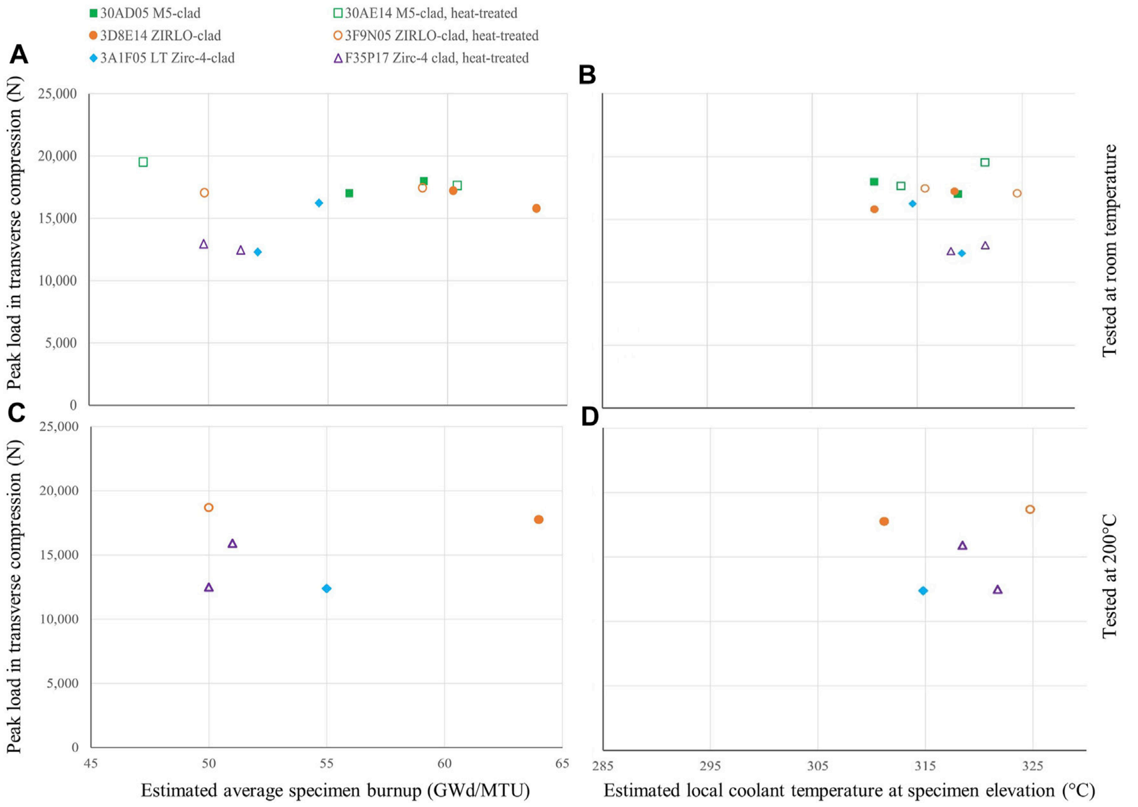

FIGURE 11
Measured transverse load bearing capability (room temperature and 200°C) for each specimen plotted as a function of **(A)**, **(B)** the estimated average specimen burnup and **(C)**, **(D)** the estimated average local coolant temperature at the specimen's in-reactor elevation.

using ring compression testing (RCT), as summarized by Billone, 2019. ORNL's RCT data provide supplementary information on the transverse load-bearing capability of intact fuel rods (cladding and pellets). Similar to RCT of cladding specimens, the fueled rod segment is loaded across its diameter in compression, as shown in Figure 10. The load as a function of crosshead displacement is measured to failure. Table 2 summarizes the results of 5 tests completed at 200°C and 12 tests completed at room temperature. The specimens typically carried load until at least one cladding fracture developed.

Fueled RCT indicates a large transverse load-bearing capability, independent of hydride reorientation, at about 16.4 kN on average, with a minimum load-bearing capability of 12.3 kN for the tested segments. No appreciable difference is observed in the maximum load-bearing capability of the segments from room temperature to 200°C, and there is no apparent difference related to the heat-treatment applied to some of the rods. When the room temperature tests and the 200°C tests are plotted with the segment average burnup (Figures 11A,B) and with the average local coolant temperature at the segment's rod elevation (Figures 11C,D), no trends are observed. However, a few points are noticeably lower in measured peak load, and suspicions were confirmed when the measured average segment waterside oxide thickness (Figure 12A) and the measured average remaining cladding wall thickness (Figure 12B) are plotted. The peak load capacity in transverse compression strongly correlates with the remaining cladding wall thickness, which is simply the thickness of the cladding wall that was not oxidized in reactor. The pelletside oxide thickness is typically thin and on the order of 10 μm, but the waterside oxidation kinetics depend on the local operating conditions and the alloy type.

Another primary observation is that the orientation of the major cracks in the pellet appear to nucleate fracture of the adjacent cladding and determine the pellet fracture plane, as illustrated in Figure 10. The observed failure of cladding correlated to cracks in the pellet suggests that relative pellet fragment motion may be important to predicting failure of the composite rod in transverse compression. ORNL measured failure loads of fuel rods that were significantly higher (about 8×) than defueled cladding-only tests, as shown in Figure 10.

4 Discussion and summary of key findings

The combined testing of the HBU sister rods provides a broad body of data supporting the extended interim storage and transportation performance of baseline HBU used fuel and vacuum-dried spent fuel for interim dry storage and eventual transport. In general, the HBU rods were found to be strong and durable in the expected loading conditions. For example, in bending, the rods retain significant flexural strength and ductility, even at HBU and after FHT. Fueled RCT indicates a large transverse load-bearing capability for both the baseline and FHT rods, independent of cladding alloy and any associated hydride reorientation, at about

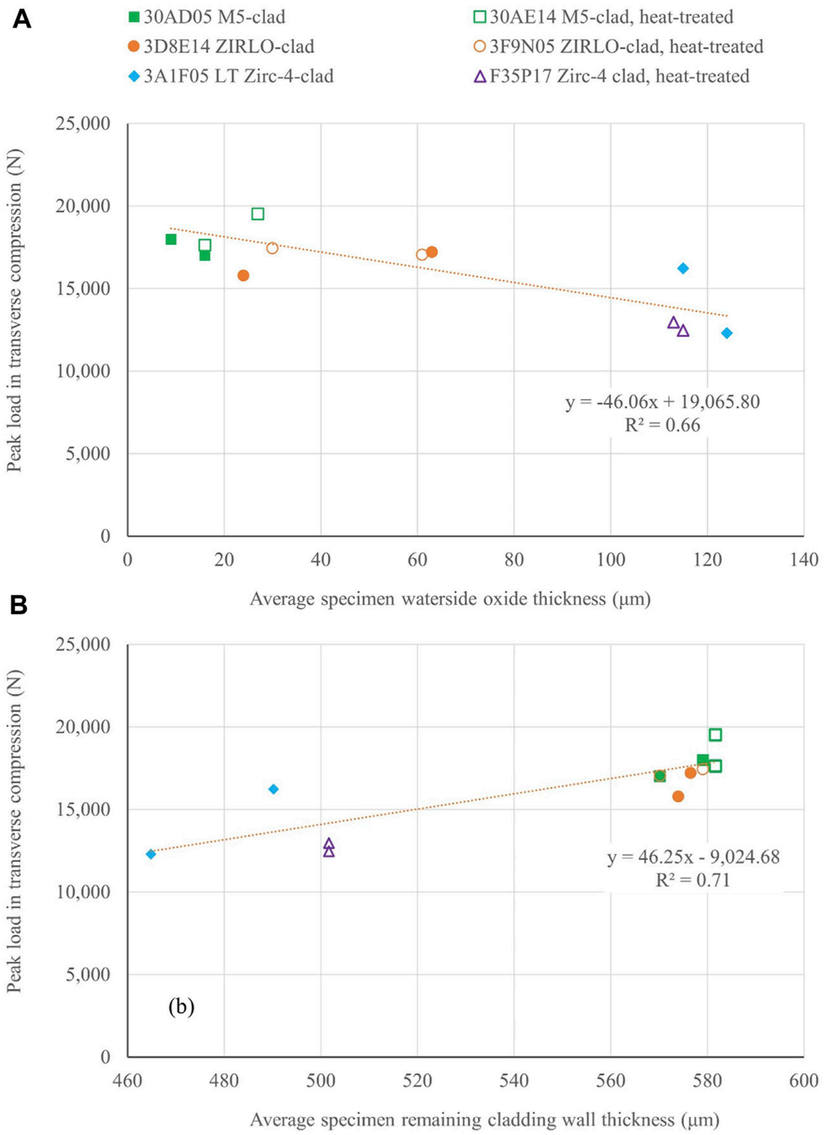

FIGURE 12
Peak load measured in transverse compression plotted with **(A)** average measured specimen waterside oxide thickness, and perhaps more appropriately, **(B)** the average remaining cladding wall thickness (measured nondestructively using eddy current (Montgomery et al., 2019a)).

8× the capacity of empty cladding. No appreciable difference exists in the RCT load-bearing capacity from room temperature to 200°C, and the peak load capacity correlates with the remaining cladding wall thickness, which is related to the waterside oxidation layer thickness developed during reactor operation.

Considering possible changes in performance related to dry storage vacuum drying, the measured cladding hydrogen content of the sister rods is slightly higher than, but consistent with, other available data. Strong correlations were observed between reactor local coolant temperature and waterside oxide thickness, and waterside oxide thickness and cladding hydrogen content. Hydride reorientation did occur at the imposed FHT temperatures and cladding stress (as generated by the as-discharged rod internal pressure); the M5 cladding had some long radial hydrides, and the other alloys had only very short radial hydrides. However, the radial hydride orientation did not degrade performance of the fuel rods.

Regarding the extended effects of the FHT unrelated to hydride reorientation, the heat-treatment (and thus vacuum-drying) resulted in decreased bending yield strength and increased ductility that are alloy dependent and we strongly suspect are related to the annealing of irradiation damage accumulated by the cladding during reactor operation and during vacuum drying. Fission and fill gas was shown to move more readily through the pellet stack in the heat-treated rods, and this is attributed to a permanent increase in the rod diameter that occurred because of the increased rod internal pressure during FHT.

One of the most important findings from the sister rod work is the observed influence of the pellet, pellet cracks, and pellet-to-cladding bonding on the strength and performance of the composite rod.

While the fatigue performance of HBU fuel rods appears to be unaffected by the FHT applied, hydride orientation, fuel rod

]

type, or cladding type, the CIRFT testing found that the fatigue performance of HBU fuel rods is degraded compared with the fatigue performance of cladding alloys. This degradation appears to be caused by stress concentrations that occur at pellet–pellet interfaces or pellet cracks under bending loads. During fatigue conditions, cracks appear to initiate from the cladding inner diameter, indicating pellet interaction effects. Further, the pellets constrain deformation of the cladding under RCT conditions, resulting in significant improvement in failure loads in transverse compression, but the orientation of the major cracks in the pellet determines the pellet fracture plane, and the cracks appear to nucleate fracture of the adjacent cladding wall. Finally, the pellet cracks have been observed to nucleate hydrides at the adjacent cladding inner diameter, and the specific influence of the precipitates at these locations deserves further study.

5 Future work

One of the primary observations from this work is the effect of in-reactor and vacuum-drying local temperatures on the rod performance. These effects are likely related to the annealing of irradiation defects within the fuel rod cladding. Future work plans focus on better defining the degree of annealing of defects with time at temperature and will include bending and fatigue tests to capture resulting effects on rod performance.

Data availability statement

The original contributions presented in the study are included in the article/Supplementary material, further inquiries can be directed to the corresponding author.

Author contributions

RM: Conceptualization, Data curation, Formal Analysis, Investigation, Methodology, Project administration, Resources, Writing–original draft, Writing–review and editing. BB: Conceptualization, Funding acquisition, Methodology, Resources, Supervision, Writing–review and editing. PC: Data curation, Investigation, Methodology, Writing–review and editing. YS: Investigation, Visualization, Writing–review and editing.

Funding

The author(s) declare financial support was received for the research, authorship, and/or publication of this article. This research was sponsored by the Spent Fuel and Waste Science and Technology Program of the US Department of Energy and was carried out at Oak Ridge National Laboratory under contract DE-AC05-00OR22725 with UT-Battelle, LLC.

Acknowledgments

The authors would like to thank the staff at the Irradiated Fuels Examination Laboratory and our collaborators at Sandia National Laboratories, Pacific Northwest National Laboratory, Oak Ridge National Laboratory, Westinghouse, Framatome, Dominion Energy, and Electric Power Research Institute.

Licenses and permissions

Notice: This manuscript has been authored by UT-Battelle, LLC, under contract DE-AC05-00OR22725 with the US Department of Energy (DOE). The US government retains and the publisher, by accepting the article for publication, acknowledges that the US government retains a nonexclusive, paid-up, irrevocable, worldwide license to publish or reproduce the published form of this manuscript, or allow others to do so, for US government purposes. DOE will provide public access to these results of federally sponsored research in accordance with the DOE Public Access Plan (http://energy.gov/downloads/doe-public-access-plan).

Conflict of interest

The authors declare that the research was conducted in the absence of any commercial or financial relationships that could be construed as a potential conflict of interest.

Publisher's note

Supplementary material

The Supplementary Material for this article can be found online at: https://www.frontiersin.org/articles/10.3389/fnuen.2024.1321627/full#supplementary-material

References

Ayanoglu, M., Montgomery, R., Harp, J., and Sasikumar, Y. (2024). Metallographic examinations and hydrogen measurements of high-burnup spent nuclear fuel cladding. *J. Nucl. Mater.* 589 (154833), 154833. ISSN 0022-3115. doi:10.1016/j.jnucmat.2023.154833

Balfour, M. G., Kilp, G. R., Comstock, R. J., McAtee, K. R., and Thornburg, D. R. (1992). *Corrosion of zircaloy-clad fuel rods in high-temperature PWRs: measurement of waterside corrosion in North Anna unit 1, TR-100408, tier 2 research Project 2757-1*. Washington, D.C., United States: Electric Power Research Institute.

Billone, M. C. (2019). *Ductility of high-burnup-fuel ZIRLO™ following drying and storage*, ANL-19/14, M2SF-19AN010201011 Rev. 3. Lemont, IL, United States: Argonne National Laboratory.

Cole, S. E., Delafoy, D., Graebert, R. F., Louf, P.-H., and Teboul, N. (2012). "Framatome optimized fuel rods for LWRs," in Proceedings of the Water Reactor Fuel Performance Meeting/Top Fuel, Manchester, UK, September, 2012, 230.

Cox, B. (1990). Pellet-clad interaction (PCI) failures of zirconium alloy fuel cladding — a review. *J. Nucl. Mater.* 172 (3), 249–292. doi:10.1016/0022-3115(90)90282-r

Garde, A. M., and Slagle, W. H. (2009). Hydrogen pick up fraction for ZIRLO™ cladding corrosion and resulting impact on the cladding integrity. *Proc. Water React. Fuel Perform. Meet. – WRFPM/Top Fuel*, 268.

Lach, T. G., Edwards, D. J., Buck, E. C., McNamara, B. K., Schwantes, J. M., and Clark, R. A. (2019). Fission recoil-induced microstructural evolution of the fuel-cladding interface [FCI] in high burnup BWR fuel. *J. Nucl. Mater.* 521, 120–125. doi:10.1016/j.jnucmat.2019.04.044

Montgomery, R., and Bevard, B. B. (2023). *Sister rod destructive examinations (FY22)*. ORNL/SPR-2023/2935. https://www.osti.gov/biblio/1986208.

Montgomery, R., and Morris, R. N. (2019). Measurement and modeling of the gas permeability of high burnup pressurized water reactor fuel rods. *J. Nucl. Mater.* 523, 206–215. ISSN 0022-3115. doi:10.1016/j.jnucmat.2019.05.041

Montgomery, R., Morris, R. N., Bruce, B., and Scaglione, J. (2019b). Key results from detailed nondestructive examinations of 25 pressurized water reactor high burnup spent nuclear fuel rods. *Nucl. Sci. Eng.* 193 (8), 884–902. doi:10.1080/00295639.2019.1573602

Montgomery, R., Bevard, B., Morris, R. N., Goddard Jr, J., Smith, S. K., and Hu, J. (2019a). *Sister rod nondestructive examination final report*, SFWD-SFWST-2017-000003 Rev. 1 (M2SF-17OR010201021)/ORNL/SPR-2017/484 Rev. 1 (ORNL/SPR-2018/801). Oak Ridge, TN, United States: Oak Ridge National Laboratory.

Motta, A. T., Couet, A., and Comstock, R. J. (2015). Corrosion of zirconium alloys used for nuclear fuel cladding. *Annu. Rev. Mater. Res.* 45 (1), 311–343. doi:10.1146/annurev-matsci-070214-020951

O Donnell, W. J., and Langer, B. F. (1964). Fatigue design basis for Zircaloy components. *Nucl. Sci. Eng.* 20 (1), 1–12. doi:10.13182/nse64-a19269

Scaglione, J. M., Montgomery, R. A., and Bevard, B. B. (2016). *Post-irradiation examination plan for high burnup demonstration Project sister rods*. SFWD-SFWST-2017-000090 ORNL/SR-2016/708. Oak Ridge, TN, United States: Oak Ridge National Laboratory.

US Nuclear Regulatory Commission (2003). *Spent fuel Project office, interim staff guidance 11 revision 3, cladding considerations for the transportation and storage of spent fuel*, SFST-ISG-11 Revision. Rockville, Maryland, United States: US Nuclear Regulatory Commission.

Wang, J.-A., and Wang, H. (2017). *Mechanical fatigue testing of high burnup fuel for transportation applications*. NUREG/CR-7198/R1.

Wang, J.-An, Wang, H., Jiang, H., and Bevard, B. (2018). High burn-up spent nuclear fuel transport reliability investigation. *Nucl. Eng. Des.* 330, 497–515. ISSN 0029-5493. doi:10.1016/j.nucengdes.2018.02.007

frontiers | Frontiers in Nuclear Engineering

TYPE Perspective
PUBLISHED 07 May 2024
DOI 10.3389/fnuen.2024.1380108

OPEN ACCESS

EDITED BY
Anne Campbell,
Oak Ridge National Laboratory (DOE),
United States

REVIEWED BY
Rinkle Juneja,
Oak Ridge National Laboratory (DOE),
United States

*CORRESPONDENCE
A. E. White,
✉ whitea@mit.edu

RECEIVED 01 February 2024
ACCEPTED 02 April 2024
PUBLISHED 07 May 2024

CITATION
White AE, Baglietto E, Bucci M, Howard NT and Rodriguez-Fernandez P (2024), Fusion plasma turbulence research beyond the burning plasma era: perspectives on transport model validation in fusion and fission.
Front. Nucl. Eng. 3:1380108.
doi: 10.3389/fnuen.2024.1380108

Fusion plasma turbulence research beyond the burning plasma era: perspectives on transport model validation in fusion and fission

A. E. White*, E. Baglietto, M. Bucci, N. T. Howard and P. Rodriguez-Fernandez

Massachusetts Institute of Technology, Cambridge, MA, United States

In fusion, the validation of turbulent transport models is undertaken with the goals of making basic physics discoveries as well as for development of new predictive models to improve the operation and enhance the performance of existing and future fusion reactors. A fusion industry is just beginning to emerge globally. Like fission, validation in fusion energy research is a vibrant research area, but unlike fusion, a fission industry exists. The fission power industry motivates validation efforts, often performed at universities with small-scale experiments and advanced models and simulations developed in-house. Because fission research spans basic physics and applications, and addresses near-term and long-term industry interests, validation is thriving. This perspective article describes the validation of turbulent transport models in both fusion research and fission research, draws parallels between the validation methods and techniques used in two areas of the fields, and presents an outlook for thriving university fusion and fission research programs underpinned by a virtual cycle of basic and applied research that supports industry needs as well as tackling intellectual grand challenges.

KEYWORDS

fusion, tokamak, validation, turbulence, fission

1 Introduction

The field of fusion and plasma physics is changing rapidly, with a new global fusion energy ecosystem set to emerge over the next decades. In the United States, recent federal advisory board reports and community activities have built consensus for a new energy mission within the US Department of Energy (DOE) Office of Fusion Energy Sciences. The report Bringing Fusion to the U.S. Grid (2021) from the US National Academies of Science, Engineering and Medicine (NASEM) noted three key recommendations; that, DOE and the private sector should demonstrate net electricity in a fusion pilot plant in the 2035–2040 timeframe; DOE should move forward now via public-private partnerships to develop and bring fusion to commercial viability; and Urgent investments by DOE and private industry are needed to resolve the remaining science and technology issues to realize a fusion pilot plant (Nasem 2021). As of early 2024, there were over 35 private fusion companies who were members of the Fusion Industry Association, which is a US-based non-profit organization composed of private companies and active in advocacy and education.

The path to fusion commercialization accelerated further, when the White House put forth a "Bold Decadal" vision for fusion in Spring 2022, announcing a new $55 Million Milestone Program for funding promising fusion pilot plant concepts. The funding opportunity called for private companies who were pursuing fusion energy systems to submit proposals for one of two tiers for funding. Tier one activities support moving a Fusion Pilot Plant to a stage called a "Preliminary Design Review". This means that an awarded Tier one company would deliver a report to the DoE that documents the design of a fusion pilot plant just 5 years after the start of the award, and that the design is mature enough such that the next two steps on the path to a pilot plant are final design and construction. In May 2023, the DoE announced eight private companies who had been awarded funding under the milestone program; with the Tier one companies aiming toward fusion pilot plants that could operate by the early 2030s. Fusion is most certainly closer to commercialization that at any point in its over 60-year history.

As academic researchers, we are often asked by colleagues what does the future hold for plasma physics and fusion research at universities once fusion is on the grid? Given the science and technology gaps identified in the NASEM report (Nasem 2021), we anticipate growth in the research and development on systems and subsystems of a fusion power plant. This will include materials that maintain performance in the extreme environment of fusion energy systems; as well as in fusion technology, such as subsystems that convert fusion neutron energy to electricity, or on superconducting magnets and cost-efficient, high-power lasers that underpin magnetic and inertial fusion confinement concepts, respectively. This will certainly bring more scientists and engineers from non-traditional science engineering academic backgrounds into the field of fusion and into fusion faculty positions at universities, as has been noted by other authors (Whyte et al., 2023).

While fusion materials and technology have always been part of research on fusion energy, most students who have pursued fusion over the years and the majority of faculty in the field have focused on plasma physics as their core traditional discipline. This can be seen by examining the fusion graduate curricula at many top universities. The emergence of energy producing fusion systems on the grid raises questions about the future of the role for plasma physics in fusion research at universities. Our answer to this question is that over time there will be an expansion of the breadth of academic fields connected to fusion, while also a deepening of fundamental plasma physics research.

In the authors' areas of research, three of us are focused on the science of fusion energy systems, through the study of plasma turbulence and the resulting transport in magnetically confined fusion plasmas. Two of us are focused on the science of fission energy systems, through the study of boiling heat transfer and turbulence in neutral fluids. This perspective article will provide an overview of turbulence and turbulent-transport model validation research in tokamaks and examples of validation research on boiling heat transfer and turbulence in neutral fluids with applications to fission power systems. We also comment on the future roles of mid-scale fusion energy research facilities for validation by drawing parallels with the fission field.

2 Validation of turbulence transport models for fusion energy

Nuclear Fusion is a physical process that combines light nuclei to make heavier nuclei. It is the process that powers every star. Fusion energy research is a branch of science and engineering dedicated to harnessing fusion reactions for the benefit of humankind. The goal of fusion energy research is to build a fusion power station to make clean electricity (or heat) from energy released in fusion reactions. Fusion energy has many advantages, including an abundant, high energy density fuel that can provide energy with no greenhouse gases, and features manageable residual radioactive waste (Freidberg 2007) and minimal proliferation risks (Glaser and Goldston, 2012).

Developing a net-energy fusion system is very challenging because of the physics and engineering involved in confining a very hot 100-million-degree Celsius plasma in steady state with high fusion performance. For the most widely studied fusion fuel, a plasma of deuterium (D) and tritium (T), high-performance would mean a plasma with large amounts of self-heating from the alpha (α) particles that are on product of the D-T fusion reaction.

$$\mathrm{D} + \mathrm{T} \rightarrow \alpha\,(3.5\,\mathrm{MeV}) + n\,(14.1\,\mathrm{MeV})$$

Before becoming ignited, the plasma will first enter a burning plasma state, where the self-heating from alpha-particles will exceed the external heating of the fuel. Once the self-heating overcomes the energy losses, due to radiation, for example, the plasma becomes self-sustaining and considered to be 'ignited' (Lawson 1957). We note there are important differences in definitions when quantifying ignition for different fusion energy confinement systems, and there are different definitions of ignition even for the same system in some cases (Wurzel 2022). For example, when the National Ignition Facility was undertaking their most recent efforts to achieve net energy, the facility first conducted experiments that conclusively reached a burning plasma state (Zylstra et al., 2022) before achieving ignition (and proved they had achieved ignition according to several definitions) (Abu-Shawareb, 2022). A few years later at the National Ignition Facility (NIF), net energy gain in the target was achieved. In the experiment described in Abu-Shawareb (2022) the target gain was 0.72, or 1.37 MJ of fusion for 1.92 MJ of laser energy. On 5 December 2022, the NIF achieved 3.15 MJ (MJ) of fusion energy output from 2.05 MJ of laser energy delivered to the target, reaching target gain above unity, and further fusion gain records were set during the year 2023 (NIF 2023).

Decades prior, the JET tokamak set plasma gain records for magnetically confined fusion, achieving a record plasma gain of Q = 0.62. It is important to emphasize that the net fusion energy gain (or target gain) in the plasma fuel, Q, is different from net energy gain for the system, often described as "Q-Engineering", QENG. Values of QENG >1 are needed to produce electricity from the fusion system. Two simple definitions that differentiate between the two are Q = (net thermal power out)/(heating power in) and QENG = (net electric power out)/(electric power in) (Freidberg 2007). There are engineering and technological challenges to achieving QENG >1, such as efficiently converting the neutrons produced from D-T reactions within a Q > 1 plasma into useable electric power and recovering and recycling the tritium for further use in the fuel.

The success of JET and other magnetic confinement devices has led to the tokamak being one of the most widely studied and most developed fusion energy systems studied. A D-T tokamak is also

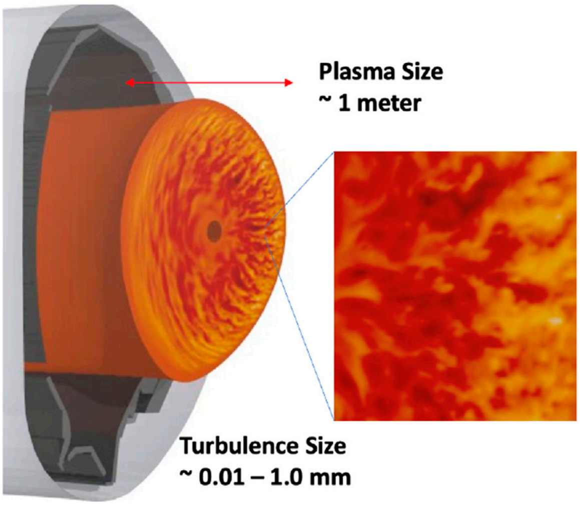

FIGURE 1
The output of a gyrokinetic simulation of micro-turbulence in a tokamak performed with the code GENE (GENE 2023) is adapted to illustrate the small length scale of the turbulent structures or "eddies" compared to the size of the plasma.

considered to be closest to a net electricity system, given the combination of fusion parameter performance (high density and high temperature) and pulse duration relative to that needed for a commercial power plant (NASEM 2021). The fusion parameter performance target can be summarized as achieving the so-called Lawson criterion. This is often described as achieving a high triple product of density, temperature, and energy confinement time, or nTτE = 8.3 atm-s at a temperature of T = 15 keV (note that the product of density and energy confinement time nτE is known as the Lawson parameter).

The fundamental physics concept behind magnetic confinement relies on motion of charged particles in a magnetic field. Charged particles are "confined" perpendicular to B field lines. The trajectory is a helix with characteristic radius (gyroradius)

$$\rho = \frac{mV_\perp}{qB} \propto \frac{\sqrt{mT}}{B} \text{ and timestep (gyrofrequency) } \omega_c = \frac{qB}{m}$$

At a magnetic field of 5T and plasma temperature of 10 keV, the electron gyroradius is ρe ~ 0.06 mm and ion gyroradius is ρi ~ 3 mm. Fuel ions are moving ~1,000 km/sec. The characteristic scale length along the field line is millions of times the gyroradius, since parallel transport is determined largely by particle coulomb collisions and the parallel mean free path several times larger than the system size. This means there is no confinement parallel to B as there is perpendicular to B. Closing the magnetic field lines or avoiding end losses is key in any magnetic confinement system. Tokamaks do this by using closed field lines and nested toroidal flux surfaces, and to date, tokamak experiments have featured some of the highest performing fusion plasmas (Wurzel 2022).

Many tokamak experiments have demonstrated high density and temperature operation but achieving high pressures simultaneously with high energy confinement time, τE, is challenging. This is because turbulence in the plasma very efficiently mixes the hot and cold plasma, limiting high pressures in the core plasma. Turbulent transport therefore limits the confinement time and therefore limits achievement of net-energy in tokamaks (and other magnetic confinement systems as well). For some time, this was not fully understood. Originally, when the observed transport levels in tokamaks exceeded what would be expected from collisional transport theory, it was called "anomalous" transport in the literature. As experiments and modeling evolved, the high transport levels were determined to be caused by turbulence. The turbulence is unavoidable, because it is driven by pressure gradients always present in the plasma, which are sources of free energy. These gradients give rise to "universal" drift-wave instabilities, which nonlinearly evolve into saturated turbulence (Horton 1999). The turbulence drives large amounts of heat and particles from the hot core to the colder edge. The turbulence is often referred to as micro-turbulence, due to the small length scale of the turbulent structures or "eddies" in the direction perpendicular to the confining magnetic field compared to the size of plasma, which is a ≈ 1 m. In contrast, the size of the turbulent structures will scale with the gyro-radii, ρe ≈ 0.06 mm, ρi ≈ 3.6 mm at 10 keV and 5.4 T, as shown in Figure 1. The broadband turbulence has frequencies ranging from 10 kHz to over 1 MHz and fluctuation amplitudes, of 0.1%–10% of equilibrium values of plasma pressure or magnetic field.

Over the past decades a standard model describing the turbulence and transport in tokamaks and other plasmas of interest for magnetic confinement fusion has merged. The turbulence in fusion plasmas is well-described by nonlinear gyrokinetics (Brizard and Hahm, 2007) and there is a large area of research in the field focused on carefully comparing experimental measurements of turbulence to simulation by a process known as validation (White 2019).

Validating gyrokinetic codes using experimental data from operating tokamaks is key for being able to use these codes to then make reliable predictions for future performance in tokamaks yet to be built and operated, such as ITER (Howard et al., 2021) and SPARC (Fernandez et al., 2020). Simply speaking, validation of a turbulent transport model proceeds as follows, nonlinear gyrokinetic codes take experimental profile data as input, and the input files must be carefully prepared. The code outputs are the heat fluxes and turbulence characteristics. Typically, only the latter are directly measured. Modern comparisons between experiment and simulation then involve sensitivity scans, error analysis, uncertainty quantification and the use of metrics. Over the years, the comparisons have led to better and better models that the codes can run. Validation has revealed importance of including realistic plasma geometry, kinetic electrons, collisions, the flow shear and turbulence-generated zonal flows, electromagnetic effects, and multi-scale effects caused by coupling between electron and ion scale turbulence.

Turbulence diagnostics have played key role in validation studies (Rhodes et al., 2011; White 2019). And of course, gyrokinetic theory itself is continuously being developed, such as recent work on the details of fast ion–turbulence interactions (Citrin and Mantica, 2023) or the effects of a non-axisymmetric 3-D equilibrium magnetic field (Wilcox et al., 2017). Numerical approaches are also evolving, for example, new gyrokinetic codes are being developed specifically to perform electromagnetic simulations of a helical model for the scrape-off-layer plasma (Hakim et al., 2020),

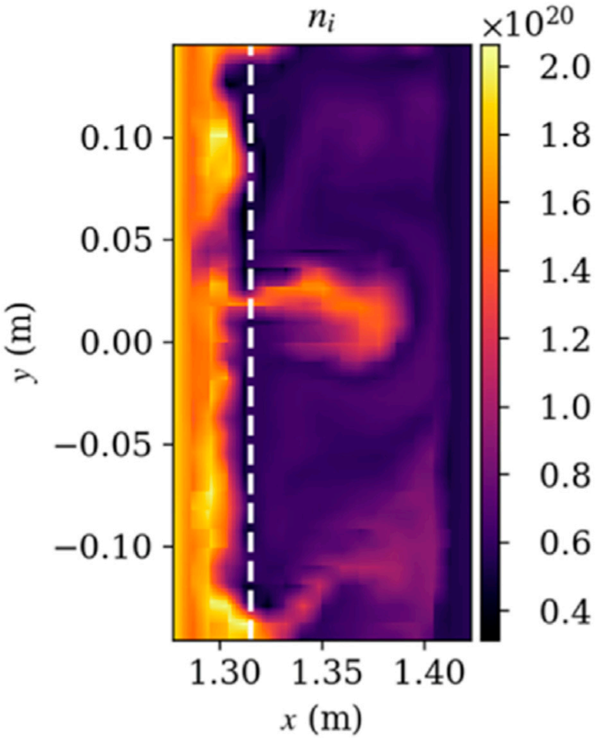

FIGURE 2
Output of an electromagnetic simulation of a helical model for the scrape-off-layer plasma in a tokamak, performed with the GEYKLL code revealing an intermittent structure with features that qualitatively resemble experimentally observed "blobs" being ejected from the source region in the simulation (left side of vertical dashed line) (Hakim et al., 2020).

revealing intermittent blob-like structures ejected from a source region, see Figure 2. While reminiscent of observations of the structure and motion of edge turbulence and "blobs" in experiments (Zweben et al., 2022), direct comparisons in this edge region remain as exciting future work.

One goal of validation in fusion is to develop reliable models that can be used to predict performance in future devices. In one example, a reduced model that is routinely used to predict profiles was improved based on multiscale turbulence studies that combined simulation with comparisons to experiments. A model called TGLF is a reduced model for the core plasma turbulent-driven transport (Staebler et al., 2007) originally developed by scientists at General Atomics. TGLF was derived via comparisons with higher fidelity gyrokinetic simulations, which had been validated against experiment. Ten years after the original TGFL model was created, a new "TGLF-SAT1" turbulent transport model was introduced (Staebler et al., 2017). This new SAT1 model included the effects of cross-scale coupling between ion-scale and electron turbulence, which were not included in the original TGLF models. This SAT1 model was developed using the nonlinear gyrokinetic simulations of multi-scale turbulence that were used for validation studies performed at the MIT tokamak, Alcator C-Mod by the MIT group (Howard et al., 2016).

Recent work used this newly developed TGLF SAT1 model to make predictions for the SPARC tokamak. This work shows important differences in physics-based model predictions for Q, the plasma gain metric, and predictions made with empirical scaling laws (Fernandez 2020). Using empirical scaling laws with conservative assumptions (H98, y2 = 1.0 and density profile peaking factors as empirically predicted) for the reference discharge in SPARC leads to a predicted Q ≈ 11. The profiles predicted for this case are shown in Figure 3. Using a new reduced model for the transport caused by the turbulence within a code called TGLF, the modeling work indicated that the current version of the SPARC design with nominal parameters will generate Pfus ≈100 MW of fusion power, with a gain of Q ≈ 9. As mentioned above, this new reduced model used in the work was itself developed from high fidelity multi-scale simulations that were validated against experiments performed at the MIT tokamak, Alcator C-Mod (Howard et al., 2014; Howard, 2016). Choosing what boundary conditions to use in the modeling also relied on another reduced model, called EPED, that has been extensively validated against experiments, including new extension to high densities relevant for SPARC using comparisons to experiments at the MIT Alcator C-Mod tokamak (Hughes et al., 2018). More recently, integrated modeling and predictive simulations indicates the tremendous value of using experimentally validated physics-based models for predicting performance of future fusion energy systems, including the use of surrogate models developed from high-fidelity codes (Fernandez et al., 2022). This is important, since the use of empirical scaling laws to predict performance in future devices can introduce significant uncertainties if used alone.

Another goal of validation in fusion is to make new, fundamental physics discoveries. For example, theory suggested a transition to subcritical turbulence occurs via an intermediate state

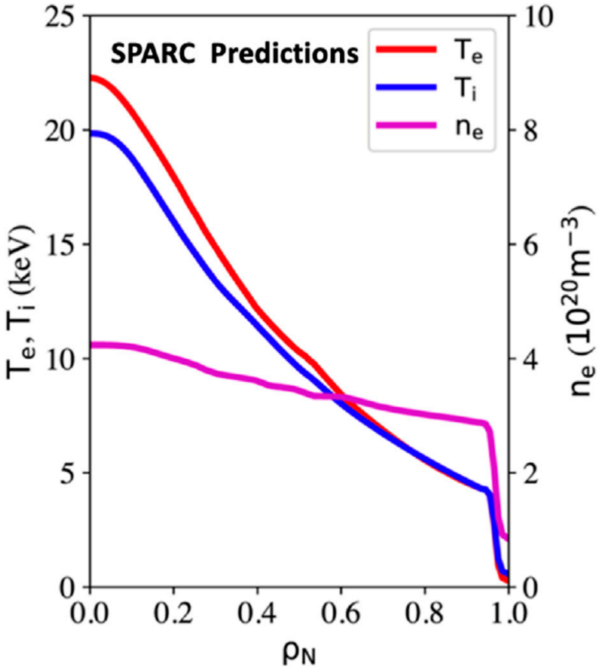

FIGURE 3
Predictions from a turbulent transport model for the temperature and density profile expected in the tokamak SPARC (Fernandez et al., 2020).

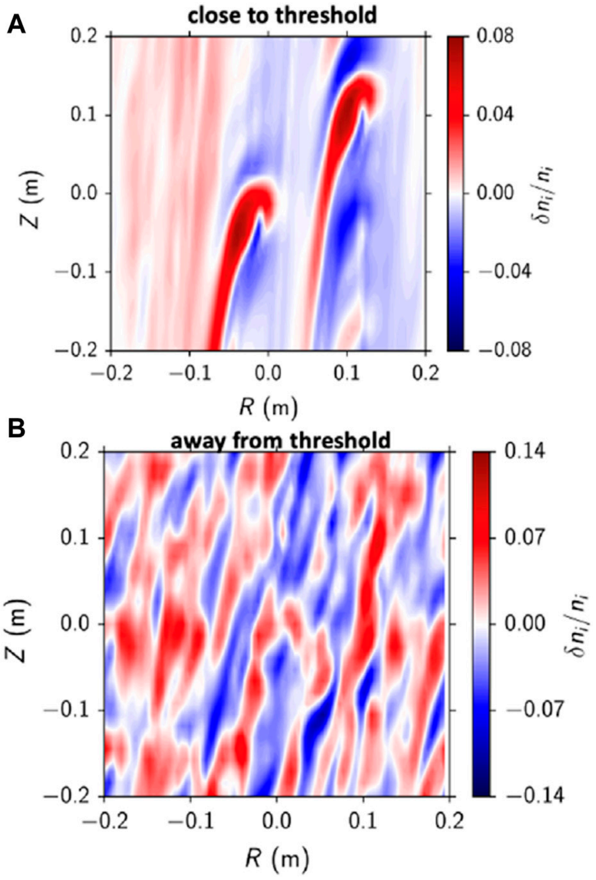

FIGURE 4
A gyrokinetic simulation output showing a low number of coherent long-lived structures **(A)** that evolve into more conventional turbulence **(B)** after the number of structures increases to fill the domain as system moves away from threshold. From Wyk (2017).

dominated by low number of coherent long-lived structures, close to threshold. Then, more conventional turbulence emerges after structures increase in number to fill domain as system moves away from threshold, as shown in Figure 4. There was a theory prediction that properties of turbulence are functions of the distance to threshold, and this could be quantified by the ion heat flux. Validation work helped corroborate this new subcritical turbulence physics result, as described in (Wyk, 2017).

3 University-based validation research in fission

Just as with fusion, validation of turbulent transport models in fission energy systems is undertaken with the goals of making basic physics discoveries as well as for development of new predictive models for operation and performance of future fission reactors.

Fission energy systems are of course dramatically different from fusion energy systems. Unlike a fusion energy system, where the fuel is a hot plasma, the fuel for operating fission power plants is a solid. Conventional fission fuel consists of uranium pellets within a fuel rod that has an outer layer of cladding, which is zirconium-based. Coolant water is used to manage the temperature of fuel rods and other parts of light water reactor (LWR) fission energy system. The study of heat transfer in the coolant water is very important for industry to support current fleet. Other coolants for advanced reactor are important to future expansion of fission energy to meet zero-carbon goals.

Boiling water is one of the most effective heat transfer mechanisms at commercial scale. Prof. Varanasi from MIT, a world-leader in field of heat transfer and surface engineering has explained, “Roughly 85 percent of the worldwide installed base of electricity relies on steam power generators, and in the U.S. it’s 90 percent,” Varanasi says. “If you’re able to improve the boiling process that produces this steam, you can improve the overall power plant efficiency.” (MIT News 2015). This underlines the importance of specific academic research (boiling fluid dynamics) to improve an ongoing, mature industry.

If nucleate boiling provides an excellent mechanism for heat removal from a heated surface, then a departure from nucleate boiling can be disastrous for the system to be cooled down (Zhang et al., 2023). When a surface is cooled by a liquid, at high heat transfer rates, the surface temperature may exceed the fluid boiling point. The liquid in contact with the surface vaporizes. Vapor bubbles nucleate and grow on top of the surface and move away. Both the process of bubble nucleation and the convective flows created by the growth and detachment of bubbles remove energy from the surface. However, at higher heat transfer rates, more and more area will be covered with bubbles. At the so-called critical heat flux (CHF), a “boiling crisis” may occur. When that happens, the surface gets suddenly covered by a stable expanding vapor patch (instead of small detaching bubbles). This instability, called departure from nucleate boiling, is very detrimental. Vapor has poor thermal conductivity. Thus, the surface is not effectively cooled down, and its temperature may even exceed its melting point.

To avoid exceeding the critical heat flux (CHF) limit, power plants are operated at a thermal power lower than they otherwise could, which limits their electric power output and cost-competitiveness.

A major validation effort in fission was led by the DOE Consortium for Advanced Simulation of Light Water Reactors (CASL), which ended in 2020 (CASL 2020). CASL was a decade-long DOE funded program for research and development, technology deployment, education, and workforce development. It was organized around several “Challenge Problems” for LWRs, across a variety of physical phenomena and processes. The CASL THM (Thermal-Hydraulics Methods) group focused on the development of predictive models for Departure from Nucleate Boiling (DNB) and Flow Regimes. To tackle this problem, the researchers realized that Multilevel Validation was needed, but there was a paucity of measurements.

Nuclear fission reactors have been historically designed based on empirical and semi-empirical correlation obtained by low-resolution diagnostics, e.g., thermocouples. These types of measurements can elucidate the physics of the phenomena only superficially. For instance, thermocouples measurements allow detecting a boiling crisis by measuring a spike in the average boiling surface temperature, but do not allow to understand the mechanisms that trigger such boiling crisis. Thus, the design of two-phase system often requires *ad hoc* experiments run in prototypical

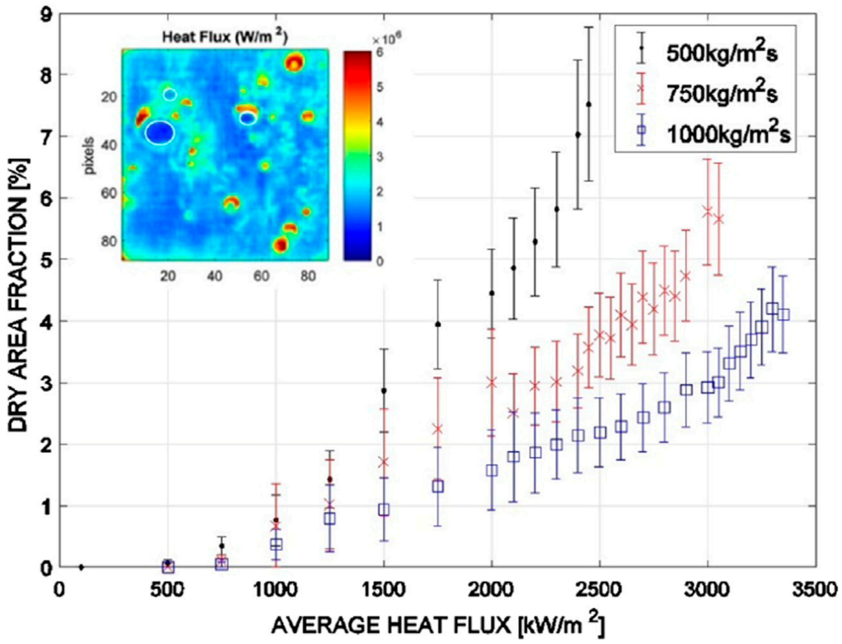

FIGURE 5
IR camera image data of nucleate boiling is used to calculate the dry area fraction as a function of applied heat flux. The inset image shows the heat flux distribution from a single IR camera frame, with darkest blue colors outlined in white indicate the dry regions (Richenderfer et al., 2018).

conditions. However, it is practically impossible to run prototypical experiment for any geometry and operating and boundary conditions. Non-prototypical data (and the attached correlations) can only be used with large margin of uncertainties, which ultimately hinder fission reactors operation and profitability.

Unlike in fusion where a large suite of turbulence diagnostics has been developed over the past 20 years, turbulence diagnostics to study water boiling systems that operate at high temperature and high pressure had not been developed until more recently. Major advances in this field have been possible thanks to the development of infrared thermometry and phase detection techniques, mostly in the last decade. These techniques rely on special heaters, consisting of a substrate, ideally transparent to both infrared and visible light, coated with a visible light transparent, but IR opaque, electrically conductive coating. This electrically conductive coating is in contact with water and releases by Joule effect the heat necessary to boil the fluid. Its thermal capacity and thermal resistance are negligible. Thus, its temperature practically coincides with the temperature at the interface between the solid and the fluid. The infrared radiation emitted by this coating can be used to measure the time-dependent temperature distribution on the boiling surface.

However, this process is complicated by the fact that the substrate is never perfectly transparent, and it tends to act as black body, it will partially absorb the radiation emitted by the ITO and re-emit radiation at a slightly different temperature (and frequency). The imperfect transparency could be used to quantify the radiation transport through the imaging surface. By solving for the various components of the IR transmission, reflections, absorption and remission, a team at MIT came up with a full radiation transport model that he could use to predict what the signal would look like. Solving this inverse problem allowed for extraction the time-dependent temperature and the heat flux distributions absolutely from the high-speed IR camera images, like the one shown in Figure 5. This new diagnostic development has unlocked the measurement of boiling parameters, such as nucleation site density, bubble growth and wait time, bubble departure diameter, and bubble size distributions, and, importantly, a parameter known as the Heat Flux Partitioning (Richenderfer et al., 2018), which was a key missing piece for the validation of two-phase modeling tools for fission energy systems (Baglietto et al., 2019).

Accessing direct measurements of the heat flux partitioning is akin to measuring turbulence directly in the tokamak case. Predictions of these parameters from a simulation are shown in Figure 6. Heat flux partitioning describes the importance of heat transfer mechanisms during bubble life cycle, including evaporation, and different modes of convection, conduction. Heat flux partitioning models use nucleation site density, bubble growth, and wait time, and bubble departure diameter as input. Given a surface temperature, the models are used to predict the total heat flux removed from the surface by predicting the heat flux removed by each of the removal mechanisms.

It is also worth noting that fission is arguably much further ahead of fusion in the approach to multimachine validation. There is a predictive simulation tools developed by CASL used to simulate many different reactors in the US fleet called Virtual Environment for Reactor Applications (VERA). VERA is being deployed as an integrated, high performance computing platform for performing multi-physics simulation for advanced Light Water Reactors ref [CASL 2020)]. As of 2020, CASL had simulated 170 operating fuel cycles across 28 reactors representing the full spectrum of designs within the US nuclear fission fleet.

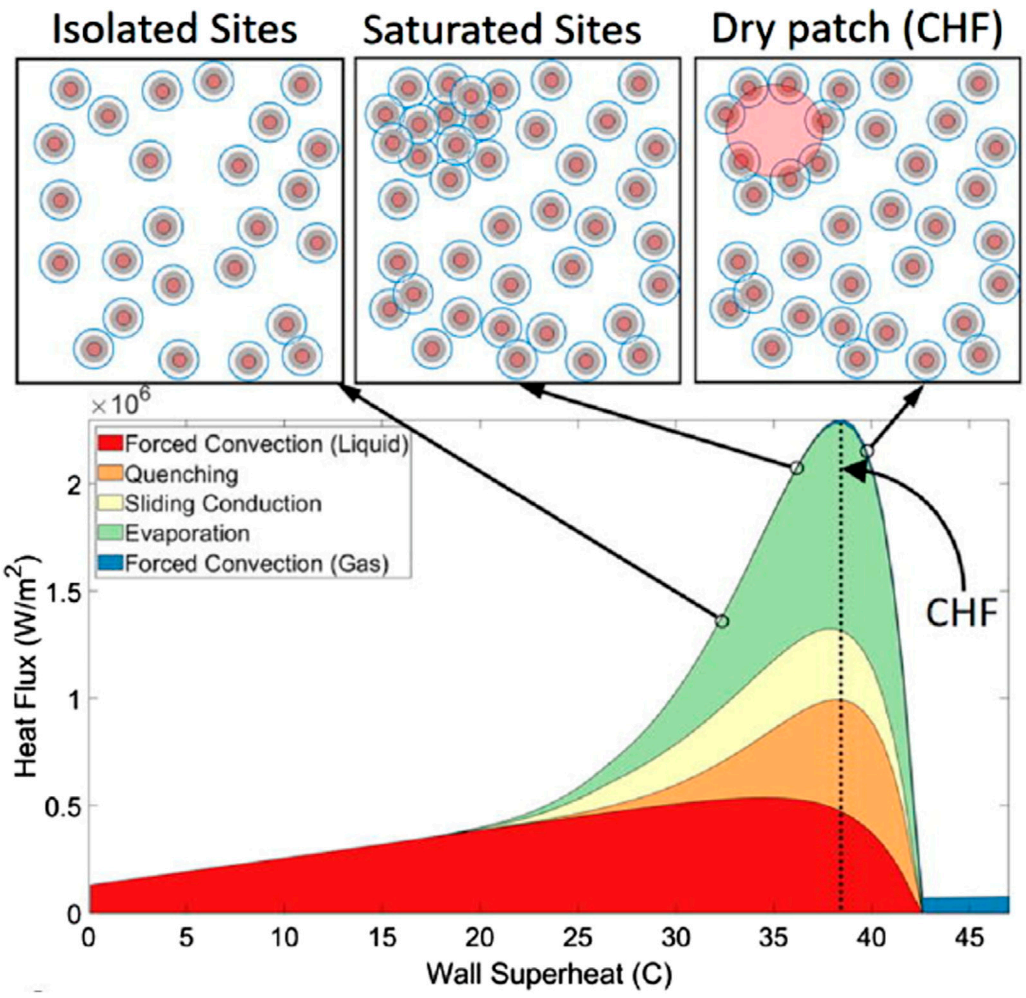

FIGURE 6
Adapted from Baglietto et al. (2019): "Illustration of CHF predictions: as the wall superheat increases, the bubbles start saturating the boiling surface, driving interactions and accelerated growth of the dry area with a sudden decrease in the total heat flux, which is the signature of CHF. The images on the top illustrate the local dry patch formation as CHF is reached."

4 Roles of small and medium-scale facilities and research reactors in fusion and fission

In a fusion power plant, like a fission power plant, there will be very limited diagnostics, so the development of better models to optimize reactors will come from small-scale and medium-scale experimental facilities at universities and labs. Research reactors, which can be sited both at universities and national labs, will also have an important role to play. Deciding what kinds of facilities are needed is driven both by fundamental physics questions as well as industry needs.

Looking at fission first, the industry needs include efforts to develop more efficient, cheaper, safer reactors. This drives academic research in small-scale platforms for the study of materials and radiation effects, as well as thermal-hydraulics and fluid-dynamics for fission applications.

Specialized small-scale facilities can address and overcome measurement challenges in detail.

Consider the new experimental platform being designed and built by Bucci and team at MIT. This first of a kind small scale facility will be capable of matching fission reactor conditions (350°C, 150 bar) to study boiling without needing a fission reactor. Several important diagnostics are deployed on this platform, such as an innovative Phase Detection technique to track phase (liquid or vapor) in contact with boiling surface using inexpensive color LEDs instead of more expensive lasers. For example, in a recent study, the CHF for a nanoengineered surface was compared at 1 bar and 4 bar conditions (Wang et al., 2024).

Fission research reactors may be considered medium and large-scale devices. There are 25 research reactors sited at universities in the US. Including a high-performance 6 MW thermal fission research reactor (the MITR) at MIT. It is the second largest university research reactor in the U.S. and the only one located on the campus of a major research university. It is also the only university research facility in the U.S. where students can be directly involved in the development and implementation of nuclear engineering experimental programs with neutron flux levels comparable to power reactors. Undergraduates can learn to operate the reactor (some go on to work in industry as operators and team leaders, others go on to PhD programs).

Such medium scale and large-scale fission reactor experiments are best augmented with extensive auxiliary measurement capabilities, both in core and outside the core. For example, the MIT CRISP is a new University-Based Collaboration with a National Laboratory. CRISP stands for the Center for Reactor Instrumentation and Sensor Physics and is a joint undertaking with MIT and INL. The CRISP Vision to advance the current state of automation in nuclear systems by developing foundational technologies, as well as existing technology for monitoring and controls of future nuclear systems. The Focus Areas include Sensing Physics and Instrumentation; Signal Processing and AI/ML-based Data Analysis; and Advanced Controls and Decision Sciences.

The fission field has placed a renewed emphasis placed in recent years on research reactors that explore the utility of advanced reactors and microreactors. For example, the U.S. DOE is building a new research reactor at Idaho National Lab (INL) for the first time in over 40 years to help researchers understand how microreactors can integrate with other technologies. This is called the Microreactor Applications Research Validation and EvaLuation or MARVEL project (Marvel 2023). The MARVEL design is a liquid-metal cooled microreactor with Stirling engines that will produce 100 kW of energy using small amounts of high-assay, low-enriched uranium (HALEU) from available research materials. Its design is primarily based on existing technology and will be built using off-the-shelf components allowing for faster construction. The reactor is being built inside the Transient Reactor Test facility (TREAT) at INL and is expected to be completed in 2025, and will be connected to a microgrid to examine decarbonization pathways. Notably, universities will play key role in validation using codes and measurements on MARVEL, as there is recognition in the field of university leadership in this area. The INL approach to engagement broadly with universities is worth examining to see how this might translate to the fusion field.

Turning now to fusion, over the past 20 years, the US has made relatively few new investments in university based fusion confinement experiments. In fact, in 2016, the Alcator C-Mod tokamak was shuttered by the DOE, as were others such as the Electric Tokamak at UCLA a decade prior. These facilities, and others were important for creating workforce training and student research opportunities. Their closure occurred during a difficult time for the US Fusion Energy Science program.

Thankfully the new FESAC Long Range Plan from 2021 Calls Out the need for Synergy Between University Based Experiments and Large Facilities. That report explains, “SPARC will be parallel and complementary to international fusion efforts, including ITER, and to other ongoing private-sector fusion endeavors. The existing DIII-D and NSTX-U national tokamak facilities are key to preparation for the study of burning plasmas in ITER and in other planned and future private devices. Continuing support of existing university tokamak programs, and utilization of US expertise in theory and simulation, is needed to find solutions to remaining technical gaps. These gaps include disruption prediction, avoidance, and mitigation; plasma-facing component integration; and FPP- relevant scenario development.”

In fusion, there is also a desire to make power plants more compact, which will make them more economically competitive. Specifically, “It is highly desirable to reduce the costs of the research path for fusion energy development, as well as making the end-product - fusion reactors–sufficiently economically attractive. Of course, the economic attractiveness of power plants is determined by many variables. Studies of nuclear fission reactor costs have shown that factors such as utility structure, reactor size, regulatory regime, and international collaboration have the largest impact”, as noted in a recent community report (FESAC 2018). It is indeed notable that most of commercial fusion companies now active, including those that have raised the most capital from investors, promise compact fusion power plant concepts.

Based on lessons learned from fission, we believe that support for a thriving fusion energy industry would also require a variety of large-scale, medium-scale and small-scale experimental platforms at universities and national labs that can bridge between the wonderful foundational research of plasma physics and the applied need for fusion energy systems on the grid. We anticipate that soon, medium-scale tokamaks, stellarators, and other fusion research devices will be desirable at universities for the training of operators at fusion power plants.

5 Outlook and discussion

There are several frontier areas to emphasize in validation in fusion, involving “Multilevel, Multichannel, and Multimachine Comparisons”. Large uncertainties and model sensitivity can lead to fortuitous agreement and difficulty discriminating between models. One approach to overcome this challenge is to make use of a “Primacy Hierarchy” (Multilevel), whereby fluctuation amplitudes, correlation lengths, cross-phase angles, and inferred heat fluxes from power balance, are all compared simultaneously with models, often using quantitative metrics (Holland 2016). It is also important to probe both electron and ion heat transport simultaneously with particle and impurity transport (Multichannel) (Sciortino et al., 2020). And finally, while Multilevel and Multichannel validation are becoming more common, applying the same turbulence models and same measurements to different tokamaks, spherical tokamaks, stellarators, and other magnetic confinement configurations (Multimachine) has yet to be done extensively.

Frontier areas in fission validation include both the development of the new measurements and the development of new high-fidelity, physics based, fast running single and multiphase computational fluid dynamics (CFD) models. Such new models can be used to make predictions of performance in existing and next-generation fission reactors to optimize operation and improve safety and cost-competitiveness. For example, new high-fidelity CFD simulations are used to predict the evolution of flow driven component failure mechanisms, with thermal fatigue accumulation being one of the most challenging to address. Since turbulent mixing causes temperature oscillations in structural components that can lead to accelerated growth of cracks and failure over time. Simulations of the fatigue evolution for primary piping locations in the reactor, as well as other internal systems performed with CFD can be combined with AI enabled digital twins to allow for innovative predictive maintenance approaches for future advanced fission reactors.

As discussed in this perspective paper, validation of turbulent transport models in fusion is an exciting and active area of research, with relevance both for advancing fusion energy through prediction of new device design, as well as fundamental plasma physics research. Similarly, validation of turbulent (and boiling) transport

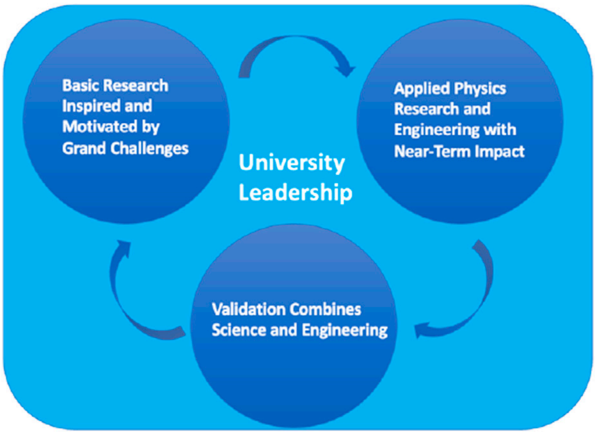

FIGURE 7
A virtuous cycle of basic research motivated by grand challenges, which in turn leads into applied science research with the goal of near-term industry impact, which is often driven by validation efforts that combine advances in experiment and simulation.

models in fission is an exciting and active area of research, with relevance for fission energy research and fundamental physics research.

Consider this concise statement about boiling heat transfer in fission systems (Kommajosyula 2020): "Boiling is an efficient mode of heat transfer and is heat removal mechanism in power systems, including fission reactors. Physics-based models that describe boiling heat transfer can be an invaluable tool to increase the performance of fission reactors. New experiments with detailed data of boiling dynamics, including fundamental bubble parameters, are essential for validating such physics-based models."

One could make a nearly identically structured statement about turbulent heat transfer in fusion systems: Turbulence is an extremely important mode of heat transfer and is a primary transport mechanism in fusion plasmas, like tokamaks. Physics-based models that describe turbulence-driven transport can be an invaluable tool to increase the performance of future fusion power plants. New experiments with detailed data of transport dynamics, including fundamental turbulence parameters, are essential for validating physics-based, predictive models.

These parallel statements for fusion turbulence and fission boiling studies help to summarize the deep connection between these two fields at a deeper level than perhaps previously explored in the literature, and considering these two statements were a helpful motivation for this perspective article.

Undoubtedly, to address climate change with fission energy and fusion energy systems, there must be a virtuous circle for university-based fission and fusion research, that attracts the most talented students from all backgrounds. The best students and faculty, researchers and scholars are always driven by grand challenges. The grand challenges can be intellectual (how does boiling work? How does plasma turbulence work?) or can be societal (how can turbulence be tamed to produce efficient, clean energy systems? How can physics understanding be used for optimization of net energy systems?).

To answer the questions posed about the future for university turbulent transport research in fusion or plasma physics research more broadly, we would argue that a fusion industry opens doors for university plasma physics research. The emergence of a new fusion energy industry will create more opportunities for fundamental research, especially in plasma turbulence and transport, at universities in the United States, not fewer. Fission power produces 20% of electricity in the USA; power plants have been reliably and safely operating over 60 years. Research on turbulence in neutral fluids is thriving at universities and has important applications for the fission industry. The fuel for fusion is a plasma, and that plasma is always turbulent.

There is a virtuous cycle of basic research motivated by grand challenges, which in turn, leads into applied science research with the goal of near-term industry impact, which is often driven by validation efforts that combine advances in experiment and simulation, Figure 7. Fusion-relevant grand intellectual challenges in plasma physics will remain long after fusion is on the grid. University researchers will engage with sponsors and collaborators including governments, national labs and private companies, and utilities around the world. Development of turbulence and transport measurements, and predictive simulation and modeling, in support of fusion and fission tell an evergreen story of innovation. The future of plasma physics research at universities is bright as we move through and beyond the era of burning plasmas to the era of ignited plasmas and fusion energy on the grid.

Data availability statement

The original contributions presented in the study are included in the article/Supplementary Material, further inquiries can be directed to the corresponding author.

Author contributions

AW: Writing–original draft. EB: Writing–review and editing. MB: Writing–review and editing. NH: Writing–review and editing. PR-F: Writing–review and editing.

Funding

The author(s) declare that no financial support was received for the research, authorship, and/or publication of this article.

Acknowledgments

The author AW is grateful to several colleagues in the fusion field for encouraging a perspective article on this topic.

Conflict of interest

The authors declare that the research was conducted in the absence of any commercial or financial relationships that could be construed as a potential conflict of interest.

Publisher's note

References

Abu-Shawareb, H., Acree, R., Adams, P., Adams, J., Addis, B., Aden, R., et al. (2022). Indirect drive ICF collaboration. *Phys. Rev. Lett.* 129, 075001. Published 8 August 2022. doi:10.1103/PhysRevLett.129.075001

Baglietto, (2021). Presented at annual nuclear review meeting ARPA-E. Available at: https://arpa-e.energy.gov/2021-annual-nuclear-review-meeting.

Baglietto, E., Demarly, E., and Kommajosyula, R. (2019). Boiling crisis as the stability limit to wall heat partitioning. *Appl. Phys. Lett.* 114, 103701. doi:10.1063/1.5080724

Brizard, A. J., and Hahm, T. S. (2007). Foundations of nonlinear gyrokinetic theory. *Rev. Mod. Phys.* 79, 421–468. doi:10.1103/revmodphys.79.421

CASL (2020). *Consortium for advanced simulation of light water reactors*. Oak Ridge, TN, USA: CASL Phase II Summary Report.

Citrin, and Mantica, P. (2023). Overview of tokamak turbulence stabilization by fast ions. *Plasma Phys. control. Fusion* 65, 033001. doi:10.1088/1361-6587/acab2b

Fernandez, P. R., Howard, N., and Candy, J. (2022). Nonlinear gyrokinetic predictions of SPARC burning plasma profiles enabled by surrogate modeling. *Nucl. Fusion* 62, 076036. doi:10.1088/1741-4326/ac64b2

Fernandez, P. R., Howard, N. T., Greenwald, M. J., Creely, A. J., Hughes, J. W., Wright, J. C., et al. (2020). Predictions of core plasma performance for the SPARC tokamak. *J. Plasma Phys.* 86 (5), 865860503. doi:10.1017/s0022377820001075

FESAC (2018). Transformative enabling capabilities for efficient advance toward fusion energy. Available at: https://science.osti.gov/-/media/fes/fesac/pdf/2018/TEC_Report_1Feb20181.pdf.

FESAC (2021). Fusion energy sciences advisory committee long Range plan report. Available at: https://usfusionandplasmas.org/.

Freidberg, J. (2007). *Plasma physics and fusion energy*. Cambridge, United Kingdom: Cambridge University Press.

GENE (2023). Gene. Available at: https://genecode.org/(Accessed online January 30, 2024).

Glaser, A., and Goldston, R. J. (2012). Proliferation risks of magnetic fusion energy: clandestine production, covert production and breakout. *Nucl. Fusion* 52, 043004. doi:10.1088/0029-5515/52/4/043004

Hakim, Mandell, N. R., Bernard, T. N., Francisquez, M., Hammett, G. W., and Shi, E. L. (2020). Continuum electromagnetic gyrokinetic simulations of turbulence in the tokamak scrape-off layer and laboratory devices. *Phys. Plasmas* 27, 042304. doi:10.1063/1.5141157

Holland, C. (2016). Validation metrics for turbulent plasma transport. *Phys. Plasmas* 23, 060901. doi:10.1063/1.4954151

Horton, W. (1999). Drift waves and transport. *Rev. Mod. Phys.* 71, 735–778. doi:10.1103/revmodphys.71.735

Howard, N. T., Holland, C., Rhodes, T., Candy, J., Rodriguez-Fernandez, P., Greenwald, M., et al. (2021). The role of ion and electron-scale turbulence in setting heat and particle transport in the DIII-D ITER baseline scenario. *Nucl. Fusion* 61, 106002. doi:10.1088/1741-4326/ac1bc2

Howard, N. T., Holland, C., White, A., Greenwald, M., and Candy, J. (2016). Multi-scale gyrokinetic simulation of tokamak plasmas: enhanced heat loss due to cross-scale coupling of plasma turbulence. *Nucl. Fusion* 56, 014004. doi:10.1088/0029-5515/56/1/014004

Howard, N. T., Holland, C., White, A. E., Greenwald, M., and Candy, J. (2014). Synergistic cross-scale coupling of turbulence in a tokamak plasma. *Phys. Plasmas* 21. doi:10.1063/1.4902366

Hughes, J. W., Snyder, P., Reinke, M., LaBombard, B., Mordijck, S., Scott, S., et al. (2018). Access to pedestal pressure relevant to burning plasmas on the high magnetic field tokamak Alcator C-Mod. *Nucl. Fusion* 58, 112003. doi:10.1088/1741-4326/aabc8a

Keilhacker, M., Gibson, A., Gormezano, C., and Rebut, P. (2001). The scientific success of JET. *Nucl. Fusion* 41, 1925–1966. doi:10.1088/0029-5515/41/12/217

Kommajosyula, R. (2020). *PhD thesis in mechanical engineering and computation*. Cambridge, MA, United States: Massachusetts Institute of Technology, Department of Mechanical Engineering. Available at: https://hdl.handle.net/1721.1/129051.

Lawson, J. D. (1957). Some criteria for a power producing thermonuclear reactor. *Proc. Phys. Soc. B* 70, 6–10. doi:10.1088/0370-1301/70/1/303

Marvel (2023). Marvel-microreactor-reaches-final-design-step. Available at: https://www.energy.gov/ne/articles/marvel-microreactor-reaches-final-design-step (Accessed January 30, 2024).

MIT News (2015). Boiling-more-efficient-less-dangerous-power-plants-0908. Available at: https://news.mit.edu/2015/boiling-more-efficient-less-dangerous-power-plants-0908 (Accessed January 30, 2024).

National Academies of Sciences, Engineering, and Medicine (2021). *Bringing fusion to the U.S. Grid*. Washington, DC: The National Academies Press. doi:10.17226/25991

NIF (2023). Lawrence livermore national laboratory website. Available at: https://lasers.llnl.gov/science/pursuit-of-ignition (Accessed January 30, 2023).

Rhodes, T. L., Holland, C., Smith, S., White, A., Burrell, K., Candy, J., et al. (2011). L-mode validation studies of gyrokinetic turbulence simulations via multiscale and multifield turbulence measurements on the DIII-D tokamak. *Nucl. Fusion* 51, 063022. doi:10.1088/0029-5515/51/6/063022

Richenderfer, A., Kossolapov, A., Seong, J. H., Saccone, G., Demarly, E., Kommajosyula, R., et al. (2018). Investigation of subcooled flow boiling and CHF using high-resolution diagnostics. *Exp. Therm. Fluid Sci.* 99, 35–58. doi:10.1016/j.expthermflusci.2018.07.017

Sciortino, F., Howard, N., Marmar, E., Odstrcil, T., Cao, N., Dux, R., et al. (2020). Inference of experimental radial impurity transport on Alcator C-Mod: bayesian parameter estimation and model selection. *Nucl. Fusion* 60, 126014. doi:10.1088/1741-4326/abae85

Staebler, G. M., Howard, N., Candy, J., and Holland, C. (2017). A model of the saturation of coupled electron and ion scale gyrokinetic turbulence. *Nucl. Fusion* 57, 066046. doi:10.1088/1741-4326/aa6bee

Staebler, G. M., Kinsey, J. E., and Waltz, R. E. (2007). A theory-based transport model with comprehensive physics. *Phys. Plasmas* 14 (5), 055909. doi:10.1063/1.2436852

Wang, C., Su, G., Akinsulire, O., Zhang, L., Rahman, Md M., and Bucci, M. (2024). Investigation of critical heat flux enhancement on nanoengineered surfaces in pressurized subcooled flow boiling using infrared thermometry. *Heat. Transf. Eng.* 45 (4-5), 417–432. doi:10.1080/01457632.2023.2191441

Wesson, J. (2011). *Tokamaks*. Oxford, United Kingdom: Oxford University Press.

White, A. E. (2019). Validation of nonlinear gyrokinetic transport models using turbulence measurements. *J. Plasma Phys.* 85 (1), 925850102. doi:10.1017/S0022377818001253

Whyte, D. G., Paz-Soldan, C., and Wirth, B. (2023). The academic research ecosystem required to support the development of fusion energy. *Phys. Plasmas* 30. doi:10.1063/5.0167369

Wilcox, R. S., Wingen, A., Cianciosa, M., Ferraro, N., Hirshman, S., Paz-Soldan, C., et al. (2017). Modeling of 3D magnetic equilibrium effects on edge turbulence stability during RMP ELM suppression in tokamaks. *Nucl. Fusion* 57, 116003. doi:10.1088/1741-4326/aa7bad

Wurzel, and Hsu, S. C. (2022). Progress toward fusion energy breakeven and gain as measured against the Lawson criterion. *Phys. Plasmas* 29, 062103. doi:10.1063/5.0083990

Wyk, F. van, Highcock, E. G., Field, A. R., Roach, C. M., Schekochihin, A. A., Parra, F. I., et al. (2017). Ion-scale turbulence in MAST: anomalous transport, subcritical transitions, and comparison to BES measurements. *Plasma Phys. control. Fusion* 59, 114003. doi:10.1088/1361-6587/aa8484

Zhang, L., Wang, C., Su, G., Kossolapov, A., Matana Aguiar, G., Seong, J. H., et al. (2023). A unifying criterion of the boiling crisis. *Nat. Commun.* 14, 2321. doi:10.1038/s41467-023-37899-7

Zweben, S., Lampert, M., and Myra, J. R. (2022). Temporal structure of blobs in NSTX. *Phys. Plasmas* 29, 072504. doi:10.1063/5.0097282

Zylstra, A. B., Hurricane, O. A., Callahan, D. A., Kritcher, A. L., Ralph, J. E., Robey, H. F., et al. (2022). Burning plasma achieved in inertial fusion. *Nature* 601, 542–548. doi:10.1038/s41586-021-04281-w

frontiers | Frontiers in Nuclear Engineering

TYPE Perspective
PUBLISHED 22 July 2024
DOI 10.3389/fnuen.2024.1308045

OPEN ACCESS

EDITED BY
Tonya Vitova,
Karlsruhe Institute of Technology (KIT),
Germany

REVIEWED BY
Christiane Heinicke,
University of Bremen, Germany

*CORRESPONDENCE
N. Dianne Bull Ezell,
bullnd@ornl.gov

RECEIVED 05 October 2023
ACCEPTED 20 June 2024
PUBLISHED 22 July 2024

CITATION
Ezell NDB (2024), Demonstrating autonomous controls on hardware test beds is a necessity for successful missions to Mars and beyond.
Front. Nucl. Eng. 3:1308045.
doi: 10.3389/fnuen.2024.1308045

Demonstrating autonomous controls on hardware test beds is a necessity for successful missions to Mars and beyond

N. Dianne Bull Ezell *

Oak Ridge National Laboratory, Nuclear and Extreme Environment Measurements Group, Fusion and Fission Energy Science Directorate, Oak Ridge, TN, United States

NASA and the Department of Defense are planning for a mission to Mars in the 2030s–2040s using nuclear thermal propulsion (NTP). NTP uses a nuclear reactor to heat flowing hydrogen and create thrust. A serious concern for crewed and uncrewed missions to Mars is the loss of reactor control. The reactor startup and initial rocket impulse are initiated in cislunar or near-earth orbital regions; therefore, radio communications between ground control and the NTP engine should occur in real time. However, radio communications can take more than 20 min, depending on planet positions, to reach Mars orbiters from ground control. To address this delay, local autonomous controls are implemented onboard the NTP engine to ensure acceptable operation. However, autonomous controls have not been demonstrated or implemented in research or power reactor contexts because of safety and reliability concerns. To enable autonomous controls development, demonstration, and validation, Oak Ridge National Laboratory has created a nonnuclear hardware-in-the-loop test bed. Sensors throughout the test bed relay system status and hardware response to the user control algorithm, including measurements of temperature, flow, pressure of a loop, control drum position, and drum speed. This paper discusses the development of this facility and user accessibility.

KEYWORDS

nuclear thermal propulsion, autonomous controls, demonstration test bed, Modelica modeling, verification and validation

1 Introduction

NASA and the US Department of Defense (DOD) aim to launch a mission to Mars in the next 2 decades using nuclear thermal propulsion (NTP). NTP uses a variation of chemical rocket engines to create thrust by ejecting burning gases in the opposite direction of the planned trajectory. Chemical rockets use a chemical reaction, creating a phase change that requires a great deal of working mass. However, nuclear rockets provide heat to create a phase change. Nuclear rockets are more appealing than chemical rockets because of their improved efficiency, their reduced size, and the independence of the heat source from the working mass. The specific impulse (Eq. 1) of the rocket engine is defined by

$$I_{sp} = \frac{F_{th}}{\dot{m} g_o}, \tag{1}$$

where F_{th} is the total impulse force determined by the rocket thrust equation (Hall, 2021), $\dot{m}$ is the mass flow rate, and g_o is the gravitational acceleration constant. This defines the efficiency of the engine, and it provides a simplified way to determine the thrust of the rocket and, ultimately, to "size" an engine for analysis (Finseth, 1991).

NASA characterizes NTP as a "game changing technology for deep space exploration" (Hall, 2018). NASA and the former Atomic Energy Commission began investigating nuclear reactors as a heat source for rocket propulsion through the Nuclear Engine for Rocket Vehicle Application (NERVA) program in 1961 (Hall, 2018). Over 2 decades (i.e., 1965–1973) under the Space Nuclear Propulsion Office, the NERVA program "established a technology base for nuclear rocket engine systems to be utilized in the design and development of propulsion systems for space mission applications" (Robbins, 1991). The reactor development origins came from the United States Air Force Project ROVER (1955–1973), executed at Los Alamos Scientific Laboratory (LASL), and focused on the development of nuclear-powered intercontinental ballistic missiles. Three ROVER reactors (i.e., Kiwi, Phoebus, and Pewee) were built and tested at LASL to characterize highly enriched uranium fuels and the nuclear material performance of graphite, beryllium, and boron. Projects ROVER and NERVA were cancelled in 1973: reactors were only ground tested. However, reactors were tested across 48 ground demonstrations in under 5 years (Finseth, 1991).

SNAP-10A, also known as *Systems for Nuclear Auxiliary Power*, was the first nuclear-powered satellite. It launched in 1965 and operated for 43 days, after which the reactor stopped functioning because of electrical component failure (Truscello, 1983). This was the first and only demonstration of a US nuclear fission reactor in space. However, many small reactor systems have been deployed in space by the former Soviet Union and China. The design of the SNAP-10 nuclear satellite was much less complex than that of nuclear rockets: the assembly included the reactor, an energy converter used to generate electricity, and a radiator to dissipate excess heat (Corliss, 1966). The overall size of the payload was greatly decreased and did not require a working mass for propulsion.

In February 1983, a resurgence in NTP research resulted in the SP-100 project. A new approach to fuel, the pebble bed concept, promised a specific impulse of 1,000 s. However, NASA deemed the SP-100 design an insufficient technology improvement over NERVA (Truscello, 1983). A summary of program dates, starts, temperatures, flow rates, and specific impulses is provided in Table 1.

Like other DOD and US Department of Energy initiatives, NTP has been a catalyst for the development of nuclear fuels, advanced instrumentation and controls (I&Cs), high-temperature materials, and other technologies. Many terrestrial nuclear concepts, such as microreactors and advanced generation IV reactors, benefit from the innovations in materials and technology. NASA, in partnership with the national laboratory complex and industry partners, restarted the NTP program in 2016 with the goal of achieving a mission to Mars in the 2030s. Figure 1 displays a side-by-side view of the original conceptual NERVA NTP engine design (Figure 1A) and the most recent NTP engine conceptual design illustration created by NASA (Figure 1B). Some discrepancies between the two images are: Figure 1A does not include the hydrogen tank but instead only illustrates the turbo-machinery, piping, reactor, and nozzle. It is difficult to visualize the nozzle on the left side of Figure 1B because this image includes the trans hab and hydrogen tank, but the image points out a key features including the nozzle and reactor core. Both of these images are good for general discussion but limited for in-depth technical discussion. Figure 1B is also a good illustration of the size of engine.

A full ground demonstration, as previously executed in ROVER/NERVA days is the preferred method for comprehensive testing. However, limitations in funding prohibit a full ground demonstration today. Therefore, Oak Ridge National Laboratory (ORNL) is supporting NASA and the NTP community in advancing I&C technology maturation through development of this test bed infrastructure. I&C test beds enable validation and verification of autonomous control algorithm with hardware-in-the-loop demonstrations; such facilities also provide exhaustive test candidate instrumentation.

2 Engine controls and test bed design

Most NTP reactor designs use liquid hydrogen as both the rocket propellant and reactor coolant. Reactor power controls are

TABLE 1 NERVA nuclear reactor engine list and test parameters.

Reactor	Test date	Starts	Average full power (MW)	Time at full power(s)	Propellant temperature (Chamber) (K)	Propellant temperature (Exit) (K)	Chamber pressure (kPa)	Flow rate (kg/s)	Vacuum specific impulse(s)
NERVA A2	Sept. 1964	2	1,906	40	2,119	2,229	4,006	34.3	811
NERVA A3	April 1965	3	1,093	990	2,189	> 2,400	3,930	33.3	> 841
NRX EST	Feb. 1966	11	1,144	830	2,292	> 2,400	4,047	39.3	> 841
NRX A5	June 1966	2	1,120	580	2,287	> 2,400	4,047	32.6	> 841
NRX A6	Nov. 1967	2	1,199	3,623	2,406	2,558	4,151	32.7	869
XE PRIME	March 1969	28	1,680	1,680	2,267	> 2,400	3,806	32.8	> 841

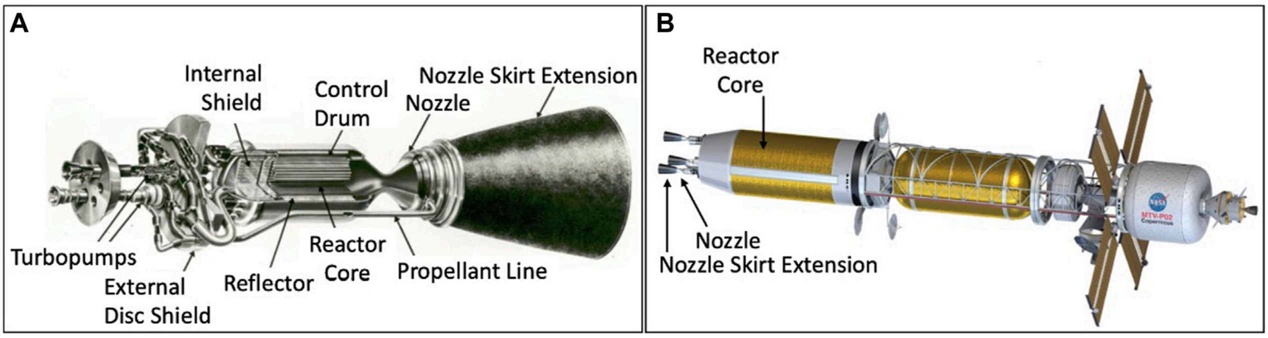

FIGURE 1
Illustrations of **(A)** NERVA and **(B)** the current NTP conceptual design (Borowski et al., 2013; Hall, 2018).

implemented using drums with graphite or beryllium on one side and boron poison on the other side. However, hydrogen flow also affects the reactivity. Therefore, control schemes for a nuclear rocket comprise two principal mechanisms: the rotation of the drums and the hydrogen flow. A serious concern for crewed and uncrewed missions to Mars is loss of reactor control. The reactor startup and initial rocket impulse are initiated in cislunar or near-earth orbital regions; therefore, radio communications between ground control and the NTP engine can occur in real time. However, currently for the Rovers on Mars's surface (mars.nasa.gov, 2020), radio communications can take more than 20 min, depending on planet positions, to reach Mars orbiters from ground control. This is not a complete loss in communication but instead a lag in signal reception. While this may not be an issue for science missions streaming data, reactors can require fine-tune controls with fast instrumentation sample rates and near-real time processing. To mitigate this issue, local (or autonomous) controls will be needed onboard the NTP engine to ensure sustainable operation. Autonomous controls are well understood and widely used in manufacturing, chemical processing, and other large-scale process industries (Antsaklis et al., 1991). However, autonomous control schemes have not been demonstrated or implemented in research or power reactor contexts because they carry heavy implications for safety and reliability. To enable autonomous controls development, demonstration, and validation, ORNL created a nonnuclear hardware-in-the-loop test bed. Sensors throughout the test bed relay system status and hardware response to the autonomous control algorithm, including measurements of temperature, flow, pressure of a loop, control drum position, and drum speed. To reduce qualification timelines, space rated systems are employed where possible.

The only control functions in an NTP engine are the reactor reactivity and the hydrogen flow. This hardware-in-the-loop test bed is designed to operate as a tightly coupled system symbolic of the nuclear rocket engine. This means, the test bed allow users to study the reactor and flow loop as a singular engine instead of two isolated systems—which is different from other available test beds. However, the test bed is modular, scalable, and rapidly reconfigurable, making it adaptable for various design criteria test cases. The support infrastructure is built of 80/20 materials for simple assembly, disassembly, and reconfiguration. The NASA NTP program invested in the development of this test bed starting in 2017. The instrumentation and actuator locations and parts were heavily influenced by the ROVER/NERVA and SNAP-10A literature. Also, the ORNL team worked closely with BWXT and AeroJet Rocketdyne to select components comparable to industry designs. As seen in Figure 2, six hollow control drums with associated motors are positioned uniformly and axially around the periphery of the mock reactor section of the test bed. Assorted materials fill the inside of the control drums to adjust the weight. This enables variable torque measurements with distinctive control responses. Motor encoders, torque meters, and resolvers monitor the performance of drum position and speed. As discussed, control drums are typically composed of two materials, one absorbing the neutrons to control reactivity. Because this is a nonnuclear test bed, the neutronics are modeled and represented physically in the system through either light generation and photon transport or conduction and heat transport, according to the user's preference. As the neutronics model steps through startup and steady-state operation, the furnace emits a correlating heat intensity. Moreover, the power of each of these mechanisms is monitored for systematic diagnostics. To sense the mock reactor neutrons, a thermocouple monitor the heat generated. The temperature measurement is symbolic to radiation detection using gas filled detectors.

Refined rotation of the control drums is only one portion of the test bed. To realize the flow portion of the engine, the mock reactor is coupled with a two-phase flow loop. The loop enables users to test pressure, flow, and temperature sensors. Because of facility limitations, flowing cryogenic liquid hydrogen (H_2), which would case a phase change, is prohibited. Therefore, a two-phase system using flowing water and gas was implemented to allow for pressure and flow measurements. The water loop and gas loop are coupled via a turbo pump and turbine. As the water flows, the turbine begins to turn a coupling between the turbine and pump, which affects flow control of the gas loop. The gas is exhausted out the top of the assembly through a printed nozzle (seen in white). Multiple flow and pressure sensors are placed throughout the loop to monitor its performance and to validate other instrumentation on the loop implemented by users. The moderator control value and turbine bypass control valve are controlled by the user control algorithm. The turbine bypass valve dictates the flow to the pump turbine, ultimately determining the total hydrogen that flows through the engine and therefore the thrust of the engine. The user is limited only by the interchangeable hardware installed on the system.

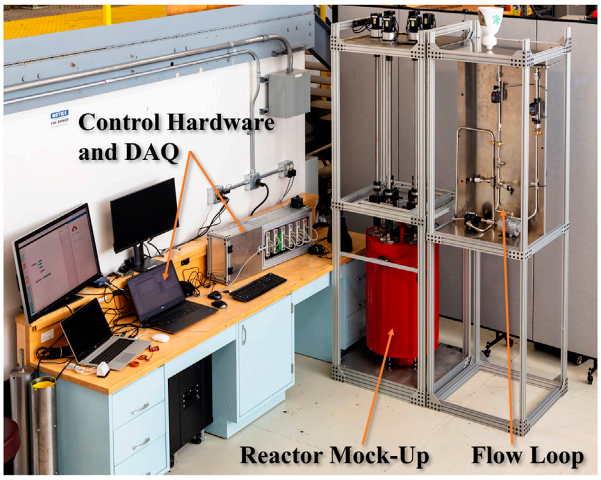

FIGURE 2
ORNL/NASA developed instrumentation and controls hardware-in-the-loop testbed.

A heat exchanger on the loop is driven by a reactor kinetics model and provides a temperature change in the loop that is representative of the hydrogen phase change. Thermocouples, resistive thermometers (i.e., resistance temperature detectors), and infrared cameras are used to monitor the temperature and feed data back into the software for analysis and implementation in the control loop. The entire loop is a scaled-down version of the anticipated loop hardware and functionality of the engine; however, the scaled-down version can provide invaluable data for modeling and simulation (M&S) of dynamic systems or digital twins.

3 Software interface

Many modern systems aim for autonomous functions, forcing real-time data analysis deeper into system control algorithms and modeling schemes, such as digital twins and dynamic system modeling (DSM). Therefore, M&S and real-time data analysis require more computational power and edge computing. Because the test bed was developed to operate in real time and demonstrate advanced autonomous controls while maintaining scalability, the data acquisition hardware should function in the same manner. The NVIDIA Jetson graphics card enables interfacing the hardware-in-the-loop instrumentation with traditional industrial programmable logic controllers (PLCs). Because edge devices are already implemented in autonomous vehicle technology with large data streams, deployment of edge computing resources in nuclear applications is not far-fetched. A PC, high-performance computing, or cloud computing system communicates with the NVIDIA Jetson, leveraging GitLab to upload and download code. Users develop autonomous control algorithms locally at their facility and upload them to GitLab, then ORNL downloads the version-controlled code and executes it on the hardware-in-the-loop test bed. This method of development was selected to reduce design to demonstration time as well as system costs. This platform is very flexible and can host various programming languages such as C++, Python, etc.

To investigate specific behaviors of I&Cs as they encounter normal and off-normal operating conditions, ORNL developed a DSM that includes reactor neutronics (i.e., a point kinetics model) (Williams et al., 2023). The model was developed in Modelica (Rader et al., 2019; Rader and Smith, 2020) for nominal operating conditions with an operational set-point of outlet temperature and pressure at the nozzle, which can be changed to control the input for the simulation. The model is parameterized to allow for testing the off-nominal operation of individual components. For example, the turbomachinery can be tested at off-nominal efficiencies to simulate performance degradation or malfunctions. Moreover, drum malfunctions, such as the drums sticking, causing reactivity changes inside the point kinetics model can also be simulated. The Functional Mock-Up (FMU) standard is used to package the simulation with the numerical solvers in a convenient black box surrogate model and is run as a real-time simulation in the hardware loop to provide calculated responses based on the first principles model.

Building a digital twin of the system can serve many purposes, including adding redundancy using digital sensors and acting as a living model. Additionally, the digital twin can actively learn and adapt to real-time information during collection. The mock reactor system design allows the user to navigate easily between the physical reality and the digital twin; the digital twin can provide surrogate models as replacements for gaps in the hardware. Through exhaustive testing and demonstration, this approach uses digital twin models as redundant instrumentation and reducing payloads to build the confidence for licensing and approvals.

4 Conclusion

NTP is one mechanism that will enable crewed missions to Mars; however, gaps in the technology must be addressed. Specifically, autonomous control of the engine in the case of communication delay or loss will be critical for ensuring the safe and reliable operation of the reactor and flowing hydrogen loop. ORNL developed a hardware-in-the-loop system to serve as a nonnuclear autonomous control test bed to address technology gaps for NTP. This test bed, coupled with Modelica modeling, provides engine developers with the ability to elevate the technology readiness levels of instrumentation and autonomous controls. This approach represents one of the only means of performing autonomous controls and instrumentation testing in the absence of a complete ground demonstration of the engine.

Data availability statement

The original contributions presented in the study are included in the article/Supplementary Material, further inquiries can be directed to the corresponding author.

Author contributions

NE: Conceptualization, Methodology, Project administration, Supervision, Writing–original draft.

Funding

The author(s) declare that financial support was received for the research, authorship, and/or publication of this article. This research is funded by NASA's Space Technology Mission Directorate under the Space Nuclear Propulsion Program.

Acknowledgments

The author would like to acknowledge NASA Marshall Space Flight Center, Aerojet Rocketdyne, and BWXT for their contributions to the design of the test bed, as well as the ORNL research staff and technicians who were instrumental in the fabrication of the system, including Brandon Wilson, Craig Gray, and Nick Termini. The data acquisition and controls hardware was developed by Charles Taylor at Louisiana State University, and the dynamic modeling software was developed by ORNL researcher Wesley Williams.

Licenses and permissions

Conflict of interest

The author declares that the research was conducted in the absence of any commercial or financial relationships that could be construed as a potential conflict of interest.

Publisher's note

References

Antsaklis, P., Passino, K., and Wang, S. (1991). An introduction to autonomous control systems. *IEEE Control Syst. Mag.* 11, 5–13. doi:10.1109/37.88585

Borowski, S. K., McCurdy, D., and Packard, T. (2013). "Nuclear thermal propulsion (NTP): a proven, growth technology for 'fast transit' human missions to mars," in AIAA SPACE 2013 Conference and Exposition 5354.

Corliss, W. R. (1966). SNAP nuclear space reactors. *Tech. Rep. U. S. At. Energy Comm.*

Finseth, J. L. (1991). Rover nuclear rocket engine program: overview of rover engine tests. Final Report. *Tech. Rep. Sverdrup Technol Inc.*

Hall, L. (2018). Nuclear thermal propulsion: game changing technology for deep space exploration

Hall, N. (2021). *Specific impulse.*

mars.nasa.gov (2020). *Mars 2020 mission perseverance rover.*

Rader, J. D., and Smith, M. B. (2020). *Dynamic nuclear thermal rocket and engine modeling.*

Rader, J. D., Smith, M. B., Greenwood, M. S., and Harrison, T. (2019). Nuclear thermal propulsion dynamic modeling with modelica

Robbins, W. (1991). "An historical perspective of the nerva nuclear rocket engine technology program," in Conference on Advanced SEI Technologies, USA, 06 September 1991.

Truscello, V. C. (1983). SNAP nuclear space reactors. *Tech. rep., U. S. Space Nucl. React. Power Program.*

Williams, W., Ramuhalli, P., and Greenquist, I. (2023). Development of microreactor automated control system (macs): surrogate plant-level modeling and control algorithms integration. doi:10.2172/1992728

frontiers | Frontiers in Nuclear Engineering

TYPE Original Research
PUBLISHED 26 July 2024
DOI 10.3389/fnuen.2024.1341754

Check for updates

OPEN ACCESS

EDITED BY
Charlotte Becquart,
Laboratoire UMET, France

REVIEWED BY
Benjamin Beeler,
North Carolina State University, United States
Siamak Attarian,
University of Wisconsin-Madison, United States

*CORRESPONDENCE
Emily De Stefanis,
✉ destee@rpi.edu
Li (Emily) Liu,
✉ liue@rpi.edu

RECEIVED 20 November 2023
ACCEPTED 22 May 2024
PUBLISHED 26 July 2024

CITATION
De Stefanis E, Ramic K, Vidal J, Zhao Y, Gallington LC, Bedell R and Liu LE (2024), Ab-initio molecular dynamics study of eutectic chloride salt: $MgCl_2$–NaCl–KCl.
Front. Nucl. Eng. 3:1341754.
doi: 10.3389/fnuen.2024.1341754

Ab-initio molecular dynamics study of eutectic chloride salt: $MgCl_2$–NaCl–KCl

Emily De Stefanis[1]*, Kemal Ramic[2], Judith Vidal[3], Youyang Zhao[3], Leighanne C. Gallington[4], Ryan Bedell[1] and Li (Emily) Liu[1]*

[1]Department of Mechanical, Aerospace, and Nuclear Engineering, Rensselaer Polytechnic Institute, Troy, NY, United States, [2]Nuclear Data Group, Oak Ridge National Laboratory, Oak Ridge, TN, United States, [3]National Renewable Energy Laboratory, Golden, CO, United States, [4]Xray Science Division, Advanced Photon Source, Argonne National Laboratory, Argonne, IL, United States

Ionic liquid materials are viable candidates as a heat transfer fluid (HTF) in a wide range of applications, notably within concentrated solar power (CSP) technology and molten salt reactors (MSRs). For next-generation CSP and MSR technologies that strive for higher power generation efficiency, a HTF with wide liquid phase range and energy storage capabilities is crucial. Studies have shown that eutectic chloride salts exhibit thermal stability at high temperatures, high heat storage capacity, and are less expensive than nitrate and carbonate salts. However, the experimental data needed to fully evaluate the potential of eutectic chloride salts as a HTF contender are scarce and entail large uncertainties. Considering the high cost and potential hazards associated with the experimental methods used to determine the properties of ionic liquids, molecular modeling can be used as a viable alternative resource. In this study, the eutectic ternary chloride salt $MgCl_2$–NaCl–KCl is modeled using ab-initio molecular dynamics simulations (AIMDs) in the liquid phase. Using the simulated data, the thermophysical and transport properties of eutectic chloride salt can be calculated: density, viscosity, heat capacity, diffusion coefficient, and ionic conductivity. For an initial model validation, experimental pair-distribution function data were obtained from X-ray total scattering techniques and compared to the theoretical pair-distribution function. Additionally, theoretical viscosity values are compared to experimental viscosity values for a similar system. The results provide a starting foundation for a $MgCl_2$–NaCl–KCl model that can be extended to predict other fundamental properties.

KEYWORDS

molten salts, chloride molten salts, Ab-initio molecular dynamics, simulations, VASP, $MgCl_2$, NaCl

1 Introduction

Next-generation technologies that require high operating temperatures to achieve a higher efficiency of power generation need a heat transfer fluid (HTF) that has high thermal stability, high heat storage capabilities, and is available in large quantities for the foreseeable future. The goal of a higher efficiency power generation method is needed due to the growing demand for energy. In order to decrease the reliance of power generation on the combustion of fossil fuels, the development of capable clean power technologies is crucial. Next-generation concentrated solar power (CSP) plants combined with thermal energy storage (TES) utilize a sCO2-Brayton power cycle instead of the traditional steam-Rankin power cycle (González-Roubaud et al., 2017). Due to the higher operating temperature of the sCO2-Brayton cycle, traditional nitrate salts, such as Hitec, used for the steam-Rankine cycle cannot be used due to the low temperature of the liquid phase of 130 °C–550 °C (Fernandez et al., 2015; Mehos, et al., 2017). Two candidate upgrades from nitrate salts are carbonate and chloride salts. Both these salts have reliable thermal stability at high temperatures and a wide liquid phase range, but carbonate salts are more expensive than chloride salts (Ding et al., 2019).

Myers Jr and Goswami (2016) analyzed 133 chloride salt systems, showing that NaCl and $MgCl_2$ are the best choices for high-temperature heat transfer and storage applications. The melting points of the separate ionic compounds NaCl, $MgCl_2$, and KCl are very high at 801°C, 714 °C, and 770 °C, respectively (Parker et al., 2022). Eutectic salt mixtures utilize the advantage of a lower melting point. $MgCl_2$–NaCl–KCl is a potential candidate for generation-3 CSP technology due to its lower melting point (≈400°C), wide liquid range, and reliable thermal stability (Xu et al., 2018). However, the available thermophysical data on this eutectic chloride system is scarce and contains large uncertainties. An alternative route to studying the physical chemistry of molten salts is molecular dynamics simulations.

From fundamental studies on local structure to investigations into thermodynamic and kinetic properties, recent research on molten salts has demonstrated that molecular dynamics (MD) simulations are a valuable alternative. MD simulations, classical and ab-initio (or first principles), are used to study and calculate the properties of molten salt systems. Classical MD simulations (CMDs) are based on the principle of statistical mechanics, describing the forces on each atom with an interatomic potential/force field. From a quantum mechanical perspective, ab-initio MD simulations (AIMDs) solve the interatomic forces using the instantaneous positions of the atoms. Due to the complexity of molten salt systems, CMD has questionable accuracy because the existing interatomic potentials do not fully capture the complex nature of the ionic liquid. AIMDs enjoy higher accuracy than CMD because the interatomic forces are calculated to solve Newton's equations of motion, which substitute the need for interatomic potentials/force fields (Marx and Hutter, 2000).

Before the research of Car and Parrinello (1985) on AIMDs, salt systems were simulated using CMDs based on interatomic potentials such as the Born–Mayer–Huggins–Tosi–Fumi (BMHTF) rigid ion interionic potential and the Buckingham pair potential. The development of the BMHTF potential approximation introduced new insights into the physical chemistry of alkali halides. The approximation estimates the potential energy of the system as a summation of all the interactions between all ion pairs. Early studies of simulated NaCl-type solid alkali halides used a variation of the BMHTF rigid-ion potential (Fumi and Tosi, 1964). However, this methodology cannot be accurately replicated for single salt ionic liquid systems due to the absence of many-body and long-range interactions that are essential for predicting the transport phenomena of ionic liquids, such as ionic conductivity (Salanne and Madden, 2011). Galamba and Costa Cabral (2007) confirmed this theory by comparing the results of a molten NaCl system that was simulated with both classical and first principles molecular dynamics. This study used the force-autocorrelation functions as a comparison to provide insight into the dependency of polarization effects. Using the basis of first-principles calculations with density functional theory (DFT), Ohtoriet al. (2015) parameterized a polarizable ion model (PIM) for single salt systems: NaCl and KCl. Their results show good agreement with the salt's experimental values of transport properties. However, this contradicted DeFever et al. (2020), who found that the PIM potentials could not produce accurate melting points for different alkali chlorides, such as NaCl and KCl. Furthermore, Zhou et al. (2022) simulated the ternary chloride salt $MgCl_2$–NaCl–KCl using a PIM and showed, in comparison with experimental results, the accuracy of the calculation for multi-component systems. The system they studied has the same components as our eutectic chloride salt but with different concentrations While Zhou et al. (2022) showed hope for the PIM, unresolved contradictions persist among the available studies that have yet to be reconciled.

The evident constraints of CMDs and PIM have prompted a shift towards the simulation of molten salt systems with AIMDs. The methodology of this study was influenced by the findings in studies using AIMDs to simulate similar chloride molten salt systems. Liang et al. (2020) simulated molten $MgCl_2$ using first-principles molecular dynamics simulation (FPMDs) and showed agreement between the theoretical model and experimental data regarding the thermo-kinetic and structural properties. In another study, they used FPMDs to demonstrate the effect of the dispersion correction term and the concentration on the prediction of thermo-kinetic properties. Other candidates for the heat transfer fluid of a CSP plant, NaCl–$CaCl_2$ and NaCl–$CaCl_2$–$MgCl_2$, were simulated by Rong et al. (2020; 2021), who investigated the thermophysical and structural properties using AMIDs. They concluded that thermophysical properties decrease with increasing temperature by observing the weakened bonding interactions. Rising temperature weakens the bonding interactions which increases the distance between the ion pairs as a result of volume expansion, thus revealing that the large ion clusters are divided into smaller dispersed clusters. It is worth noting that they used Car–Parrinello dynamics with CPMD computational software package. Furthermore, this research utilizing AIMDs to model similar chloride molten salt systems have lain the groundwork for the methodology explored in this study.

The present study utilizes the Vienna ab-initio simulation package (VASP). Previous work simulated eutectic salt systems similar to the present study to predict thermo-kinetic properties such as NaCl–$MgCl_2$ (Xu et al., 2020; Duemmler et al., 2022), $MgCl_2$–KCl (Xu, et al., 2021), and NaCl–KCl–$MgCl_2$ (Li, 2020) at different compositions than ours. These studies have shown the applicability of AIMD simulations for molten salt systems. However, because the interactions between the ions are calculated at every step, AIMD is computationally expensive, resulting in limits to the simulation system size and total simulation time. Bengtson et al. (2014) showed in a convergence study with a simulated LiCl–KCl molten salt system that the properties of the system with 64 atoms were consistent with a 1,000 atom system. They also showed that a minimal simulation time of 6–12 picoseconds (ps) is enough for statistical physical analysis. Duemmler et al. (2023) disputed these claims, arguing that the minimum total simulation time needed to calculate thermo-kinetic or thermophysical properties is 300 ps. Their results underestimated the diffusion coefficient compared to experimental values reported by Janz and Bansal (1982), as did the results published by Bengtson et al. (2014), but were closer to the experimental values. Duemmler et al. (2023) claimed that the results of Bengtson et al. (2014) "…overpredicted […] the actual DFT-predicted diffusion coefficient, which led their results to be more accurate compared to experiment," thus concluding that their methodology was more accurate, robust, and thorough than those of Janz and Bansal (1982). These studies have shown that AIMDs are a reliable alternative resource for studying chloride molten salt systems.

The aim of this research is to investigate the applicability of first principles AIMD simulations to predict the transport and thermophysical properties of eutectic chloride salt in the liquid phase range. Its data consists entirely of unpublished results and will be used to improve the future model. This research attempts to fill gaps in the fundamental understanding and vital literature needed to access the compatibility of an ionic liquid as a heat transfer fluid.

The implications of the findings of this study extend beyond the realm of fundamental research into the practical applications of next-generation CSP and MSR technologies. As highlighted previously, the demand for high-efficiency power generation methods necessitates HTFs with specific characteristics such as high thermal stability and heat storage capabilities. By leveraging AIMDs, this study contributes to ongoing efforts to accurately understand and predict the behavior of molten salt systems. The application of AIMDs in predicting these properties offers a cost-effective and less hazardous alternative to traditional experimental methods.

2 Methodology

2.1 Computational methods

2.1.1 Simulation details

First-principles AIMD simulations were performed using the Vienna Ab-Initio Simulation Package (VASP) based on density functional theory (DFT) and the Born–Oppenheimer approximation with periodic boundary conditions (Vosko et al., 1980; Kresse and Hafner, 1993; Kresse and Hafner, 1994; Kresse and Furthmüller, 1996a; Kresse and Furthmüller, 1996b). The interactions between electrons and nucleus are defined by the projector augmented wave (PAW) method, and the revised Perdew–Burke–Ernzerhof (rPBE) DFT of the generalized gradient approximation (GGA) is used for the electron exchange-correlation. The kinetic energy cutoff is 400 eV, and the system has a 1 × 1 × 1 k-point mesh. The timestep chosen is two femtoseconds (fs) to avoid energy drift. Fermi smearing with a smearing parameter of 0.2 eV was used for the partial occupancies of the wave function (Grimme, 2006a; Grimme et al., 2011; Hacene, et al., 2012; Hutchinson and Widom, 2012).

In this research, the molten salt system under investigation is a ternary chloride salt $MgCl_2$–NaCl–KCl, 44.8 mol% $MgCl_2$–29.4 mol % NaCl–25.8 mol% KCl, provided by NREL. Based on the experimental compositions, two systems were generated and used in this study: 142-atom (26 Mg_2+, 17 Na+, 15 K+, 84 Cl-, 58 cations and 84 anions) (Grimme et al., 2010) and 83-atom (15 Mg_2+, 10 Na+, 9 K+, 49 Cl-, 34 cations and 49 anions). The following were regarded as the valence electrons: Mg_2+ 3s2, Na+ 2s22p63s1, K+ 3s23p64s1, and Cl 3s23p5. The 83-atom system was used for the initial evaluation of the dispersion forces. Both systems were used to predict the structure and properties of the ternary salt.

The starting configuration file of the two systems was generated using PACKMOL, which calculated the initial geometries of the system by randomly packing atoms into a given volume based on the experimental composition and density at a specified temperature (Martínez et al., 2009). The cell sizes for the 83-atom system ranged 13.75–14.20 Å; the cell sizes for the 142-atom system ranged 16–17 Å. Before these initial configuration files could be used for AIMD simulations, the system needed to be pre-equilibrated with classical interatomic potential molecular dynamic (IPMD) simulations. These were performed with a Large-scale Atomic/Molecular Massively Parallel Simulator (LAMMPS) and utilized the Born–Mayer–Huggins potentials for each component of our system (Mayer, 1933; Fumi and Tosi, 1964; Tosi and Fumi, 1964; Thompson, et al., 2022). Even though there were limitations with the force field potentials for complex ternary salts, the accuracy of the pre-equilibration stage was not essential. The pre-equilibration IPMD simulation used an NVT ensemble at the specified temperature for 5 ps to lose the memory of the initial configuration from PACKMOL (Martínez et al., 2009). This method of pre-equilibration using IPMD followed Bengtson et al. (2014) and Nam, et al. (2014) The final configuration of the IPMD simulation was used for the following AIMD simulations. With the final configuration of the system from the IPMD simulation, the configuration underwent another step of equilibration using an isobaric–isothermal (NPT) ensemble for total simulation time (Steinmann and Corminboeuf, 2011). A generalized-gradient approximation exchange hole model was used for dispersion coefficients of approximately 100 ps at the respective temperature with a timestep of 1 fs and pressure of 1 atm. The NPT ensemble used the Langevin thermostat with a temperature coefficient set to 10 ps^{-1}. The goal of the NPT equilibration was to evaluate the density and energy of the system. The configuration used for the next simulation was selected from the trajectory of the NPT equilibration simulation. This configuration was selected from a timestep where the density of the system was approximately its average density from the overall simulation. With this selected configuration file, the system underwent an NVT ensemble using a Nosè thermostat for 100 ps with a timestep of 2fs, referred to as the "production run". The production runs from each temperature were used to estimate the thermodynamic properties at that temperature. The first 5 ps from the production run were neglected from the analysis and served as further equilibration. The simulated temperatures for both the 83-atom and 142-atom systems are 723 K, 773 K, 823 K, 873 K, 923 K, and 973 K.

2.1.2 Calculation methods of thermo-kinetic and transport properties

Properties were predicted using the trajectories from the production runs at the respective temperature. Each trajectory had a total simulation time of approximately 100 ps, used an NVT ensemble, and then was analyzed using MDANSE (Goret, 2017). The results given in Section 3.1 were simulated with an NPT ensemble while those in Section 3.2 were simulated with an NVT ensemble—the production runs.

2.1.2.1 Diffusion coefficient

The diffusion coefficient was calculated using Einstein's equation, which states that the self-diffusion coefficient is evaluated from the slope of the mean-squared displacement (MSD) (Einstein, 1905). The MSD is a statistical analysis of the particle trajectory in the simulation and was calculated using MDANSE (Eq. 1). The diffusion coefficient was calculated from the MSD (Eq. 2).

$$MSD = \langle \Delta\bar{r}(t)^2 \rangle = \frac{1}{N} \langle \sum \left| r_{i(t)} - r_{i(0)} \right| \rangle \tag{1}$$

$$D = \lim_{t\to\infty} \frac{1}{6} \frac{d\left[\Delta\bar{r}(t)^2\right]}{dt} = \lim_{t\to\infty} \frac{1}{6} \frac{d[\mathrm{MSD}]}{dt} \tag{2}$$

2.1.2.2 Ionic conductivity

Ionic conductivity was calculated for each ion with Nernst–Einstein approximation (Eq. 3). It is a scalar quantity of the diffusion coefficient (Bockris and Reddy, 1998).

$$\sigma = D\frac{nq^2}{k_B T} \tag{3}$$

where q is the charge of the ion, n is the unit volume concentration of carrier ions, D is the diffusion coefficient for the respective ion, k_B is the Boltzmann constant, and T is the temperature.

2.1.2.3 Viscosity

Viscosity was calculated using the Einstein–Stokes approximation (Eq. 4) (Zwanzig, 1983; Alonso & March, 1999).

$$\mu = \frac{k_B T}{D\lambda} \tag{4}$$

where λ is the effective atomic diameter, k_B is the Boltzmann constant, T is the temperature, and D is the diffusion coefficient. The effective atomic diameter is determined by the radius at which the first peak appears—the radial distribution function (RDF) of the system, calculated using MDANSE.

2.1.2.4 Heat capacity

Heat capacity was calculated at each temperature using Einstein's model for heat capacity of an oscillator modulated by the phonon spectrum (Eq. 5). $\tau = k_B T$. When the temperature is large, $Nk_B \approx nR$ (Kittel, 2005).

$$C_V = \left(\frac{\partial U}{\partial T}\right)_V = Nk_B\left(\frac{\hbar\omega}{\tau}\right)^2 \frac{e^{\frac{\hbar\omega}{\tau}}}{\left(e^{\frac{\hbar\omega}{\tau}} - 1\right)^2} \tag{5}$$

This equation is solved using the vibrational density of states (VDOS) of the system, which are calculated from MDANSE. The equation used to calculate heat capacity is shown as Eq. 6:

$$C_V = 3R\int_0^\infty \left(\frac{\omega}{k_B T}\right)^2 \frac{e^{\frac{\omega}{k_B T}}}{\left(e^{\frac{\omega}{k_B T}} - 1\right)^2} VDOS(\omega)d\omega \tag{6}$$

2.2 Experimental techniques

2.2.1 Density measurement

The density of the salt in the molten phase was measured with a density meter employing Archimedes' principle of buoyancy. This meter utilizes the weight of an object, such as high purity nickel cylinder, and a quartz container, which holds the molten salt. The measurement relies on measuring the object's mass before and after submerging in the molten salt. The scale used had a full capacity of 50 g and an uncertainty of ±0.1%. Utilizing the disparity in the mass between the object in air and submerged in molten salt, the density of the molten salt across various temperatures is calculated using Eq. 7:

$$\rho_f = \frac{\Delta M}{M}\rho_M \tag{7}$$

where ΔM is the difference in the weight of the object before and after submerging caused by the buoyancy force of the molten salt, M is the weight of the object measured in air, ρ_M is the density of the object, and ρ_f is the density of the molten salt. This method has been utilized in the literature with good reliability. The systematic error of the experimental density can be calculated using the partial derivative error propagation method based on Eq. 7 (Wang et al., 2021; Xu, et al., 2018).

2.2.2 Total scattering techniques

For comparison and validation of our AIMD simulation results, X-ray total scattering techniques are utilized to investigate the atomic structure of a material system by collecting Bragg, diffuse, and inelastic scattering. The diffraction pattern of a system is obtained from the scattering pattern. In total scattering studies, the pair distribution function (PDF) is obtained by performing a Fourier transformation on the system's scattering pattern. The PDF illustrates the probability of finding interatomic distances between pairs of atoms in a system (Egami and Billinge, 2012). The experimental PDF will be compared to the PDF of the simulated system.

A scattering experiment measures the probability of X-rays scattered at a certain angle and with a certain energy. X-ray scattering experiments collect the static scattering function of a sample, $I(\vec{Q})$. The angle is translated to the wavevector transfer $\vec{Q}$, which is related the incident and scattered wave-vector of the neutron or X-ray that hit the sample. In principle, the static scattering function is only determined by the structure of a sample and does not depend on the energy of the incident particle. The intensity of the static scattering function is related to the system's intra-particle structure factor $P(\vec{Q})$ and the inter-particle structure factor $S(\vec{Q})$. In liquid systems, the general equation for the static structure factor is:

$$I\left(\vec{Q}\right) = nP\left(\vec{Q}\right)S\left(\vec{Q}\right) \tag{8}$$

Here, n is the number density of particles in a sample. The inter-particle structure factor is extracted from the experimental static scattering function data after subtracting the background. This inter-particle structure factor, $S(\vec{Q})$, is converted to the pair distribution function $G(r)$ via a sine Fourier transform (8) (Egami and Billinge, 2012):

$$G(r) = \frac{2}{\pi}\int_0^\infty \vec{Q}\left[S\left(\vec{Q}\right) - 1\right]\sin\left(\overrightarrow{Qr}\right)d\vec{Q} \tag{9}$$

Total X-ray scattering data were collected on the 11-ID-B beamline at the Advanced Photon Source at Argonne National Laboratory. (Borkiewicz et al., 2019). The sample container was a

TABLE 1 Evaluation of exchange-correlation functionals at 973 K.

Functional + dispersion correction term	Density (g/cm^3)	Standard deviation
GGA PBE	1.31819	0.04732
GGA PBE + DFT-D3-BJ	1.72881	0.05127
GGA PBE + DFT-D2	1.69488	0.07015
GGA PBE + DFT-D3-0D	1.70422	0.0525
GGA BLYP	1.27859	0.0429
GGA BLYP + DFT-dDsC	1.74373	0.04263
GGA BLYP + DFT-D2	1.66392	0.06576
GGA rPBE	1.25629	0.10203
GGA rPBE + DFT-D3-0D	1.7107	0.04535
GGA rPBE + DFT-dDsC	1.55789	0.04368
GGA rPBE + DFT-D3-BJ	1.77661	0.05573
revPBE-vdW	1.57249	0.03959
GGA PBEsol	1.5878	0.08539
Experimental Density	1.56254	-

1 mm diameter quartz tube 75% filled with our salt sample. The incident X-ray wavelength was 0.2115 Å. The X-ray scattering measurements were converted to X-ray diffraction patterns with GSAS-II (Toby and Von Dreele, 2013). The diffraction patterns were then converted into experimental PDFs with PDFgetx2 (Qiu, 2004).

3 Results and discussion

The findings of this study help fill the fundamental gaps in the existing literature on molten salt systems, specifically regarding the application of AIMDs in predicting thermophysical and transport properties. By employing AIMDs, this research explores the atomistic behavior of eutectic ternary chloride salt in its liquid phase. The simulated data thus obtained can be used to calculate properties crucial for evaluating the capability of this salt as a HTF, including density, viscosity, heat capacity, diffusion coefficient, and ionic conductivity.

3.1 Effects of exchange-correlation functionals with and without Van der Waals dispersion correction term

The first simulations were performed using generalized gradient approximation (GGA) exchange-correlation functionals (ecf), such as Perdew–Burke–Ernzerhof (PBE) (Perdew et al., 1996), revised PBE (rPBE) (Zhang & Yang, 1998), Becke's ecf with Lee–Yang–Parr (BLYP) hybrid functional (Vosko et al., 1980; Stephens, Devlin, Chabalowski and Frisch, 1994), and revised PBE for solids (PBEsol) (Perdew et al., 2008). Additionally, a different type of functional was also tested for comparison: Van der Waals density functional (vdW-DF), which consists of a semi-local exchange-correlation functional that is improved with an added term that accounts for dispersion interactions (Dion, Rydberg, Schroder, Langreth and Lundqvist, 2004; Roman-Perez and Soler, 2009; Klimes et al., 2010; Klimes et al., 2011; Zhang & Yang, 1998). Dispersion forces that were tested with the above exchange-correlation functionals are DFT D2 (Grimme, 2006a), DFT D3-0D zero-damping function (Grimme et al., 2010), DFT D3-BJ with Becke–Johnson damping function (Grimme, Antony, Ehrlich, and Krieg, 2010; Grimme et al., 2011), and a density-dependent energy correction DFT dDsC (Steinmann and Corminboeuf, 2011). The different exchange-correlation functionals with and without dispersion correction terms combinations that were tested are listed in Table 1.

Each combination of exchange-correlation functional with or without a dispersion correction term listed in Table 1 was simulated with an 83-atom system using an NPT ensemble for 100 ps at 973 K with a timestep of one femtosecond. The trajectory files were analyzed using Molecular Dynamics Analysis for Neutron Scattering Experiments (MDANSE) software. The density values were calculated from analysis of the trajectory with MDANSE. Table 1 shows the calculated density of the system of each simulated system after the first 5 ps. The standard deviation is calculated from the calculated density after the first 5 ps. Included in Table 1 is the experimental density of the salt at that temperature. The experimental density of this salt system was provided by Dr. Vidal's group from the National Renewable Energy Laboratory (NREL).

Of the 13 combinations of exchange-correlation functionals with or without dispersion forces, only three fell within 2% of the experimental density: GGA rPBE DFT-dDsC, revPBE-vdW, and PBEsol. However, PBEsol was not tested further because it was optimized for solid materials. When no dispersion correction term is included, the simulations that rely solely on the exchange-correlation functionals (GGA: PBE, rPBE, and BLYP) underestimate the density. Bengtson et al. (2014) concluded that GGA PBE with the semi-empirical DFT-D2 method dispersion correction term provided accurate results for ionic liquid systems, but it overestimated the density of our system. The simulated salt system is LiCl-KCl (Bengtson et al., 2014). The two cases that produced a density data within 1% and were tested further at the lower temperatures in the liquid phase are a) GGA rPBE DFT-dDsC and b) revPBE-vdW. The system was simulated with an NPT ensemble at temperatures of 723 K, 773 K, 823 K, 873 K, and 923 K with a and b exchange-correlation functionals and dispersion force terms. Figure 1 shows the calculated density from these simulated systems using functionals a and b. The data was calculated after the first 5 ps of the simulation. The standard deviation of the simulated density was calculated over 95 ps. The experimental data included in this figure was provided by Dr. Judith Vidal's group at NREL. The method used to obtain this experimental data is described in Section 2.2.1.

In Figure 1, the calculated density of the simulated system's a and b are compared to the experimental density of the salt system. For Case A, GGA rPBE DFT dDsC, the timestep for the simulation was 1fs and ran for 100 ps. The error bars for the calculated density are wide enough to be comparable with the experimental density values. For Case B, revPBE-vdW, the timestep of the simulation was 3fs and ran for 40ps. The error

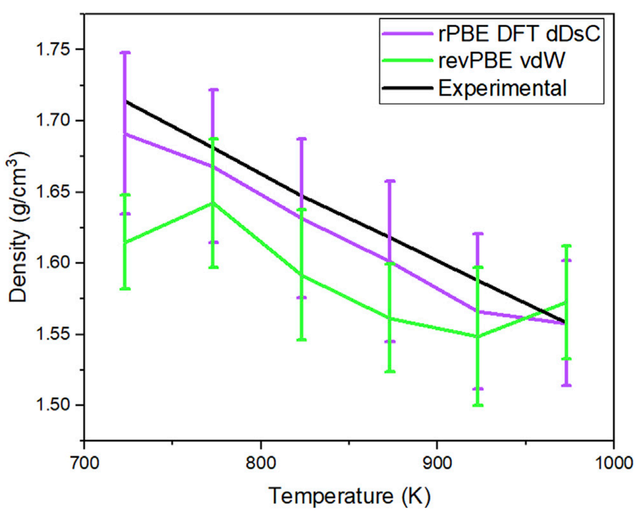

FIGURE 1
Density comparison of the 83-atom system simulated with GGA rPBE DFT dDsC and revPBE-vdW compared with the experimental density of the salt.

bars for some of the temperatures are wide enough to barely be comparable with the experimental density. Cases A and B were run at different timesteps and total simulation times because the computational cost of Case B is much more expensive than A. For example, in the time taken for the calculations GGA rPBE dDsC for 600 timesteps, revPBE-vdW calculates 60 timesteps. Based on the calculated density of the simulated system and considering computational cost, the exchange-correlation functional and dispersion correction term that will be used for the remainder of this research is GGA rPBE DFT-dDsC.

3.2 Testing convergence

3.2.1 Testing convergence with simulation time

The 83-atom system was used to observe the effect of the total simulation time of the production runs in the calculated properties. Figure 2 show the thermo-kinetic properties of the 83-atom system with a shorter and longer total simulation time of production run. The trajectory simulation time for the shorter simulation was approximately 25 ps, and the longer simulation was approximately 100 ps. For both simulations, the first 5 ps of the production run is neglected in the calculation as the original trajectory length was 5 ps longer. The methods for calculation of the properties are given in Section 2.1.2.

Figure 2 compare the shorter vs. longer simulation time for the 83-atom system. The properties calculated were the diffusion coefficient of each species (total, Cl, K, Mg, Na) (upper left quadrant), ionic conductivity of each species (Cl, K, Mg, Na) (upper right quadrant), and the viscosity and (4) heat capacity of the system. The results of the properties were predicted for the 83-atom system with a total simulation time of 25 ps (shorter) and 100 ps (longer). The experimental values of these properties for our salt system with the same composition are limited and are not available for comparison. In Figure 2, the calculated diffusion coefficient at each temperature for the 83-atom system with shorter and longer simulation times shows that the simulation time does not have a significant effect on the results. At temperatures below 825 K, there is very little difference between the diffusion coefficients from the shorter and longer simulations. This trend can also be seen in the comparison of the calculated ionic conductivity values for the 83-atom system shorter and longer simulation times (Figure 2). The accuracy of this calculation is questionable, considering that the ionic conductivity should theoretically increase with increasing temperature and there is little difference between values at the lowest and highest temperature. In Figure 2, the calculated viscosity values are shown for the 83-atom system with shorter and longer simulation times. This shows that there is very little difference between the values from the shorter and longer simulation times. This trend can also be seen in Figure 2 for the comparison of the calculated heat capacity values.

3.2.2 Testing convergence with unit cell size

Figure show the thermo-dynamic properties for the 142- and 83-atom systems. The methods for calculation were discussed in section 2.1.2. The trajectory used for analysis had a simulation time of approximately 100 ps and a timestep of 1fs and 2fs for the 83-atom and 142-atom systems, respectively. In Figure, the properties calculated were (a) diffusion coefficient of each species (total, Cl, K, Mg, Na), (b) ionic conductivity of each species (Cl, K, Mg, Na), and the (c) viscosity and (d) heat capacity of the 83- and 142-atom systems simulated at 723 K–973 K, respectively. The experimental values of these properties for our salt system with the same composition are limited and are not available for comparison.

Figure 3 shows the comparison of the calculate diffusion coefficient from the 83- and 142-atoms systems. The calculated diffusion coefficient for the 142-atom system is almost consistent with theoretical predictions, with temperature increasing as the diffusion coefficient increases. Figure 3 shows the ionic conductivity of the 83- and 142-atom systems. Since the ionic conductivity is a scalar of the diffusion coefficient, it is a safe assumption that it also follows the same temperature dependency trend. Figure 3 shows the viscosity values for the 83- and 142-atom systems. Theoretically, viscosity should decrease as the temperature increases, and the viscosity values for the 142-atom system follow that trend. This is one example where it is evident that the 142-atom system is more accurate than the 83-atom system. The calculations for the 142-atom simulation shows near consistency with theoretical predictions— as temperature increases, viscosity decreases. Figure 3 shows the calculated heat capacity values for the 83- and 142-atom systems. In theory, the heat capacity of the molten salt should increase with increasing temperatures. It can be seen in this comparison how the unit cell size affects the predicted properties. The values for the 142-atom system are consistent with the theory that heat capacity increases with increasing temperature. The line for the 142-atom system is quite straight without much scatter, unlike the rest of the calculations; this is concerning but the calculations have been reviewed.

This method of calculating viscosity and heat capacity has questionable accuracy because the Stokes–Einstein relationship assumes that the system has spherical particle random motion, which is not the case for fluids with intermediate range structures, such as ionic liquids. In future calculations, a more sophisticated method of statistical mechanics, such as green-kubo

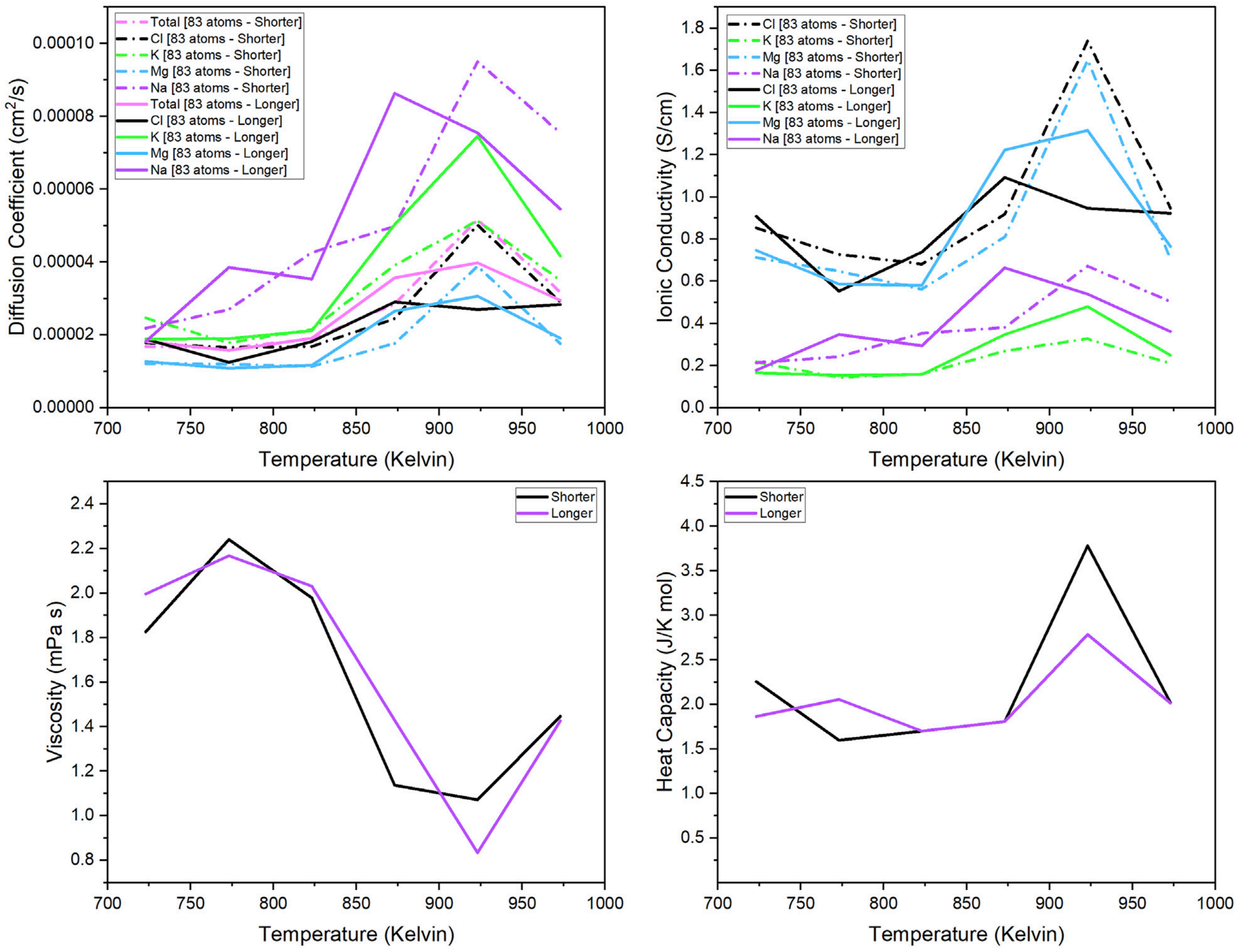

FIGURE 2
Diffusion coefficient of each component (total, Mg, Na, K, Cl); Ionic conductivity of each separate component (Mg, Na, K, Cl); Viscosity and heat capacity of the 83-atom system simulated at 723 K–973 K.

analysis, will be used for viscosity and heat capacity calculation. This requires the calculation of the autocorrelation function of the system's stress tensor.

3.3 Total scattering techniques results

Total scattering measurements were taken for comparison against the AIMD simulation results. The x-ray PDF data for the $MgCl_2$–NaCl–KCl salt in the liquid phase was obtained through the sine Fourier transform of the scattering pattern (Section 2.2.2). Figure 4 shows the PDF of the salt in the liquid phase. These measurements were taken for comparison against the PDF of our simulated salt system.

3.4 Comparison of theoretical and experimental results

Comparisons between the theoretical and existing experimental data provide insights into the accuracy and reliability of AIMDs in modeling molten salt systems. Initial validation efforts include the comparison of the theoretical and experimental PDF of the eutectic system in the liquid phase to confirm the molten environment. Additionally, the theoretical viscosity values predicted from the AIMDs are compared to the experimental viscosity of a similar system. These comparisons serve to establish the credibility of predicting properties of molten salts systems with AMIDs.

3.4.1 Pair distribution function

In Figure 5, the experimental PDF of the liquid system was compared to the theoretical PDF from the simulated system at the specified temperature. The trajectory was from the 142-atom production run with a simulation time of approximately 100 ps. The theoretical PDF was obtained from MDANSE. It can be seen at both 723 K and 973 K that the positions of the first and second major peak in the PDF are at the same interatomic distance, approximately 2.4 and 3.6 Å, respectively. The literature values for the bond length between Mg–Cl, Na–Cl, and K–Cl in the solid phase are 2.8, 2.36, and 2.7 Å (Bickelhaupt, Sola and Fonesca Guerra, 2007). The slight difference between the first peak and the Na–Cl bond length is due to the system being in a liquid phase. The difference between them is the magnitude of the intensity, for which it can be assumed that the

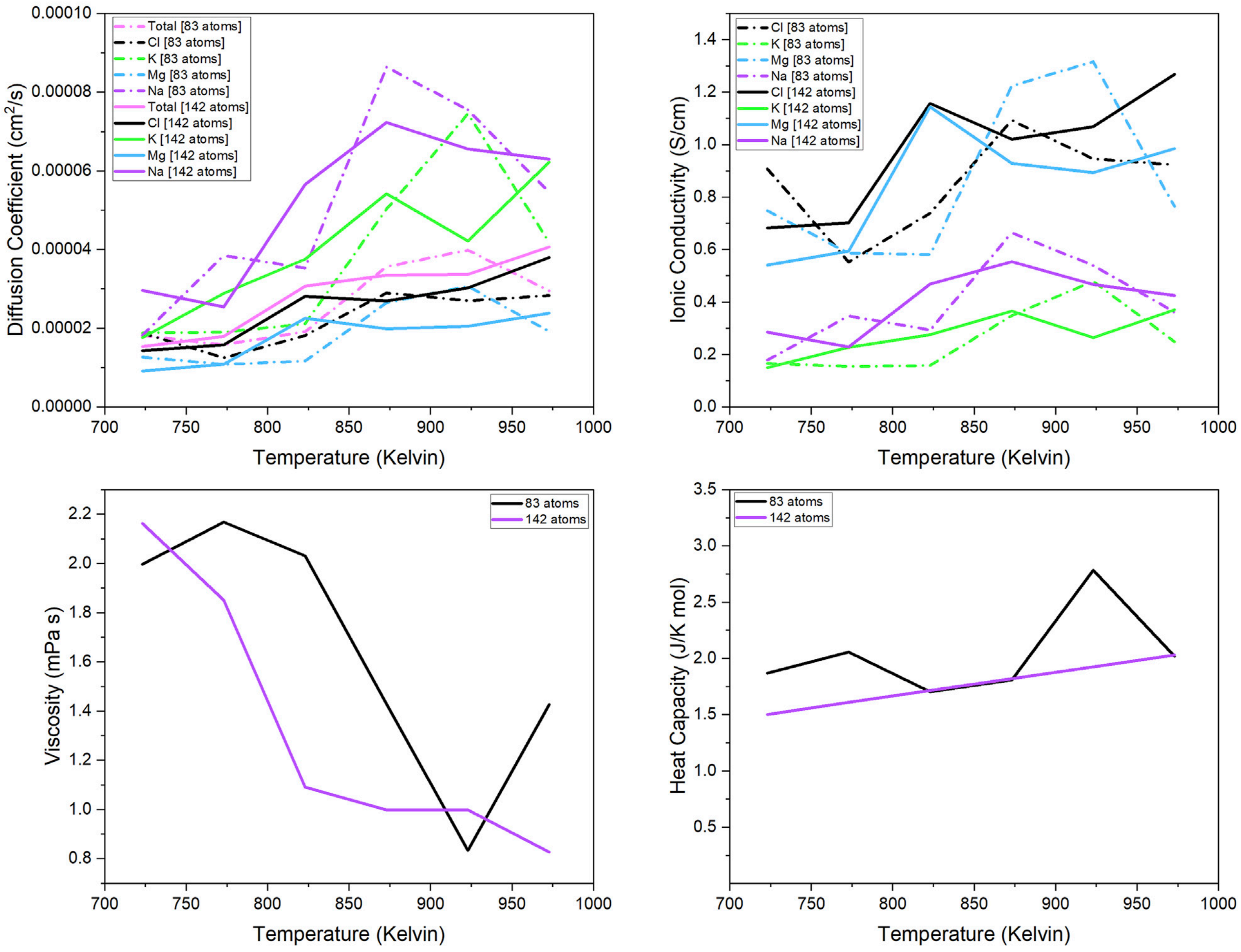

FIGURE 3
Diffusion coefficient of each component (total, Mg, Na, K, Cl); Ionic conductivity of each separate component (Mg, Na, K, Cl); Viscosity and heat capacity of the 83- and 142-atom systems simulated at 723 K–973 K.

simulated system is in a fully diffusive regime. The discrepancy between the two systems is caused by the calculation of the simulated PDF not considering the periodicity of the simulation cell. Non-consideration of the periodicity also makes the theoretical PDF go to 0 instead of 1. These results show that the AIMD simulation estimates both the short- and medium-range atomic structure.

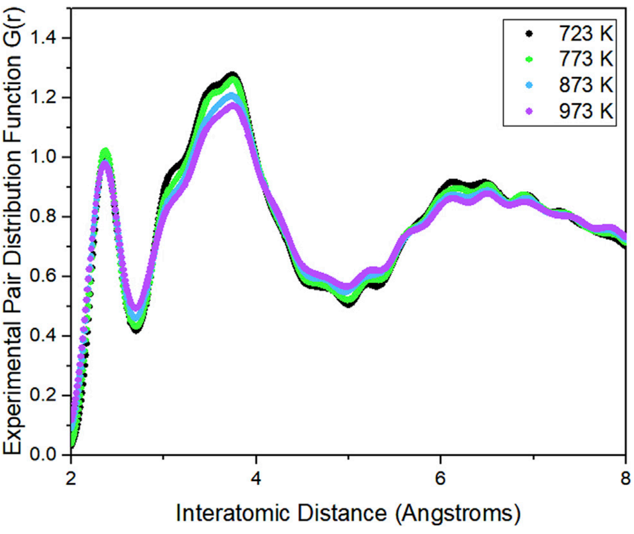

FIGURE 4
Experimental PDF obtained from X-ray scattering experiment from 11-ID-B.

3.4.2 Viscosity

To contextualize our findings and attempt to fill the gaps in the fundamental knowledge of molten salts, the theoretical viscosity values of our system are compared to the experimental viscosity values of a similar system (Figure 6). Both systems have the same main components, but the difference is the concentration of each. Wang et al. (2021) measured $MgCl_2$–NaCl–KCl at the concentration of (wt%) 45.98%–15.11%–38.91%. These experimental values were reported in centi-Poise, which is equal to our units of milli-pascal seconds.

The theoretical viscosity value was calculated using the Einstein–Stokes approximation. The viscosity values of this system can be calculated using this approximation because the eutectic salt exhibits Brownian motion in the molten phase. However, the disparity

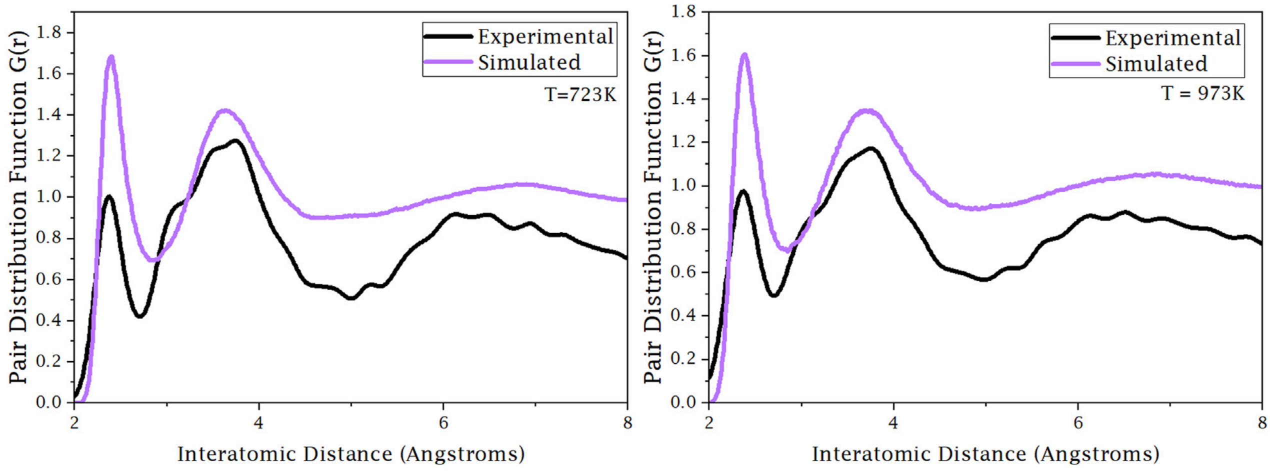

FIGURE 5
Experimental and theoretical PDF comparison at 723 K and 973 K.

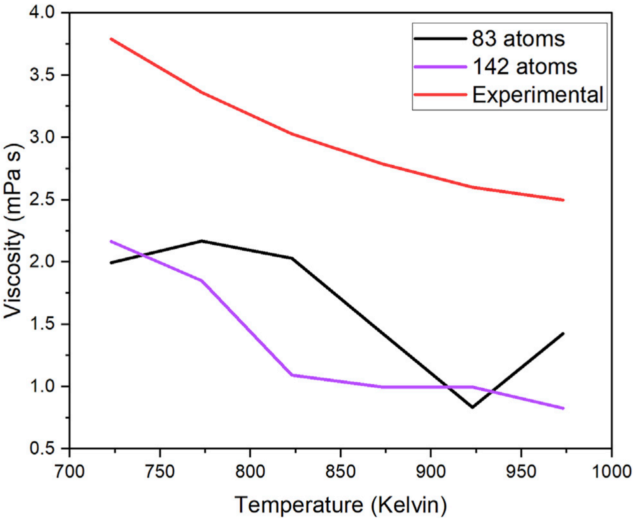

FIGURE 6
Experimental and theoretical viscosity value comparison.

observed between the theoretical and experimental viscosity values may stem from the possibility that the calculation relies on the assumption of the minimal interactions between ions, a factor critical for this approximation. This results in an underestimation of viscosity values due to the interactions of ions not being negligible. It is also possible that the size of the 142-atom system is not sufficient to capture the atomic behavior. While theoretical viscosity values do not display the same magnitudes as the experimental values, they do exhibit the same trend: viscosity decreases with increasing temperature.

4 Conclusion

In this study, AIMD simulations are utilized to study the ternary chloride salt system in the liquid phase range: 723K–973 K. Through a comprehensive evaluation of various exchange-correlation functionals and dispersion forces, it was determined that the GGA rPBE exchange-correlation functional with the dDsC dispersion correction term provides the most accurate description of our system. The production run trajectories were then used to predict key properties such as diffusion coefficient, ionic conductivity, viscosity, and heat capacity.

The impact of simulation parameters, including total simulation time and unit cell size, was systematically examined. Results indicate that the predicted properties exhibit minimal sensitivity to changes in simulation time for an 83-atom system. Additionally, comparing properties between 83- and 142-atom systems reveal that the larger system aligns more closely with theoretical predictions. It is worth noting that the calculation of heat capacity yielded invalid values, considering the assumed units shown.

Further validation was conducted through comparison with experimental data, PDF, and viscosity measurements. For the PDF, the location of the peaks in the theoretical PDF differs slightly from the experimental PDF, affirming the assumption that the simulation captures short- and medium-range atomic interactions. The disparity found between the theoretical and experimental PDF is the difference in magnitudes of the G(r). The discrepancy between the magnitudes of intensity is due to not considering the periodicity of the simulation cell. This shows that our simulated liquid phase structure is similar to the real liquid phase structure. Additionally, a disparity was observed between the theoretical and experimental viscosity values, possibly due to assumptions made in the calculation process.

Overall, this research helps address fundamental gaps in the understanding of molten salt systems at an atomic level. The insights gained by leveraging AIMDs can inform the design and optimization process of HTFs for clean energy technologies, thus supporting advancements in sustainable energy generation. Future directions for research include investigating simulation parameters and how the properties are affected. In the context of existing literature, this research contributes to ongoing efforts to advance clean energy technologies. By providing insights into the thermo-kinetic properties of eutectic chloride salts, this study supports the optimization and design of HTFs for high-efficiency power generation, thus addressing the growing demand for clean and sustainable energy.

Data availability statement

The data that support the findings of this study are available from the corresponding author upon reasonable request.

Author contributions

ES: Writing–original draft, Writing–review and editing, Investigation, Data curation, Formal Analysis, Visualization. KR: Investigation, Conceptualization, Methodology, Writing–review and editing. JV: Investigation, Writing–review and editing. YZ: Resources, Writing–review and editing. LG: Resources, Writing–review and editing. RB: Resources, Writing–review and editing. LL: Writing–review and editing, Conceptualization, Funding Acquisition, Project administration, Resources, Supervision.

Acknowledgments

This material is based upon work supported by the U.S. Department of Energy's Office of Energy Efficiency and Renewable Energy (EERE) under the Generation 3 Concentrated Solar Power (CSP) Systems award number DE-EE0008380. The identification of any commercial product or trade name does not imply endorsement or recommendation by the National Institute of Standards and Technology, nor does it imply that the materials or equipment identified are necessarily the best available for the purpose. This research used resources at Spallation Neutron Source, a DOE Office of Science User Facility operated by the Oak Ridge National Laboratory (IPTS 23984). This research used the resources of the Advanced Photon Source, a U.S. Department of Energy (DOE) Office of Science User Facility operated for the DOE Office of Science by Argonne National Laboratory under Contract No. DE-AC02-06CH11357. AIMD simulations were performed on the supercomputer at RPI, CCI-AIMOS.

Licenses and permissions

This manuscript has been authorized by UT-Battelle, LLC, under contract DE-AC05-00OR22725 with the US Department of Energy (DOE). The US government retains and the publisher, by accepting the article for publication, acknowledges that the US government retains a nonexclusive, paid-up, irrevocable, worldwide license to publish or reproduce the published form of this manuscript or to allow others to do so for US government purposes. DOE will provide public access to these results of federally sponsored research in accordance with the DOE Public Access Plan.

Conflict of interest

The authors declare that this research was conducted in the absence of any commercial or financial relationships that could be construed as a potential conflict of interest.

Publisher's note

References

Alonso, J. A., and March, N. H. (1999). Relation between transport and thermodynamic properties in liquid sp-electron metals near freezing. *Phys. Rev. E* 60 (4), 4125–4129. doi:10.1103/physreve.60.4125

Bengtson, A., Nam, H. O., Saha, S., Sakidja, R., and Morgan, D. (2014). First-principles molecular dynamics modeling of the LiCl–KCl molten salt system. *Comput. Mater. Sci.* 83, 362–370. doi:10.1016/j.commatsci.2013.10.043

Bickelhaupt, F., Sola, M., and Fonesca Guerra, C. (2007). Table salt and other alkali metal chloride oligomers: structure, stability, and bonding. *Inorg. Chem.* 46, 5411–5418. doi:10.1021/ic070328u

Bockris, J., and Reddy, A. K. (1998) *Modern electrochemistry: an introduction to an interdisciplinary area*, 1. USA: Plenum Press.

Borkiewicz, O. J., Ruett, U., Beyer, K., and Gallington, L. (2019). New capabilities at beamline 11-ID-B of the advanced Photon source. *Found. Crystallogr.* 75, a352. doi:10.1107/s0108767319096570

Car, R., and Parrinello, M. (1985). Unified approach for molecular dynamics and density-functional theory. *Phys. Rev. Lett.* 55 (22), 2471–2474. doi:10.1103/physrevlett.55.2471

DeFever, R. S., Wang, H., Zhang, Y., and Maginn, E. J. (2020). Melting points of alkali chlorides evaluated for a polarizable and non-polarizable model. *J. Chem. Phys.* 153 (1), 011101. doi:10.1063/5.0012253

Ding, W., Bonk, A., and Bauer, T. (2019). Molten chloride salts for next generation CSP plants: selection of promising chloride salts and study on corrosion of alloys in molten chloride salts. *AIP Conf. Proc.* 2126, 200014. doi:10.1063/1.5117729

Dion, M., Rydberg, H., Schroder, E., Langreth, D. C., and Lundqvist, B. I. (2004). Van der Waals density functional for general geometries. *Phys. Rev. Lett.* 92 (24), 246401. doi:10.1103/physrevlett.92.246401

Duemmler, K., Woods, M., Karlsson, T., Gakhar, R., and Beeler, B. (2022). An *ab initio* molecular dynamics investigation of the thermophysical properties of molten NaCl-MgCl 2. *J. Nucl. Mater.* 570, 153916. doi:10.1016/j.jnucmat.2022.153916

Duemmler, K., Woods, M., Karlsson, T., Gakhar, R., and Beeler, B. (2023). First-principles-derived transport properties of Molten chloride salts. *Jounral Nucl. Mater.* 585, 154601. doi:10.1016/j.jnucmat.2023.154601

Egami, T., and Billinge, S. (2012) *Underneath the Bragg peaks: structural analysis of complex materials*. Second Edition. Pergamon, Elmsford, NY: Elsevier.

Einstein, A. (1905). "On the movement of small particles suspended in stationary liquids required by the molecularkinetic theory of heat." . *Ann.d. Phys.* 17, 549–560. doi:10.1002/andp.19053220806

Fernandez, A. G., Galleguillos, L., Fuentealba, E. L., and Perez, F. J. (2015). Thermal characterization of HITEC molten salt for energy storage in solar linear concentrated technology. *J. Therm. Analysis Calorim.*, 122, 3–9. doi:10.1007/s10973-015-4715-9

Fumi, F. G., and Tosi, M. P. (1964). Ionic sizes and born repulsive parameters in the NaCl-type alkali halides—I: the Huggins-Mayer and Pauling forms. *J. Phys. Chem. Solids* 25: 31–43. doi:10.1016/0022-3697(64)90159-3

Galamba, N., and Costa Cabral, B. J. (2007). First principles molecular dynamics of molten NaCl. *J. Chem. Phys.* 126 (12), 124502. doi:10.1063/1.2711187

González-Roubaud, E., Pérez-Osorio, D., and Prieto, P. (2017). Review of commercial thermal energy storage in concentrated solar power plants: steam vs. molten salts. *Renew. Sustain. Energy Rev.* 80, 133–148. doi:10.1016/j.rser.2017.05.084

Goret, G. B., Aoun, B., and Pellegrini, E. (2017). MDANSE: an interactive analysis environment for molecular dynamics simulations. *J. Chem. Inf. Model.* 57 (1), 1–5. doi:10.1021/acs.jcim.6b00571

Grimme, S. (2006a). Semiempirical GGA-type density functional constructed with a long-range dispersion correction. *J. Comput. Chem.* 27 (15), 1787–1799. doi:10.1002/jcc.20495

Grimme, S., Antony, J., Ehrlich, S., and Krieg, H. (2010). A consistent and accurate*ab initio*parametrization of density functional dispersion correction (DFT-D) for the 94 elements H-Pu. *J. Chem. Phys.* 132 (15), 154104. doi:10.1063/1.3382344

Grimme, S., Ehrlich, S., and Goerigk, L. (2011). Effect of the damping function in dispersion corrected density functional theory. *J. Comput. Chem.* 32 (7), 1456–1465. doi:10.1002/jcc.21759

Hacene, M., Anciaux-Sedrakian, A., Rozanska, X., Klahr, D., Guignon, T., and Fleurat-Lessard, P. (2012). Accelerating VASP electronic structure calculations using graphic processing units. *Jounral Comput. Chem.* 33 (32), 2581–2589. doi:10.1002/jcc.23096

Hutchinson, M., and Widom, M. (2012). VASP on a GPU: application to exact-exchange calculations of the stability of elemental boron. *Comput. Phys. Commun.* 183 (7), 1422–1426. doi:10.1016/j.cpc.2012.02.017

Janz, G. J., and Bansal, N. P. (1982). Molten salts data: diffusion coefficients in single and multi-component salt systems. *J. Phys. Chem. Reference Data* 11 (3), 505–693. doi:10.1063/1.555665

Kittel, C. (2005) *Introduction to solid state physics*, 195b. New York: John Wiley and Sons Inc.

Klimes, J., Bowler, D. R., and Michaelides, A. (2010). Chemical accuracy for the van der Waals density functional. *J. Phys. Condens. Matter* 22, 022201. doi:10.1088/0953-8984/22/2/022201

Klimes, J., Bowler, D. R., and Michaelides, A. (2011). Van der Waals density functionals applied to solids. *Phys. Rev. B* 83 (19), 195131. doi:10.1103/physrevb.83.195131

Kresse, G., and Furthmüller, J. (1996a). Efficiency of ab-initio total energy calculations for metals and semiconductors using a plane-wave basis set. *Comput. Mater. Sci.* 6 (1), 15–50. doi:10.1016/0927-0256(96)00008-0

Kresse, G., and Furthmüller, J. (1996b). Efficient iterative schemes for *ab initio* total-energy calculations using a plane-wave basis set. *Phys. Rev. B* 54 (16), 11169–11186. doi:10.1103/physrevb.54.11169

Kresse, G., and Hafner, J. (1993). *Ab initio*molecular dynamics for open-shell transition metals. *Condens. Matter* 48, 13115–13118. doi:10.1103/physrevb.48.13115

Kresse, G., and Hafner, J. (1994). Norm-conserving and ultrasoft pseudopotentials for first-row and transition elements. *J. Phys. Condens. Matter* 6 (40), 8245–8257. doi:10.1088/0953-8984/6/40/015

Kresse, G. a., and Joubert, D. (1999). From ultrasoft pseudopotentials to the projector augmented-wave method. *Phys. Rev. b* 59 (3), 1758–1775. doi:10.1103/physrevb.59.1758

Li, X. N., Liu, W., Tang, Z., and Wang, J. (2020). Unrevealing the thermophysical properties and microstructural evolution of MgCl2–NaCl–KCl eutectic: FPMD simulations and experimental measurements. *Sol. Energy Mater. Sol. Cells* 210, 110504. doi:10.1016/j.solmat.2020.110504

Liang, W., Wu, J., Ni, H., Lu, G., and Yu, J. (2020). First-principles molecular dynamics simulations on the local structure and thermo-kinetic properties of molten magnesium chloride. *J. Mol. Liq.* 298, 112063. doi:10.1016/j.molliq.2019.112063

Martínez, L., Andrade, R., Birgin, E. G., and Martínez, J. M. (2009). PACKMOL: a package for building initial configurations for molecular dynamics simulations. *J. Comput. Chem.* 30 (13), 2157–2164. doi:10.1002/jcc.21224

Marx, D., and Hutter, J. (2000). “Modern methods and algorithms of quantum chemistry,” in *John von Neumann Institute for Computing, Jülich, Germany, 2000. Julich, Germany: John von Neumann Institute for Computing*. Editor J. Grotendorst (Germany: IEEE).

Mayer, J. E. (1933). Dispersion and Polarizability and the van der Waals Potential in the Alkali Halides. *J. Chem. Phys.* 1 (4), 270–279. doi:10.1063/1.1749283

Mehos, M., Turchi, C., Vidal, J., Wagner, M., Ma, Z., Ho, C., et al. (2017) *Concentrating solar power Gen3 demonstration roadmap*. Golden, CO: NREL. No. NREL/TP-5500-67464. National Renewable Lab (NREL).

Myers Jr, P. D., and Goswami, D. Y. (2016). Thermal energy storage using chloride salts and their eutectics. *Appl. Therm. Eng.* 109 (2016): 889–900. doi:10.1016/j.applthermaleng.2016.07.046

Nam, H. O., Bengtson, A., Vörtler, K., Saha, S., Sakidja, R., and Morgan, D. (2014). First-principles molecular dynamics modeling of the molten fluoride salt with Cr solute. *J. Nucl. Mater.* 449 (1-3), 148–157. doi:10.1016/j.jnucmat.2014.03.014

Ohtori, N., Mathieu, S., and Madden, P. A. (2015). Calculations of thermal conductivities of ionic materials by simulation with polarizable interaction potentials. *J. Chem. Phys.* 113 (17-18), 2422–2450. doi:10.1063/1.3086856

Parker, S. S., Long, A. M., Lhermitte, C. R., Monreal, M., and Jackson, J. R. (2022). Thermophysical properties of liquid chlorides from 600 to 1600 K: Melt point, enthalpy of fusion, and volumetric expansion. *J. Mol. Liq.* 346, 118147. doi:10.1016/j.molliq.2021.118147

Perdew, J. P., Burke, K., and Ernzerhof, M. (1996). Generalized gradient approximation made simple. *Phys. Rev. Lett.* 77 (18), 3865–3868. doi:10.1103/physrevlett.77.3865

Perdew, J. P., Ruzsinszky, A., Csonka, G. I., Vydrov, O. A., Scuseria, G. E., Constantin, L. A., et al. (2008). Restoring the density-gradient expansion for exchange in solids and surfaces. *Phys. Rev. Lett.* 100 (13), 136406. doi:10.1103/physrevlett.100.136406

Qiu, X. J., Thompson, J. W., and Billinge, S. J. L. (2004). PDFgetX2: a GUI-driven program to obtain the pair distribution function from X-ray powder diffraction data. *J. Appl. Crystallogr.* 37 (4), 678. doi:10.1107/s0021889804011744

Roman-Perez, G., and Soler, J. M. (2009). Efficient implementation of a van der Waals density functional: application to double-wall carbon nanotubes. *Phys. Rev. Lett.* 103 (9), 096102. doi:10.1103/physrevlett.103.096102

Rong, Z., Ding, J., Wang, W., Pan, G., and Liu, S. (2020). Ab-initio molecular dynamics calculation on microstructures and thermophysical properties of NaCl–CaCl2–MgCl2 for concentrating solar power. *Sol. Energy Mater. Sol. Cells* 216, 110696. doi:10.1016/j.solmat.2020.110696

Rong, Z., Pan, G., Lu, J., Liu, S., Ding, J., Wang, W., et al. (2021). Ab-initio molecular dynamics study on thermal property of NaCl–CaCl2 molten salt for high-temperature heat transfer and storage. *Renew. Energy* 163, 579–588. doi:10.1016/j.renene.2020.08.152

Salanne, M., and Madden, P. A. (2011). Polarization effects in ionic solids and melts. *Mol. Phys.* 109 (19), 2299–2315. doi:10.1080/00268976.2011.617523

Steinmann, S. N., and Corminboeuf, C. (2011). A generalized-gradient approximation exchange hole model for dispersion coefficients. *J. Chem. Phys.* 134 (4), 044117. doi:10.1063/1.3545985

Stephens, P. J., Devlin, F. J., Chabalowski, C. F., and Frisch, M. J. (1994). *Ab initio* calculation of vibrational absorption and circular dichroism spectra using density functional force fields. *J. Phys. Chem.* 98 (45), 11623–11627. doi:10.1021/j100096a001

Thompson, A. P., Aktulga, H. M., Berger, R., Bolintineanu, D. S., Brown, W. M., Crozier, P. S., et al. (2022). LAMMPS-a flexible simulation tool for particle-based materials modeling at the atomic, meso, and continuum scales. *Comput. Phys. Commun.* 271, 108171. doi:10.1016/j.cpc.2021.108171

Toby, B. H., and Von Dreele, R. B. (2013). GSAS-II: the genesis of a modern open-source all purpose crystallography software package. *J. Appl. Crystallogr.* 46 (2), 544–549. doi:10.1107/s0021889813003531

Tosi, M. P., and Fumi, F. G. (1964). Ionic sizes and born repulsive parameters in the NaCl-type alkali halides—II: the generalized Huggins-Mayer form. *J. Phys. Chem. Solids* 25 (1), 45–52. doi:10.1016/0022-3697(64)90160-x

Vosko, S. H., Wilk, L., and Nusair, M. (1980). Accurate spin-dependent electron liquid correlation energies for local spin density calculations: a critical analysis. *Can. J. Phys.* 58 (8), 1200–1211. doi:10.1139/p80-159

Xu, T., Li, X., Guo, L., Wang, F., and Tang, Z. (2020). Powerful predictability of FPMD simulations for the phase transition behavior of NaCl-MgCl2 eutectic salt. *Sol. Energy* 209, 568–575. doi:10.1016/j.solener.2020.09.038

Xu, T., Li, X., Li, N., Liu, M., Wang, F., and Tang, Z. (2021). In-depth explorations on the microstructural, thermodynamic and kinetic characteristics of MgCl2-KCl eutectic salt. *J. Mol. Liq.* 347, 118275. doi:10.1016/j.molliq.2021.118275

Xu, X., Dehghani, G., Ning, J., and Li, P. (2018). Basic properties of eutectic chloride salts NaCl-KCl-ZnCl2 and NaCl-KCl-MgCl2 as HTFs and thermal storage media measured using simultaneous DSC-TGA. *Sol. Energy* 162, 431–441. doi:10.1016/j.solener.2018.01.067

Zhou, W., Zhang, Y., and Salanne, M. (2022). Effects of fluoride salt addition to the physico-chemical properties of the MgCl2-NaCl-KCl heat transfer fluid: a molecular dynamics study. *Sol. Energy Mater. Sol. Cells* 239, 111649. doi:10.1016/j.solmat.2022.111649

Zwanzig, R. (1983). On the relation between self-diffusion and viscosity of liquids. *J. Chem. Phys.* 79 (9), 4507–4508. doi:10.1063/1.446338

frontiers | Frontiers in Nuclear Engineering

TYPE Original Research
PUBLISHED 01 August 2024
DOI 10.3389/fnuen.2024.1382695

OPEN ACCESS

EDITED BY
Anne Campbell,
Oak Ridge National Laboratory (DOE),
United States

REVIEWED BY
Juliana P. Duarte,
University of Wisconsin-Madison, United States
Axel Liebscher,
Federal Company for Radioactive Waste
Disposal, Germany

*CORRESPONDENCE
Aditi Verma,
✉ aditive@umich.edu

RECEIVED 06 February 2024
ACCEPTED 09 April 2024
PUBLISHED 01 August 2024

CITATION
Verma A (2024), Reckoning with the wicked problems of nuclear technology: pedagogical philosophy, design, and method underlying a course on nuclear technology, policy, and society.
Front. Nucl. Eng. 3:1382695.
doi: 10.3389/fnuen.2024.1382695

Reckoning with the wicked problems of nuclear technology: pedagogical philosophy, design, and method underlying a course on nuclear technology, policy, and society

Aditi Verma*

Nuclear Engineering and Radiological Sciences and Fastest Path to Zero Initiative, University of Michigan, Ann Arbor, MI, United States

Many problems at the intersection of nuclear technology, policy, and society can be thought of as wicked problems. Wicked problems—a formulation put forward in what is now a landmark paper by Rittel and Webber (design and planning scholars respectively)–are those that lack definitive formulations, resist durable resolution, do not have an exhaustively identifiable set of true or false solutions, and are often framed entirely differently by different entities experiencing the problem. Every attempt to solve a wicked problem is a solution attempt made in the real world and thus has consequences and implications that can potentially be far-reaching. This paper describes the underlying philosophy, design, and implementation of a course on "Nuclear Technology, Policy, and Society" taught in the Department of Nuclear Engineering and Radiological Sciences at the University of Michigan. The course explores some of nuclear technology's most pressing challenges (or its 'wicked problems'). Through this course students explore the origins of these problems–be they social or technical, they are offered tools–conceptual and methodological–to make sense of these problems, and guided through a semester-long exploration of how engineers can work towards their resolution, and to what degree these problems can be solved through institutional transformation and/or a transformation in our own practices and norms as a field. The underlying pedagogical philosophy, implementation, and response to the course are described here for other instructors who might wish to create a similar course, or for non-academic nuclear engineers, who might perhaps, in these pages, find a vocabulary for articulating and reflecting on the nature of these problems as encountered in their praxis.

KEYWORDS

nuclear energy, ethics, energy justice, environmental justice, wicked problems, nuclear ethics, engineering education, future of nuclear engineering

Introduction

With a growing global emphasis on the need to decarbonize energy systems, key decision-makers in many countries are calling for a significant expansion of nuclear energy–with projections calling for a doubling or tripling of nuclear capacity around the globe by mid-century[1]. These expansions in capacity projected, include in many cases, the use of nuclear technologies in entirely new places and contexts–countries that have never before built and operated nuclear reactors, applications of nuclear energy technologies in remote and off-the-grid locations, as well as the use of nuclear technologies for generating process heat for a wide variety of industrial applications. Beyond the technical work needed to rapidly develop and commercialize nuclear energy systems over these challenging timescales for use across a potentially vast set of use contexts, a range of problems–political, ethical, social, environmental, and economic–must also be acknowledged and explored if nuclear energy technologies are to become significantly integrated into our energy systems of the future[2]. Achieving this requires that nuclear engineers of the future must be equipped with the intellectual frameworks and tools to make sense of these problems–both as they manifest in the context of nuclear technologies and industries as we know them today and learn to anticipate the forms these problems might take in the future. Traditionally, these skills and ways of thinking often consigned to the category of "non-technical" or "soft", have been relegated to footnotes and sidebar discussions, never occupying a central place in the intellectual canon of nuclear engineering. Yet a growing number of young people[3, 4] entering the discipline of nuclear engineering, are increasingly expressing an interest in reckoning with these difficult–or what we will call here, the "wicked problems" of nuclear engineering.

Wicked problems—a formulation put forward in what is now a landmark paper by Rittel and Webber[5] (design and planning scholars respectively)–are those that lack definitive formulations, resist durable resolution, do not have an exhaustively identifiable set of true or false solutions, and are often framed entirely differently by different entities experiencing the problem. Every attempt to solve a wicked problem is a solution attempt made in the real world and thus has consequences and implications that can potentially be far-reaching. (A fuller discussion of wicked problems in a nuclear context is contained in the subsequent section. See also Table 1).

Many, if not all problems, at the intersection of nuclear technology, policy, and society bear all these (and other, as shown in Table 1 above) hallmarks of wickedness. These include difficulties within the nuclear sector in seeing through new technological designs from the inception to implementation[6]; cost overruns, financing difficulties, and the recent mismanagement of nuclear plant construction projects (Lovering et al., 2016); the presence of regulatory institutional infrastructures that in both real and perceived ways can curtail meaningful learning; a rigid ways of thinking about risk and safety within the nuclear sector which have unintentionally led to the creation of an antagonistic expert-public divide (Verma and Djokić, 2021); our failures to successfully engage communities in the siting and technology development process (Verma et al., 2021); the still unresolved problem of long-term nuclear waste management which even if regarded as a technically solved problem, remains unresolved in a real sense (Saraç-Lesavre, 2021); the dual-use nature of nuclear technologies that create security and non-proliferation concerns; and a myriad of environmental justice issues that pervade the nuclear fuel cycle and even several aspects of nuclear policymaking (Turner et al., 2020). The list is not exhaustive. It goes on and is subject to change. The form these problems take is likely to change as our technologies evolve and as they are potentially used on an ever larger scale–as many nuclear engineers intend them to be. What then is our responsibility to society? Or more immediately, what is our responsibility to future nuclear engineers? How must we prepare them to reckon with these problems?

To these questions, this paper offers some answers and offers a set of propositions on how nuclear engineers, part of their education,

---

[1] aditive@umich.edu

[2] While some, having observed these wicked problems, have viewed their existence as grounds for not pursuing the development of nuclear technology or even for the extinction of the field as a whole, this author takes the stance that every field of engineering has it is own variation of these problems. Consider, for example the significant societal and environmental impacts of critical minerals extraction needed for the development of solar and wind energy, or the many potential and actual misuses of artificial intelligence and machine learning, including facial recognition technology, or large scale systemic organizational and institutional failures leading to accidents in airplanes and spacecraft. Rather than call for an end to the fields that produce these technologies (an unlikely occurrence over the timescale of any single generation), this author takes the stance that the researchers and practitioners within these fields (nuclear engineering included) must be trained (as students) to thoroughly recognize their ethical responsibilities to society and the environment.

[3] This study focused on the University of Illinois Urbana Champaign, University of Tennessee Knoxville, University of Michigan, North Carolina State University, and University of New Mexico. This study was completed just prior to the introduction of the course described in this paper which is therefore not reflected in its analysis.

[4] This study focused on MIT.

[5] It would certainly be interesting to explore whether and how nuclear engineering coursework in other countries offers courses on ethics or integrates these considerations in existing offerings. Such an analysis is beyond the scope of this paper but would make for an important and fascinating follow-up study. It should also be noted that faculty outside nuclear engineering departments have been offering courses on history with a nuclear focus. Here, notable examples are courses offered by Gabrielle Hecht and Sonja Schmid–both historians of technology–at their respective institutions.

[6] To be clear, these are extrapolations of the futures most nuclear engineers hope for or imagine. These extrapolations, if achieved, will present new policy challenges for which the discipline and the sector is ill-prepared.

TABLE 1 This table describes the 10 attributes of wicked problems as laid out by Rittel and Webber, with brief examples of nuclear technology problems that illustrate their 'wicked' nature.

Attributes of wicked problems (Rittel and Webber, 1973)	How 'tame' problems differ from wicked problems (paraphrased from rittel and Webber) (Rittel and Webber, 1973)	Further description of the wicked problem attribute (paraphrased from rittel and Webber) (Rittel and Webber, 1973)	A nuclear example (most nuclear policy problems possess each of these attributes. For the sake of brevity only one example is included to illustrate each attribute)
1. Do not have a definitive formulation	"tame problems" have exhaustive formulations containing all the information needed to solve the problem	"The information needed to understand a problem depends on one's idea for solving it." The understanding and solution of the problem are inextricably linked to each other "One cannot understand the problem without knowing about its context; one cannot meaningfully search for information without the orientation of a solution concept"	Nuclear waste Is spent fuel waste? Should it be buried or recycled? Should we build in retrievability?
2. Do not have a stopping rule	The problem solver knows when they have done their job. There are criteria that indicate or specify that a solution has been found.	"No ends to the causal chains that link interacting open systems". The planner can always do better. Additional investment of effort might lead to a better solution. A planner stops working on a problem not because it is perfectly solved but because the planner has run out of time. The planner has to satisfice	Nuclear safety We will always need to remain vigilant about nuclear safety, always need to ensure we have public consent, and always need to ensure that nuclear technologies and materials are not used to build weapons. Nuclear regulators can always do additional things to make plants safer
3. Wicked problems do not have solutions that are true-or-false, but good-or-bad	Tame problems have identifiable solutions. The problem solver knows whether the solution is right or wrong, true or false	There are no true or false answers. Solutions to wicked problems impact many parties and these impacts may vary. Some may perceive the impacts to be desirable and good while others may find the impacts are harmful and undesirable	Siting of a nuclear plant When a nuclear plant is sited, some people in a nearby community may be strongly opposed to it and have concerns about safety, whereas others may be pleased about plant siting and possible economic opportunities the siting may bring
4. Do not have an immediate or ultimate test of a solution	It is possible to immediately determine whether a solution attempt has been successful. The test of a solution is under the control of a limited number of people. For example, designing the interior of a house	Solutions to wicked problems generate "waves of consequences" over an extended period of time. The solution attempt cannot be fully evaluated until the waves of consequences have been allowed to play out and are themselves assessed. Planners typically satisfice and stop studying outcomes due to resource constraints	Nuclear waste For a deep geological repository, the ultimate test of safe confinement is only possible at the of the containment period which can be upwards of a hundred thousand years. In this case, there is an 'ultimate test' of the solution but it lies beyond human timescales too deep in the future to be verifiable by the designers of the repository
5. Every solution attempt has real world consequences	Many problem solutions may be attempted analytically, in a simulation or in a lab with little to no impact on the real world. Because of this minimal impact, a very large number of solution attempts are possible. Trial and error is an acceptable approach to problem-solving	Every implemented solution has real-world consequences, creating traces that cannot be undone; "half-lives" of consequences are very long. Every trial counts	Nuclear innovation Decisions to fund a particular nuclear technology or design, also involve decisions to not fund others (which may ultimately have turned out to be superior to the designs that were funded). These unfunded designs and companies may not continue and may be shut down
6. Wicked problems do not have a finite set of potential solutions	There is a well-defined solution or a set of possible solutions	There may be a vast number of unknowable solutions or even the absence of a single solution. The size of the solution set cannot be quantified because the number and "goodness" of the solutions depend on the entities impacted by the problem and solution	Nuclear waste How should a nuclear waste repository be designed to minimize societal and environmental impact? Who is considered while evaluating impact? If the set of people, communities, and non-human actors considered expands, the possible facility design solutions also expand

(Continued on following page)

TABLE 1 (*Continued*) This table describes the 10 attributes of wicked problems as laid out by Rittel and Webber, with brief examples of nuclear technology problems that illustrate their 'wicked' nature.

Attributes of wicked problems (Rittel and Webber, 1973)	How 'tame' problems differ from wicked problems (paraphrased from rittel and Webber) (Rittel and Webber, 1973)	Further description of the wicked problem attribute (paraphrased from rittel and Webber) (Rittel and Webber, 1973)	A nuclear example (most nuclear policy problems possess each of these attributes. For the sake of brevity only one example is included to illustrate each attribute)
7. Each wicked problem is unique	These problems may be arranged into 'classes' or 'types' of problems	While wicked problems may share some similarities, there are likely to be additional distinguishing properties that make it impossible to replicate the solution of a wicked problem attempted elsewhere	Nuclear Waste Approaches to nuclear waste siting which have been tried (successfully) in Scandinavian countries may not work if replicated exactly in the US because of the unique history of the nuclear sector and its impacts on communities
8. Every wicked problem is a symptom of another wicked problem	These problems may be connected to each other but not necessarily or always	Wicked problems are symptoms of other problems. One must carefully choose the 'level' at which the problem is solved and choose a level that is neither to high and 'abstract' nor too specific and concrete	Nuclear proliferation Nuclear proliferation is the symptom of another 'problem' - the discovery of nuclear fission and the spread of nuclear technologies around the world. Nuclear proliferation as a problem could be solved by reversing the spread of nuclear technology (not possible but attempted in a limited sense) or policing every instance of use of nuclear technology (attempted but also in a limited sense)
9. A wicked problem can be represented or framed in more than one way	These problems can typically be represented simply and without discrepancies	Representation and explanation of wicked problems depend upon the person explaining or representing the problem. Problem solvers tend to pick the representations that best fit the solutions that are available to them	Nuclear safety A nuclear plant designer may view safety as a design problem, a regulator might view safety as a problem of sufficient oversight of plant designers and operators, and a plant operator might view safety as being a problem related to organizational pressures and insufficiency of resources to ensure safe operation
10. The planner or policymaker has no right to be wrong	Trial and error is an acceptable solution approach as solution attempts have little real-world impact	Planners are morally responsible for every solution attempt which has real-world impacts that might be far-reaching	Cost of electricity Failures to design a plant carefully or manage a construction project well may lead to significant cost escalations which could increase electricity prices for hundreds of thousands of households

can be taught how to reckon with these problems. This paper describes the underlying pedagogical philosophy, design, and implementation of a course on "Nuclear Technology, Policy, and Society" taught in the Department of Nuclear Engineering and Radiological Sciences at the University of Michigan. The course explores some of nuclear technology's most pressing challenges (or its 'wicked problems'). Through this course students explore the origins of these problems–be they social or technical, they are offered tools–conceptual and methodological–to make sense of these problems, and guided through a semester-long exploration of how engineers can work towards their resolution, and to what degree these problems can be solved through institutional transformation and/or a transformation in our own practices and norms as a field. The underlying pedagogical philosophy, implementation, and response to the course are described here for other instructors who might wish to create a similar course, or for non-academic nuclear engineers, who might perhaps, in these pages, find a vocabulary for articulating and reflecting on the nature of these problems as encountered in their praxis. The paper is structured as follows: a background section describes the emergence of ethics as an area of emphasis within engineering education and research, as well as prior nuclear policy-related pedagogical efforts at the University of Michigan. This is followed by a brief section on the contributions of this paper and the course that it describes, followed by a section on method which describes the pedagogical philosophy and design of the course. This section in turn is followed by a discussion of course outcomes, recommendations to others considering developing or teaching similar courses, and a section that concludes.

Background

With the creation of the first engineering ethics standards in the late 19th century, many engineering societies began to draft their own codes of ethics by the early 20th century (NSPE, 2021). In the nuclear sector–this has included codes of ethics for both academic and professional engineers (as created by the American Nuclear Society in the US (American Nuclear Soceity, 2022), for example) as well as codes of ethics for nuclear operating organizations (as created by the International Atomic Energy Agency (INTERNATIONAL ATOMIC ENERGY AGENCY, 2019)). With the widespread adoption of codes of ethics, the Accreditation Board for Engineering and Technology (ABET) also started calling for the inclusion of ethics in engineering education and began auditing its presence as part of its accreditation processes. Yet, what ethics means, and how it is implemented in engineering pedagogy, varies widely across engineering disciplines–as does the understanding of what constitutes the ethical responsibility of an engineer (Fiesler et al., 2020; Das et al., 2023a). This, in part, has to do with the breadth of expertise of engineering instructors, their ability and interest in teaching ethics, as well as institutional barriers and constraints that might prevent the meaningful inclusion of ethics, as well as other social and policy considerations in engineering education (Das et al., 2023b; Saadi et al., 2023). Many have critiqued the concept of ethics itself as operationalized in engineering education as being too narrow, calling instead for a focus not just on ethics but on justice (Riley and Riley, 2008; Nieusma and Riley, 2010). Reviews of engineering literature reveal that until recently engineers have typically been hesitant to adopt a pro-justice positionality (Das et al., 2023c). One possible explanation of this is that the adoption of such a stance is an implicit acceptance of the politicization of engineering (Cech, 2013)–an ideology that engineers have long rejected. Yet a growing body of research on how engineers and designers make design decisions, how they often unintentionally encode their designs with their values and biases, "designing for a 'reference' individual or user" they are able to easily imagine, while often failing to recognize the needs of many others, is leading to a growing consensus across fields of engineering that engineers need to frame and solve design problems keeping in mind a much broader range of possible users and constituents, and design with these individuals and communities wherever possible (D'Ignazio and Klein, 2023; Costanza-Chock, 2020). These logics which are rapidly becoming mainstream in fields such as product design (Dayan and Colak, 2008), AI (Gabriel, 2022), and robotics (Ostrowski et al., 2022), are gradually also reaching fields of engineering concerned with the design of complex systems–systems that do not have a single or even a handful of users but instead a complex web of rightsholders.

Infusing ethical considerations in nuclear engineering education

Approaches to instruction that emphasize ethics and justice, as well as the importance of community and user engagement, are gradually making their way into nuclear engineering coursework. A comparative study of nuclear engineering curricula across five American institutions (Kendall and Arkhurst, 2023) found while fourteen courses across these five institutions partially embedded ethics, no single course was devoted to an in-depth exploration of ethics and nuclear technology. The authors of this study concluded that "in a field with such consequential history and heavy importance of ethical considerations and quality of communication, the availability of a course devoted to the intersections between ethics, communication, history, technology, and policy could show the dedication of universities to these standards". (Fisher et al., 2023). A separate study focusing on design pedagogy in engineering and traditional design departments (such as architecture and urban planning) at a leading engineering institution (Fisher et al., 2023) found that while nuclear engineering coursework at that institution reckoned with the history of the nuclear field, it did so from the dominant perspective–failing to reckon with complicated and disparate impacts of nuclear technologies on different communities and regions (Das et al., 2023a) (such as the impacts of uranium mining, weapons development and testing on indigenous communities as pointed out by the authors of the previously mentioned study).

Interdisciplinary nuclear technology studies at the University of Michigan

It is significant that the course described here is being taught at the University of Michigan–home to the first research initiative dedicated to the interdisciplinary study of nuclear energy. This initiative—the Michigan Memorial Phoenix Project was created in 1948–is headquartered in a physical building on the University of Michigan's North Campus at 2,301 Bonisteel Boulevard. The Memorial was imagined as "a living memorial to the 585 university alumni, students, faculty, and staff members who gave their lives in World War II" devoted to the "peaceful, useful, and beneficial applications and implications of nuclear science and technology for the welfare of the human race" (Michigan Memorial Phoenix Project, 1948). The Memorial, which predated the Department of Nuclear Engineering and Radiological Sciences, brought together researchers of many intellectual stripes–physicists, engineers, lawyers, political scientists, and sociologists, to study nuclear energy and its applications. Regrettably, over time, this momentum faded, and the purpose and mission of the memorial were all but forgotten until 2022 when the Memorial was rededicated to its original mission (an initiative led by the new department chair, Professor Todd Allen). The preceding year also marked the return of the Department of Nuclear Engineering and Radiological Sciences to the Michigan Memorial Phoenix Project building. The Phoenix building is also currently home to Fastest Path to Zero–an interdisciplinary initiative at the University of Michigan whose purpose is to help communities reach their climate goals.

A brief history of curricular development at the University of Michigan

Even preceding these developments, various faculty at the University of Michigan have taught courses on the history and policy of nuclear technology. Most recently, Professor Todd Allen taught a course on nuclear policy. The course, taught in a hybrid fashion in Fall 2020 (during the pandemic), brought a diverse array of policymakers who lectured on the structure and functioning of their respective institutions. Dr. Patricia Schuster taught a course on the history of nuclear weapons. This course was offered in Fall 2018.

Going further back, NERS Professor Emeritus Ron Fleming briefly taught a course on the history of nuclear weapons, and Professor Gabrielle Hecht, during her tenure in the history department, taught courses on the history of nuclear energy. All but Hecht's courses in the History department were one-off offerings. Following widespread student demand (including an initiative by some students to themselves create and teach a course–an initiative that ultimately was not realized), and on the recommendations of the Department's Advisory Board (a group of senior practitioners, researchers, and policymakers), a decision was made to create a new, recurring course–which is the course created by the author and described in this paper.

The instructor's background

An ideology of logical positivism and depoliticization (Cech, 2013) pervades the natural sciences and engineering. Peer-reviewed writings are written in the third person, describing the logical order of research questions, methods, results, analysis, and discussion–thus projecting a veneer of pure objectivity and linearity in the research process. Often, the actual research process could not be further from reality. Bold discoveries and inventions are sometimes purely accidental–not the result of deliberate planning and design, but fortunate serendipity (Kauffman and Mayo, 1997; Ban, 2006; Buckner, 2012), and often unexpected results that precede the research questions, with the results once realized prompting researchers to return to an earlier phase of exploration and self-inquiry to ponder whether the correct questions were being asked or indeed what are the questions to which the unexpected results are the answer. Observing the circuitous nature of the process of research and discovery but the nevertheless linear account of it presented in publications has prompted many researchers, including a Peter Medawar–a Nobel Laureate in Medicine (1960), to speculate whether the structure of a research paper is a 'fraud' (Medawar, 1963). The structure of the research paper tells us little about the manner in which the actual work proceeded and indeed effaces all the quirks and happenstances that are a feature, not a bug, of the research process. Drawing from another body of work–the study of design–one might go even further to say that yet another important aspect of research the research process is obscured–the identity and expertise of the researcher/author, their background, and how their particular set of proclivities led them to the results described in the paper (Cross, 2004; Verma, 2021a). In an emerging tradition in many fields of study, authors start by describing their own backgrounds and why understanding their backgrounds is essential to understanding their work. It is with this emerging tradition that I align myself. Though the remainder of the paper is written in the third person, I pause here to explain my own background as a way for the reader to make sense of the key decisions made in the design and implementation of this course.

I was drawn as a high school student to the field of nuclear engineering precisely because of its policy problems. Having grown up in India where, even during the 1990s, blackouts, and brownouts were a frequent occurrence, I viewed nuclear energy technologies as having enormous potential for good. A handful of experiences participating in simulated sessions of the IAEA helped me realize that nuclear technology's policy problems could only be solved by having a deep understanding of the science and engineering underlying the technology as well as access to conceptual frameworks and tools that lay outside the field–in history, economics, political science, and many other disciplines.

Though initially intending to major in both physics and economics, I ultimately chose nuclear engineering. The choice of a signal major made it possible, once I had completed my core coursework as an undergraduate and then doctoral student, to take many elective courses from other departments. This interdisciplinary coursework included courses on theories of the state and economy; theories of innovation; comparative political economy; energy economics; engineering, regulation, and management of the electric power sector; design of social science research projects; and qualitative research methods. This coursework was supplemented with extensive reading (both supervised and unsupervised) on foundational texts in social theory, the history, and sociology of technology, design research, and a broad (though not exhaustive as the field is immense) selection of works from risk studies. The broad range of conceptual frameworks and methodological tools drawn from these courses and readings have shaped key decisions in the design of this particular course. For example, as described in the section on underlying course philosophy, I explain how in every course session that focuses on a particular policy problem, students learn about the empirical status and framing of that problem, while also learning to view that problem through one or more conceptual frameworks–many of which were gleaned from the coursework and reading described above and which continue to shape my thinking today. My growing interdisciplinary intellectual identity took further shape in my thesis project–a study of how reactor designers make decisions in the early, foundation stages of design. This was an effort that brought to bear my grounding in nuclear engineering with research methods from the social sciences, and theoretical frameworks from the field of design research. Each of these disciplines was represented on my dissertation committee.

The decade of study and research at the Massachusetts Institute of Technology was followed by a 2-year position at the OECD Nuclear Energy Agency where a final tool in my toolbox was acquired–an understanding of how policymakers conceptualize and make decisions about the problems that had drawn me to the field. This experience too shapes the course. As described in the section on underlying philosophy–a key tenet of the course is the need for students to be able to understand problems at the intersection of nuclear technology policy, and society from multiple, even conflicting, perspectives.

A return to academia at the Harvard Kennedy School of Government for a postdoctoral fellowship led to a new area of inquiry–the study of pedagogical practices, particularly as they pertain to design across engineering as well as non-engineering disciplines. How did designers–engineers or not–engage (or not) with society and how? How did they make sense of their responsibilities? A review of over 200 syllabi yielded important insights–that few courses treated questions of ethics and justice meaningfully, and many that did tend to over-intellectualize these questions–removed from the lived experience of people, from reality (Das et al., 2023a). These learnings too shape this course. Writings by community members, even activists, appear alongside readings by researchers and policymakers. As part of course assignments, students engage with people to explore their understandings of and views on nuclear technology.

Contributions and underlying pedagogical philosophy

The contributions of the course are best understood by unpacking how the course prepared students to rigorously approach problems at the intersection of technology, policy, and society.

A central tenet of the course is that students must learn not only what to think but how to think about a broad range of problems at the intersection of nuclear technology, policy, and society. This is because problems framed in a certain way today might be framed entirely differently in the future and further, problems regarded as pressing today may not be as pressing in the future, with still other problems, we have not yet imagined, rising to the fore. For example, a relatively well-developed system of export controls and safeguards is applied today particularly to countries that are “non-nuclear” weapons states and make use of nuclear technologies for peaceful applications. However, in a potential future when no new nuclear weapons remain, instruments such as safeguards and even export controls may need to be applied even more rigorously to prevent re-armament or the re-development of nuclear weapons. Another example might be drawn from nuclear waste management–while waste volumes are relatively small today and require the identification of one or at most a couple of sites for deep geological repositories in each country using nuclear energy technologies, a future (one desired by many nuclear engineers) in which nuclear energy technologies–both fission and fusion–are potentially used at a much larger scale, is one in which waste volumes might be sufficiently significant to prompt concern and require siting of multiple, possibly even highly localized repositories. As a third example, though uranium resources are regarded as plentiful today, a possible expansion of fission energy technologies might prompt a surge in demand, leading either to an increase in mining (which would require weighing the benefits of procuring uranium against the environmental and social harms of mining) or a normalization of reprocessing technologies (Abdulla et al., 2017). When the time comes, and as the tenor and framing of nuclear policy problems change, nuclear professionals of tomorrow–our students today–need to be prepared to knowledgeably grapple with these problems, however implausible and speculative these problems might seem today.

Just as students learn analytical rigor in their other engineering courses, so too must analytical rigor be applied to problems at the intersection of technology, policy, and society, even if these problems seldom, if ever, yield to everlasting solutions. In this course students learn the ability to approach these problems rigorously by:

1. **Understanding multiple, even conflicting perspectives on the same problems**. For example in an early course session on the role of nuclear energy in decarbonized energy systems, students learn arguments put forward both for and against nuclear energy technologies and learn how to weigh these arguments without vilifying the originators of the arguments.
2. **Understanding multiple framings of an identical problem from numerous standpoints**. Students examine nuclear policy problems as framed by engineers, citizens and community members, and policymakers themselves. For example, in a session about the siting of new nuclear energy facilities, students learn the state and federal approaches to siting facilities, they read research studies by scholars from the field of planning, while also reading perspectives from community-based organizations offering support and critique of said facility. The goal is not to single out a particular framing of the problem as right or wrong–but rather to make sense of`why so many perspectives are able to co-exist and what the origins of diverging framings might be, including how the positionality of the persons or organizations approaching the problem, shapes their framing of it.
3. **Linking theory to practice**. Students are offered one or more conceptual and theoretical frameworks through which to make sense of the policy problems they are examining. For example, initial course sessions focus on the history of nuclear energy technology development and the emergence of light water reactors as the leading or dominant technology. To make sense of this history–students complete and are led through a discussion of research from the sociology of technology on the social construction of technology (Pinch and Bijker, 1984), interpretive flexibility, and technological momentum (Hughes, 1987) and lock-in (Cowan, 1990) alongside research on theories of innovation on creative destruction (Schumpeter, 2013), disruptive innovation (Christensen et al., 2018), and the emergence of dominant designs (Suárez and Utterback, 1995) as well as critiques of innovation itself (Russell and Vinsel, 2018; Lepore, 2023). Similarly, in a following session on the global nature of the nuclear industry and international transfers of technology (Metzler, 2012; Hansen et al., 2020), students learn about theories about early and late industrial development (Gerschenkron, 2015) and technological leapfrogging (Amsden, 2001; Breznitz, 2007), alongside work on complex product systems (Davies and Brady, 2000)–of which nuclear reactors are an archetypal example. While it is true that entire courses could be offered on these theories (and are) in political science and economics departments, the intent behind including these theories and conceptual frameworks in an applied manner in the course is to show students how practice and empirical reality can be related to theory; how other disciplines, including seemingly intellectually distant ones, might offer crucial tools for grappling with problems at the intersection of technology policy, and society; to imbibe enough of the language and jargon from these disciplines to be able to immerse themselves further and engage with scholars and practitioners from these disciplines, if they so desire; and most of all to understand the limits of their own expertise and appreciate that of others, while being willing to transgress traditional disciplinary boundaries in service of a greater good, as needed.

Methods: course design

This section of the paper describes the underlying course philosophy as well as course design.

Framing nuclear technology problems as ‘wicked problems’

The course begins by framing problems at the interaction of technology, policy, and society as wicked problems. Table 1 below shows the ten attributes of wicked problems as laid out by Rittel and Webber (Rittel and Webber, 1973). It also describes how ‘tame’ problems differ from wicked problems and offers examples of nuclear problems as ‘wicked problems.’ In the first course session, having learned about wicked problems and their attributes, students are invited to reflect on whether problems at the intersection of nuclear technology, policy, and society, of which they are aware, exhibit these different attributes of wickedness. (This initial course session is followed by a related assignment described below.) The wicked problem framing has proved to be very useful in the course as we often return to this way of thinking about problems at the intersection of technology, policy, and society several times during the semester including during sessions on nuclear waste, safety, innovation, siting of new nuclear facilities, economics, and proliferation.

An elective course

The course is an elective with the students in the class last year (Winter 2023) being a mix of senior undergraduate students from the Department of Nuclear Engineering and Radiological Sciences (NERS) as well as masters and Ph.D. students from the department. While the majority of students enrolled in the course this term are again from NERS, the course also includes students from Chemical Engineering, Computer Science, Mechanical Engineering, and the Business School. On the first day of class when students are invited to share what brought them to the course, the students from outside NERS shared that their interest in nuclear energy and technologies and in some cases, internships or approaching employment in the nuclear sector drew them to the course. In the first year of the course, the course was only advertised internally within the department, leading to an enrollment of 10 students. The number of students enrolled in the course has doubled this year (with some students deciding whether they will take the course for credit or audit it). Students auditing the course are not required to complete weekly assignments or the term project but are encouraged to participate in the “Nuclear in the News” exercise and complete the required readings before each course session.

It should be added that while the course is strictly an elective for most students, doctoral students in NERS taking the fission-policy track are required to take the course and are tested on it as part of their written candidacy exam.

Course structure

The course unfolds over 16 weeks with two 80-min lectures a week. The list of topics covered in the lecture is shown in Table 2 below. Not included in the list of topics are the sessions devoted to student presentations. Following the initial lecture on the framework of wicked problems and how this framework can be applied to problems examined as part of this course, students are led through sessions on social construction of technologies and a history of nuclear technologies, sessions on innovation, technology selection and the role of startups, and global transfers of nuclear technologies. Following these initial sessions on history and innovation, the course pivots for a week to focus on economics and financing. A session on speculative design is included in the Winter 2024 course offering as a resource for the students for their term projects. Following this, a series of sessions focus on safety, risk, regulation, and accidents. The course then shifts to focus on the siting of nuclear facilities. This includes sessions on nuclear waste, consent based siting, siting of new nuclear facilities, and the impacts of legacy facilities. These sessions on siting are followed by two lectures on security and non-proliferation. A final session on reimagining nuclear engineering–which invites the students to envision possible futures for the nuclear field, including futures in which wicked problems have been solved–wraps up the lectures. The semester ends with sessions in which students present their projects.

Each lecture is informed by a series of guiding questions the students are expected to be able to knowledgeably reflect and write about based on their learnings from each lecture. For example, the fourth and fifth course sessions focus on innovation in the nuclear sector and technology selection, demonstration, and the role of startups respectively. The guiding questions for these two sessions are shown in the Table 3 below.

Students are asked to complete (typically) two to three readings before each lecture. For students interested in exploring the topic further, a number of additional optional readings are also offered. Students in the initial course offering in Winter 2023 found these readings especially helpful particularly when their term projects were on a related subject. As an additional resource, students are given an annotated bibliography template and encouraged to fill this out as they complete their readings over the course of the semester. The annotated bibliography is not graded. Students are encouraged to create it so that it might serve as a resource for them to be able to revisit the course readings after the completion of the semester.

Nuclear in the news

Class participation and discussion are central to the course and students are encouraged to ask questions throughout the lecture (and do) starting from the very first course session. Beyond the active discussion encouraged in every lecture, another significant opportunity for class participation is at the start of every lecture. The first fifteen to 20 minutes of each class are devoted to discussing nuclear technology topics in the news (this the ‘Nuclear in the News’) component of the course. At the start of the course, the students are invited to select two topical keywords (a list of the keywords is shown in Table 4 below) and read a total of two news articles before each session (or peruse other sources of information—such as podcasts, documentaries, or youtube videos). As a starting point, students are offered an initial set of potential resources and news outlets where they may begin their

TABLE 2 A list of lecture topics are included below.

Lecture topics
Introduction to the course + Nuclear policy problems as wicked problems
Technologies as socially constructed + a brief history of the nuclear technologies and institutions
The role for nuclear energy in a clean energy system?
Innovation in the nuclear sector
Technology selection, demonstration, and the role of startups
Technology transfer–The nuclear industry as a global industry
Cost - a primer on engineering economics
Financing nuclear projects
Speculative design
Safety–what is a safe reactor?
Risk–The engineer's framing of risk
Risk–Framing, perception, and reality
Accidents and what we can learn from them
Nuclear waste: a history of management and mismanagement
Consent-based siting and nuclear waste management
Siting nuclear facilities
New Nuclear Communities
Legacy, contamination, and cultural heritage
Uranium mining and markets: local and global impacts
Security–security by and for whom?
Nuclear energy, equity, environmental justice
Reimagining nuclear engineering - what does a reflexive, inclusive field look like?

reading but are encouraged to read broadly and identify new sources and share them with the class. When perusing these different sources of information, students are encouraged to read between the lines and reflect critically on the source of the information, the affiliation of the author, potential biases of the author or publication outlet, and how these biases might color what is being written about. Prior to each lecture session, students summarize both what they have learned as well as reflect critically on the article or other source on sticky notes on an online course mural. Additionally, students are encouraged to find connections between their readings and those of their classmates or between current and previous readings and identify trends or connections where they may exist.

Use of technology in the classroom

In addition to Mural–which is used for the Nuclear in the News segment, as well as for in-class workshops, the course also makes use of Menti. Menti is a helpful tool for eliciting student responses live during a lecture. Gathering student responses through Menti is particularly helpful for gathering background information or understanding of a particular problem or topic by the students.

TABLE 3 Guiding questions for the sessions on innovation in the nuclear nuclear sector and technology selection, demonstration, and the role of startups respectively.

Innovation in the nuclear sector	Technology selection, demonstration, and the role of startups
What do we mean by 'innovation'?	The technology lifecycle and the emergence of dominant technologies
Where, when, and how does innovation take place?	Should the state pick 'winners' and shape the emergence of winning technologies?
What is the role of the state in stimulating or stewarding innovation?	Are the winning technologies always the 'best' technologies?
Where does innovation occur in the nuclear sector?	How did the light water reactor become the dominant technology?
Has innovation in the nuclear sector been equitable historically? Can innovation in the nuclear sector be equitable in the future?	Are we likely to see the emergence of dominant reactor technologies in the future?
The importance of innovation and maintenance	What role do large companies vs. startups play in an innovation ecosystem?
	How does private vs. government funding impact innovation decisions?
	What is the state of innovation and technology development in the fusion sector?

For example, Figure 1 below shows student responses gathered using Menti to the question "what does the word 'policy' mean to you?". Students were asked this question on the first day of class.

Course readings and resources

The course does not have a required textbook. As noted above, students are required to complete two to three readings prior to each course session. Additionally, the syllabus includes as a resource several readings on the historical, sociological, and anthropological studies of nuclear organizations and institutions, as well as a list of books on the history and sociology of technology broadly. The syllabus also lists several podcasts as resources. These include "Press the Button", "The Sketch Model Podcast", "The Received Wisdom", and "Things that go Boom".

In addition to these resources, all students in the course in Winter 2024 received a copy each of two books on speculative design–The Extrapolation Factory (Montgomery and Woebken, 2016) and Speculative Everything (Dunne and Raby, 2013). These books offer conceptual frameworks and methods students are encouraged but not necessarily required to explore as part of their term projects.

Suffusing questions of ethics and justice across sessions

While the course is not solely about questions of ethics and justice–these themes suffuse every session of the course. For example, in the initial sessions on innovation, students are invited to think critically about innovation practices: is

TABLE 4 Nuclear in the News keywords.

Nuclear in the news keywords	
Decarbonization	Nuclear construction
Coal to nuclear	Critique of the nuclear sector
Nuclear supply chain	Nuclear regulation
Reprocessing Technology	Microreactors
Spent fuel/waste management	Decommissioning
Uranium enrichment	Government
Uranium mining and markets	Nuclear safety
Small modular reactors (SMRs)	Nuclear security
Demonstration projects	Fusion Technology
Contamination and cleanup	Nuclear Innovation
Space propulsion	

TABLE 5 Prompts for envisioning nuclear futures.

Prompts for envisioning nuclear futures
What do nuclear energy technologies - fission and fusion–look like in 2,100 and how and where are they being used? Who is using these technologies?
Have we averted the worst effects of climate change? If so, what role have nuclear energy technologies played in accomplishing this?
How much nuclear waste have we produced? Where is that nuclear waste being stored? Is that waste still regarded as 'waste'?
Have we repaired the legacy environmental and health impacts of nuclear technologies?
How many nuclear weapons exist in 2,100? Who has these weapons? If there are no weapons, what have we done to prevent countries from rearming?
How are nuclear materials safeguarded in 2,100?
What roles do nuclear engineers play in society? Are we trusted?
What are some new cutting-edge areas of nuclear science and technology that have emerged? (quantum computing, space nuclear propulsion, transformative new materials for use in extreme environments?)

innovation necessarily always desirable and ethical? Who has a voice in the innovation process (and who does not)? How, in the process of innovation and design, can inequities become embedded in our technologies? What does it mean for companies, researchers, and government agencies to make ethical and judicious use of public funding?

In sessions on safety and risk students reflect on how experts and publics (plural as the public is not a monolithic group) differently perceive and frame risks and how engineers, instead of dismissing public perceptions of risk as affective and irrational, can make sense of them and try to engage meaningfully with publics, without 'acceptance' of a technology being an instrumental goal framing such engagement. In the sessions on nuclear waste management, nuclear facility siting, legacy, contamination, and cultural heritage, students reckon with the complicated history of the nuclear sector and often disproportionate impacts of nuclear technology development (weapons technologies especially) on indigenous communities in particular. They reflect on what measures might be taken to correct historical wrongdoings as well as what measures might be taken to ensure responsible and ethical development and use of nuclear technologies in the future–and how communities might be able to directly participate in this decision-making.

As a culmination of all of this thinking, the final course session before the student presentations is on "Reimagining nuclear engineering - what does a reflexive, inclusive field look like?". In this course session, the students discuss and reflect on what a socially and environmentally responsible, reflexive, and inclusive nuclear field could look like and what institutional structures, engineering practices, and power dynamics need to change to achieve this shift. As an assignment concurrent with to this session students are invited to do three things:

(1) Write a code of ethics for nuclear engineers informed by all that they have learned throughout the course
(2) Draft a letter to their future selves describing what brought them to this course, what 'wicked' problems in the nuclear sector they hope their future selves will have helped solve, and what they have learned over the course of the semester that they would like their future selves to remember. Students are encouraged to use a service such as futureme.org to send this letter to their future selves.
(3) Envision and visualize possible futures for nuclear technologies as well as nuclear professionals in the year 2,100. Some questions students were asked to consider while imagining these futures are shown in Table 5 below. Students are asked to use AI image generators to create images depicting these futures.

Course deliverables

In addition to periodic assignments students are required to complete two key deliverables–an op-ed and a term project.

Periodic assignments

Students complete periodic assignments. These assignments do not have a weekly cadence. For the first course offering, the students completed four such assignments. As part of the second course offering the number of assignments has been increased to six. The timing and cadence of the assignments are aligned with other recurring deliverables (such as the op-ed, mid-semester and final presentation, and the final term paper). These periodic assignments, either call on students to delve deeper into a reading, to reflect on it, or to collect and analyze original data. For example, in the very first course assignment, students choose a problem at the intersection of technology, policy, and society and then, using the wicked problems framework paper as a framework, examine whether the problem they have chosen meets each of the criteria for wicked problems as identified in the Rittel and Webber (1973) paper, and whether the problem they have chosen has other aspects of wickedness not captured in the paper. In a subsequent paper, having completed readings on

FIGURE 1
A transformation in nuclear engineering from a discipline that narrowly views our roles as nuclear engineers and the interactions of our technologies with society to a richer, more complex (and complicated) understanding of the origins and impacts of our technologies.

technological lock-in and dominant designs (and having discussed these topics and theories in class), students are asked to imagine that they are in a position of leadership at the DOE and tasked with designing a program of research and innovation funding that meets the following criteria: (1) pursuit and development of if not the 'best' then at least clearly superior technology options and designs; (2) A moderately rapid pace of innovation and technology commercialization, attuned to the urgencies of the looming climate crisis; (3) responsible and accountable use of taxpayer dollars. Another example of an assignment is one in which students collect and analyze the mission and vision statements of nuclear companies (fission and fusion), along with details on the source of funding of the companies and the backgrounds of their founders. Students are then asked to analyze where there are patterns that appear across and within the fission and fusion companies, and what their data tells them about the nature and state of innovation in the nuclear sector, as well as what and who is driving it.

Op-ed

The inclusion of the op-ed as a course deliverable was a deliberate decision stemming from the instructor's desire that engineers ought to be able to communicate clearly and effectively with publics and well as decision-makers. Students in the course are invited to author an op-ed on any topic of their choosing (selected in consultation with the instructor) and are welcome to submit the op-ed at any point in the semester. Many students chose op-ed topics that were closely related to their term projects. The only significant limiting criterion for the op-ed was the word limit (a range of 600–1,000 words). Many students expressed that while they found it challenging to express their viewpoints concisely, they appreciated the challenge and the opportunity to develop a new set of skills through the writing of the op-ed. Op-ed topics from the first course offering included the impact of the Russian-Ukrainian conflict on the commercial nuclear industry, the need for nuclear energy in a low-carbon economy, the environmental and societal challenges associated with mining uranium, and the need for the US to adopt a no first use nuclear weapons policy, to name some. In the Winter 2024 course offering, selected Op-Eds will be invited for publication as part of a new ANS NSTOR open access collection on "Reimagining Nuclear Futures: Emerging Voices on Technology, Policy, and Society" (Nuclear Newswire, 2023).

Term project

In addition to periodic assignments, and an op-ed, each student in the course also completes a term project. Students select and define their term project (in consultation with the instructor) by the mid-semester mark and present their mid-semester progress to the class. The term project deliverables include a written research paper (five to seven thousand words) as well as a final presentation. During the first course offering, all student term projects were research-based. Students were offered a range of possible term paper topics by the instructor while also being given the option of designing a topic of their choosing. From the first course offering, student term projects include:

1. The value of flexible, load-following reactors in distributed nuclear-renewable energy systems
2. Expert assessments of the prospects for commercial fusion energy

3. Regulatory and environmental challenges and opportunities for nuclear fusion
4. Innovative financing approaches for SMRs
5. Stockpile modernization across nuclear weapon states

For the second-course offering in Winter 2024, the term projects are a creative rather than research endeavor. Students have been tasked with interpreting, exploring, or offering solutions to nuclear policy problems through the lens of storytelling or play. While student projects are still at an early stage–it is clear that students are interested in exploring a range of mediums through their work including music, documentary videos, podcasts, and video games.

Tutorials and workshops

In addition to lectures, students also participate in workshops and tutorials that take place during the regular class sessions. During the first course offering students received a tutorial on how to write op-eds as well as a tutorial on how to use a GIS-based nuclear energy facility siting tool developed at the University of Michigan by the Fastest Path to Zero initiative.

Examples of workshops include one on the nuclear innovation ecosystem. As part of this workshop, students, working in teams of two to three, were tasked with reflecting on the purpose of innovation in the nuclear sector, identifying key actors (individuals, organizations, government agencies), and marking how these actors are connected by flows of funds, people, and information. This exercise quickly revealed to the students the complex, interconnected, convoluted, and not perfectly knowable nature of an innovation ecosystem. Through this exercise, they learned to appreciate that a key feature of these ecosystems is the asymmetry of information as held by various actors, and the critical role that connecting organizations–including government agencies can play in stewarding and tending to these systems of innovation. These observations resonate strongly with research on the role of governments–as clearinghouses of innovation (Rodrik, 2004)– in modern industrial ecosystems. (Students learned about this theory in a subsequent course session).

Grading

The final grade students receive for the course is distributed in such a way that no single deliverable is overwhelmingly significant. This choice was made deliberately for two reasons:

(1) the most beneficial learning experience in this course is one in which students are actively engaged in every aspect of the course (readings, in-class discussion, periodic assignments, op-ed development, and term project) throughout the semester as each element of the course supports the students in achieving a deeper and more layered understanding of the course material.
(2) Given that the course is non-traditional and calls for the development and exercise of what for most students will be a new set of skills and ways of thinking, overweighting any particular assignment or deliverable is likely to create an unnecessarily stressful, high stakes environment which is ultimately counterproductive to learning in this course. As a result, no single element of the course counts significantly, because all elements are important. This is among the first pieces of information students receive at the start of the semester.

Course outcomes

In its first offering, the course received overwhelmingly positive student evaluations. In their course evaluations students, when asked to comment on the quality of the course, offered unanimously positive input. They commented on (paraphrased or quoted verbatim from student responses):

- The “exceptional” quality of the course
- The “robustness” of the syllabus
- The wide array of topics and an appreciation for the breadth of material covered
- An appreciation that the topics covered applied not only to nuclear engineering but “engineering and science in general”
- Thoroughness of the materials covered
- Having learned a lot of valuable things they could use in their career
- The engaging nature of the lectures and discussions
- The instructor’s willingness to adapt the flow of the lecture to the interests of the students
- The instructor’s respectful treatment of the students in the course

When asked for areas of improvement for future course offerings, students suggested that they would have appreciated more time to complete readings, which could be posted earlier, possibly more than a week ahead of each lecture, as well as better pacing course deliverables towards the end of the semester when several deliverables were due in quick succession. These recommendations have been incorporated into the current course offering.

To the statement “I think it is important for nuclear engineers to learn about the social, policy, and ethical implications of nuclear technologies” all students chose the “strongly agree” option. Similarly, all students also chose the “strongly agree” option in their course evaluations that all nuclear engineers should take the course.

Discussion: Recommendations for those developing similar courses

The initial course offering and the second course iteration currently in progress, as well as the student evaluations suggest that the course development efforts have been successful. While there are specific aspects of lectures, including readings, and the details of assignments, that will continue to evolve over the years, it is the instructor’s intent that the course structure described here will be sustained.

For those who are considering developing and offering similar courses at their own institutions, the course framings, topics, and structure–including readings, deliverables, in-class workshops and tutorials as they are implemented in the course–might offer a

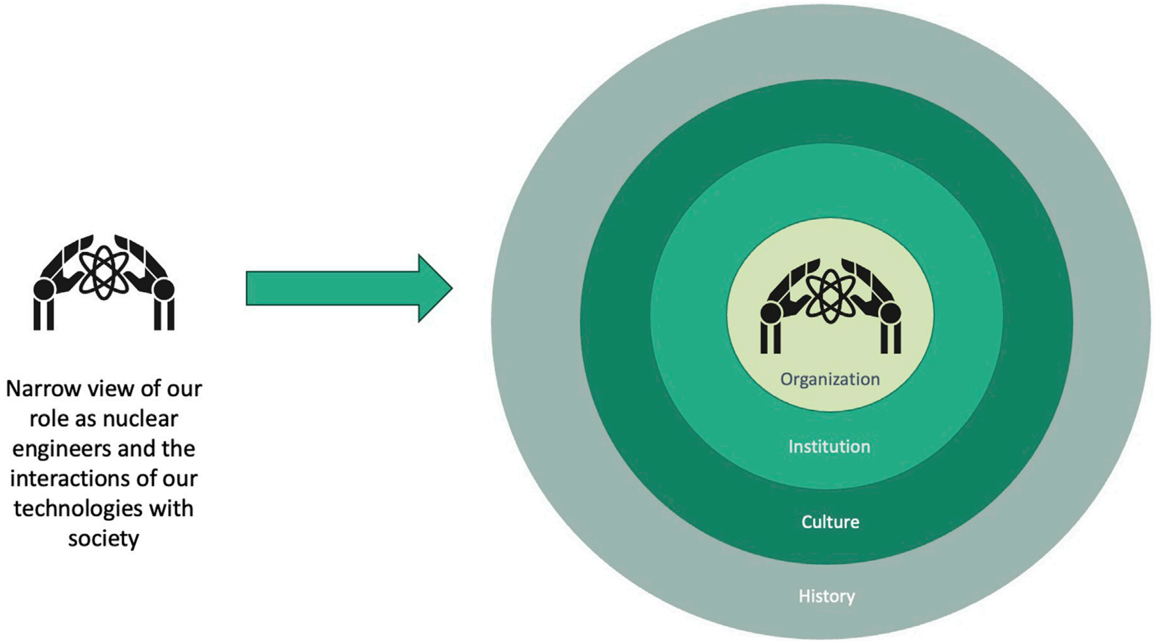

FIGURE 2
A transformation in nuclear engineering from a discipline that narrowly views our roles as nuclear engineers and the interactions of our technologies with society to a richer, more complex (and complicated) understanding of the origins and impacts of our technologies.

starting point for course development. Alternatively, those who wish to replicate the course syllabus are welcome to do so. A few aspects of the course that make it a meaningful learning and teaching experience bear repeating:

1. As is evident from the wicked problems framing, and as explicitly stated, problems at the intersection of technology, policy, and society do not yield to well-defined and permanent solutions. Often these problems and their potential solutions are viewed in diametrically opposite ways by different entities. This is a fundamental feature of these problems that must be acknowledged. Doing so can lead to intellectual discomfort–particularly as the sciences and engineering–built as they are around positivism – tend to seek the 'best' solutions. However, as noted earlier, wicked problems do not have 'best' solutions–they only have good or bad ones such that goodness and badness lie in the eye of the beholder or assessor. Therefore, in a course such as this one, it is important for students to hold opposing truths, be comfortable with not being able to find singular 'right' answers but also appreciate that these are not reasons for not looking for *any* answers, but instead, for trying harder and looking further.
2. A second key aspect of this course, as described earlier, is that it is important for students to be able to both learn how to think and what to think about wicked problems. This is a crucial skill to develop as the manifestation of these problems will continue to evolve over time.
3. A third important aspect of the course relates to viewing the classroom–both students and the instructor–as a community of learning and practice. The course is as much an opportunity for the instructor to learn about and question their own assumptions about problems at the intersection of technology, policy, and society (assumptions that come to light while responding to student questions–which themselves may be founded in still other assumptions). For this reason, building a teaching and learning environment in which students feel comfortable asking questions, even offering opposing viewpoints, is essential. In this manner the classroom becomes a living laboratory (Hossain et al., 2019) for the exploration of wicked problems.

To conclude this section, the development and offering of this course comes at a time when national funding agencies are increasingly supporting interdisciplinary research that seeks to bring engineers and social scientists together to work on complex sociotechnical issues that call for inter- and even trans-disciplinary solutions. Drawing together researchers and practitioners from these previously intellectually distant fields and their working successfully together will require the development of a shared language and set of norms (Verma, 2021b). Courses such as the one described here can lay the ground for these inter- and even trans-disciplinary collaborations, thus enabling us to tackle grand societal challenges–in areas of energy, environment, health, infrastructure–at the scale and scope at which they present themselves.

Conclusion

This paper has described the design, implementation, and outcomes of a course on Nuclear Technology, Policy, and Society at the University of Michigan. As noted at the start of this paper, topics covered in this course have historically been regarded as 'soft', 'non-technical' and not relevant to an engineering education. However, the design and implementation of this course is proof that topics and problems at the intersection of technology, policy, and society can and should be treated in rigorous ways–even if these problems do not yield everlasting solutions, and even if these solutions are not universally accepted or satisfying.

The course outcomes–in particular the student evaluations, suggest that students find the course to be a valuable, even essential part, of their nuclear engineering education. All of this suggests a potential repositioning of how we view what constitutes nuclear engineering: We have typically understood our technologies and conceptualized our role as nuclear engineers in narrow ways. We have concerned ourselves with the science and engineering details of our technologies and designs. Our conceptualization of what constitutes engineering and our conceptualization of our roles as engineers in society can be broader (as visualized in Figure 2), particularly as the field matures, as it is now doing. As part of this broader view, we should think of our technologies and our roles relative to them in the fullness, richness and complexity of how our technologies interact with society, and in so doing, we must expand our notion of what it means to be a nuclear engineer.

Data availability statement

The course syllabus is available to anyone who would like to consult it. Requests to access the datasets should be directed to aditive@umich.edu.

Author contributions

AV: Conceptualization, Methodology, Resources, Writing–original draft, Writing–review and editing.

Funding

The author(s) declare that financial support was received for the research, authorship, and/or publication of this article. The author acknowledges the Fastest Path to Zero Initiative for supporting the open access publication charges for this article.

Conflict of interest

The author declares that the research was conducted in the absence of any commercial or financial relationships that could be construed as a potential conflict of interest.

Publisher's note

References

Abdulla, A., Ford, M. J., Morgan, M. G., and Victor, D. G. (2017). A retrospective analysis of funding and focus in US advanced fission innovation. *Environ. Res. Lett.* 12, 084016. doi:10.1088/1748-9326/aa7f10

American Nuclear Soceity (2022). Code of ethics. Available at: https://www.ans.org/about/coe/.

Amsden, A. H. (2001). *The rise of 'the rest': challenges to the west from late-industrializing economies*. Oxford, United Kingdom: Oxford University Press.

Ban, T. A. (2006). The role of serendipity in drug discovery. *Neurosci* 8, 335–344. doi:10.31887/dcns.2006.8.3/tban

Breznitz, D. (2007). *Innovation and the state: political choice and strategies for growth in Israel, taiwan, and Ireland*. New Haven, Connecticut: Yale University Press.

Buckner, R. L. (2012). The serendipitous discovery of the brain's default network. *Neuroimage* 62, 1137–1145. doi:10.1016/j.neuroimage.2011.10.035

Cech, E. A. (2013). The (mis) framing of social justice: why ideologies of depoliticization and meritocracy hinder engineers' ability to think about social injustices. *Eng. Educ. Soc. justice Crit.*

Christensen, C., Raynor, M. E., and McDonald, R. (2018). Disruptive innovation. Available at: https://www.innosight.com/wp-content/uploads/2018/01/Innosight_HBR_What-is-Disruptive-Innovation.pdf.

Costanza-Chock, S. (2020). *Design justice*.

Cowan, R. (1990). Nuclear power reactors: a study in technological lock-in. *J. Econ. Hist.* 50, 541–567. doi:10.1017/s0022050700037153

Cross, N. (2004). Expertise in design: an overview. *Des. Stud.* 25, 427–441. doi:10.1016/j.destud.2004.06.002

Das, M., Ostrowski, A. K., Ben-David, S., Roeder, G. J., Kimura, K., D'Ignazio, C., et al. (2023a). Auditing design justice: the impact of social movements on design pedagogy at a technology institution. *Des. Stud.* 86, 101183. doi:10.1016/j.destud.2023.101183

Das, M., Roeder, G., Ostrowski, A. K., Yang, M. C., and Verma, A. (2023c). What do we mean when we write about ethics, equity, and justice in engineering design? *J. Mech. Des.* 145, 061402. doi:10.1115/1.4057056

Das, M., Saadi, J. I., Santos, M., Roeder, G., Ostrowski, A. K., Lee, S., et al. (2023b). How and why instructors include and exclude social, policy, and ethical considerations in design education. *Proc. Des. Soc.* 3, 2085–2094. doi:10.1017/pds.2023.209

Davies, A., and Brady, T. (2000). Organisational capabilities and learning in complex product systems: towards repeatable solutions. *Res. Policy* 29, 931–953. doi:10.1016/s0048-7333(00)00113-x

Dayan, M., and Colak, M. (2008). The role of procedural justice in the new product development process. *Eur. J. Innovation Manag.* 11, 199–218. doi:10.1108/14601060810869866

D'Ignazio, C., and Klein, L. F. (2023). *Data feminism*. Massachusetts, United States: MIT Press.

Dunne, A., and Raby, F. (2013). *Speculative everything: design, fiction, and social dreaming*. Massachusetts, United States: MIT Press.

Fiesler, C., Garrett, N., and Beard, N. (2020). *What do we teach when we teach tech ethics? A syllabi analysis*, 289–295.

Fisher, R. J., Nicolls, H., and Munk, M. (2023). "Nuclear engagement education with context of impacted tribal nations," in ANS Student Conference, Amelia Island, Florida, 6-9 February 2023.

Gabriel, I. (2022). Toward a theory of justice for artificial intelligence. *Daedalus* 151, 218–231. doi:10.1162/daed_a_01911

Gerschenkron, A. (2015). *Economic backwardness in historical perspective (1962)*. Cambridge MA: Harvard University.

Hansen, J. K., Dixon, B. W., Cuadra-Gascon, A., and Todosow, M. (2020). *Retrospective analysis of US LWR technology commercialization: lessons for today's nuclear industry*.

Hossain, M., Leminen, S., and Westerlund, M. (2019). A systematic review of living lab literature. *J. Clean. Prod.* 213, 976–988. doi:10.1016/j.jclepro.2018.12.257

Hughes, T. P. (1987). "The evolution of large technological systems," in *The social construction of technological systems*.

INTERNATIONAL ATOMIC ENERGY AGENCY (2019). *Establishing a code of ethics for nuclear operating organizations*, 1–29. Available at: https://www.iaea.org/publications/7823/establishing-a-code-of-ethics-for-nuclear-operating-organizations.

INTERNATIONAL ATOMIC ENERGY AGENCY (2020). “Energy, electricity and nuclear power estimates for the period up to 2050,” in *Energy, electricity and nuclear power estimates for the period up to 2050*, 1–137.

Kauffman, G. B., and Mayo, I. (1997). The story of nitinol: the serendipitous discovery of the memory metal and its applications. *Chem. Educ.* 2, 1–21. doi:10.1007/s00897970111a

Kendall, B. A., and Arkhurst, B. K. (2023). “Applying early-stage energy justice metrics to nuclear engineering,” in ASME 2023 International Conference on Environmental Remediation and Radioactive Waste Management V001T06A004, Stuttgart, Germany, October 2023.

Lepore, J. (2023). The disruption machine. Available at: https://facultygovernance.mit.edu/.

Lovering, J. R., Yip, A., and Nordhaus, T. (2016). Historical construction costs of global nuclear power reactors. *Energy Policy* 91, 371–382. doi:10.1016/j.enpol.2016.01.011

Medawar, P. B. (1963). Is the scientific paper a fraud. *Listener* 70, 377–378.

Metzler, F. (2012). *Global nuclear power supply chains and the rise of China’s nuclear industry*.

Michigan Memorial Phoenix Project (1948). *Michigan memorial Phoenix project – home for Michigan memorial Phoenix project*. Available at: https://mmpp.engin.umich.edu/.

Montgomery, E. P., and Woebken, C. (2016). *Extrapolation factory operator’s manual. (Extrapolationfactory.com)*.

Nieusma, D., and Riley, D. (2010). Designs on development: engineering, globalization, and social justice. *Eng. Stud.* 2, 29–59. doi:10.1080/19378621003604748

NSPE (2021). *NSPE ethics reference guide*.

Nuclear Newswire (2023). UMich offers online collection on ‘Nuclear Futures’. Available at: https://www.ans.org/news/article-5469/umich-offers-online-collection-on-nuclear-futures/.

Ostrowski, A. K., Walker, R., Das, M., and Yang, M. E. (2022). *Equity, and justice in human-robot interaction: a review and future directions. 2022 31st ieee*.

Pinch, T. J., and Bijker, W. E. (1984). The social construction of facts and artefacts: or how the sociology of science and the sociology of technology might benefit each other. *Soc. Stud. Sci.* 14, 399–441. doi:10.1177/030631284014003004

Riley, D. (2008). “Engineering and social justice,” in *Engineering and social justice*. Editor D. Riley (Cham: Springer International Publishing), 47–106.

Rittel, H. W. J., and Webber, M. M. (1973). Dilemmas in a general theory of planning. *Policy Sci.* 4, 155–169. doi:10.1007/bf01405730

Rodrik, D. (2004). *Industrial policy for the twenty-first century Available at SSRN 666808*.

Russell, A. L., and Vinsel, L. (2018). After innovation, turn to maintenance. *Technol. Cult.* 59, 1–25. doi:10.1353/tech.2018.0004

Saadi, J. I., Das, M., Roeder, G., Ostrowski, A. K., Lee, S., Santos, M., et al. (2023). “Incorporating social, policy, and ethical considerations in engineering and design education: an examination of barriers and resources,” in ASME 2023 International Design Engineering Technical Conferences and Computers and Information in Engineering Conference V006T06A019, Boston Park Plaza, Boston, August 20–23, 2023.

Saraç-Lesavre, B. (2021). Deep time financing? ‘Generational’ responsibilities and the problem of rendez-vous in the U.S. nuclear waste programme. *J. Cult. Econ.* 14, 435–448. doi:10.1080/17530350.2020.1818601

Schumpeter, J. A. (2013). *Capitalism, socialism and democracy*. England, UK: Routledge.

Suárez, F. F., and Utterback, J. M. (1995). Dominant designs and the survival of firms. *Strateg. Manage. J.* 16, 415–430. doi:10.1002/smj.4250160602

Turner, K., Borja, L., Djokić, D., Munk, M., and Verma, A. (2020). A call for antiracist action and accountability in the US nuclear community. *Bull. Atomic Sci.*

Verma, A. (2021a). What can nuclear engineers learn from design research? A review of the theory and evidence from contemporary American and French nuclear reactor design. *Nucl. Eng. Des.* doi:10.1016/j.nucengdes.2021.111114

Verma, A. (2021b). The nuclear, humanities, and social science nexus: challenges and opportunities for speaking across the disciplinary divides. *Nucl. Technol.* 207. doi:10.1080/00295450.2021.1941663

Verma, A., Ahmad, A., and Giovannini, F. (2021). Nuclear energy, ten years after Fukushima. *Nature* 591, 199–201. doi:10.1038/d41586-021-00580-4

Verma, A., and Djokić, D. (2021). Reimagining nuclear engineering. *Issues Sci. Technol.*

frontiers | Frontiers in Nuclear Engineering

TYPE Brief Research Report
PUBLISHED 08 August 2024
DOI 10.3389/fnuen.2024.1379996

OPEN ACCESS

EDITED BY
Anne Campbell,
Oak Ridge National Laboratory (DOE),
United States

REVIEWED BY
Jean-Emmanuel Groetz,
University of Franche-Comté, France
Frankie White,
Oak Ridge National Laboratory (DOE),
United States

*CORRESPONDENCE
Bianca Schacherl,
Bianca.schacherl@kit.edu
Martina Benešová-Schäfer,
m.benesova@dkfz.de

†PRESENT ADDRESS
Chemical Sciences Division (CSD), Lawrence Berkeley National Laboratory (LBNL), Berkeley, CA, United States

RECEIVED 31 January 2024
ACCEPTED 20 June 2024
PUBLISHED 08 August 2024

CITATION
Schacherl B, Maurer K, Schäfer M, Remde Y, Geyer F, Fried A, Happel SA and Benešová-Schäfer M (2024), Concept validation of separations for thorium-based radionuclide generator systems for medical application.
Front. Nucl. Eng. 3:1379996.
doi: 10.3389/fnuen.2024.1379996

Concept validation of separations for thorium-based radionuclide generator systems for medical application

Bianca Schacherl[1]*†, Kiara Maurer[1], Martin Schäfer[2],
Yvonne Remde[2], Frank Geyer[1], Annika Fried[1],
Steffen Alexander Happel[4] and Martina Benešová-Schäfer[3]*

[1]Karlsruhe Institute of Technology (KIT), Institute for Nuclear Waste Disposal (INE), Karlsruhe, Germany, [2]German Cancer Research Center (DKFZ), Service Unit for Radiopharmaceuticals and Preclinical Trials, Im Neuenheimer Feld 280, Heidelberg, Germany, [3]German Cancer Research Center (DKFZ), Research Group Molecular Biology of Systemic Radiotherapy, Heidelberg, Germany, [4]TrisKem International, Bruz, France

Targeted alpha therapy (TαT) represents an emerging and cutting-edge treatment option for patients dealing with highly challenging metastatic cancer diseases. Critically, the limited supply of alpha-particle-emitting radionuclides, so-called alpha *in vivo* nanogenerators, hampers wider utilization of TαT in clinical settings. This could effectively be circumvented by alternative production routes, including straightforward purification and reformulation strategies. Radionuclide generators offering great potential in simple and robust elution strategies can be provided that still adhere to high radioisotopic, radionuclidic, and radiochemical purity criteria. This study takes a first step towards novel separation strategies by providing additional sources of alpha *in vivo* nanogenerators for TαT through experiments with various metal surrogates. With different systems, ^{232}Th/^{nat}Ba was used as a radionuclide generator analogue to ^{227}Th/^{223}Ra, and ^{232}Th/^{nat}Ba/^{nat}La was used as a triplet analogue to ^{229}Th/^{225}Ra/^{225}Ac. Three selective resins (UTEVA, TEVA, DGA-N) were evaluated for the ^{232}Th/^{nat}Ba system. Two perturbations of the best-performing resin were further evaluated using a larger diameter column and 1 week of equilibration. For the ^{232}Th/^{nat}Ba/^{nat}La separation system, a combined column with two selective resins (TK200, TK101) was employed and evaluated. The results thus obtained pave the way for alternative separation strategies in radioactive proof-of-concept validation in the near future.

KEYWORDS

targeted alpha therapy, alpha *in vivo* nanogenerators, thorium, radium, radionuclide generators, radionuclide separation

1 Introduction

Targeted alpha therapy (TαT) is a treatment method that systematically addresses cancer types that include advanced prostate and neuroendocrine malignancies (Kratochwil et al., 2017; Lindén et al., 2021; Yadav et al., 2022). TαT uses alpha-particle-emitting radionuclides (α-emitters), in contrast to targeted radionuclide therapy (TRNT) that commonly applies beta-minus-particle-emitting radionuclides (β^--emitters) (Kim and Brechbiel, 2012). Both TαT and TRNT selectively deliver cytotoxic radiation to cancer cells. However, TαT demonstrates overall higher treatment efficiencies due to the higher linear energy transfer (LET) and smaller tissue penetration observed for α particles (Kratochwil et al., 2018). Within this concept, the most promising α-emitters are represented by actinium-225 (^{225}Ac), thorium-227 (^{227}Th), and radium-223 (^{223}Ra).

The radionuclide ^{225}Ac decays with a half-life of 9.9 days while generating 4α + 2β$^-$emissions with one branching ratio for ^{213}Bi. Currently, ^{225}Ac represents the most promising alpha *in vivo* nanogenerator for the clinical management of various cancer types (Królicki et al., 2020; Ma et al., 2022; Yadav et al., 2022) and can be produced:

i) *via* the cyclotron bombardment of ^{226}Ra (Parker et al., 2018; Higashi et al., 2022), e.g.,

$$^{226}_{88}Ra\,(p,2n)\,^{225}_{89}Ac$$

ii) *via* photonuclear reaction on ^{226}Ra within the ^{225}Ra/^{225}Ac generator principle (Maslov et al., 2006; Diamond and Ross, 2021), e.g.,

$$^{226}_{88}Ra\,(\gamma,n)\,^{225}_{88}Ra\,(\beta^-)\,^{225}_{89}Ac$$

iii) or in a nuclear reactor within the ^{229}Th/^{225}Ra/^{225}Ac generator principle (Robertson et al., 2018), e.g.,

$$^{226}_{88}Ra\,(3n,g)\,^{229}_{88}Ra\,(\beta^-)\,^{229}_{89}Ac\,(\beta^-)\,^{229}_{90}Th\,(\alpha)^{225}_{88}Ra\,(\beta^-)^{225}_{89}Ac$$

The radionuclide ^{227}Th decays with a half-life of 18.7 days while generating 5α + 2β$^-$emissions with one branching ratio for ^{211}Bi. ^{227}Th is pre-clinically tested for application in several solid as well as hematologic malignancies (Hagemann et al., 2019; Frantellizzi et al., 2020; Karlsson et al., 2023). ^{227}Th can be produced *via* a neutron activation of ^{226}Ra within the ^{227}Ra/^{227}Ac/^{227}Th generator principle (Henriksen et al., 2001; Larsen et al., 2007), e.g.,:

$$^{226}_{88}Ra\,(n,\gamma)\,^{227}_{88}Ra\,(\beta^-)\,^{227}_{89}Ac\,(\beta^-)\,^{227}_{90}Th$$

The radionuclide ^{223}Ra with a half-life of 11.4 days practically shares the decay chain of its mother radionuclide ^{227}Th. Radium is an alkaline earth metal ion and accumulates in bones through an analogical mechanism such as calcium. Based on this property, $^{223}RaCl_2$ (Xofigo®, Bayer Healthcare) found its main clinical application in the treatment of bone metastases. ^{223}Ra is usually gained within the ^{227}Ac/^{227}Th/^{223}Ra generator principle (Abou et al., 2017), e.g.,:

$$^{227}_{89}Ac\,(\beta^-)\,^{227}_{90}Th\,(\alpha)\,^{223}_{88}Ra$$

Based on limiting challenges of, for example, high costs, regulations, and the scarce availability of these radionuclides, the optimization, research, and broader availability of radionuclide generators are essential for prospective application in cancer therapies (Kim and Brechbiel, 2012; Elgqvist et al., 2014; Parker et al., 2018).

In general, three main principles for radionuclide generator build-up are known: i) sublimation generator, ii) extraction generator, and, most versatile, iii) column generator (Rösch and Knapp, 2011). Furthermore, a rapid and uncomplicated chemical separation should be ensured to enable seamless implementation, such as in hospitals. The desired daughter radionuclide should be eluted with high radioisotopic and radionuclidic purity, crucial for not only medical applications but also for subsequent radiolabeling of various pharmaceuticals.

The working principle of the radionuclide generator is based on a "genetic relationship" between mother and (grand)daughter radionuclide(s) and can be "milked" several times after ingrowth of the (grand)daughter radionuclide(s). In contrast to expensive cyclotron and/or nuclear reactors procedures, the radionuclide generator offers an affordable alternative that is easier to maintain and operate. Currently, the number of generator concepts is limited, however, the demand for α-emitters in the pre-clinical and clinical settings is increasing. Additionally, present political strains are critically impacting ^{225}Ac availability for the wider application of α-emitters in cancer treatment (van Cleve et al., 2019; Causey et al., 2020). Therefore, it is essential to research, evaluate, and produce alternate radionuclides which are suitable for TαT and subsequent (pre-)clinical purposes. In this study, we systematically validated separation strategies for two thorium-based generator concepts using extraction chromatographic resins and corresponding metal surrogates. These surrogates were chosen on chemical similarity; ideally, chemically identical isotopic surrogates are chosen. In this study, this was the case for the surrogate ^{232}Th for $^{227/229}$Th. If such surrogates are unavailable, chemically similar elements were chosen. Here, $^{223/225}$Ra was surrogated by ^{nat}Ba and ^{225}Ac by ^{nat}La, although these are not ideal since there are slight differences in their documented chemical behavior. A fully developed generator system should be tested with isotopic surrogates or the desired radionuclides itself.

2 Materials and methods

Milli-Q water (18.2 MΩ cm; Milli-Q Plus, Merck Millipore, Darmstadt, Germany) and ultra-pure-grade acids (VWR International GmbH, Darmstadt, Germany) were used. A column (Figure 1) made from a 1 mL-syringe (Omnifix B. Braun, Melsungen, Germany) with a filter plate (TrisKem International, Bruz, France) was filled with 0.3 mL resin which approximately corresponds to 100 mg. The resins used in this work were UTEVA, TEVA, DGA-N, TK101, and TK200 (TrisKem International, Bruz, France). The resin was covered by another filter plate and connected to a 5 mL syringe (Omnifix B. Braun, Melsungen, Germany) and an outlet tube *via* connectors (Altmann Analytik GmbH & Co. KG, Munich Germany).

For the ^{227}Th/^{223}Ra system, the columns with a single resin (UTEVA, TEVA, DGA-N) were loaded with 56 µL of 0.001 mg/mL ^{232}Th solution (56 ng Th) and 90 µL of 0.001 mg/mL ^{nat}Ba solution (90 ng Ba), both solutions in 0.5 mol/L HNO_3. The liquid was carefully and slowly pushed onto the resin with a 5 mL syringe and allowed to equilibrate over 2.5 h. The collected eluate was labeled "loading fraction".

Successively for the elution of Ba, 3 mol/L HNO_3 was applied and collected in five fractions of 0.5 mL in individual screw cap vessels (PE, Sarstedt Ag & Co. KG, Nümbrecht, Germany). To avoid cross-contamination in the small fractions, 7.5 mL air was flushed through the resin. Finally, the eluent was changed to 0.05 mol/L HCl for Th elution and five fractions of 0.2 mL each were collected before flushing 7.5 mL air through the resin again.

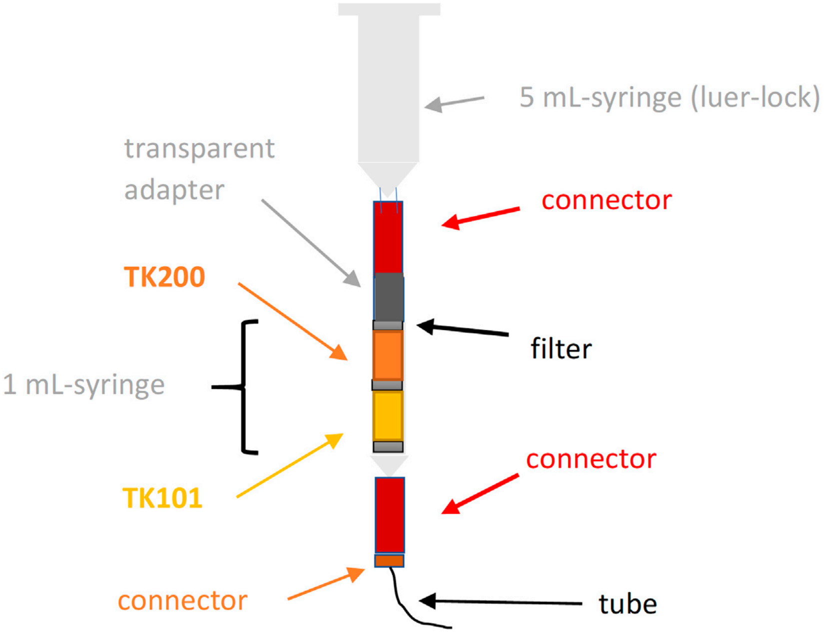

FIGURE 1
General elution set-up shown for examined generator systems. For the binary generator system, i.e. $^{227}Th/^{223}Ra$, only a single resin (UTEVA, TEVA or DGA-N) was used. All columns were pre-conditioned with 3 mL 3 mol/L HNO_3; the eluate was collected as ten fractions of 0.3 mL each in a screw-cap vessel (polypropylene (PP), Zinsser Analytic, Fürstenfeldbruck, Germany).

Both a "blind column" and a "spiked blind column" were prepared for each resin set-up. Blind columns were not loaded with corresponding elements, while the washing and elution procedure remained unchanged. This enabled the evaluation of contaminants potentially present in applied resins or solvents. To verify the selected analytical method, the respective amount of evaluated elements (^{232}Th, ^{nat}Ba) was added after elution to each of the "spiked blind column" eluent fractions, serving as a positive control for the sensitivity and quantification of examined elements.

For the $^{229}Th/^{225}Ra/^{225}Ac$ system, the combined column (TK200/TK101) was washed with ten times its volume (6 mL 0.5 mol/L HNO_3). Subsequently, it was loaded with 90 µL 0.001 g/L ^{nat}Ba solution (0.66 nmol Ba) and 56 µL 0.001 g/L ^{232}Th solution (0.24 nmol Th). In addition, 36 µL of 0.01 g/L concentrated ^{nat}La solution (2.6 nmol La) was loaded onto the column and allowed to equilibrate over 1.5 h. The first five eluted fractions were chosen to be of 0.2 mL H_2O each to evaluate whether La could be eluted without acidic conditions.

In the next step, 0.05 mol/L HNO_3 was chosen to enable proper elution of La. To avoid cross-contamination in the small fractions, 7.5 mL air was flushed through the resin. Ba was then eluted with 6 mol/L HNO_3 (5 × 0.2 mL fractions), and, in a final step, Th was eluted with 0.1 mol/L HCl in 5 × 0.2 mL fractions. To evaluate potential retarding effects of the TK200 resin on the Ba elution profile, this procedure was first repeated with a column of the combined resins (TK200+TK101) and then with a column containing only 0.3 mL of TK101 resin afterwards.

Before ICP-MS measurements, all wash, loading, and Ba elution fractions were diluted with 4.5 mL deionized water, whereas the Th elution fractions were diluted with 4.8 mL 2% HNO_3. The eluents were measured by HR-ICP-MS (ELEMENT XR by Thermo Fisher Scientific, Dreich/Bremen, Germany) and with Q-ICP-MS (Nexion-5000 by Perkin Elmer) while assessing essential limits of detection (LOD) for all three tested elements (Table 1; Supplementary Table S8).

3 Results

3.1 $^{227}Th/^{223}Ra$ separation system surrogated by $^{232}Th/^{137}Ba$

The first system investigated the separation of $^{227}Th/^{223}Ra$ surrogated by $^{232}Th/^{nat}Ba$. Considering a prospective application of the depicted separation processes, we readily implemented the possible impact of nanogram tracer amounts into this proof-of-concept. The results of the $^{227}Th/^{223}Ra$ separation are shown in Figure 2.

It is noteworthy that the wash fraction (No. 1–3) of all resins indicated Ba impurities much higher than the detection limit (Figure 2A), effectively hindering the quantification of non-retained Ba. In spite of these background values, clear differences are apparent in qualitative comparisons between resins such as TEVA and UTEVA, which show only a negligible retention of Ba in contrast to DGA-N. For TEVA and UTEVA, Ba is already washed out with the loading fraction (No. 4) and up to fraction No. 6 the elution is complete, while the DGA-N resin enables the Ba elution to be separated from the loading in fractions No. 6 to No. 12 (Figure 2A).

The elution profile of Th (Figure 2B) clearly shows low cross-contaminations of Th in Ba fractions, which is highly desirable for a

TABLE 1 HR-ICP-MS detection limits for eluents.

Samples	Detection limit for ^{nat}Ba [ng/fraction]	Detection limit for ^{232}Th [ng/fraction]	Detection limit for ^{nat}La [ng/fraction]
Wash fractions	0.47	0.03	0.02
Loading fraction	1.18	0.08	0.06
Elution fractions	1.18	0.08	0.06

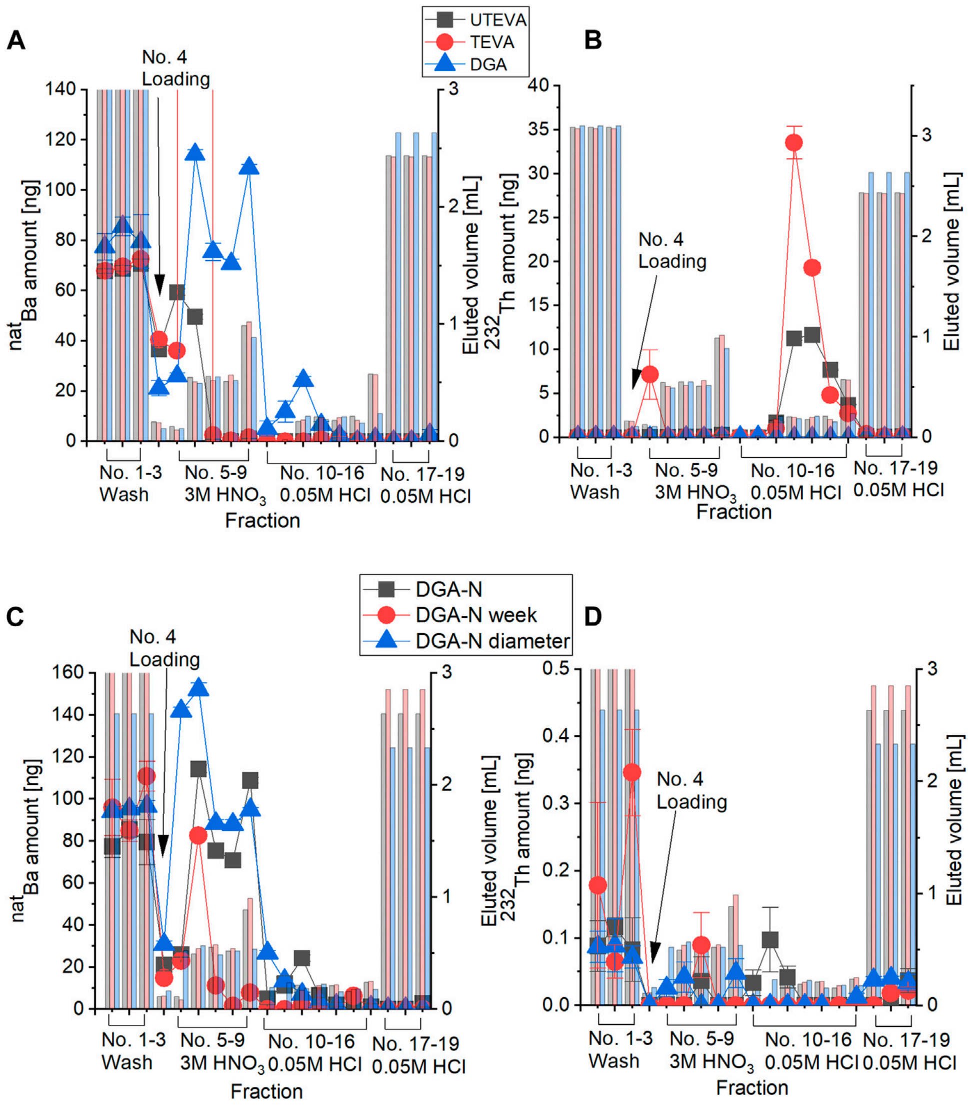

FIGURE 2
Eluted amount per fraction for Ba **(A, C)** and Th **(B, D)** with the following resins: **(A, B)** UTEVA (black), TEVA (red), and DGA-N (blue). **(C, D)** Comparison of the unperturbed DGA-N column results with equilibration times of 1 week and at an increased column diameter of 13 mm. Elution volume profiles are shown in mL as bars on the right y-axis. The errors were calculated by error propagation.

system with a Th mother radionuclide. However, overall yields of Th remain low with a DGA-N resin, possibly due to the high affinity of Th to the DGA-N according to known k' values (TrisKem International, 2015a; TrisKem International, 2015b; TrisKem International, 2015c; TrisKem International, 2023a; TrisKem International, 2023b). Furthermore, experiments at increased acidic concentrations have shown improved Th-retention on UTEVA and TEVA resins. Nevertheless, Ba target fractions should preferentially be eluted in diluted acids to ensure more efficient radiolabeling of prospective pharmaceuticals.

The DGA-N resin showed ideal separation results through high Th-retention and favorable Ba-elution behavior in the presence of less concentrated acids (Roesch, 2012; International Atomic Energy Agency, 2016). Based on these results, the DGA-N resin was chosen for further tests under variable conditions.

Several Th/Ra separation approaches have been reported, ranging from extraction-based approaches (Shishkin et al., 2011; Havelka, 2016) to methods using ion exchange resin like Dowex-1/Dowex-50 (Mokhodoeva et al., 2015; Abou et al., 2017) or Dipex-2 and AG50W-X12 for the separation of ^{223}Ra (Henriksen et al., 2001). However, Henriksen et al. (2001) used ^{223}Ra-stripping concentrations of 8 mol/L HNO_3 which, compared to 3 mol/L HNO_3 applied in this study, are unfavorable for the subsequent radiolabeling within the intended radiopharmaceutical approach. In comparison, Mastren et al. (2017) have reported on successful Ra isotope separation on a larger scale with radiochemical purities of 99.99%—very similar to the resins tested in this study.

Moreover, we chose to investigate two crucial parameters in the DGA-N experiments. Firstly, larger column diameters can result in less interaction between stationary and mobile phases, which can result in different resolution profiles of the evaluated elements. To examine this, we chose to increase the column diameter from 5 mm to 13 mm while retaining the volume of the applied resin. Secondly, equilibration times on the column can affect the durability, potential degradation, or other reactions of applied resins and nuclides. Therefore, we chose to elute a week after loading the column.

While the diameter variation revealed no difference to the elution profiles (Figures 2C, D), the equilibration time seems to impact the retrievability of Ba. Considering the background of Ba in the resin, Figure 2C shows similar amounts of eluted Ba in the wash fractions (No. 1–3). In contrast, the elution of Ba from the one-week equilibrated column was generally lower and ended five fractions earlier than in the directly eluted columns. This is clearly disadvantageous when considering that this component is applied in generator set-ups with contact times of up to a whole year. To counteract this lower retrievability, tests were performed in which the eluent was heated to 60 °C (Supplementary Figure S1; Supplementary Tables S1, S2). In general, this resulted in a higher retrievability of Ba but also in higher backgrounds in the wash fraction, making a quantitative comparability impossible. The implementation of radioisotope ^{133}Ba could potentially circumvent this problem, as it should be possible to determine the elution profile *via* gamma spectroscopy.

Very strong adhesion of Th was found for all columns, with detected values being close to the ICP-MS detection limit. In general, repeated experiments verified trends and profiles (Supplementary Figure S2; Supplementary Tables S3, S4), albeit with different Ba backgrounds. As indicated by our results, the elution of Ba is strongly sensitive to temperature. It is possible that these results might have been affected by fluctuating laboratory temperatures or different ICP-MS devices.

3.2 ^{229}Th/^{225}Ra/^{225}Ac separation system surrogated by ^{232}Th/^{137}Ba/^{139}La

The second system investigated the separation of ^{229}Th/^{225}Ra/^{225}Ac surrogated by ^{232}Th/^{nat}Ba/^{nat}La. We compared the combination of TK200 and TK101 resins to the elution profile of sole TK200 resin retaining only Th.

In this system, the elution profile of La (Figure 3A) indicates an efficient La retention on the column and no elution with the loading fraction. Additionally, we evaluated the necessity of acidic elution conditions by applying deionized water on the combined TK200/TK101 set-up. The water-eluted amount of La corresponds to 18% of the initially loaded La onto the column. In contrast, 57% ± 3% of the initially loaded La was successfully eluted from the TK200 column using 0.05 mol/L HNO_3. Comparing the profiles of the TK200 (Figure 3B) and TK200/TK101 columns (Figure 3A), it is evident that an elution using water is ideally possible when only TK200 is applied. Thus, it can be hypothesized that La was partially retained on TK101 during the elution with deionized water, which is in congruence with K_D values of La on the TK101 resin. The K_D values are about 3 mL/g at 10^{-2} mol/L HNO_3 and decrease for 0.1 mol/L HNO_3 (TrisKem International, 2023b).

Figure 3C demonstrates the high efficiency of combined resins in retaining the majority of applied Ba. However, the elution of Ba in 6 mol/L HNO_3 continued into the Th target fractions and resulted in cross-contamination. Applying a larger volume of 6 mol/L HNO_3 could potentially deter this problem but might lead to potential difficulties in subsequent radiolabeling procedures. In comparison to Ba, Ra is less strongly bound to TK101 at 6 mol/L HNO_3 (TrisKem International, 2023a), and the feasibility of both Ra extraction and elution from environmental samples was proven with TK100, which is a direct derivative of the crown-ether-based TK101 resin (van Es et al., 2017). The elution profiles with TK200 (Figure 3D) conclude that Ba is present in all loading fractions, confirming that TOPO ligands in the applied resin offer subpar Ba-complexation properties (Ghose et al., 1975).

On a final note, Th was successfully retained on combined (TK200/TK101; Figure 3E) and single (TK200; Figure 3F) resin columns with a low recovery of only 2.9%, similar to Th on the DGA-N resin, which is congruent with conditions applied in practical radionuclide generator systems. During generator operation, Th, as the mother nuclide, should be retained and only washed from the column to protect the resin from undesired radiolytic effects in case a reloading strategy would prove feasible. These results of the previous elution profiles of the repeated experiments are nearly identical; however the total recovery of Ba is again lower.

In this study, the quantities of examined surrogates for potential generator settings were chosen in accordance with established ones to allow for comparisons with real radionuclide generator systems. For instance, 100 MBq of ^{229}Th and ^{227}Th respectively correspond to 13.7 mg and 87.9 ng, and 100 MBq of ^{225}Ra and ^{223}Ra to 69.4 ng and 52.6 ng.

A similar approach of combining two separate resins was performed by Lin et al. (2023). They chose different resins to combine, but their elution profiles strongly resemble ours. Our study thus reinforces the application of sequentially combined resins in a single column for multi-radionuclide separation purposes.

3.3 Purity and retrievable yields

For TαT purposes, the purity of the applied radionuclide is the decisive factor, and a specific purity limit must be ensured prior to

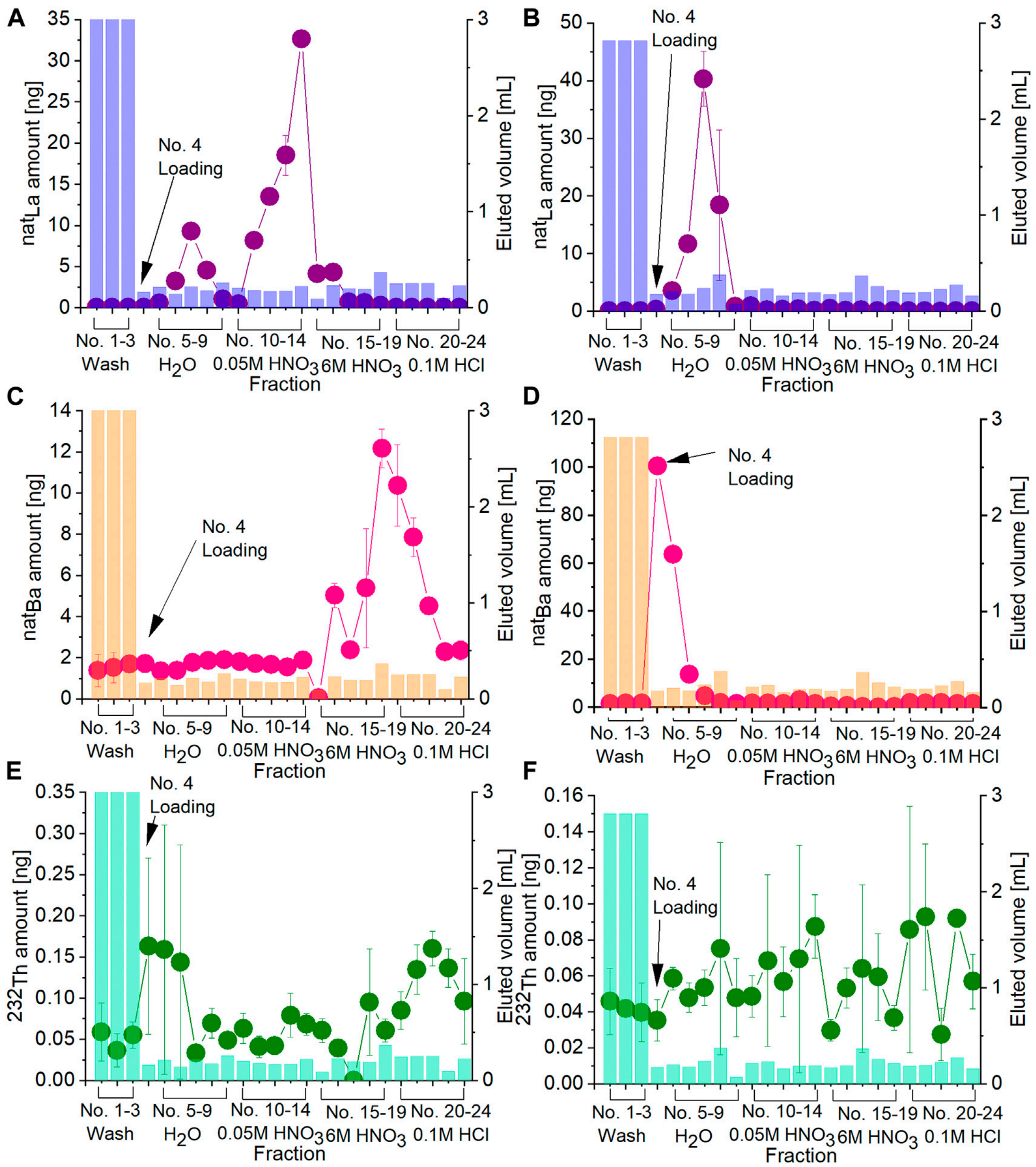

FIGURE 3
Eluted amount per fraction for La **(A, B)**, Ba **(C, D)**, and Th **(E, F)**. **(A, C, E)** show separation using the combination of two resins (TK200+TK101) while **(B, D, F)** show the separation using only the TK200 resin. Additionally, elution volume profiles are shown in mL as bars on the right y-axis. The errors were calculated by error propagation.

application. As established in various radionuclide generators, subsequent purification steps are often attached to the radionuclide production procedure itself (Guseva and Dogadkin, 2010).

Since the ^{232}Th/^{137}Ba separation system is a surrogate for ^{227}Th/^{223}Ra, ^{223}Ra represents the desired radionuclide. Consequently, the fraction with high radionuclidic purity is of utmost importance for the Ba fraction (cf. Table 2). While UTEVA can provide high nuclidic purities of 99.7% ± 0.1%, higher purities of 99.99% ± 0.01% are possible when using DGA-N. In the case of TEVA, a breakthrough of Th reduced the overall purities to 91% ± 6%. For all applied resins, retrievability remained impossible to quantify as Ba impurities remained present before loading (Figure 2A). Despite being a potential TαT nuclide (Frantellizzi et al., 2020; Karlsson et al., 2023), ^{227}Th showed generally low retrievability, especially on DGA-N resin, which would prevent a dual use of the generator.

In the system ^{229}Th/^{225}Ra/^{225}Ac, ^{225}Ac is the desired radionuclide to separate for application in TαT. Therefore, it is preferable to obtain the La fraction in high nuclidic purity from the ^{232}Th/^{nat}Ba/^{nat}La separation system. Our data indicate reasonably efficient separation strategies, with La purities of 85% ± 13% observed. Nevertheless, future research should focus on delivering not only higher nuclidic purities but also increased retrievability. In this study, only 57% ± 3% of the introduced La were recovered

TABLE 2 Amounts of eluted nuclide in respective target fractions (defined in Figures 2 and 3 of the specific nuclide). Additionally, nuclidic purity is listed as the ratio, expressed as an atom percentage, of the desired nuclide amount to the total amount of nuclides in the target fraction. The retrievability in the target fractions is given as the percentage of the spike added. Due to the Ba impurities detected in all resins, the values exceed 100%.

System investigated	Resin	Element	Portion of total yield in target fractions [%]	Nuclidic purity [%]	Total retrievable yield [%]
Th/Ba separation system	UTEVA	Ba Th	75 ± 2 98 ± 3	99.7 ± 0.1 100.00 ± 0.01	164 ± 4 65 ± 2
	TEVA	Ba Th	49 ± 3 90 ± 4	91 ± 6 94 ± 4	90 ± 4 111 ± 5
	DGA-N	Ba Th	84 ± 2 85 ± 42	99.99 ± 0.01	462 ± 14 0.4 ± 0.1
	DGA-N + 1 week equilibration time	Ba Th	84 ± 4 31 ± 8	99.99 ± 0.01	150 ± 10 0 ± 1
	DGA-N column with larger diameter	Ba Th	87 ± 2 52 ± 10	99.99 ± 0.01	650 ± 2 detection limit
Th/Ba/La separation system	Combined TK101/TK200	La Ba Th	90 ± 4 35 ± 7 34 ± 8	85 ± 13 71 ± 26	57 ± 3 79 ± 13 3 ± 1
	TK200 only	La Ba Th	98 ± 24 2 ± 1 29 ± 11	44 ± 42 68 ± 22	43 ± 11 119 ± 18 2 ± 1

successfully, which is a range of 57%–71% compared to other proposed ^{223}Ra-generator concepts (Henriksen et al., 2001; Abou et al., 2017).

4 Discussion and conclusion

This study acquired preliminary data towards separation strategies of TαT-suitable radionuclides from experimental series using cold metal surrogates.

In our study, two separation systems were set-up and analyzed: i) the binary ^{232}Th/^{137}Ba system representing the generator pair ^{227}Th/^{223}Ra and ii) the tertiary ^{232}Th/^{137}Ba/^{139}La system representing the generator triplet ^{229}Th/^{225}Ra/^{225}Ac.

In the Th/Ba separation system, the performances of TEVA, UTEVA, and DGA-N resins were thoroughly studied using analytes in nanogram amounts. All tested analyte contents were observed to be well below the capacities of evaluated extraction chromatographic resins for the examined elements, which is in the order of 15–50 mg/g of resin. The best-performing resin (DGA-N) was further evaluated under varied parameters at both increased column diameters (13 mm), heated eluents, and equilibration time (1 week). For the Th/Ba/La separation system, a column with a successive resin combination (TK200/TK101) and a sole resin (TK200) was evaluated and compared.

The DGA-N resin was found to be the most effective in separating Th from Ba. In the case of UTEVA, the lowest percentage of Ba and Th retrieval in the target fractions were obtained. Similarly, elution yields of Th decreased to 0.4%, possibly due to high affinities of Th to DGA-N. In prolonged equilibration times of 1 week, only 0.8% of the Th could be recovered. Essentially, the nanogram amounts of Th were strongly retained in all systems. While overall elution yields remained low, the strong retention of Th on the examined resin(s) can prospectively be of advantage in (^{227}Th/^{223}Ra) separation systems in which Th is utilized as a mother radionuclide.

In the Th/Ba/La system using a combination of TK101/TK200 resins, La was separated sufficiently and was almost exclusively collected in the target fractions. Ba was successfully retained by TK101 and only eluted with 6 mol/L HNO_3 at the onset of the target fractions. Nevertheless, Ba contaminations leaked into subsequent fractions, which could potentially be counteracted by a larger volume of the eluent. As the D_w values of Ra on the resin are lower compared to Ba, this would most probably not be relevant to the same extend for the real generator system. As with the DGA-N resin, Th was strongly retained on TK200 and could hardly be eluted with the amounts used.

These results raise new questions that call for follow-up research in the near future. To study different factors, further resins could be implemented and tested at varied parameters analogous to our studies—for example, TK200 in Th/Ba separation systems. In addition, eluents and acids of different kinds and concentrations could be applied. Potential complexing agents might be tested, especially given the low retrievability of Th found by this research.

To further understand and develop additional separation systems, more surrogates, deriving from daughter radionuclides of ^{229}Th and ^{227}Th two-decay series, should be implemented in experiments. Finally, if practical approaches are desired, the surrogates should be replaced with the desired radionuclides to facilitate a transfer in research and medical application. To conclude, this research sheds light on radionuclide generator development for TαT and demonstrates that many existing and new questions remain to be investigated.

Data availability statement

The original contributions presented in the study are included in the article/Supplementary Material; further inquiries can be directed to the corresponding author.

Author contributions

BS: conceptualization, formal analysis, methodology, project administration, resources, supervision, validation, visualization, writing–original draft, writing–review and editing. KM: data curation, formal analysis, investigation, validation, visualization, writing–review and editing. MS: investigation, methodology, writing–review and editing. YR: investigation, methodology, writing–review and editing. FG: data curation, methodology, writing–review and editing. AF: data curation, methodology, writing–review and editing. SH: conceptualization, writing–review and editing. MB-S: conceptualization, methodology, supervision, validation, writing–review and editing.

Funding

The author(s) declare that financial support was received for the research, authorship, and/or publication of this article. It was funded by the Federal Ministry of Education and Research (BMBF) and the Baden-Württemberg Ministry of Science as part of the Excellence Strategy of the German Federal and State Governments. The authors acknowledge funding from the European Research Council (ERC) Consolidator Grant 2020 under the European Union's Horizon 2020 research and innovation program (grant agreement no. 101003292). Co-funding of this project was made available through the joint strategic alliance between the German Cancer Research Center (DKFZ) and Bayer AG. The authors declare that this study received funding from Bayer AG. The funder was not involved in the study design, collection, analysis, interpretation of data, the writing of this article, or the decision to submit it for publication.

Acknowledgments

The authors sincerely acknowledge the support of Harun Taş from the German Cancer Research Center (DKFZ) in Heidelberg for his valuable and profound comments as well as thorough adjustment of the manuscript's format, structure, and style.

Conflict of interest

Author SH is employed by TrisKem International.

The remaining authors declare that the research was conducted in the absence of any commercial or financial relationships that could be construed as a potential conflict of interest.

Publisher's note

Supplementary material

The Supplementary Material for this article can be found online at: https://www.frontiersin.org/articles/10.3389/fnuen.2024.1379996/full#supplementary-material

References

Abou, D. S., Pickett, J., Mattson, J. E., and Thorek, D. L. (2017). A radium-223 microgenerator from cyclotron-produced trace actinium-227. *Appl. Radiat. Isotopes* 119 (1), 36–42. Available at:. doi:10.1016/j.apradiso.2016.10.015

Causey, P., Perron, R., and Gendron, D. (2020). Production of actinium-225 at the Canadian Nuclear Laboratories: operation of a thorium generator and quality control of Ac-225. *J. Nucl. Med.* 61 (Suppl. 1), 467.

Diamond, W. T., and Ross, C. K. (2021). Actinium-225 production with an electron accelerator. *J. Appl. Phys.* 129 (10). Available at:. doi:10.1063/5.0043509

Elgqvist, J., Frost, S., Pouget, J. P., and Albertsson, P. (2014). The potential and hurdles of targeted alpha therapy – clinical trials and beyond. *Front. Oncol.* 3, 324. Available at:. doi:10.3389/fonc.2013.00324

Frantellizzi, V., Cosma, L., Brunotti, G., Pani, A., Spanu, A., Nuvoli, S., et al. (2020). Targeted alpha therapy with thorium-227. *Cancer Biotherapy Radiopharm.* 35 (6), 437–445. Available at:. doi:10.1089/cbr.2019.3105

Ghose, A. K., Šebesta, F., and Starý, J. (1975). Synergistic extraction of radium and barium using 1-phenyl-3-methyl-4-benzoylpyrazol-5-one and trioctylphosphine oxide. *J. Radioanalytical Chem.* 24 (2), 345–351. Available at:. doi:10.1007/bf02518432

Guseva, L. I., and Dogadkin, N. N. (2010). A generator system for production of medical alpha-radionuclides Ac-225 and Bi-213. *J. Radioanalytical Nucl. Chem.* 285 (3), 667–673. Available at:. doi:10.1007/s10967-010-0593-6

Hagemann, U. B., Ellingsen, C., Schuhmacher, J., Kristian, A., Mobergslien, A., Cruciani, V., et al. (2019). Mesothelin-targeted thorium-227 conjugate (MSLN-TTC): Preclinical evaluation of a new targeted alpha therapy for mesothelin-positive cancers. *Clin. Cancer Res.* 25 (15), 4723–4734. doi:10.1158/1078-0432.ccr-18-3476

Havelka, M. (2016). Preparation of (228)Ra standard solution. *Appl. Radiat. isotopes Incl. data, Instrum. methods use Agric. industry Med.* 109, 222–225. Available at:. doi:10.1016/J.APRADISO.2015.11.062

Henriksen, G., Hoff, P., Alstad, J., and Larsen, R. H. (2001). 223Ra for endoradiotherapeutic applications prepared from an immobilized 227Ac/227Th source. *Radiochim. Acta* 89 (37165), 661–666. Available at:. doi:10.1524/ract.2001.89.10.661

Higashi, T., Nagatsu, K., Tsuji, A. B., and Zhang, M. R. (2022). Research and development for cyclotron production of 225Ac from 226Ra—the challenges in a country lacking natural resources for medical applications. *Processes* 10 (6), 1215. Available at:. doi:10.3390/pr10061215

International Atomic Energy Agency, (IAEA) (2016). Human health campus - decay properties for generators of short-lived radionuclides. Available at: https://humanhealth.iaea.org/HHW/Radiopharmacy/VirRad/Eluting_the_Generator/Generator_Module/Design_principles/Non_99mTc_generators/table.html (Accessed November 25, 2023).

Karlsson, J., Schatz, C. A., Wengner, A. M., Hammer, S., Scholz, A., Cuthbertson, A., et al. (2023). Targeted thorium-227 conjugates as treatment options in oncology. *Front. Med.* 9 (January), 1071086–1071089. Available at:. doi:10.3389/fmed.2022.1071086

Kim, Y. S., and Brechbiel, M. W. (2012). An overview of targeted alpha therapy. *Tumor Biol.* 33 (3), 573–590. Available at:. doi:10.1007/s13277-011-0286-y

Kratochwil, C., Bruchertseifer, F., Rathke, H., Bronzel, M., Apostolidis, C., Weichert, W., et al. (2017). Targeted α-therapy of metastatic castration-resistant prostate cancer with 225 Ac-PSMA-617: dosimetry estimate and empiric dose finding. *J. Nucl. Med.* 58 (10), 1624–1631. Available at:. doi:10.2967/jnumed.117.191395

Kratochwil, C., Bruchertseifer, F., Rathke, H., Hohenfellner, M., Giesel, F. L., Haberkorn, U., et al. (2018). Targeted a-therapy of metastatic castration-resistant prostate cancer with 225 Ac-PSMA-617: Swimmer-plot analysis suggests efficacy regarding duration of tumor control. *J. Nucl. Med.* 59 (5), 795–802. Available at:. doi:10.2967/jnumed.117.203539

Królicki, L., Kunikowska, J., Bruchertseifer, F., Koziara, H., Królicki, B., Jakuciński, M., et al. (2020). 225Ac- and 213Bi-substance P analogues for glioma therapy. *Seminars Nucl. Med.* 50 (2), 141–151. Available at:. doi:10.1053/j.semnuclmed.2019.11.004

Larsen, R. H., Borrebaek, J., Dahle, J., Melhus, K. B., Krogh, C., Valan, M. H., et al. (2007). Preparation of Th 227 -labeled radioimmunoconjugates, assessment of serum stability and antigen binding ability. *Cancer Biotherapy Radiopharm.* 22 (3), 431–437. Available at:. doi:10.1089/cbr.2006.321

Lin, Y., Wang, J., Shao, K., Zhang, G., Wang, X., Liu, T., et al. (2023). Two-step separation of Th, La and Ba using combined chromatographic columns. *J. Radioanalytical Nucl. Chem.* 332 (4), 1245–1252. Available at:. doi:10.1007/s10967-023-08761-3

Lindén, O., Bates, A. T., Cunningham, D., Hindorf, C., Larsson, E., Cleton, A., et al. (2021). 227Th-Labeled anti-CD22 antibody (bay 1862864) in relapsed/refractory CD22-positive non-hodgkin lymphoma: a first-in-human, phase i study. *Cancer Biotherapy Radiopharm.* 36 (8), 672–681. Available at:. doi:10.1089/cbr.2020.4653

Ma, J., Li, L., Liao, T., Gong, W., and Zhang, C. (2022). Efficacy and safety of 225Ac-PSMA-617-Targeted alpha therapy in metastatic castration-resistant prostate cancer: a systematic review and meta-analysis. *Front. Oncol.* 12 (February), 796657. Available at:. doi:10.3389/fonc.2022.796657

Maslov, O. D., Sabel'nikov, A. V., and Dmitriev, S. N. (2006). Preparation of ^{225}Ac by ^{226}Ra(γ, n) photonuclear reaction on an electron accelerator, MT-25 microtron. *Radiochemistry* 48 (2), 195–197. doi:10.1134/S1066362206020184

Mastren, T., Radchenko, V., Owens, A., Copping, R., Boll, R., Griswold, J. R., et al. (2017) 'Simultaneous separation of actinium and radium isotopes from a proton irradiated thorium matrix', *Sci. Rep.* 7:1, pp. 8216–8217. doi:10.1038/s41598-017-08506-9

Mokhodoeva, O., Guseva, L., and Dogadkin, N. (2015). Isolation of generator-produced 223Ra in 0.9-% NaCl solutions containing EDTA for direct radiotherapeutic studies. *J. Radioanalytical Nucl. Chem.* 304 (1), 449–453. Available at:. doi:10.1007/s10967-014-3777-7

Parker, C., Lewington, V., Shore, N., Kratochwil, C., Levy, M., Lindén, O., et al. (2018). Targeted alpha therapy, an emerging class of cancer agents: a review. *JAMA Oncol.* 4 (12), 1765–1772. Available at:. doi:10.1001/jamaoncol.2018.4044

Robertson, A. K. H., Ramogida, C. F., Schaffer, P., and Radchenko, V. (2018). Development of ^{225}Ac radiopharmaceuticals: TRIUMF perspectives and experiences. *Curr. Radiopharm.* 11 (3), 156–172. Available at:. doi:10.2174/1874471011666180416161908

Roesch, F. (2012). Maturation of a key resource – the germanium-68/gallium-68 generator: development and new insights. *Curr. Radiopharm.* 5 (3), 202–211. Available at:. doi:10.2174/1874471011205030202

Rösch, F., and Knapp, F. F. F. (2011). "Radionuclide generators," in *Handbook of nuclear chemistry*. Editor A. Vertes (Boston, MA: Springer US), 1935–1976. Available at:. doi:10.1007/978-1-4419-0720-2_40

Shishkin, D. N., Krupitskii, S. V., and Kuznetsov, S. A. (2011). Extraction generator of 223Ra for nuclear medicine. *Radiochemistry* 53 (4), 404–406. Available at:. doi:10.1134/S1066362211040126

TrisKem International (2015a). *Product sheet DGA resin (normal and branched).*

TrisKem International (2015b). *Product sheet TEVA resin*.

TrisKem International (2015c). *Product sheet UTEVA resin, product sheet*.

TrisKem International (2023a). Product sheet TK100/TK101 resins. Available at: www.triskem.com.

TrisKem International (2023b). *Product sheet TK200 resin, product sheet*.

van Cleve, S., Boll, R., Benny, P., Dyke, T., Kehn, J., and Phillips, K. (2019). Thorium-229 generator production of actinium-225 at Oak Ridge National laboratory. *J. Med. Imaging Radiat. Sci.* 50 (1), S11–S12. Available at:. doi:10.1016/j.jmir.2019.03.037

van Es, E. M., Russell, B. C., Ivanov, P., García Miranda, M., Read, D., Dirks, C., et al. (2017). The behaviour of 226Ra in high-volume environmental water samples on TK100 resin. *J. Radioanalytical Nucl. Chem.* 312 (1), 105–110. Available at:. doi:10.1007/s10967-017-5203-4

Yadav, M. P., Ballal, S., Sahoo, R. K., and Bal, C. (2022). Efficacy and safety of 225Ac-DOTATATE targeted alpha therapy in metastatic paragangliomas: a pilot study. *Eur. J. Nucl. Med. Mol. Imaging* 49 (5), 1595–1606. Available at:. doi:10.1007/s00259-021-05632-5

Frontiers in
Nuclear Engineering

Advances and applications in nuclear science, technology, and engineering

A forum for the nuclear research community working across fission and fusion physics, power generation, safety and waste management, materials and modelling to find new applications.

Discover the latest Research Topics

See more →

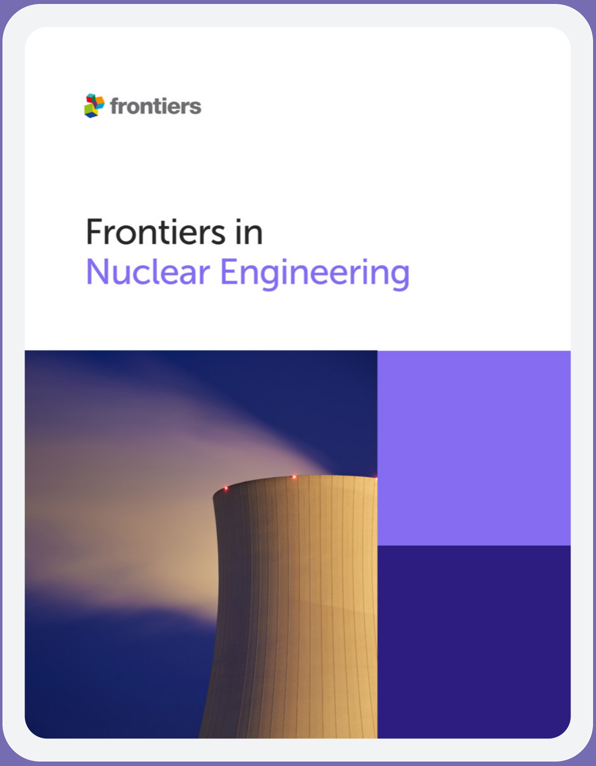

frontiers

Frontiers in
Nuclear Engineering

Frontiers

Avenue du Tribunal-Fédéral 34
1005 Lausanne, Switzerland
frontiersin.org

Contact us

+41 (0)21 510 17 00
frontiersin.org/about/contact